UILU-ENG-80-2016

CIVIL ENGINEERING STUDIES
STRUCTURAL RESEARCH SERIES NO. 482

# EXPERIMENTS TO STUDY EARTHQUAKE RESPONSE OF R/C STRUCTURES WITH STIFFNESS INTERRUPTIONS

By
JACK P. MOEHLE
and
METE A. SOZEN

A Report to the
NATIONAL SCIENCE FOUNDATION
Research Grant PFR 78-16318



UNIVERSITY OF ILLINOIS
at URBANA-CHAMPAIGN
URBANA, ILLINOIS
AUGUST 1980

50272-101

| REPORT DOCUMENTATION PAGE | 1. REPORT NO. NSF/RA-800496 | 2. | 3. Recipient's Accession No. PB81-183915 |
|---|---|---|---|

**4. Title and Subtitle**
Experiments to Study Earthquake Response of R/C Structures with Stiffness Interruptions

**5. Report Date**
August 1980

**6.**

**7. Author(s)**
J. P. Moehle, M. A. Sozen

**8. Performing Organization Rept. No.**
UILU-ENG-80-2016

**9. Performing Organization Name and Address**
University of Illinois
Department of Civil Engineering
Urbana, IL 61801

**10. Project/Task/Work Unit No.**
SRS-482

**11. Contract(C) or Grant(G) No.**
(C)
(G) PFR7816318

**12. Sponsoring Organization Name and Address**
Office of Planning and Resources Management (OPRM)
National Science Foundation
1800 G Street, N.W.
Washington, D.C. 20550

**13. Type of Report & Period Covered**
Ph.D. Dissertation

**14.**

**15. Supplementary Notes**

**16. Abstract (Limit: 200 words)**

An experimental study was undertaken to investigate the response to strong earthquakes of reinforced concrete (R/C) structures having abrupt interruptions in adjacent story stiffness. Four structures (of approximately one-twelfth scale), comprising two nine-story, three-bay frames or two frames and a wall which acted in parallel were tested. The first story was twice the height of other stories. The experimental variable was the wall height with structures having either no wall or walls which were one-, four-, or nine-stories tall. Experimental measurements include displacements, accelerations, and forces between frames and walls at each level. Observed behavior was interpreted using simple, design-oriented numerical models. Studies using linear models included (1) comparison of modal-spectral and equivalent static procedures and (2) estimates of response maxima using SDOF oscillators. Studies using nonlinear models included (1) interpretation of behavior for a monotonic lateral loading distribution and (2) estimates of displacement maxima and waveform using SDOF models.

**17. Document Analysis a. Descriptors**

Earthquakes
Reinforced concrete
Walls
Structures
Loading
Stiffness methods
Nonlinear systems
Linear Systems
Displacement
Structural analysis

**b. Identifiers/Open-Ended Terms**

Seismic response
SDOF oscillators

**c. COSATI Field/Group**

Earthquake Hazards Mitigation

| 18. Availability Statement | 19. Security Class (This Report) | 21. No. of Pages |
|---|---|---|
| NTIS | 20. Security Class (This Page) | 22. Price |

(See ANSI-Z39.18) See Instructions on Reverse

OPTIONAL FORM 272 (4-77)
(Formerly NTIS-35)
Department of Commerce

# EXPERIMENTS TO STUDY EARTHQUAKE RESPONSE OF R/C STRUCTURES WITH STIFFNESS INTERRUPTIONS

by

Jack P. Moehle

and

Mete A. Sozen



A Report to the
NATIONAL SCIENCE FOUNDATION
Research Grant PFR-78-16318

University of Illinois
at Urbana-Champaign
Urbana, Illinois
August, 1980

# ACKNOWLEDGMENT

The work described in this report is part of a continuing investigation of the response of reinforced concrete structures to strong earthquake motions being carried out in the Structural Research Laboratory of the University of Illinois Civil Engineering Department. The work is sponsored by the National Science Foundation under grant PFR 78-16318. Opinions, findings, and conclusions or recommendations in this report do not necessarily represent those of the National Science Foundation.

Appreciation is expressed to the kind and patient assistance of many who were involved with the project, several of whom are mentioned below.

Members of the panel of consultants are thanked for criticisms and suggestions which led to and guided the work described in this report. The panel included M. H. Eligator, Weiskopf and Pickworth; A. E. Fiorato, Portland Cement Association; W. D. Holmes, Rutherford and Chekene; R. G. Johnston, Brandow and Johnston; J. Lefter, Veteran's Administration; W. P. Moore, Jr., Walter P. Moore and Associates; and A. Walser, Sargent and Lundy.

Gratitude is due Professors Gamble, Pecknold, and Schnobrich for criticisms and advice. D. P. Abrams is thanked for advice during early stages of the work. Valuable discussion during various phases of the project were given by research assistants B. B. Algan, F. Castilla, N. D. Gilbertsen, M. E. Kreger, D. G. Morrison, and C. E. Wolfgram.

N. D. Gilbertsen, M. E. Kreger, and T. E. Kuo are thanked for careful conduct of static member tests.

Professor V. J. McDonald provided invaluable direction and assistance with instrumentation and data reduction. G. Lafenhagen was indispensable

for his conscientious assistance with instrumental setup and experimental conduct. O. H. Ray and his staff helped in fabricating test specimens and hardware.

Laura Goode, Patricia Lane, and Julia Hubbard are thanked for patience and care in typing the report. R. Winburn and T. Kuo are thanked for figure drafting.

The CDC-Cyber 175 Computer System of the Department of Computer Science was used for data reduction and analyses.

This report was prepared as a doctoral dissertation by J. P. Moehle under the direction of Professor M. A. Sozen.

TABLE OF CONTENTS

# LIST OF TABLES

# LIST OF FIGURES

# 1. INTRODUCTION

The performance of multistory buildings during strong earthquake motion depends on distributions of weight, stiffness, and strength in both the horizontal and vertical planes of the building. Experience during past earthquakes and experimental and analytical investigations into the behavior of buildings having "regular" configurations have resulted in a relative sense of comfort within the design community in dealing with "regular" structures and comparative discomfort in dealing with buildings having "irregular" configurations. Design provisions for irregular buildings are understandably cautious and generally include conservative and relatively complicated design procedures which tend to discourage the use of such configurations. Unfortunately, choice of building configuration is seldom the prerogative of the designer who must consider seismic response, and irregular configurations will often be required to fulfill functional or economical requirements. The objective of this study is to investigate experimentally the effect on response to strong earthquake motion of irregularities in the vertical plane of multistory, reinforced concrete structures and to study the possibilities of using simple design and analysis procedures to estimate observed responses.

To achieve the objective, four small-scale, nine-story, test structures were constructed and subjected experimentally to one horizontal component of a measured earthquake motion. The test structures (which were approximately one-twelfth of full scale) were effectively two-dimensional and comprised either two frames situated opposite one

another and parallel to the base motion or two frames with a centrally-located, "slender" wall which was constrained to displace the same as the frames at each story level. Frames had three bays and carried equal weights at each level to increase vertical and lateral forces. Vertical irregularities in story stiffness and strength were introduced (1) by including a first story in each structure which was twice the height of other individual stories and (2) by varying the height of the centrally-located wall element. One test structure comprised only two frames. Three subsequent structures had walls extending from the base through levels one, four, and nine (full height of the frames).

Frame and wall elements were proportioned for the first (design) earthquake simulation using principles of the substitute structure design method [32].* That design method features modal-spectral analysis with "substitute" member stiffnesses and effective damping factors selected to account for intended inelastic behavior. In designing the test structures, the design objective was to limit inelastic behavior to beams and walls and to limit displacement maxima within some "tolerable" bound (approximately 1.5 percent drift). The experiment (in which the test structures are subjected to design earthquake motions) is a direct test of the design procedure.

Several simple design and analysis procedures are studied to determine if the procedures are reasonable for obtaining estimates of earthquake response. Equivalent-static-force and modal-spectral design

---

*References are listed alphabetically in the List of References. Numbers in brackets [ ] are the number of the reference.

procedures are compared for several assumed distributions of member stiffnesses to determine whether consideration of the modal properties of the test structures provides additional insight into the relative distributions of member design forces. The adequacy of using a linear model with linear response spectra to estimate response maxima is also investigated. Static, monotonic loading of an analytical model which considers the inelastic behavior of individual members is investigated to determine whether static procedures may be used to evaluate the effects of the stiffness "interruptions" considered in this study. A concluding study investigates the use of "economical," nonlinear SDOF models for obtaining estimates of displacement maxima and waveforms.

# 2. DESIGN OF TEST STRUCTURES

Design of test structures was considered on two levels. Experimental design, which is discussed in the first section of this chapter, describes the choice of test structure configurations and testing motions. The latter portion of the chapter describes the design model, design forces, and reinforcement of specimens.

## 2.1 Experimental Design

### (a) Test Structure Configuration

The overall configuration of the test structures was determined by the objectives of the tests and by equipment limitations. The simplest test arrangement that would allow study of reinforced concrete wall-frame interaction was considered to be the most desirable. An effectively two-dimensional arrangement of coupled frames and walls was selected. In that arrangement, two nine-story, three-bay frames (of approximately one-twelfth scale) were situated opposite and parallel to one another with a prismatic wall element located centrally between (Fig. 2.1). The frames carried a weight at each story level (Fig. 2.1) which increased lateral inertial forces and which provided a lateral shear "link" to couple the frames and wall into a single unit. For simplicity, and concurrence with an analytical model, the frames and wall were fixed at the base by casting them monolithically with very stiff base girders. To maintain the two-dimensional character of the test arrangement, testing was conducted by subjecting the base of the structure to a simulated earthquake motion in one horizontal direction parallel to the plane of the structure.

Frame and wall elements in test structures were selected so that the effect of wall height on the earthquake response of multistory, reinforced concrete, wall-frame structures could be observed. For this purpose, test structure geometries were maintained nearly the same for the four test structures, the only geometric variable being the height of the wall. Wall heights varied from no wall (or a structure composed only of frames) through walls extending from the base to levels one, four, and nine (Fig. 2.2). Designations of the four tests structures used throughout this report are as follows:

| Designation | Structural Elements |
|---|---|
| FNW | Frames with No Wall |
| FSW | Frames with One-Story ("Stub") Wall |
| FHW | Frames with Four-Story ("Half") Wall |
| FFW | Frames with Nine-Story (Full-Height) Wall |

Elements and overall geometries in test structures were not chosen with intent to obtain optimal proportions nor to model elements and geometries of any real buildings.

(b) Frames and Walls

Particular dimensions of frames and walls evolved from dimensions used in previous tests of small-scale structures at the University of Illinois. Tests of frames with uniform story heights [ 6 ] indicated serviceable behavior in framed structures. Tests of frames with moderately tall first and top stories (20% taller than intermediate stories) indicated little consequent change in overall behavior [17,24]. Subsequent

tests coupled a full-height wall with uniform frames for the purpose of studying frame-wall interaction [1]. To investigate further the response of frame and wall-frame structures, frames and walls in this study were chosen with intent to introduce stiffness variations along the height of the structure. Overall geometries were maintained similar to those of the previously tested frame and wall-frame test structures.

Frames were made nonuniform by providing a first story twice the height of other stories (Fig. 2.2). Frames were nine stories tall, so that a multistory system was represented, and had three bays at uniform widths so as to include interior and exterior beam-column joints. Aspect ratios of beams and columns were chosen to be typical of those in real buildings. Cross-sectional member dimensions were established from small-scale reinforcement requirements.

Wall depth was chosen so that neither frame nor wall would dominate overall response. Preliminary design analyses using a full-height wall indicated a 200-mm depth would result in a system in which the wall resisted most of the shear in the "tall" first story and the frames resisted most of the shear in upper stories. Subsequent analyses with terminated walls indicated a four-story wall could effect nearly the same shear distribution in lower stories and reduced frame shears in upper stories. Finally, a one-story wall was chosen so that the effect of stiffening only the tall first story could be observed.

Wall depth was established at 200 mm for all walls and wall heights for three different structures set at one, four, and nine stories (Fig. 2.2). A fourth structure comprised frames only.

(c) Story Weights

Story weights (nominally 454 kg each) were made as massive as test equipment would permit. Because masses were used to couple frames and wall, they were also made very stiff. Mass-to-wall and mass-to-frame connections were designed so that vertical load was carried only by the frames and distributed equally to all columns at a story level. The connections provided lateral coupling with negligible rotational restraint. Details are provided in Appendix A.

(d) Base Motions

The unidirectional base acceleration was modelled after El Centro NS, 1940 and was the same for all test structures. For the simulations, the time scale of the prototype was compressed by 2.5 so that realistic ratios of test structure and base motion frequencies would result. The peak acceleration was amplified to 0.4 g so the small-diameter reinforcing bars would yield during the "design" earthquake simulation.

## 2.2 Design of Specimens

Design forces were determined from modal spectral analyses of the four structures. The design method closely paralleled the substitute structure method [ 32 ] in the assumption of member stiffnesses and energy dissipations and in the use of a linear design spectrum. Combination of modal forces differed from that design method. Design assumptions, design forces, and distributions of reinforcement are described below.

(a) Analytical Model

The planar analytical model for design consisted of a frame and wall constrained to have equal lateral deflections at each level (Fig. 2.3).

Flexural and shear deformations were considered in all members. Axial deformations were permitted only for columns. Rigid beam-column joint cores and base fixity of frame and wall were also assumed. Equal masses possessing lateral inertias only were lumped at each of nine story levels. Modal spectral forces for the idealized model were calculated using a linear modal-spectral analysis computer program.

(b) Design Assumptions

Design decisions are inherently arbitrary in the absence of legal stipulations. Designs may vary depending on building location or function. Designs may also be organized on several levels, e.g., certain requirements may be based on providing occupant comfort and others on maintaining structural (or nonstructural) integrity. One basis of designing structures subject to earthquake loading is that of limiting expected displacements within some designer-specified tolerable limits. For structures in this study, design requirements were based on providing minimum strengths so that a set of maximum tolerable displacements would not likely be exceeded. In the absence of absolutes, "tolerable" was taken as approximately 1.5 percent interstory drift.

Component stiffnesses were arbitrarily selected with the intent of economically satisfying the design requirements of limiting displacement maxima. Following the procedure prescribed by the substitute structure method [ 32 ], components responding in the inelastic range could be substituted with components responding linearly at a softened stiffness. This softening of stiffness by a "damage ratio" (as illustrated in Fig. 2.4) has the advantage of accounting for nonlinear behavior with a linear response model. Another distinct advantage is that member strength

requirements can be varied to satisfy design criteria by arbitrarily assigning different damage ratios to different elements. As is true with most design models, inaccuracies in assumed stiffness or strength can be expected to result in premature yield of certain elements. Thus, implicit in the design method is the capacity of the structure to "smear" the effects of these inaccuracies over the entire structure through the provision of adequate member ductility and overall geometric redundancy. For structures with geometric interruptions such as those considered in this study, use of a design method which arbitrarily assigns stiffnesses is questionable. Thus, designing these test structures by this method is a test on limitations of the method.

To account for the effects of inelastic behavior on energy dissipation, increases in energy dissipations with increasing damage ratio can be estimated for a member by the expression below.

$$\beta_{SM} = \frac{[1 - (1/\mu)^{1/2}]}{5} + 0.02 \qquad (2.1)$$

where $\beta_{SM}$ = substitute damping factor in a member

and $\mu$ = damage ratio in member

This formulation for energy dissipation in a member was derived from experimentally observed response of reinforced concrete elements [ 35 ] and one-story frames [ 13 ]. Contributions of individual elements to energy dissipation of the overall structure are estimated by smearing dissipation in proportion with strain energy distributions for each mode.

For design of test structures, a smooth linear design spectrum was chosen to represent the "expected" earthquake (Fig. 2.5). Using that

spectrum, preliminary analyses were performed to determine damage ratios that would result in tolerable displacement limits. Damage ratios of one for columns, three for walls, and six for beams were selected as final design values. Design flexural stiffnesses are summarized in Table 2.1. Substitute damping factors were found to range from ten to twelve percent for the first mode and less for higher modes. However, because (1) substitute-structure damping is an approximate quantity indicating a range rather than a precise value, (2) only slight variations in calculated design response occur by varying assumed damping between ten and twelve percent, and (3) calculated effects of varying wall height could be more clearly viewed by assuming the same substitute damping for each structure, a conservative value of ten percent critical damping was assumed for the four structures. To simplify design calculations, ten percent damping was assumed for higher modes as well. Analyses considered only the first three modes of vibration. Modes higher than the third were not considered because of inherent calculation errors and because of increasingly negligible effect on displacement response.

(c) Calculated Design Quantities

Design response was calculated using the previously described analytical model and design assumptions. The first three mode shapes and frequencies are summarized in Table 2.2. Calculated displacements are plotted in Fig. 2.6 and listed in Table 2.3. From these quantities, it can be seen that the full-height wall would be expected to provide substantial stiffness to the frames (the first-mode design frequency for structure FFW was 14 percent higher than that for FNW). In addition,

interstory drifts in lower stories would be expected to be reduced by use of the full-height wall. Displacement response of the structure with the four-story wall was expected to be similar to that for the full-height wall. The one-story wall could be expected to stiffen significantly the tall first story but to result in a kink and "high" interstory drifts above the wall cutoff.

Calculated member forces are summarized for the first mode in Fig. 2.7 and for the root sum square (RSS) of the first three modes in Fig. 2.8. Interaction among the frames and wall in the structure with full-height wall resulted in a more uniform distribution of column and beam end moments as compared with the frame structure. A force reversal at the top of the full-height wall resulted in a wall moment opposing the overall structure moment in the upper stories and resulted in increased beam and column moments at the top of the structure. The four-story wall had no such force reversal. However, the one- and four-story walls increased design modal-spectral accelerations resulting generally in higher design beam and column end moments above cutoffs as compared with moments in the frame structure. Relatively large column moments immediately above the cutoffs were indicated by design analyses but were considered to be within reasonable limits from the viewpoint of satisfying flexural reinforcement requirements.

(d) Reinforcement Requirements

Distributions of flexural reinforcement were selected so that the provided flexural strengths would match or exceed design strengths. Provided capacities were allowed to exceed design strengths so that a reasonably uniform distribution of steel would result. Small-scale

reinforcing bar sizes were selected so that all specimens could be reinforced with the same size bar for beams and columns and for walls. A minimum of two bars per face was required for confinement of concrete.

Design forces were taken as the RSS of forces for the first three modes. Flexural strength requirements were taken generally as the RSS forces with no factor of safety. However, to insure that yielding be limited to beams, column design requirements were factored by 1.2 at all beam-column joints.

Flexural reinforcement selected for beams and columns was No. 13 g wire (2.32 mm dia.) with a yield stress of 399 MPa. Flexural reinforcement for walls was No. 2 g wire (6.65 mm dia.) with a yield stress of 339 MPa. Flexural strengths were calculated using conventional methods and assumed concrete strength of 38 MPa. Because specimens were to be cast horizontally, no strength-reduction factor was used in calculating column strengths. Details concerning steel and concrete are presented in Appendix A.

Design requirements for beams and walls are compared in Fig. 2.8a and 2.8d. Requirements for columns are presented in the interaction diagram of Fig. 2.9. Axial force in columns includes dead load which was distributed uniformly among columns at a story level. Variation of axial force due to overturning required consideration of two axial force conditions for exterior columns. As may be concluded from comparison of design forces (Fig. 2.8 and 2.9), the structures with walls (FSW, FHW, and FFW) could be reinforced identically with two bars per face in all elements. The structure with no wall (FNW) required additional reinforcement in the lower stories. Distributions of flexural reinforcement selected for the structures are indicated in Fig. 2.10a.

(e) Details of Reinforcement

Typical reinforcement details are presented in Fig. 2.10. Flexural steel was continuous with no splices or welds along floor levels for beams and along structure height for columns and walls. Extension of flexural steel into stubs was provided at beam and column ends for additional development of steel. Where column longitudinal steel requirements changed from four to two bars per face in structure FNW, cutoffs were made 64 mm above story-level centerlines where the extra steel was no longer required. Anchorage of longitudinal column and wall steel within the base girders which supported a structure was provided by welding to anchorage plates (Fig. 2.10d and 2.10e).

Transverse reinforcement was designed so that flexural strengths could be achieved with a minimum factor of safety of three considering no concrete resistance. The intent of the "stringent" requirement for transverse reinforcement was to minimize the possibility of primary failure in shear. Transverse reinforcement in beams and columns was rectangular-shaped spirals(Fig. 2.10b). Transverse reinforcement in walls was made of bent stirrups (Fig. 2.10c). Beam-column joint cores were reinforced with helical reinforcement so that joint distress would be avoided (Fig. 2.10b). Steel tubing was used for all beam-column joints and for walls at each story level so that deterioration at the connection between elements and story weights would be minimized (Fig. 2.10b).

# 3. EXPERIMENTAL PROGRAM

Four small-scale, reinforced-concrete test structures were constructed and tested. Test structures were effectively two-dimensional, fixed-base representations of frame and coupled wall-frame structures. Both dynamic and static tests were conducted. This chapter describes the test structures and testing program. Additional details appear in Appendix A. A description of static tests of members and beam-column assemblies which were typical of those composing test structures is presented in Appendix B.

## 3.1 Test Structures

The overall configuration of a test structure is shown in Fig. A.1a. A photograph of a test structure is shown in Fig. 3.1. The structures were effectively two-dimensional, nine-story systems with a first story twice as tall as other stories. One of the test structures was composed only of two frames which were situated opposite and parallel to one another and which carried a mass at each level. Three subsequent structures included prismatic walls of varying height which were situated centrally between the frames. Wall heights in the latter structures were one-story, four-stories, and nine-stories tall.

Frames and walls were fabricated using small-aggregate concrete and small-diameter reinforcement. Mean concrete strengths (Table A.5) varied between 35 and 40 MPa. Longitudinal reinforcement for frames was No. 13 gage wire (2.32 mm dia.) and for walls was knurled No. 2 gage (6.65 mm dia.). Mean yield stresses of No. 13 and No. 2 gage wires were 399 and 339 MPa (Fig. A.4). All longitudinal steel was continuous so that there were no welds or splices within members or joints. Transverse reinforcement

(No. 16 gage wire) was in the form of rectangular spirals for beams and columns and closed stirrups for walls (Fig. 2.10). Frames and walls were cast monolithically in a horizontal position with stiff base girders. After curing, the frames and wall were positioned on the earthquake-simulator platform as described in Fig. A.1.

A story weight with mass of approximately 454 kg was supported between the frames at each of nine story levels. Masses and connections were designed so that displacements of frames and walls would be effectively the same at each story level. Masses were fabricated from steel and concrete with a central opening to allow space for the centrally-located walls (Fig. A.1b). Each was positioned vertically so that mass centers coincided with story levels. A system of steel cross-channels distributed vertical load equally to all beam-column joints at a level without eccentricity either parallel or transverse to the plane of the frames (Fig. A.1c). A steel link transmitted in-plane horizontal force between the mass and wall at each level with negligible rotational restraint (Fig. A.1d). A system of diaphragms connected between masses restrained motion transverse to the major plane of a structure.

Instrumentation of a test structure was organized so that absolute accelerations, relative displacements, and wall-frame interactive forces were measured. Instrument location and orientation are shown in Fig. A.7. Accelerometers measured (1) base accelerations, (2) in-plane accelerations at each level of both the north and south frames, (3) vertical accelerations of columns and wall, and (4) top-level transverse accelerations. LVDT's measured (1) displacements of the test platform and (2) in-plane displacements of each level relative to the test platform. Wall-frame interaction

forces were inferred from measured strains in the steel connecting links. Electrical signals from instruments were recorded continuously on analogue tape for dynamic tests and at intervals for static tests.

Details of structure fabrication and instrumentation are presented in Appendix A.

## 3.2 Testing Procedure

The primary test for each structure was an earthquake simulation for which a single direction of base motion was modelled after a measured earthquake acceleration record. Complementary testing measured response in free vibration, response to sinusoidal base motion at several frequencies (steady-state tests), and response to a static lateral force applied alternately at each of nine levels (static test). A typical testing sequence is depicted in Fig. 3.2. The sequence was performed three times with the only variable being the earthquake simulation intensity. Following the third sequence the structure was subjected to another steady-state test (at "higher" amplitude) and to a strength test in which the top level was loaded laterally to failure. A check of connecting bolts and permanent transverse deformation followed each test. A detailed description of each test follows.

Base accelerations for earthquake simulations were modelled after the N-S accelerations measured in El Centro, California, 1940. Time scales of simulations were compressed by a factor of 2.5 so that reasonable ratios of base-motion to test-structure frequencies would result. The peak acceleration of the first simulation was anticipated at 0.4 g. This was the motion for which the test structures had been designed. Subsequent simulations had nominal intensities two and three times the design-basis

motion. Crack patterns were recorded immediately before and after each simulation.

Free-vibration tests were conducted by laterally displacing and suddenly releasing the top level of a test structure (Fig. A.6). The force used to displace the structure was the same for each test.

Base motions for steady-state tests were displacement-controlled, sinusoidal motions at constant amplitude of approximately one mm. Frequency of motion was increased in steps from below to above the apparent fundamental resonance frequency of each structure. Following the third sequence (Fig. 3.2), a higher-amplitude steady-state test was conducted with exciting amplitude of approximately two mm.

A static test involved applying a static lateral force to one level of a structure. The load was increased in three equal increments up to the design shear that had been estimated for that story level using the design model presented in Chapter 2. Loading progressed from the top level down. Loads were released from the current level before proceeding to the next so that only one level was loaded at a time. Loads were applied at each level in the same direction. Following the completion of all other tests, the top level was loaded in increments to apparent failure.

# 4. RESPONSE TO SIMULATED EARTHQUAKES

The structures were tested following the procedure described in Section 3.2. In this chapter, recorded signals representing displacement, acceleration, and force response to simulated earthquakes are presented. Concrete cracking and crushing are used as indicators of structural damage.

## 4.1 Nature of Data

### (a) Response Histories

Instrumentation used to measure response to simulated earthquakes is shown schematically in Fig. A.7. Base accelerations were measured on the top of base girders of both north and south frames of each test structure. Base displacements were measured between the test platform and the strong floor of the Structural Research Laboratory. Displacements of each level of a structure were measured relative to a stiff A-frame which was fixed to the test platform. In-plane accelerations of each level were measured on both north and south frames. Vertical accelerations were measured on tops of columns and walls and transverse accelerations were measured on the top-level mass. Wall forces were measured between mass and wall centerlines.

Response signals and electrical calibrations were recorded in analogue form using four magnetic-tape analogue recorders. Data were subsequently digitized at a rate of 200 points per second. A common signal was recorded on each of the four analogue recorders as an aid to synchronize starting and ending points of records recorded on different analogue tapes. However, because of inherent variation in recorder speeds,

slight time discrepancies are likely in records from different analogue tapes. Instrument layout on each recorder is indicated in Fig. A.9.

Instruments were calibrated initially using known physical quantities. Calibrations were corrected for electrical changes with time by monitoring changes in electrical calibrations. Shear and moment responses were calculated by using story heights and masses as additional calibration factors. The effect of gravity forces acting through story displacements (P-delta effect) was included in determining moments acting on a test structure.

Response histories presented in this chapter could be verified only by comparing them with each other and with responses measured in previous experiments. Displacements viewed at a given instant indicated reasonably smooth displaced shapes. Story-level accelerations measured on north and south frames of a structure were nearly identical. In addition, an accelerometer fixed to the top-level mass indicated the same accelerations as those fixed to the top level of frames so that equal motion of masses and frames was inferred. Because of the similarity of acceleration records, only those recorded for the south frame are presented here. Construction forces which were likely before testing could not be monitored because of probable electrical drift occurring during the approximately two-week construction period. The forces between the wall and the frames were measured with the zero defined as the reading of the initiation of the first test run. Symmetric patterns of measured wall base-moment indicated that assumed wall forces were close to the actual forces although the possibility of error in individual readings cannot be discounted.

Displacement and acceleration histories are plotted in Fig. 4.1 for the purpose of illustrating various features of response waveforms. Test-structure designation, simulation number, and the type of data being plotted versus time are indicated above each plot. The starting point relative to initial motion of the test platform was the same for each record. The actual duration of base motion is indicated in Fig. 4.1. No residuals were assumed at the start of the initial simulation. Residuals incurred during prior testing were retained for subsequent simulations.

Response histories are not presented for all measured responses. Displacement, shear, and moment responses are presented for alternate levels because of similarities of responses measured at adjacent levels. Acceleration responses are presented at every level for the first simulation and at alternate levels for the second simulation. No response histories are presented for the third simulation because trends for that simulation could be inferred from trends in previous test runs. For convenience, Table 4.1 summarizes all response waveforms and their location in the text.

(b) Response Distributions

Distributions of response over the height of a test structure were determined at discrete intervals during each earthquake simulation. Displacement, lateral force, story shear, and story moment were plotted versus height (eg. Fig. 4.10). Distributions are presented only at times near the synchronization points (Section 4.1a) so that synchronization of records is assured. Because of space limitations, distributions are not plotted at all times during a simulation. Rather, distributions were

plotted for only a few times before, during, and following cycles of maximum displacement response.

(c) Sign Convention of Measured Response

Positive senses of displacements, in-plane accelerations, and wall forces were in the same direction (east). Vertical accelerations were positive in the upward direction. Positive direction for transverse accelerations was north. Positive sense of inertial forces was determined from D'Alembert's principle. Shear and moment senses were such that positive shear and moment resulted from positive force at an upper level.

(d) Cracking and Spalling Patterns

Cracking and spalling patterns are presented typically as in Fig. 4.2. The maximum crack width at a level is also presented. Cracks were observed immediately before testing and following each earthquake simulation. Observation of the smaller cracks (widths less than 0.05 mm) was aided by a fluorescent fluid which, when washed over specimens, collected in cracks and reflected black light.

## 4.2 Terminology

Certain terms used to describe response may not be standard in usage and require definition. As used in this report, the term "mode" refers to an apparent phase relation among motions observed at various levels. "First" or "fundamental" mode refers to the "appearance" of motion at all levels being in phase, and "higher modes" refers to motion being generally out of phase at different levels. "Node" or "nodal point" refers to a point on a structure where motion is negligibly small relative to motions at other levels (in the same frequency range) and where

the apparent phase relation of a higher mode changes. The second-mode has one node, the third-mode has two, and so on. The term "double amplitude" is used to describe the amplitude between adjacent peaks of response (Fig. 4.1).

## 4.3 Response During the First Earthquake Simulation

### (a) Condition Before Testing

Some cracking of specimens before testing was likely because of shrinkage and unintentional handling and construction stresses. Cracks observed before testing (Fig. 4.2) were all less than 0.05 mm in width. Wall cracks tended to be concentrated near the base. Cracks in frames were concentrated near beam-column interfaces and near the base of first-story columns.

### (b) Base Motions

Measured base accelerations for the first simulation are plotted in Fig. 4.3. Peak accelerations in the negative directions were 0.39, 0.34, 0.41, and 0.32 g for structures FNW, FSW, FHW, and FFW. Direct comparison of intensities is difficult because of differences in high-frequency content of the records. Base accelerations below approximately ten Hz were similar for FSW, FHW, and FFW. High frequencies apparent in the record for FHW beginning at 2.5 seconds were beyond the apparent third-mode frequency of test structures and thus were unlikely to affect response significantly. The base accelerations for FNW appeared "stronger" than for the other structures. This was especially true for frequencies ranging approximately between ten and thirty Hz. A comprehensive discussion of base accelerations is presented in Chapter 5 in terms of Fourier amplitude and spectral-response curves.

Maximum base displacements (Fig. 4.3) were 19.5, 18.2, 17.6 and 17.3 mm for structures FNW, FSW, FHW, and FFW, respectively. High frequencies observed in corresponding acceleration records were not apparent in base-displacement records.

(c) Displacements

Displacement response histories are plotted in Fig. 4.4 and displaced shapes measured at several instances are plotted in Fig. 4.10. Response at the time of maximum top level displacement is tabulated in Table 4.2.

Each structure underwent approximately the same number of large-amplitude displacement cycles. The peak top-level displacements, which occurred during the interval between two and three seconds, were 26.3, -22.4, -23.2, and -26.1 mm for structures FNW, FSW, FHW, and FFW, respectively. With the exception of response amplitude (which was larger for structure FFW), top-level waveforms for FHW and FFW were nearly identical. Waveforms for both of structures FNW and FSW differed perceptibly from those of the other structures.

A salient feature of displacement response, as indicated by the similarity among waveform shapes at different levels of a structure, was the predominance of the apparent fundamental mode. Higher modes were most apparent during intervals of low-amplitude response. Relative contributions of higher modes to overall displacement response appeared higher for structures FNW and FSW but did not exceed ten percent of the maximum apparent fundamental-mode response measured at the top level.

Because of its apparent dominance on displacement response, changes in the fundamental period could be observed indirectly and approximately

by measuring the time interval between adjacent displacement peaks. For each structure, the apparent period observed at the beginning of the test had at least doubled by the time of the maximum response (Fig. 4.4). Apparent periods observed during free-vibration response (after base motion had ceased) were longer than those observed during response at the maximum amplitude. Comparison throughout the test duration indicated similar periods for structures FHW and FFW and successively longer periods for structures FSW and FNW.

Displaced shapes (Fig. 4.10) were different for the four test structures as indicated below.

FNW: The largest interstory drifts occurred in the first story. Story drift decreased with height.

FSW: Drifts were small in the first story but "large" immediately above the first-story wall cut off. Above the third level, story drifts decreased with height.

FHW: Story drifts increased to the fourth or fifth level (wall cut off at fourth level) and decreased above the fifth level.

FFW: Story drifts along the height were more uniform than for the other test structures with the larger drifts occurring between levels two and six.

At the instant of maximum top-level displacement, maximum story drifts were approximately 2.0, 1.9, 1.4, and 1.4 percent of story height for structures FNW, FSW, FHW, and FFW, respectively.

Residual displacements at the end of the test (Fig. 4.4) served as an indicator that inelastic response had occurred. Top-level residuals

were nearly equal (0.06 percent) but in opposite directions for structures FNW and FSW. Residuals for FHW and FFW were in the same direction as for FSW but approximately three and four times as large. For all structures, the top-level residual was in the same direction as the maximum displacement for that structure and appeared to have been incurred during that maximum.

(d) Accelerations

Response acceleration histories (Fig. 4.5) appeared to be closely synchronized with measured displacement histories. However, in contrast with displacement response, acceleration waveforms revealed considerable frequency content higher than that corresponding to the apparent first-mode response. Accelerations measured at the first level were similar to base-level accelerations, especially for the structure with one-story wall (FSW). Acceleration response attributable apparently to the second and third modes was observed at several levels. For all test structures, apparent nodal points were between the sixth and seventh levels for the second mode and near levels four and eight for the third mode.

Lateral force distributions inferred from measured accelerations and masses were strongly influenced by higher-mode response (Fig. 4.10). Because of the different apparent characteristics of various modes, and because of the "random" nature of the base accelerations, distributions of inertial force underwent continuous change. Even near times of large-amplitude displacement response (Fig. 4.10) when displaced shapes remained almost constant, distributions of lateral inertial forces were observed to vary considerably.

Comparison of maximum base-acceleration amplification is difficult because of differences in the high-frequency characteristics of base motions which resulted in meaningless peak base accelerations. The maximum absolute acceleration (in units of g) at several story levels is presented below.

| Level | FNW | FSW | FHW | FFW |
|---|---|---|---|---|
| 9 | 0.49 | 0.67 | 0.62 | 0.82 |
| 7 | 0.42 | 0.49 | 0.52 | 0.55 |
| 4 | 0.37 | 0.38 | 0.42 | 0.42 |
| 1 | 0.43 | 0.34 | 0.32 | 0.36 |
| Base | 0.39 | 0.34 | 0.41 | 0.32 |

The maxima in upper stories were significantly higher for structures with walls, despite apparently weaker base motions for those structures as compared with the structure with no wall. At the seventh level, where contributions of higher modes were low, approximate comparison of base-acceleration amplification indicated similar amplifications for structures with walls (approximately 1.5) and lower amplification for the structure with no wall (approximately 1.0).

Transverse accelerations measured on the east end of the top-level mass (Fig. 4.6) were distinctly different for the four structures. The maximum observed for any structure (0.07 g) was an order of magnitude lower than measured in-plane acceleration maxima. For each structure, the lowest apparent frequency in the transverse direction was higher than the observed in-plane fundamental frequency. Comparison of transverse

accelerations on opposite ends of the top-level mass indicated the accelerations were primarily torsional as opposed to translational.

(e) Wall Forces

The wall force history for FSW is presented in Fig. 4.8 and those for FHW and FFW in Fig. 4.7. Electrical difficulties were encountered with the tests of structure FFW. Electrical leakage before the beginning of earthquake simulations (when electrical equipment was turned on) caused zero shifts in the force readings (Fig. 4.7). The shifts were of approximately equal magnitude and in the same sense at all levels except level eight where gauges had been wired in the opposite sense. The only observed shifts occurred immediately before the simulations of structure FFW. The zero level was taken as the reading immediately before motion of the test platform began. Symmetric patterns of base level wall moments which resulted from the estimated zero levels (Fig. 4.9) indicate that the estimated zeroes were close to the true zeroes. Problems with electrical equipment were corrected for tests FSW and FHW so that no electrical leakage was observed.

Wall-force histories (Fig. 4.7 for FHW and FFW and 4.8 for FSW) measured at different levels exhibited characteristics which, to varying degrees, resembled characteristics of displacements and accelerations measured at the same level. For levels 2 through 8 of structures FHW and FFW, wall-force waveforms resembled and were synchronized with measured acceleration responses. All forces (at the apparent fundamental period) measured below the ninth level were in the same sense as displacements. At the ninth level of structure FFW the force history was synchronized with

but opposite to the top-level displacement. Wall forces measured at the first level were dominated by the apparent fundamental period. For structure FSW, the first-level force history was nearly identical in shape to the first-level displacement history.

Differences and similarities among wall-frame interaction in the three structures with walls were apparent from comparison of measured wall forces at various levels (Fig. 4.7 and 4.10). One such difference was the force reversal at the top of the wall in structure FFW, which indicated the restraint of frames on wall at that level. Similar reversals were not observed at any level for other structures. Between levels one and nine for structure FFW, the similarity, at any level, between frequency content amd amplitude of lateral inertial forces and wall forces indicated the possibility that wall forces depended primarily on the inertial force applied at a level. However, complications introduced by residual forces made direct comparison of inertial and wall forces difficult. These residuals also indicated that, although wall forces may have depended primarily on the lateral inertial force applied at the same level, interaction resulting from overall deformation along the height of the structure was an important consideration. First-level wall forces for structures FHW and FFW were similar throughout the simulation. The limited interaction for structure FSW, where the wall force was apparently controlled by the first-level displacements, resulted in a significantly different force history. Forces were typically three times as large as first-level forces measured in FHW and FFW and comparatively negligible degradation in the force history was observed.

Residual wall forces (Fig. 4.7 and 4.8) indicate that inelastic response had occurred during the "design" earthquake for every test structure having a wall. Barring relative motion of base girders and instrument error, the existence of residual forces is attributable to inelastic response in at least one of the elements or, more likely, to differences in the hysteretic characteristics of the walls and the frames.

Changes in the wall-frame interaction were observed during the first three seconds for structures FHW and FFW. Up to the time of 2.3 seconds, first-level wall forces were observed to decrease while displacement amplitudes increased. After this interval, the first-level wall forces dropped suddenly despite high-amplitude displacements. In addition, sudden and opposite shifts in the reference points of second and fourth level wall forces occurred at the same time. A likely cause of these changes was faster rate of stiffness-reduction in walls relative to frames in the first story.

Because of the different deformation characteristics of frames and walls, and because of the previously mentioned sensitivity of wall forces to acceleration response, no typical distribution of wall forces could be attributed to the different structures, either at different amplitudes in the same displacement cycle or at similar amplitudes of different cycles (Fig. 4.10).

(f) Shears and Moments

Shear and moment histories are plotted in Fig. 4.8 and 4.9 and distributions along the height are plotted in Fig. 4.10. In those figures, shears and moments resisted by the total structure and those resisted by the wall are superimposed for comparison. Shear and moment carried by

the frames alone is noted to be the difference between total structure response and wall response at each level.

Because shears and moments on the total structure were determined by combining lateral inertial forces, higher-mode effects could be expected in upper story levels. However, the relative contribution of higher modes to structure shear and moment in the lower stories decreased because opposing forces for a particular mode tended to cancel. Thus base shear and moment acting on the total structure were dominated by the apparent fundamental mode.

Wall shears and moments for structure FSW, which resulted from the single force acting at the first level of the wall, were controlled by the first-level displacements. For structure FHW, higher-mode effects near the top of the wall tended to cancel near the base so that base shear and moment were dominated by the first mode. For structure FFW, the top-level force reversal resulted in an inflection point along the wall height. Shears and moments near the top of the wall were dominated by this reversal and tended to oppose total structure shear and moment. Wall forces below the top level tended to cancel the effect of the force reversal so that relatively small shears and moments were observed near levels seven and three, respectively. Near these levels, higher-mode response in shear and moment was apparent. Below these levels, shears and moments resisted by the wall increased, in the same sense as total structure shear and moment, and were again dominated by the apparent fundamental period.

The maximum base shears and moments observed during the simulation are summarized below.

| Test Structure | Base Shear, kN | | Base Moment, kN-m | |
|---|---|---|---|---|
| | Structure | Wall | Structure | Wall |
| FNW | 12.2 | -- | 19.3 | -- |
| FSW | 12.8 | 12.3 | 21.2 | 5.6 |
| FHW | 13.2 | 8.2 | 22.7 | 5.3 |
| FFW | 14.0 | 8.2 | 23.8 | 5.0 |

The quantities listed indicate that the maximum structure base responses were higher for structures with higher walls. Maximum base shears resisted by walls in structures FHW and FFW were essentially equal with each resisting approximately sixty percent of the total during high amplitudes of displacement early in the test. The shear resisted by the one-story wall in structure FSW was approximately fifty-percent larger than that for other walls. That wall carried nearly the entire structure base shear. Shear carried by first-story columns was negligible. Maximum wall base moments were apparently limited by yield levels (Appendix B). Although walls continued to resist similar proportions of total base shear throughout a test, comparison is difficult because of residuals incurred during maximum response cycles (Fig. 4.8).

Distributions of total structure shear and moment were similar for all structures at times of high base shear and moment (Fig. 4.10). Because of the different wall heights, proportions of total force that had to be carried by the frames varied. Although the frames in structure FSW carried very little first-story shear, maximum frame shear above the first-level wall cutoff (12.1 kN) was nearly the same as the maximum carried in structure FNW (12.2 kN). Structure FFW had the smallest maximum frame shear (10.1 kN).

However, because of the force reversal at the top of the wall, the upper three stories in that structure also carried the largest frame shears of the four structures tested. In comparison with structure FFW, the frames in structure FHW tended to carry a slightly larger proportion of total shear in intermediate stories (maximum of 10.6 kN) but considerably less in upper stories.

(g) Crack Patterns

The majority of observed frame cracks* were located at beam-column interfaces and, for structures FNW and FSW, in the first story columns (Fig. 4.11). No shear distress or crushing was observed. Distributions of residual crack widths in frames (Table 4.4) correlated with observed distributions of drift maxima for each structure but did not compare well for different structures. Wall cracks consisted primarily of flexural cracks near the base and a crisscross pattern of small-width (less than 0.02 mm) "shear" cracks in the first story (Fig. 4.11). Observed cracking in the four-story wall was relatively light despite the similarity in loading conditions of first-story portions of walls in structures FFW and FHW.

Maximum wall crack widths, which were located near and parallel to the wall base, were 0.05, 0.60, and 0.70 mm for structures FSW, FHW, and FFW.

---

* Because of equipment necessary to carry the story masses illustrated in Fig. A.1, it was not possible to inspect in detail the entire surface of each wall and frame.

## 4.4 Response During the Second Earthquake Simulation

### (a) Base Motions

Base accelerations and displacements measured for the second earthquake simulation are plotted in Fig. 4.12. The shapes of the curves were similar for the four structures. High frequency accelerations which were prominent for the first simulations were not observed in acceleration histories. Peak base accelerations in the negative direction were 0.78, 0.59, 0.48, and 0.55g for structures FNW, FSW, FHW, and FFW, respectively. Peak base displacements were 36, 33, 31, and 32 mm.

Discussion of base motion in terms of spectral response curves and frequency content is presented in Chapter 5.

### (b) Displacements

Displacement waveforms and shapes are plotted for the second earthquake simulation in Fig. 4.13 and 4.18. Distributions of response measured at the time of maximum top-level displacement are summarized in Table 4.3.

Although many of the characteristics observed during the first simulation were observed during the second test, displacement histories were distinctly different from the previous test. For structures FNW and FSW, large-amplitude displacements were distributed more uniformly throughout the test duration. As in the first simulation, displacement waveforms for structures FHW and FFW were nearly identical. Overall waveform shapes for FHW and FFW resembled waveforms measured for structure FNW during the first simulation. Although displacement waveforms for all structures were dominated by an apparent fundamental mode, the waveforms were generally less periodic in nature. Average periods were longer but increases in apparent period were less than increases observed during the first test run.

Top-level displacement maxima were 44, 40, 40, and 44 mm for structures FNW, FSW, FHW, and FFW. These maxima ranged from 1.7 to 1.8 times those observed during the first simulation.

Displaced shapes (Fig. 4.18) were similar to shapes observed during the first simulation. However, for structures with walls, drifts in the first story were observed to increase more than drifts in other stories, indicating a possible decay in the stiffening effect of the walls. Maximum interstory drifts measured at the time of maximum top-level displacement were 3.1, 3.1, 2.6, and 2.6 percent for structures FNW, FSW, FHW, and FFW. The maximum drift for structure FFW which had occurred at intermediate stories during the first simulation, was located in the first story during the second simulation. For other structures, stories of maximum drift did not shift noticeably between the two simulations.

Top-level displacement residuals (of -1, 2, 5, and 5 mm for structures FNW, FSW, FHW, and FFW) were similar in magnitude to those observed following the first simulation even though displacement maxima were nearly twice as large during the second simulation. In addition, observed drifts were not all in the same direction as the observed displacement maximum, indicating that inelastic response was not limited to the cycle of maximum displacement and that residual drifts were not a good measure of maxima nor of overall damage.

(c) Accelerations

Acceleration waveforms (Fig. 4.14) were generally more erratic than those observed during the first simulation, indicating a greater contribution of higher modes to overall acceleration response. The greater influence of higher modes was apparent in distributions of lateral inertial forces over the structure height (Fig. 4.18). As in the first simulation, response

near the seventh level was dominated by the apparent fundamental mode. Examination of phasing of various frequencies indicated that nodal points for the second and third modes did not change noticeably from those observed during the first simulation.

Maximum base-acceleration amplifications were 1.2, 1.6, 1.9, and 2.0 for structures FNW, FSW, FHW, and FFW, respectively. As for the first simulation, amplification at the seventh level, where higher-mode contributions were small, were similar for structures with walls (approximately 1.2) and lower for the structure with no wall (approximately 0.75). The latter amplifications represented approximately twenty-percent decreases from those observed during the first simulation.

(d) Wall Forces

Wall force histories (Fig. 4.15 and 4.16) and distributions of wall force with height (Fig. 4.18) indicate several trends which were similar to those observed for the first simulation. As in the previous test, forces at levels one and nine were dominated by the first mode while forces measured between these levels revealed frequencies comparable with frequencies observed for lateral inertial forces.

Maximum wall forces in structure FFW did not increase significantly except at the top level, despite increases in lateral inertial forces and displacements. The top-level force increased by approximately fifty percent of that observed during the first simulation. In structure FHW, increases in wall forces above the first level ranged from fifty to one-hundred percent over forces measured during the first simulation. For all structures, amplitudes of first-level wall forces were similar to forces in the previous test.

During the first two seconds of the second simulation, the phasing of wall forces at all levels was the same as in the previous test so that the only apparent force-reversal occurred at the top level of structure FFW. During the interval between two and three seconds, when displacement maxima occurred, the phasing of the first-level wall force in structures FHW and FFW changed so that force reversals were also observed at that level (Fig. 4.15). The reversal indicated the frames were loaded by the wall at the first level, in contrast to observations in the previous test, and also pointed to the decaying "stiffness" at the base of the walls. This observation was consistent with ovserved increases in first-story drifts for structures FHW and FFW (Section 4.4b).

(e) Shears and Moments

Shear and moment histories for structures and walls are superposed in Fig. 4.16 and 4.17 and distributions over height are plotted in Fig. 4.18. As for the first simulation, observed structure and wall shears and moments were closely synchronized with displacement histories.

The increased contribution of higher modes to lateral inertial forces was apparent in structure shear and moment histories at all levels. An apparent effect of the increase in higher-mode contributions was that lateral inertial forces were often concentrated in upper stories of a test structure resulting in nearly uniform shear distribution over the height of a structure (Fig. 4.18). Whereas the effect of higher modes on base shear and moment was small, the concentration of forces near the top of a test structure resulted in upper-story shears and moments which were considerably higher than observed during the first test run.

Shears and moments resisted by walls exhibited trends similar to those observed in the previous test. One difference was higher wall shears and moments at intermediate levels of the four story wall in structure FHW. In addition, for structure FFW the higher-amplitude of the (reversed) top-level force resulted in a lower point of contraflexure along the wall height (Fig. 4.18). Despite apparent damage at the base of the walls in structures FHW and FFW, as indicated by the development of a force reversal at the first level (Fig. 4.15), shear histories (Fig. 4.16) indicate that walls continued to carry a large portion of total structure base shear.

Maximum base shears and moments measured during the second simulation are summarized below.

| Test Structure | Base Shear, kN | | Base Moment, kN-m | |
|---|---|---|---|---|
| | Structure | Wall | Structure | Wall |
| FNW | 12.6 | -- | 23.2 | -- |
| FSW | 13.9 | 12.8 | 25.1 | 5.8 |
| FHW | 15.5 | 9.7 | 25.8 | 5.6 |
| FFW | 16.8 | 10.4 | 25.8 | 5.3 |

As in the first simulation, maximum structure base shear and moment tended to be larger for structures with taller walls. The maximum structure base shears and moments were larger than those observed during the first test, but increases were smaller than increases in top-level displacement maxima (approximately fifteen percent increases in shear and moment versus approximately seventy percent increases in displacement). At the time of maximum base shear, proportions of total base shear resisted

by walls were similar to those observed for the first test (approximately sixty percent for structures FHW and FFW and ninety percent for structure FSW). The maximum shear resisted by the wall in FSW was apparently limited by strength of the wall. At times other than the maximum, that wall resisted nearly the total base shear, although comparison was complicated by an apparent residual wall force. Maximum wall base moments for all walls were probably limited by flexural capacities and showed increases of three to five percent over maxima observed during the first test.

Proportions of maximum shear carried by frames were similar to those in the first simulation. In structure FSW, the maximum above the wall cutoff was 14.3 kN compared with 12.6 kN in the first story for structure FNW. Maximum frame shears in structures FHW and FFW were 13.0 and 11.8 at levels two and three, respectively. Frames of structure FHW carried larger shears in intermediate stories than did structure FFW during times of large displacements. However, the top-level wall force in structure FFW, for which the reversal was larger than that observed during the first simulation, resulted in large frame shears in upper levels of that structure (Fig. 4.18).

(f) Crack Patterns

Crack patterns observed following the second earthquake simulation are shown in Fig. 4.19 and distributions of maximum frame crack widths are tabulated in Table 4.4. Distributions of frame crack sizes (Table 4.4) correlated well with distribution of maximum story drift for each structure. For walls, new cracks were observed in most stories although crack patterns in the four-story wall were notably different from those in other walls.

Maximum wall crack widths were 0.20, 1.8, and 1.5 mm for structures FSW, FHW, and FFW. Minor spalling (as indicated in Fig. 4.19) was observed at the base of walls in structures FHW and FFW. In addition, a shear displacement of 0.50 mm to the east across the main flexural wall crack was observed for structure FFW. The displacement indicated that sliding had occurred at the wall base during the second tests.

# 5. DISCUSSION OF OBSERVED BEHAVIOR

Base motions are studied in the first portion of this chapter. Behavior of test structures during dynamic tests is then interpreted using measured response quantities.

## 5.1 Base Motions

Base motions were studied so that responses of different test structures could be compared and also so that the responses of individual structures to different intensity motions could be studied. Base acceleration and displacement histories recorded in the first two simulations for each test structure (Fig. 4.3 and 4.12) were compared in Chapter 4. This section describes base motions using Fourier-amplitude spectra, linear response spectra, and spectrum intensities.

### (a) Fourier-Amplitude Spectra

Fourier-amplitude spectra were calculated from base-acceleration histories using a discrete Fast Fourier Transform [15]. The Fourier-amplitude spectrum is a measure of the final energy in zero-damped, single-degree-of-freedom (SDOF) oscillators subjected to the base motion [20]. In this regard, it should be similar to the zero-damped velocity spectrum which represents the maximum response of the system. Because the maximum response is probably of more interest to an engineer, the response spectrum will be of greater value for estimating response. The Fourier-amplitude spectrum is still of considerable value because peaks on the spectrum represent frequencies at which the earthquake motion has input higher amounts of energy to a system.

Fourier-amplitude spectra determined for the first two earthquake simulations and normalized to a maximum Fourier coefficient of one are compared in Fig. 5.1. For first simulations, spectra for the four tests are nearly the same for frequencies below eight Hz. Above eight Hz, two differences among the four spectra are apparent: (1) the spectrum for structure FNW indicates more energy than the other motions between eight and eighteen Hz, and (2) the spectrum for FHW indicates more energy above approximately thirty Hz. These higher-frequency contents could be identified in sharper acceleration peaks in the record for FNW and in high-frequency "noise" for FHW (Fig. 4.3).

Fourier-amplitude spectra for the second simulation (Fig. 5.1) also indicated similar frequency content up to eight Hz and higher content for FNW between eight and eighteen Hz. The "high" frequencies indicated for FHW in the first simulation were not apparent in the second. Spectra for the third simulation were nearly the same as those for the second "simulation."

(b) Response Spectra

Linear response spectra were calculated from measured base-acceleration histories. The calculation procedure involved solution of the convolution integral for a general impulse motion to determine the response of linear single-degree-of-freedom systems at several natural frequencies and percentages of critical damping. The time step used in the calculation was 0.005 second. Records measured on base girders of south frames were used for the calculations. Records measured on north frames produced nearly identical spectra. Tripartite psuedo-velocity spectra are plotted for the first two simulations of each test for damping ratios of 0.0,

0.02, 0.05, 0.10, and 0.20 and over a frequency range of 1.0 to 50.0 Hz in Fig. 5.2. Relative displacement and absolute acceleration spectra are plotted in linear format for all three simulations for damping ratios of 0.02, 0.05, 0.10, and 0.20 and over a frequency range of 1.0 to 40.0 Hz in Fig. 5.3.

Displacement spectra had nearly the same shapes for all simulations (Fig. 5.3). The overall trend of displacement spectra was for displacements to increase as periods increased to 0.4 sec, decrease as periods lengthened to 0.5 sec, and then increase again as the period increased to 1.0 sec. For frequencies higher than eight Hz, where differences in Fourier-amplitude spectra of base accelerations were most apparent, displacement spectra (Fig. 5.3) indicated low displacement response. Differences in base motions at these high frequencies should have negligible influence on displacement response.

Shapes of acceleration spectra were generally different for different earthquake simulations (Fig. 5.3). An apparent reason for the differences was the sensitivity of response accelerations to high frequencies which varied considerably for different base-acceleration records. The acceleration spectra for FNW deviated from the other spectra with relatively high response accelerations in the range between eight and thirty Hz. For frequencies below eight Hz, spectra shapes were similar for all simulations.

Ten-percent-damped spectra for the first simulation of each test structure are compared in Fig. 5.4. The expected peak acceleration in this design-basis simulation was 0.4 g as compared with measured

acceleration maxima of -0.39, -0.34, -0.41, and -0.32 g for structures FNW, FSW, FHW, and FFW.

Ten-percent damped displacement spectra for the first simulation of each test structure (Fig. 5.4a) were similar in shape. Calculated amplitudes were also similar for the four base motions with differences in amplitude varying for different periods. At a period of 0.5 sec. (which was close to the lowest apparent test-structure periods during maximum displacement response) the calculated spectral displacements were 14.5, 14.1, 14.3, and 13.8 mm, or effectively 14 mm for all four cases.

Ten-percent damped acceleration spectra for the first simulation (Fig. 5.4b) were nearly identical for periods longer than 0.4 sec. and matched closely the design spectrum for periods between 0.4 and 0.8 sec. For periods between 0.2 and 0.4 sec., the calculated spectra exceeded the design by approximately twenty percent. For shorter periods, the spectrum for structure FNW matched the design spectrum reasonably well and spectra for FSW, FHW, and FFW were generally well below the design. Because apparent fundamental periods of the test structures were in the range where calculated and design spectra were nearly the same, it would appear that actual base motions of the first earthquake simulation were close to the design-basis motion.

In order to estimate relative intensities of different portions of the earthquake simulations, displacement and acceleration spectra for the first test of structure FHW are compared for the first three and first six seconds in Fig. 5.5. Comparisons for other tests were similar. The ten-percent damped spectra are identical for these two intervals. The two-percent damped spectra, for which an oscillator would not dissipate

energy as quickly, showed some response increase during the interval between three and six seconds. Spectra for full durations were identical to those for the first six seconds. Based on these spectra for partial durations, maximum response of test structures might be expected to occur early during an earthquake simulation.

(c) Spectrum Intensities

Spectrum intensity is a convenient measure of the severity of an earthquake motion because it is a single number by which different motions can be compared. As used for this study, spectrum intensity is defined as the area under the velocity spectrum between periods of 0.04 and 1.0 sec. This definition is derived from that used by Housner [ 19 ] with period shifts consistent with time-scale compressions used for the simulations.

Spectrum intensities calculated at ten percent of critical damping are listed in Table 5.1. For the first simulation, the highest spectrum intensity was for structure FNW. Spectrum intensities for structures FSW, FHW, and FFW were 87, 89, and 83 percent of the intensity for test FNW. Spectrum intensities for second and third simulations were generally less than two and three times the intensities of the first simulations (Table 5.1).

The adequacy of spectrum intensity in representing the severity of the earthquake simulations is questionable and warrants consideration. By definition, spectrum intensity is an average of the velocity responses of a series of linear SDOF systems. This intensity might be a reasonable measure of effects on inelastic response for motions with similar durations of "strong shaking," as is the case for these tests. However,

by nature of being an "average," spectrum intensity cannot be a precise measure of the effects on a particular structure unless the base motions being considered are identical. Care must be exercised in comparing intensities for base motions which have different frequency characteristics as occurred for the first simulations of the test structures. Calculated velocity spectra for first simulations (Fig. 5.2) indicated higher spectral response for test FNW in the frequency range between eight and twenty Hz. This would tend to "inflate" the spectrum intensity for that test relative to other tests if response was limited primarily to response below that frequency range. High frequencey noise indicated for test FHW (Fig. 5.1) was beyond the integration limits used to calculate intensity and would not influence the intensity.

Spectrum intensities for several damping factors are compared with spectrum intensity calculated for ten-percent damping in Fig. 5.6.

Spectrum intensities generally increased with increasing peak base acceleration but correlation between these two measures was poor (Fig. 5.7). Because acceleration maxima are largely attributable to peaks or "spikes" at frequencies beyond the apparent response frequencies of the test structures, spectrum intensity is the better measure of simulation intensity. However, for comparison of responses in the low-frequency range (below eight Hz), response spectra (Fig. 5.3) are a better indicator of simulation intensity for these tests.

## 5.2 Frequency Content of Measured Responses

When a multistory structure responds to earthquake loading, different frequency contents can be expected in different responses. Such behavior

was observed for the tests studied in this report (see Chapter 4 for measured responses). Evaluation of the frequency content of particular records can be important in terms of understanding overall response, especially if apparent modal characteristics can be associated with the response. The frequency content of various measurements is analyzed in this section.

The analysis procedure involved manipulation of measured waveforms using the discrete Fast-Fourier transform. Measured responses were decomposed from the time domain to the frequency domain and relative amplitudes of the harmonic components were plotted versus frequency in Fourier-Amplitude spectra (eg., Fig. 5.8a). "Filtered" waveforms were constructed by setting amplitudes of particular harmonic components to zero and performing an inverse operation to transform back to the time domain.

Fourier-amplitude spectra and measured and filtered response waveforms are plotted in Fig. 5.8. In that figure, waveforms were filtered to exclude all harmonic components above 4.0 Hz and the filtered record (solid curve) superposed on the measured record (broken curve). Data are presented only for the first earthquake simulation of structure FFW. Responses of the other test structures and during subsequent tests indicated trends similar to those presented for structure FFW.

(a) Displacement Response

Fourier-amplitude spectra indicate that displacement response was dominated by response at frequencies below 4.0 Hz (Fig. 5.8a). A

negligibly small influence of response at a frequency near ten Hz is indicated in Fourier-amplitude spectra of the lower story-levels. Filtered waveforms are nearly the same as measured waveforms. Some mismatch of the two waveforms is apparent during the first 1.2 seconds of the test. This mismatch is attributable to a higher frequency of response before the structure was subjected to "large" displacements.

(b) Acceleration Response

Acceleration responses were influenced by several frequency ranges (Fig. 5.8b). As indicated by Fourier-amplitude spectra for accelerations, response of all levels was dominated by frequencies below 4.0 Hz. Response at upper levels indicated more-pronounced influence of response below 4.0 Hz than at lower levels. Response of the first level contained several frequencies apparent in base accelerations (Fig. 5.8b).

Apparent modal characteristics can be identified on Fourier-amplitude spectra of accelerations (Fig. 5.8b). Three bands of frequencies are apparent near 2.5, 10, and 22 Hz. Although response periods associated with these bands lengthened during a test, the relative amplitudes at different levels did not change appreciably and tended to resemble amplitudes expected for the three lowest modes. Response amplitude near the 2.5 Hz range was higher near the top of the test structure as would be expected for the first-mode response. Amplitudes of response at frequencies near ten Hz were low at the seventh level and amplitudes near the 22 Hz range were low at levels four and eight, suggesting apparent nodal points for the second and third modes. Nodal points determined using the design model (Fig. 2.6) were approximately the same as those apparent in the Fourier-amplitude spectra.

(c) Structure Shear and Moment Response

Frequency content of structure shear and moment response is presented in Fig. 5.8c and d. Because shears and moments were calculated from inertial forces, the frequency content in upper levels was similar to that observed in upper-story acceleration responses. The influence of higher modes on shear and moment responses was less pronounced in lower stories because forces associated with higher-mode responses tended to cancel near the base while first-mode inertial forces were all in phase and "accumulated" over the structure height. Fourier-amplitude spectra indicate that base shear in test structures was dominated by the apparent fundamental mode with a small second-mode component. Base moment contained very little frequency content above the apparent fundamental-mode frequency.

## 5.3 Measured Hysteretic Behavior of Test Structures

The dynamic characteristics of a structure are largely dependent on the effective stiffness characteristics. For example, a structure which is "flexible" in an overall sense is expected to have longer response periods than one which is "stiff". For structures responding in the inelastic range, progressive softening should be reflected in progressively-lengthening apparent response periods. In addition to providing an indication of overall structure stiffness, study of hysteretic behavior of the test structures should give a qualitative indication of the energy dissipation characteristics.

Construction of load-deformation curves for individual structural members was not possible for the tests discussed in this report because

of equipment limitations and difficulty in synchronizing records recorded on different tape recorders (see Appendix A). Because it was considered important to obtain a measure of the hysteretic response of the test structures, instrumentation for dynamic tests was organized so that synchronized records of top-level displacement and base-level moment were obtained. The predominance of the apparent fundamental mode on top displacement and base moment (almost to the exclusion of higher modes) is convenient because hysteretic relations between these two measures can be viewed as if test structures were single-degree-of freedom systems. The two responses are compared in this section.

(a) General Characteristics of Hysteretic Response

The measured relationship between base moment and top displacement (to be called the moment-displacement relationship in this section) obtained from the first earthquake simulation of structure FFW is plotted for successive two-second intervals in Fig. 5.9. The hysteretic curves are reasonably smooth, especially at high displacement amplitudes where the first-mode response dominated. Because a positive top-level displacement in a higher mode could result in a small negative base moment, higher-mode response typically appears as S-shaped waves superimposed on the "first-mode" hysteresis loops (Fig. 5.9). The hysteretic curves must be viewed cautiously during response at low amplitudes where higher modes can dominate the overall response, resulting in loops oriented approximately perpendicular to the "first-mode" loops.

As indicated by the hysteretic response in Fig. 5.9, the overall stiffness tended to decrease with increasing displacement amplitude previously experienced by a test structure. Response of the "undamaged" structure (up to approximately 1.1 seconds for structure FFW) was nearly

linear. Up to this time, the appearance of hysteresis is probably caused by higher-mode effects and, because the curves pass through the origin, it is unlikely that significant energy dissipation through inelastic response has occurred. As indicated by slopes in Fig. 5.9, the first appreciable excursion into the inelastic range occurred after the top displacement exceeded approximately 2 mm (approximately 1.15 seconds for structure FFW) after which inelastic rebound of the structure is apparent. Beyond this apparent elastic limit, the "peak-to-peak" stiffness of the test structures decreased whenever a new displacement maximum was reached. A small stiffness reduction observed if a test structure oscillated a second time at a displacement amplitude equal to the previous maximum was similar to the reduction observed in static tests of members which composed the test structures (see Appendix B). As in static tests, a third oscillation resulted in no apparent stiffness loss.

An interesting feature of the hysteretic response of a test structure was that, while an overall characteristic of a structure was to become softer as new displacement maxima were reached, response at displacements below the previous maximum (in the inelastic range) was that of a stiffening system. This stiffening behavior, which is apparent in the small-amplitude response for structure FFW in the interval between 4.0 and 6.0 seconds (Fig. 5.9), was the result of "pinching" of the moment-displacement curve at low moment levels. Similar behavior observed in static tests of members (Fig. B.5) is attributed to reinforcement slip. Full-scale reinforced concrete elements have exhibited similar behavior [2, 16, 29].

Pinching of the moment-displacement relation (low incremental stiffness at low moments followed by increasing stiffness) might be expected to reduce the energy-dissipation capacity of a test structure, as indicated by the narrowness of hysteresis loops for responses at amplitudes which do not exceed previous maxima by a significant amount (Fig. 5.9). Pinching also results in lower effective stiffness for low displacement amplitudes than for higher amplitudes. The alternating softening-stiffening behavior of the test structures can be expected to result in an interesting interplay between response amplitude and apparent frequency (see Section 5.4).

(b) Comparison of Overall Stiffnesses of Test Structures

Base moment-top displacement relations of each test structure measured during the first earthquake simulation are compared in Fig. 5.10. The curves indicate similar trends. Stiffnesses of the "undamaged" structures generally decreased as the maximum displacement increased. Pinching (low incremental moment-displacement slopes at low moment levels) was apparent for all of the test structures. Relatively wide hysteresis loops resulted whenever maximum displacement significantly exceeded a previous maximum but narrower loops resulted for all other responses because of pinching in the low moment region.

Pinching of hysteresis loops at low displacement amplitudes was more pronounced for structures FNW and FSW than for structures FHW and FFW. This observation can be explained qualitatively by comparing displaced shapes (Fig. 5.19) with measured hysteretic behavior of members composing the test structures (Fig. B.5, B.6, and B.7). Measured moment-displacement relations for members indicated that pinching became more pronounced as

displacement amplitudes (distortions) increased. Displaced shapes of test structures indicate that top-level displacements (which were similar for all test structures during the first test) were composed of concentrations of high interstory drifts for structures FNW and FSW and more uniform distributions for FHW and FFW. The larger distortions in structures FNW and FSW should be expected to result in more pronounced pinching characteristics similar to those observed for large distortions in the static member tests.

"Primary" curves were estimated from measured responses to all three earthquake simulations so that stiffnesses and strengths of the test structures could be compared. The curves (Fig. 5.11) were constructed by tracing base moment-displacement curves and interpolating between measured peaks to obtain smooth curves. The primary curves indicate two apparent break points which might be attributed to the onset of "significant" cracking and "significant" yielding of the test structures. Beyond the onset of significant yielding, moments continue to increase at a decreasing rate as displacements increase. This behavior is to be expected as yielding spreads throughout a structure before the formation of a complete failure mechanism.

An apparent trend indicated in Fig. 5.11 is that, in terms of top-level displacement and base moment, structures FSW, FHW, and FFW had nearly equal stiffness and strength and that structure FNW had perceptibly less stiffness and strength. However, it should be emphasized that the stiffnesses suggested in Fig. 5.11 are effectively those of a single-degree-of-freedom system and that top-level displacement and base moment are not complete descriptors of that SDOF system. Characteristics of response as SDOF systems are considered in Sec. 6.2.

## 5.4 Measured Dynamic Characteristics of Test Structures

### (a) Low-Amplitude Frequency Response

Frequency-response curves were obtained from steady-state tests which were carried out after earthquake simulations. Base displacements for the tests were approximately sinusoidal and varied in steps from a frequency below the apparent first-mode resonant frequency to a frequency beyond resonance. Steady-state (constant-amplitude) response was attained before data were taken and the excitation frequency was increased to the next step. Base-displacement amplitudes were approximately 1 mm for the steady-state tests following each earthquake simulation. A higher-amplitude test was conducted following the third steady-state test with base-displacement amplitude of approximately 2 mm.

Frequency-response data are plotted in Fig. 5.12. Smooth curves drawn through datum points were selected arbitrarily to resemble response curves for linear systems. Nevertheless, the response curves resemble suspiciously those expected of nonlinear systems. Although it is not a specific objective of this study to investigate the frequency-response of nonlinear systems to sinusoidal excitations, brief consideration is deemed essential so that the relevance of these specialized, low-amplitude tests in estimating response to earthquake excitation can be placed in perspective. More-detailed analytical investigations can be found in the literature [5, 21, 22, 36, 37]. Several experimental investigations of the response of real buildings have also been reported (eg. Ref. [8, 10, 21, 25]). These experimental studies were conducted on structures that were "less damaged" and subjected to lower excitation levels than were test structures considered in this study.

Steady-state responses should be strongly influenced by the stiffness characteristics during the tests. Because maximum displacements during steady-state tests were less than half the maximum during previous earthquake simulations, the stiffnesses should be similar to the "pinched", low-moment stiffnesses observed during the simulations (Fig. 5.10). Hysteretic relations measured during resonant response of structures FNW and FFW to the first and second steady-state tests (Fig. 5.13) indicate various degrees of stiffening. Depending on the extent of stiffening, jump phenomena (sudden changes in response amplitude with small change in frequency) might occur in the frequency response curves (Fig. 5.12). Apparent jumps in the first tests of FNW and FSW are indicated by broken curves in that figure. Jumps were not observed for any other tests of those structures nor for any tests of structures FHW and FFW.

The tendency of a structure to stiffen with increasing displacement amplitude does not of itself guarantee that a "jump" will occur. All test structures were observed to stiffen as amplitudes approached previous maxima during earthquake simulations but jumps were not observed in all steady-state tests. The response amplitude in these steady-state tests were insufficient to result in the extent of stiffening required for a jump. Two factors controlling the amplitude were the energy dissipation (at low moment levels) and the excitation level. Different response characteristics would have been observed for different base-displacement amplitudes. This is apparent from the "high-amplitude" tests following the third earthquake simulations which resulted in frequency-response curves which were different from those observed for the lower-amplitude tests.

The relevance of the frequency-response curves to estimating response during earthquake excitation is obviously limited; these steady-state responses might indicate the extent and effects of "pinching" of the hysteretic response relationship (which were caused by the previous earthquake response) but provide limited insight into dynamic characteristics (such as energy dissipation and effective period or stiffness) which prevailed during the maximum earthquake response.

(b) Frequencies

Apparent modal frequencies were estimated from responses of test structures to free-vibration, steady-state, and earthquake-simulation tests. Resonant frequencies observed during steady-state tests (Fig. 5.12) were taken as estimates of first-mode frequencies. Averages of the three lowest apparent frequencies over durations of free-vibration and earthquake simulation tests were estimated from peaks on Fourier-amplitude spectra of top-level accelerations (Fig. 5.14 and 5.15). Additional estimates of fundamental frequencies were made from base-moment periods during the cycle of maximum response in earthquake simulations. The frequencies obtained by these estimates are plotted versus response history in Fig. 5.16 and 5.17. The maximum top-level displacement incurred during or before the indicated test is used to represent response history.

Initial frequencies estimated from free-vibration responses before the earthquake simulation are compared along the zero-displacement ordinate in Fig. 5.16. Measured first-mode frequencies were nearly identical for the three structures with walls and approximately twenty-percent lower for structure FNW. Second- and third-mode frequencies were different for all test structures, indicating that increasing the

wall height above the first level had an appreciable effect on "uncracked" higher-mode frequencies but little effect on the apparent first-mode frequency. Calculated uncracked frequencies (based on mean concrete modulus and uncracked transformed section properties) are listed in Table 5.2 and indicate similar ratios of first:second:third mode frequencies as those observed. The measured first-mode frequencies were between 5 and 10 per cent below calculated uncracked frequencies. Possible sources of discrepancy between measured and calculated values in an experimental environment have been discussed in several reports [1, 2, 13] and are not considered in detail here so as to avoid redundancy and also because of the limited relevance of "uncracked" properties on inelastic earthquake response. Reductions in stiffness attributable to concrete cracking before the tests (Fig. 4.2) are the main source of the discrepancy.

Apparent frequencies of all test structures decreased as the maximum top-level displacement experienced by a test structure increased (Fig. 5.16 and 5.17). The apparent first-mode frequencies measured in all tests were normalized with respect to measured initial frequencies so that relative decreases with increasing maximum displacement would be apparent (Fig. 5.18). The highest rate of decrease in frequencies occurred during the first earthquake simulation and at a progressively lower rate during subsequent tests. Expected variation in frequency was inferred from secant stiffnesses of measured base moment-top displacement primary curves (Fig. 5.11) by assuming a constant first-mode shape. The inferred curve is consistent with measured frequencies (Fig. 5.18) which indicated

a high rate of frequency-reduction for small displacements as cracking spread through a test structure.

Apparent frequencies varied not only with the maximum previous displacement experienced by a test structure but with the amplitude at which the frequency was measured (Fig. 5.17). The variation of frequencies normalized to the initial frequencies (Fig. 5.18) indicates trends which are similar for all test structures and which can be interpreted in terms of measured hysteretic relations (Fig. 5.10). Those hysteretic relations indicate that the structures generally softened as displacement maxima increased but that stiffness was effectively lower for low-amplitude motion which followed a maximum because of pinching in the low moment region. As should be expected, frequencies estimated from the cycles of maximum response were approximately the same as those inferred from measured secant stiffnesses (Fig. 5.18). Frequencies estimated from Fourier-amplitude spectra of earthquake responses (which were averages over response durations and would be dominated by response in the "pinched" region) were lower than those inferred from secant stiffnesses except in one case. Frequencies estimated from steady-state tests (which included response primarily in the pinched region) were also lower than the inferred relation (Fig. 5.18). Frequencies estimated from the free-vibration tests (which had the smallest top-level displacement of less than one mm) indicated a stiffer structure at very low amplitudes, which is opposite the trend apparent for the other frequency measures. Although it was not possible to measure stiffnesses at this low amplitude during dynamic tests, it is likely that some "threshhold" force was required before reinforcement slip could be initiated and that stiffness below that threshhold level was relatively high. This interpretation is

supported by observation of a threshhold and high stiffness below the threshhold in static tests of members which composed the test structures (Fig. B.5 ). Similar "threshhold" levels have been observed in static tests of full-scale members [3, 16, 29].

(c) First-Mode Shapes

Study of frequency content of measured responses in Section 5.2 indicated that displacements were dominated by response of an apparent fundamental mode. Characteristics of the observed first-mode shapes are studied in this section. The characteristics of these shapes are important for design considerations because of their dominant effect on displacements and interstory drifts. Shapes were obtained by filtering out all response components above 4.0 Hz which, as indicated in Fig. 5.8a, had little effect on observed shapes but insured that higher-mode components would be avoided.

Displaced shapes of the test structures determined from maximum responses to earthquake simulations are plotted in Fig. 5.19. Shapes were normalized to have the same top-level value. The influence of the wall on the shapes is apparent. With no wall, distortions were largest in the relatively-tall first story. With a one-story wall, distortions were markedly reduced in the first story with distortions above the wall cutoff only slightly larger than the maximum observed for the structure with no wall. The four- and nine-story walls apparently resulted in more uniform distributions of story distortion over the height. It is especially important to note that no distress was indicated (by sudden slope increases) above the wall-cutoff for structure FHW.

Moderate changes of the displaced shapes (Fig. 5.19) give an indication of progressive deterioration in relative story stiffnesses for earthquake simulations of increasing intensity. For structure FNW, changes in shape were small, indicating that relative story stiffnesses did not change much as response amplitude increased. For structure FSW, stiffnesses apparently decreased most rapidly in the upper stories of the frames rather than in stories immediately above the one-story wall cutoff. For structures FHW and FFW, the most rapid rate of deterioration occurred in the first story and was probably precipitated by deterioration in "shear" stiffness of the wall at the base (shear-sliding was observed across the flexural crack at the base of the walls during third earthquake simulations). The importance of these observed shapes and inferred deteriorations in relative story stiffnesses is that the most rapid deterioration did not appear to occur in stories where vertical interruptions in story stiffness had been introduced in the various structures.

To investigate the characteristics of the apparent mode shapes and to gage the effects of observed changes in shapes, test structures were reduced to effective SDOF systems based on observed shapes and test structure dimensions. The same procedure has been used in an experimental investigation by Abrams [1]. Quantities of interest include the mode shape, participation factor, and effective height and modal weight of the equivalent SDOF oscillator. The quantities are defined for an N-degree-of-freedom system as

$$\text{Participation Factor} = \frac{\sum_{i=1}^{N} m_i \phi_i}{\sum_{i=1}^{N} m_i \phi_i^2} \qquad (5.1)$$

$$\text{Effective Height} = \frac{\sum_{i=1}^{N} m_i \phi_i h_i}{\sum_{i=1}^{N} m_i \phi_i} \tag{5.2}$$

$$\text{Effective Modal Weight} = \frac{(\sum_{i=1}^{N} m_i \phi_i)^2}{\sum_{i=1}^{N} m_i \phi_i^2} \times g \tag{5.3}$$

where

$m_i$ = mass at level i

$\phi_i$ = ordinate of mode shape at level i

$h_i$ = height of level i above the base

g = gravity acceleration.

These are listed in Tables 5.3 and 5.4 for shapes observed during maximum response to earthquake simulations and steady-state tests. The small changes in these quantities for responses at different amplitudes indicate that test-structure responses which were dominated by the apparent fundamental mode could be represented by a SDOF system with unchanging mass and height. Responses in this category include displacements, base moment and, to a lesser extent, base shear. Similar observation had been made by Abrams for structures with "uniform" stiffness distribution over height. The interruptions studied in this report did not apparently affect this modal characteristic.

(d) Measures of Energy Dissipation

Measures of energy dissipation or effective damping factors can be determined from any dynamic test given arbitrary assumptions. The

measures so determined are equally arbitrary but can be useful within certain limitations. In this section, effective damping factors are determined for low-amplitude free-vibration and steady-state tests by viewing responses as if they were those of linear, viscously-damped, SDOF oscillators. It was considered reasonable to obtain equivalent viscous damping factors for these tests because response characteristics were reasonably constant and could be substituted by equivalent linear systems. The relevance of these damping factors to estimating response to earthquake simulations is probably small because of the low amplitudes of these tests relative to simulations.

Effective first-mode damping factors were determined from free-vibration responses by applying the log-decrement method to filtered top-level acceleration responses (Fig. 5.14). The estimated damping factors are listed in Table 5.5. Because free-vibration responses were probably at an amplitude below that required to initiate pinching in the moment-displacement relation, it is likely that damping factors determined from these tests reflect the extent and effect of concrete cracking. Changes in effective damping factors (Fig. 5.20) suggest damping factors below two percent for "uncracked" specimens and increasing to as much as ten percent for heavily-cracked specimens.

Response amplitude in steady-state tests was sufficiently large to cause reinforcement slip and pinching in the moment-displacement relation (Fig. 5.13). Estimates of effective damping factors were made at two different amplitudes for each test. The first estimate related damping as one-half of the reciprocal of the observed resonant amplification. A half-power bandwidth method was used to obtain a second estimate as

$$\beta = \frac{\omega_2 - \omega_1}{2\omega_r} \qquad (5.4)$$

where $\beta$ = damping factor

$\omega_1$ and $\omega_2$ = frequencies at response amplification of $1/\sqrt{2}$ times maximum amplification

and $\omega_r$ = resonant frequency $\approx 1/2 * (\omega_1 + \omega_2)$ .

The calculation procedure assumed that maximum magnification had not been measured. An arbitrary maximum amplification was selected from which one value of $\beta$ could be evaluated using expression 5.1 and a second value evaluated as half the reciprocal of the assumed maximum. A correct solution was assumed when the "arbitrary" amplification resulted in two identical estimates of $\beta$. This procedure should give an effective damping factor at an amplitude below the observed resonant amplitude.

The damping factor estimates are listed in Table 5.6. For the first tests of structures FNW and FSW, the half-power estimates were higher than the estimates based on maximum observed resonant response. The estimate based on the observed resonant response would be effective specifically for a linear, viscously-damped system responding at maximum amplification. The estimate based on the half-power method would specifically be effective for a lower amplitude. The lower effective damping inferred at the higher amplitude would be expected because the hysteresis is narrowly pinched as the test structure begins to stiffen (Fig. 5.13). For all tests other than the first tests of FSW and FNW, damping factor estimates by either method were essentially the same and may have reflected the observation that stiffening was less pronounced for these tests. The damping estimates ranged between five and twenty percent of critical (Table 5.6).

# 6. INTERPRETATION OF RESPONSE USING LINEAR MODELS

This chapter investigates briefly the use of linear models to interpret the earthquake response of the test structures. In the first section, three analytical models based on different assumptions of member stiffness are used to compare modal-spectral and static lateral-force procedures for the test structures. One of the analytical models, for which member stiffnesses were inferred from experimental measurements, may be used to verify approximately the first-mode characteristics measured during earthquake simulations. The latter section of this chapter compares measured response maxima with maxima estimated using linear response spectra and measured first-mode properties.

## 6.1 Comparison of Modal-Spectral Analysis with an Equivalent Static Procedure

Two analysis procedures are generally recognized for design of buildings for earthquakes. These are modal-spectral analysis and static analysis using a set of equivalent lateral forces. Modal-spectral analysis is intended to account approximately for modal characteristics of a building and for effects of base excitation on each response mode. Equivalent static force procedures prescribe a set of lateral story forces (or story shears) for which a building is to be analyzed. The magnitude of lateral forces is either directly or indirectly based on the fundamental period of the building, with higher-mode effects approximated through the selection of the particular force distribution. Neither method can be described as being preferable in all cases; modal analysis may provide better estimates of forces for unusual structures but in most cases will not be worth the extra computational effort. The methods are compared below for the structures investigated in this report.

(a) Description of Linear Models and Analysis Procedure

The analytical model was the same as that used for design of the test structures (Sec. 2.2a and Fig. 2.3). To investigate the influence of stiffness assumptions on calculated quantities three different assumptions of member stiffness were considered. To parallel current design practice, member stiffnesses for the first model were based on uncracked section. Member stiffnesses for a second model were based on fully-cracked section. A third model ("experimental" model) had stiffnesses which were inferred from the experiment.

Stiffnesses for the "experimental" model were inferred from measured dynamic responses of test structures and measured static properties of members which composed the test structures (App. B). As discussed in App. B, column stiffnesses could be represented satisfactorily by fully-cracked section (Fig. B.8). Wall stiffnesses were based on uncracked section unless maximum story moments measured during the initial earthquake simulation exceeded the cracking moment, in which case the stiffness was based on fully-cracked section (Fig. B.12). Beam stiffnesses were derived from the measured curves for the beam-column assemblies (Fig. B.9). The stiffness was obtained by connecting the origin to a point on the measured envelope corresponding to the maximum displacement recorded during the initial earthquake simulation for each story (Table 4.2). In addition, rotational springs were included at the base of walls and columns to account for deformation concentrations observed in static component tests. The values of the wall spring stiffnesses were calculated as the stiffness required to obtain measured first-story displacements for the wall moment distributions measured at the time of maximum response. Rotational springs

at the base of columns for FNW were selected so that the calculated and measured ordinate of the first-mode shape would be the same at the first-story level. Stiffnesses are summarized in Table 6.1.

It should be noted that the models based on gross- or cracked-section member properties can be obtained for design analyses. The experimental model would not be available for design of a building. It is used in this study to provide a "best" estimate of effective linear stiffnesses in the test structures so that the static and modal-spectral methods may be compared more critically.

The equivalent-static-lateral-force method used lateral story forces which were proportional to height (linear distribution). Other distributions are possible. Modal-spectral analyses were performed using the design spectrum proposed by Shibata [ 32 ] at ten percent damping (Fig. 2.5). This spectrum represents the simulated El Centro record satisfactorily (Fig. 5.4b). All modal-spectral quantities were taken as the RSS of the lowest three modes. Damping was equal for all modes.

All calculated quantities were normalized for a unit base shear so that static and modal-spectral quantities could be compared independently of a prescribed design base-shear coefficient. No attempt is made in this section to estimate response maxima.

(b) Comparison of Calculated Responses for Unit Base Shear

Mode shapes calculated for the three linear models are compared in Fig. 6.1. Also shown are the apparent first-mode shapes measured at the time of maximum response (see Section 5.4c). Modal participation factors are included. The shapes calculated for experimentally-obtained stiffnesses compare closely with the measured shapes. However, except at the

first level of structures with walls, the shapes were insensitive to the assumed distribution of stiffness.

Calculated modal frequencies are listed in Table 6.2. As would be expected, frequencies were sensitive to stiffness assumptions. The fundamental frequencies for the experimentally-inferred model compare closely with those measured during the earhtquake simulations. Although an infinite number of "incorrect" stiffness assumptions could result in the "correct" frequency, it is likely that the agreement between calculated and measured frequencies indicates a nearly correct distribution of assumed stiffnesses because of the procedure used to obtain the experimentally-inferred model.

Story shears obtained using the static and modal-spectral procedures are compared in Fig. 6.2 . There is no consistent trend in comparing the shears for different stiffness assumptions because different modal shapes and frequencies result in different modal-spectral shears. However, for design purposes, either of the static or modal-spectral procedures resulted in practically the same story shears for the test structures.

One reason for the similarity between story shears obtained using the two procedures lies in the similarities between the first mode shapes and the linear shape. For the models considered, the higher-mode shears add most noticeably to the upper-story shears, resulting in modal story shears which are close to the linear distribution. Another reason for the similarity in story shears is that all shears were normalized to a base shear equal to one. However, this does not have a significant influence on the comparison because higher-mode shears tend to be small near the base because of phase relations of the higher-mode story forces.

Story shears may tend to be an insensitive measure by which to compare the equivalent static and modal-spectral procedures. Because the test

structures had "abrupt" interruptions in adjacent story stiffness or strength, calculated column moments provide an interesting and sensitive measure for comparisons. It will be noted that modal-spectral column moments are taken as the RSS of the individual modal moments.

Interior column moments obtained from modal-spectral analysis are plotted in Fig. 6.3 . Column moments obtained using the static procedure are not plotted because they were nearly identical to those obtained using the modal-spectral procedure. By the two procedures, the maximum difference between calculated maximum column moments in a story was approximately ten percent. For these structures, modal-spectral analysis provided no additional insight into forces in vertical members near the "interruptions" for any of the assumed stiffness distributions. This is because of the similarity between the first-mode and linear force-distribution shapes and because higher-mode shapes were similar for test structures with and without wall cut-offs (Fig. 6.1 ).

Assumptions of member stiffnesses had significantly more influence on calculated member forces than the analysis procedure. Column base moments changed substantially in structures with walls when stiffnesses were changed from gross-section to cracked-section stiffness and again when changed from cracked-section stiffness to the experimentally-inferred stiffness (Fig. 6.3). Although less apparent in intermediate and upper stories, column moments changed markedly at several locations because of differences in the relative member stiffnesses as different member stiffness assumptions were used. Although none of the distributions in Fig. 6.3 can be assumed correct, it is apparent that the assumption of member stiffness had a more significant effect on distribution of "design" forces than did the analysis procedure for these structures.

## 6.2 Evaluation of Response to Earthquake Simulations Using SDOF Oscillators

Comparison of linear modal-spectral and equivalent-static-force procedures in Sec. 6.1 indicates that, for a particular assumed distribution of effective member stiffnesses, either method is "equally suitable" for determining the relative distributions of member forces for the test structures. However, no attempt was made to estimate the magnitude of "design" forces. In this section, estimates of maximum base forces and top-level displacements are made using a SDOF oscillator with properties based on measured "first-mode" characteristics. Before the estimates are made, the suitability of representing the test structures by linear SDOF systems is discussed.

Response measurements indicate that test structures responded inelastically during design and subsequent earthquake simulations. Despite the inelastic response and the intentional introduction of abrupt changes in story stiffnesses of adjacent stories, observed displaced shapes were observed to be similar for different response amplitudes. In addition, measured displacements, base shears, and base moments were dominated by responses of apparent fundamental modes. These characteristics suggest that test structure responses might be interpreted using SDOF oscillators.

Representative SDOF systems can be defined by measured effective heights and masses and by measured envelopes of load versus deformation. Effective heights and masses were based on displaced shapes measured at the time of maximum response during earthquake simulations (Table 5.3). Envelopes of base moment versus SDOF displacement can be derived from measured envelopes of base moment versus top-level displacement (Fig. 5.11) by factoring the top-level displacement axis by the ratio of top-level displacement to SDOF displacement. The ratios (participation factors) are listed in Table 5.3.

Approximate envelopes of base-shear and top-level displacement can be scaled from corresponding peaks on top-level and base-shear waveforms. The envelopes can then be normalized to SDOF displacement. The base moment and shear envelopes are plotted on Fig. 6.4.

To be consistent with the SDOF concept, base shear and moment for a particular displacement should be related by the effective SDOF height. However, the measured envelopes (Fig. 6.4) could not be related by an effective height because of the contributions of higher modes to inertial forces. To demonstrate the influence of higher modes, distributions of response over structure height are plotted for initial and third simulations of structure FNW (Fig. 6.5). In that figure, actual inertial forces are compared with forces which were filtered at 4.0 Hz to provide a comparison with forces expected based on the apparent first-mode displacement response. The influence of higher modes on inertial forces was significant, particularly for third simulations. Maximum base shear and moment did not in all instances occur simultaneously and, if they did, often resulted from loading distributions which were different from the assumed first-mode shape. Thus, it should not be expected that a SDOF representation which relies on an assumed shape will provide accurate estimates of base shears or base moments.

As indicated above, the treatment of test structures as SDOF systems cannot provide precise representation of all response quantities. The concept is useful, however, in design applications where multidegree-of-freedom systems are represented by several SDOF oscillators having natural frequencies equal to those of individual response modes. To evaluate the validity of this concept, maximum top-level displacements, base shears, and base moments were estimated for earthquake simulations using linear response spectra (Fig. 5.3). Use of the spectra required estimates of effective periods, damping factors, and modification of the spectra as described below.

Response periods during cycles of maximum response were difficult to measure because of higher-modes, base-motion effects, and residuals. For this reason, fundamental periods were approximated using envelopes of moment-displacement response (Fig. 6.4a) and measured first-mode shape characteristics (Table 5.3). The estimated variations of frequency with displacement amplitude agree well with frequencies inferred from cycles of maximum response (Fig. 6.6).

Effective damping factors could not be estimated reliably from steady-state or free-vibration tests because of the low response amplitudes obtained in those tests. Rather, a range of damping factors was estimated using a procedure analogous to that used for estimating member damping in the design process (Sec. 2.2). Fully-cracked stiffness of a test structure was calculated as the base-moment per unit top-level displacement using the design analytical model (Fig. 2.3), fully-cracked section properties for members, and a triangular loading distribution. An overall structure damage ratio for a particular earthquake simulation was calculated as the ratio of fully-cracked to measured secant stiffness at maximum dispalcement. A substitute damping factor for the entire structure was then evaluated using expression 2.1. Damage ratios and estimated damping factors are summarized in Table 6.3. It is worth noting that the listed damping factors were within the range of factors estimated from free-vibration and steady-state tests (Tables 5.5 and 5.6).

Displacement spectra were used to estimate maximum top-level displacement by (1) estimating the range of frequencies from the beginning of the simulation to the end using Fig. 6.6, (2) estimating maximum SDOF displacement for the calculated damping factor as the maximum displacement ordinate for that range of frequencies, and (3) modifying the SDOF displacement

using measured first mode shapes for a particular test structure to obtain top-level displacement. The calculated displacements are compared with measured displacements in Fig. 6.7a. Displacements calculated by assuming ten percent critical damping are compared in Fig. 6.8a.

The displacements estimated from calculated damping factors agree exceptionally well with measured displacements for the design simulation. Estimates for subsequent simulations are satisfactory (within twenty percent of measured displacements). Estimates of top-level displacement based on the arbitrarily-selected ten-percent damping do not agree as well for the first simulation. However, all the estimates were satisfactory.

Base shear and moment estimates were made directly from estimates of SDOF displacements by using first-mode response frequencies (Fig. 6.6) and first-mode shape characteristics. The estimated base forces are plotted versus measured forces in Fig. 6.7 and 6.8 for the calculated damping factors and for the arbitrarily-selected ten-percent damping. The calculated quantities do not agree with the measured quantities as well as the displacements did. This is to be expected because of the influence of higher modes on the measured base shears and moments.

In summary, responses of test structures to earthquake simulations were viewed using SDOF systems having measured displaced shape characteristics. Base shears and moments were found to be influenced moderately by higher modes so that precise definition of a SDOF system was not possible. However, for design applications, a SDOF approach yielded satisfactory estimates of response. Fundamental frequencies could be estimated with measured stiffnesses and reasonable damping factors could be estimated by viewing an entire structure as a single member. Effective damping factors ranged from 6 to 13 percent of critical. Estimates of response maxima that would be suitable for

for design were estimated using linear response spectra, effective frequencies, and effective damping factors.

# 7. INTERPRETATION OF RESPONSE USING NONLINEAR MODELS

Test-structure responses are studied in this chapter using simple nonlinear models to interpret stiffness, strength, and time-response characteristics. Limiting strengths are interpreted using a rigid-plastic model with static member strengths obtained from static tests of members composing the test structures. A model which considers inelastic load-deformation characteristics of individual members is used to obtain estimates of the overall load-deformation characteristics of the test structures not provided by the rigid-plastic model. Measured and calculated stiffness and strength characteristics are used with a simple SDOF model to estimate the time responses of test structures. It should be noted that simple models are adopted where possible so that the possible uses of such models for design and analysis may be investigated.

## 7.1 Strength of Test Structures

Strength of a multistory building is not a unique quantity. It varies depending on the distributions of external loading and of internal strength. Measured envelopes of base moment versus top-level displacement which were presented in Sec. 5.3 implied base-moment strengths for test structures during dynamic tests. Bounds of base shear strength were also estimated based on maximum measured base shears (Fig. 6.4). Because of the influence of varying inertial load distributions, the quantities of maximum base shear and moment did not in all instances occur simultaneously and did not define unique strength quantities. Strengths of test structures are evaluated in terms of base shear and moment in this section so that

the credibility of measured quantities may be studied.

(a) Assumed Strength Distribution in Test Structures

Strength distributions in test structures are defined as distributions of member strengths throughout a structure. Distributions of frame and wall reinforcement are listed in Fig. 2.10a and nominal member dimensions are presented in Fig. 2.1 and 2.10. Measured mean gross dimensions and clear cover to reinforcing steel in frames and walls were nearly identical to the nominal dimensions (Tables A.1 and A.2). Based on known dimensions and material properties, distributions of flexural strength can be estimated and can be verified by strengths observed from static tests of small-scale members which were representative of test-structure members (App. B). The calculation methods (which are indicated in App. B) produced satisfactory agreement with measured static strengths of beam-column assemblies, columns, and walls. It should be noted, however, that measured beam strengths consistently exceeded the calculated strengths by between five and ten percent. Calculated flexural strengths are summarized in Table 7.1. Shear strength in members was not a primary concern because of excesses of transverse reinforcement.

(b) Strength Under Static Loading

After the third earthquake simulation, a lateral load was applied at the centroid of the top-level mass of each test structure. This load was increased until failure occurred or appeared imminent so that the static strength of the structure could be estimated for a particular loading. It should be noted that displacements on the order of four percent of height had been reached during the previous earthquake simulation.

Load-deformation curves measured during static strength tests are presented in Fig. 7.1. The curves originate at the displacement residual

incurred during previous testing and load initially at a relatively-high slope. Incremental stiffnesses decreased gradually as apparent strengths were approached. For structure FNW, failure was preceded by plastic hinging of beams over the structure height (as judged by crack widths). The maximum load was followed by sudden collapse of the first story. For structure FSW, plastic hinging appeared to occur in members above the wall cutoff. For FHW and FFW, apparent collapse mechanisms included columns and walls at the base and beams at all levels. Total collapse of structures FSW, FHW, and FFW was avoided.

Comparison of calculated stiffnesses (based on fully-cracked section for all elements) with those measured (Fig. 7.1) indicates that initial slopes for the structures with walls were close to the fully-cracked slopes. The perceptible deviation for FNW may be attributed to larger drifts experienced by that structure and to the effect of vertical loads on column moments in the first story (approximately half of the top displacement occurred in the first story).

Strengths for test structures with a single load at the top level were investigated using a rigid-plastic limit analysis. Plastic hinges were allowed to form at any beam-column face (so that rigid joint cores were recognized), at the base of first-story columns, and at the base or any story level of walls. Assumed flexural strengths of members were based on calculated ultimate capacities (Table 7.1). Using the principle of virtual work, the combination of plastic hinges which was geometrically admissible and which resulted in the minimum external work of the applied force was assumed to indicate the collapse load and mechanism.

Calculated collapse mechanisms for the static tests are depicted in Fig. 7.2. The mechanisms were the same as those observed in static tests

for FNW, FSW, and FFW. For FHW, calculated hinging was indicated only in the frame above the wall cutoff. The observed mechanism for FHW included yield over the full height of the frames and the base of the wall. The calculated load was seven percent higher for the observed mechanism than for the calculated mechanism.

The loads required to form the calculated collapse mechanisms are compared with observed strengths in Fig. 7.1. Observed strengths exceeded calculated strengths by 8, 19, 14, and 20 percent of calculated strengths for structures FNW, FSW, FHW, and FFW, respectively. The discrepancy between measured and calculated strengths cannot be attributed to error in the estimate of wall strength because calculated wall strengths were nearly identical to strengths measured during static tests (Fig. B.13) and because the wall participated in the calculated mechanism only for structure FFW. It is also unlikely that underestimation of column strengths accounted for the discrepancy because column strengths did not contribute significantly to the overall resistance. Required increases in beam flexural strengths, based on the calculated mechanisms, were 8, 27, 30, and 29% above calculated strengths. These increases could not be accounted for based on the 5 to 10 percent increases in beam strength indicated by static tests of beam-column assemblies (App. B).

It may be possible that actual beam strengths were increased at large deformations because of restraint of the connections used to attach story weights to beam-column joints (Fig. A.1). In a test structure, adjacent joints would tend to separate after cracking as beam-column interfaces rotated relative to one another. Upper bounds of joint separation were estimated using the model illustrated in Fig. 7.3. Beams were assumed to rotate about column faces at a neutral axis depth of 5 mm (which is less

than the probable depth at strength for lightly reinforced beams). Using measured mean dimensions, the calculated separation between adjacent joints was as follows:

| Joint Rotation, (radians) | Joint Separation (mm) |
|---|---|
| 0.01 | 1/3 |
| 0.02 | 2/3 |
| 0.03 | 1 |
| 0.04 | 5/4 |

Allowable joint separations measured for the connectors were approximately one mm. Based on the sum of residual crack widths measured following third simulations, separations exceeding 0.7 mm were credible. By comparison with the calculated upper-bound joint separations listed above, increases in beam strength caused by the experimental setup would not occur until joint rotations or interstory drifts (which would be composed almost entirely of inelastic rotations) exceeded approximately two percent. In light of the large displacements attained during the strength tests, it is likely that excesses of strength can be attributed to the experimental setup.

The static tests do indicate limits of forces which could be carried by the first-story of test structures.

The maximum base-moment measured during the static tests (including the P-delta moment) was approximately 29 kN-m for structures with walls and 26 kN-m for structure FNW. The limiting moment that could be carried by elements framing into the foundation can be estimated as

$$M_b = M_w + \Sigma M_c + d \times T \qquad (7.1)$$

where

$M_b$ = limiting base moment capacity

$M_w$ = static wall flexural strength

$\Sigma M_c$ = sum of static column flexural strengths

$d$ = centerline distance between exterior columns

and

$T$ = change in axial force in exterior column.

Considering dead load and tensile strength of flexural reinforcement, the maximum change in axial force for an exterior column was 12.3 kN for structures with walls and 19.5 kN for FNW. Using Eq. 7.1, limiting base-moment capacities are 29 and 39 kN-m for structures with and without walls. The strengths for structures with walls were apparently limited by moment capacity, while the strength of structure FNW was not.

The observed collapse mechanism for structure FNW involved formation of yield hinges at tops and bottoms of first-story columns. The first-level displacement before the collapse was 50 mm, resulting in a P-delta moment of 2.0 kN-m. Using calculated flexural strengths of columns less the P-delta moment, the calculated collapse base shear for this mechanism is 10.0 kN which is nearly identical to the observed collapse load. This indicates that the strength for FNW was limited by base shear capacity, even for the case of a single load at the top.

(c) Strengths During Earthquake Simulations

Strengths observed during static tests cannot be used to estimate the strengths observed during earthquake simulations because of differences in loading distributions for the tests. During earthquake simulations, several distributions of inertial loads were observed for each test structure (Fig. 4.10, 4.18, and 4.20). Depending on the magnitude and distributions of the loadings over the structure height, several collapse mechanisms were possible for a particular test structure.

One loading distribution which is convenient because it is easy to use and because it is similar to the first mode shape is a linear distribution with forces varying linearly from zero at the base to a maximum at the top level. Collapse mechanisms were calculated using the limit-analysis model described in Sec. 7.16. The calculated mechanisms and base forces are shown in Fig. 7.4. It should be noted that collapse mechanisms and base forces were nearly identical to those calculated using loading distributions proportional to the measured first-mode shapes (Table 5.3).

Calculated collapse base shears and moments for the linear loading distribution are compared for various mechanisms in Fig. 7.5. For each structure, mechanisms were assumed to originate at the base and to extend to various levels. Additional mechanisms for FSW and FHW considered the story above the wall cutoff to be the lowest story to participate in the mechanism. The mechanisms illustrated in Fig. 7.4 correspond to the minimum collapse base forces in Fig. 7.5. However, considering that several different mechanisms resulted in nearly-minimum base forces, it must be concluded that the actual mechanisms cannot be described with certainty.

The loading distributions measured during dynamic tests could be expected to result in a wide variety of calculated collapse mechanisms.

The rate at which the story-force distributions changed was significant during design simulations. The rates increased during subsequent simulations because of increased contributions of higher modes (Fig. 6.5). Calculation of mechanisms for dynamic loadings was not applicable because of the rapidly-changing force distributions. In addition, mechanisms could not be based on filtered components of measured inertial forces because filtering resulted in "smooth", illusory forces whereas actual inertial forces resulted from "spiked" acceleration histories.

In contrast with individual inertial forces, changes in base shears and moments were "slower". Strengths of test structures during earthquake simulations are evaluated relative to these base forces. Base-moment capacity was estimated using Eq. 7.1 with the maximum axial-force change in columns taken as the sum of the limiting beam shears in an external bay. For FNW, the limiting base-shear capacity was estimated as the shear required to reach flexural strengths at tops and bottoms of first-story columns, including effects of the P-delta forces.

Calculated base-moment capacities are compared with measured maxima for the first two earthquake simulations. The third earthquake simulation is not included in the comparison because of possible beam strength increases during that test due to test setup restraints (See Sec. 7.1b). The calculated and measured base moment quantities (in kN-m) are

| Structure Base Moment | | FNW | FSW | FHW | FFW |
|---|---|---|---|---|---|
| Calculated | | 21.0 | 22.7 | 22.7 | 22.7 |
| Measured: | Run 1 | 19.3 | 21.3 | 22.7 | 23.8 |
| | Run 2 | 23.2 | 25.1 | 25.8 | 25.8 |

Maximum base moments exceed the calculated strengths by 10, 11, 14, and 14 percent of calculated for structures FNW, FSW, FHW, and FFW. Possible sources of discrepancy include an underestimate of beam strengths (strengths in static member tests consistently exceeded calculated strengths by 5 percent) and strain rate effects.

To investigate possible strain rate effects, wall base moments measured during dynamic loading are compared with measured static flexural strengths (in kN-m) below. The measured dynamic moments are taken as one-half of the maximum and minimum base moment measured in a test so that possible error resulting from unrecorded construction forces is avoided.

| Wall Base Moment | FSW | FHW | FFW |
|---|---|---|---|
| Static | 4.9 | 4.9 | 4.9 |
| Dynamic | 5.8 | 5.2 | 5.2 |
| $\frac{\text{Dynamic}}{\text{Static}}$ | 1.18 | 1.06 | 1.06 |

Increases in dynamic wall flexural strength over the static strengths were between 6 and 18 percent as compared with increases in test-structure base-moment capacity between 10 and 14 percent. As estimated from base-moment waveforms, wall and structure base moments increased from zero moment to the maximum in less than 0.1 sec. In addition, calculated structure base-moment capacity relied on beam strengths which may have been subjected to higher loading rates because of the more rapidly changing inertial forces in upper story levels. In light of observed high loading rates, the observed strength increases are credible.

The measured maximum base shear for FNW during the third simulation was 12.6 kN. Including the equivalent base shear due to gravity forces acting

through the first-story displacements, the effective maximum base shear was 14.0 kN. Base-shear capacity was calculated as 14.6 kN.

(d) Summary of Observed Strengths

Calculated capacities were compared with those measured during static and dynamic tests of the test structures. The comparison indicates that strength increases were likely at large displacements because of restraint of the experimental setup. The experimental setup is not expected to have influenced strengths in the first and second earthquake simulations. For the dynamic tests, explicit collapse mechanisms could not be calculated because of the rapidly-changing inertial forces acting at each level. Base-moment capacities were nearly reached during the first (design) simulations. Base moments measured during the second simulations exceeded the calculated capacities by as much as 14 percent. The increase is attributed to strain rate effects.

## 7.2 Interpretation of Test Structure Stiffness Under Monotonic Loading

The stiffnesses of the test structures are not readily defined because of the abrupt changes in stiffness and strength in adjacent stories. A quantitative measure of the change in stiffness is also difficult to define. Two alternatives for investigating analytically the effects of the stiffness interruptions, in the inelastic range of response, are dynamic response analyses or static analyses for a monotonically-increasing lateral force distribution. The static approach is adopted here because it provides a controlled environment in which to view critically the behavior of the test structures. A linear distribution of lateral loads is selected to approximate the first-mode distribution so as to provide insight into displacement responses which were dominated by the apparent first mode.

Numerical computations for the analyses were performed using a computer program written by K. Emori [ 7 ]. The program was developed to investigate the inelastic response of uniform, multistory wall-frame structures and was modified for the present study to handle nonuniform story heights. The program is capable of performing dynamic-response analyses. For this study, only the static-analyses was used. For simplicity, a distribution of lateral forces with loads proportional to height was used to approximate a "first-mode" loading. It should be noted that calculated responses were relatively insensitive to the small differences between the linear and "first-mode" distributions of loading.

(a) Analytical Procedure

The model used for analysis is depicted in Fig. 7.6. The model considered a frame and wall connected in parallel with rigid links at story levels and with elements fixed at the base. Members were represented by line elements (coincident with member centerlines) which considered flexural, shear, and axial deformations with the exception that beams were axially rigid. The line elements representing beams and columns were connected by rigid joint cores. Geometric nonlinearities (such as the effect of gravity force acting through lateral displacements) were ignored. For the test structures and for the range of displacements investigated, these effects are small.

Beams and columns were idealized as elastic line elements with inelastic rotational springs located at member ends. Load-rotation of the spring operated on a trilinear curve. For computational efficiency the rotational springs at opposite ends of a member were uncoupled by assuming points of contraflexure at midlength of the member. This should result in negligible error for beams. The idealization is incorrect for columns where points of

contraflexure are expected to shift. Considering that load-deformation relations of the test structures were dominated by inelastic response of the beams, the idealization should be satisfactory.

For a slender wall, line elements are considered to be acceptable. To account for the more general distribution of moment over the wall height, a multiple-spring model is used. The model consists of line elements of variable length (Fig. 7.6) connected in series. The moment-curvature relation of each element operates on a trilinear curve. The centroid of each element is used to define the current element flexibility.

The model was loaded with lateral loads applied at each story-level centerline. The model responds linearly during each load increment. Stiffnesses are reevaluated following the increment and unbalanced forces resulting from change in member stiffness are added to the next load increment. A monotonically increasing static loading with forces proportional to height was used for the present study. Forty load increments were used to define response to top-level displacements equal to two percent of height.

Details of the computer program and analysis assumptions are given in Reference [ 7 ].

(b) Assumed Member Properties

Load-deformation properties of members were calculated based on assumed material properties. Modifications to calculated beam and first-story wall properties were required to obtain responses representative of responses obtained from static member tests (App. B).

Assumed steel and concrete properties were based on measured properties (Fig. 7.7). To account approximately for the uncertain effects of concrete shrinkage and construction stresses on cracking moments, moduli

of rupture were artificially reduced to one-half of the mean measured moduli. Moment-curvature relations were calculated using these assumed properties and the assumption of linear strain across a section. End rotations due to reinforcement pullout were based on the model in Fig. 7.8 and an assumed bond stress of 2.0 MPa [ 11 ]. Shear deformations were calculated with an arbitrarily assumed shear modulus equal to one-fourth of the initial compression modulus for concrete. The relatively large reduction was intended to account approximately for reductions in effective shear modulus due to concrete cracking. It should be noted that shear stiffness was not a primary concern because deformations were predominantly flexural.

Moment-rotation relations for beams and columns were calculated using the above assumptions and column axial loads indicated in Fig. 7.6. Moment was assumed to vary linearly along the member length. End rotations due to curvature were calculated by taking the moment of curvatures along the length (Fig. 7.9). Additional end rotations due to shear deformations and reinforcement pullout were added. The calculated moment-rotation relations are idealized as trilinear curves with breakpoints at calculated cracking and yield moments (Fig. 7.10). The calculated slopes compare satisfactorily with measured slopes (App. B) for columns. For beams the calculated second breakpoint was below the measured breakpoint resulting in a low yield moment and high slope to ultimate. A modified relation, as inferred from static member tests, is represented by the broken curve in Fig. 7.10a.

Moment-curvature relations for walls were determined from the assumed material properties. Because the computer program used for analyses of test structures did not automatically include effects of reinforcement

pullout at the base of walls, modified moment-curvature relations were required for wall elements located in the first story. The additional first-level displacement due to reinforcement pullout was taken from static wall tests (App. B). Modified effective moment-curvature relations were then calculated based on assumed moment distributions equal to those measured at the time of maximum displacement during design simulations (Fig. 4.10). The resulting moment-curvature relations are idealized as trilinear curves in Fig. 7.10b.

(c) Calculated Response to Monotonic Loading

Responses to a monotonically-increasing, linear load distribution were calculated initially using the calculated moment-rotation relations for members. It should be noted that calculated relations for beams did not compare satisfactorily with measured relations. Results of these analyses are compared in this section with results obtained using beam moment-rotation relations inferred from measured beam behavior to establish the sensitivity of calculated results to assumed member properties.

The calculated moment-displacement response of test structures based on the calculated beam properties can be interpreted using Fig. 7.11. The models responded linearly to base moments of approximately five kN-m after which cracking was indicated. Calculated yield occurred first in beams, at top-level displacement of approximately five mm. Beam yield was followed in gradual succession by yield in columns and walls, resulting in a rounded "yield" for overall response. The steep loading slope of the models beyond apparent yield is attributable primarily to the "steep" post-yield slope calculated for the beams.

In comparison with moment-displacement relations inferred from measured hysteresis in test structures (Fig. 5.11), the calculated response exhibited

yield at a lower moment but continued at a relatively steep slope for a longer displacement range: the calculated transition range was longer than the observed one. The earlier yield of the numerical models was due to the assumed beam yield moments which were smaller than those measured in tests of beam-column assemblies. Further comparison with the measured structure responses indicates that slopes beyond apparent yield were closely approximated by the static analyses. However, it must be pointed out that the program assumes no limit to individual member capacities. Accordingly, the program does not automatically indicate limits to overall strength and will continue to produce output which may be comparable to measured overall response but which is associated with absurdly high internal moments. Beyond top displacements of one percent of height, calculated interactions among members are questionable because of excessively high forces assumed to be resisted by beams.

Because of the above-mentioned discrepancies and because calculated beam behavior did not represent the best available information, interpretations of test-structure responses for the remainder of this section are based on the modified beam moment-rotation relations (broken curves in Fig. 7.10a). Calculated responses of test structures using the modified beam properties are interpreted in relation to Fig. 7.12 which compares calculated moment-displacement response for the test structures subjected to the monotonic static loading.

Initial elastic stiffnesses compare well with measured base-moment stiffnesses (Fig. 7.12a). The comparison is also good up to base moments of 10 kN-m, suggesting that the artificial reduction of concrete rupture moduli (to account for uncertain initial stresses) was reasonable.

Calculated slopes to top displacements of ten mm were consistently higher than measured slopes (see Fig. 7.16 for comparison of slopes based on measured hysteresis of test structures). The discrepancy could have been caused by error in the estimated virgin secondary slopes for members. More likely, the discrepancy was attributable to stiffness reductions in test structures caused by reversed loading conditions during earthquake simulations.

Differences in the calculated and measured "break points" corresponding to significant yield in the test structures cannot be ascribed to any single cause with certainty. During the dynamic tests, softening caused by cyclic loading would tend to increase the displacement at which yield would be noticeable. High strain rates would tend to increase the yield stress and strain at which overall structure yield would appear. In addition, actual loading distributions were generally different from the assumed linear distribution and might result in moderately different moment and shear stiffnesses and strengths.

One trend should be noted in comparing the calculated and measured "yield" transitions and slopes beyond yield (Fig. 7.12a and b). As discussed in Sec. 6.2 and 7.1, participation of higher modes increased as the base-motion intensity was increased in successive simulations, resulting in inertial force distributions which deviated significantly from the linear distribution. In Fig. 7.12a, calculated and measured base-moment stiffnesses after yield were most similar for FFW with greater discrepancy observed for structures in order of decreasing wall height. Using the principle of virtual work, the base-moment capacity of FFW should be independent of loading distribution because of the nearly-linear displaced

shape [ 1 ]. In contrast, the best agreement between measured and calculated base-shear stiffness (Fig. 7.12b) occurs for FNW, with decreasing correlation between calculated and measured stiffness as the wall height increases. Again using virtual work principles, base-shear resistance for a structure in which displacements are equal at all levels should be independent of loading distribution. The measured displaced shapes for structure FNW were nearly equal to the shape with equal displacements at all levels. It is reasonable to conclude that differences in loading distribution accounted at least partially for discrepancies between measured and calculated stiffnesses beyond apparent yield.

Although it is certain that loading distributions and loading reversals during earthquake simulations influenced internal member force distributions, a reasonable interpretation of the internal responses and failure patterns can be made using the calculated monotonic response. However, it should be recognized that responses beyond apparent yield depended on assumed member stiffnesses after member yield and that post-yield stiffnesses are difficult to estimate for reinforced concrete members. This was pointed out previously in relation to calculated and measured beam behavior.

Calculated yield patterns are illustrated in Fig. 7.13 for the left halves of frames (symmetric with right portion) and walls, and the calculated displacement at first yield is indicated in Fig. 7.14. As calculated, yield was expected to initiate in beams at top displacements of approximately 0.4 percent of height. Calculated yield spread rapidly over the structure height for FFW because of the nearly-linear displaced shape. Yield spread over intermediate and lower stories of the other structures.

For elasto-plastic member behavior, a collapse mechanism is defined by a combination of yield "hinges" which allows incremental displacement without increasing load. For test structures, effective yield mechanisms were calculated to have formed at top displacements of approximately 1.5 percent of height (Fig. 7.13). The mechanisms agree with those calculated using limit analyses (Sec. 7.1). Because of the small but perceptible stiffnesses assumed for members after yield, the calculated mechanisms spread to adjacent stories as loads and displacements were increased. The extent of spreading was subject to the assumed post-yield stiffnesses which, as discussed previously, cannot be defined with certainty.

It is noteworthy that calculated base response of walls in FHW and FFW were nearly identical (Fig. 7.14). Yield was expected to occur at essentially equal top displacements, and the percentages of total base shear resisted by the wall were nearly identical for various stages of structural "damage." The calculations simulate correctly the base-shear responses measured during dynamic tests in that approximately 60 percent of the total shear was resisted by the wall in each structure. The calculated response for the wall in FSW was significantly different from that in FHW and FFW. In near agreement with measured response, the wall resisted approximately 90 percent of the total base shear. The measured percentage was slightly higher.

Calculated displaced shapes for top displacements equal to 0.5, 1.0, and 2.0 percent of overall height are plotted in Fig. 7.15, The shapes are compared with those observed at times of maximum top displacement in first and second simulations. Top drifts in these simulations were approximately 1.0 and 2.0 percent. Comparison indicates little change in calculated shapes for this drift range. Calculated shapes compare

satisfactorily with observed shapes. Small differences in slopes for FNW, FSW and FHW indicate larger measured interstory drifts in upper stories relative to lower stories. These may have been caused by concentrations of inertial forces in upper levels which were not included in the static analyses. Comparisons of shapes of FHW and FFW for drifts of two percent of height indicate larger measured first-story drifts than calculated. These discrepancies were caused by wall sliding at the base during dynamic tests. Wall sliding was not considered for the analytical model.

The similarity between measured and calculated displaced shapes (Fig. 7.15) indicates that the monotonic loading simulates satisfactorily the relative stiffness of adjacent stories in the test structures. Moderately-high story drifts in the lower stories for FNW and FSW were estimated well. Despite the interruption in story stiffness introduced by the wall cutoff in FHW, the analysis correctly estimated the "smooth" transition between levels with and without the wall. It should be noted that, for these structures, similar patterns of story drift were also indicated by elastic analyses (See Sec. 6.1).

The relatively large drifts in stories immediately above the wall cutoff in FSW would be expected because of the large transition in story "shear stiffness" caused by "cutting off" the wall and because of the large shears in lower stories. Large drifts might be expected in FHW above the wall cutoff, also. However, it should be observed that the walls in FHW and FFW, while resisting large proportions of total base shear, deformed primarily in flexure. As indicated by the experiment and by the calculations, relatively-large interstory drifts occurred in intermediate stories with relatively low shear forces acting on the wall. The large drifts without correspondingly-high shears were possible because of all wall rotation attributable to flexural deformations in lower stories of the walls.

## 7.3 Study of Dynamic Response Using Nonlinear SDOF Models

Static analysis using a monotonic loading provides a simple but satisfactory measure of the overall force-deformation characteristics of the test structures. Using static analysis, an understanding of the stiffness, strength, and failure patterns may be obtained without complications introduced by multidegree-of-freedom nonlinear dynamic analyses. However, interpretations of response are incomplete without an estimate of the magnitude of lateral forces or, preferably, of the maximum displacement that can be expected for a particular base motion or class of base motions. It was demonstrated in Sec. 6.2 that the displacement maxima could be estimated satisfactorily using modal-spectral analyses. In this section, an approach to estimating displacement maxima and waveform is investigated using simple nonlinear SDOF models. The sensitivity of this approach is investigated using measured and calculated force-deformation primary curves, two simple hysteresis models, and two approximate approaches to satisfying dynamic equilibrium. The study is an extension of work initiated by Saiidi [31].

### (a) Analysis Procedures for the Nonlinear SDOF Models

Two approaches to modelling the test structures as SDOF oscillators were investigated in this study. Both approaches use approximations to represent mass and stiffness properties, so neither should be expected to provide a "correct" result. Rather, the models are investigated to determine whether simple models may be used to estimate the dynamic response of structures which are similar to those tested in the course of this study. The first model, which was developed and used extensively by Saiidi [31], is referred to as the Q-model. The second, which is developed in this study, is a modified Q-Model and will be referred to as the MQ-Model.

The equation of motion for the Q-Model is derived from Biggs [4]. For an N-degree-of-freedom structure, the undamped SDOF equation of motion is

$$M_{eff}\,\ddot{X} + KX = -\,M_T\,\ddot{X}_g \tag{7.2}$$

where

$$M_{eff} = \frac{1}{\phi_X}\,\frac{\sum_{i=1}^{N} m_i\,\phi_i^2}{\sum_{i=1}^{N} m_i\,\phi_i}\,M_T$$

$m_i$ = mass at level i

$\phi_i$ = ordinate of mode shape at level i

X = displacement of an arbitrary point on the structure relative to the base (having the ordinate $\phi_X$)

K = stiffness of structure for load distribution equal to distribution of external forces

$M_T$ = total mass of structure

$\ddot{X}_g$ = base acceleration.

For the Q-Model, both the displaced shape and stiffness are defined using lateral forces varying linearly from zero at the base to a maximum at the top (linear distribution). An effective height, which is used to relate base shear to base moment, is taken as

$$L_{eff} = \frac{\sum_{i=1}^{N} m_i\,\phi_i\,h_i}{\sum_{i=1}^{N} m_i\,\phi_i} \tag{7.3}$$

where

$h_i$ = height of level i above the base.

The Q-Model was demonstrated by Saiidi to produce reasonable estimates of response for several small-scale structures. However, the Q-Model, while simple to use, relies on a derivation resulting in expressions for stiffness and mass not conveniently interpretable in terms of physical concepts (see pp. 116-119 in Biggs for the derivation and original expression for the SDOF system). For this reason, an alternative approach, the MQ-Model, was developed. In deriving the equation of motion for the MQ-Model it is assumed that the structure oscillates in a shape which does not change for different response amplitudes. The equation of motion can be written from equilibrium as

$$\sum_{i=1}^{N} (\ddot{X}_g + \ddot{X}_i)\, m_i + V = 0 \qquad (7.4)$$

where

$X_i$ = displacement of level i relative to the base

and

V = base shear.

Using the assumed shape, Eq. 7.4 may be rewritten

$$\left(\frac{1}{\phi_X} \sum_{i=1}^{N} m_i\, \phi_i\right) \ddot{X} + V = - M_T\, \ddot{X}_g \qquad (7.5)$$

In Eq. 7.5, the base shear can be expressed as a function of the displacement, X, for a particular loading. Because the predominant

distribution of inertial forces observed during the earthquake simulations was proportional to the apparent first-mode shape, the effective height given by Eq. 7.3 is used to relate base shear and base moment. In addition, displaced shapes and stiffnesses can be calculated using the linear load distribution (which approximates the first mode).

For both the Q- and MQ-Models the monotonic load-deformation curve is idealized as either a bilinear or trilinear relation. These load-deformation relations and assumptions for load reversal are discussed in Sec. 7.3b.

Equivalent viscous damping was assumed to be two percent of critical based on the initial circular frequency. The frequency is calculated as the square root of the ratio of initial stiffness to effective mass.

The equations of motion for the SDOF models were solved numerically using the computer program LARZAK and a modified hysteresis model. The first six seconds of base motion were analyzed. The program is described in References [30] and [31].

(b) Stiffness and Mass Properties

Stiffnesses of the SDOF models under monotonic loading were based on envelopes of base moment versus top displacement and on the effective heights defined by Eq. 7.3. The arbitrary choice of base moment rather than base shear was made because of lower contributions of higher modes to base moment responses observed during earthquake simulations.

Three different moment-displacement primary curves were used for each test structure to calculate response histories:

(1) A measured moment-displacement relationship based on an envelope to maxima observed in earthquake simulations (Sec. 5.3).

(2) A moment-displacement relationship calculated for a linear lateral-load distribution using the program developed by Emori [ 7 ] (Sec. 7.2).

(3) A moment-displacement relationship estimated using the simple procedure described below.

The "estimated" moment-displacement relationship was assumed to be trilinear. Breakpoints were selected at the intersection of the uncracked stiffness with the "cracking strength" and at the intersection of the fully-cracked stiffness with the "limit strength." Stiffnesses were calculated for a linear load distribution with member stiffnesses based on either uncracked or fully-cracked section. The "limit strength" was obtained for the linear load as described in Sec. 7.1c. Because of uncertainties in construction and shrinkage stresses, only an approximation of the structure "cracking strength" is considered justified. Thus, the cracking strength is calculated by substituting member cracking strengths (based on one-half of the measured rupture modulus) for flexural strengths in Eq. 7.1 with the change in column axial load taken as the sum of limiting beam "cracking" shears in an exterior bay. The slope of the linear segment from the second breakpoint was selected arbitrarily at five percent of the slope from the origin to the second breakpoint.

The measured, calculated, and estimated primary curves are compared for the four test structures in Fig. 7.16. As may be observed in that figure, the estimated curves approximate closely the measured and calculated envelopes for displacements below the onset of member yielding. As would be expected, the estimated curves do not represent yielding well. A measure of the "goodness" of the estimated curve beyond yield might be defined by an overall structure damage ratio which is taken as the ratio of fully-cracked

stiffness to secant stiffness. For top-level displacements ranging between 1.0 and 1.5 percent of height (which is considered reasonable for design), the damage ratios of the calculated and estimated curves compare closely (Table 7.2). Based on this damage ratio, the estimated curve appears to provide a quick and acceptable estimate of the secant stiffness beyond yield. The "goodness" of the estimated curve is compared further in the discussion of calculated response histories (Sec. 6.3c).

For convenient analysis of the response of the SDOF models, the primary curves (Fig. 7.16) were idealized into trilinear curves. Breakpoints were selected to represent significant cracking and yielding. An ultimate point was selected on the envelope curve at a top displacement equal to two percent of height. The selected breakpoints are sumaarized in Table 7.3.

Effects of load reversals are modelled with one of two hysteresis models which operated on either the trilinear curve or a bilinear curve with a single breakpoint at yield (second breakpoint in Table 7.3). The "bilinear" model (Q-Hyst model) was developed by Saiidi [31]. The "trilinear" model, which was devleoped for this study, was a modified Q-Hyst model which operated on the trilinear envelope. These are described briefly below.

The bilinear (Q-Hyst) model is linearly elastic for displacements below the assumed yield point. Subsequent loading follows the envelope curve to ultimate. Unloading follows the slope given by

$$S_{unl} = \left(\frac{\delta_y}{\delta_m}\right)^{1/2} S_y \qquad (7.6)$$

where

$S_{unl}$ = unloading slope

$\delta_m$ = maximum previous displacement in either direction

$\delta_y$ = yield displacement

$S_y$ = slope from origin to yield point

Reloading in either direction follows a path to a point symmetric on the envelope curve corresponding to $\delta_m$.

The trilinear model is linearly elastic to the "cracking" breakpoint. Subsequent loading follows the envelope curve. Unloading from a point beyond the yield breakpoint on the envelope curve has a slope

$$S_{unl} = \left(\frac{\delta_y}{\delta_m - \delta_r}\right)^{1/2} S_y \qquad (7.7)$$

where $\delta_r$ is selected to result in a desired residual when unloading from the yield breakpoint. Based on measured hysteresis for the test structures, the selected residual was 20 percent of the displacement at yield. Between the cracking and yielding breakpoints, unloading slopes vary linearly between the uncracked slope and the slope given by Eq. 7.7. Reloading is identical to reloading in the bilinear model.

It should be noted that these hysteresis models are quite simple by comparison with other models [31]. The bilinear model has only four rules. In the trilinear model, the loading and unloading slopes are "switched" after the yield displacement has been reached in either direction, so little additional complication is introduced. The simplicity of the models is consistent with the simplicity of the SDOF concept.

Displaced shapes for the models are based on the shapes measured at maximum displacement, calculated at top displacement equal to one percent of height, or based on fully-cracked member properties for the measured, calculated, and estimated envelope curves, respectively. These shapes are tabulated in Tables 5.3 and 7.4.

Effective masses based on Eq. 7.2 or 7.5 for the Q- and MQ-Models, respectively, were calculated from the displaced shapes and story masses. To be consistent with stiffnesses (which were defined relative to top displacement), the effective masses (Table 7.3) were calculated relative to the top displacement. Using these masses and stiffnesses, the SDOF model can be solved to obtain directly the top-level displacement response. Effective heights (which relate approximately the base shear to base moment) are also summarized in Table 7.3.

(c) Comparison of Measured and Calculated Responses

Top-displacement and base-moment response histories were calculated for the first six seconds (half the test duration) of base acceleration measured on the south frames of test structures during the first earthquake simulation. Calculated response histories are compared with the measured responses in Fig. 7.17 and 7.18 for the Q- and MQ-Models. In those figures, responses of all four test structures calculated using the bilinear hysteresis with the measured primary curve are compared first. Subsequent responses are compared for the four structures using the trilinear hysteresis with the measured, calculated, and estimated primary curves, respectively. Base accelerations, displacements, and moments have units of g, m, and kN-m. Calculated and measured displacement maxima are compared over the height of a structure in Fig. 7.19. The measurements refer to the instant at which the maximum top-displacement was recorded.

In comparing calculated and measured responses, it should be recognized that the calculated maximum base moment is an insensitive quantity

which is effectively limited by the strength assigned to the model. However, base moment provides a good measure of the response period because it does not incur residuals. In the following discussion, comparison of measured and calculated waveform shapes and maxima refers to the displacement response.

The response waveforms calculated using the bilinear measured curve do not match the measured waveforms well (7.17a and 7.18a). Calculated initial periods are longer than the measured periods because of the low initial slope in the bilinear hysteresis. After approximately 1.2 sec. the calculated responses exceed measured responses because no energy is dissipated through hysteresis until the yield displacement is reached. Because calculated response maxima exceed measured maxima, the model becomes excessively "soft" for high-amplitude responses, with consequently longer response periods. For structure FNW, which had the most pronounced "pinching" in measured hysteresis loops (see Sec. 5.3), the "softened" SDOF model provides the most satisfactory match with the measured waveform. However, it should be noted that pinching is not explicitly included in this hysteresis model, and that the satisfactory agreement between measured and calculated responses for FNW is a consequence of the excessively large responses during the first few seconds of the calculation.

Maximum displacements calculated using the bilinear hysteresis do not deviate severely from those measured (Fig. 7.19a), but considering that equally good estimates of maxima could be obtained using modal-spectral methods with the correct damping, use of the bilinear hysteresis would not be justified for these structures. For this reason, all subsequent responses in this chapter are calculated using the trilinear hysteresis.

Using the trilinear hysteresis with the measured primary curves resulted in better estimates of the waveforms for all but structure FNW (Fig. 7.17b and 7.18b). It should be noted that the waveforms match more closely throughout the duration for structures with taller walls. The poorer performance for FNW and FSW may in part be attributed to the more pronounced "pinching" observed in hysteresis loops for these structures. It should also be noted that the SDOF models do not indicate displacement residuals accurately. This might be attributed to the fact that the hysteresis model is "damaged" symmetrically about the origin, wheareas the test structures may not be damaged symmetrically.

Comparison of waveforms for the Q- and MQ-Models (Fig. 7.17b and 7.18b), respectively) indicates similar estimates of response waveforms were obtained with either model. Comparison of displacement maxima (Fig. 7.19b) indicates that the MQ-Model provides a moderately better estimate for these structures. However, on the basis of waveform shape and maxima, either model may be considered satisfactory.

The SDOF response estimates based on the trilinear hysteresis with the calculated primary curves are presented in Fig. 7.17c, 7.18c, and 7.19c. Measured and calculated waveform shapes for FHW and FFW match closely. However, the Q-Model underestimates the response maxima and both the Q- and MQ-Models underestimate the response near the end of the analysis. The response for FNW and FSW do not compare as favorably. Both models underestimate the responses of FNW and FSW at the time of maximum measured response. However, with the exception of maximum response amplitudes and slightly smaller periods as a consequence, the overall waveform shapes are satisfactory.

Maximum displacements are compared in Fig. 7.19c. The comparison between measured and calculated maxima is perceptibly better for the MQ-Model, although it should be noted that the calculated maximum for FSW does not occur at the same time as the measured maximum. The maximum responses obtained using the calculated primary curves compare as well with the measured maxima as do the responses obtained using the measured primary curves (Fig. 7.19b).

Response waveform obtained using the "estimated" primary curves (which were based on linear stiffnesses and limiting strengths) are plotted in Fig. 7.17d and 7.18d. With the Q-Model, calculated and measured waveforms compare well for FSW and FHW. The calculated waveform for FFW is markedly different throughout the duration, probably because of the large error in the "estimated" yield breakpoint (Fig. 7.16). The response for FNW is similar to responses estimated using the measured and calculated primary curves. The MQ-Model produces better estimates of the waveform shape for all four test structures than does the Q-Model.

Response maxima obtained using the estimated primary curves are compared in Fig. 7.19d. Estimated maxima for FNW and FFW obtained using the Q-Model are low by more than 25 percent. Response maxima for the MQ-Model are satisfactory for all test structures and compare favorably with those obtained using the more-sophisticated nonlinear monotonic analyses (Sec. 7.3).

In summary, it was found that the bilinear hysteresis model produced reasonable estimates of response maxima but failed to reproduce the waveform satisfactorily. This was because the bilinear hysteresis does not model

stiffness characteristics and hysteretic energy dissipation below the yield displacement. The trilinear hysteresis model, which was developed to model closely the hysteresis below the yield displacement, produced better estimates of the response in most instances. Neither the bilinear nor trilinear models account explicitly for stiffness loss attributable to slip of reinforcement, which may have been the reason for poorer estimates of response for FNW. However, because the extent of the stiffness loss is not generally known for a structure and because of the additional complications involved in estimating that stiffness loss, it is not recommended to model this behavior for the simple SDOF analysis.

Performance of the Q- and MQ-Models was comparable when using the trilinear hysteresis with the measured or calculated primary curves. However, the Q-Model tended to underestimate response maxima. The MQ-Model produced estimates of maxima that would be suitable for design using all three primary curves.

The economy of either the Q- or MQ-Models used with the "estimated" primary curves is noteworthy. Calculation of the waveform using the "calculated" or "estimated" primary curves requires the same effort. However, the "estimated" primary curve can be obtained using readily-available concepts and analysis procedures whereas the "calculated" primary curve may not be so readily obtained. Considering that the "design" earthquake motion cannot be "predicted" accurately, inaccuracies resulting from defining the primary curve with elastic stiffnesses and limiting strengths are not unreasonable.

# 8. SUMMARY AND CONCLUSIONS

## 8.1 Object and Scope

The objectives of this study were (1) to investigate experimentally the inelastic earthquake response of multistory, reinforced concrete structures with nonuniform distributions of stiffness and strength in the vertical plane and (2) to investigate analytically the use of simple linear and nonlinear models to obtain estimates of observed responses.

(a) Experimental Work

Four small-scale structures (total height of 2.29 meters) were built and tested (Fig. 2.1 and 2.2). The effectively two-dimensional test structures were composed either of two frames which were situated parallel and opposite one another or of two frames with a centrally-located "slender" wall. The frames had nine stories with the first story twice the height of other stories. One test structure comprised frames only. Three other structures had walls extending from the base to levels one, four, and nine (top level), respectively. In the experimental setup, the frames and wall were constrained to displace equally at each story level. Story weights (460 kg each including tributary weight of structure) were carried vertically by the frames at each level.

Frames and walls in a test structure were cast monolithically with stiff foundation girders using a small-aggregate concrete having mean compressive strength of 38 MPa. Flexural reinforcement in frames was 2.32 mm dia. wire (mean yield stress of 399 MPa) and in walls was 6.65 mm dia. wire (mean yield stress of 339 MPa).

Distributions of flexural reinforcement were determined using principles of the substitute structure method [ 32 ] with design flexural

stiffnesses for columns, beams, and walls equal to fully-cracked stiffness, one-sixth of fully-cracked stiffness, and one-third of fully-cracked stiffness, respectively. Distributions of flexural reinforcement (Fig. 2.10a) were identical in the three test structures with walls. Additional flexural reinforcement was provided in lower stories of the structure without a wall. Transverse reinforcement was provided in all members to preclude primary failure in shear.

Tests included three earthquake simulations of successively increasing intensity, free-vibration tests, steady-state tests with sinusoidal base excitation, and static tests with lateral loads applied to individual story levels. All dynamic excitations and loadings were in the plane of the structures. Earthquake simulations were modelled after El Centro NS-1940 with the time scale compressed by a factor of 2.5. The first simulation had a nominal peak acceleration of 0.4 g and was the motion for which the test structures were designed.

Measurements during testing include base motions and response displacements, accelerations, and forces acting between frames and wall. Story shears and moments were determined from test-structure dimensions and measured responses.

(b) Data and Studies

Simulated earthquake response data are presented and discussed in Chapter 4.

Base motions are evaluated in terms of Fourier-amplitude spectra, linear response spectra, and spectrum intensities in Sec. 5.1.

Discussion of measured frequency response, hysteretic relations between top displacement and base moment, apparent first-mode characteristics, and effective damping in low-amplitude tests is given in Chapter 5. The

interrelation among these quantities is also discussed.

Modal characteristics were calculated using a linear model with various member stiffness assumptions in Chapter 6. Comparison is made between modal-spectral and equivalent static analyses for the test structures. Response estimates are made using measured "first-mode" properties and linear spectral-response curves.

Limiting strengths of test structures are evaluated in Sec. 7.1.

Stiffness and collapse characteristics are investigated for a monotonically-increasing, linear distribution of lateral loads using a nonlinear computer program developed by Emori [ 7 ] in Sec. 7.2.

A nonlinear SDOF model is used to obtain estimates of measured displacement responses in Sec. 7.3. The effects of various assumptions related to SDOF mass, stiffness, and hysteretic properties are studied. A simple approximation to representing the test structures as SDOF systems is introduced.

## 8.2 Observations

### (a) Observations Related to the Experiment

The following observations are made on the basis of measured responses.

(1) Responses to design (initial) earthquake simulations were in the inelastic range as demonstrated by measured hysteretic relations and by displacement and wall-force residuals. Apparent fundamental periods during the design simulation lengthened to approximately twice the measured initial ("uncracked") periods. Overall structure damage ratios, which are defined as the ratios of elastic stiffness (for a linear distribution of lateral loads and members fully-cracked) to secant stiffness observed during design earthquake simulations, were between 1.6 and 1.9.

(2) Top-level displacement maxima (approximately one percent of height

during the design test) were similar for the test structures subjected to nearly identical base motions, despite differences in the vertical distribution of stiffness and strength. Top-displacement waveforms were nearly identical for the structures with four- and nine-story walls, with perceptible differences observed for the structures with no wall and one-story wall.

(3) For a given test structure, displaced shapes were nearly constant for all top displacements exceeding approximately 0.2 percent of height. For different structures, the displaced shapes were different (Fig. 5.19). Maximum observed story drifts during design simulations were 2.0, 1.9, 1.4, and 1.4 percent of story height for structures in order of increasing wall height.

(4) The design procedure used to proportion flexural reinforcement was successful in terms of observations (2) and (3) above.

(5) Envelopes of base moment versus top displacement were nearly identical for the three structures with walls and lower for the structure without a wall. Structures with taller walls tended to resist greater base shear, particularly during second and third earthquake simulations. During design simulations, ratios of maximum structure base shear to total structure weight were approximately 0.3 for all four test structures.

(6) The maximum force acting between a wall and frame was nearly the same for the structures with four- and nine-story walls and more than twice as large for the one-story wall (where approximately 95 percent of the total structure base shear was transferred to the wall at the first level).

(7) During design simulations, walls in the structures with four- and nine-story walls resisted approximately 60 percent of the total structure base shear, and the one-story wall resisted approximately 95 percent of

the total. The corresponding maximum nominal shear stresses at the base of walls were 1.0 and 1.6 MPa.

(8) Measured hysteretic relations between top displacement and base moment can be described as those of a "softening-stiffening" system. Secant stiffnesses were softer whenever new displacement maxima (in the inelastic range) were attained. However, after the apparent "yield" displacement had been exceeded, incremental stiffnesses at low amplitudes increased with increasing displacement (Fig. 5.10). This is consistent with measured hysteresis of constituent members (App. B).

(9) Measured base moment-top displacement hysteresis relations, which resembled those for a SDOF system, could be used with apparent first-mode shapes to interpret measured frequencies, effective damping factors, and responses to steady-state sinusoidal base excitation, all of which varied with the maximum previous displacement and with the displacement amplitude at which the measurement was made.

(b) Observations Related to the Use of Simple Models

The following observations are made on the basis of linear and nonlinear analytical studies.

(1) For the same assumed distribution of member stiffness and for equal base shears , modal-spectral analysis provided little additional insight into "design" forces over that provided by an equivalent static procedure (with lateral forces proportional to height and mass). The assumption of member stiffness had a more significant effect on "design" member forces than did the analysis procedure.

(2) Displacement maxima could be interpreted using linear SDOF systems with "effective" stiffness defined by base moment-top displacement secant stiffnesses. Using a procedure analogous to that used in the

substitute structure design method [ 32], maximum displacements could be estimated reliably using linear response spectra and frequencies and damping estimated from the ratio of fully-cracked to "effective" stiffness (overall structure damage ratio).

(3) Limiting base shears and moments were estimated in terms of strengths which could be developed by those members connecting to the foundation. Principles of limit analysis (using static member strengths) could not be used to estimate maximum base forces. This discrepancy was attributed to the influence of high loading rates at intermediate and upper levels of the test structures.

(4) Measured moment-displacement relations, displaced shapes, wall base forces, and failure patterns could be interpreted using monotonic loading (linear force distribution) of an analytical model which accounted for inelastic behavior of constituent members. However, the analysis, which is costly in terms of time and momey, can err if incorrect assumptions of member properties are used. For the test structures, an approximation of the measured moment-displacement relation of the overall structure could be obtained economically using elastic member stiffnesses and estimated "cracking" and limit strengths (Sec. 7.3).

(5) Displacement waveforms and maxima of the multistory test structures could be approximated by a nonlinear SDOF model. Results based on a SDOF model as defined by Saiidi [ 31] and on a similar model defined in this study were both satisfactory. Estimates of response improved if force-displacement models accounting for hysteretic energy dissipation before overall structure yield were used.

## 8.3 Concluding Discussion

The four test structures responded during design earthquake simulations near the bounds estimated by the design method. Maximum displacement at the top level exceeded the design displacement by a maximum of five percent. Measured first-story drifts exceeded the design values. Drifts in other stories were within the design bounds. As judged by residual crack widths, yield was limited primarily to beams and walls. It is concluded that the distribution of reinforcement specified by the design method resulted in the type of behavior intended.

Response during design and subsequent simulations was in the inelastic range. The overall hysteretic behavior of the test structures (defined by the relation between base moment and top displacement) was similar to the complicated hysteresis of members composing the test structures. Response characteristics depended not only on the maximum displacement attained previously but on the response amplitude at which measurements were made. Quantities such as effective period or effective damping could be estimated during low-amplitude tests following earthquake simulations, but the estimates cannot be expected to represent the same quantities that were effective during higher-amplitude responses.

Effects of terminating walls at intermediate levels in the test structures cannot be interpreted in terms of "shear stiffness" of a story. Although the walls resisted large proportions of total base shear, deformations were primarily flexural so that large interstory drifts were possible in intermediate stories without large shear forces in the wall. Interaction among the frames and wall for a representative distribution of lateral forces should be considered. In this study, modal analysis and static analysis (with lateral forces proportional to height and mass) both provided

satisfactory estimates of effects of the "interruptions" in terms of measured relative story distortions. Simple equivalent-lateral-force analysis would have been satisfactory to determine the member force distributions (relative strengths of beams, columns, and walls) in the test structures.

Displacement response could be determined by modelling test structures as SDOF oscillators. Close estimates of displacement maxima could be obtained using modal-spectral analysis. Using a procedure developed previously for one-story frames or single members [13], estimates of effective damping suitable for design were obtained based on the overall structure "damage ratio," which is defined (Sec. 6.2) as the ratio of overall, fully-cracked structure stiffness to effective stiffness for a particular displacement amplitude. Displacement waveforms and maxima could be estimated using nonlinear SDOF models and response-history analysis. Response of the nonlinear SDOF model could be approximated by:

(1) obtaining elastic stiffness for a lateral distribution of forces proportional to height and mass,

(2) obtaining limiting strengths using conventional limit-analysis,

(3) defining SDOF mass properties based on actual masses and elastic displaced shapes, and

(4) calculating the response history for a particular base motion.

With the above procedure, estimates of response suitable for design can be obtained using simple structural concepts and modest computational facilities.

# LIST OF REFERENCES


1. Abrams, D.P., and M.A. Sozen, "Experimental Study of Frame-Wall Interaction in Reinforced Concrete Structures Subjected to Strong Earthquake Motions," Civil Engineering Studies, Structural Research Series No. 460, University of Illinois, Urbana, May, 1979.

2. Aristizibal-Ochoa, J.D., and M.A. Sozen, "Behavior of Ten-Story Reinforced Concrete Walls Subjected to Earthquake Motions," Civil Engineering Studies, Structural Research Series No. 431, University of Illinois, Urbana, October, 1976.

3. Bertero, V.V., and E.P. Popov, "Seismic Behavior of Ductile Moment-Resisting Reinforced Concrete Frames," in Reinforced Concrete Structures in Seismic Zones, Publication SP-53, American Concrete Institute, Detroit, 1977, pp. 247-291.

4. Biggs, J.M., Introduction to Structural Dynamics, McGraw-Hill Book Co., 1964.

5. Caughey, T.K., "Sinusoidal Excitation of a System with Bilinear Hysteresis," Paper No. 60-APM-8, Journal of Applied Mechanics, Vol. 27, December, 1960, pp. 640-643.

6. Cecen, H.M., "Response of Ten-Story Reinforced Concrete Frames to Simulated Earthquakes," Doctoral Dissertation, Graduate College, University of Illinois, Urbana, May, 1979.

7. Emori, K., and W.C. Schnobrich, "Analysis of Reinforced Concrete Frame-Wall Structures for Strong Motion Earthquakes," Civil Engineering Studies, Structural Research Series No. 457, University of Illinois, Urbana, December, 1978.

8. Englekirk, R.E., and R.B. Matthiesen, "Forced Vibration of an Eight-Story Reinforced Concrete Building," Report No. 66-8, Department of Engineering, University of California, Los Angeles, January, 1966.

9. Ferguson, P.M., Reinforced Concrete Fundamentals, John Wiley and Sons, Inc., 1958.

10. Foutch, D.A., "A Study of the Vibrational Characteristics of Two Multi-story Buildings," Earthquake Engineering Research Laboratory, California Institute of Technology, Pasadena, September, 1976.

11. Gavlin, N., "Bond Characteristics of Model Reinforcement," Civil Engineering Studies, Structural Research Series No. 427, University of Illinois, Urbana, April, 1976.

12. Gilbertsen, N.D., and J.P. Moehle, "Experimental Study of Small-Scale R/C Columns Subjected to Axial and Shear Force Reversals," Civil Engineering Studies, Structural Research Series No. 481, University of Illinois, Urbana, July, 1980.

13. Gulkan, P., and M.A. Sozen, "Inelastic Response of Reinforced Concrete Structures to Earthquake Motions," Journal of the American Concrete Institute, Vol. 71, No. 12, December, 1974, pp. 601-609.

14. Gulkan, P., and M.A. Sozen, "Response and Energy Dissipation of Reinforced Concrete Frames Subjected to Strong Base Motions," Civil Engineering Studies, Structural Research Series No. 377, University of Illinois, Urbana, May, 1971.

15. Hamming, R.W., Numerical Methods for Scientists and Engineers, McGraw-Hill Book Co., 1973.

16. Hanson, N.W., "Seismic Resistance of Concrete Frames with Grade 60 Reinforcement," Journal of the Structural Division, ASCE, Vol. 97, No. ST6, Proc. Paper 8180, June, 1971, pp. 1685-1700.

17. Healey, T.J., and M.A. Sozen, "Experimental Study of the Dynamic Response of a Ten-Story Reinforced Concrete Frame with a Tall First Story," Civil Engineering Studies, Structural Research Series No. 450, University of Illinois, Urbana, August, 1978.

18. Hognestad, E., "Study of Combined Bending and Axial Load in Reinforced Concrete Members," Engineering Experiment Station Bulletin Series No. 399, University of Illinois, Urbana, November, 1951.

19. Housner, G.W., "Behavior of Structures During Earthquakes," Journal of the Engineering Mechanics Division, ASCE, Vol. 85, No. EM4, Proc. Paper 2220, October, 1959, pp. 108-129.

20. Housner, G.W., "Strong Ground Motion," in Earthquake Engineering, ed. R.L. Wiegel, Prentice-Hall, Inc., 1970, pp. 75-92.

21. Ibanez, P., "Identification of Dynamic Structural Models from Experimental Data," UCLA-ENG-7225, School of Engineering and Applied Science, University of California, Los Angeles, March, 1972.

22. Jennings, P.C., "Periodic Response of a General Yielding Structure," Journal of the Engineering Mechanics Division, ASCE, Vol. 90, No. EM2, Proc. Paper 3871, April, 1964, pp. 131-166.

23. Kreger, M.E., and D.P. Abrams, "Measured Hysteresis Relationships for Small-Scale Beam-Column Joints," Civil Engineering Studies, Structural Research Series No. 453, University of Illinois, Urbana, August, 1978.

24. Moehle, J.P., and M.A. Sozen, "Earthquake-Simulation Tests of a Ten-Story Reinforced Concrete Frame with a Discontinued First-Level Beam," Civil Engineering Studies, Structural Research Series No. 451, University of Illinois, Urbana, August, 1978.

25. Nielsen, N.N., "Dynamic Response of Multistory Buildings," Earthquake Engineering Laboratory, California Institute of Technology, Pasadena, 1964.

26. Otani, S., and M.A. Sozen, "Behavior of Multistory Reinforcement Concrete Frames During Earthquakes," Civil Engineering Studies, Structural Research Series No. 392, University of Illinois, Urbana, November, 1972.

27. Otani, S., and M.A. Sozen, "Simulated Earthquake Tests of R/C Frames," Journal of the Structural Division, ASCE, Vol. 100, No. ST3, March, 1974, pp. 687-701.

28. Park, R., and T. Paulay, Reinforced Concrete Structures, John Wiley and Sons, Inc., 1975.

29. Popov, E.P., "Seismic Behavior of Structural Subassemblages," Journal of the Structural Division, ASCE, Vol. 106, No. ST7, Proc. Paper 15519, July, 1980, pp. 1451-1474.

30. Saiidi, M., "User's Manual for the LARZ Family," Civil Engineering Studies, Structural Research Series No. 466, University of Illinois, Urbana, November, 1979.

31. Saiidi, M., and M.A. Sozen, "Simple and Complex Models for Nonlinear Seismic Response of Reinforced Concrete Structures," Civil Engineering Studies, Structural Research Series No. 465, University of Illinois, Urbana, August, 1979.

32. Shibata, A., and M.A. Sozen, "Substitute-Structure Method for Seismic Design in R/C," Journal of the Structural Division, ASCE, Vol. 102, No. ST1, Proc. Paper 11824, January, 1976, pp. 1-18.

33. Sozen, M.A., S. Otani, and N.N. Nielsen, "The University of Illinois Earthquake Simulator," Proceedings, Fourth World Conference on Earthquake Engineering, Santiago, Chile, January 13-18, 1969, Vol. III, Session B5, pp. 139-150.

34. Staffier, S.R., and M.A. Sozen, "Effect of Strain Rate on Yield Stress of Model Reinforcement," Civil Engineering Studies, Structural Research Series No. 415, University of Illinois, Urbana, February, 1975.

35. Takeda, T., M.A. Sozen, and N.N. Nielsen, "Reinforced Concrete Response to Simulated Earthquakes," Journal of the Structural Division, ASCE, Vol. 96, No. ST12, Proc. Paper 7759, December, 1970, pp. 2557-2573.

36. Thomson, W.T., Theory of Vibrations with Applications, Prentice-Hall, Inc., 1972.

37. Timoshenko, S.P., D.H. Young, and W. Weaver, Vibration Problems in Engineering, John Wiley and Sons, Inc., 1974.

38. Whitney, C.S., "Plastic Theory of Reinforced Concrete Design," Trans. ASCE, Vol. 107, 1942, pp. 251-282.

Table 2.1 Flexural Stiffnesses Used in Design

| Level or Story | Inertias, $10^4 mm^4$* | | | | | | |
|---|---|---|---|---|---|---|---|
| | Structure with No Wall (FNW) | | | Structures with Walls (FSW,FHW,FFW) | | | |
| | Beams | Interior Columns | Exterior Columns | Beams | Interior Columns | Exterior Columns | Walls |
| 9 | 0.76 | 10.2 | 10.2 | 0.76 | 10.2 | 10.2 | 530 |
| 8 | 0.76 | 10.2 | 10.2 | 0.76 | 10.2 | 10.2 | 530 |
| 7 | 0.76 | 10.2 | 10.2 | 0.76 | 10.2 | 10.2 | 530 |
| 6 | 0.76 | 10.2 | 10.2 | 0.76 | 10.2 | 10.2 | 530 |
| 5 | 0.76 | 10.2 | 10.2 | 0.76 | 10.2 | 10.2 | 530 |
| 4 | 0.76 | 10.2 | 10.2 | 0.76 | 10.2 | 10.2 | 530 |
| 3 | 1.05 | 10.2 | 10.2 | 0.76 | 10.2 | 10.2 | 530 |
| 2 | 1.05 | 17.9 | 10.2 | 0.76 | 10.2 | 10.2 | 530 |
| 1 | 1.05 | 17.9 | 17.9 | 0.76 | 10.2 | 10.2 | 530 |

*Assumed Concrete Modulus of 21000 MPa.

Table 2.2 Frequencies and Mode Shapes Used in Design

| | Test Structure | | | | | | | | | | | |
|---|---|---|---|---|---|---|---|---|---|---|---|---|
| | FNW | | | FSW | | | FHW | | | FFW | | |
| Mode | First | Second | Third | First | Second | Third | First | Second | Third | First | Second | Third |
| Freq., Hz | | | | | | | | | | | | |
| | 1.47 | 4.63 | 9.06 | 1.56 | 5.13 | 9.82 | 1.65 | 5.34 | 11.4 | 1.68 | 6.51 | 15.4 |
| Shapes | | | | | | | | | | | | |
| Level | | | | | | | | | | | | |
| 9 | 1.00 | 1.00 | 1.00 | 1.00 | 1.00 | 1.00 | 1.00 | 1.00 | 1.00 | 1.00 | 1.00 | 1.00 |
| 8 | 0.95 | 0.66 | 0.17 | 0.95 | 0.60 | 0.09 | 0.94 | 0.58 | -0.08 | 0.91 | 0.53 | 0.02 |
| 7 | 0.88 | 0.23 | -0.61 | 0.87 | 0.12 | -0.71 | 0.86 | 0.07 | -0.89 | 0.81 | 0.05 | -0.73 |
| 6 | 0.79 | -0.23 | -0.97 | 0.77 | -0.37 | -0.98 | 0.75 | -0.42 | -0.96 | 0.70 | -0.37 | -0.97 |
| 5 | 0.68 | -0.63 | -0.74 | 0.64 | -0.75 | -0.58 | 0.62 | -0.77 | -0.28 | 0.59 | -0.69 | -0.63 |
| 4 | 0.56 | -0.88 | -0.06 | 0.50 | -0.93 | 0.21 | 0.48 | -0.87 | 0.50 | 0.46 | -0.85 | 0.09 |
| 3 | 0.43 | -0.93 | -0.63 | 0.35 | -0.86 | 0.89 | 0.35 | -0.72 | 0.75 | 0.34 | -0.83 | 0.78 |
| 2 | 0.30 | -0.79 | -0.94 | 0.20 | -0.60 | 1.03 | 0.22 | -0.51 | 0.75 | 0.22 | -0.66 | 1.08 |
| 1 | 0.17 | -0.51 | -0.76 | 0.08 | -0.29 | 0.67 | 0.11 | -0.29 | 0.52 | 0.11 | -0.39 | 0.86 |

Table 2.3 Maximum Displacements Calculated Using Design Model

| Level | Displacement , mm | | | | | | | | | | | |
|---|---|---|---|---|---|---|---|---|---|---|---|---|
| Structure | FNW | | | FSW | | | FHW | | | FFW | | |
| Mode | First | Second | Third | First | Second | Third | First | Second | Third | First | Second | Third |
| 9 | 26.7 | 3.05 | 0.54 | 25.2 | 2.95 | 0.60 | 24.2 | 2.91 | 0.43 | 24.6 | 2.50 | 0.22 |
| 8 | 25.4 | 2.00 | 0.09 | 23.8 | 1.78 | 0.05 | 22.8 | 1.69 | -0.03 | 22.4 | 1.32 | 0.00 |
| 7 | 23.6 | 0.69 | -0.33 | 21.9 | 0.34 | -0.43 | 20.8 | 0.21 | -0.38 | 20.0 | 0.13 | -0.16 |
| 6 | 21.2 | -0.71 | -0.52 | 19.4 | -1.10 | -0.59 | 18.2 | -1.22 | -0.41 | 17.3 | -0.93 | -0.21 |
| 5 | 18.2 | -1.92 | -0.40 | 16.2 | -2.22 | -0.35 | 15.0 | -2.25 | -0.12 | 14.4 | -1.72 | -0.14 |
| 4 | 14.8 | -2.68 | -0.03 | 12.6 | -2.74 | 0.12 | 11.7 | -2.54 | 0.21 | 11.3 | -2.11 | 0.03 |
| 3 | 11.4 | -2.84 | 0.34 | 8.7 | -2.55 | 0.54 | 8.4 | -2.09 | 0.32 | 8.3 | -2.07 | 0.17 |
| 2 | 8.0 | -2.41 | 0.50 | 4.9 | -1.78 | 0.62 | 5.4 | -1.49 | 0.32 | 5.3 | -1.65 | 0.23 |
| 1 | 4.7 | -1.57 | 0.41 | 2.0 | -0.84 | 0.41 | 2.8 | -0.83 | 0.22 | 2.7 | -0.99 | 0.19 |

Table 4.1 Key to Figures and Tables of Measured Response

| | Run 1 | Run 2 |
|---|---|---|
| Figures: | | |
| Base Motions | 4.3 | 4.12 |
| Displacements | 4.4 | 4.13 |
| Accelerations | 4.5 | 4.14 |
| Transverse Accelerations | 4.6 | --- |
| Wall Forces | 4.7 | 4.15 |
| Shears | 4.8 | 4.16 |
| Moments | 4.9 | 4.17 |
| Response Distributions | 4.10 | 4.18 |
| Crack Patterns* | 4.11 | 4.19 |
| Tables: | | |
| Response at Time of Maximum Displacement | 4.2 | 4.3 |
| Maximum Frame Crack Widths | 4.4 | 4.4 |

* Crack Patterns before first test run are given in Fig. 4.2

Table 4.2 Response at Time of Maximum Displacement in Test Run One

(a) Structure FNW

| Level/ Story | Displacement (mm) | Acceleration (g) | Wall Force (kN) | Shear (kN) | | Moment (kN-m) | |
|---|---|---|---|---|---|---|---|
| | | | | Structure | Wall | Structure | Wall |
| 9 | 26.3 | -0.44 | - | 1.97 | - | - | - |
| 8 | 25.1 | -0.42 | - | 3.85 | - | 0.46 | - |
| 7 | 23.9 | -0.38 | - | 5.56 | - | 1.34 | - |
| 6 | 22.9 | -0.32 | - | 7.02 | - | 2.62 | - |
| 5 | 20.4 | -0.26 | - | 8.19 | - | 4.24 | - |
| 4 | 18.1 | -0.23 | - | 9.23 | - | 6.13 | - |
| 3 | 16.2 | -0.22 | - | 10.2 | - | 8.25 | - |
| 2 | 13.1 | -0.22 | - | 11.2 | - | 10.6 | - |
| 1 | 9.3 | -0.21 | - | 12.2 | - | 13.2 | - |
| Base | - | - | - | - | - | 18.8 | - |

Table 4.2 Response at Time of Maximum Displacement in Test Run One

(b) Structure FSW

| Level/ Story | Displacement (mm) | Acceleration (g) | Wall Force (kN) | Shear (kN) | | Moment (kN-m) | |
|---|---|---|---|---|---|---|---|
| | | | | Structure | Wall | Structure | Wall |
| 9 | -22.4 | 0.43 | - | -1.94 | - | - | - |
| 8 | -21.7 | 0.46 | - | -4.00 | - | -0.45 | - |
| 7 | -20.6 | 0.48 | - | -6.19 | - | -1.37 | - |
| 6 | -18.9 | 0.48 | - | -8.35 | - | -2.79 | - |
| 5 | -16.4 | 0.38 | - | -10.1 | - | -4.72 | - |
| 4 | -13.2 | 0.25 | - | -11.2 | - | -7.04 | - |
| 3 | -9.6 | 0.10 | - | -11.6 | - | -9.61 | - |
| 2 | -5.2 | -0.04 | - | -11.4 | - | -12.3 | - |
| 1 | -2.2 | -0.11 | -12.3 | -10.9 | -12.3 | -14.9 | - |
| Base | - | - | - | - | - | -19.9 | -5.61 |

Table 4.2 Response at Time of Maximum Displacement in Test Run One

(c) Structure FHW

| Level/ Story | Displacement (mm) | Acceleration (g) | Wall Force (kN) | Shear (kN) | | Moment (kN-m) | |
|---|---|---|---|---|---|---|---|
| | | | | Structure | Wall | Structure | Wall |
| 9 | -23.2 | 0.45 | - | -2.03 | - | - | - |
| 8 | -22.5 | 0.41 | - | -3.86 | - | -0.47 | - |
| 7 | -21.4 | 0.38 | - | -5.57 | - | -1.36 | - |
| 6 | -19.5 | 0.38 | - | -7.28 | - | -2.64 | - |
| 5 | -17.3 | 0.36 | - | -8.89 | - | -4.32 | - |
| 4 | -14.5 | 0.29 | -1.60 | -10.2 | -1.60 | -6.37 | - |
| 3 | -11.5 | 0.23 | -0.86 | -11.3 | -2.46 | -8.72 | -0.37 |
| 2 | - 8.2 | 0.19 | -0.64 | -12.1 | -3.10 | -11.3 | -0.93 |
| 1 | - 5.5 | 0.09 | -3.22 | -12.5 | -6.32 | -14.1 | -1.64 |
| Base | - | - | - | - | - | -19.9 | -4.53 |

Table 4.2 Response at Time of Maximum Displacement in Test Run One

(d) Structure FFW

| Level/ Story | Displacement (mm) | Acceleration (g) | Wall Force (kN) | Shear (kN) | | Moment (kN-m) | |
|---|---|---|---|---|---|---|---|
| | | | | Structure | Wall | Structure | Wall |
| 9 | -26.1 | 0.58 | 3.64 | -2.64 | 3.64 | - | - |
| 8 | -23.8 | 0.52 | -1.62 | -5.00 | 2.01 | -0.61 | 0.83 |
| 7 | -21.6 | 0.45 | -1.81 | -7.08 | 0.20 | -1.77 | 1.29 |
| 6 | -18.9 | 0.39 | -1.36 | -8.84 | -1.16 | -3.40 | 1.34 |
| 5 | -16.1 | 0.34 | -0.48 | -10.4 | -1.63 | -5.44 | 1.07 |
| 4 | -13.4 | 0.27 | -1.67 | -11.6 | -3.30 | -7.83 | 0.70 |
| 3 | -10.6 | 0.20 | -0.73 | -12.5 | -4.04 | -10.5 | -0.06 |
| 2 | - 7.5 | 0.13 | -0.19 | -13.1 | -4.23 | -13.4 | -0.98 |
| 1 | - 5.0 | 0.07 | -2.19 | -13.5 | -6.42 | -16.4 | -1.95 |
| Base | - | - | - | - | - | -22.6 | -4.88 |

Table 4.3 Response at Time of Maximum Displacement in Test Run Two

(a) Structure FNW

| Level/ Story | Displacement (mm) | Acceleration (g) | Wall Force (kN) | Shear (kN) | | Moment (kN-m) | |
|---|---|---|---|---|---|---|---|
| | | | | Structure | Wall | Structure | Wall |
| 9 | 43.8 | -0.46 | - | 2.07 | - | - | - |
| 8 | 41.5 | -0.49 | - | 4.25 | - | 0.48 | - |
| 7 | 39.3 | -0.50 | - | 6.51 | - | 1.47 | - |
| 6 | 37.8 | -0.50 | - | 8.78 | - | 2.97 | - |
| 5 | 31.6 | -0.42 | - | 10.7 | - | 5.00 | - |
| 4 | 28.1 | -0.20 | - | 11.6 | - | 7.47 | - |
| 3 | 25.2 | -0.01 | - | 11.6 | - | 10.1 | - |
| 2 | 19.8 | -0.01 | - | 11.7 | - | 12.8 | - |
| 1 | 14.3 | 0.00 | - | 11.7 | - | 15.5 | - |
| Base | - | - | - | - | - | 20.9 | - |

Table 4.3 Response at Time of Maximum Displacement in Test Run Two

(b) Structure FSW

| Level/ Story | Displacement (mm) | Acceleration (g) | Wall Force (kN) | Shear (kN) | | Moment (kN-m) | |
|---|---|---|---|---|---|---|---|
| | | | | Structure | Wall | Structure | Wall |
| 9 | 39.8 | -0.47 | - | 2.11 | - | - | - |
| 8 | 37.9 | -0.52 | - | 4.43 | - | 0.49 | - |
| 7 | 37.3 | -0.58 | - | 7.05 | - | 1.51 | - |
| 6 | 33.4 | -0.57 | - | 9.65 | - | 3.14 | - |
| 5 | 28.2 | -0.50 | - | 11.9 | - | 5.37 | - |
| 4 | 24.0 | -0.33 | - | 13.4 | - | 8.11 | - |
| 3 | 17.5 | -0.11 | - | 13.9 | - | 11.2 | - |
| 2 | 10.5 | -0.03 | - | 14.0 | - | 14.4 | - |
| 1 | 5.2 | 0.01 | 11.4 | 13.9 | 11.4 | 17.6 | - |
| Base | - | - | - | - | - | 24.0 | 5.22 |

Table 4.3 Response at Time of Maximum Displacement in Test Run Two

(c) Structure FHW

| Level/ Story | Displacement (mm) | Acceleration (g) | Wall Force (kN) | Shear (kN) | | Moment (kN-m) | |
|---|---|---|---|---|---|---|---|
| | | | | Structure | Wall | Structure | Wall |
| 9 | 40.1 | -0.47 | - | 2.14 | - | - | - |
| 8 | 39.1 | -0.45 | - | 4.18 | - | 0.49 | - |
| 7 | 37.3 | -0.46 | - | 6.28 | - | 1.46 | - |
| 6 | 35.5 | -0.43 | - | 8.23 | - | 2.91 | - |
| 5 | 3.07 | -0.44 | - | 10.2 | - | 4.81 | - |
| 4 | 26.5 | -0.49 | -2.09 | 12.5 | -2.09 | 7.17 | - |
| 3 | 22.3 | -0.36 | 4.49 | 14.1 | 2.40 | 10.0 | -0.48 |
| 2 | 16.4 | -0.26 | 2.78 | 15.3 | 5.18 | 13.3 | 0.07 |
| 1 | 11.4 | -0.16 | 4.32 | 16.0 | 9.50 | 16.8 | 1.26 |
| Base | - | - | - | - | - | 24.2 | 5.60 |

Table 4.3 Response at Time of Maximum Displacement in Test Run Two

(d) Structure FFW

| Level/ Story | Displacement (mm) | Acceleration (g) | Wall Force (kN) | Shear (kN) | | Moment (kN-m) | |
|---|---|---|---|---|---|---|---|
| | | | | Structure | Wall | Structure | Wall |
| 9 | 44.0 | -0.49 | -5.36 | 2.21 | -5.36 | - | - |
| 8 | 40.8 | -0.48 | 1.55 | 4.40 | -3.81 | 0.52 | -1.23 |
| 7 | 37.1 | -0.49 | 1.53 | 6.62 | -2.28 | 1.55 | -2.10 |
| 6 | 34.8 | -0.49 | 1.84 | 8.86 | -0.44 | 3.07 | -2.62 |
| 5 | 28.7 | -0.46 | 1.53 | 11.0 | 1.09 | 5.13 | -2.72 |
| 4 | 25.4 | -0.40 | 0.17 | 12.8 | 1.26 | 7.66 | -2.47 |
| 3 | 21.3 | -0.38 | 1.44 | 14.6 | 2.70 | 10.6 | -2.19 |
| 2 | 16.7 | -0.31 | 4.53 | 16.0 | 7.23 | 14.0 | -1.57 |
| 1 | 11.7 | -0.19 | 1.68 | 16.8 | 8.91 | 17.6 | 0.09 |
| Base | - | - | - | - | - | 25.4 | 4.16 |

Table 4.4 Maximum Frame Crack Widths, mm

(Run One)

| Story/ Level | Structure | | | |
|---|---|---|---|---|
| | FNW | FSW | FHW | FFW |
| 9 | - | - | - | - |
| 8 | - | - | - | - |
| 7 | - | - | - | - |
| 6 | - | - | - | - |
| 5 | - | 0.05 | - | - |
| 4 | - | 0.15 | 0.10 | - |
| 3 | - | 0.15 | 0.15 | - |
| 2 | 0.05 | 0.15 | 0.05 | - |
| 1 | 0.15 | 0.15 | 0.05 | - |

(Run Two)

| Story/ Level | Structure | | | |
|---|---|---|---|---|
| | FNW | FSW | FHW | FFW |
| 9 | - | - | - | 0.10 |
| 8 | 0.05 | 0.05 | - | 0.10 |
| 7 | 0.05 | 0.05 | 0.05 | 0.10 |
| 6 | 0.10 | 0.15 | 0.10 | 0.10 |
| 5 | 0.10 | 0.20 | 0.10 | 0.10 |
| 4 | 0.20 | 0.20 | 0.20 | 0.10 |
| 3 | 0.20 | 0.30 | 0.20 | 0.10 |
| 2 | 0.30 | 0.30 | 0.20 | 0.10 |
| 1 | 0.30 | 0.25 | 0.20 | 0.10 |

Table 5.1 Spectrum Intensities for a Damping Factor of 0.10*

| Test Run | Test Structure | | | |
|---|---|---|---|---|
| | FNW | FSW | FHW | FFW |
| 1 | 218 | 190 | 193 | 182 |
| 2 | 379 | 352 | 329 | 335 |
| 3 | 555 | 575 | 484 | 491 |

* Calculated between periods of 0.04 and 1.0 sec.
Units are mm.

Table 5.2 Calculated Uncracked Test Structure Frequencies*

| Mode | Frequency, Hz | | | |
|---|---|---|---|---|
| | FNW | FSW | FHW | FFW |
| First | 4.4 | 5.5 | 5.5 | 5.5 |
| Second | 14 | 17 | 18 | 19 |
| Third | 28 | 31 | 34 | 40 |

* Assumed concrete modulus of 22,000 MPa.

Table 5.3 Apparent First-Mode Shapes during Earthquake Simulations

| Test Structure | FNW | | | FSW | | | FHW | | | FFW | | |
|---|---|---|---|---|---|---|---|---|---|---|---|---|
| Test Run | 1 | 2 | 3 | 1 | 2 | 3 | 1 | 2 | 3 | 1 | 2 | 3 |
| Top-Level Displacement, mm | 26 | 44 | 93 | 20 | 40 | 76 | 22 | 41 | 69 | 24 | 44 | 73 |
| Level | | | | | | | | | | | | |
| 9 | 1.00 | 1.00 | 1.00 | 1.00 | 1.00 | 1.00 | 1.00 | 1.00 | 1.0 | 1.00 | 1.00 | 1.00 |
| 8 | 0.96 | 0.97 | 0.96 | 0.97 | 0.97 | 0.96 | 0.96 | 0.97 | 0.97 | 0.91 | 0.92 | 0.93 |
| 7 | 0.93 | 0.90 | 0.93 | 0.93 | 0.90 | 0.87 | 0.92 | 0.93 | 0.93 | 0.83 | 0.84 | 0.85 |
| 6 | 0.88 | 0.88 | 0.87 | 0.86 | 0.83 | 0.78 | 0.84 | 0.87 | 0.86 | 0.72 | 0.78 | 0.78 |
| 5 | 0.78 | 0.73 | 0.78 | 0.72 | 0.70 | 0.64 | 0.74 | 0.74 | 0.76 | 0.61 | 0.64 | 0.68 |
| 4 | 0.69 | 0.65 | 0.72 | 0.61 | 0.58 | 0.52 | 0.61 | 0.63 | 0.65 | 0.52 | 0.56 | 0.59 |
| 3 | 0.61 | 0.58 | 0.64 | 0.46 | 0.43 | 0.37 | 0.48 | 0.53 | 0.55 | 0.41 | 0.47 | 0.50 |
| 2 | 0.49 | 0.54 | 0.60 | 0.29 | 0.26 | 0.22 | 0.34 | 0.38 | 0.42 | 0.29 | 0.36 | 0.40 |
| 1 | 0.33 | 0.34 | 0.39 | 0.14 | 0.13 | 0.10 | 0.23 | 0.27 | 0.30 | 0.19 | 0.25 | 0.29 |
| Participation Factor | 1.24 | 1.26 | 1.23 | 1.25 | 1.28 | 1.31 | 1.28 | 1.26 | 1.26 | 1.38 | 1.35 | 1.34 |
| Effective* Weight, kN | 37.3 | 37.4 | 37.4 | 33.2 | 33.4 | 32.4 | 35.3 | 36.1 | 36.6 | 34.5 | 35.9 | 36.6 |
| Effective Height, m | 1.54 | 1.54 | 1.51 | 1.64 | 1.64 | 1.67 | 1.60 | 1.58 | 1.56 | 1.63 | 1.59 | 1.57 |

* The total weights of structures FNW, FSW, FHW, and FFW were 40.5, 40.6, 40.7, and 40.9 kN, respectively.

Table 5.4 Apparent First-Mode Shapes during Steady-State Tests

| | Structure FNW | | | | Structure FSW | | | |
|---|---|---|---|---|---|---|---|---|
| | After Run 1 | After Run 2 | After Run 3 | "High" Amplitude | After Run 1 | After Run 2 | After Run 3 | "High" Amplitude |
| Level | | | | | | | | |
| 9 | 1.00 | 1.00 | 1.00 | 1.00 | 1.00 | 1.00 | 1.00 | 1.00 |
| 8 | 0.96 | 0.98 | 0.96 | 0.95 | 0.98 | 0.99 | 0.99 | 0.97 |
| 7 | 0.91 | 0.93 | 0.92 | 0.90 | 0.92 | 0.93 | 0.92 | 0.88 |
| 6 | 0.86 | 0.88 | 0.89 | 0.88 | 0.85 | 0.85 | 0.83 | 0.80 |
| 5 | 0.78 | 0.79 | 0.78 | 0.77 | 0.74 | 0.72 | 0.68 | 0.65 |
| 4 | 0.68 | 0.68 | 0.67 | 0.66 | 0.61 | 0.57 | 0.51 | 0.50 |
| 3 | 0.59 | 0.57 | 0.56 | 0.54 | 0.45 | 0.40 | 0.37 | 0.35 |
| 2 | 0.47 | 0.44 | 0.42 | 0.40 | 0.27 | 0.23 | 0.22 | 0.22 |
| 1 | 0.31 | 0.27 | 0.27 | 0.26 | 0.12 | 0.10 | 0.09 | 0.09 |
| Participation Factor | 1.26 | 1.24 | 1.25 | 1.26 | 1.25 | 1.25 | 1.27 | 1.29 |
| Effective Weight, kN | 37.1 | 36.5 | 36.4 | 36.2 | 33.6 | 32.7 | 32.1 | 31.9 |
| Effective Height, m | 1.54 | 1.56 | 1.57 | 1.57 | 1.63 | 1.65 | 1.67 | 1.68 |

Table 5.4 (cont'd) Apparent First-Mode Shapes during Steady-State Tests

| | After Run 1 | After Run 2 | After Run 3 | "High" Amplitude | After Run 1 | After Run 2 | After Run 3 | "High" Amplitude |
|---|---|---|---|---|---|---|---|---|
| Level | | | | | | | | |
| 9 | 1.00 | 1.00 | 1.00 | 1.00 | 1.00 | 1.00 | 1.00 | 1.00 |
| 8 | 0.99 | 0.97 | 0.97 | 0.97 | 0.91 | 0.92 | 0.91 | 0.91 |
| 7 | 0.92 | 0.91 | 0.92 | 0.92 | 0.81 | 0.81 | 0.80 | 0.80 |
| 6 | 0.84 | 0.82 | 0.84 | 0.83 | 0.71 | 0.71 | 0.72 | 0.70 |
| 5 | 0.74 | 0.70 | 0.69 | 0.70 | 0.58 | 0.59 | 0.59 | 0.60 |
| 4 | 0.60 | 0.57 | 0.56 | 0.56 | 0.50 | 0.49 | 0.48 | 0.49 |
| 3 | 0.48 | 0.44 | 0.46 | 0.46 | 0.39 | 0.40 | 0.38 | 0.39 |
| 2 | 0.34 | 0.35 | 0.31 | 0.33 | 0.26 | 0.29 | 0.27 | 0.26 |
| 1 | 0.22 | 0.22 | 0.21 | 0.22 | 0.15 | 0.19 | 0.20 | 0.20 |
| Participation Factor | 1.27 | 1.29 | 1.29 | 1.29 | 1.39 | 1.39 | 1.40 | 1.40 |
| Effective Weight, kN | 35.2 | 35.0 | 34.7 | 34.9 | 33.6 | 34.2 | 34.0 | 34.1 |
| Effective Height, m | 1.60 | 1.61 | 1.61 | 1.61 | 1.65 | 1.63 | 1.64 | 1.64 |

Table 5.5 Estimated Damping Factors in Free-Vibration Tests*

| Structure | Before Run One | Following Run One | Following Run Two | Following Run Three |
|---|---|---|---|---|
| FNW | 4 | 7 | 10 | 10 |
| FSW | 2 | 6 | 6 | 8 |
| FHW | 2 | 4 | 6 | 6 |
| FFW | 2 | 6 | 7 | 8 |

*Percent of Critical Damping

Table 5.6 Estimated Damping Factors in Steady-State Tests*

| Structure | Following Run One | | Following Run Two | | Following Run Three | | "High Amplitude" | |
|---|---|---|---|---|---|---|---|---|
| | ** | *** | ** | *** | ** | *** | ** | *** |
| FNW | 5 | 15 | 13 | 14 | 14 | 14 | 13 | 12 |
| FSW | 6 | 14 | 15 | 16 | 19 | -- | 17 | 18 |
| FHW | 7 | 8 | 9 | 9 | 12 | 11 | 14 | 14 |
| FFW | 8 | 7 | 10 | 9 | 12 | 13 | 10 | 14 |

* Percent of Critical Damping
** $\beta$ = 1/2 times observed resonant response
***Half-power bandwidth estimate

Table 6.1 Stiffnesses Used for Experimentally-Inferred Model*

| Level/ Story | FNW | | | FSW | | |
|---|---|---|---|---|---|---|
| | Interior Column | Exterior Column | Beam | Column | Beam | Wall |
| 9 | 11.0 | 11.0 | 3.9 | 11.0 | 5.9 | 0.0 |
| 8 | 11.0 | 11.0 | 3.9 | 11.0 | 4.9 | 0.0 |
| 7 | 11.0 | 11.0 | 4.2 | 11.0 | 3.5 | 0.0 |
| 6 | 11.0 | 11.0 | 3.1 | 11.0 | 2.6 | 0.0 |
| 5 | 11.0 | 11.0 | 2.0 | 11.0 | 2.0 | 0.0 |
| 4 | 11.0 | 11.0 | 2.6 | 11.0 | 1.7 | 0.0 |
| 3 | 11.0 | 11.0 | 2.8 | 11.0 | 1.5 | 0.0 |
| 2 | 19.6 | 11.0 | 2.1 | 11.0 | 1.6 | 0.0 |
| 1 | 19.6 | 19.6 | 1.7 | 11.0 | 2.6 | 1730 |
| Rotational Spring | 7.0 | 7.0 | -- | -- | -- | 200 |

* Inertias ($10^4$ $mm^4$) and Spring Stiffnesses ($10^4$ kN-mm/rad)

Table 6.1 (contd.) Stiffnesses Used for Experimentally-Inferred Model

| Level/ Story | FHW | | | FFW | | |
|---|---|---|---|---|---|---|
| | Column | Beam | Wall | Column | Beam | Wall |
| 9 | 11.0 | 5.9 | 0.0 | 11.0 | 2.5 | 3600 |
| 8 | 11.0 | 4.9 | 0.0 | 11.0 | 2.5 | 3600 |
| 7 | 11.0 | 3.4 | 0.0 | 11.0 | 2.2 | 1730 |
| 6 | 11.0 | 2.7 | 0.0 | 11.0 | 2.1 | 1730 |
| 5 | 11.0 | 2.2 | 0.0 | 11.0 | 2.1 | 1730 |
| 4 | 11.0 | 2.0 | 3600 | 11.0 | 2.0 | 1730 |
| 3 | 11.0 | 1.8 | 1730 | 11.0 | 2.0 | 1730 |
| 2 | 11.0 | 1.9 | 1730 | 11.0 | 2.0 | 1730 |
| 1 | 11.0 | 2.1 | 1730 | 11.0 | 2.2 | 1730 |
| Rotational Spring | -- | -- | 59 | -- | -- | 59 |

Table 6.2 Calculated Test-Structure Frequencies, Hz

| Test Structure | Mode | Model (Stiffness)* | | |
|---|---|---|---|---|
| | | Gross Section | Cracked Section | "Experimentally" Inferred |
| FNW | 1 | 4.4 | 2.7 | 1.9 |
| | 2 | 14 | 8.1 | 6.6 |
| | 3 | 28 | 15 | 13 |
| FSW | 1 | 5.5 | 3.1 | 2.2 |
| | 2 | 17 | 9.6 | 7.8 |
| | 3 | 31 | 17 | 14 |
| FHW | 1 | 5.5 | 3.2 | 2.2 |
| | 2 | 18 | 9.9 | 7.9 |
| | 3 | 34 | 19 | 17 |
| FFW | 1 | 5.5 | 3.2 | 2.2 |
| | 2 | 19 | 12 | 9.2 |
| | 3 | 40 | 26 | 23 |

* See Section 6.1 for description of models

Table 6.3 Structure Damage Ratios and Damping Factors*

| Test Structure | FNW | | FSW | | FHW | | FFW | |
|---|---|---|---|---|---|---|---|---|
| Run No. | μ** | β*** | μ | β | μ | β | μ | β |
| 1 | 1.6 | 0.06 | 1.7 | 0.07 | 1.7 | 0.07 | 1.9 | 0.08 |
| 2 | 2.4 | 0.09 | 2.6 | 0.10 | 2.7 | 0.10 | 2.9 | 0.10 |
| 3 | 4.6 | 0.13 | 4.5 | 0.13 | 4.2 | 0.12 | 4.4 | 0.12 |

* See Section 6.2 for explanation

** $\mu$ = Overall damage ratio (Fully-cracked structure stiffness/measured secant stiffness)

***$\beta$ = Structure damping factor $= \frac{(1- (1/\mu)^{1/2}]}{5} + 0.02$

Table 7.1 Member Strengths Assumed for Limit Analyses*

| | FNW | | | FSW, FHW, FFW | | |
|---|---|---|---|---|---|---|
| | Interior Columns | Exterior Columns | Beams | Columns | Beams | Wall |
| Level/ Story | | | | | | |
| 9 | 167 | 167 | 122 | 167 | 122 | 4900 |
| 8 | 177 | 177 | 122 | 177 | 122 | 4900 |
| 7 | 187 | 187 | 122 | 187 | 122 | 4900 |
| 6 | 197 | 197 | 122 | 197 | 122 | 4900 |
| 5 | 207 | 207 | 122 | 207 | 122 | 4900 |
| 4 | 217 | 217 | 122 | 217 | 122 | 4900 |
| 3 | 227 | 227 | 168 | 227 | 122 | 4900 |
| 2 | 313 | 237 | 168 | 237 | 122 | 4900 |
| 1 | 398 | 398 | 168 | 247 | 122 | 4900 |

* Flexural strengths in units of kN-mm.

Table 7.2 Overall Structure Damage Ratios for Assumed SDOF Primary Curves*

| Top Displacement (% of Height) | Test Structure | Primary Curve "Measured" | Primary Curve Calculated | Primary Curve Estimated |
|---|---|---|---|---|
| 1.0 | FNW | 1.5 | 1.7 | 1.6 |
| | FSW | 1.7 | 1.9 | 2.0 |
| | FHW | 1.7 | 1.9 | 1.9 |
| | FFW | 1.8 | 1.7 | 1.7 |
| 1.5 | FNW | 2.1 | 2.4 | 2.5 |
| | FSW | 2.3 | 2.7 | 2.9 |
| | FHW | 2.4 | 2.7 | 2.9 |
| | FFW | 2.4 | 2.5 | 2.5 |

* Overall structure damage ratio is defined as the ratio of elastic stiffness (all members fully cracked and structure loaded with linear distribution) to the secant stiffness of primary curve.

Table 7.3 Stiffness and Mass Properties Used for Nonlinear SDOF Analyses

| Structure/ Envelope | First Breakpoint | | Second Breakpoint | | Ultimate | | $M_{eff}$ | | $L_{eff}$ |
|---|---|---|---|---|---|---|---|---|---|
| | $\delta_{top}$ (mm) | $M_{base}$ (kN-m) | $\delta_{top}$ (mm) | $M_{base}$ (kN-m) | $\delta_{top}$ (mm) | $M_{base}$ (kN-m) | Q-Model (kg) | MQ-Model (kg) | (mm) |
| FNW | | | | | | | | | |
| Meas. | 2.3 | 6.0 | 19.0 | 18.9 | 45.0 | 23.5 | 3.32 | 3.07 | 1.54 |
| Calc. | 1.3 | 5.6 | 12.5 | 16.2 | 45.0 | 19.7 | 3.46 | 3.24 | 1.52 |
| Est. | 1.8 | 5.8 | 14.3 | 18.3 | 45.0 | 19.2 | 3.24 | 2.92 | 1.57 |
| FSW | | | | | | | | | |
| Meas. | 1.5 | 6.0 | 15.5 | 20.0 | 45.0 | 25.6 | 3.29 | 2.69 | 1.64 |
| Calc. | 0.9 | 6.0 | 11.5 | 17.1 | 45.0 | 21.6 | 3.38 | 2.78 | 1.63 |
| Est. | 1.6 | 7.3 | 11.7 | 18.9 | 45.0 | 19.8 | 3.19 | 2.56 | 1.66 |
| FHW | | | | | | | | | |
| Meas. | 1.5 | 6.0 | 16.8 | 20.6 | 45.0 | 26.2 | 3.23 | 2.81 | 1.60 |
| Calc. | 0.9 | 6.0 | 11.2 | 18.0 | 45.0 | 22.5 | 3.32 | 2.89 | 1.59 |
| Est. | 1.6 | 7.3 | 11.8 | 20.3 | 45.0 | 21.3 | 3.15 | 2.58 | 1.65 |
| FFW | | | | | | | | | |
| Meas. | 1.5 | 6.0 | 16.8 | 20.6 | 45.0 | 26.2 | 3.02 | 2.54 | 1.63 |
| Calc. | 0.9 | 6.0 | 13.2 | 20.2 | 45.0 | 23.9 | 3.06 | 2.60 | 1.62 |
| Est. | 1.6 | 7.3 | 13.2 | 22.6 | 45.0 | 23.7 | 3.03 | 2.47 | 1.65 |

Table 7.4 Calculated and Estimated Shapes Used with Nonlinear SDOF Analysis

| Structure Level | Calculated* FNW | Calculated* FSW | Calculated* FHW | Calculated* FFW | Estimated** FNW | Estimated** FSW | Estimated** FHW | Estimated** FFW |
|---|---|---|---|---|---|---|---|---|
| 9 | 1.00 | 1.00 | 1.00 | 1.00 | 1.00 | 1.00 | 1.00 | 1.00 |
| 8 | 0.99 | 0.98 | 0.98 | 0.93 | 0.97 | 0.96 | 0.96 | 0.92 |
| 7 | 0.96 | 0.95 | 0.94 | 0.85 | 0.92 | 0.89 | 0.89 | 0.84 |
| 6 | 0.92 | 0.89 | 0.88 | 0.76 | 0.84 | 0.79 | 0.79 | 0.73 |
| 5 | 0.86 | 0.79 | 0.78 | 0.66 | 0.74 | 0.68 | 0.66 | 0.63 |
| 4 | 0.77 | 0.64 | 0.65 | 0.54 | 0.64 | 0.54 | 0.53 | 0.50 |
| 3 | 0.66 | 0.45 | 0.50 | 0.43 | 0.53 | 0.39 | 0.39 | 0.38 |
| 2 | 0.53 | 0.27 | 0.36 | 0.31 | 0.42 | 0.23 | 0.26 | 0.25 |
| 1 | 0.38 | 0.10 | 0.22 | 0.19 | 0.31 | 0.09 | 0.14 | 0.14 |

* Calculated shape is obtained from nonlinear static analysis (see Sec. 7.2)
** Estimated shape is the shape obtained using fully-cracked member properties and linear load distribution

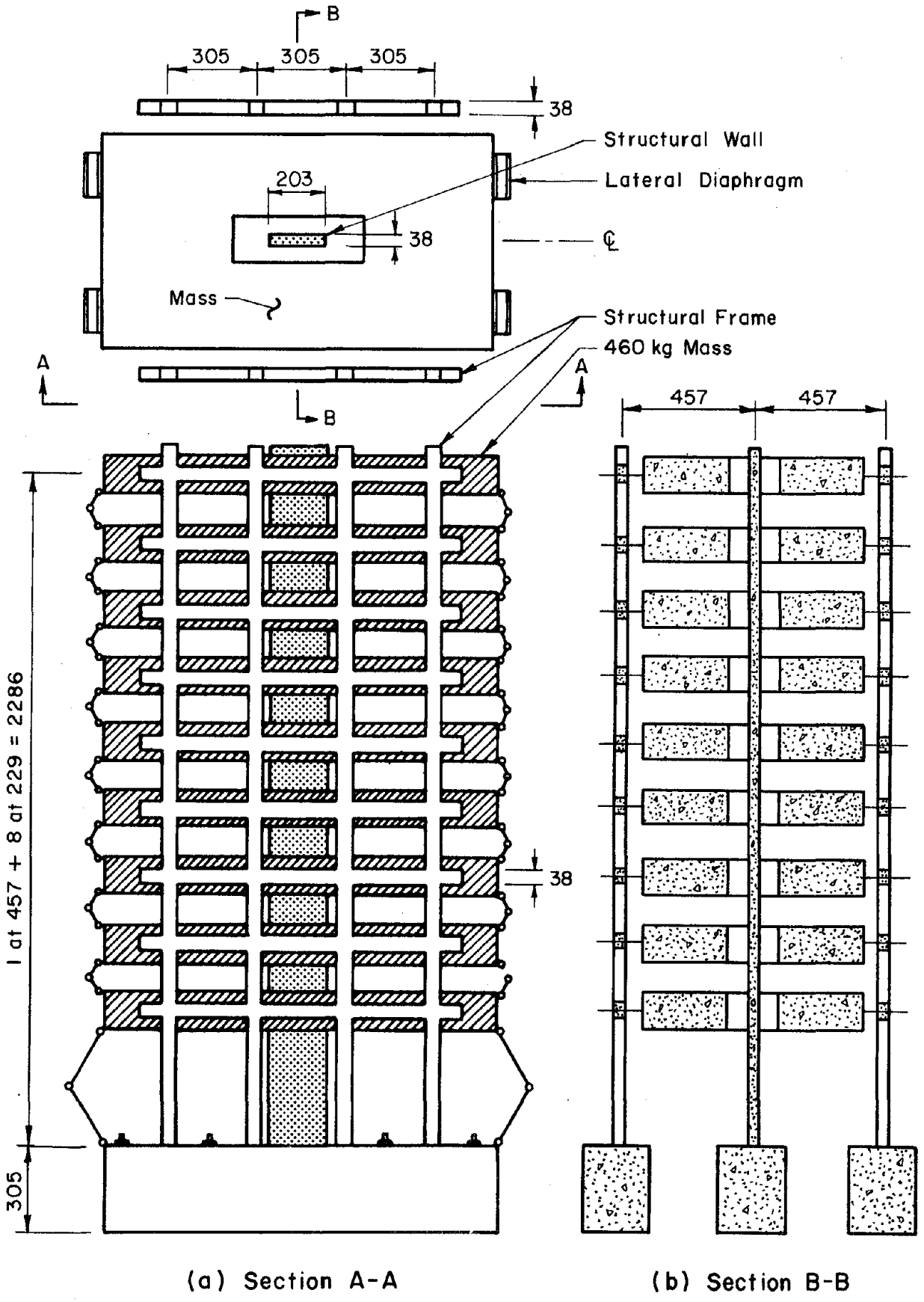


Fig. 2.1 Test Structure Configuration

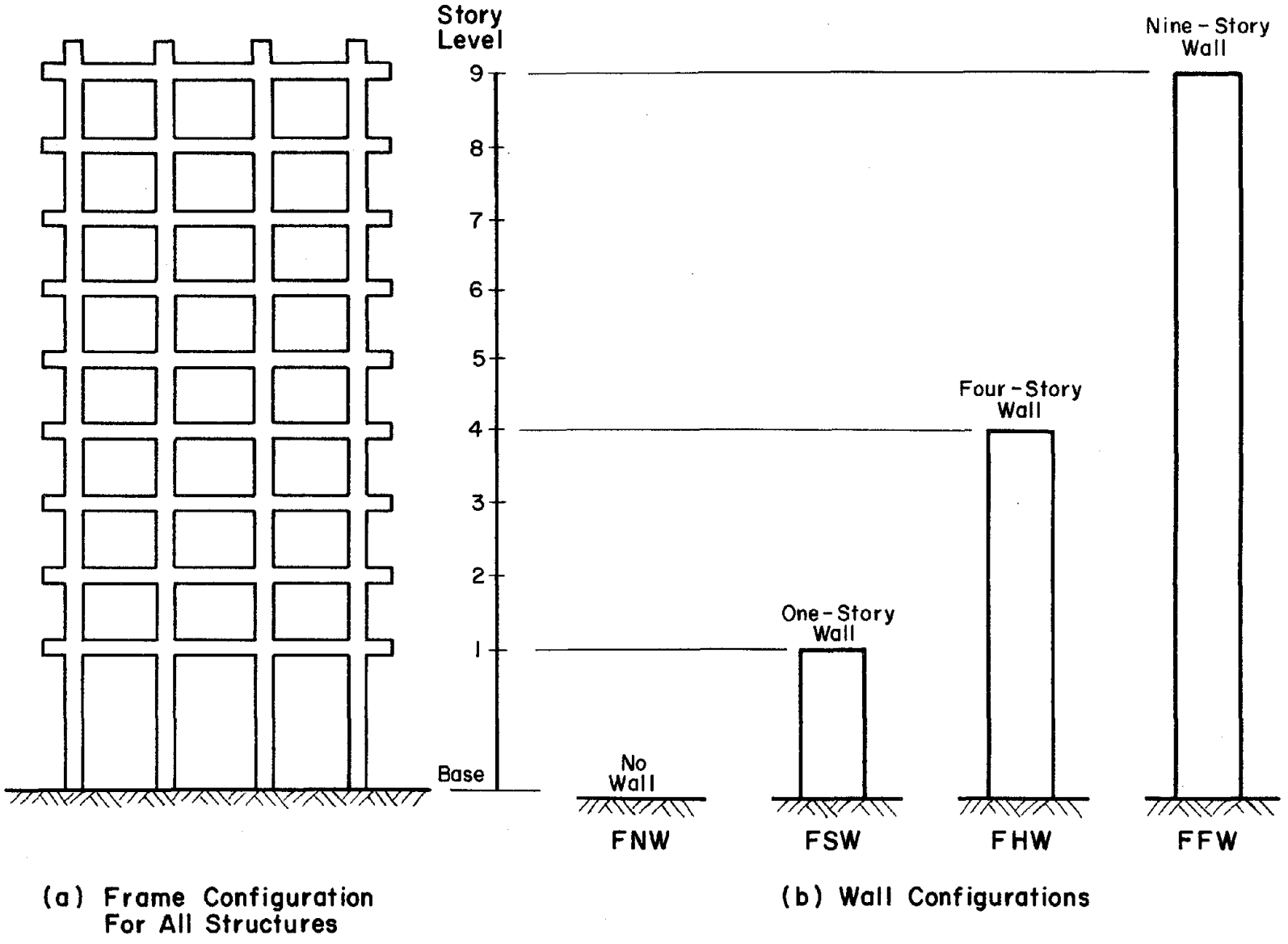


Fig. 2.2 Wall and Frame Configurations of Test Structures

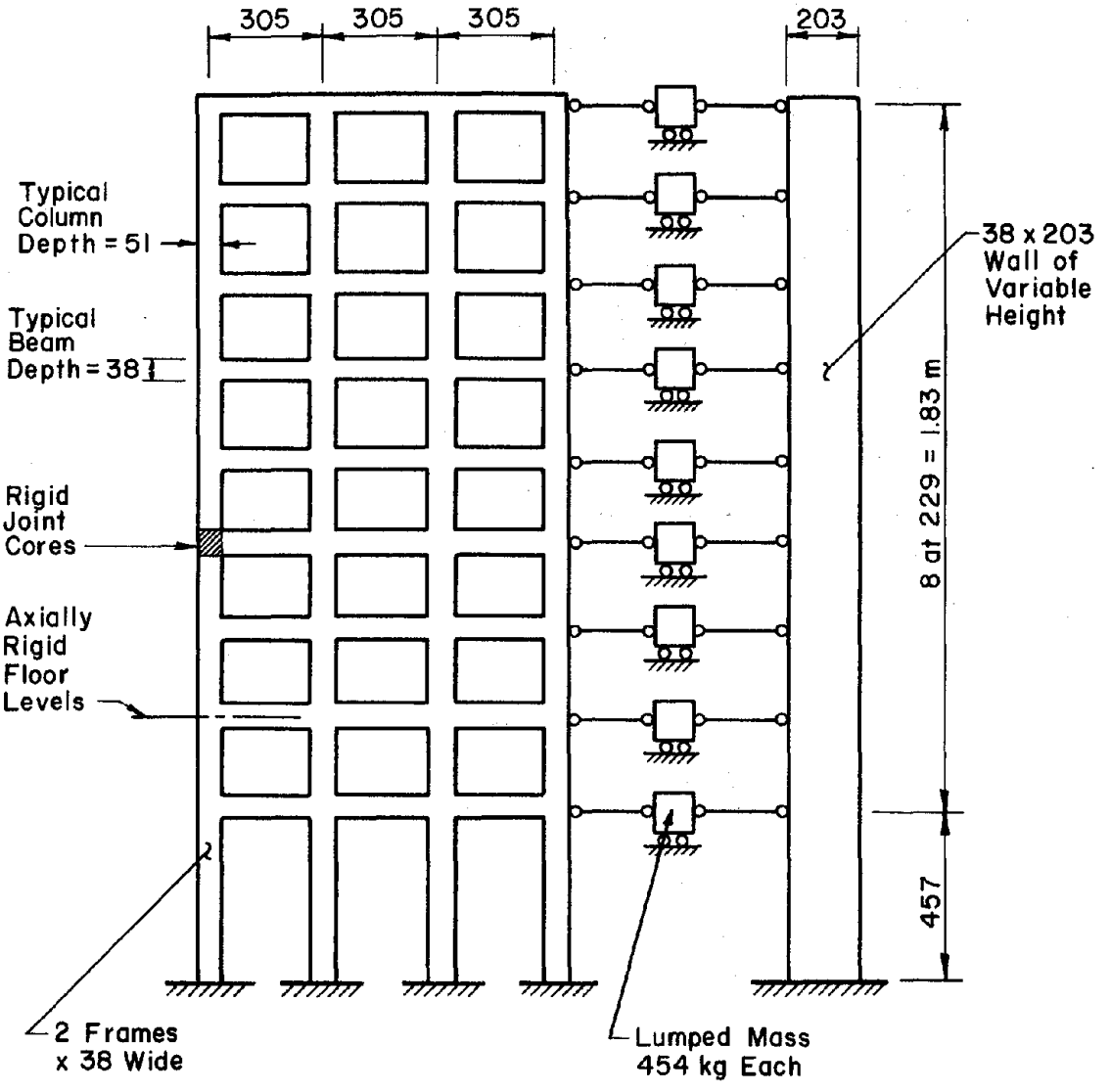


(All Dimensions In Millimeters Unless Noted)

Fig. 2.3 Analytical Model Used for Design

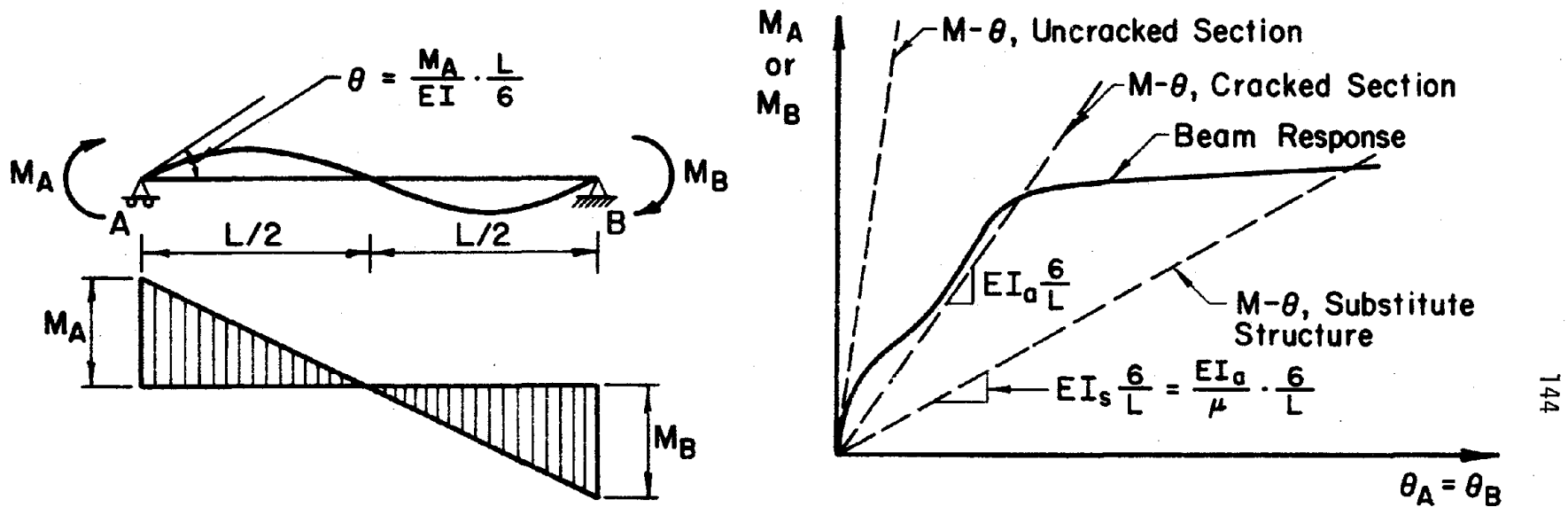


Fig. 2.4 Interpretation of Damage Ratio

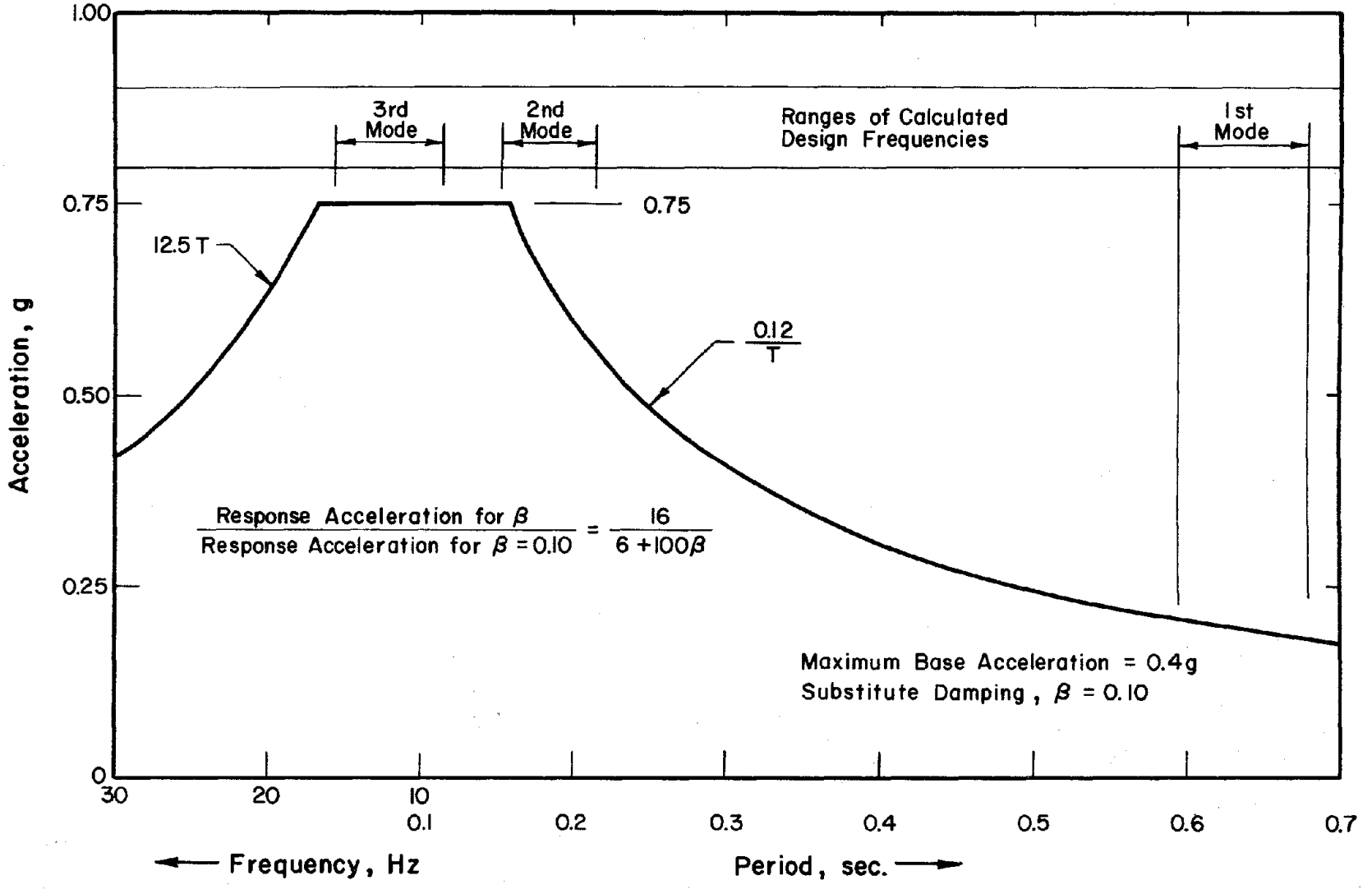


Fig. 2.5 Linear Acceleration Spectrum Used for Design

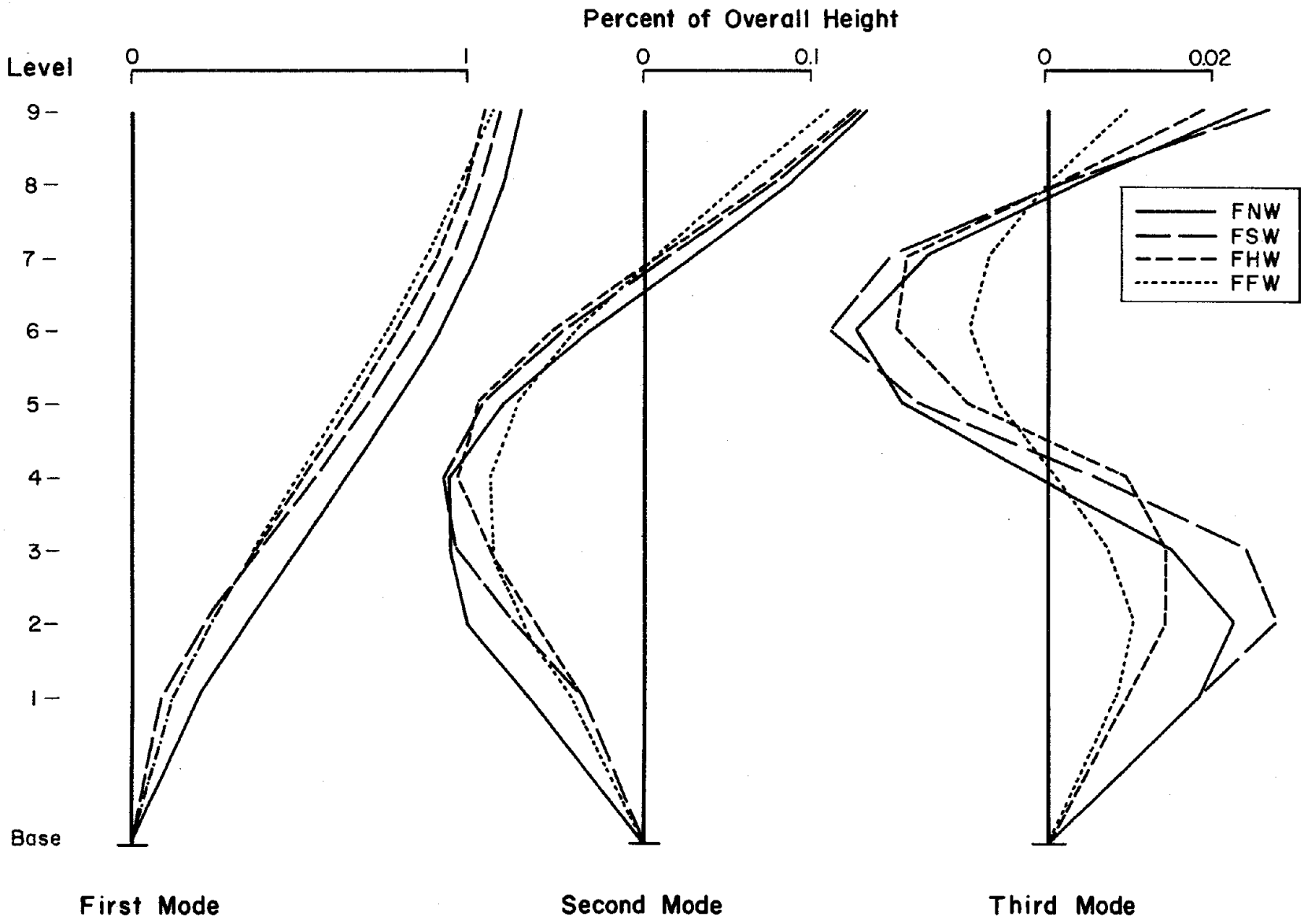


Fig. 2.6 Design Displacements for First Three Modes

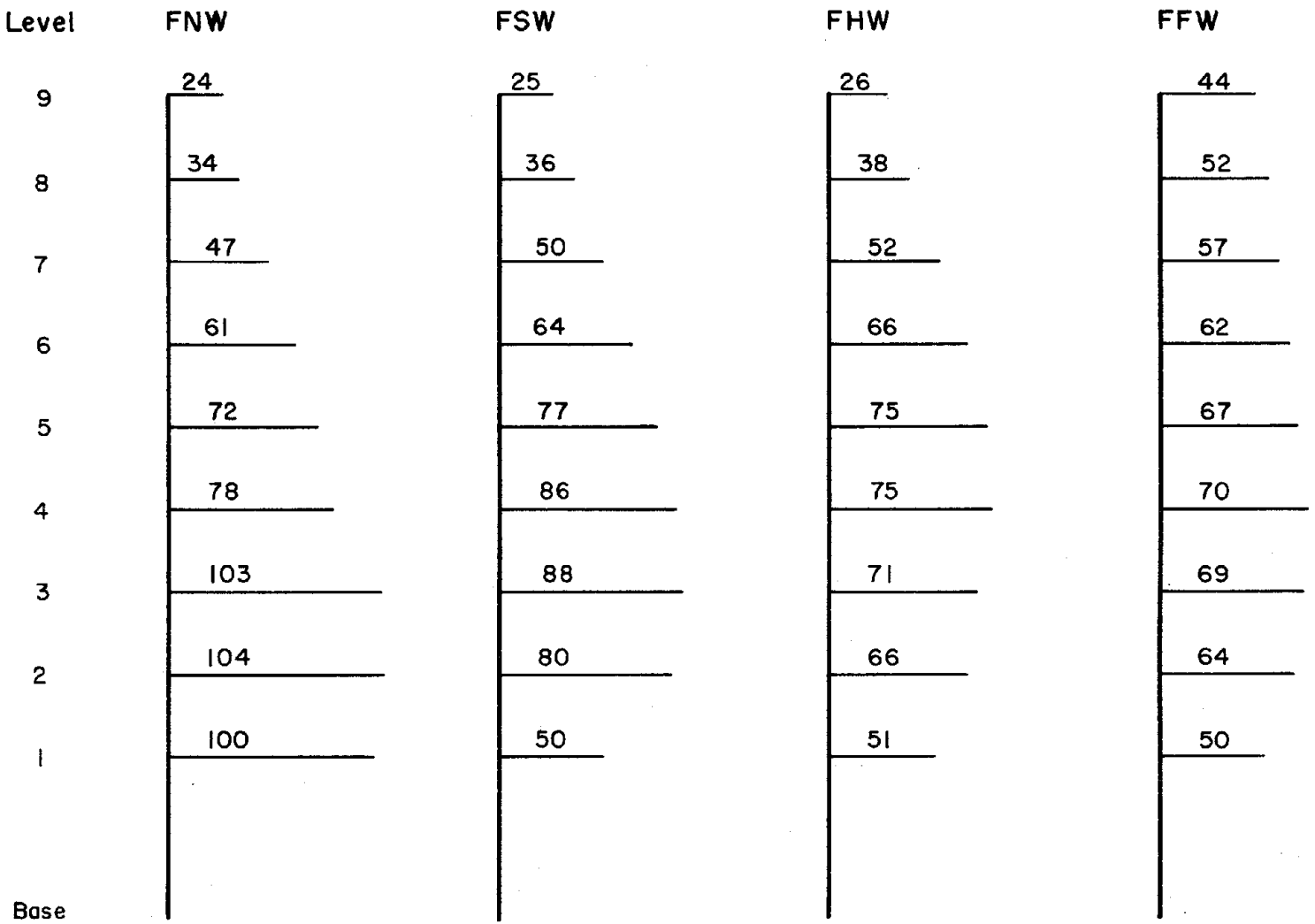


(a) Beam End Moments, kN-mm

Fig. 2.7 First-Mode Member Forces Calculated for Design Model

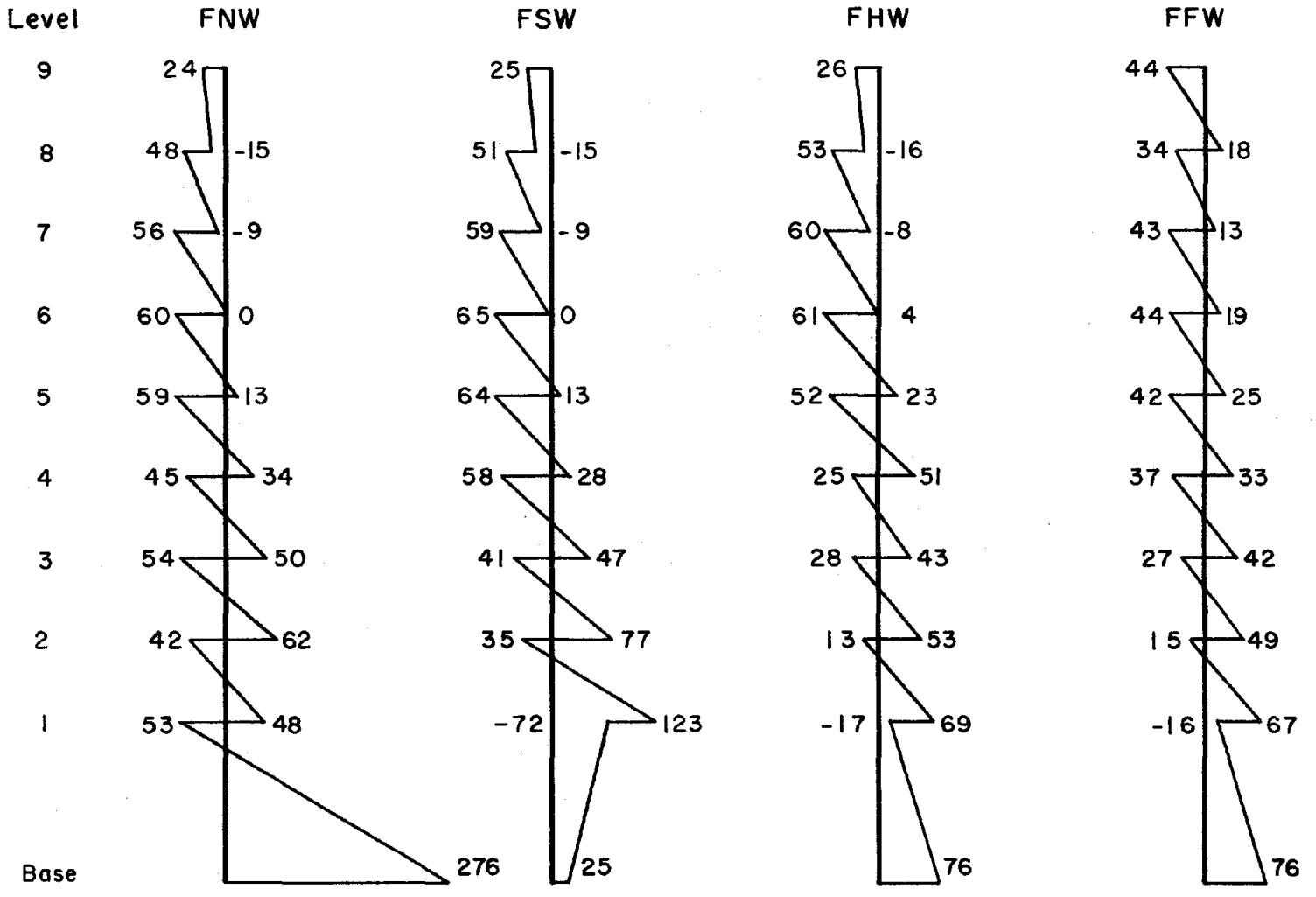


(b) Exterior Column End Moment, kN−mm

Fig. 2.7 (contd.) First-Mode Member Forces Calculated for Design Model

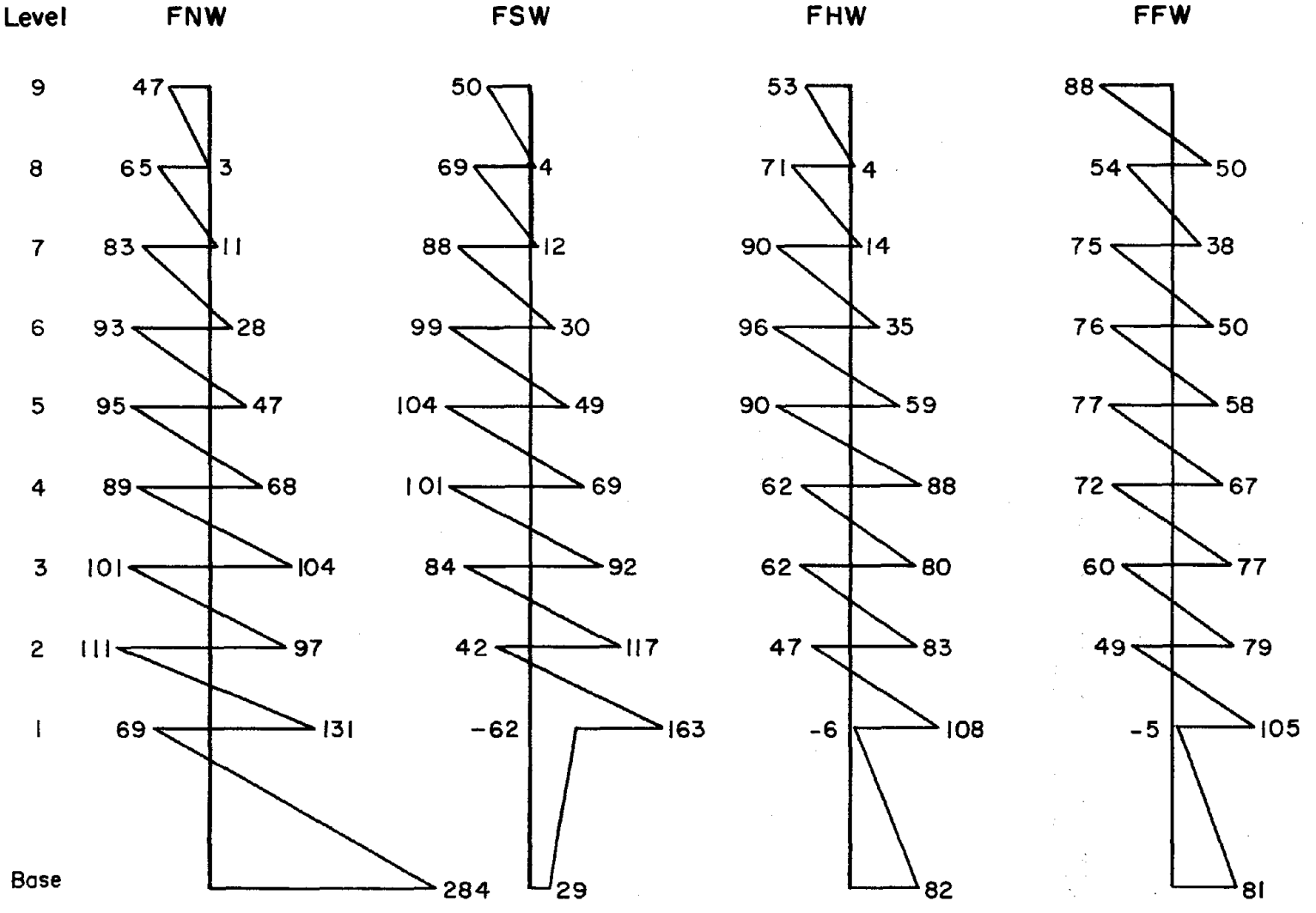


(c) Interior Column End Moments, kN−mm

Fig. 2.7 (contd.) First-Mode Member Forces Calculated for Design Model

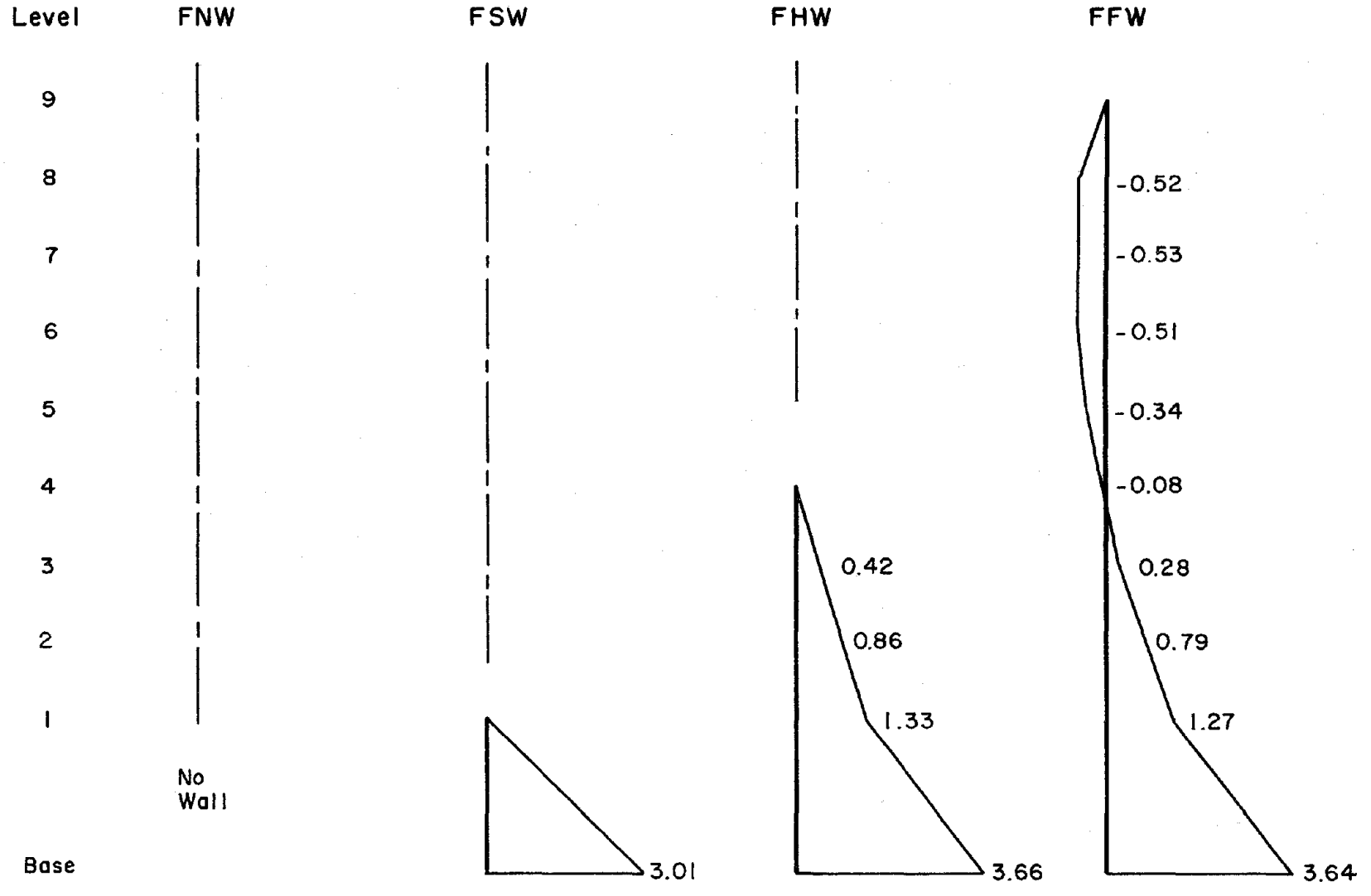


(d) Wall Moments , kN-m

Fig. 2.7 (contd.) First-Mode Member Forces Calculated for Design Model

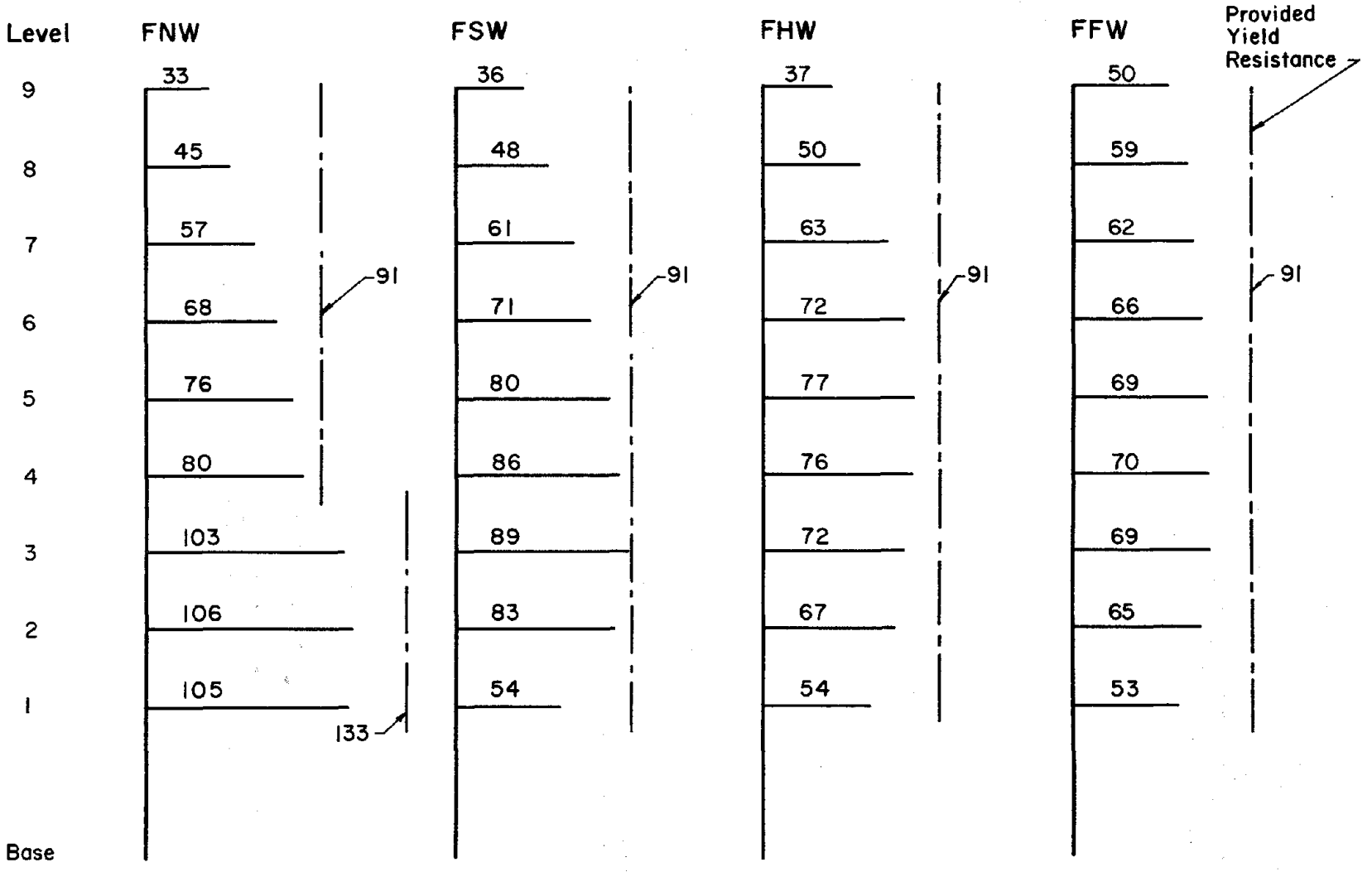


(a) Beam End Moments, kN-mm

Fig. 2.8 RSS Member Forces Calculated for Design Model

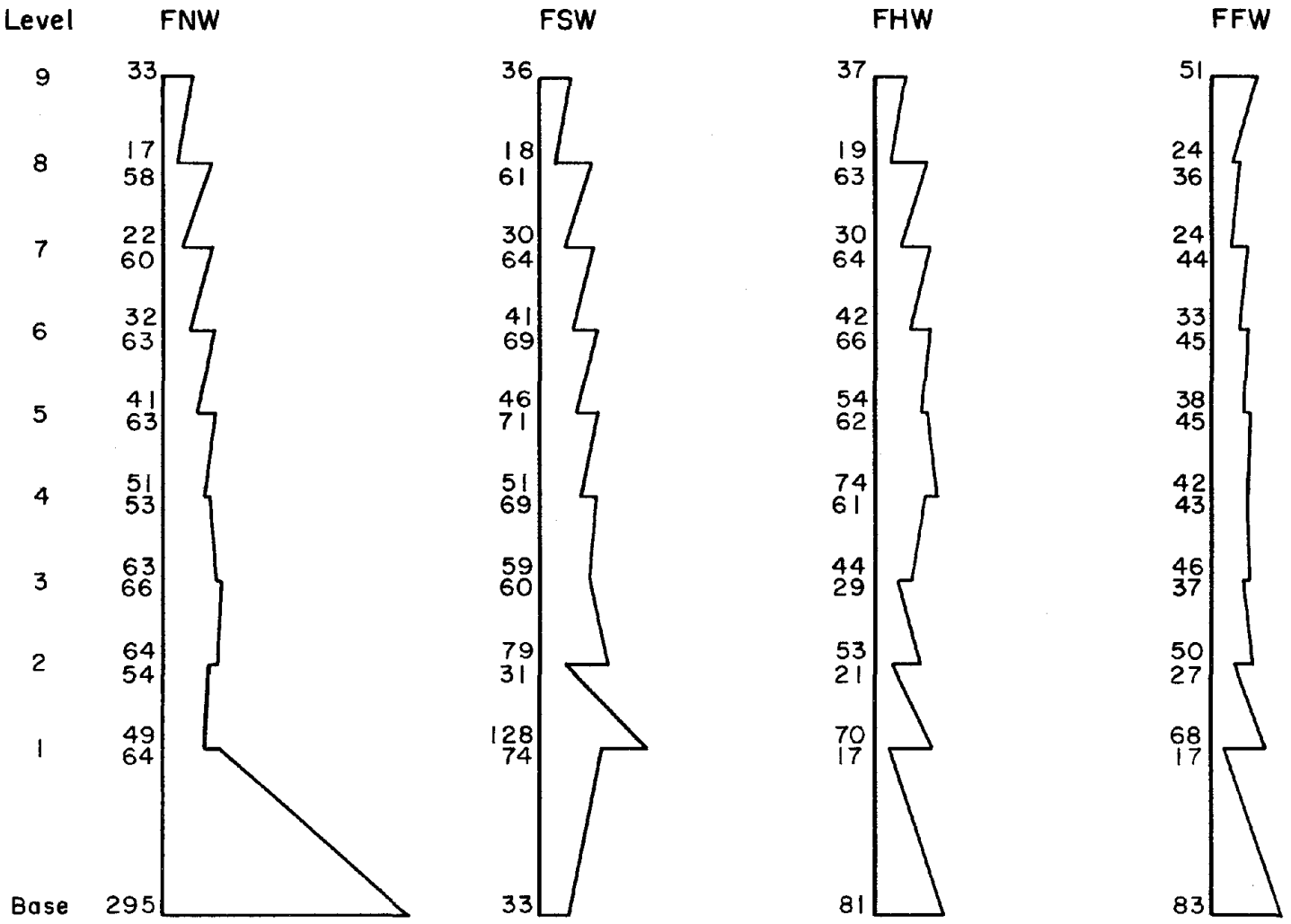


(b) Exterior Column End Moments, kN-mm

Fig. 2.8 (contd.) RSS Member Forces Calculated for Design Model

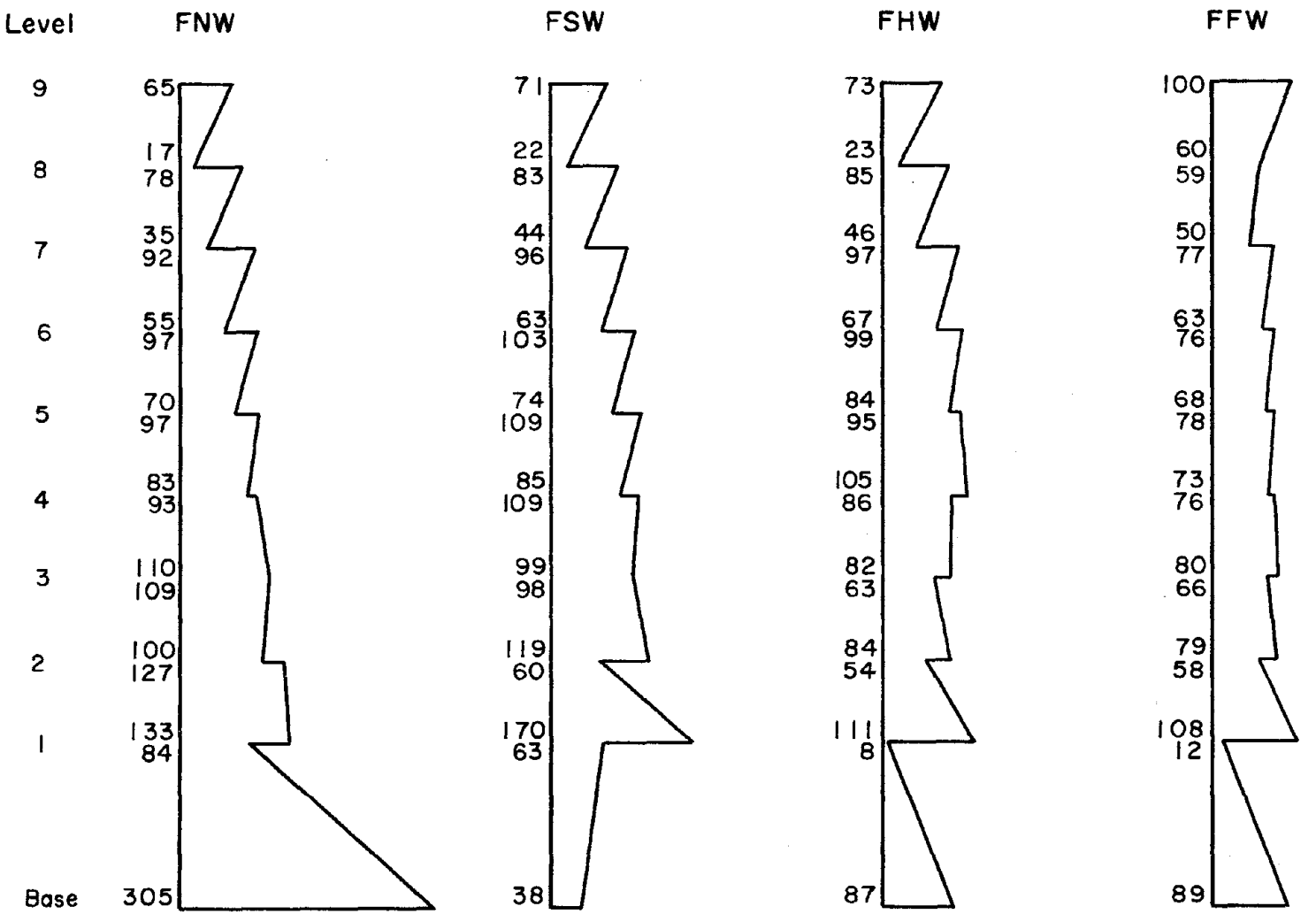


**(c) Interior Column End Moments, kN-mm**

Fig. 2.8 (contd.) RSS Member Forces Calculated for Design Model

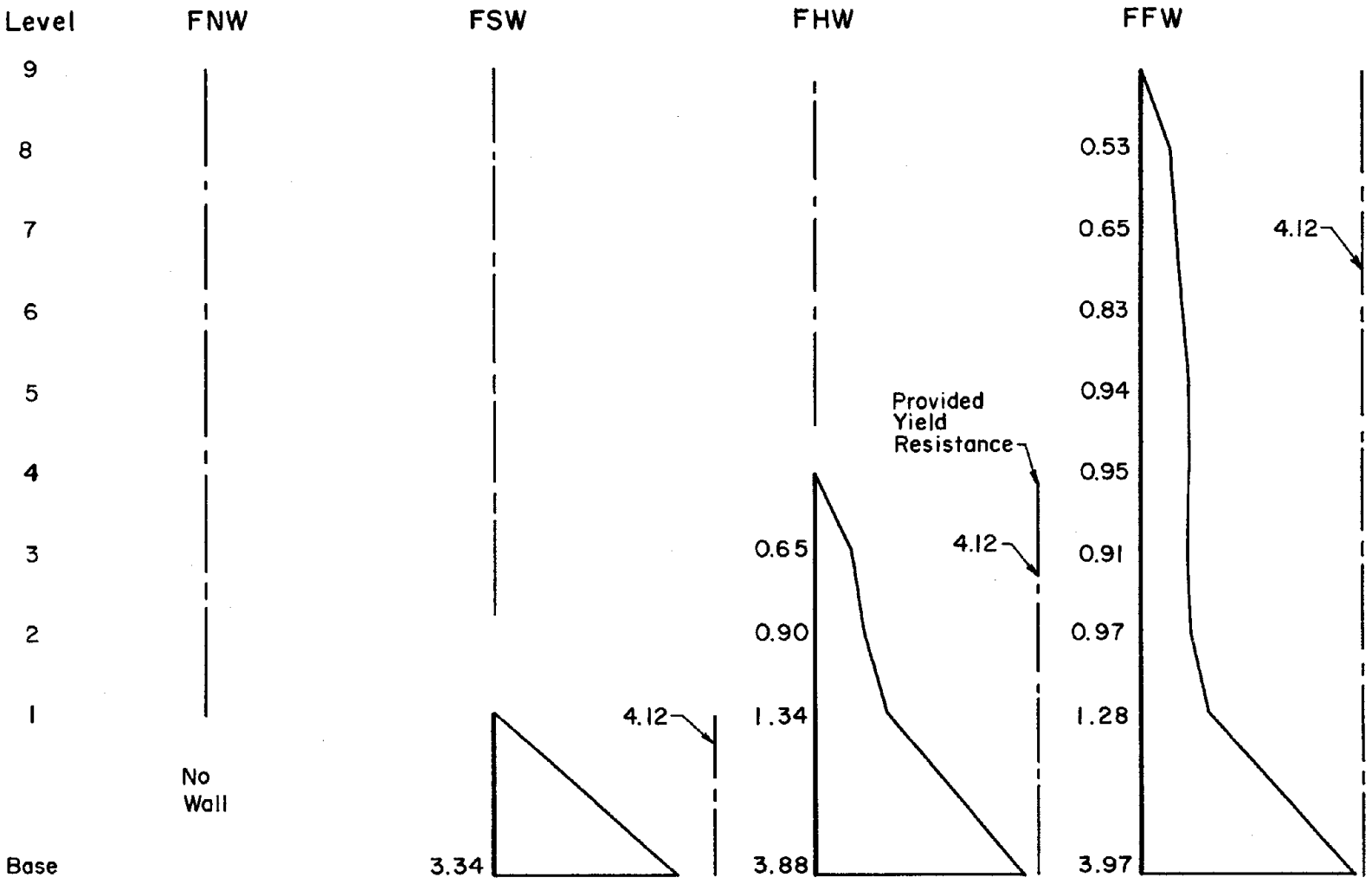


(d) Wall Moments, kN-m

Fig. 2.8 (contd.) RSS Member Forces Calculated for Design Model

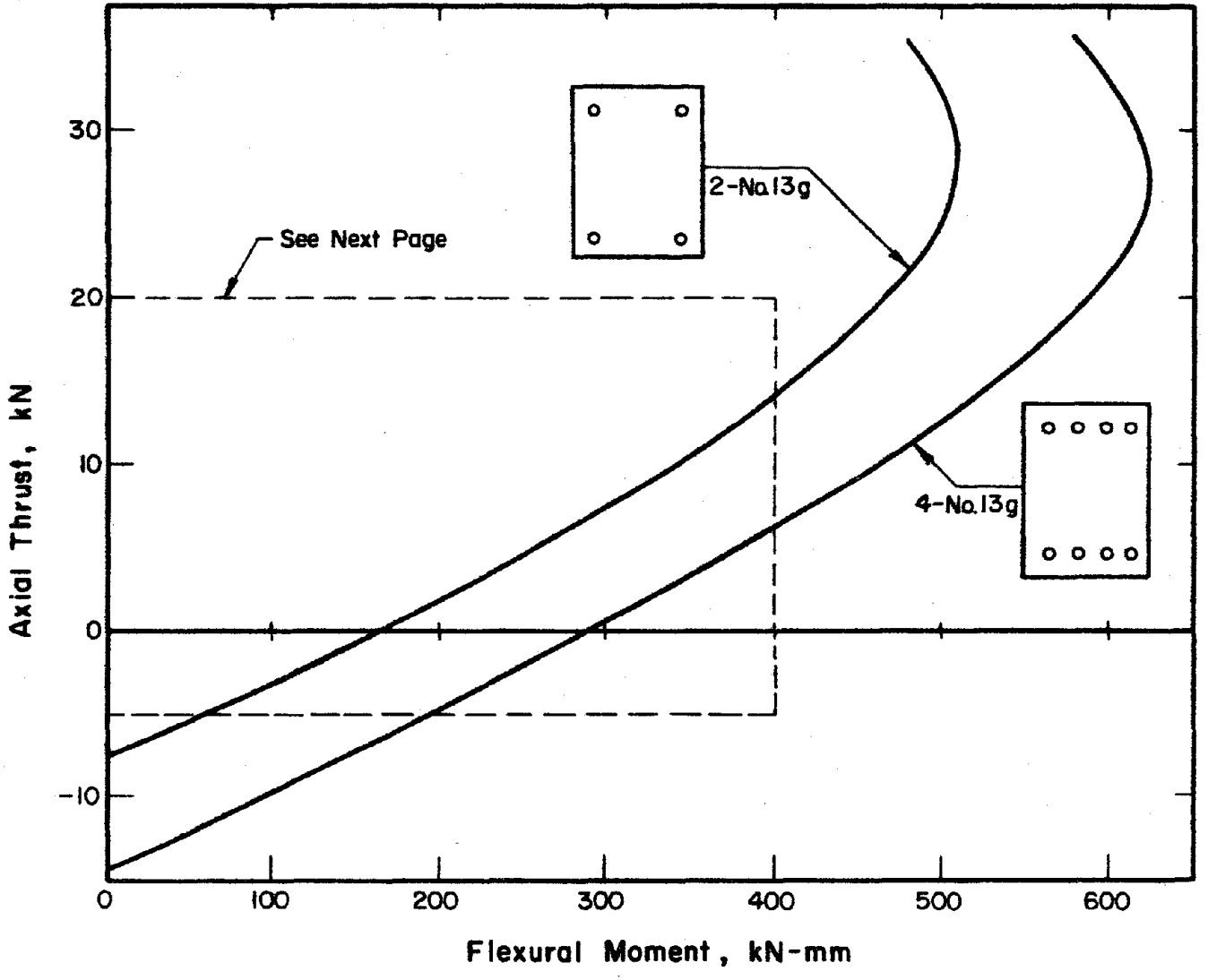


Fig. 2.9 Column Interaction Diagram

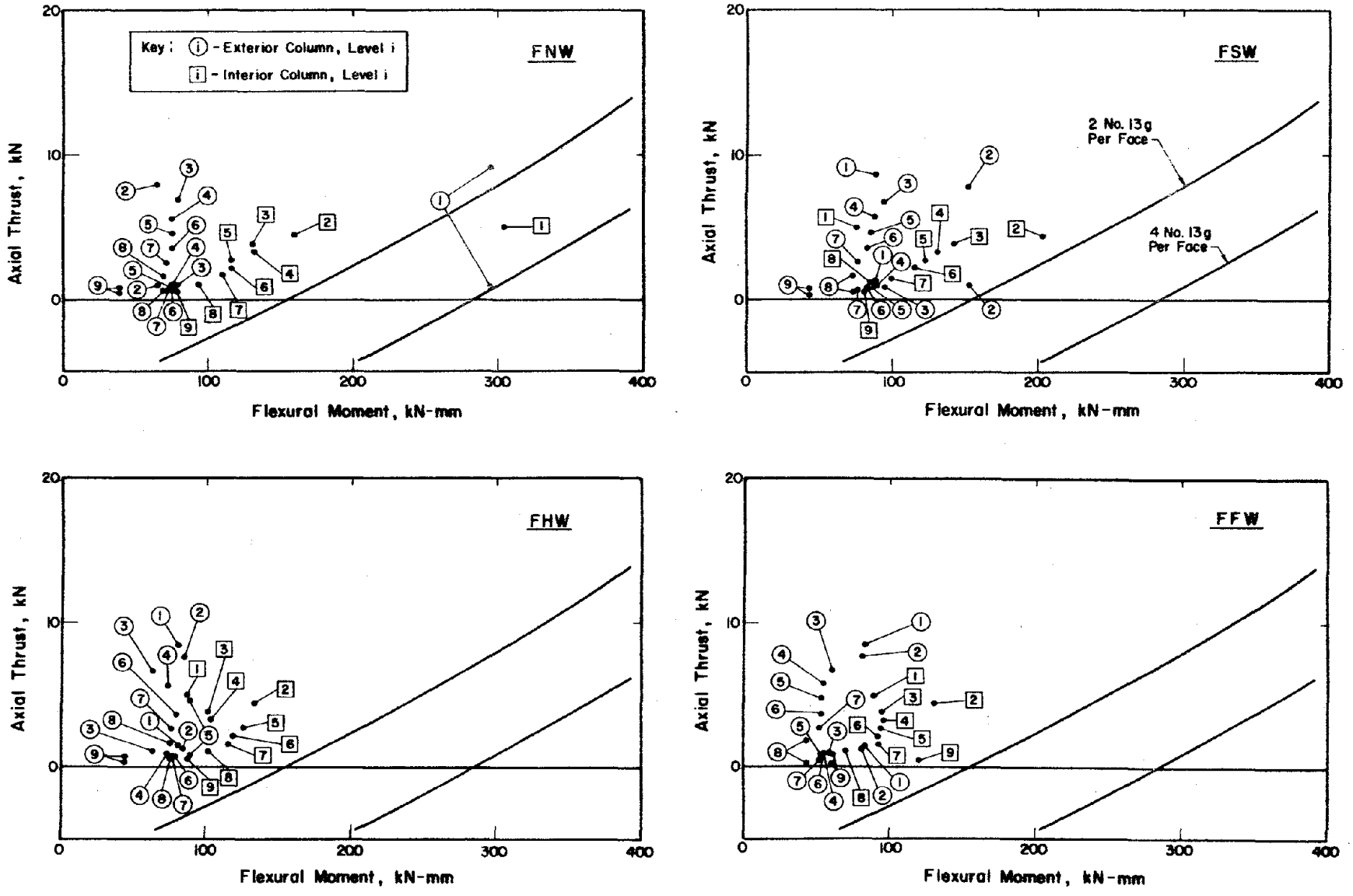


Fig. 2.9 (contd.) Column Interaction Diagram

# REINFORCEMENT RATIOS (x 100)

| | FRAME STRUCTURE | | | FRAME-WALL STRUCTURES | | |
|---|---|---|---|---|---|---|
| LEVEL | EXTERIOR COLUMNS | INTERIOR COLUMNS | BEAMS | COLUMNS | BEAMS | WALL |
| 9 | 0.88 | 0.88 | 0.74 | 0.88 | 0.74 | 0.90 |
| 8 | ↕ | ↕ | ↕ | ↕ | ↕ | ↕ |
| 7 | ↕ | ↕ | ↕ | ↕ | ↕ | ↕ |
| 6 | ↕ | ↕ | ↕ | ↕ | ↕ | ↕ |
| 5 | ↕ | ↕ | ↕ | ↕ | ↕ | ↕ |
| 4 | ↕ | ↕ | 0.74 | ↕ | ↕ | ↕ |
| 3 | ↕ | 0.88 | 1.10 | ↕ | ↕ | ↕ |
| 2 | 0.88 | 1.75 | 1.10 | ↕ | ↕ | ↕ |
| 1 | 1.75 | 1.75 | 1.10 | 0.88 | 0.74 | 0.90 |

(a) Reinforcement Schedule

Fig. 2.10 Reinforcement Details

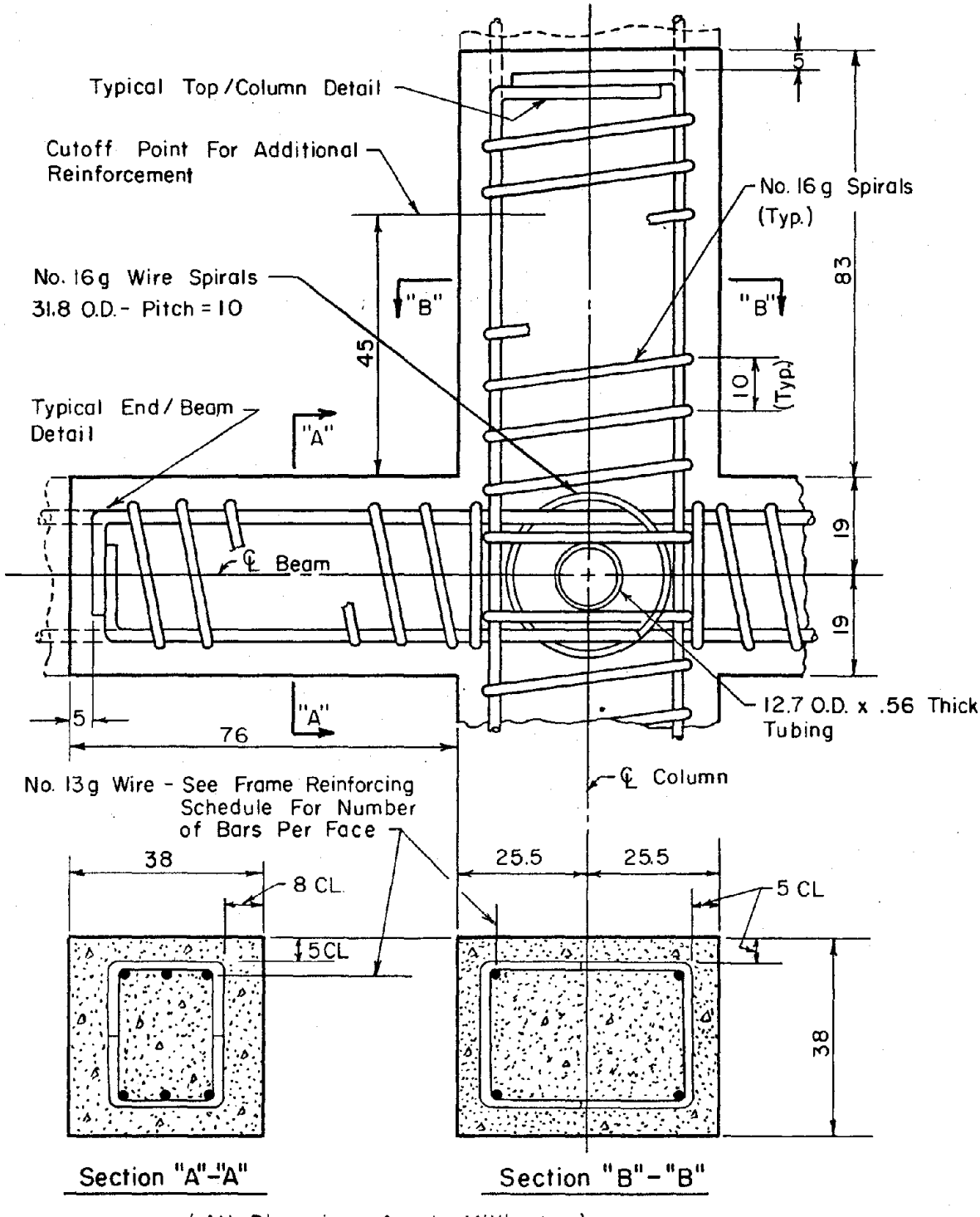


**(b) Frame Detail**

Fig. 2.10 (contd.) Reinforcement Details

(All Dimensions Are In Millimeters)

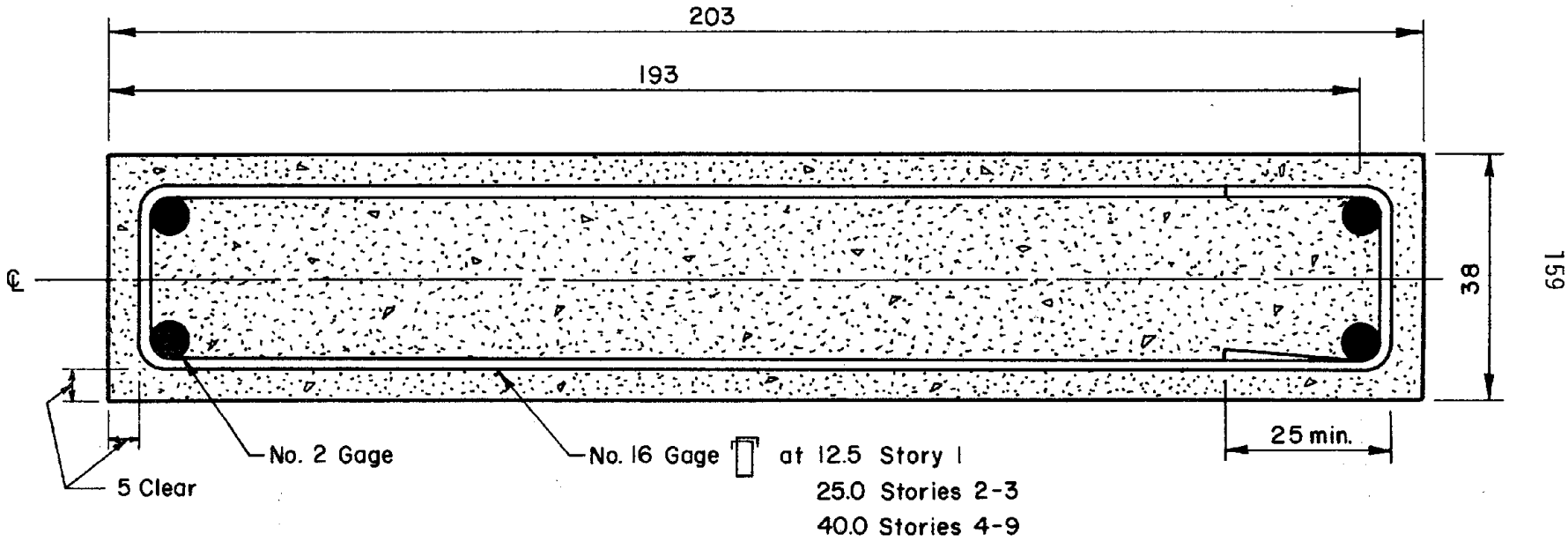


**(c) Wall Detail**

Fig. 2.10 (contd.) Reinforcement Details

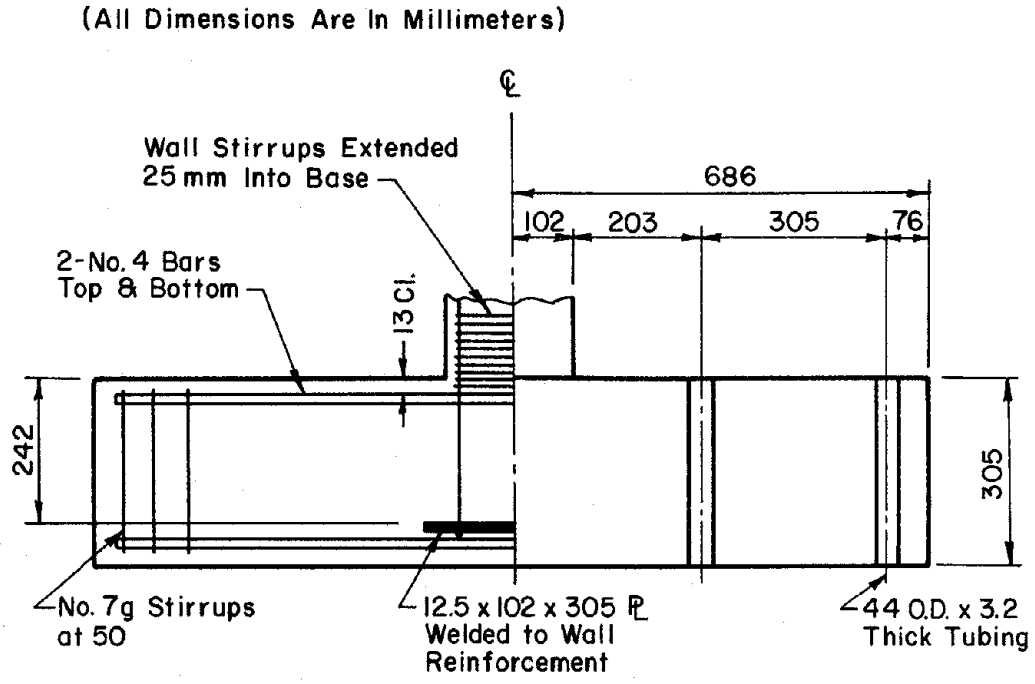


(d) Wall Base Anchorage

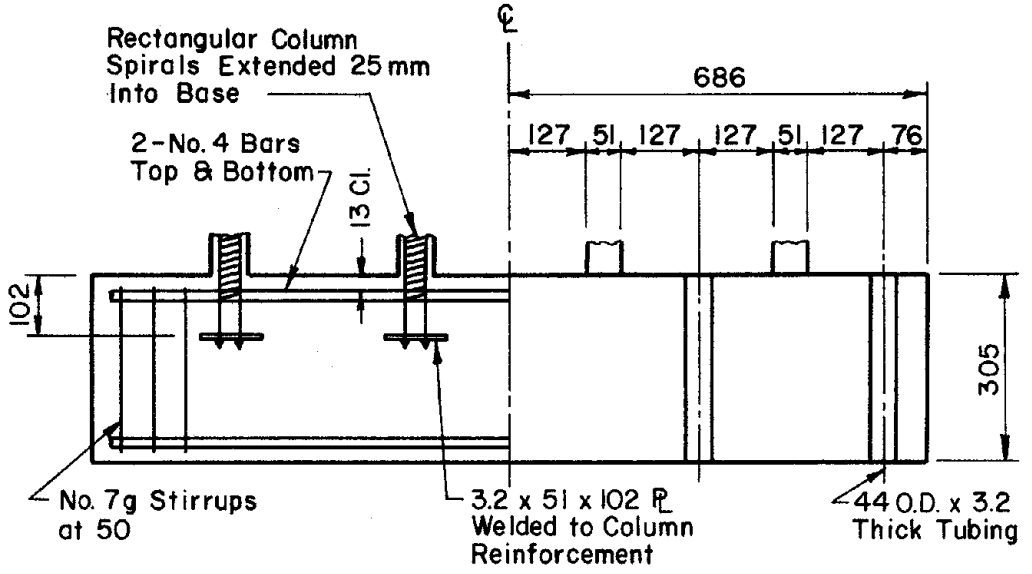


(e) Frame Base Anchorage

Fig. 2.10 (contd.) Reinforcement Details

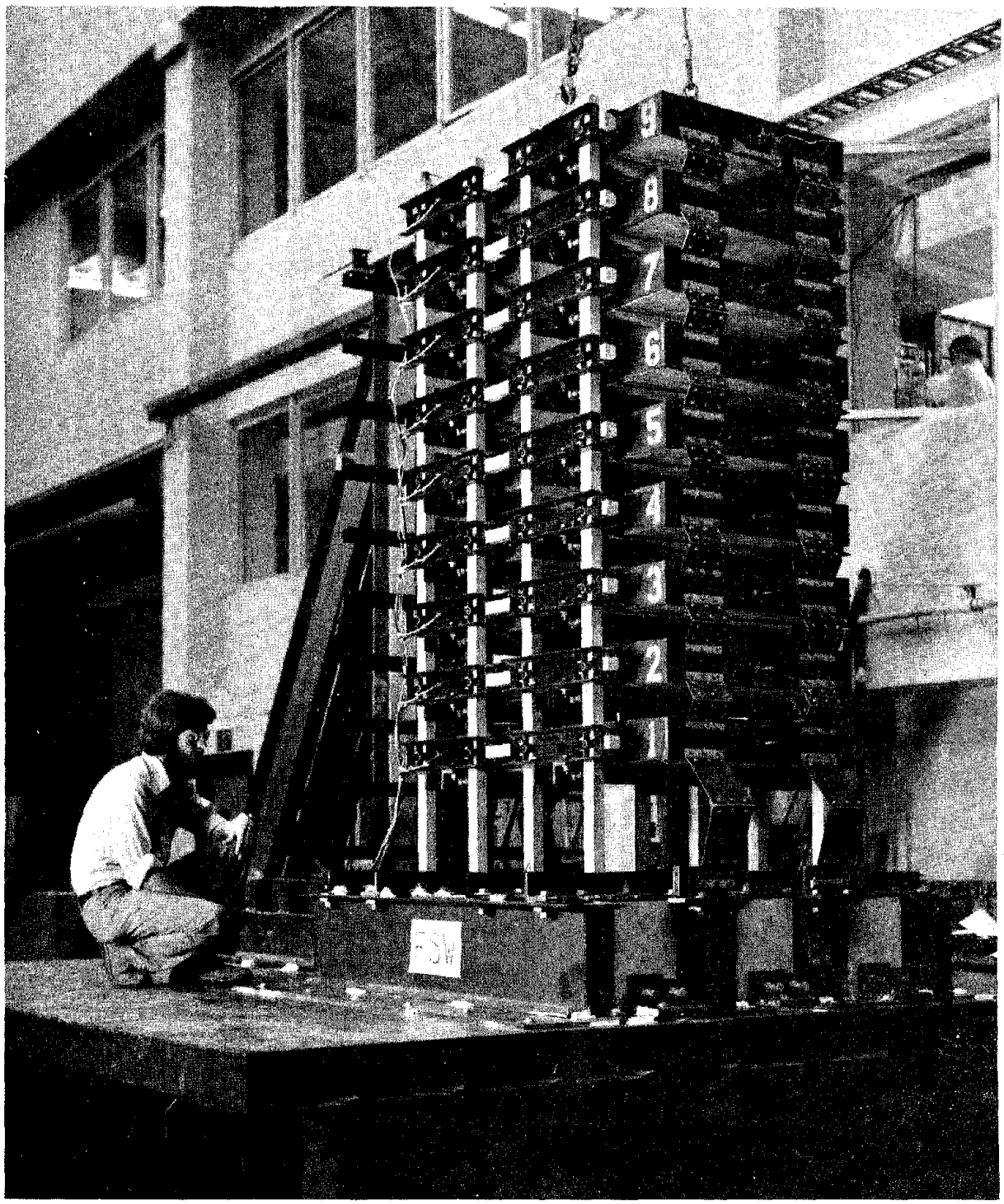


Fig. 3.1 Photograph of Test Structure

1. TEST RUNS ONE, TWO, AND THREE*

   (A) FREE-VIBRATION TEST

   (B) EARTHQUAKE SIMULATION

   (C) FREE-VIBRATION TEST

   (D) STEADY-STATE TEST

   (E) STATIC TEST

2. HIGH-AMPLITUDE STEADY-STATE TEST

3. STRENGTH TEST

* SEQUENCE (A) THROUGH (E) CONDUCTED THREE TIMES WITH EARTHQUAKE-SIMULATION INTENSITY INCREASED EACH TIME.

Fig. 3.2 Testing Sequence

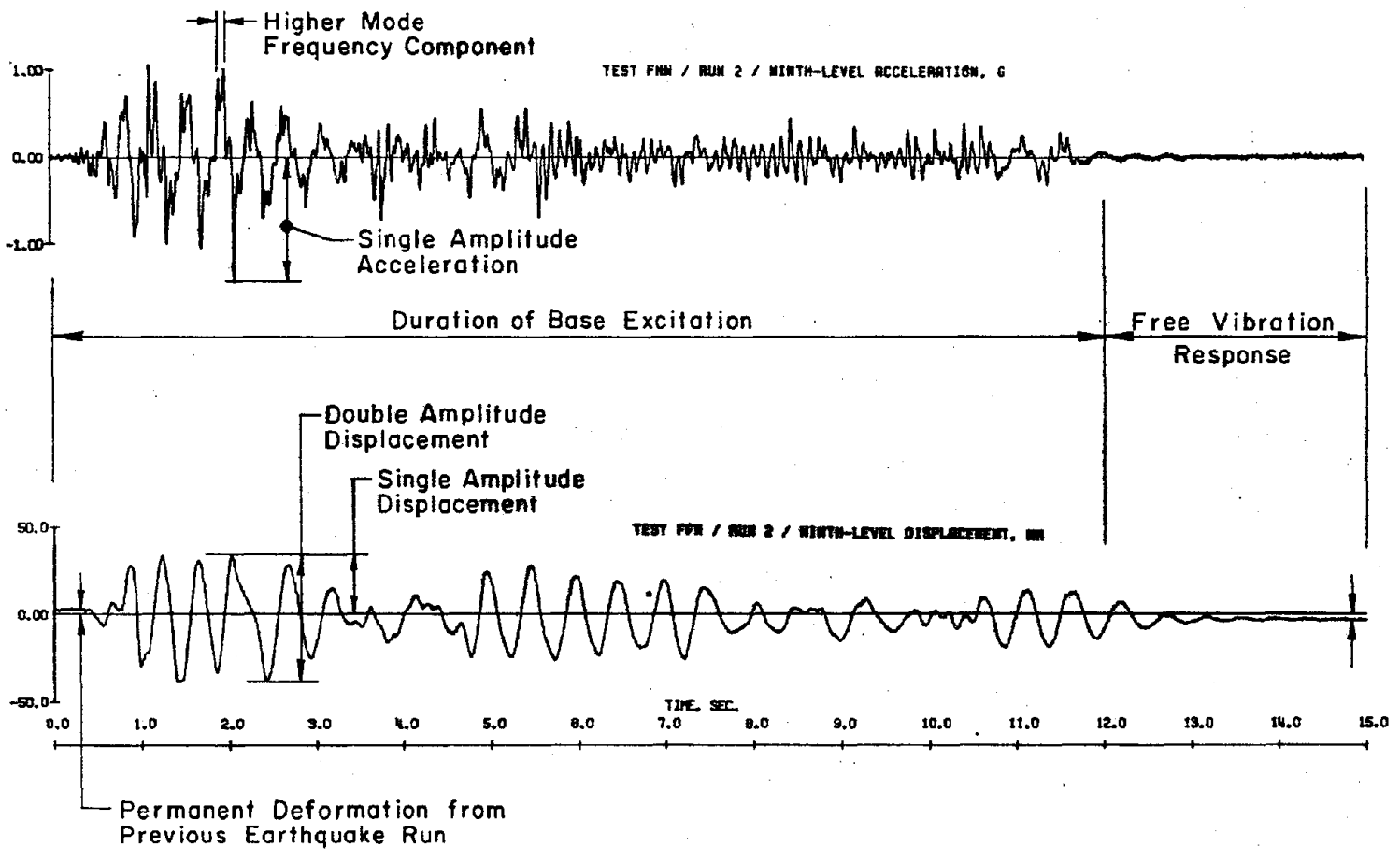


Fig. 4.1 Illustration of Terms Used to Describe Waveforms

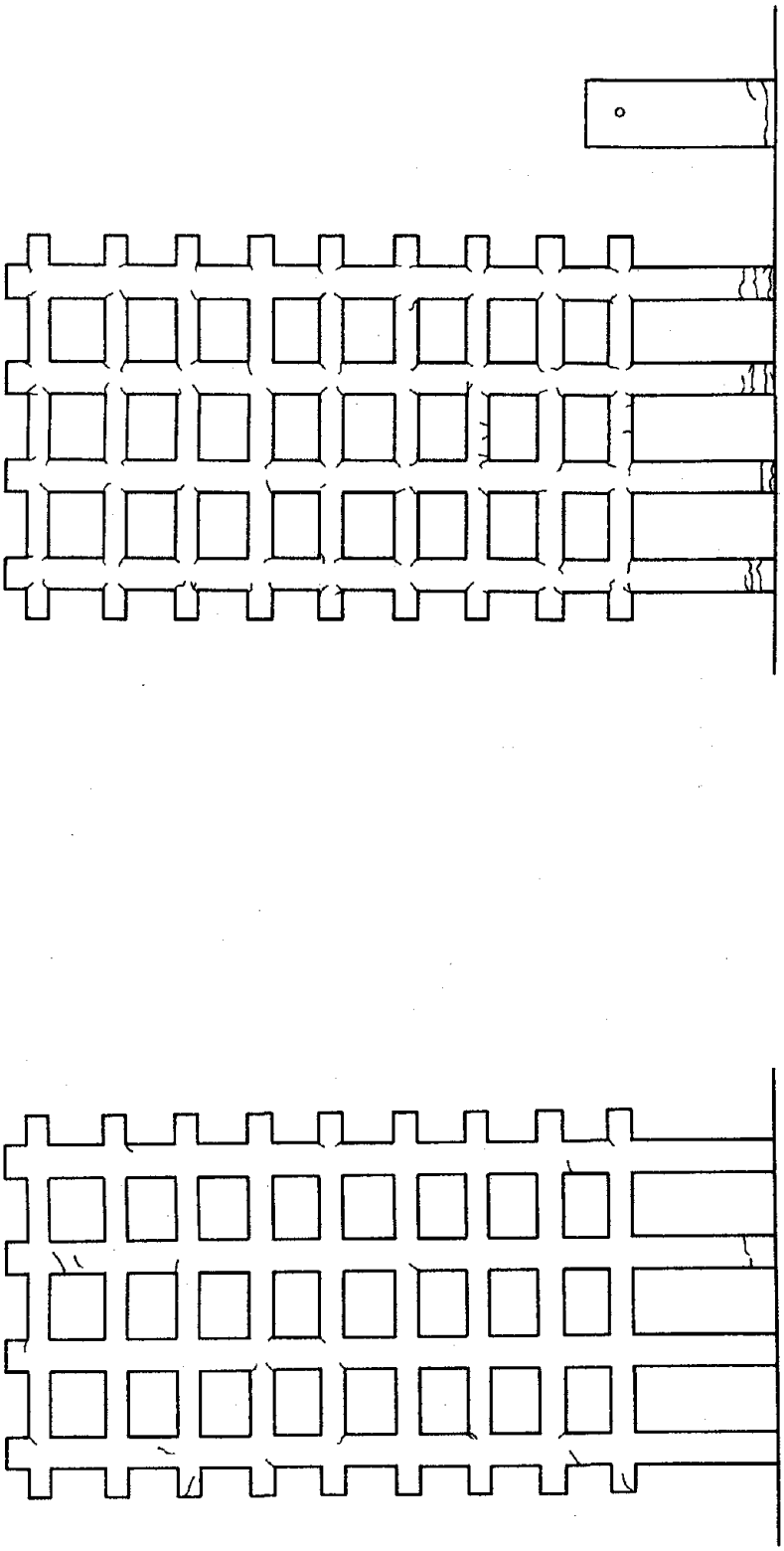

Fig. 4.2 Cracks Observed before Testing

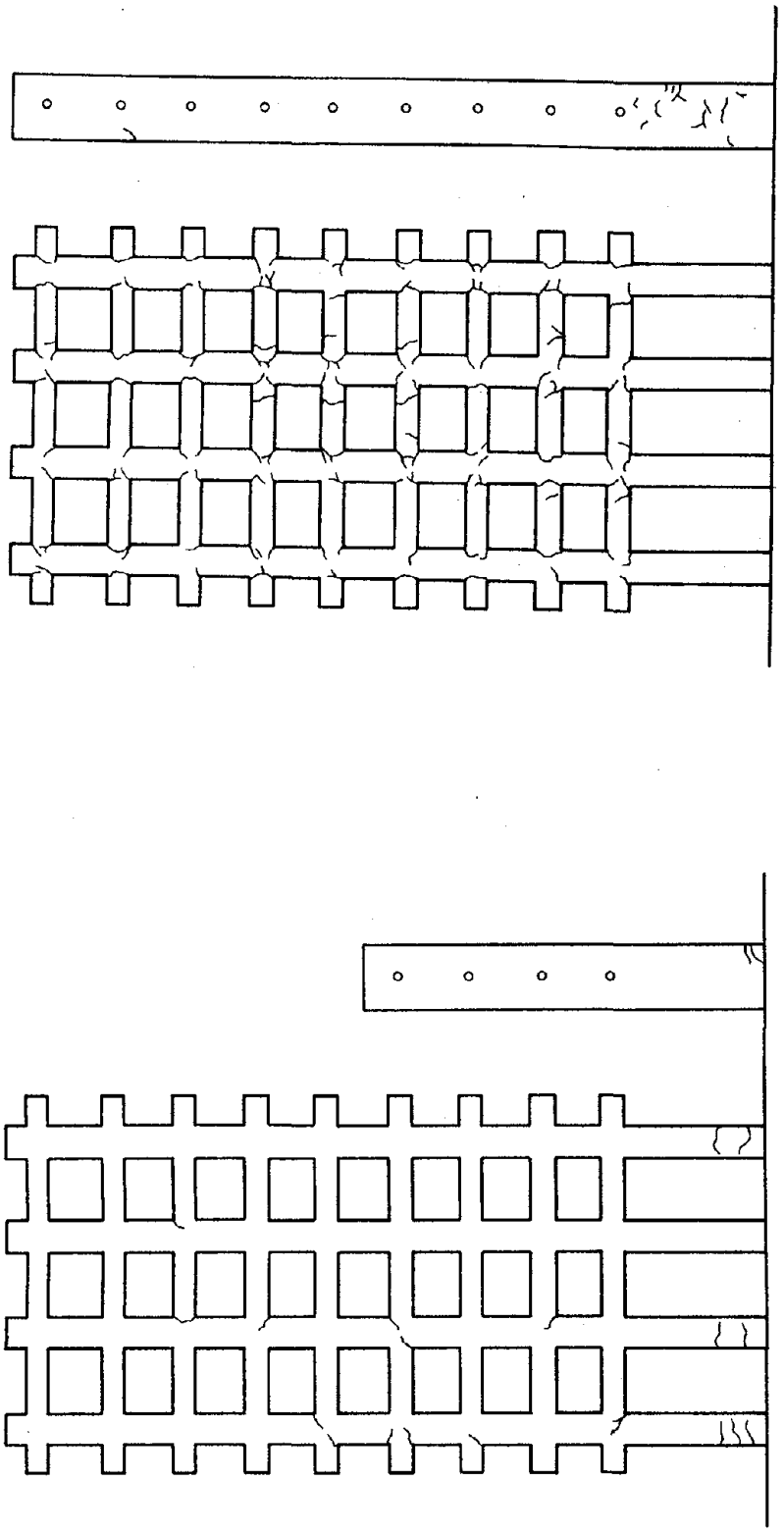

Fig. 4.2 (contd.) Cracks Observed before Testing

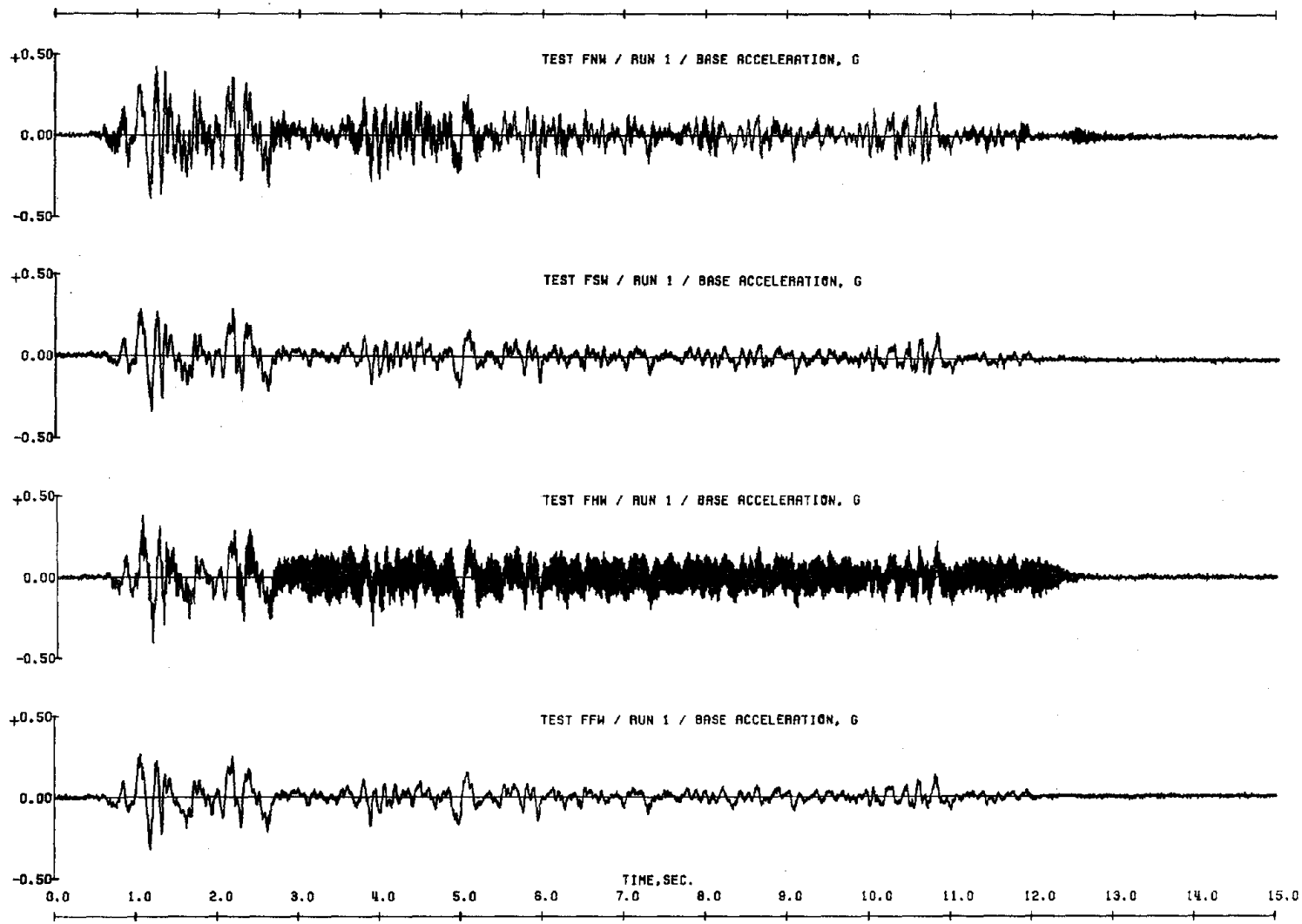


Fig. 4.3 Base Accelerations and Displacements Measured during Initial Simulation

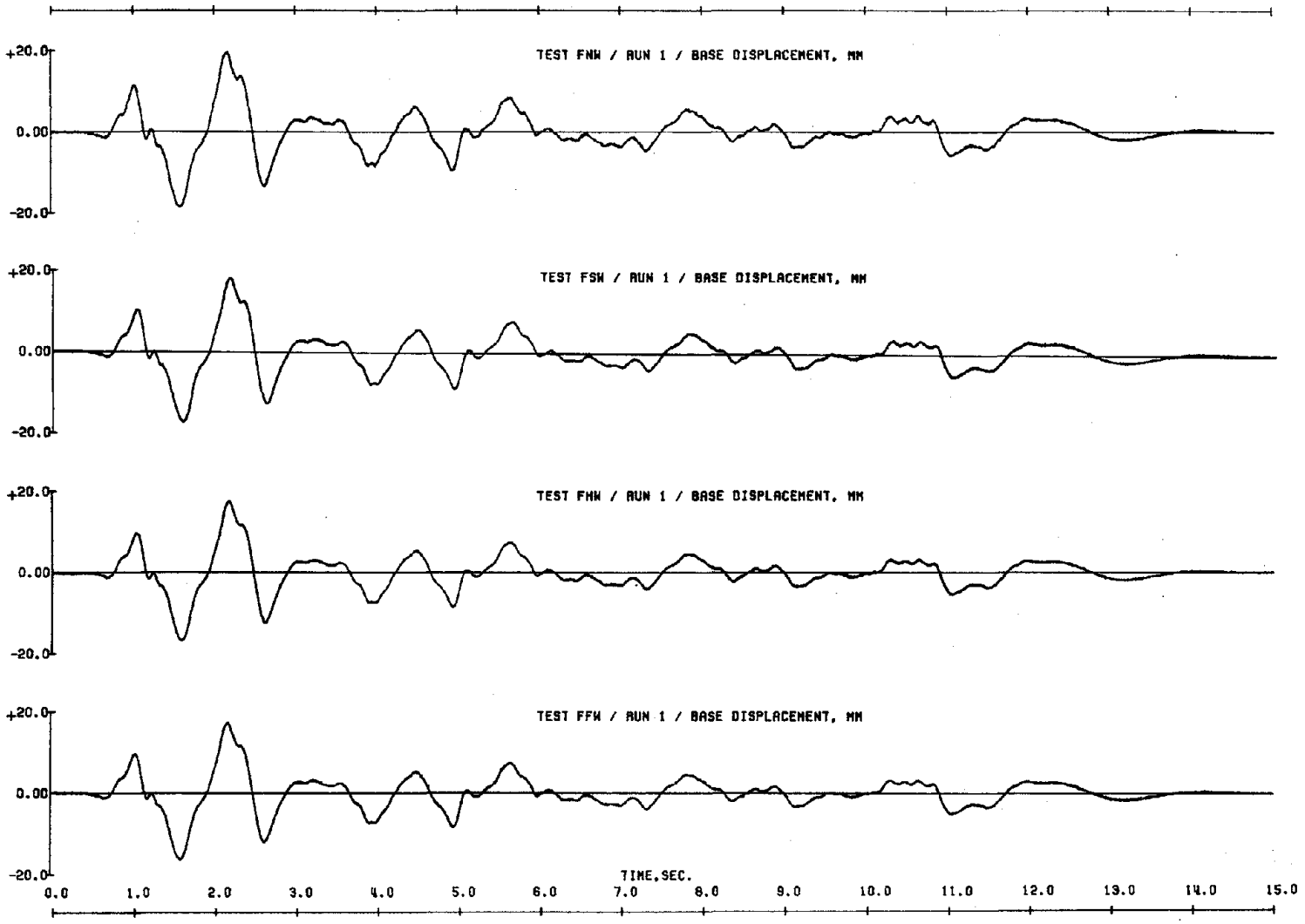


Fig. 4.3 (contd.) Base Accelerations and Displacements Measured during Initial Simulation

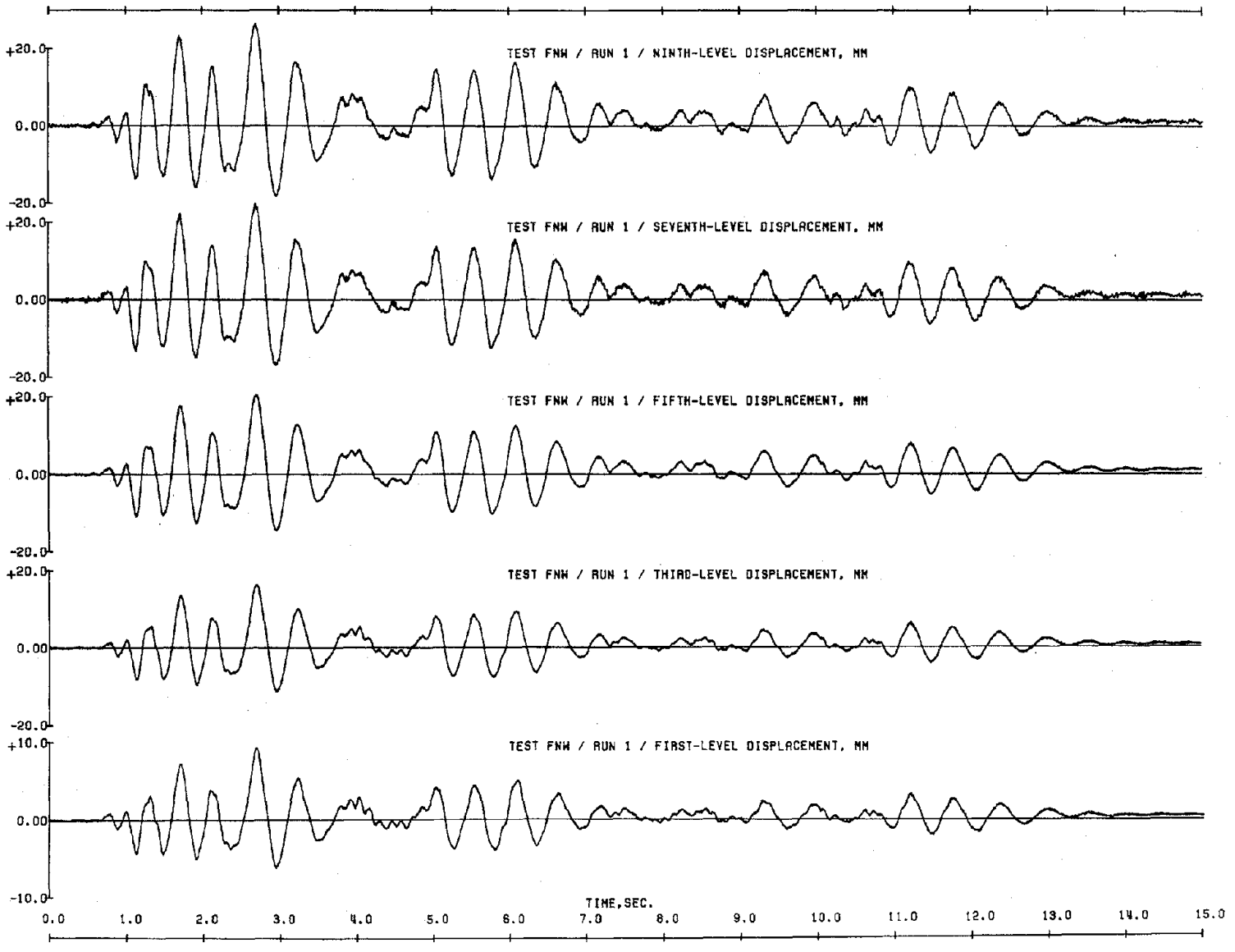


Fig. 4.4 Displacement Response Measured during Initial Simulations

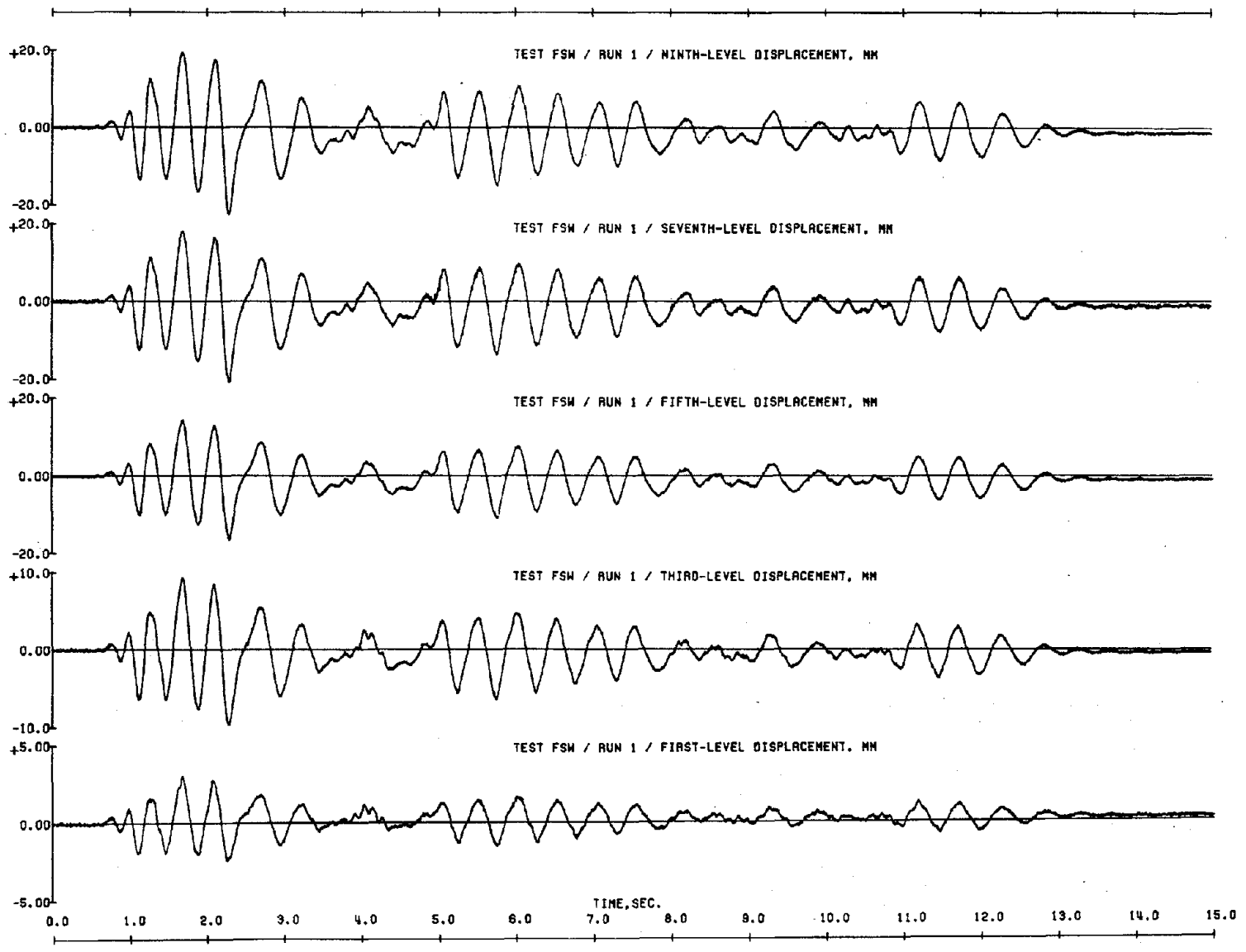


Fig. 4.4 (contd.) Displacement Response Measured during Initial Simulations

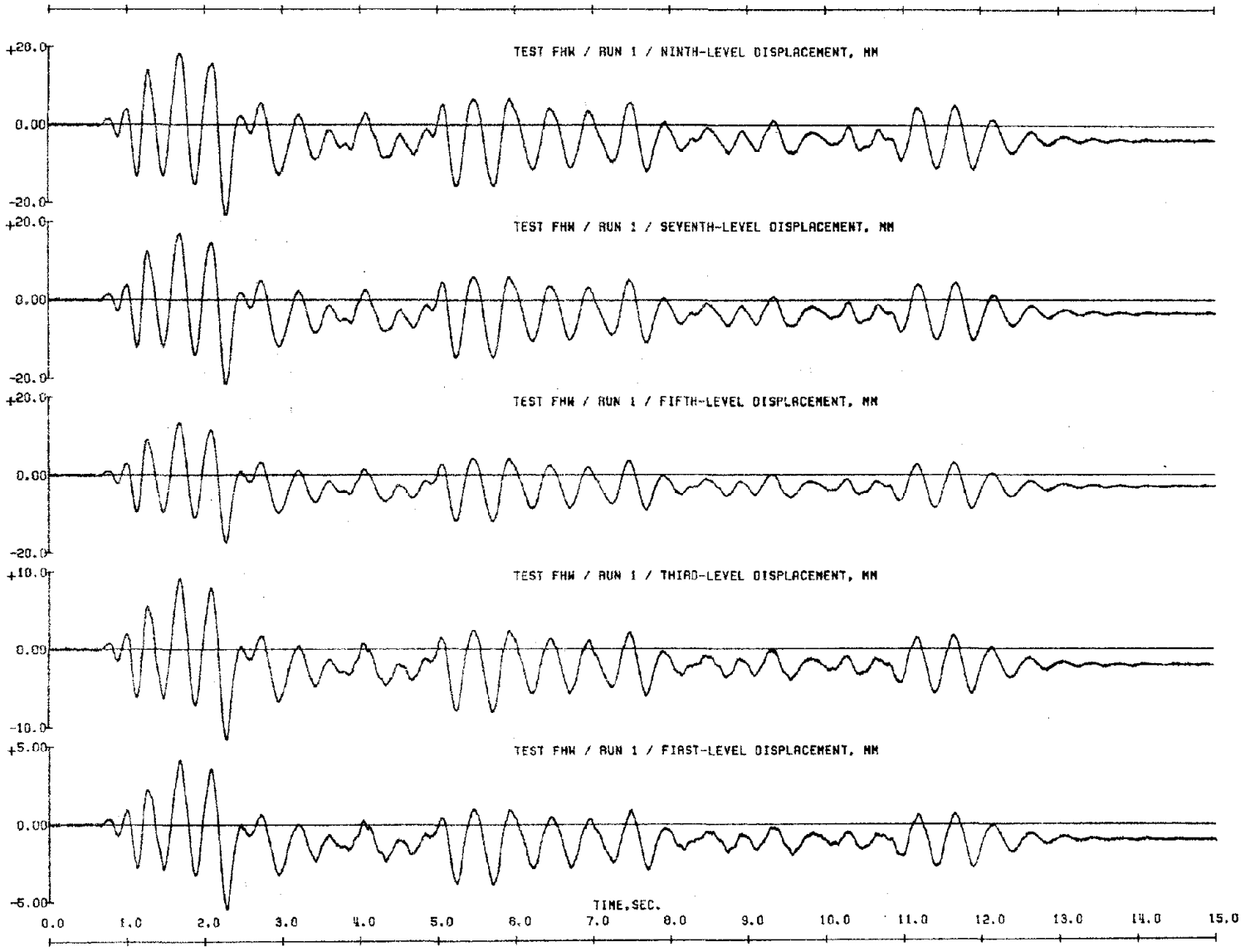


Fig. 4.4 (contd.) Displacement Response Measured during Initial Simulations

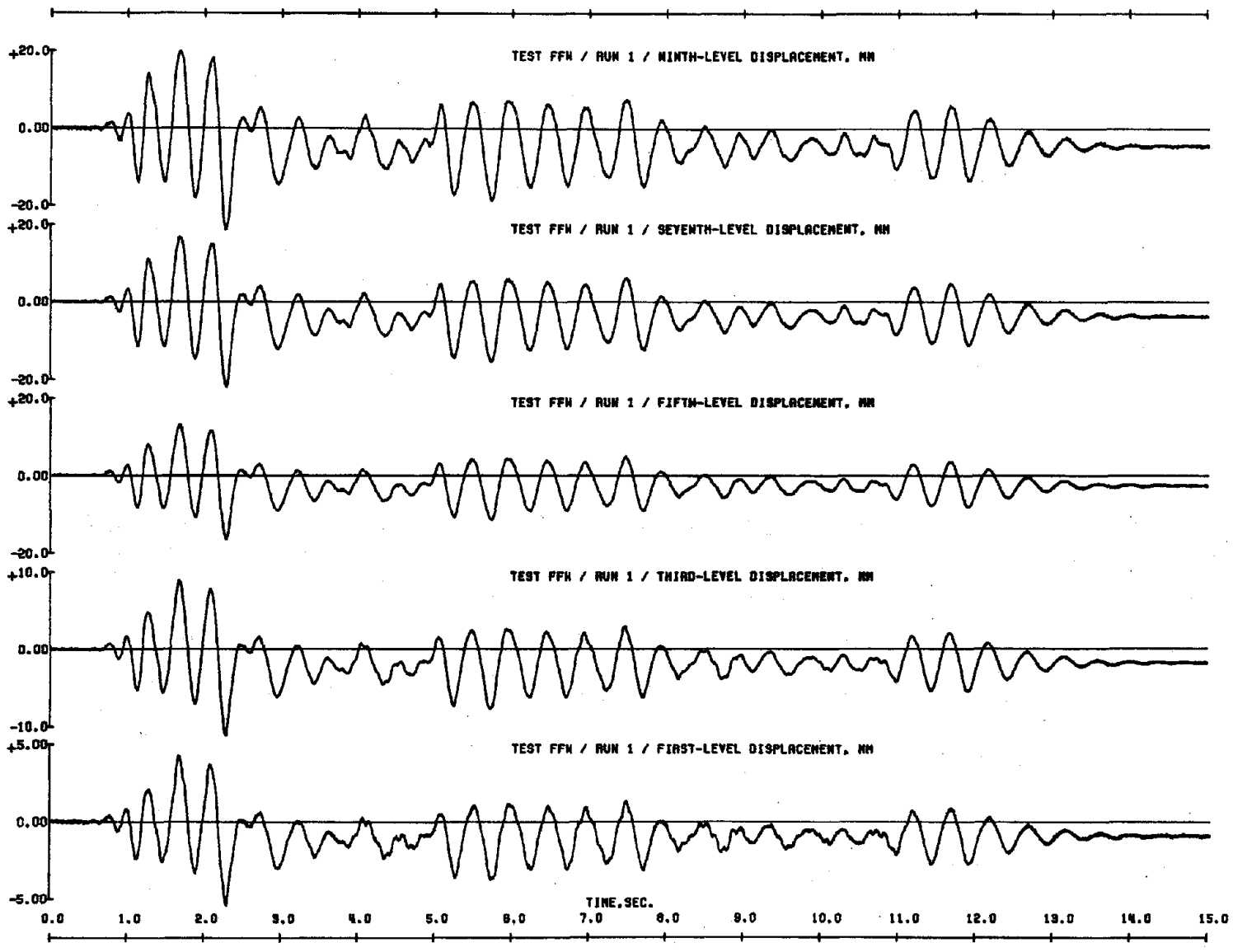


Fig. 4.4 (contd.) Displacement Response Measured during Initial Simulations

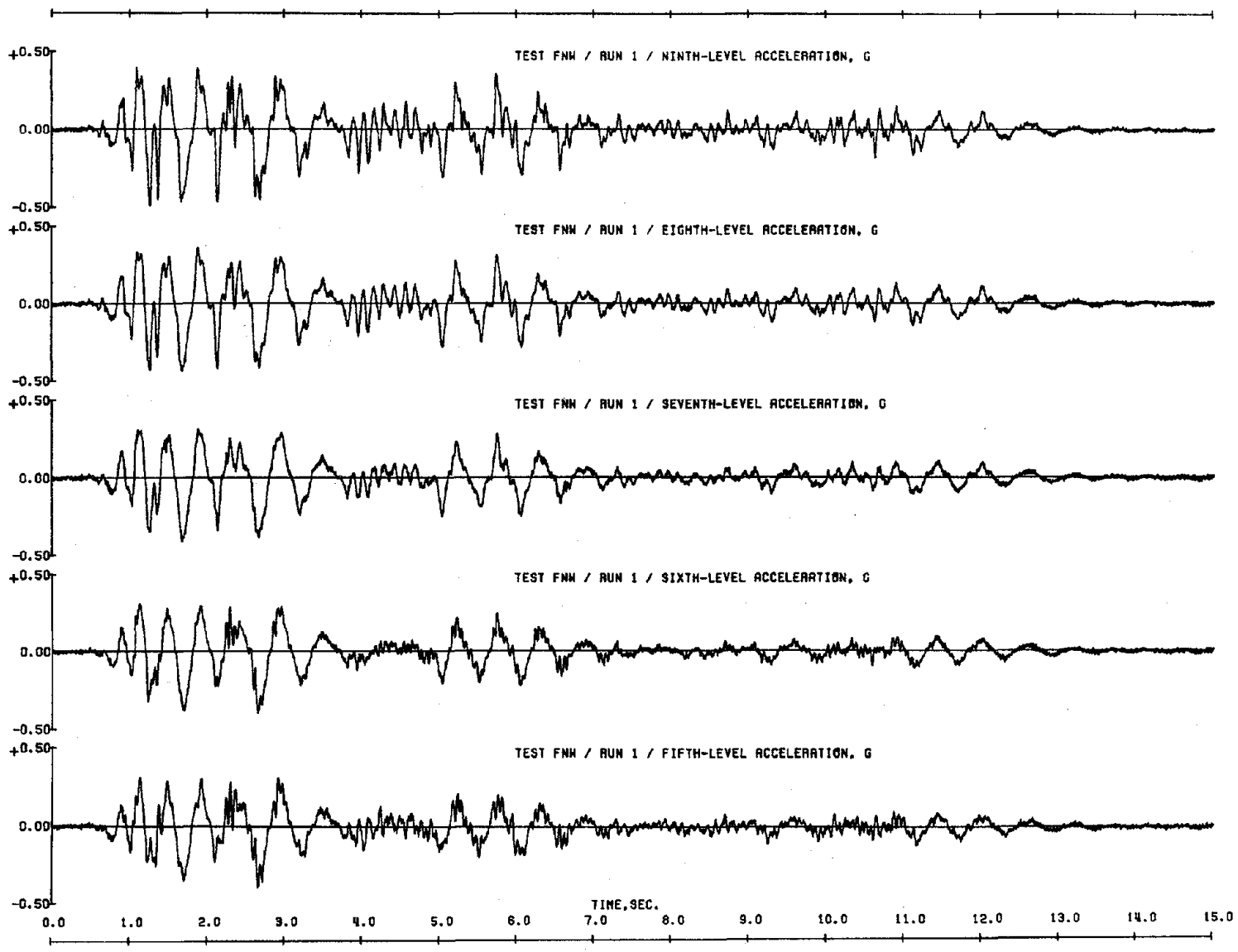


Fig. 4.5 Acceleration Response Measured during Initial Simulations

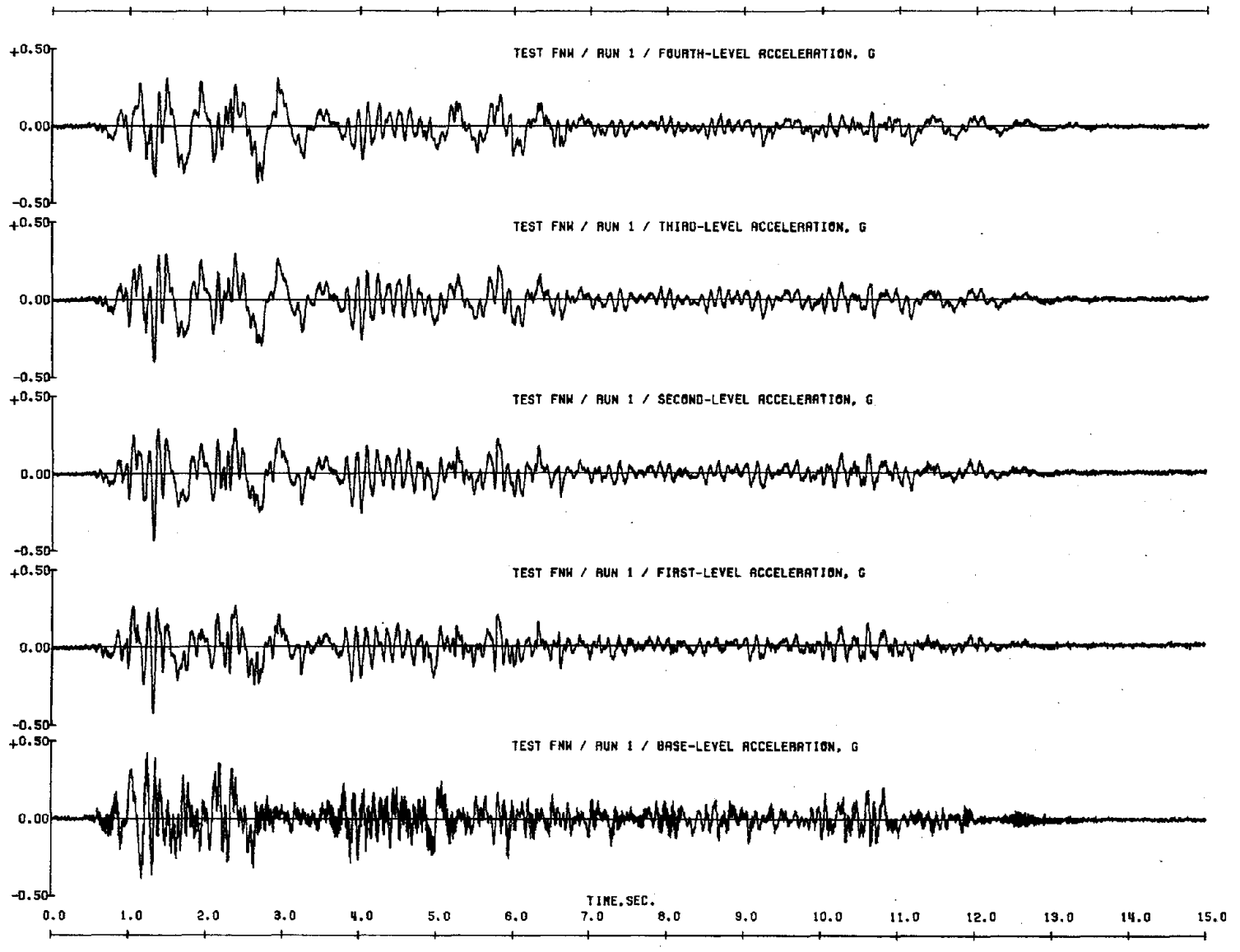


Fig. 4.5 (contd.) Acceleration Response Measured during Initial Simulations

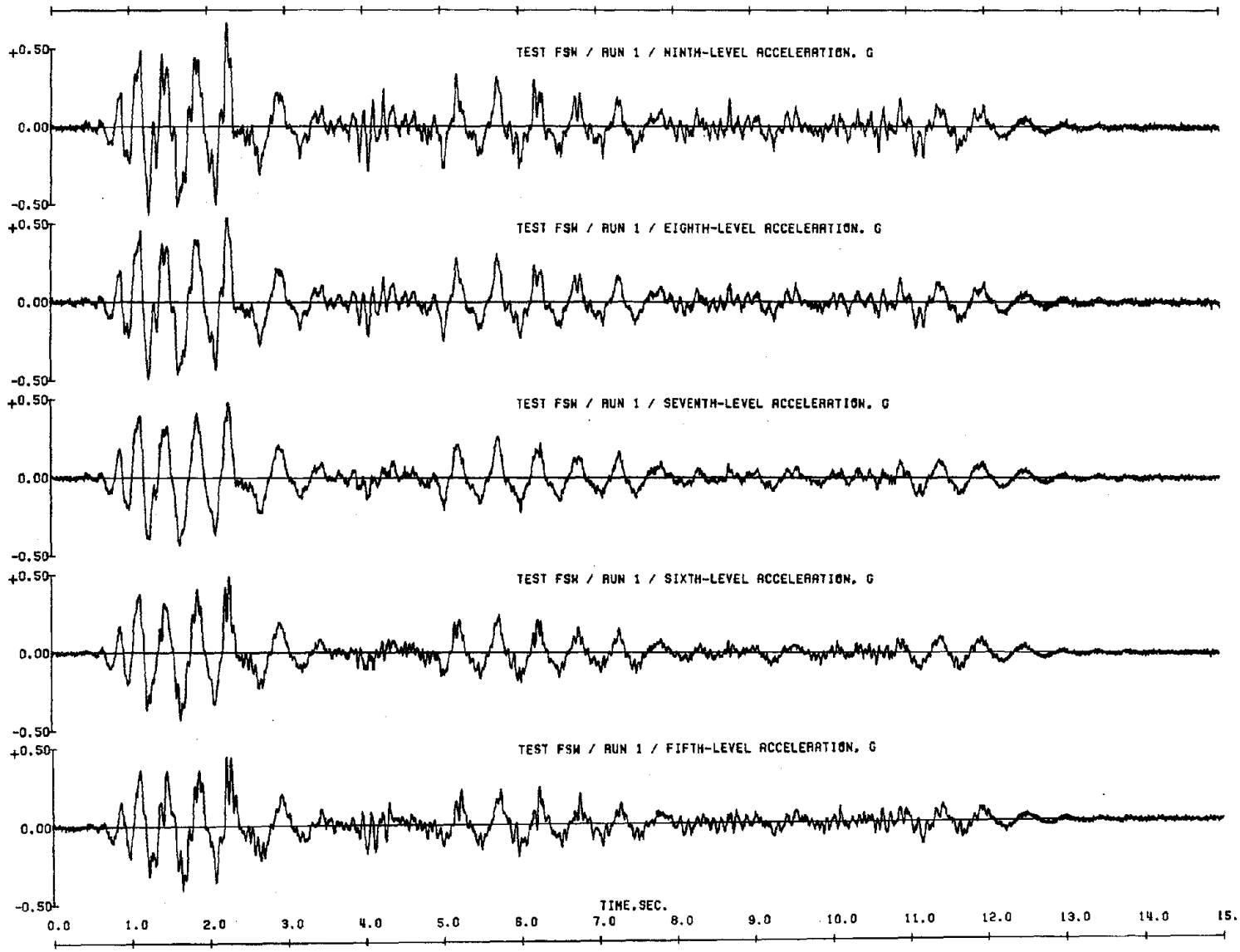


Fig. 4.5 (contd.) Acceleration Response Measured during Initial Simulations

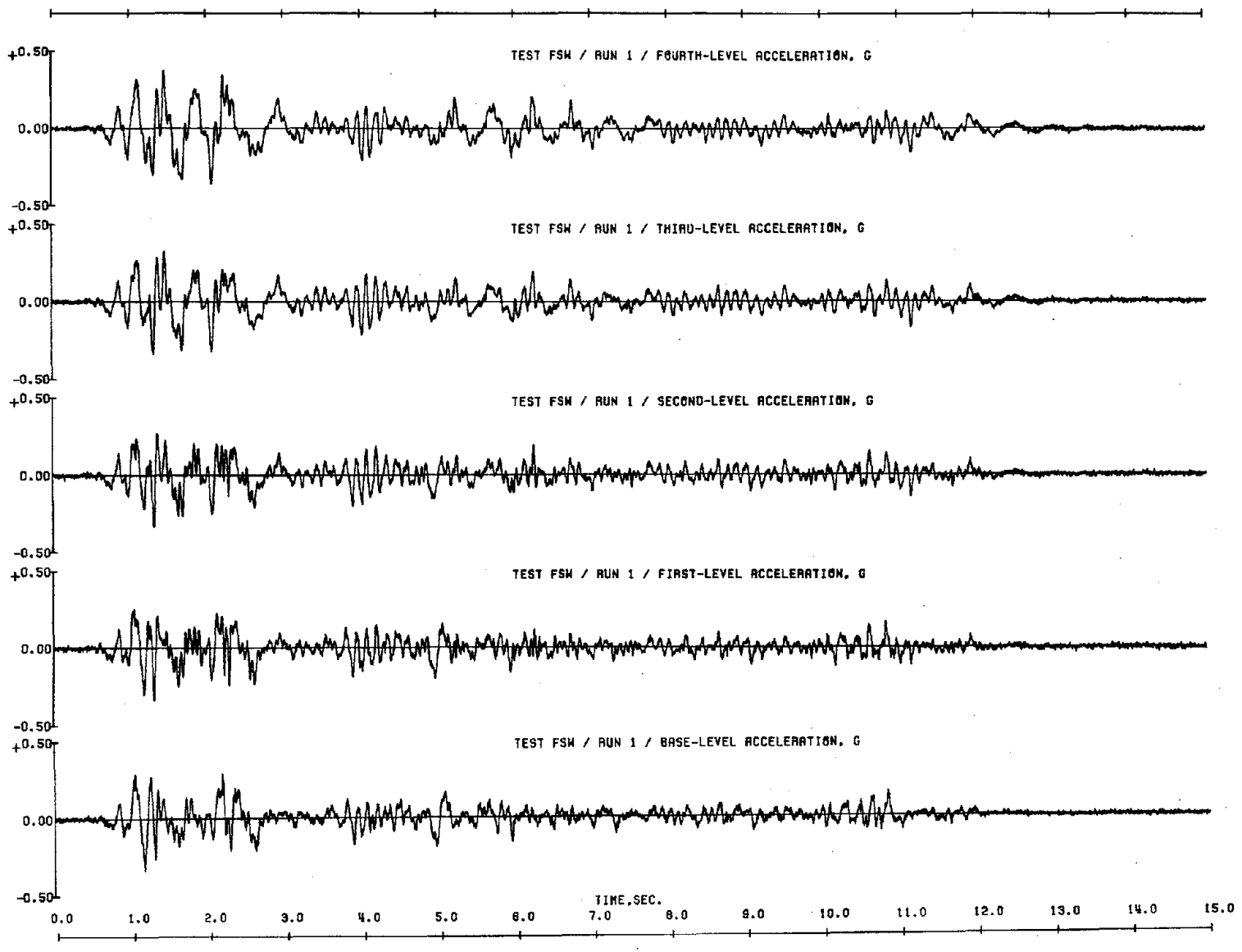


Fig. 4.5 (contd.) Acceleration Response Measured during Initial Simulations

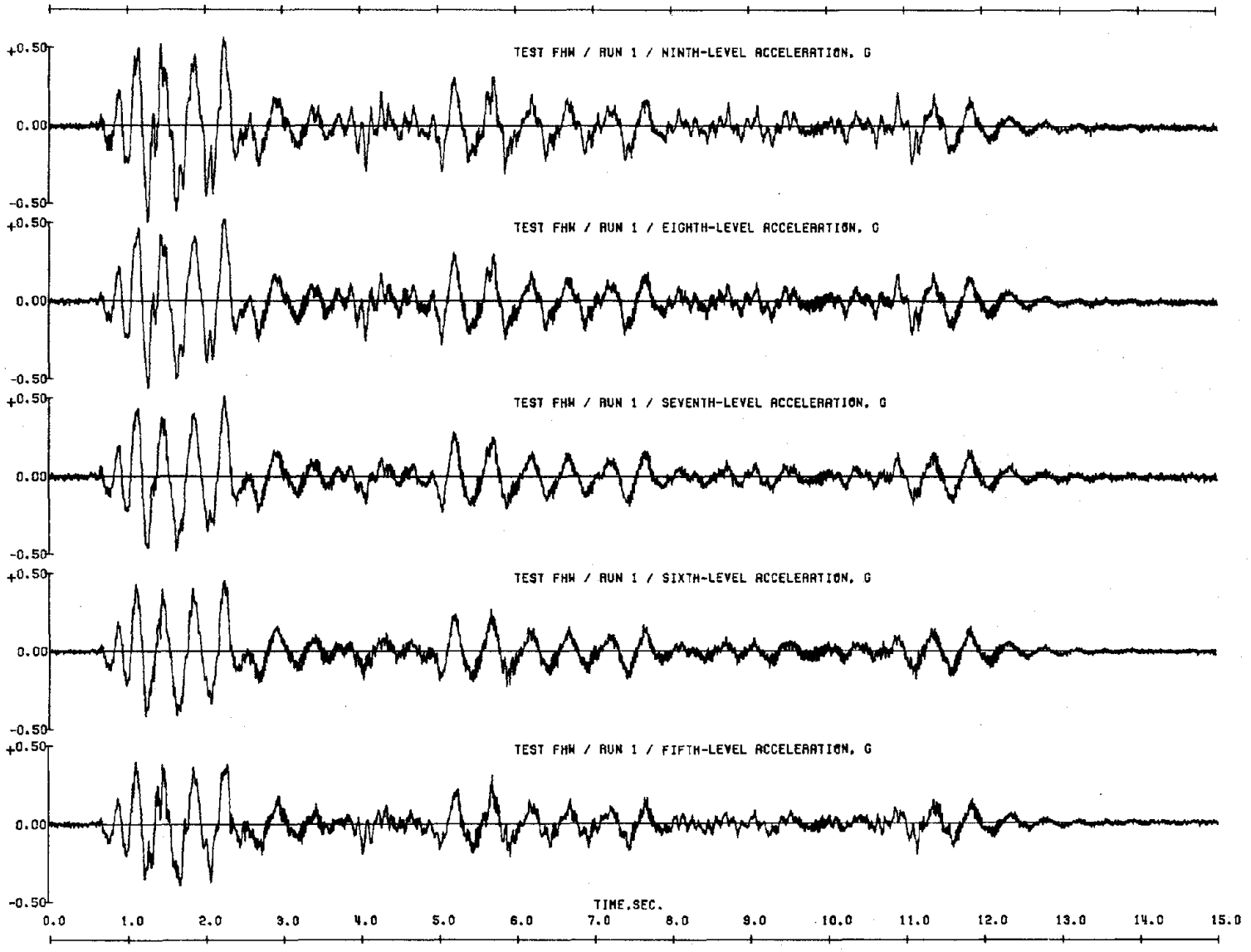


Fig. 4.5 (contd.) Acceleration Response Measured during Initial Simulations

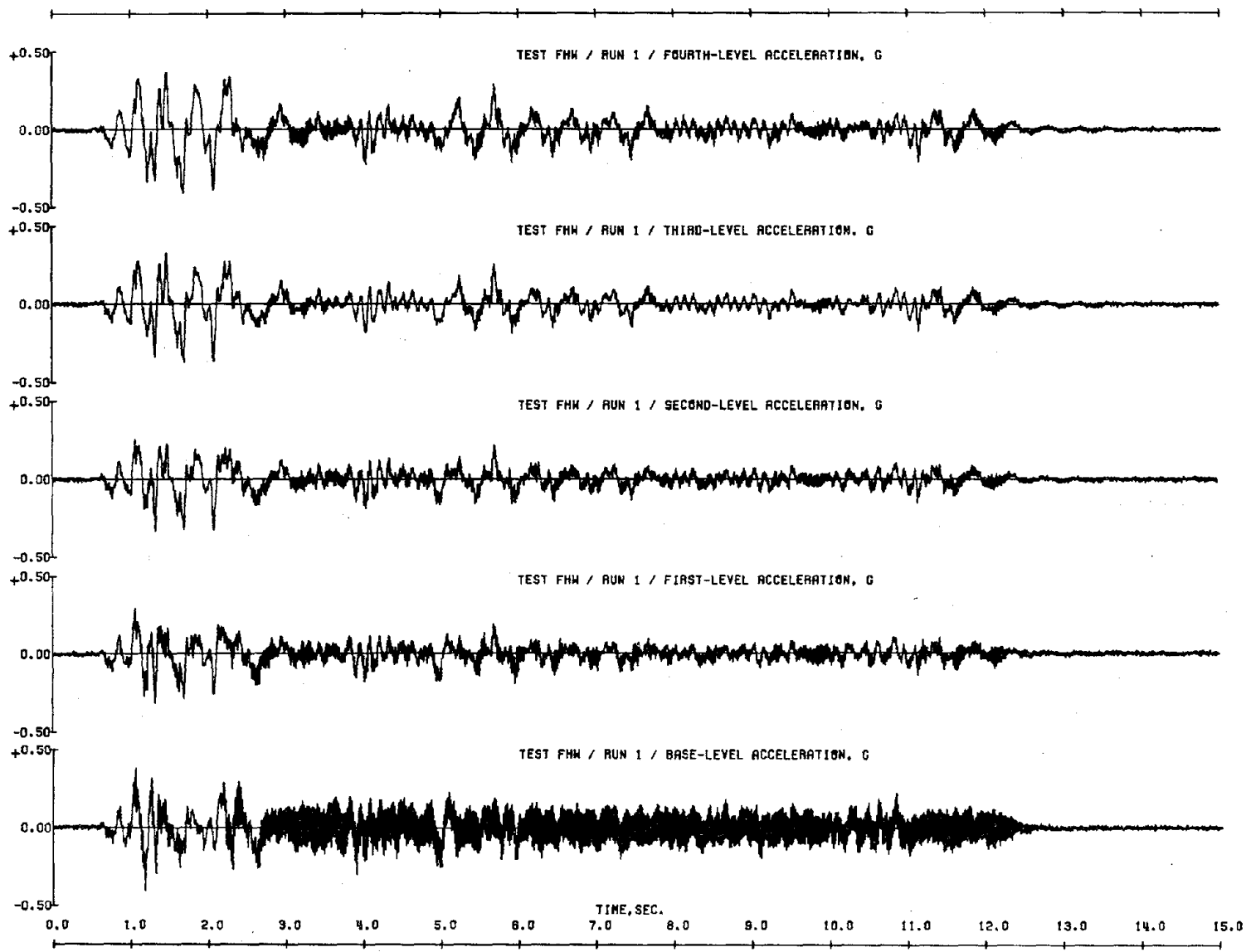


Fig. 4.5 (contd.) Acceleration Response Measured during Initial Simulations

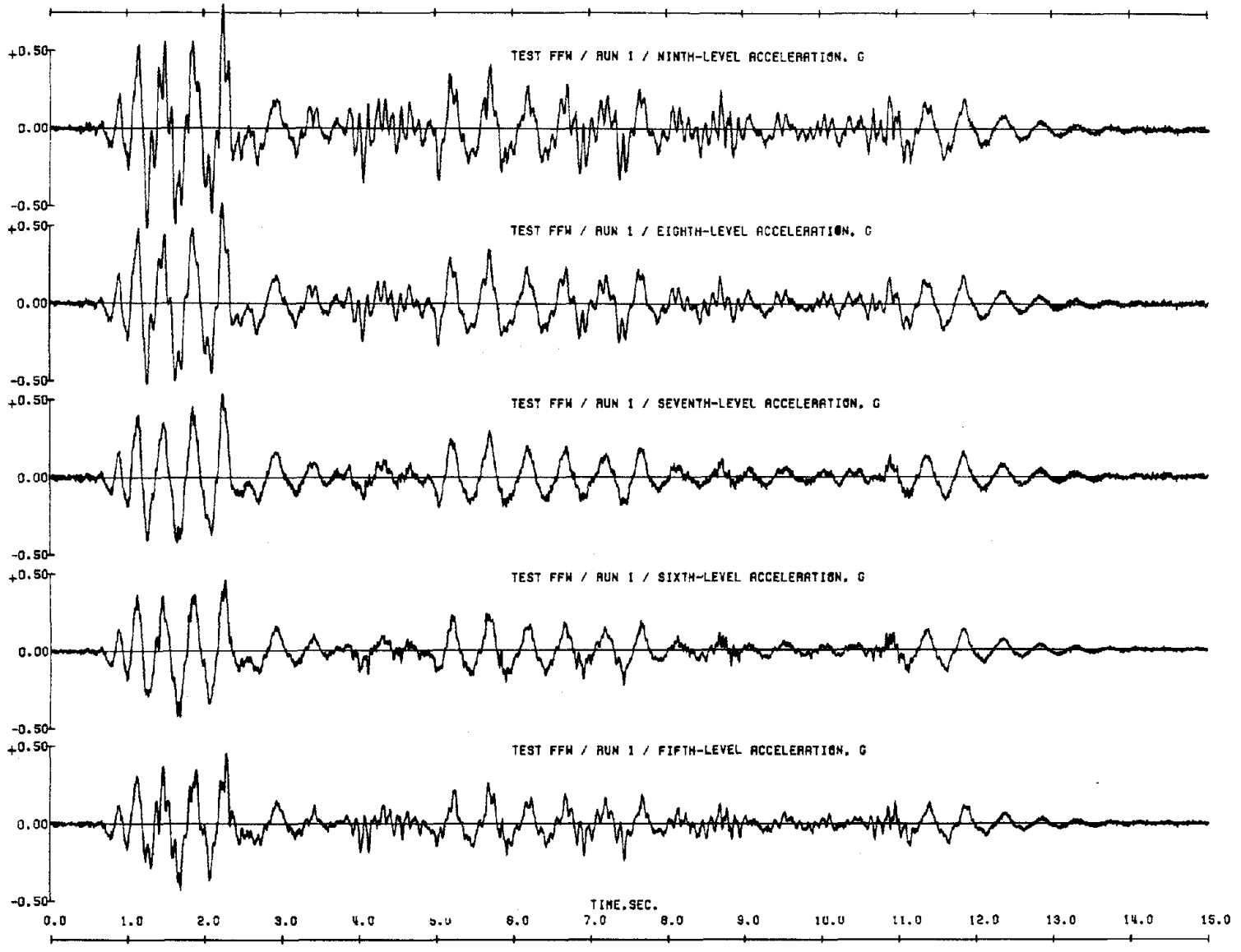


Fig. 4.5 (contd.) Acceleration Response Measured during Initial Simulations

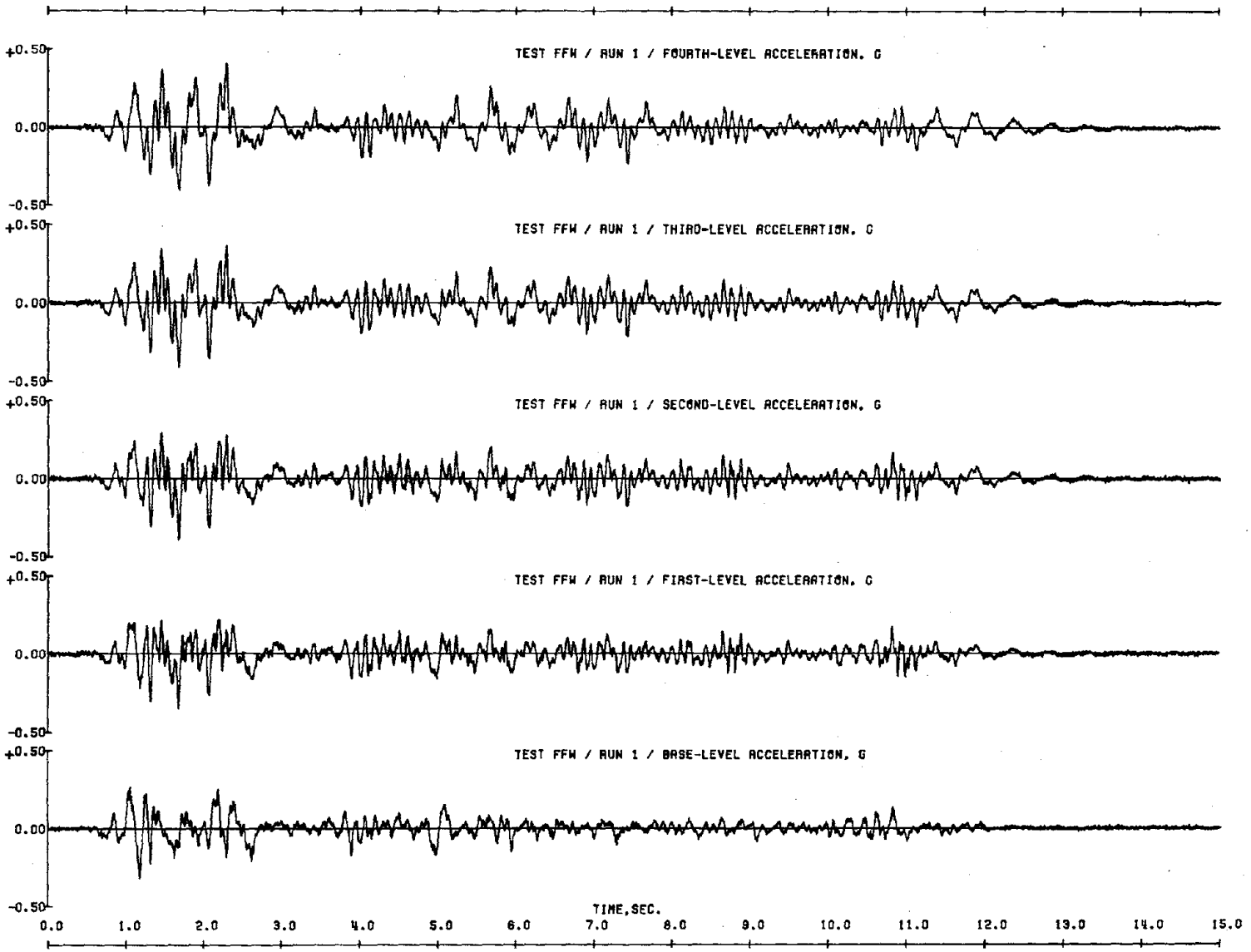


Fig. 4.5 (contd.) Acceleration Response Measured during Initial Simulations

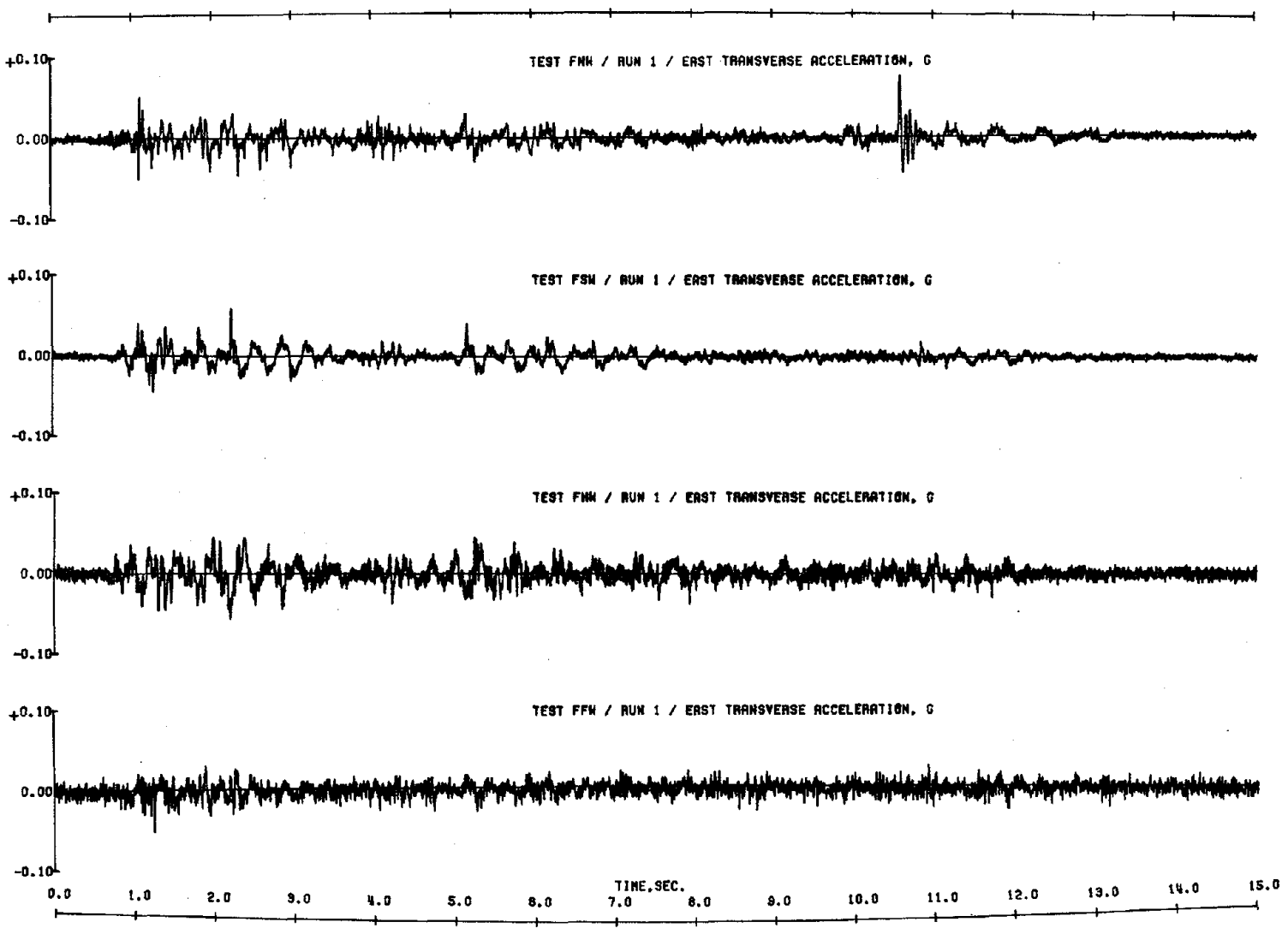


Fig. 4.6 Transverse Accelerations Measured during Initial Simulations

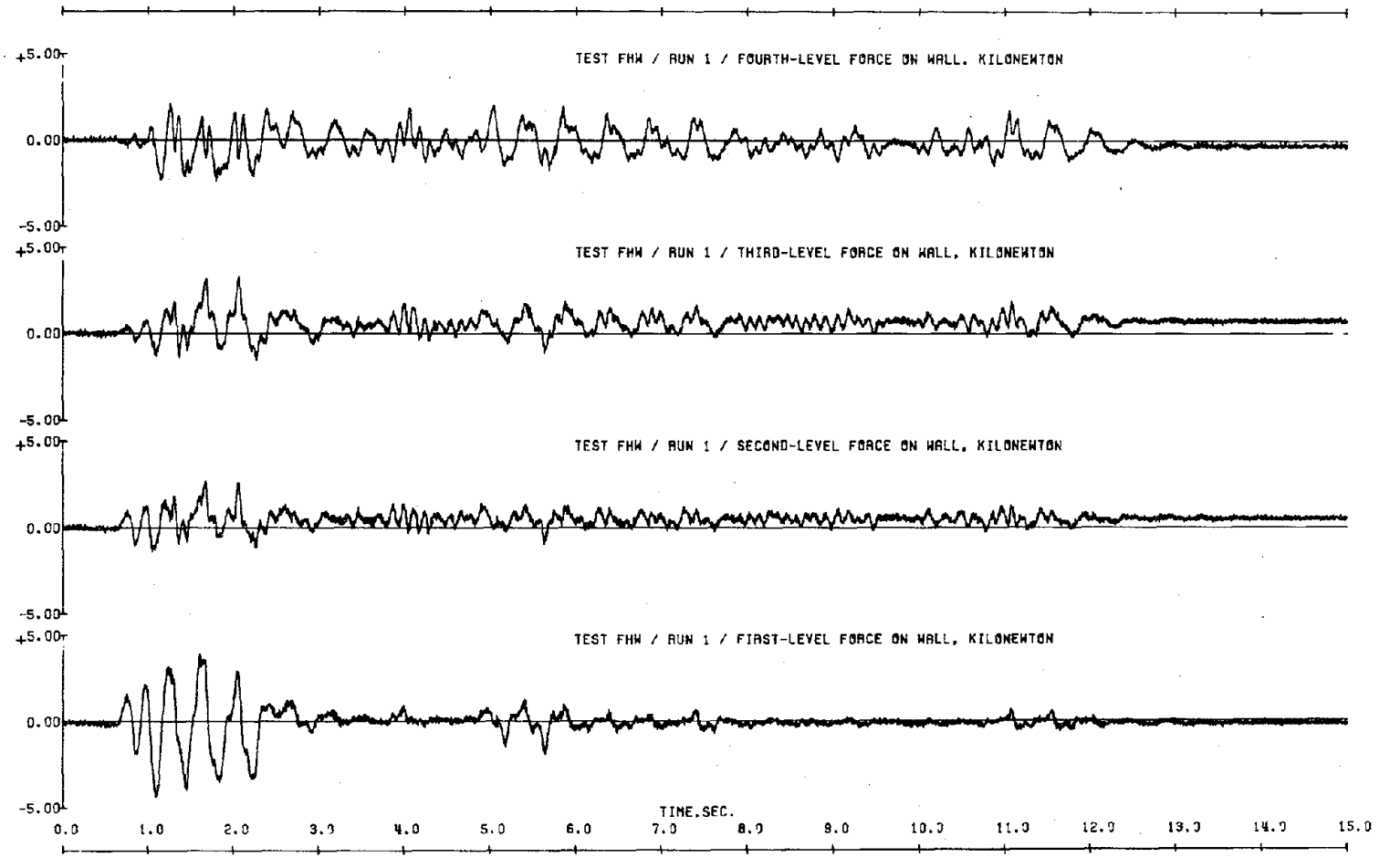


Fig. 4.7 Wall Forces Measured during Initial Simulations

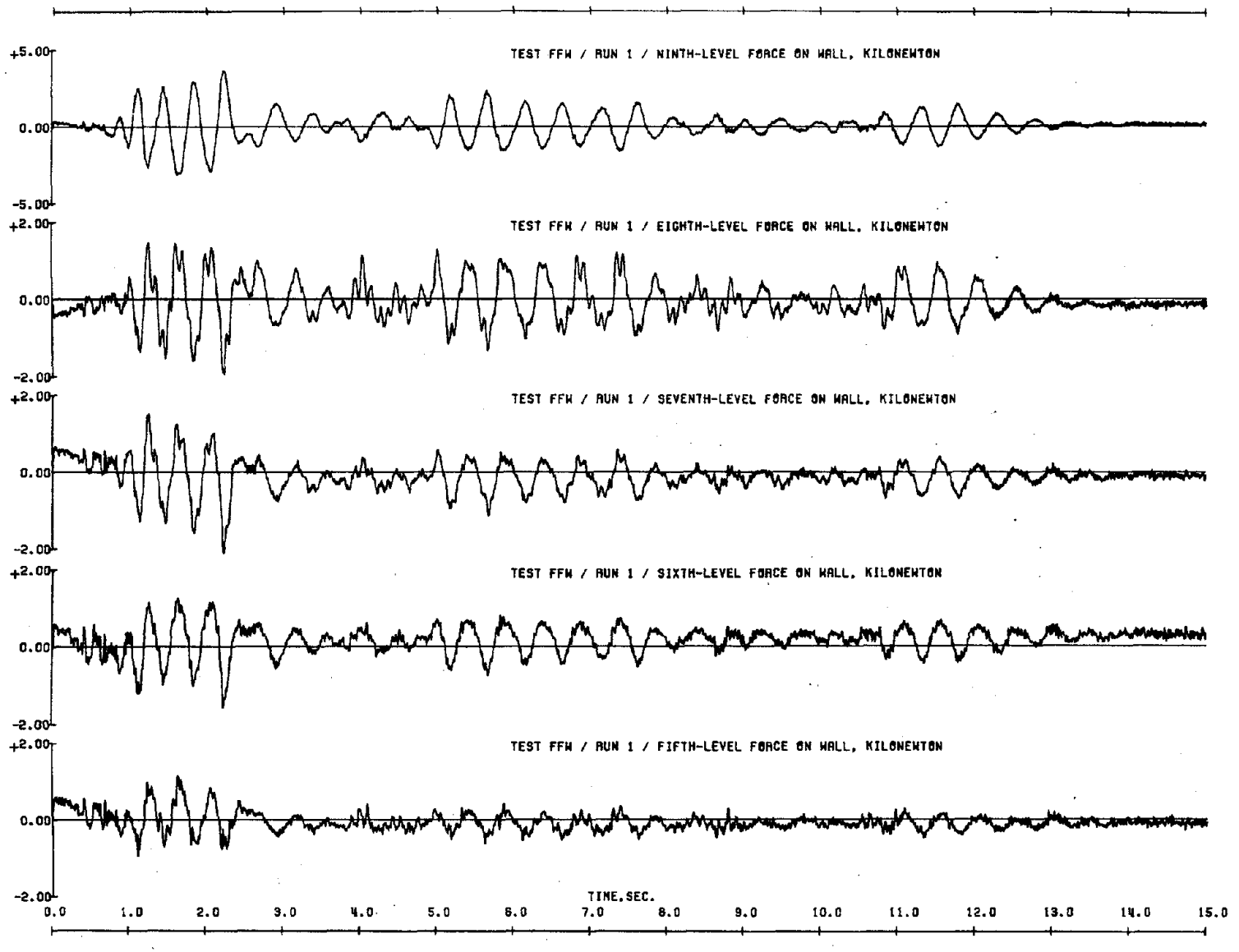


Fig. 4.7 (contd.) Wall Forces Measured during Initial Simulations

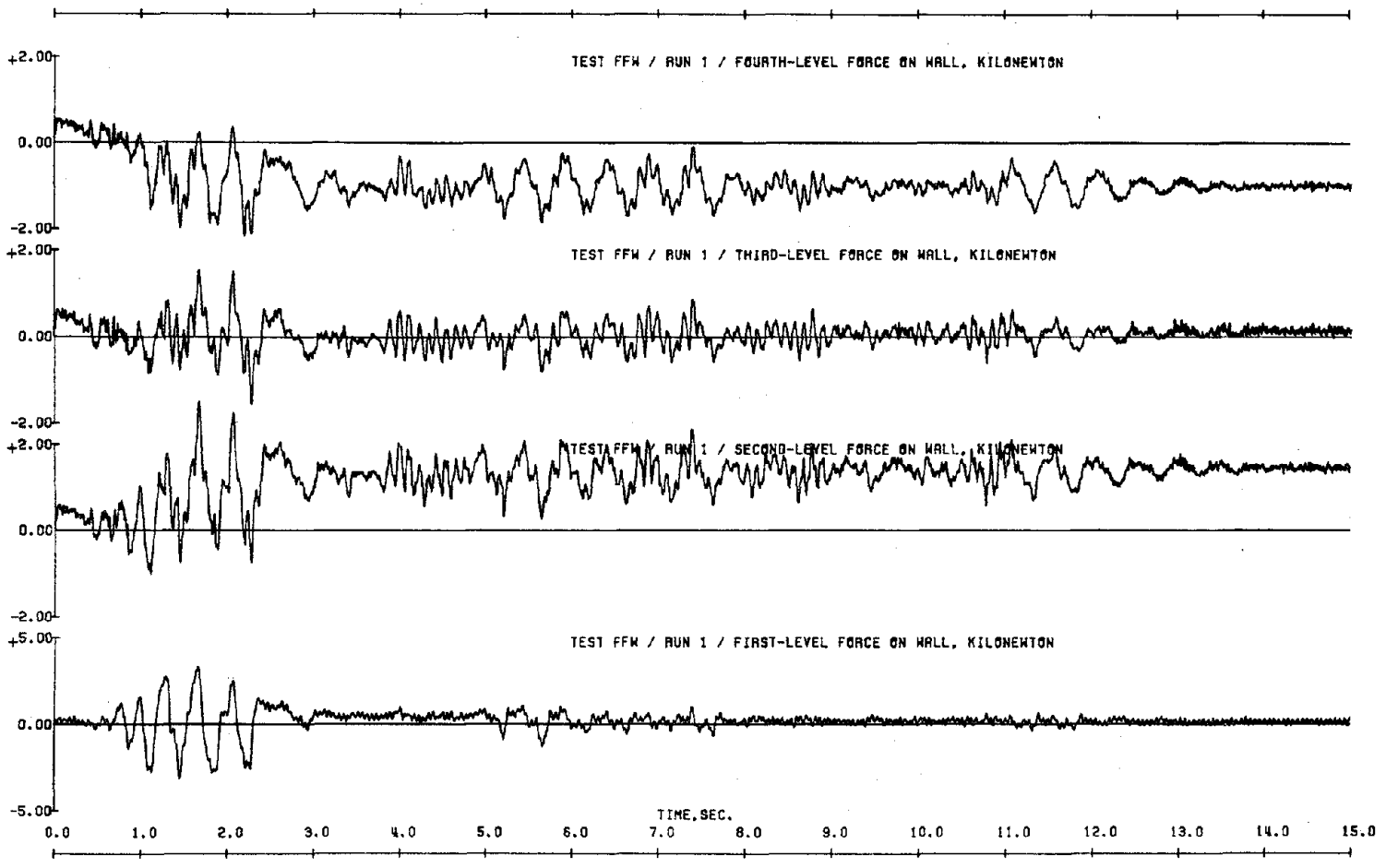


Fig. 4.7 (contd.) Wall Forces Measured during Initial Simulations

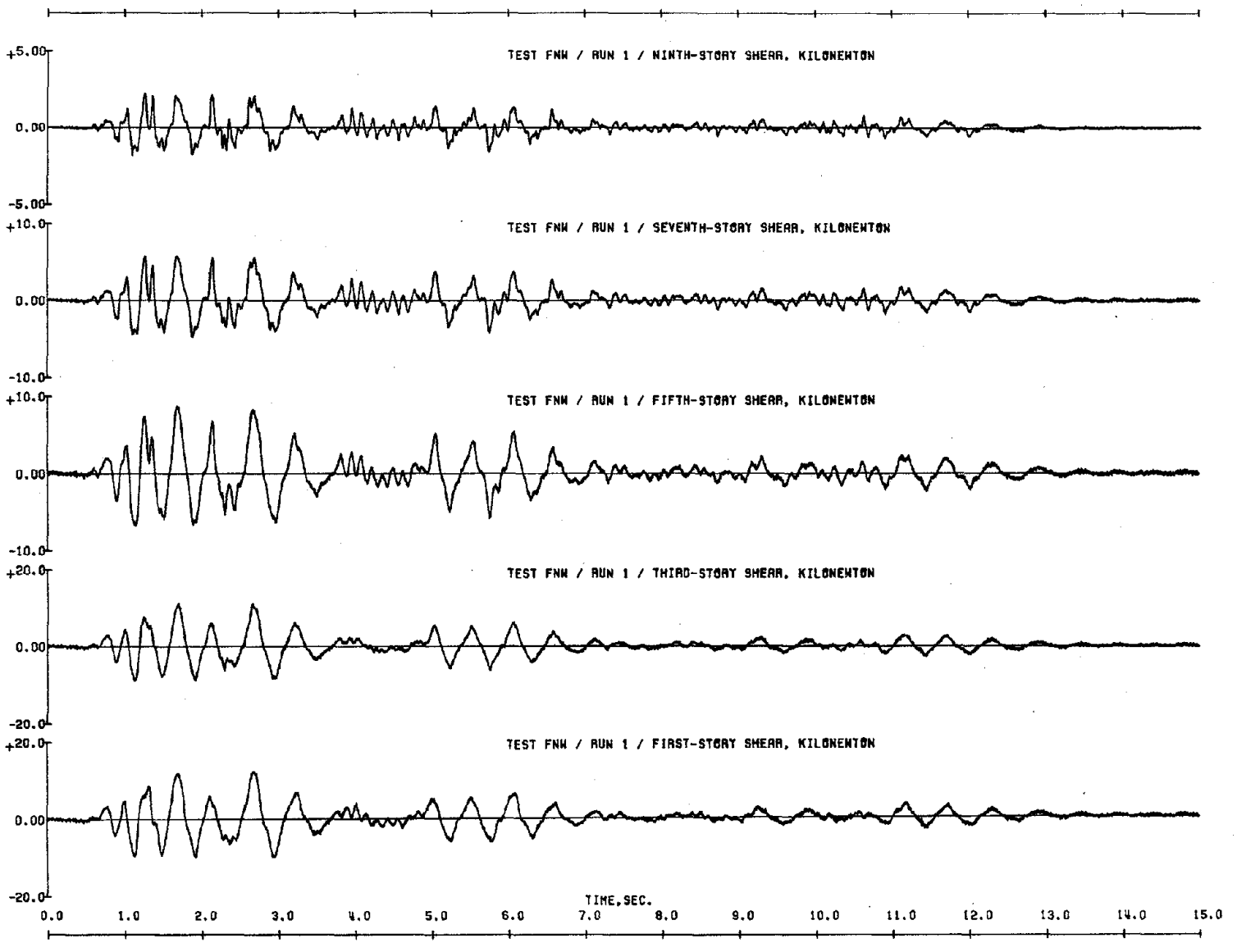


Fig. 4.8 Shear Response to Initial Simulations

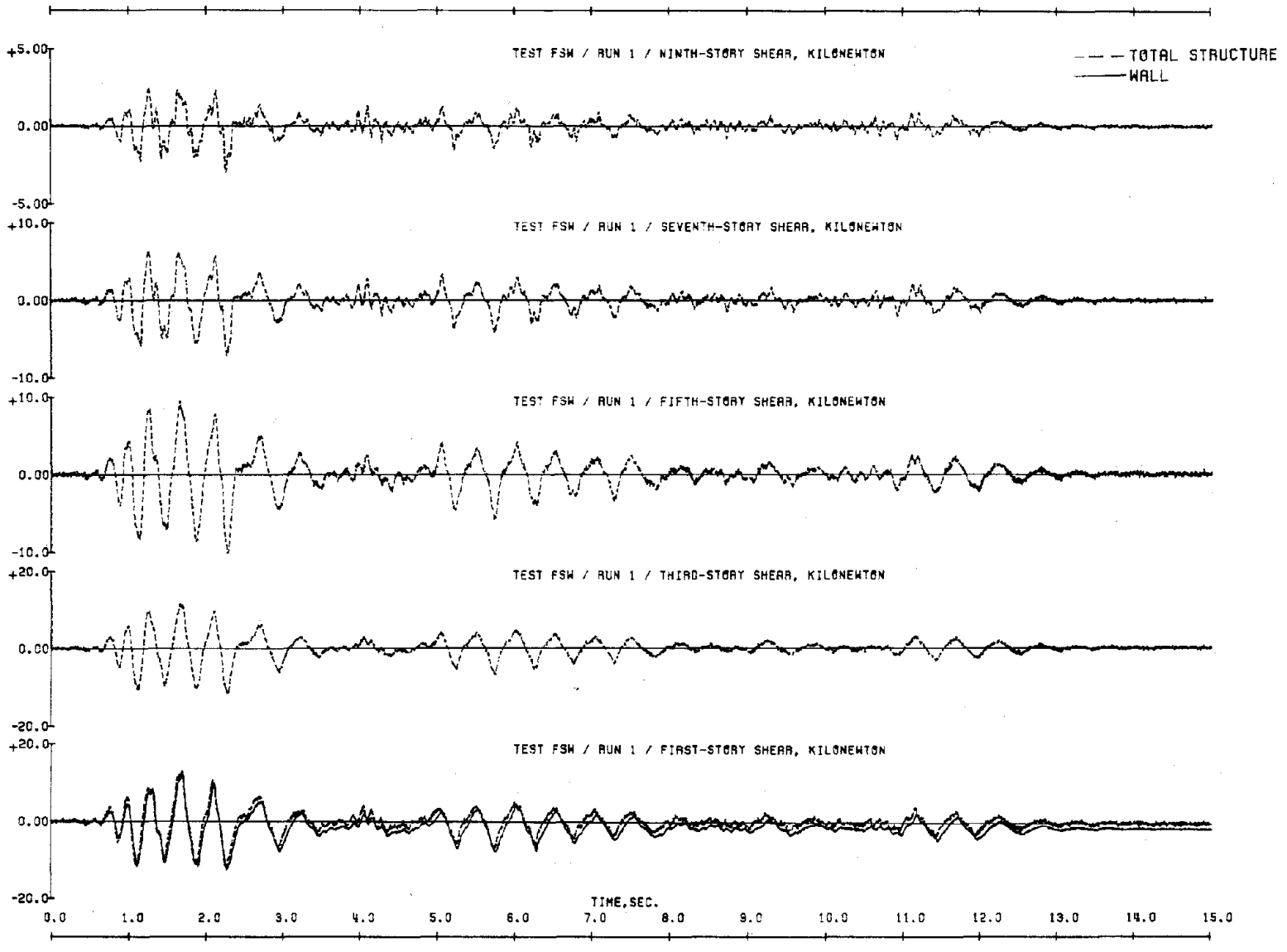


Fig. 4.8 (contd.) Shear Response to Initial Simulations

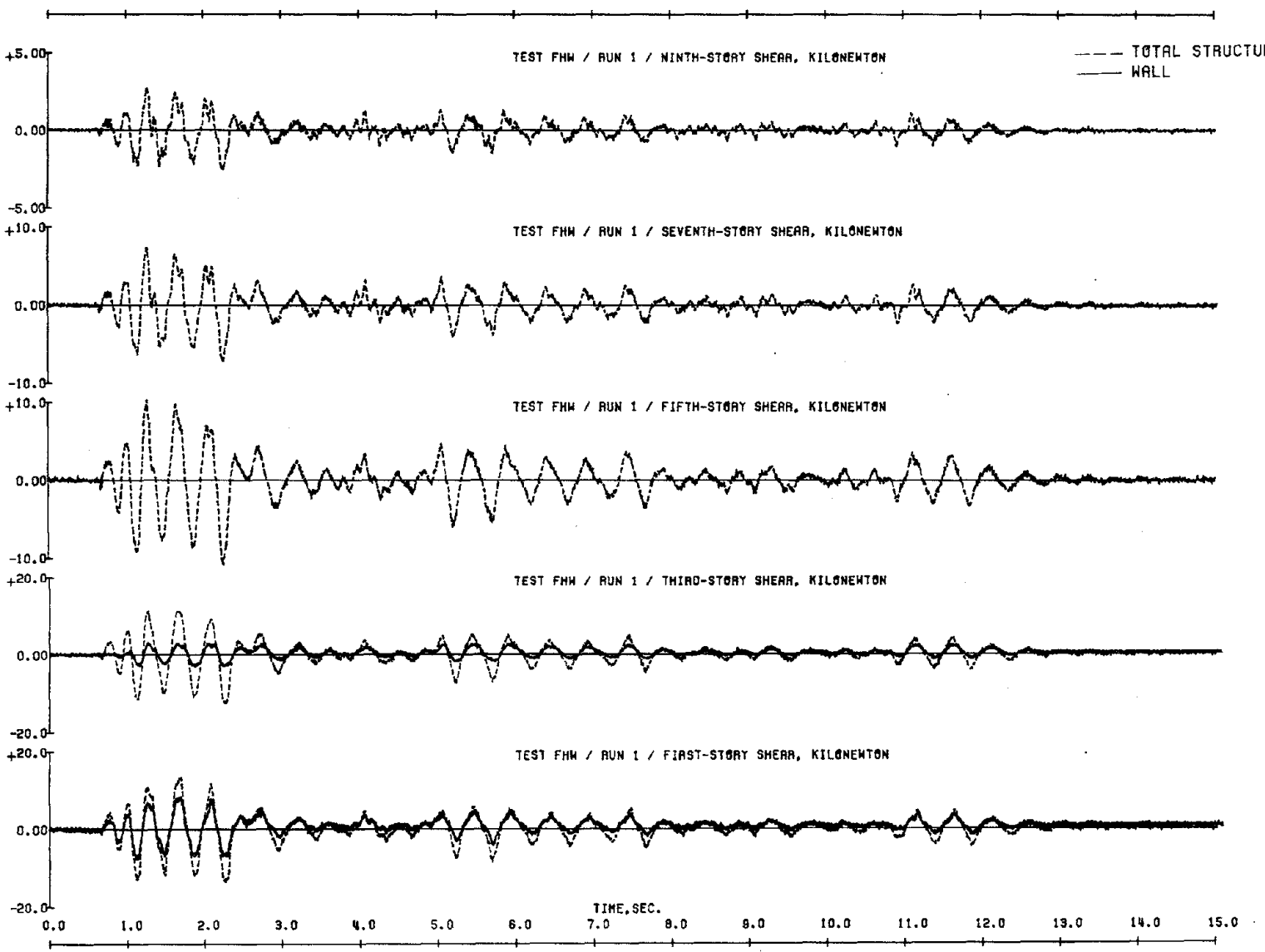


Fig. 4.8 (contd.) Shear Response to Initial Simulations

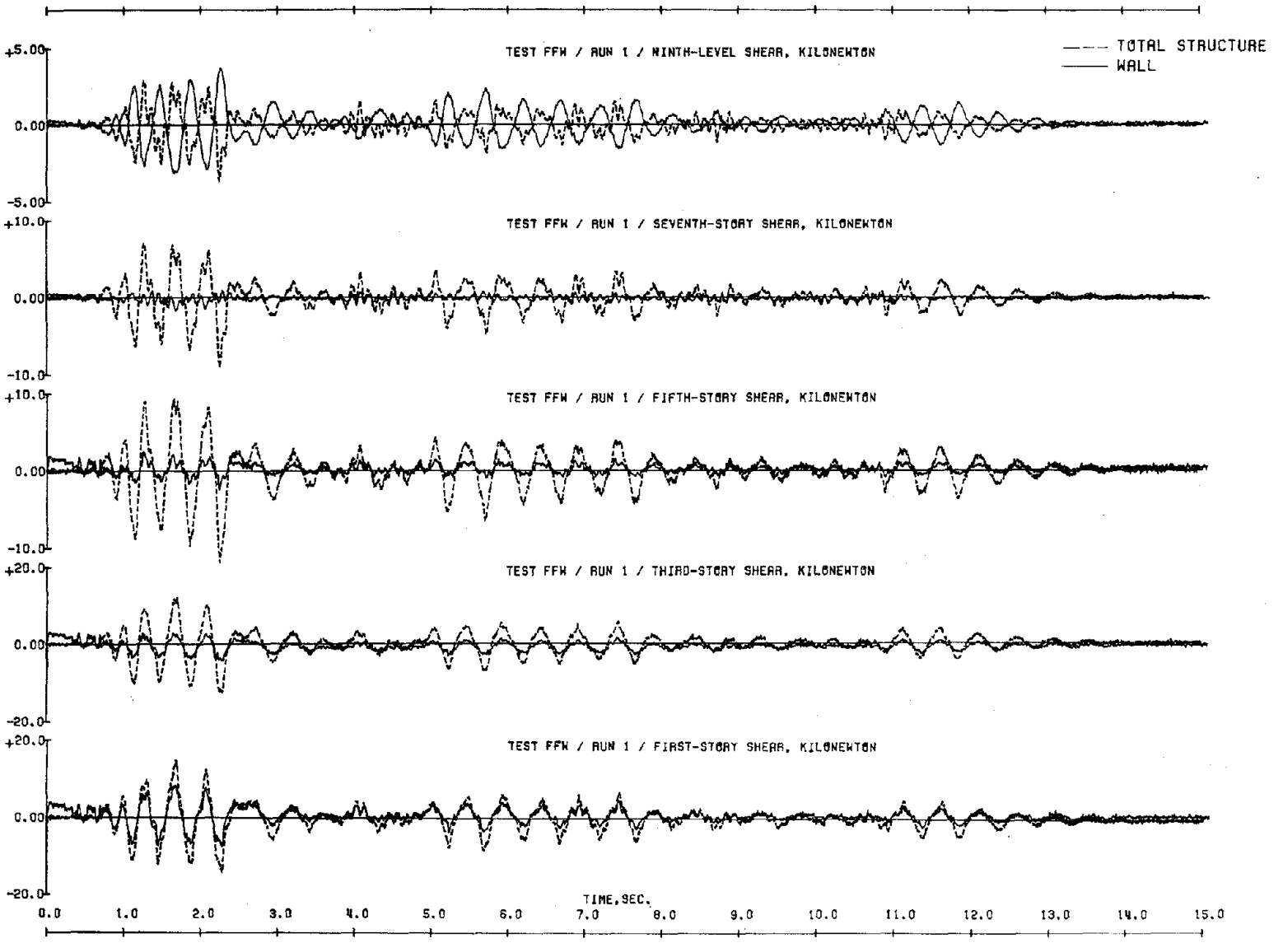


Fig. 4.8 (contd.) Shear Response to Initial Simulations

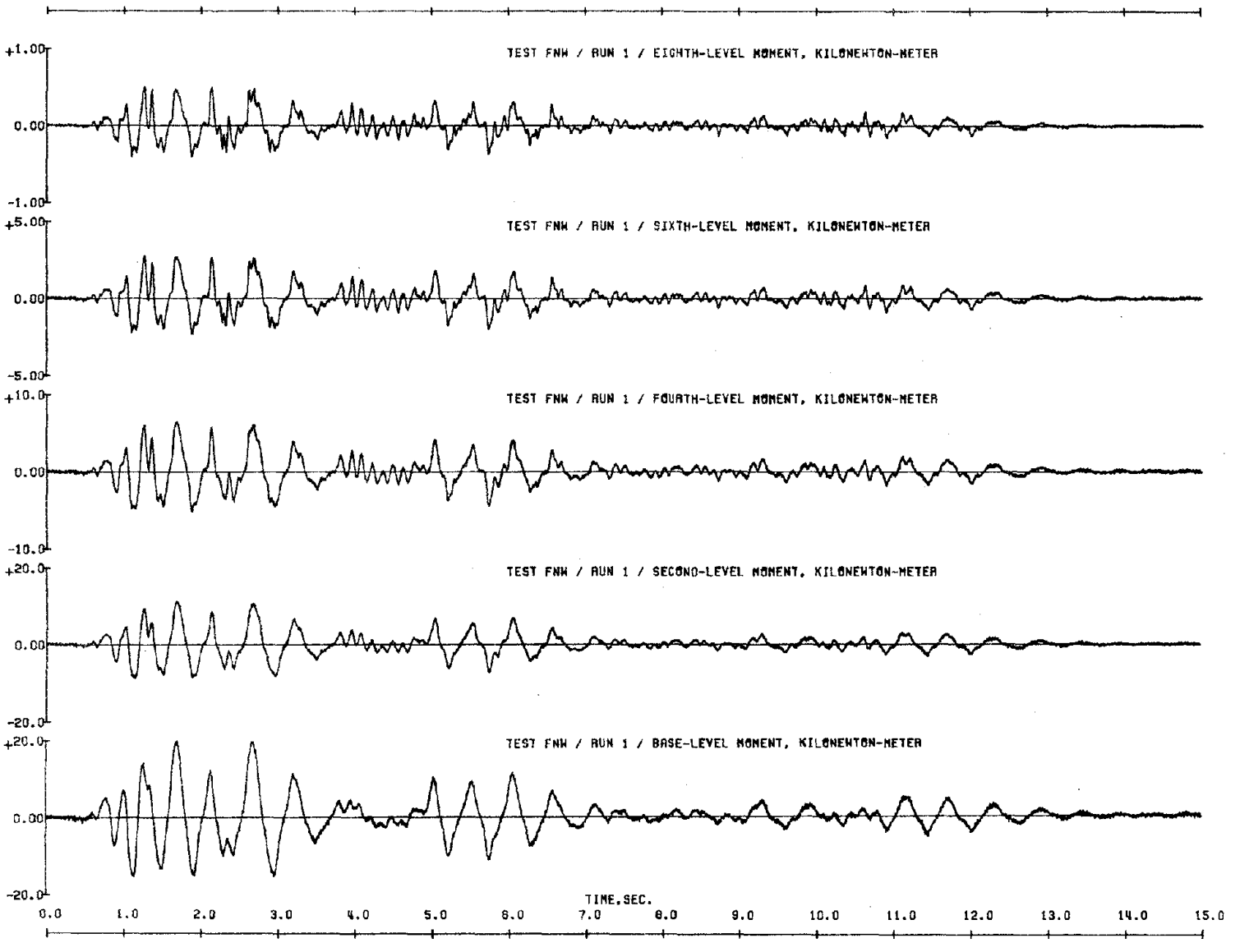


Fig. 4.9 Moment Response to Initial Simulations

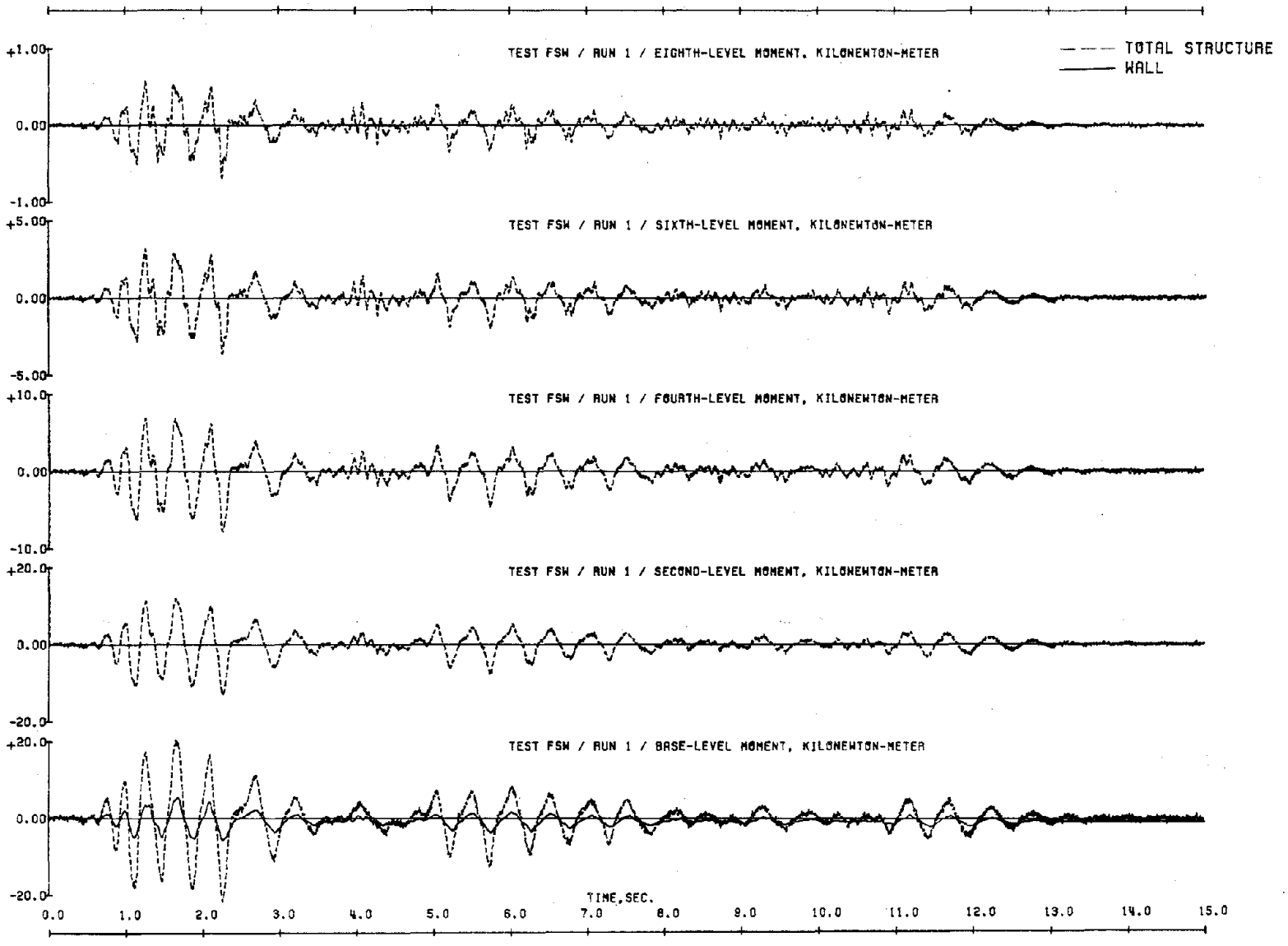


Fig. 4.9 (contd.) Moment Response to Initial Simulations

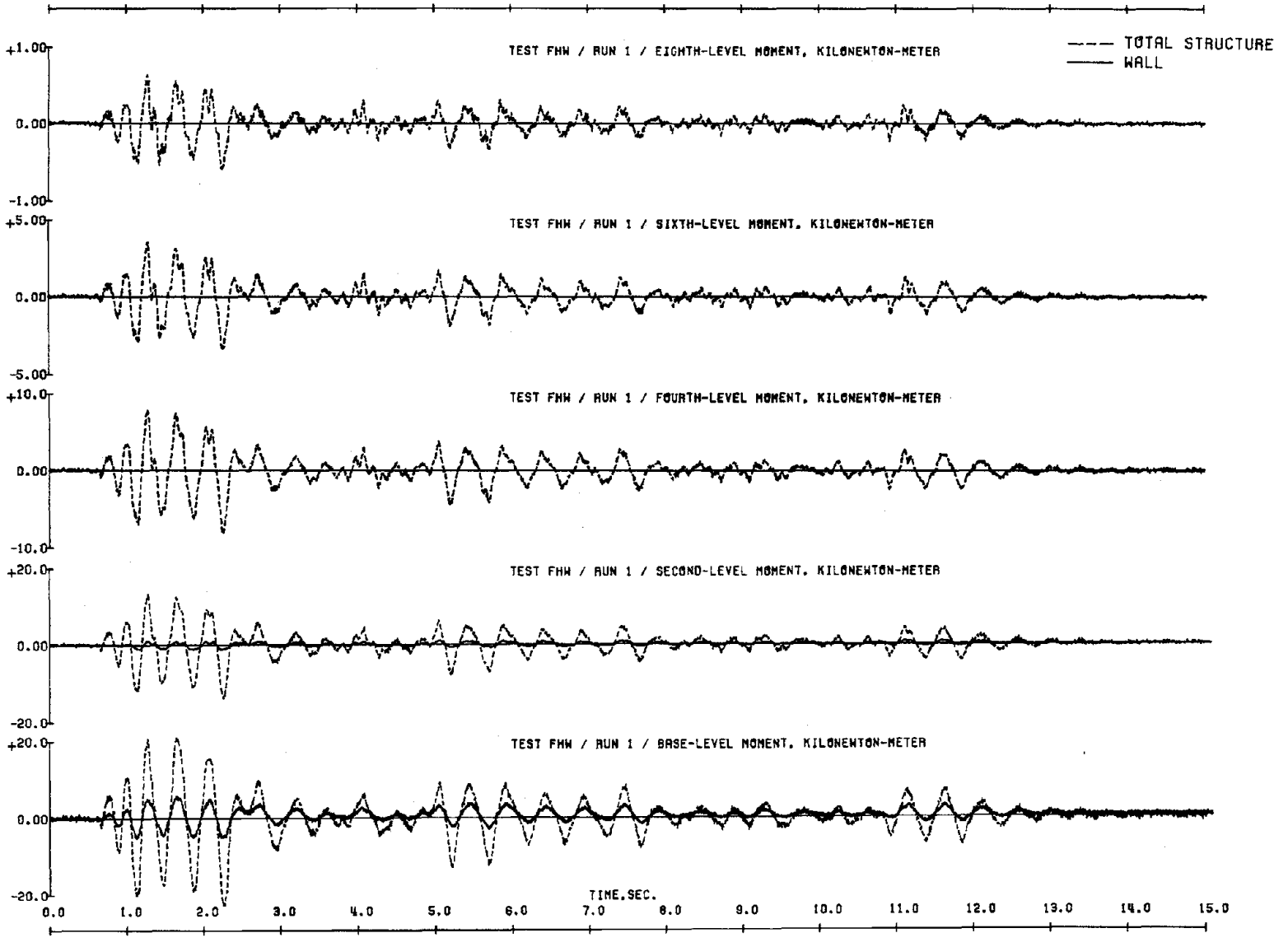


Fig. 4.9 (contd.) Moment Response to Initial Simulations

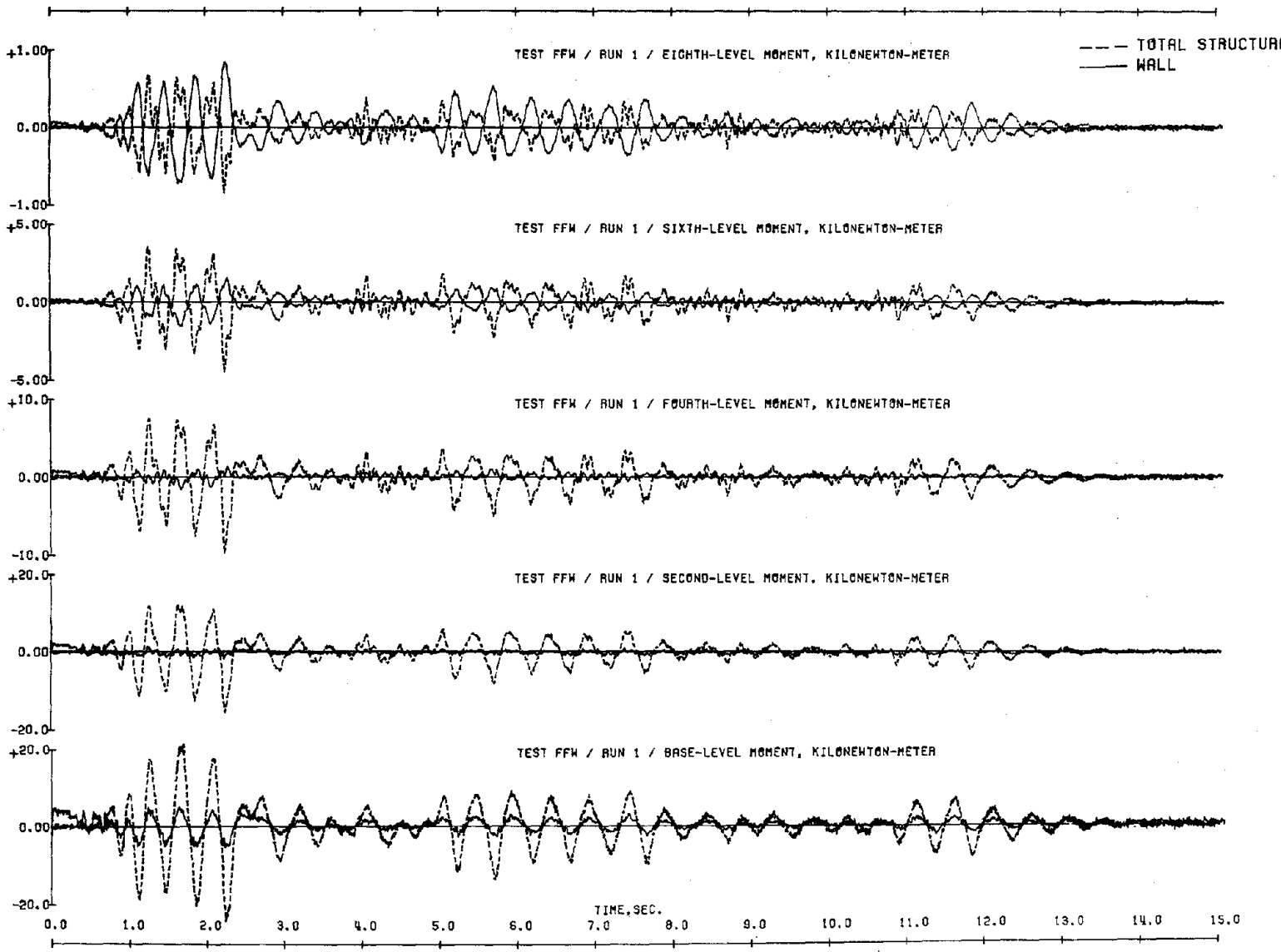


Fig. 4.9 (contd.) Moment Response to Initial Simulations

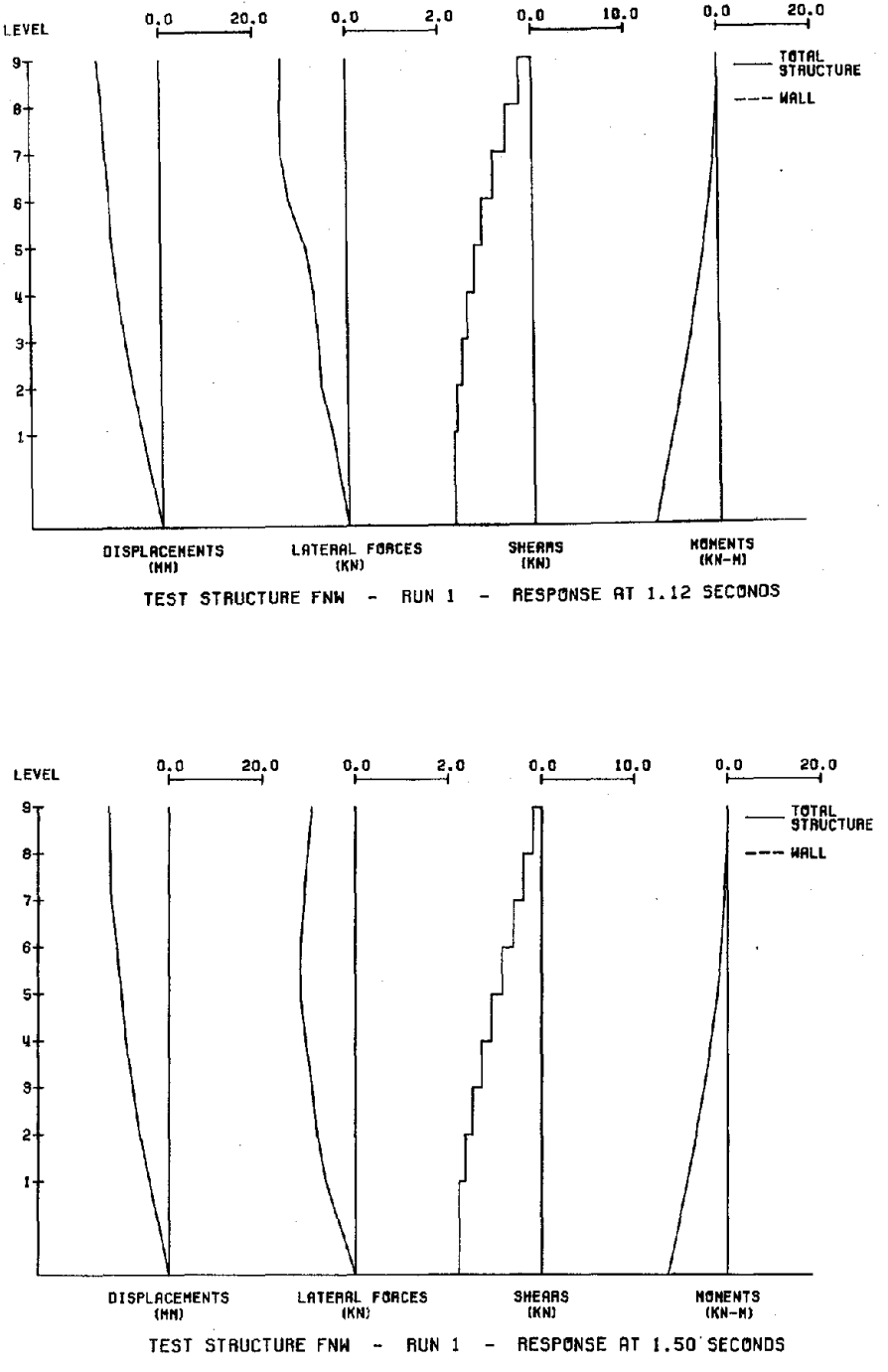


Fig. 4.10 Distributions of Response to Initial Simulations

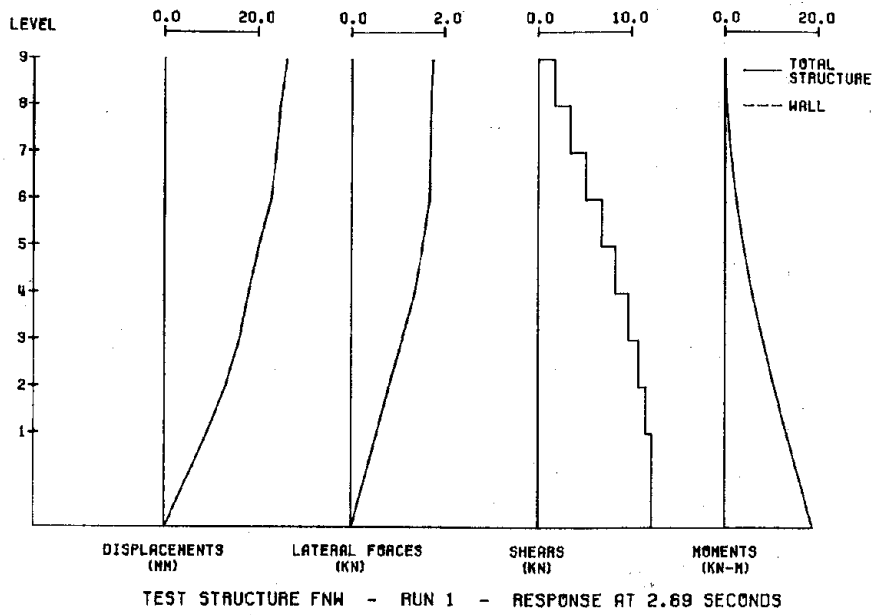


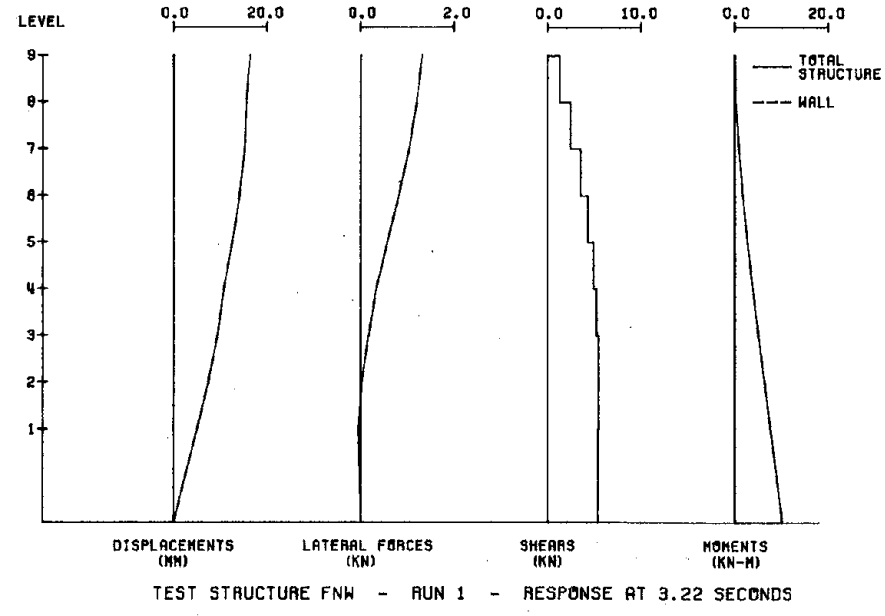


Fig. 4.10 (contd.) Distributions of Response to Initial Simulations

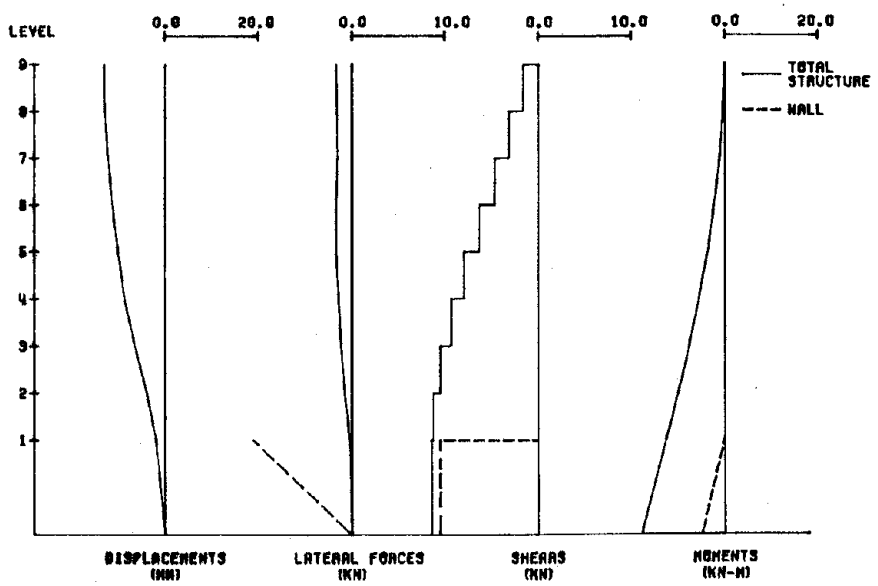


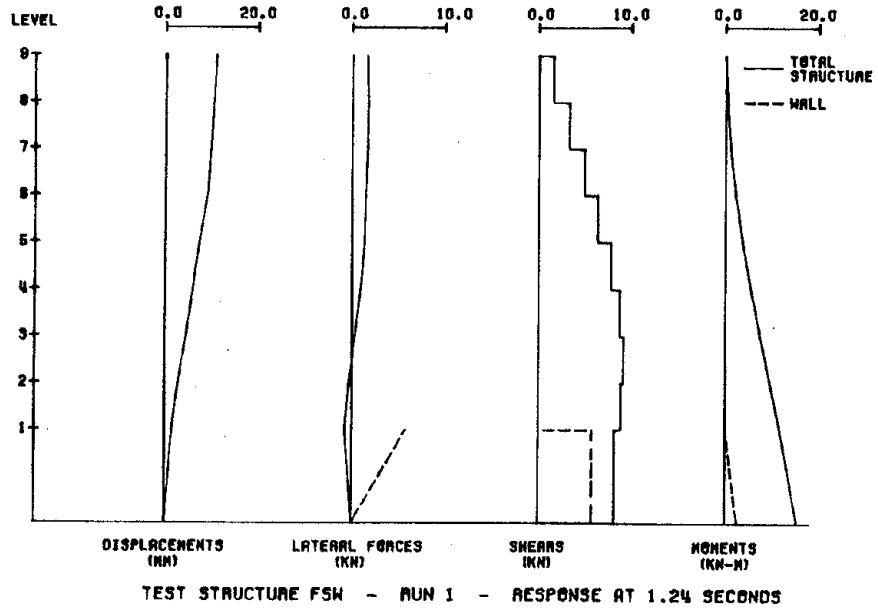


Fig. 4.10 (contd.) Distributions of Response to Initial Simulations

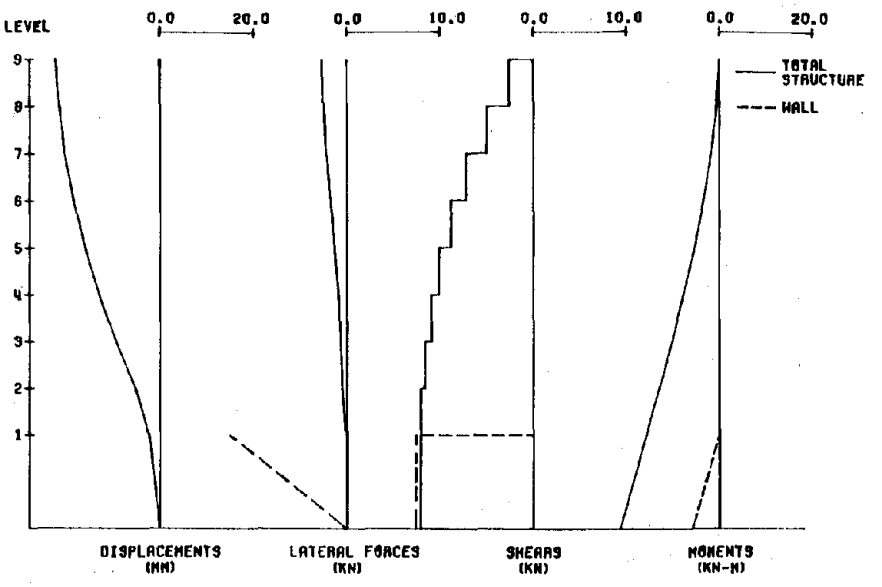


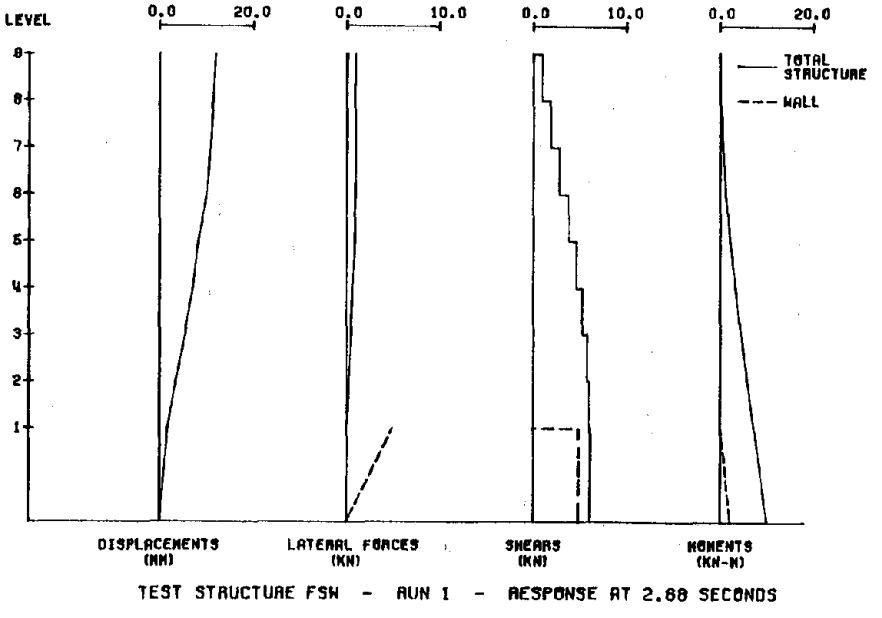


Fig. 4.10 (contd.) Distributions of Response to Initial Simulations

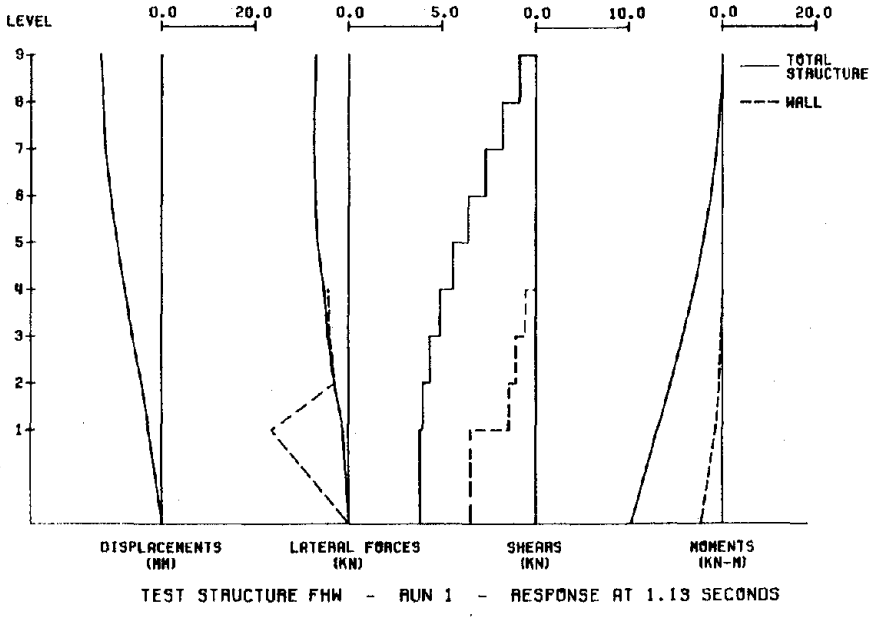


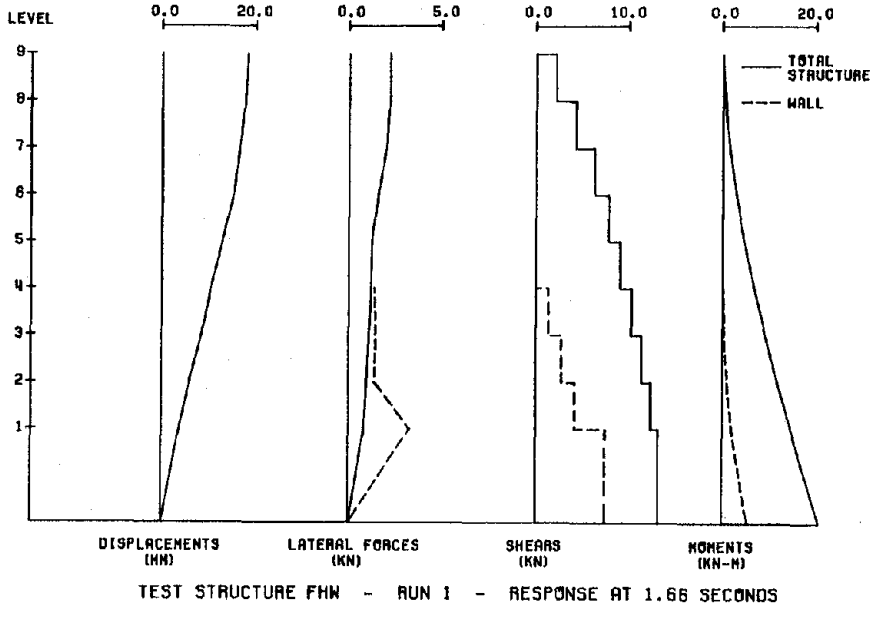


Fig. 4.10 (contd.) Distributions of Response to Initial Simulations

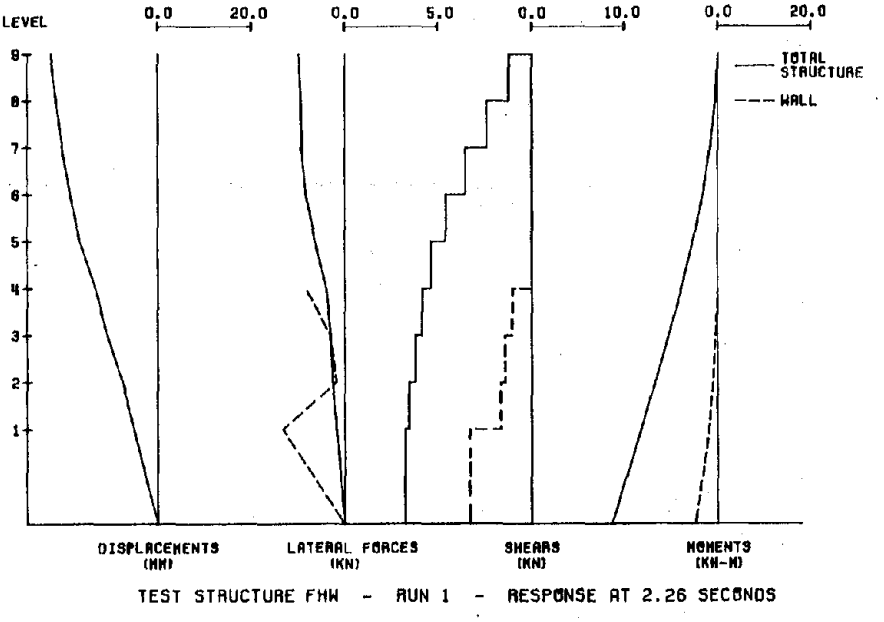


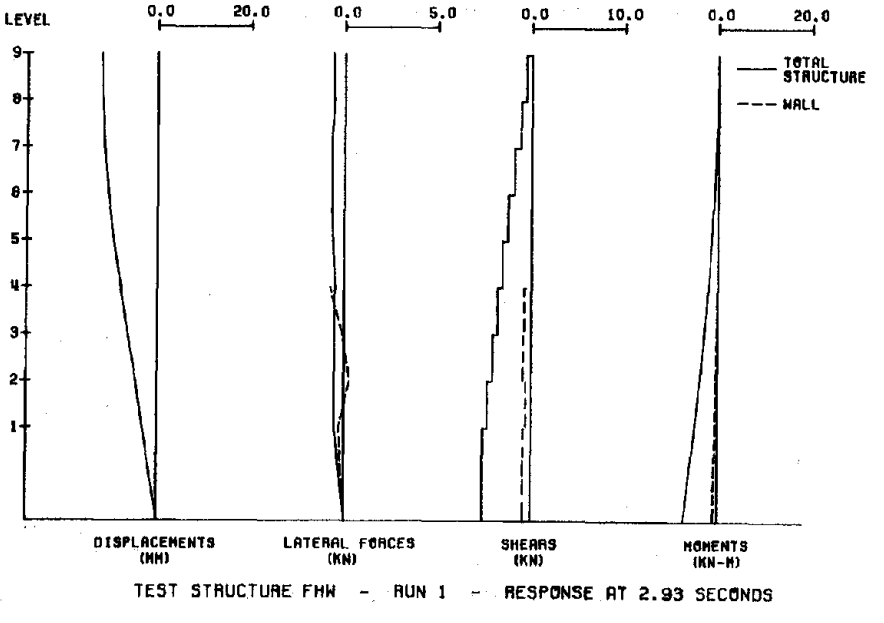


Fig. 4.10 (contd.) Distributions of Response to Initial Simulations

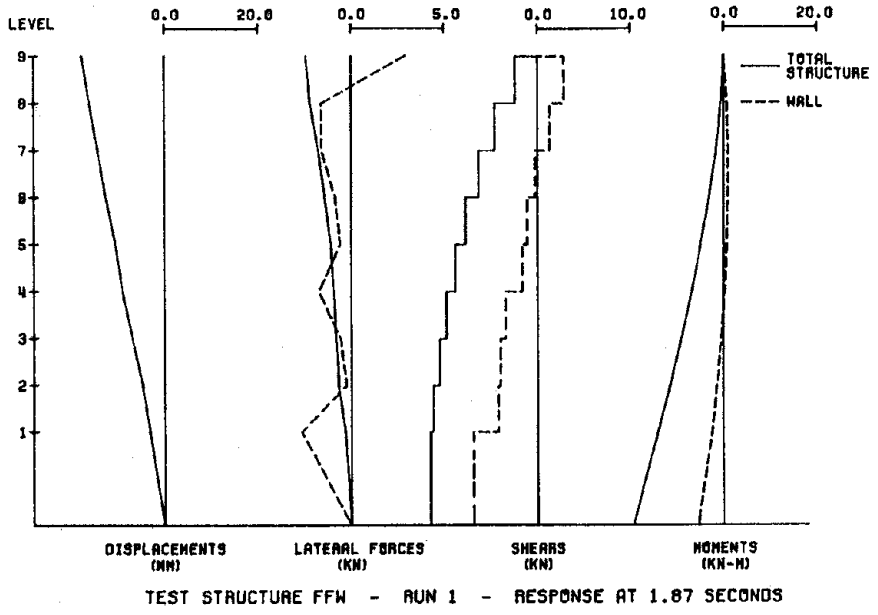


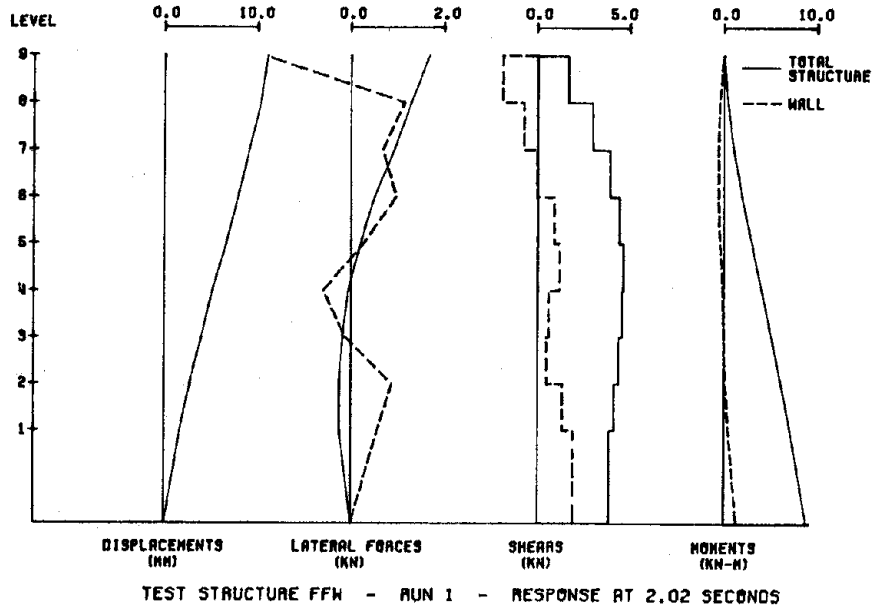


Fig. 4.10 (contd.) Distributions of Response to Initial Simulations

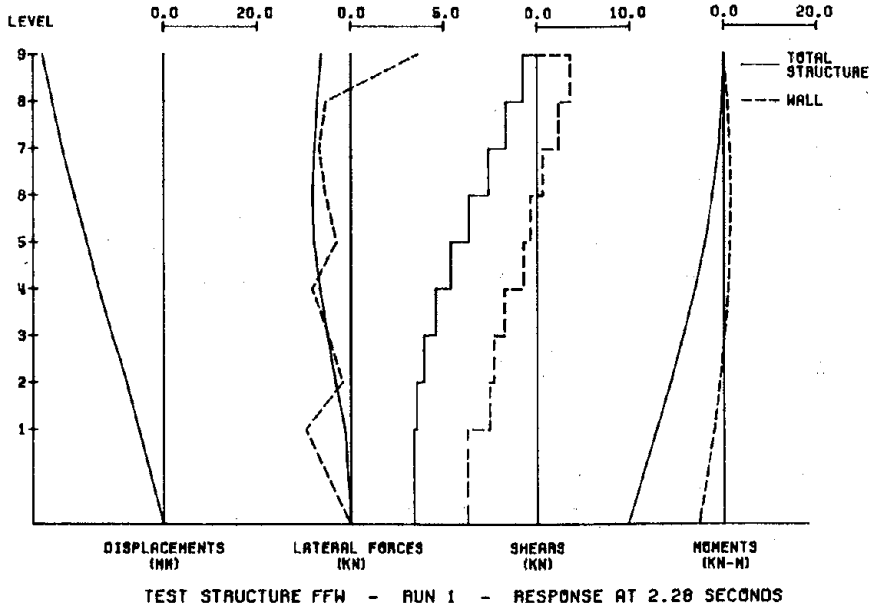


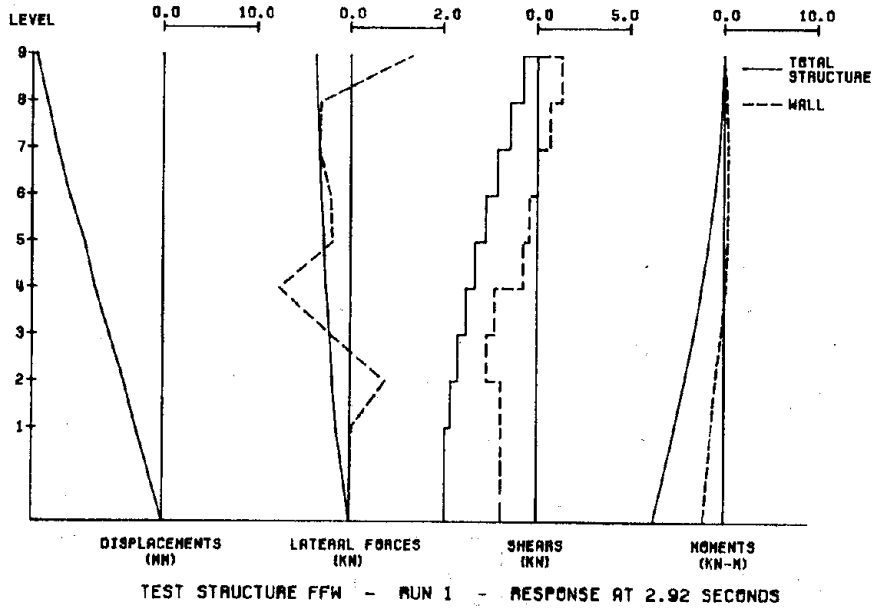


Fig. 4.10 (contd.) Distributions of Response to Initial Simulations

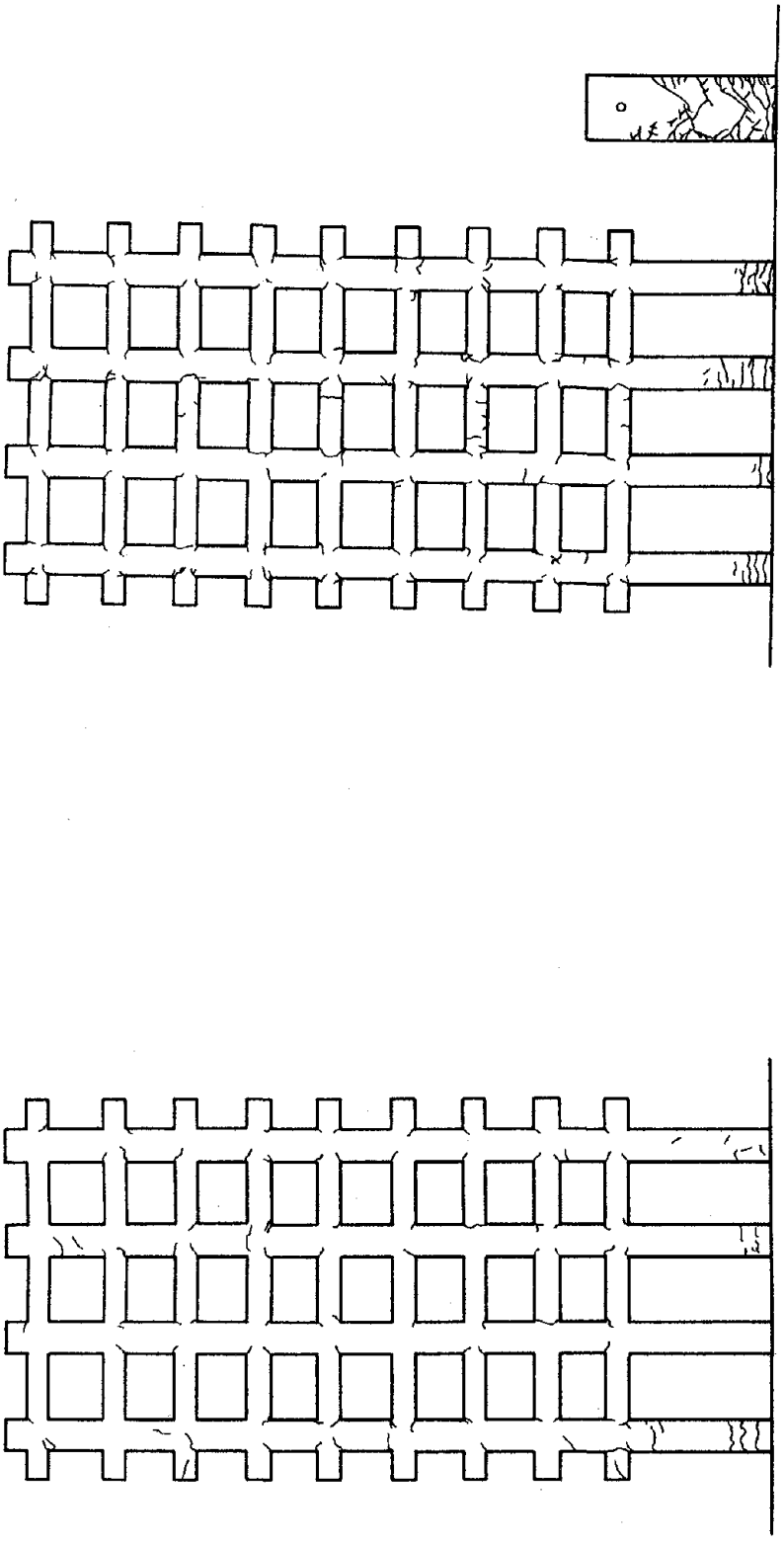

Fig. 4.11 Cracks Observed following Initial Simulations

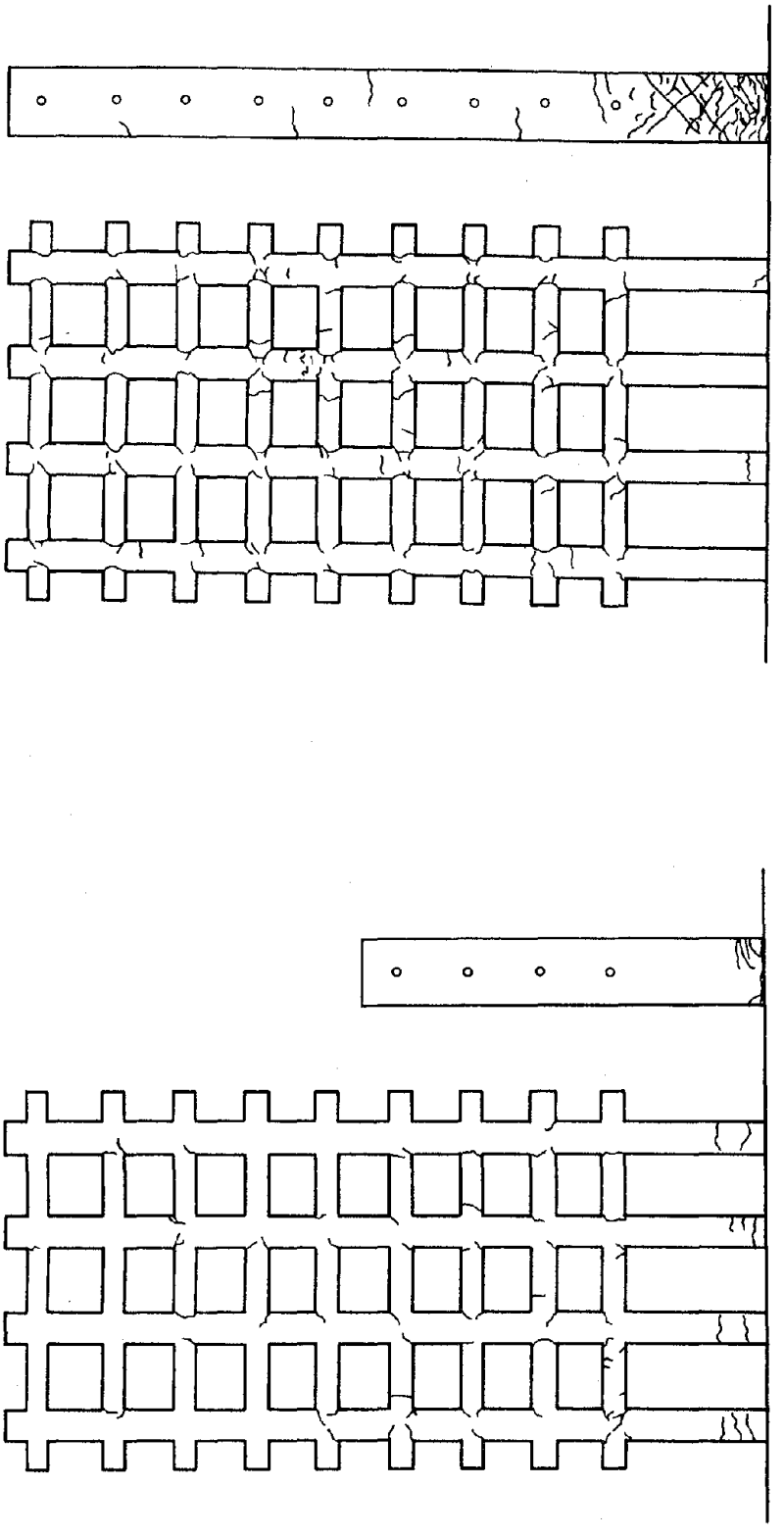

Fig. 4.11 (contd.) Cracks Observed following Initial Simulations

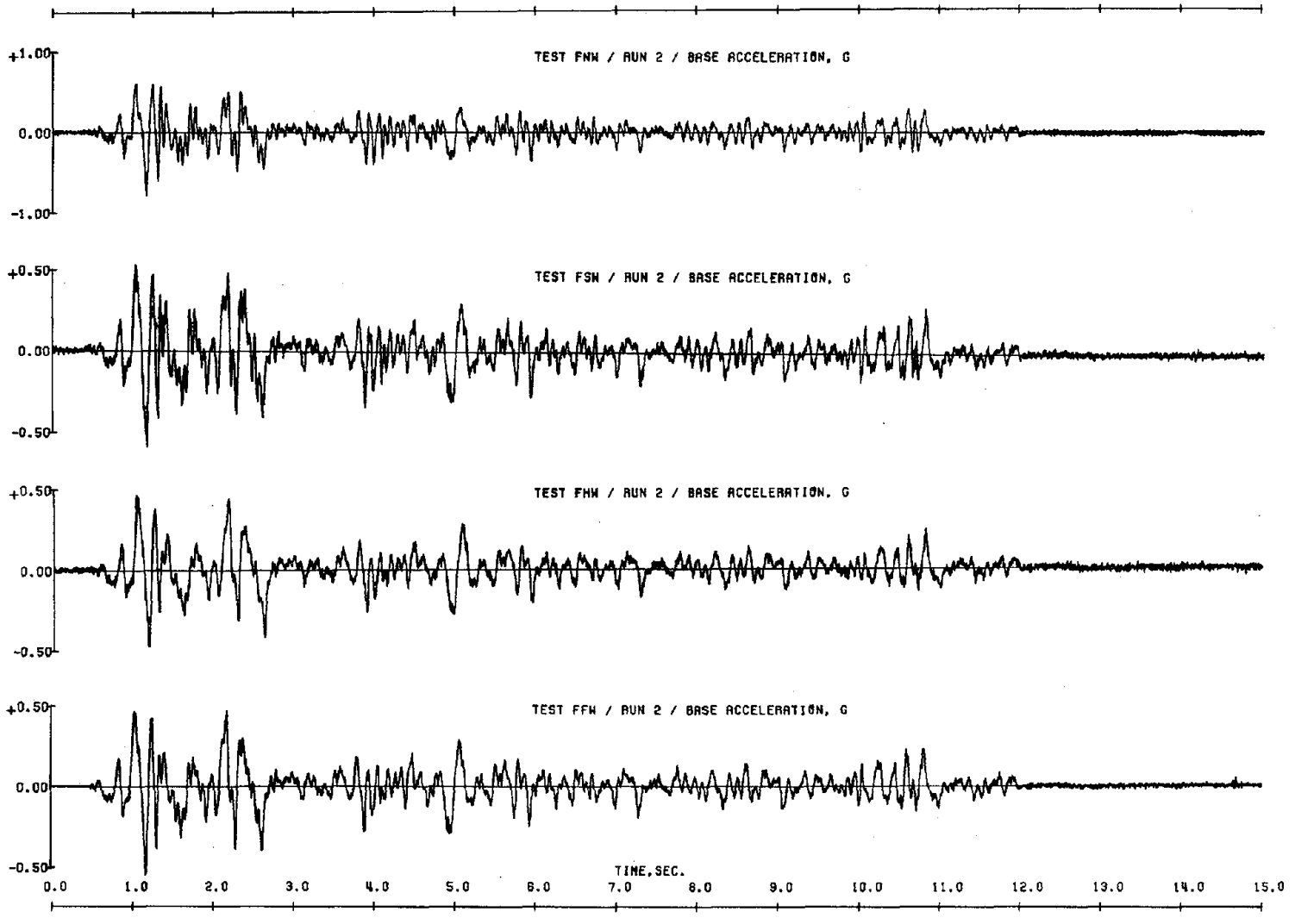


Fig. 4.12 Base Accelerations and Displacements Measured during Second Simulations

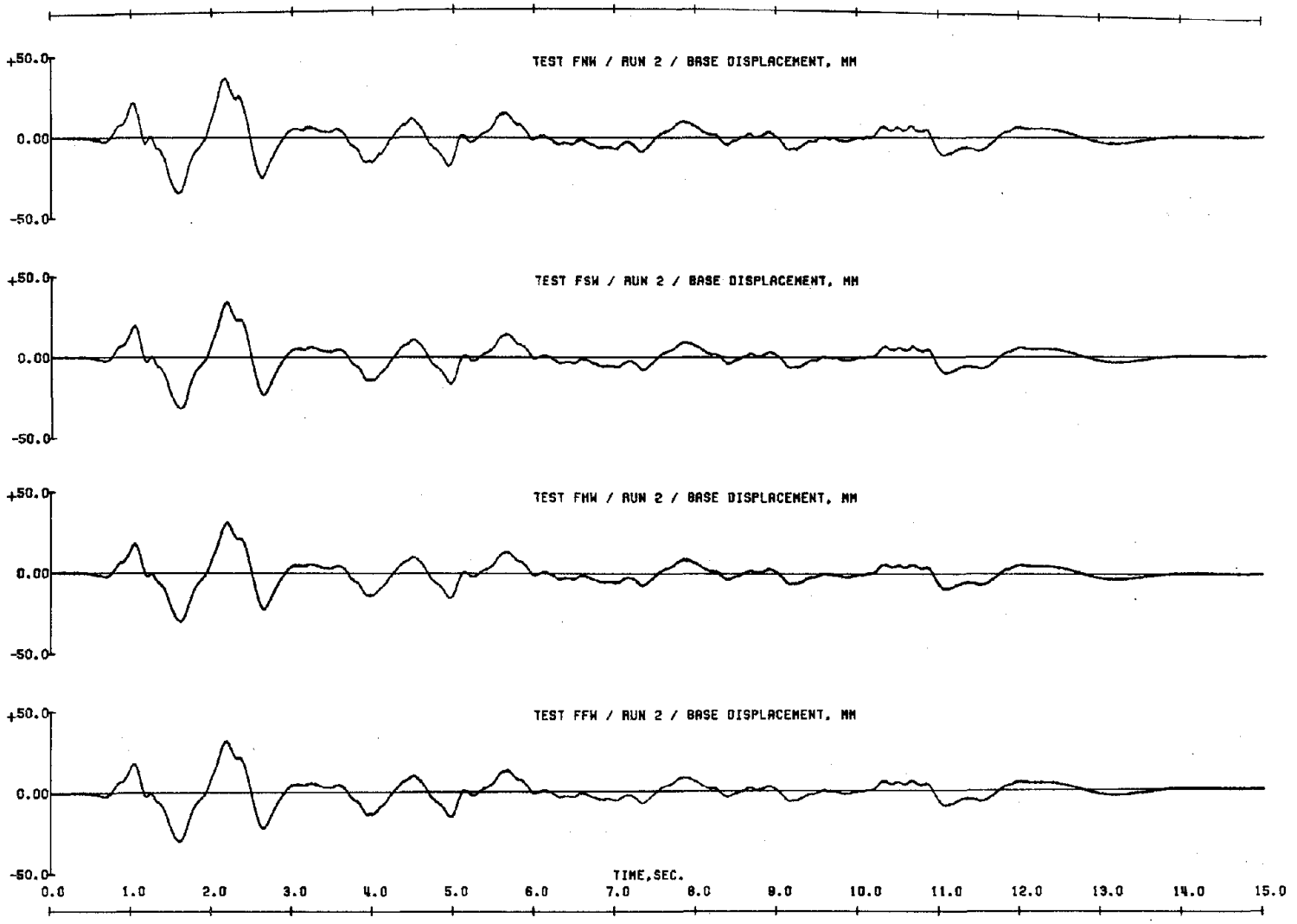


Fig. 4.12 (contd.) Base Accelerations and Displacements Measured during Second Simulations

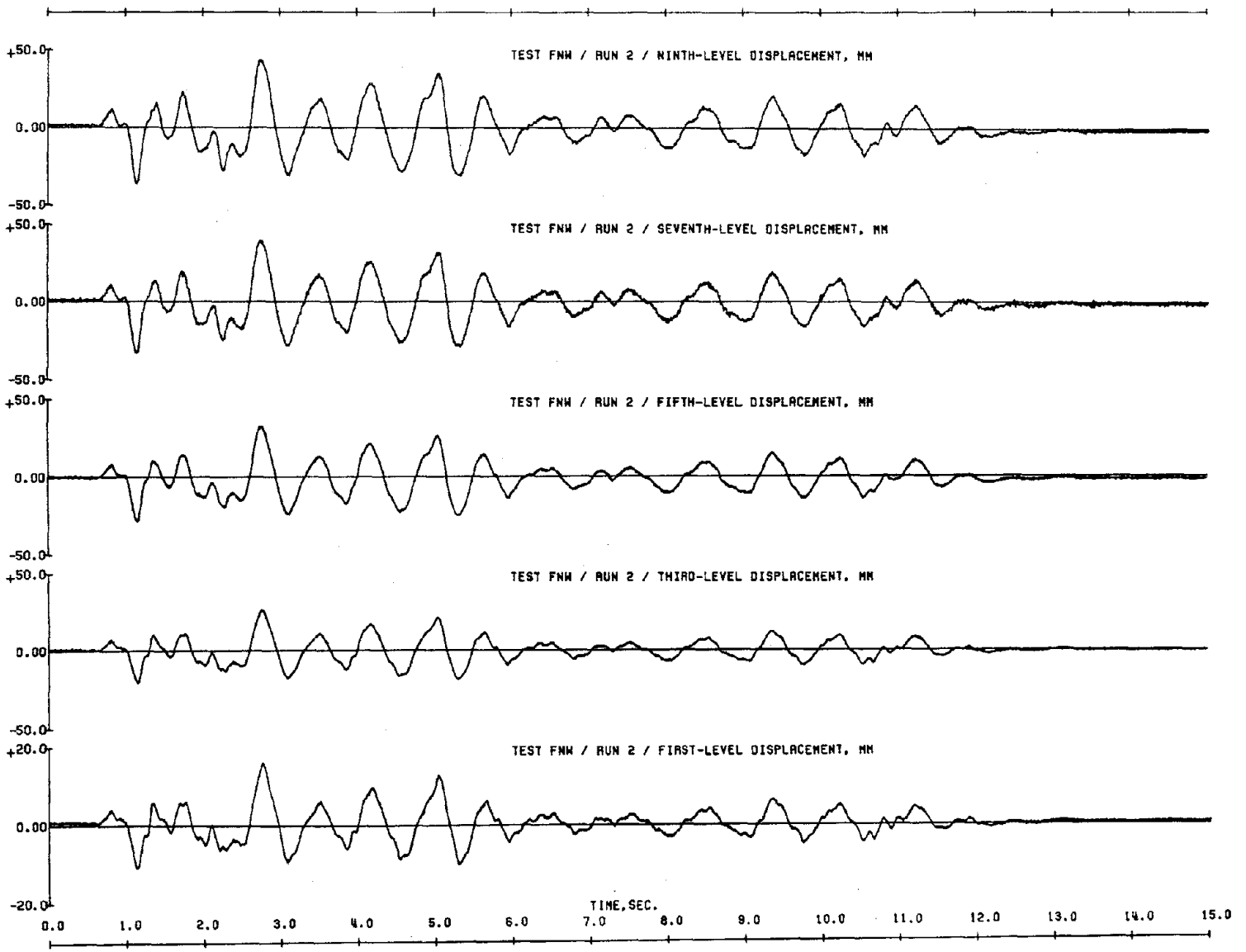


Fig. 4.13 Displacement Response Measured during Second Simulations

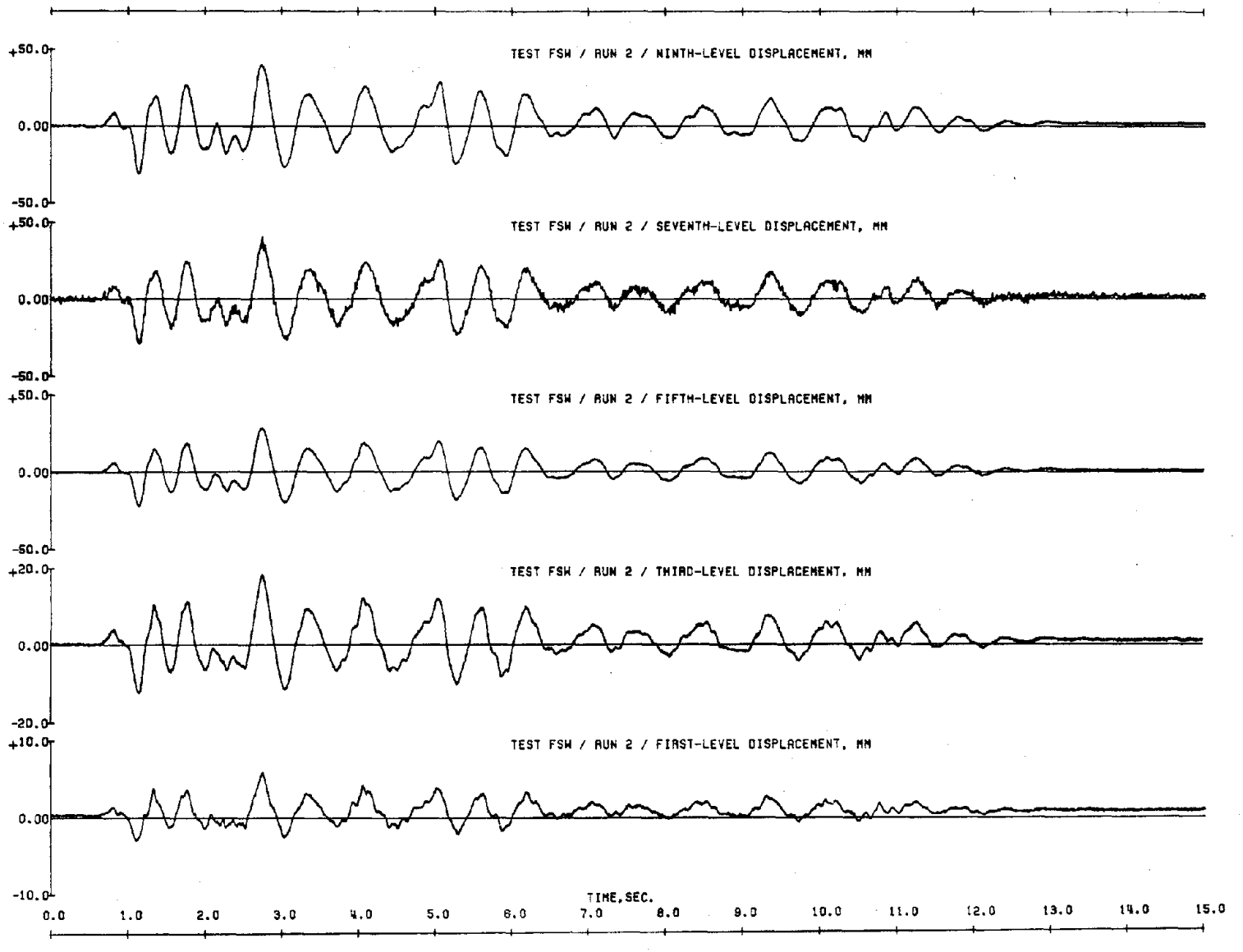


Fig. 4.13 (contd.) Displacement Response Measured during Second Simulations

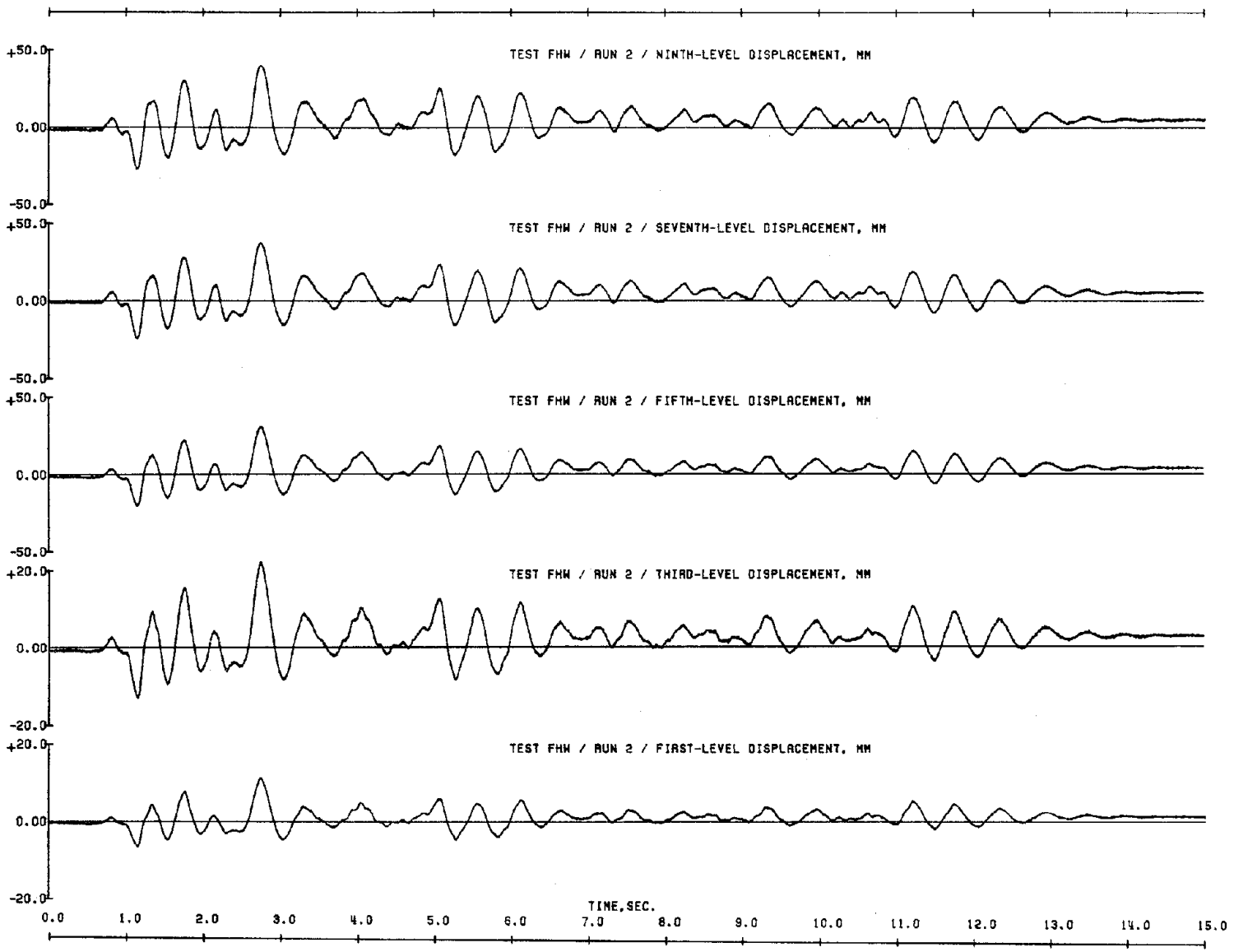


Fig. 4.13 (contd.) Displacement Response Measured during Second Simulations

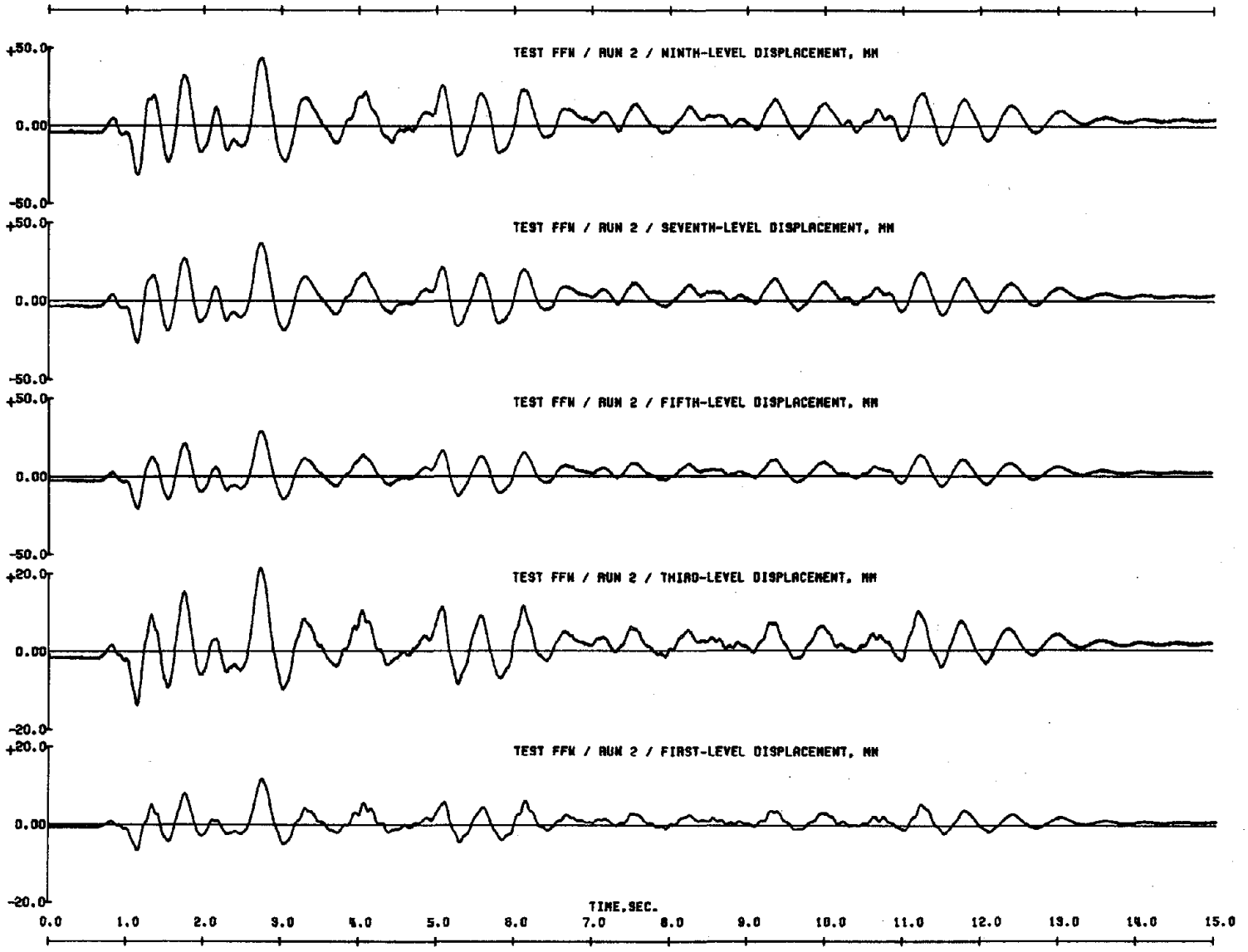


Fig. 4.13 (contd.) Displacement Response Measured during Second Simulations

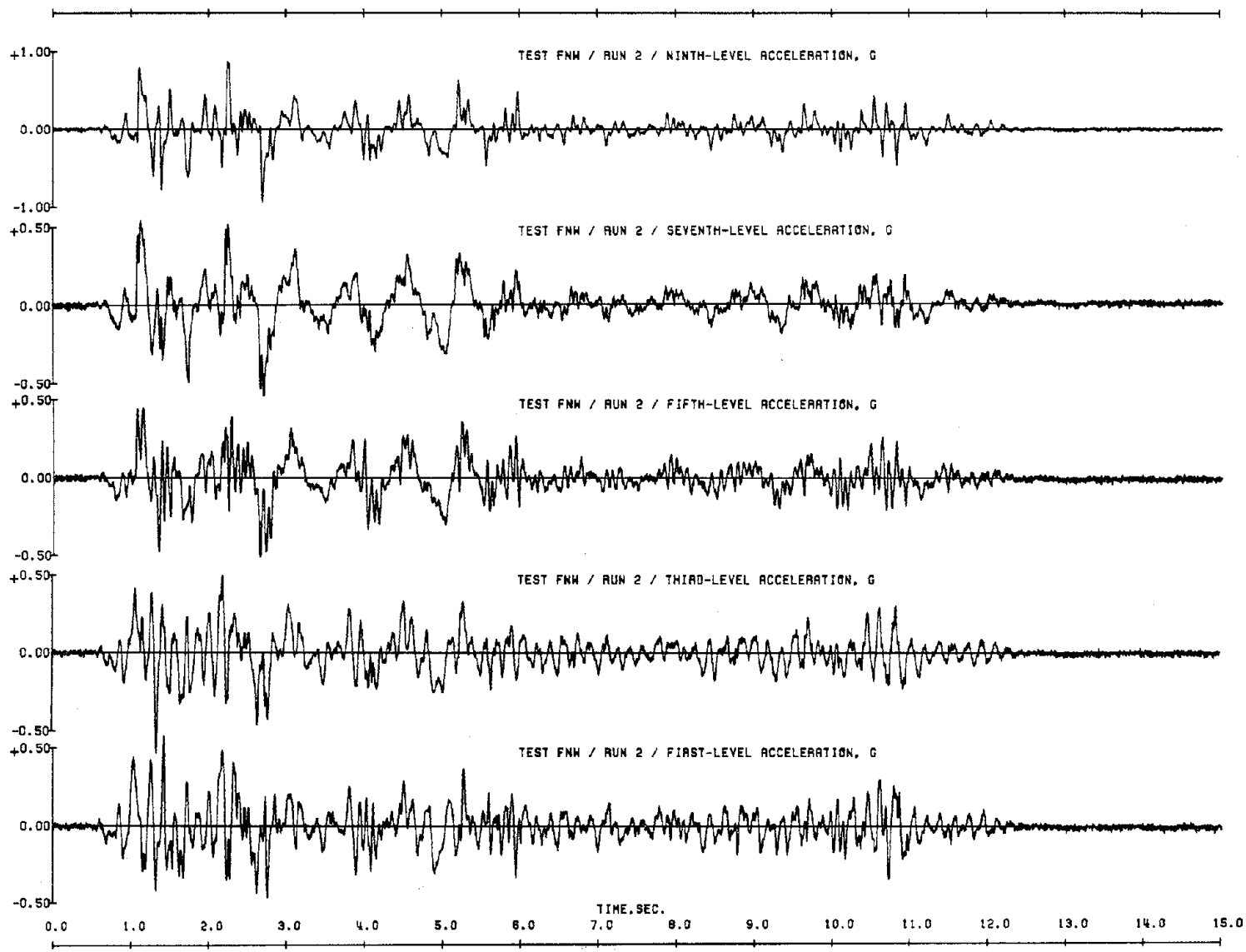


Fig. 4.14 Acceleration Response Measured during Second Simulations

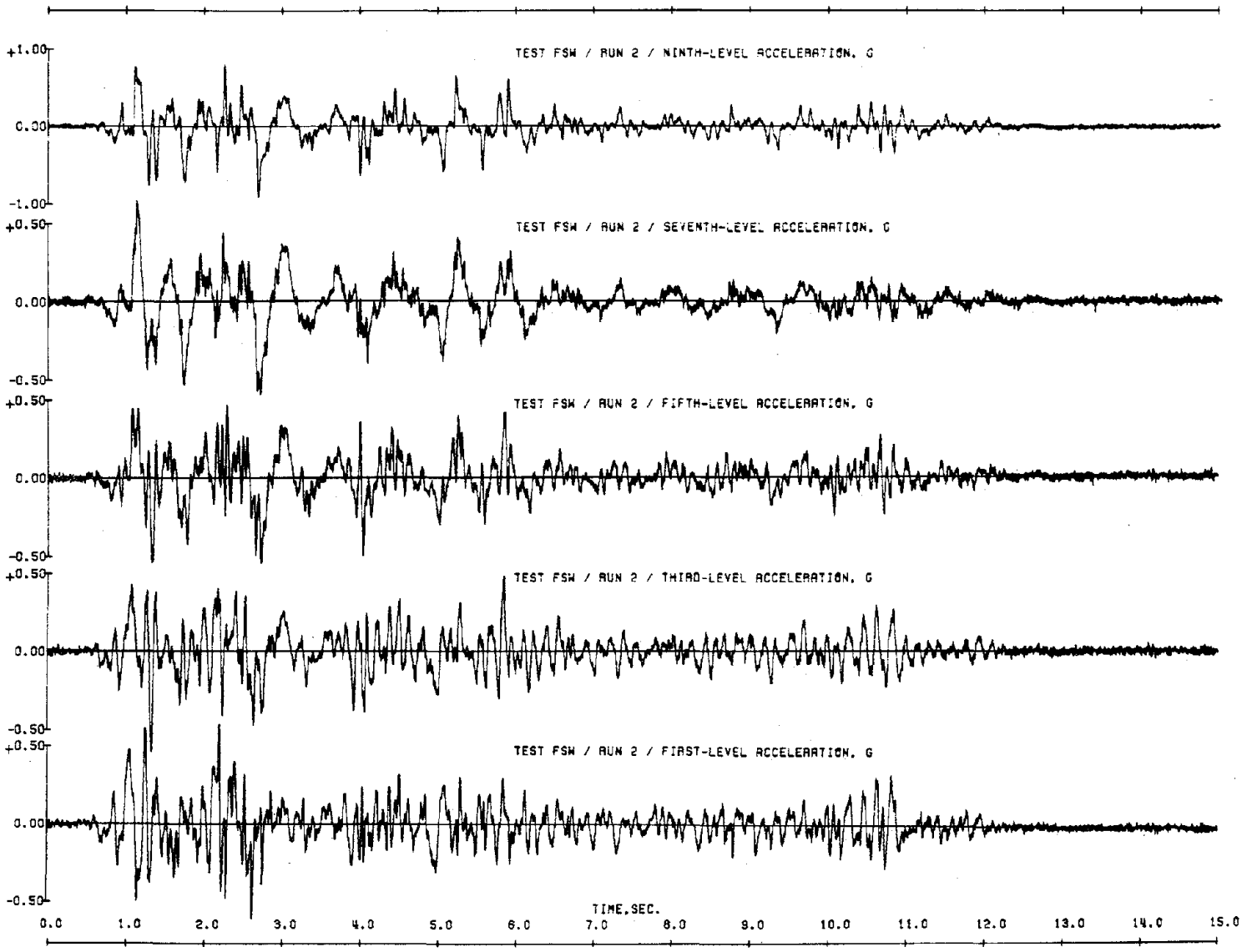


Fig. 4.14 (contd.) Acceleration Response Measured during Second Simulations

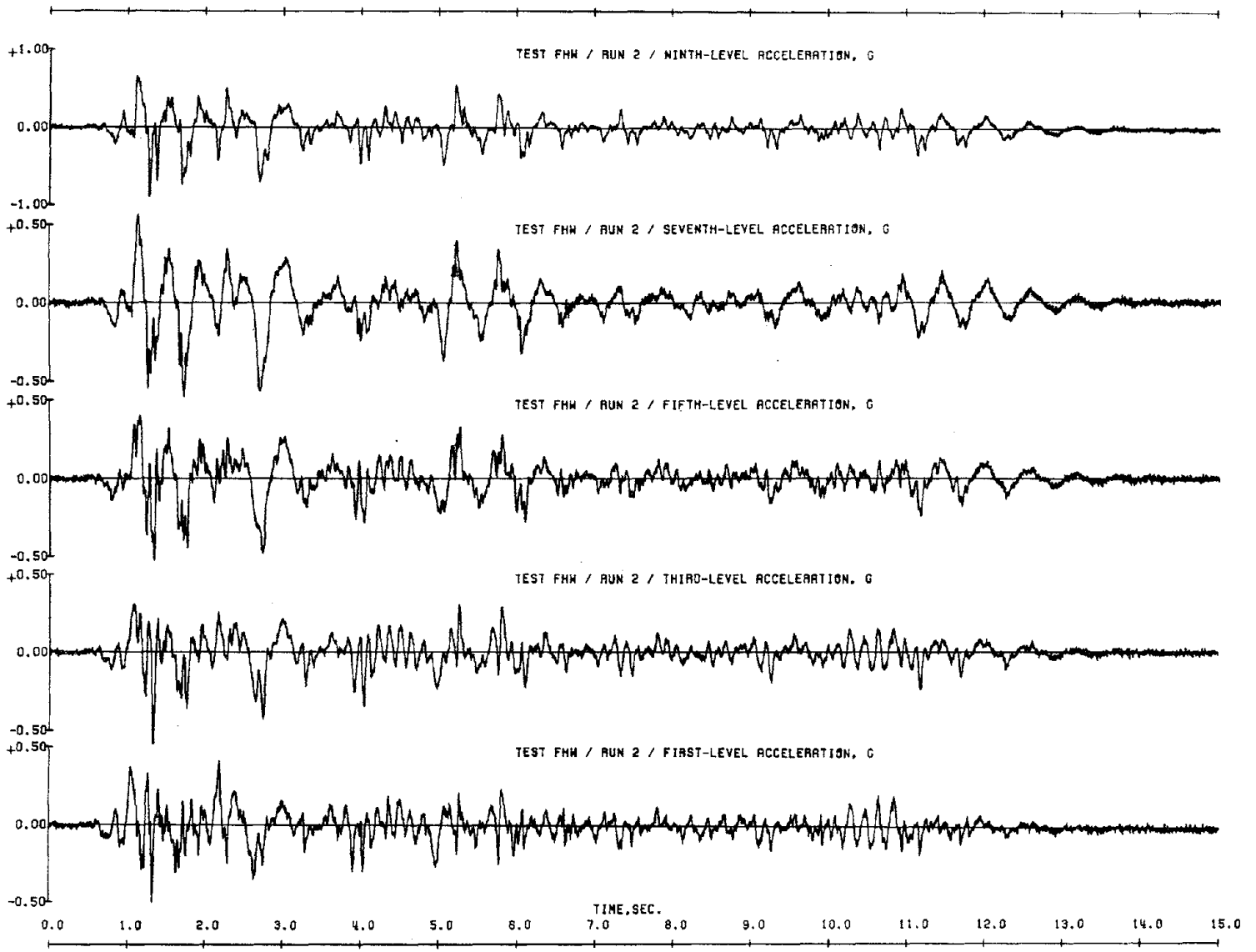


Fig. 4.14 (contd.) Acceleration Response Measured during Second Simulations

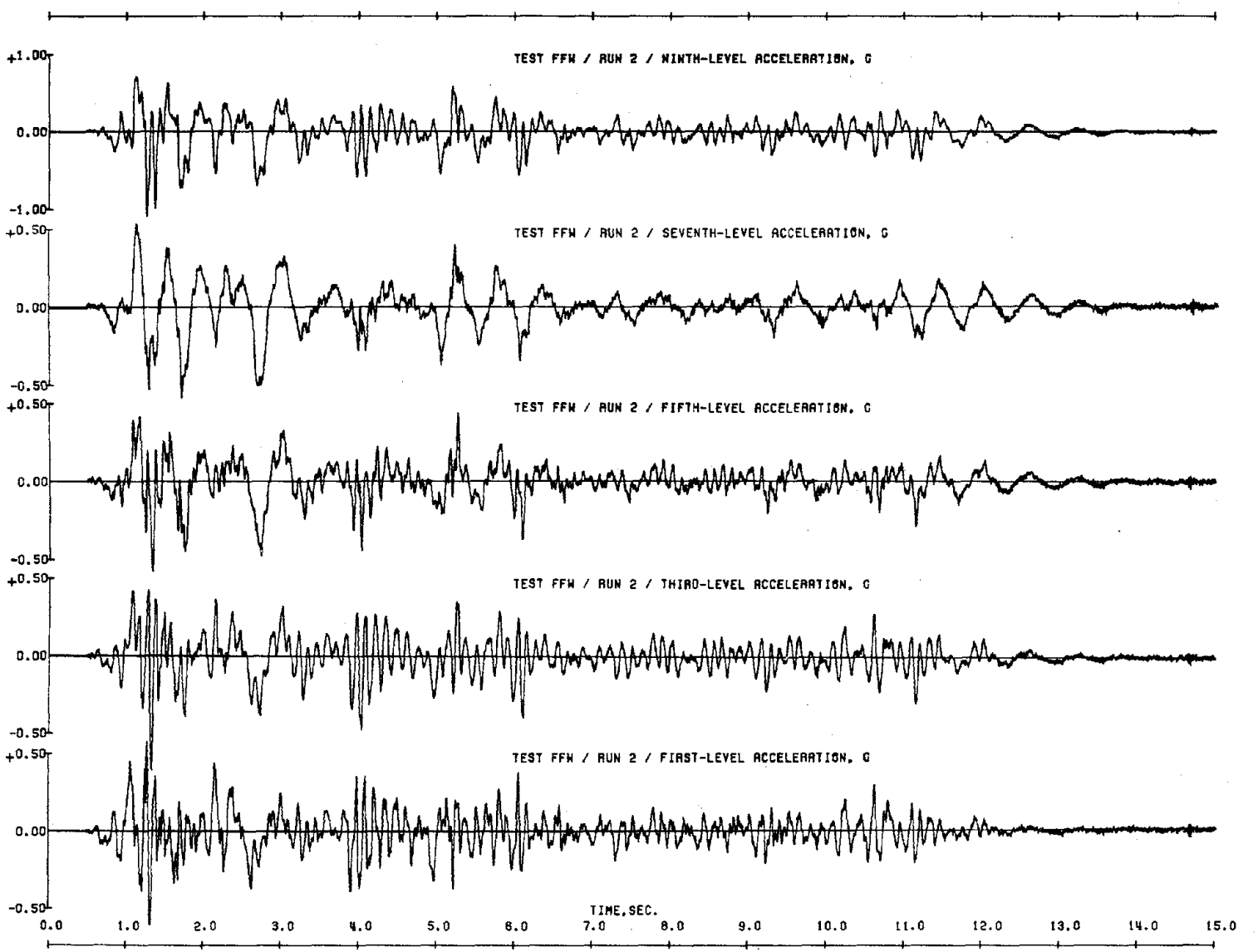


Fig. 4.14 (contd.) Acceleration Response Measured during Second Simulations

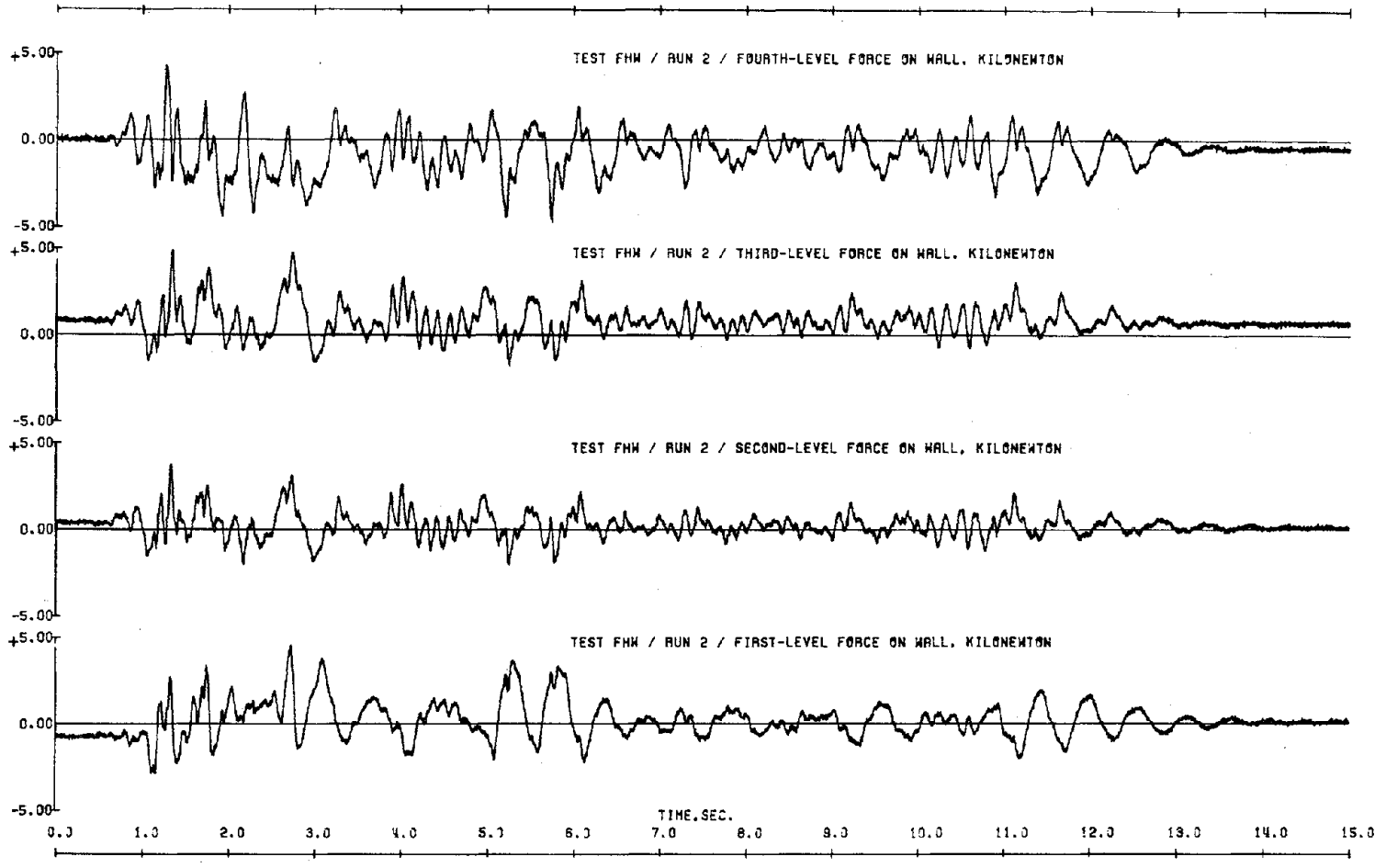


Fig. 4.15 Wall Forces Measured during Second Simulations

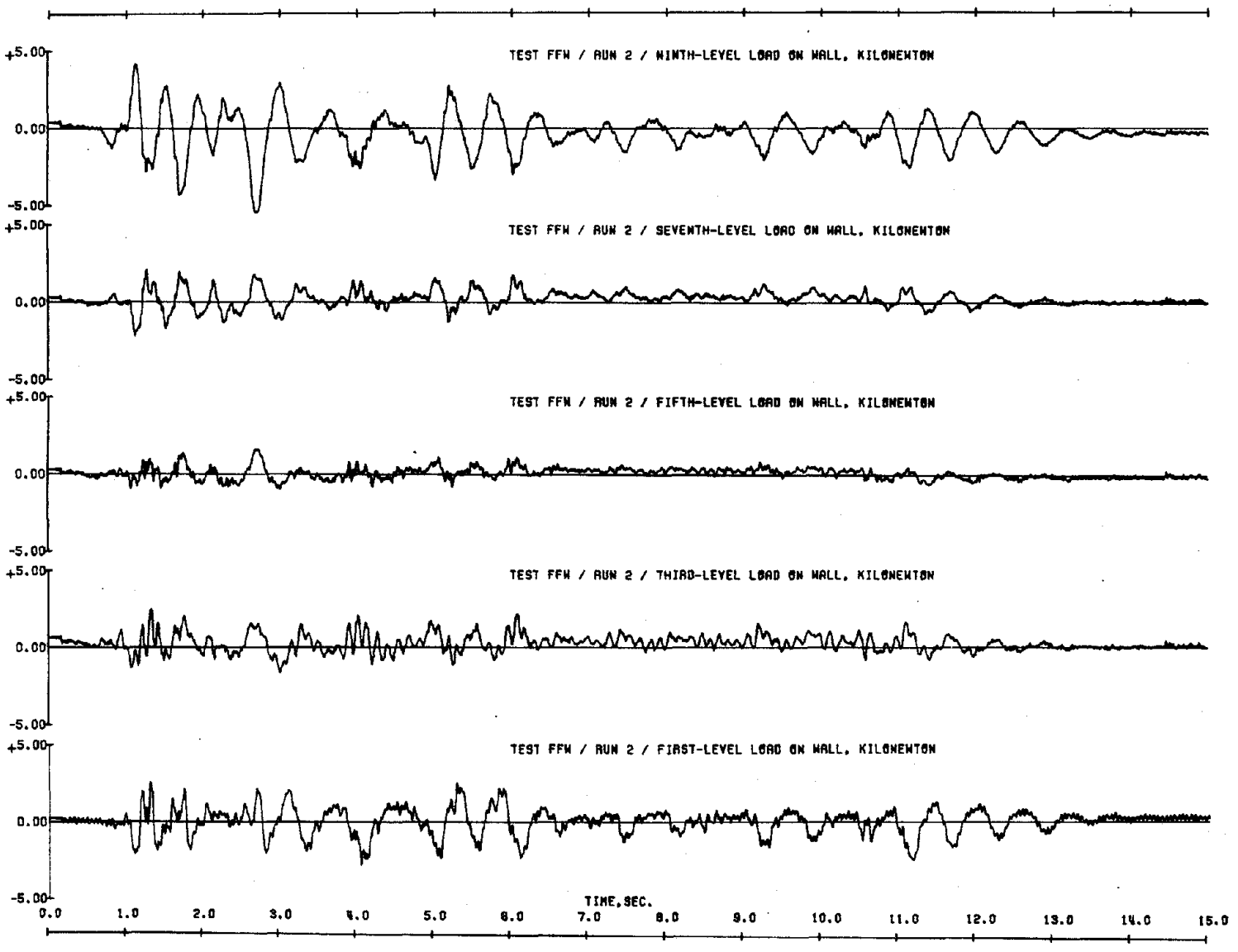


Fig. 4.15 (contd.) Wall Forces Measured during Second Simulations

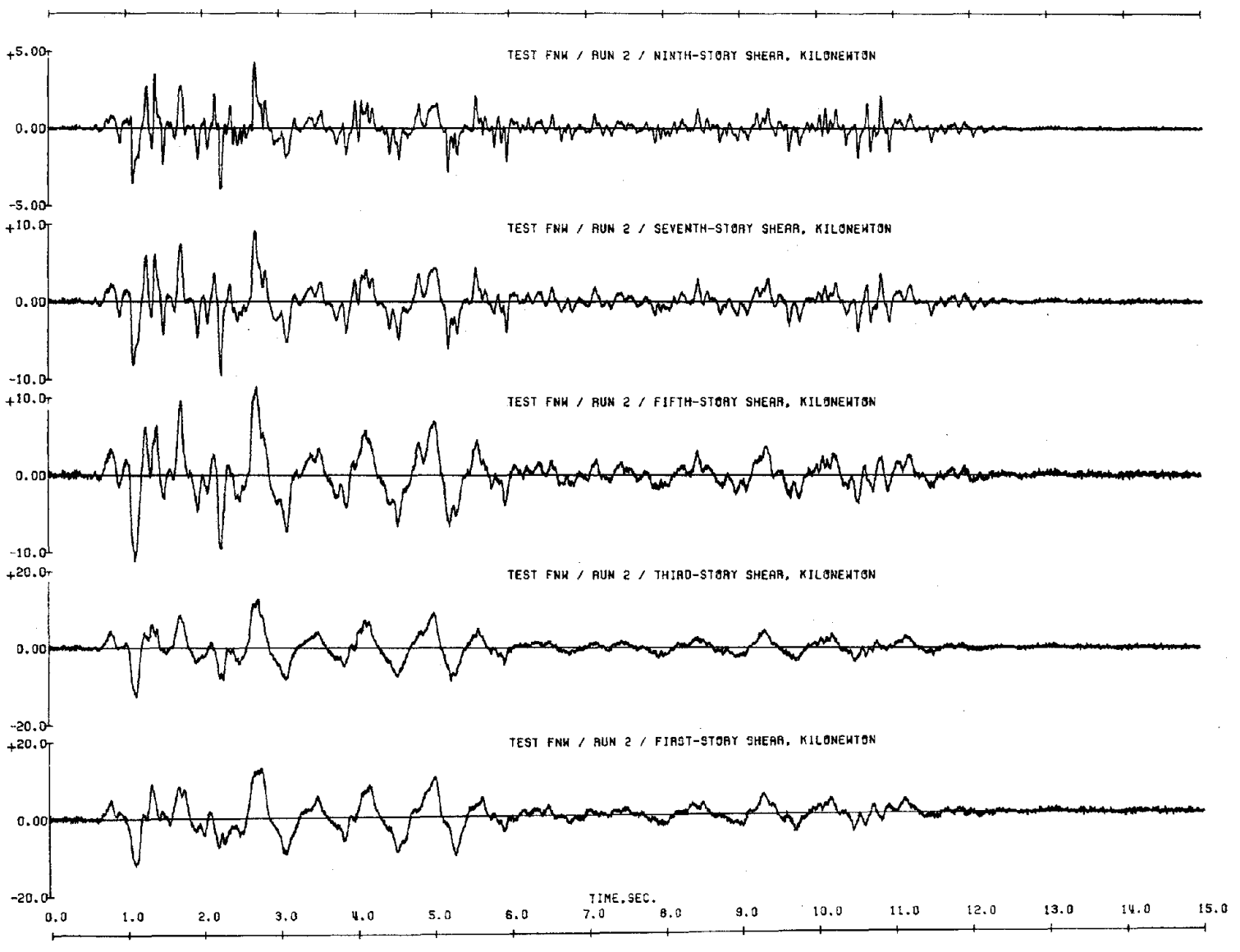


Fig. 4.16 Shear Response to Second Simulations

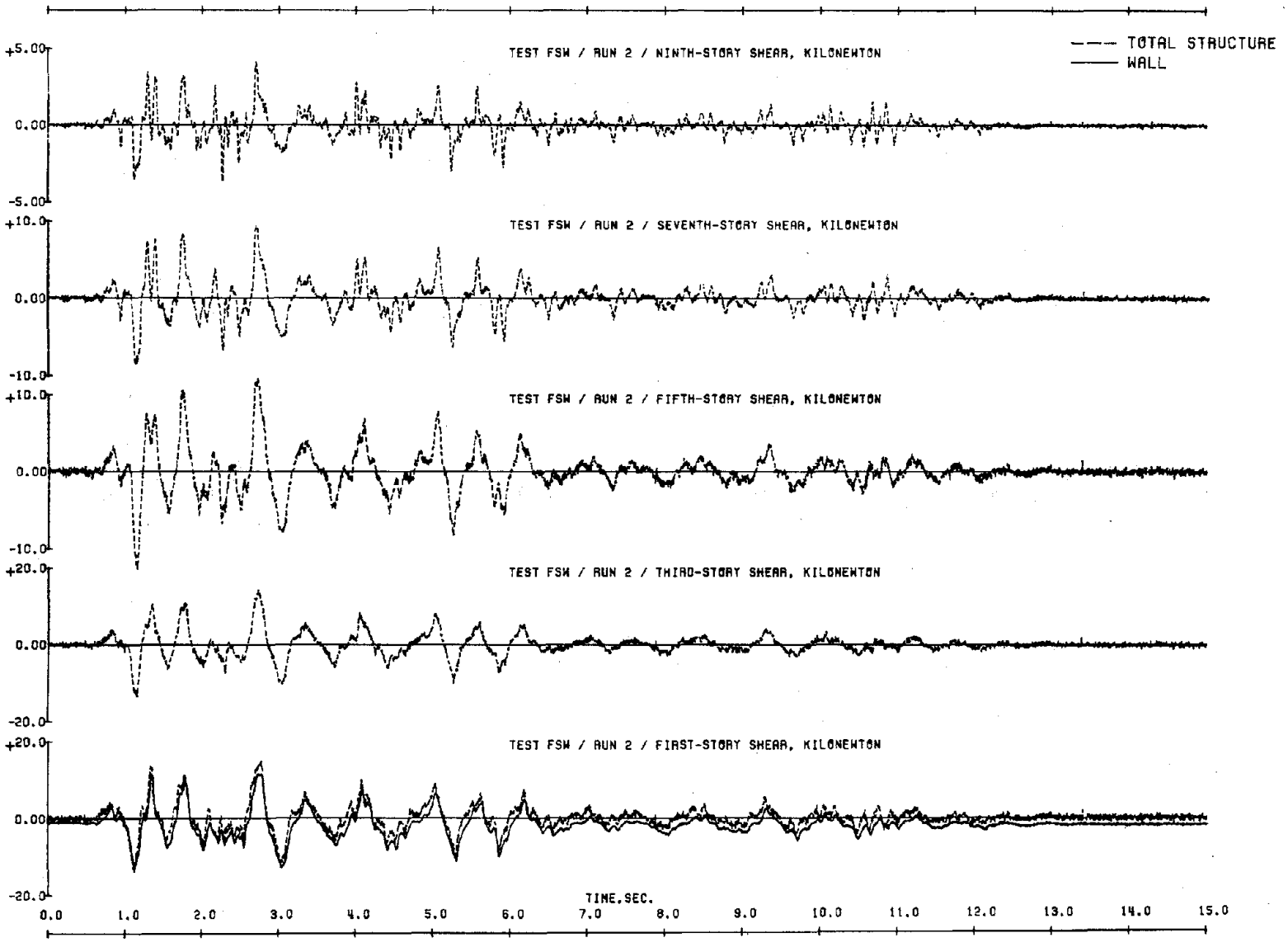


Fig. 4.16 (Contd.) Shear Response to Second Simulations

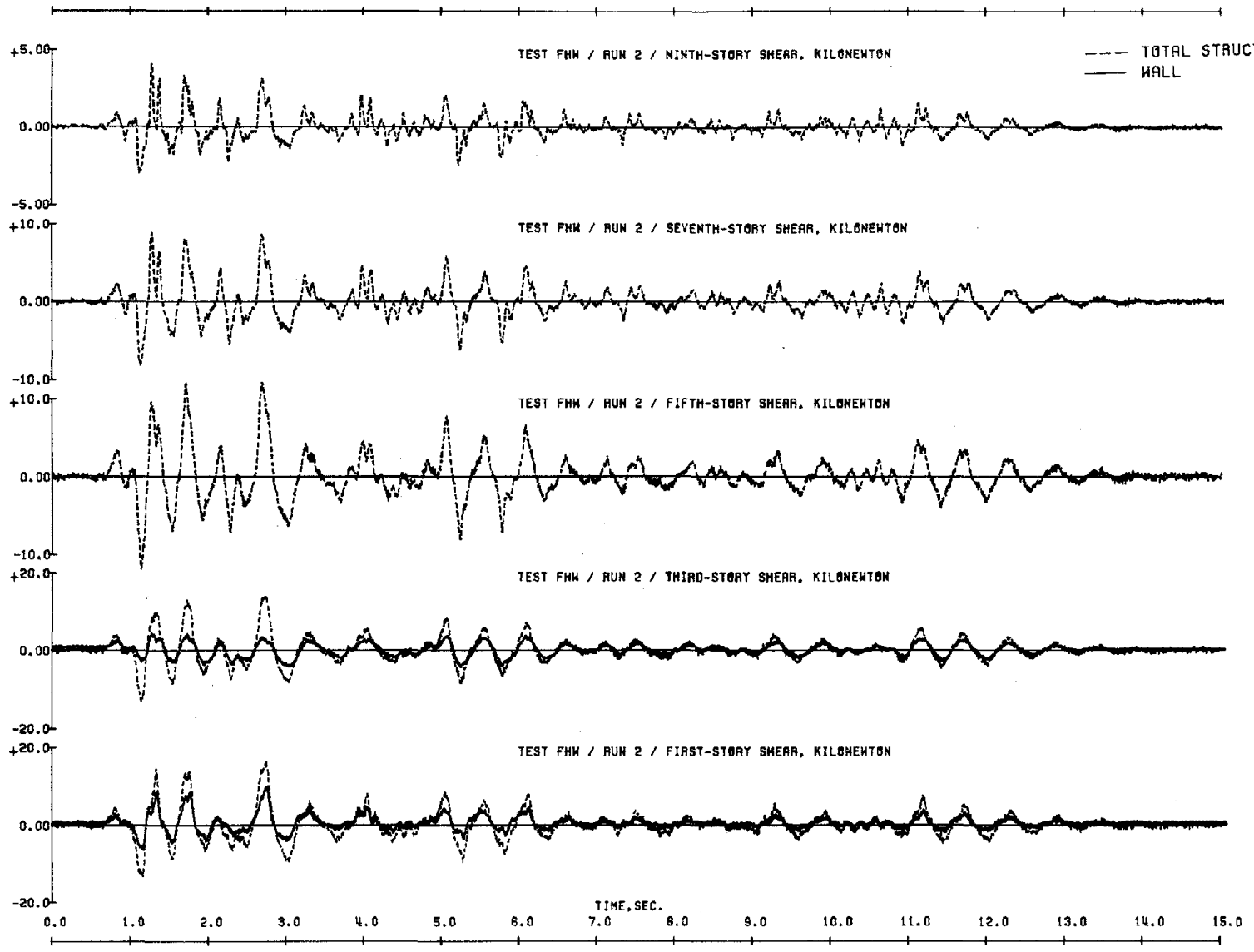


Fig. 4.16 (contd.) Shear Response to Second Simulations

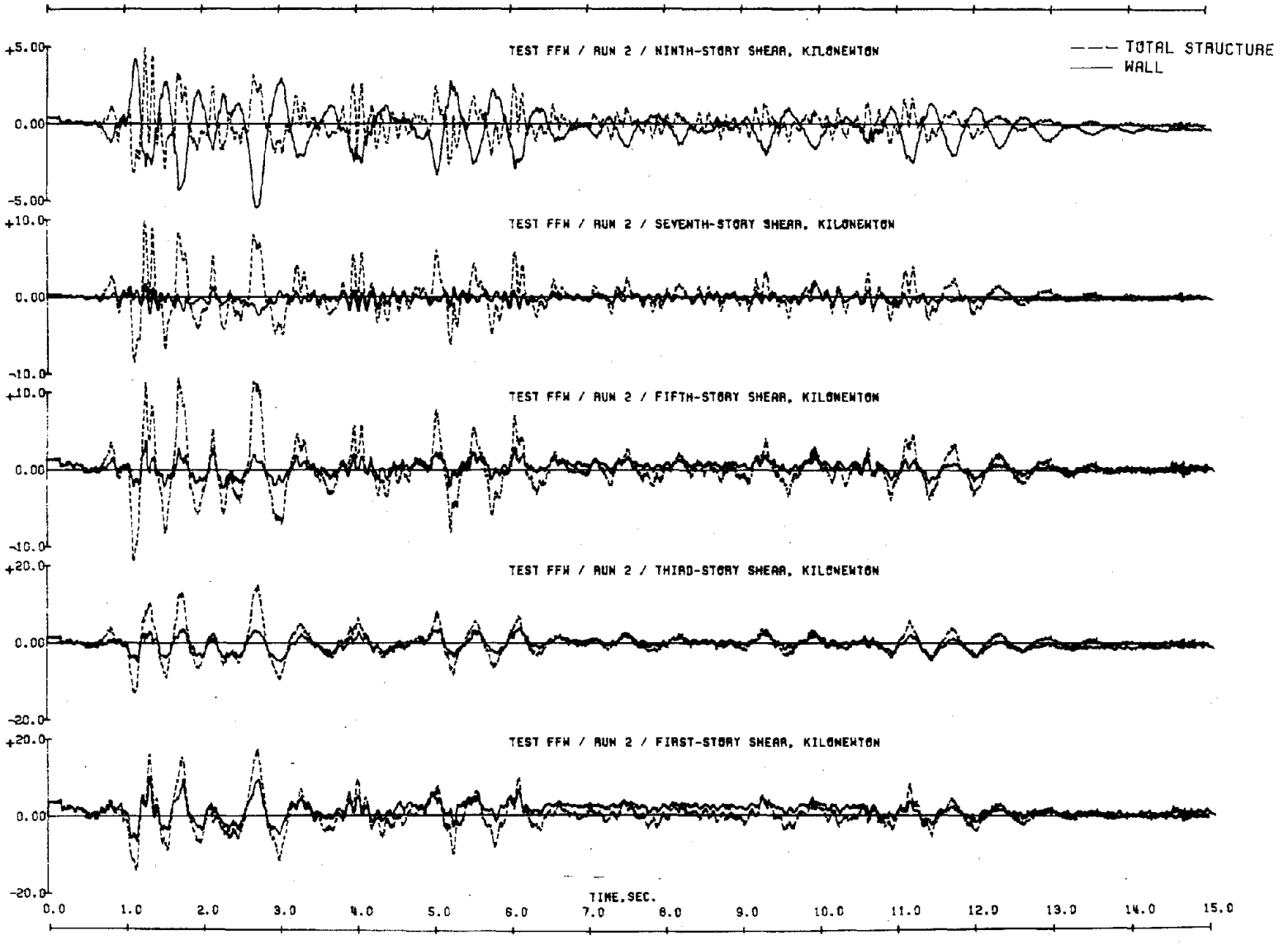


Fig. 4.16 (contd.) Shear Response to Second Simulations

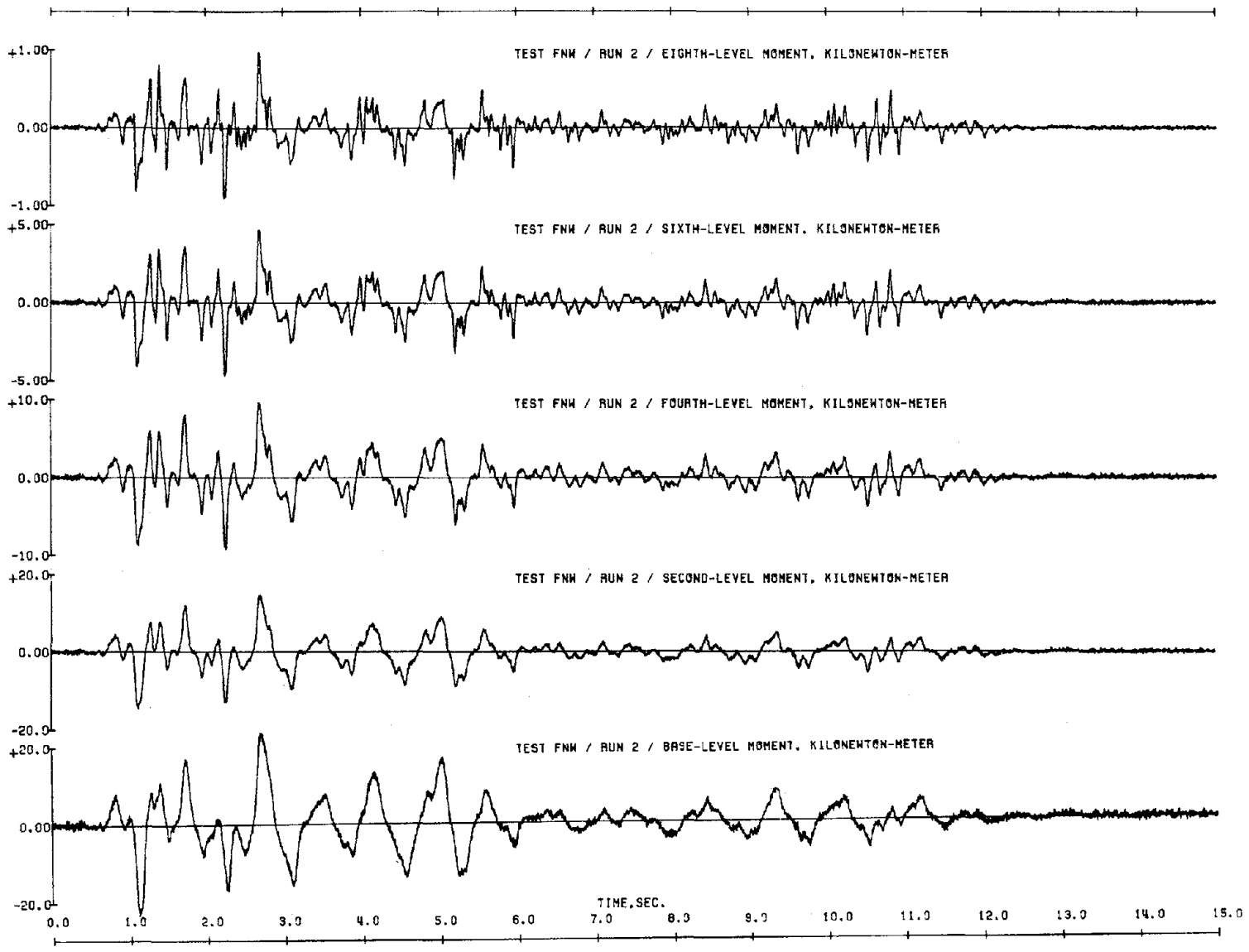


Fig. 4.17 Moment Response to Second Simulations

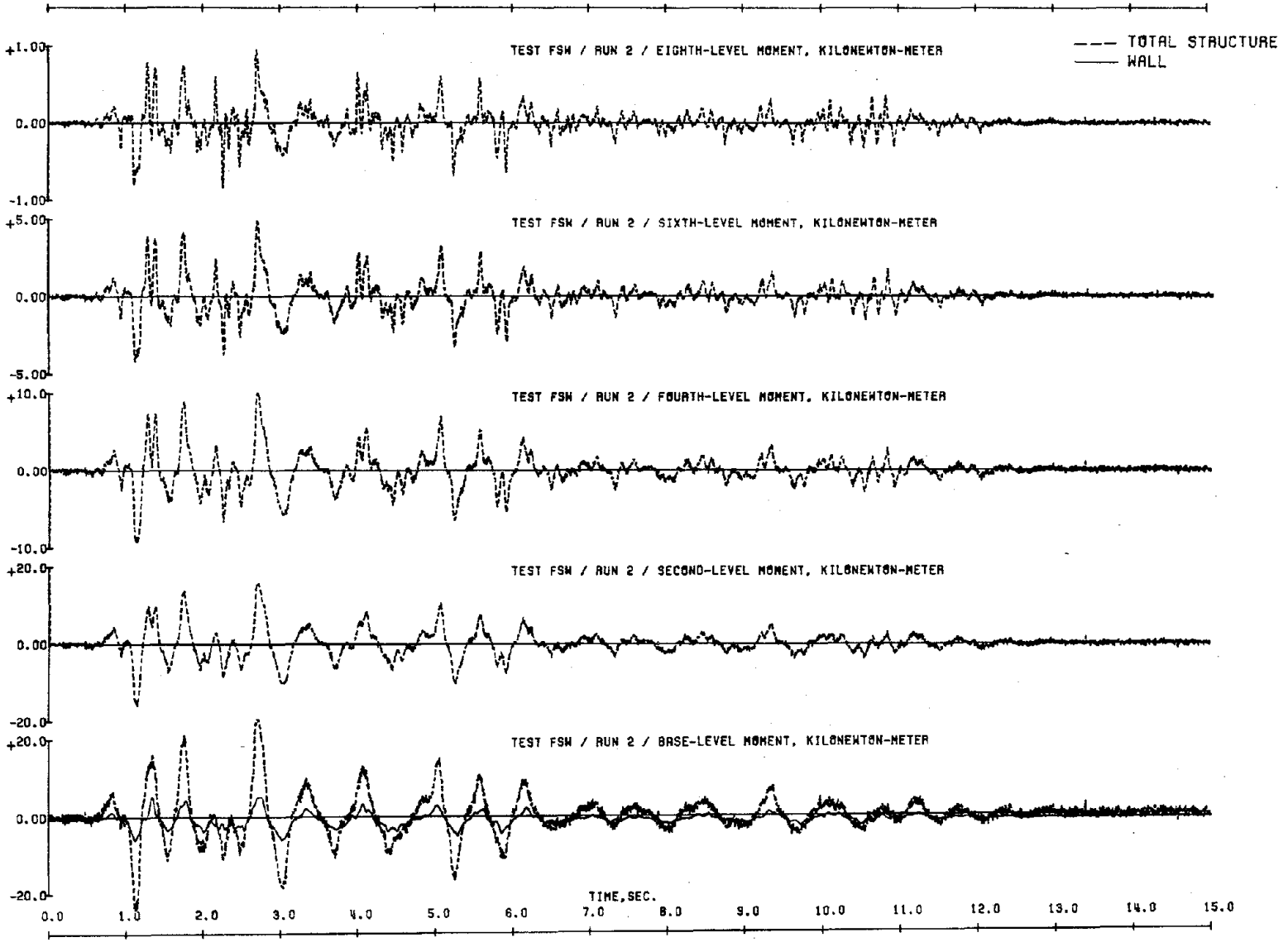


Fig. 4.17 (contd.) Moment Response to Second Simulations

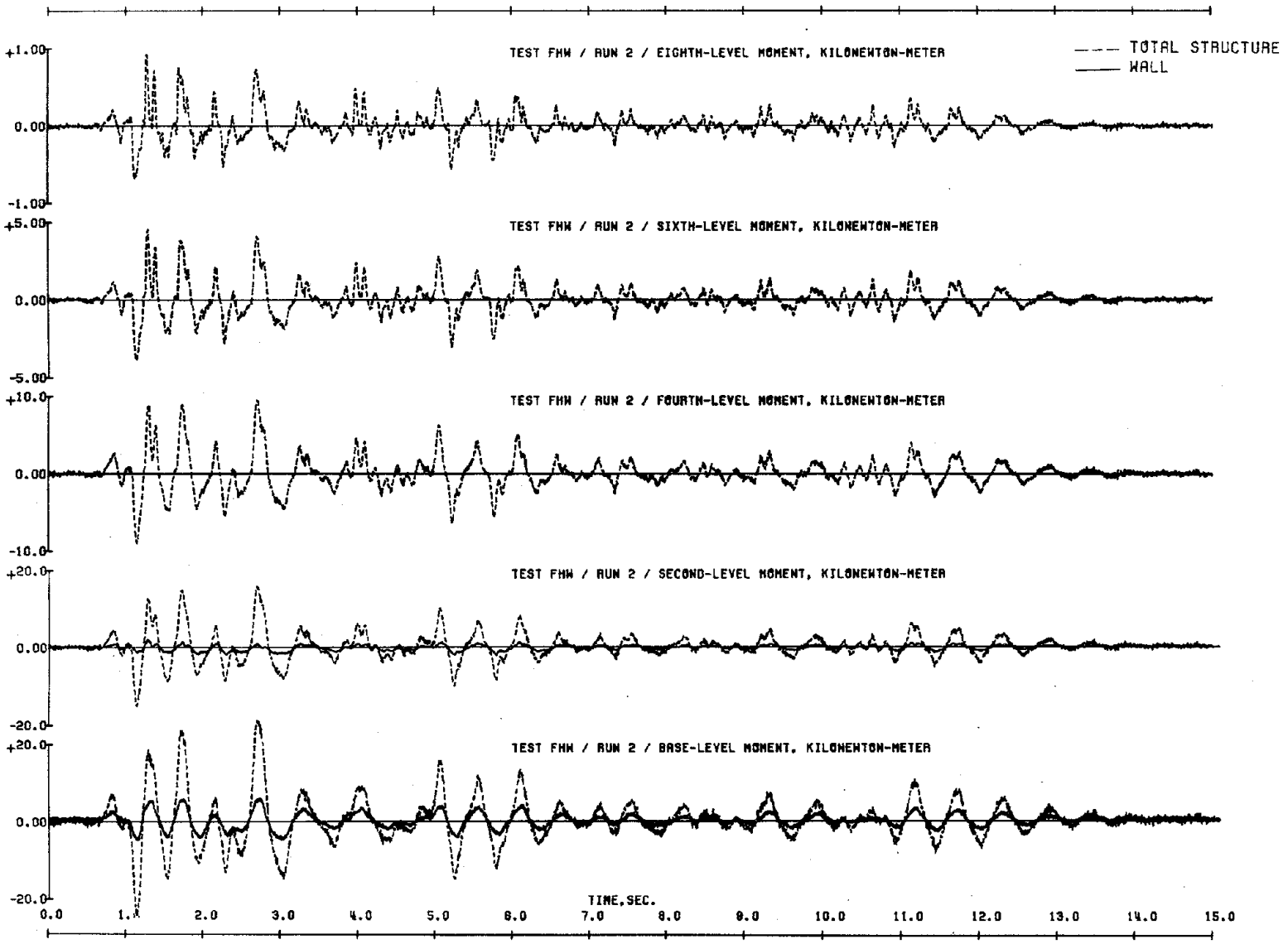


Fig. 4.17 (contd.) Moment Response to Second Simulations

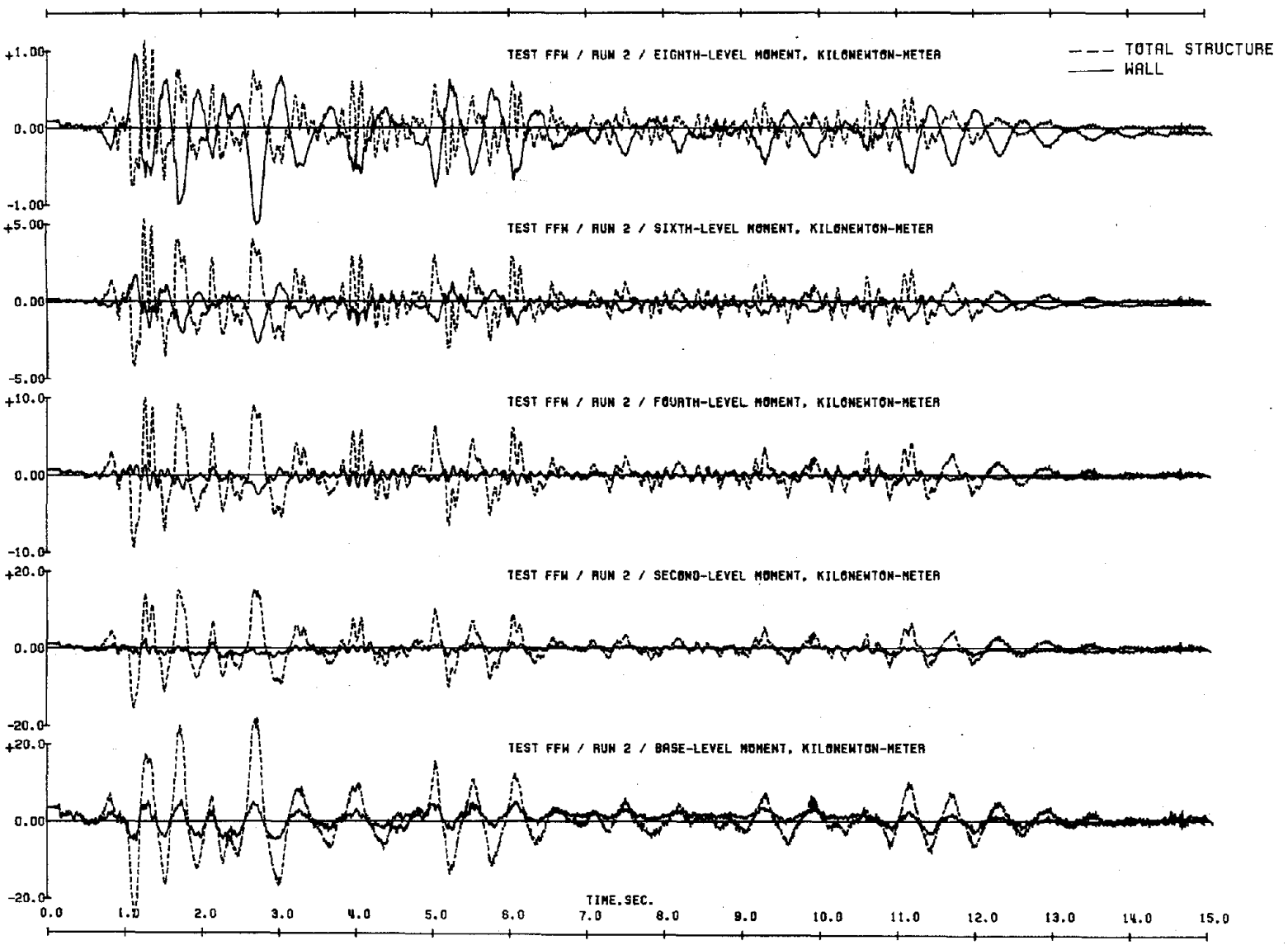


Fig. 4.17 (contd.) Moment Response to Second Simulations

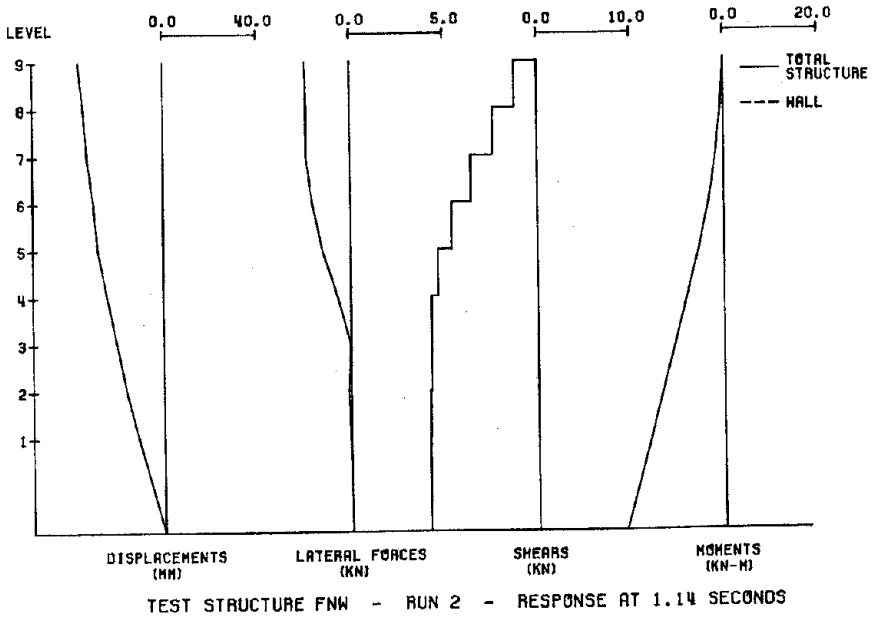


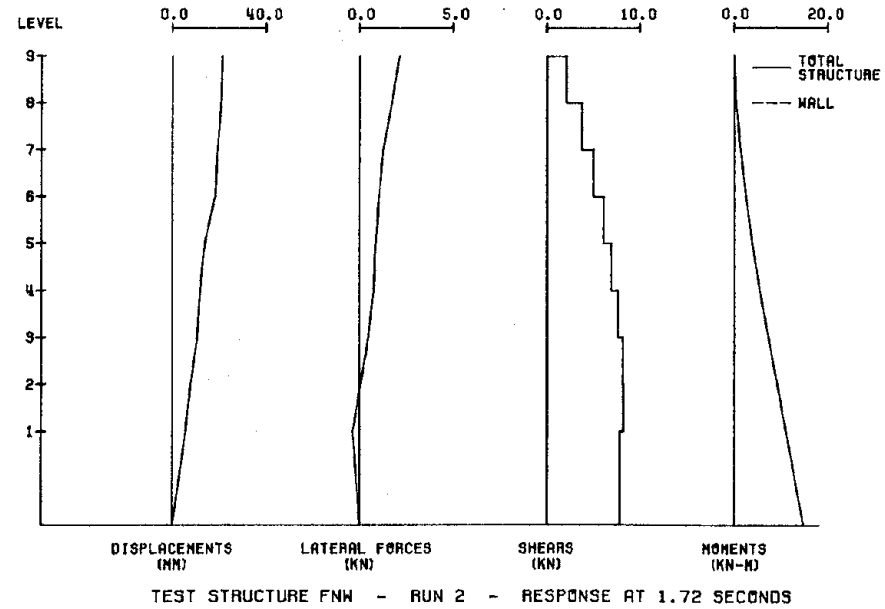


Fig. 4.18 Distributions of Response to Second Simulations

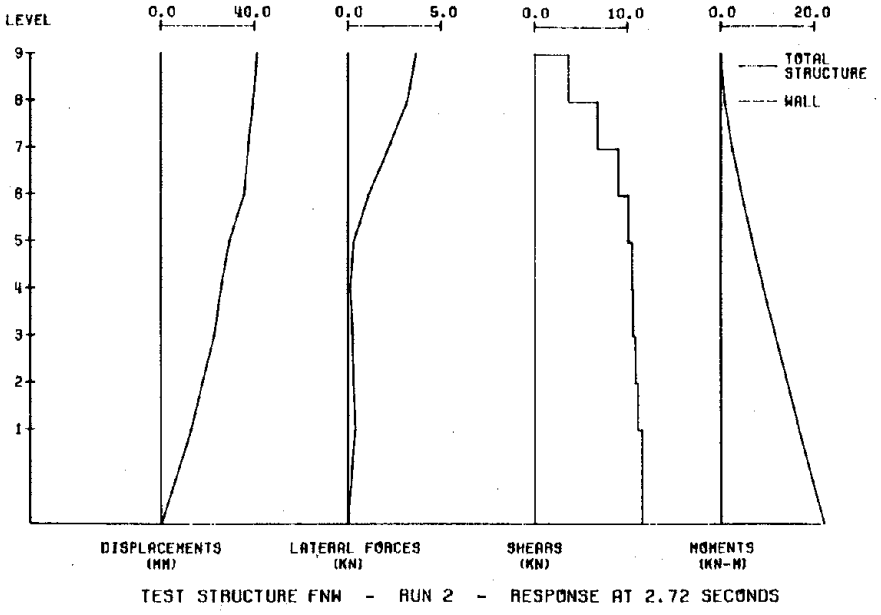


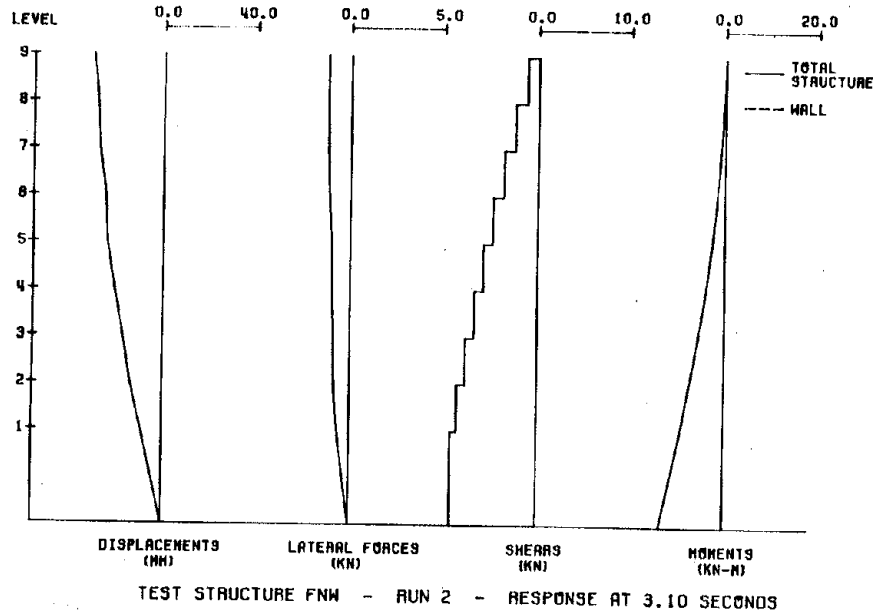


Fig. 4.18 (contd.) Distributions of Response to Second Simulations

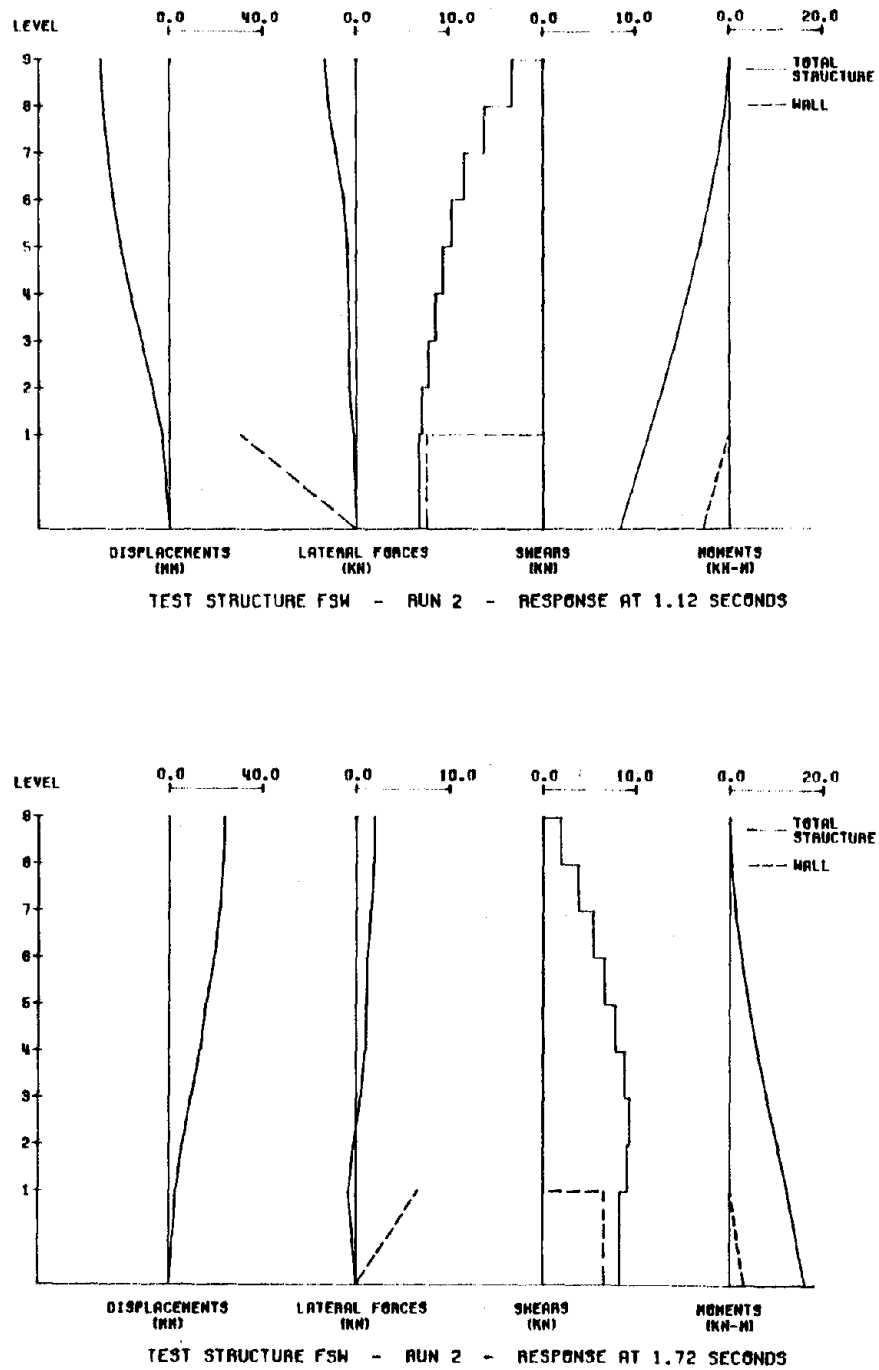


Fig. 4.18 (contd.) Distributions of Response to Second Simulations

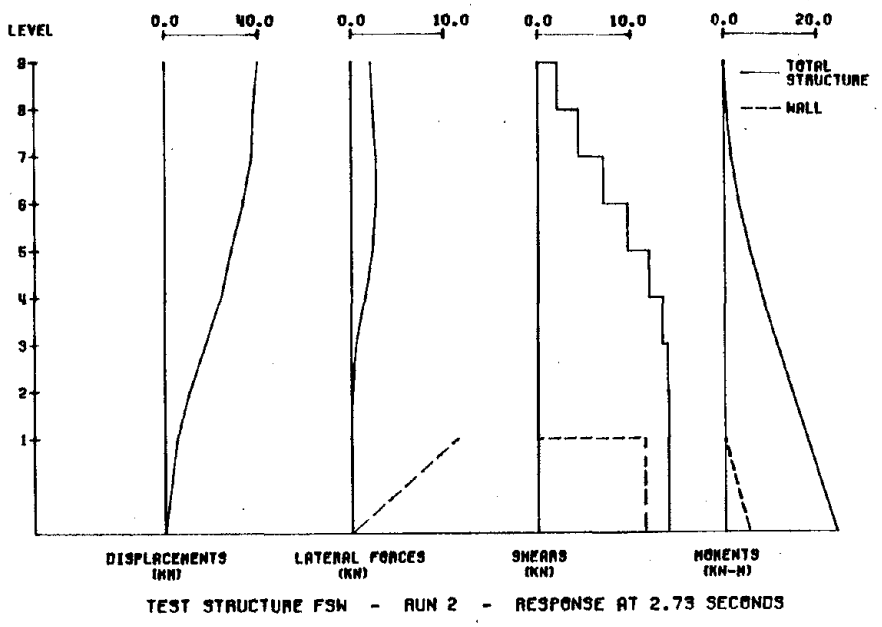


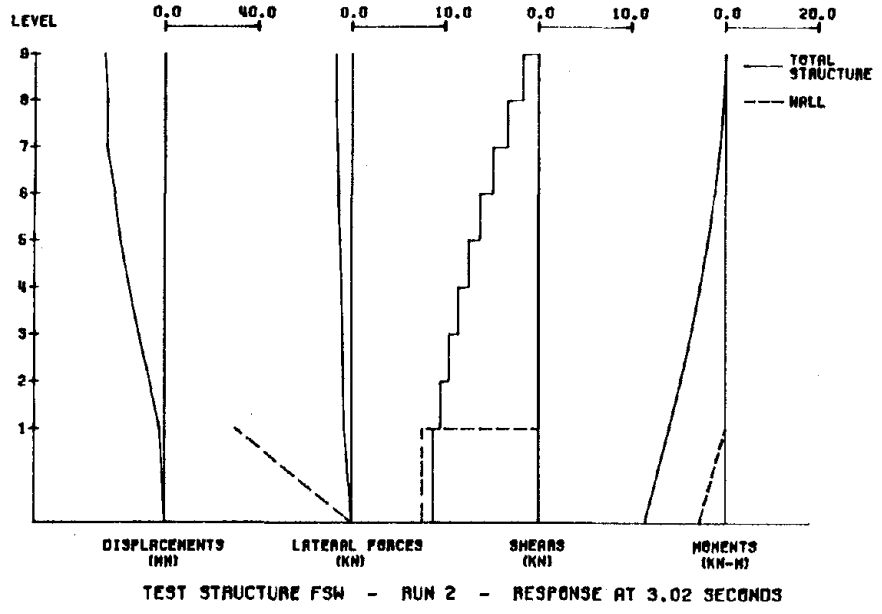


Fig. 4.18 (contd.) Distributions of Response to Second Simulations

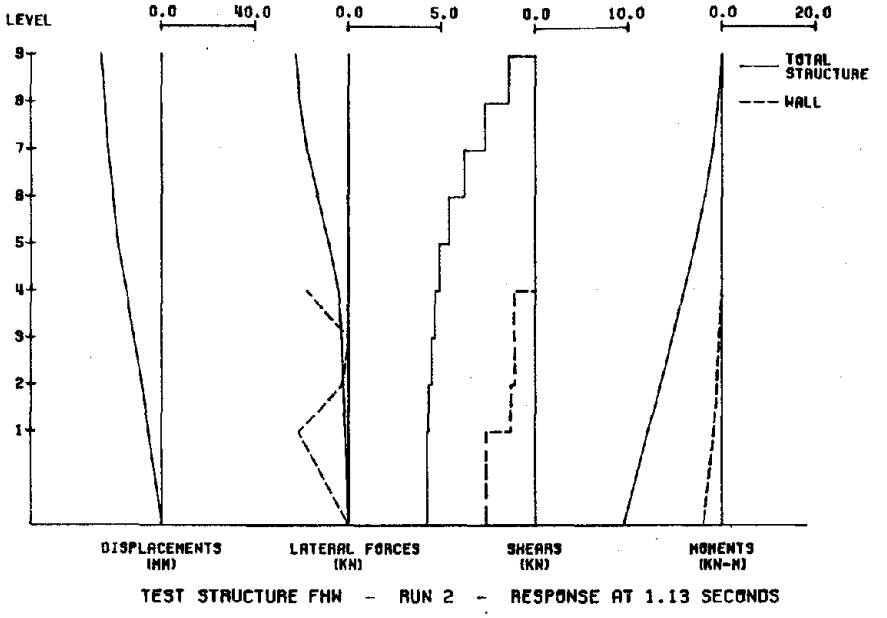


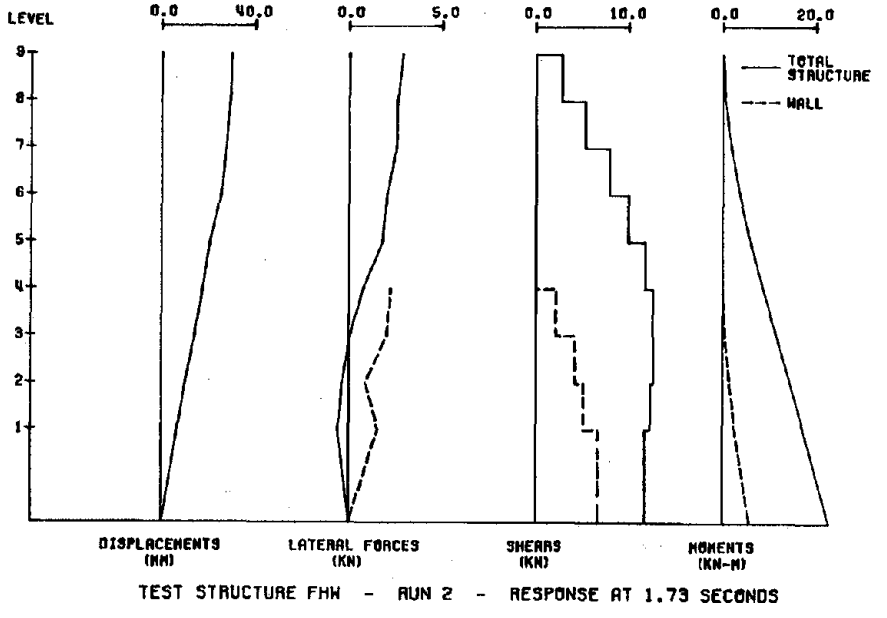


Fig. 4.18 (contd.) Distributions of Response to Second Simulations

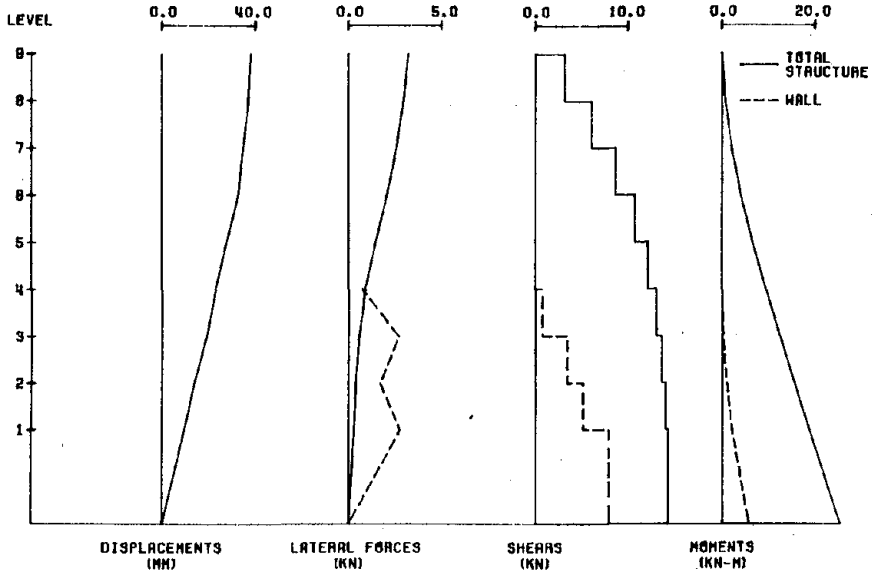


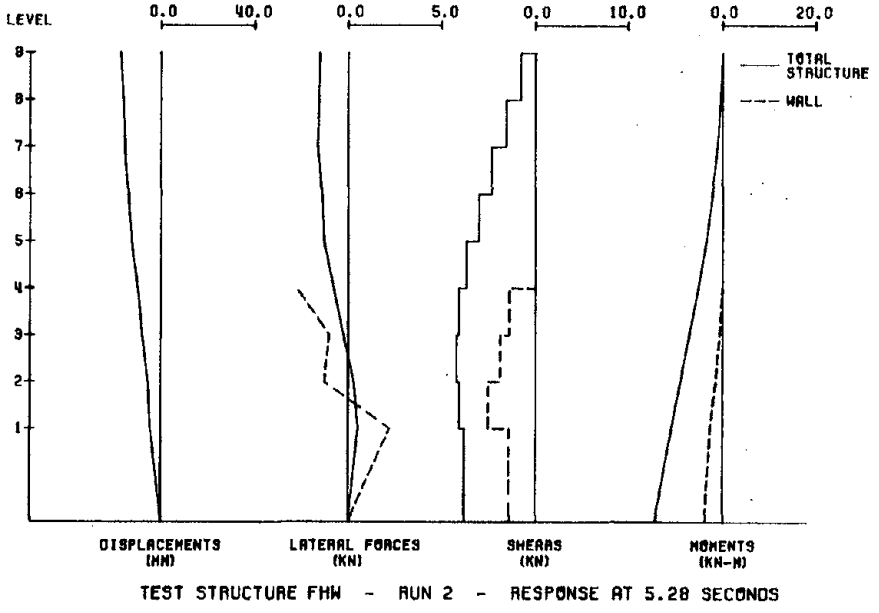


Fig. 4.18 (contd.) Distributions of Response to Second Simulations

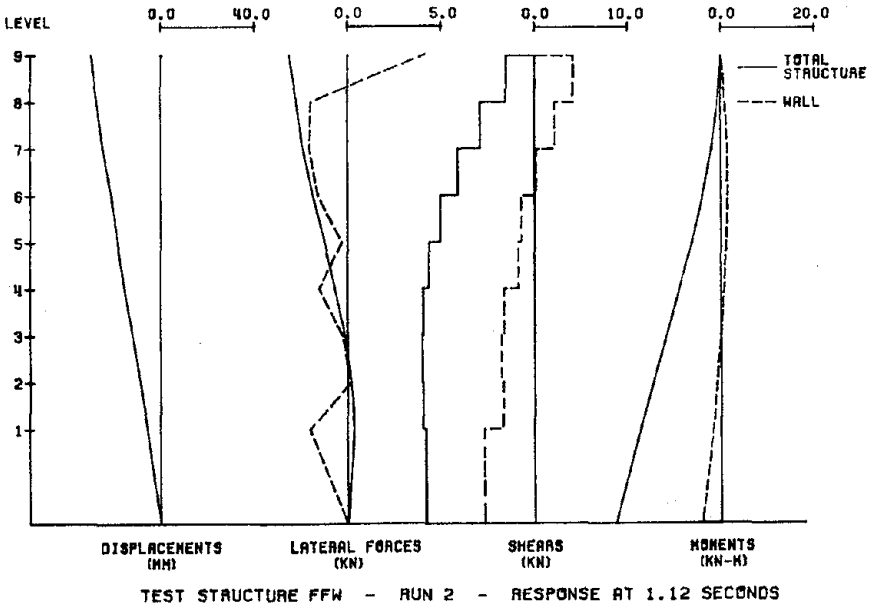


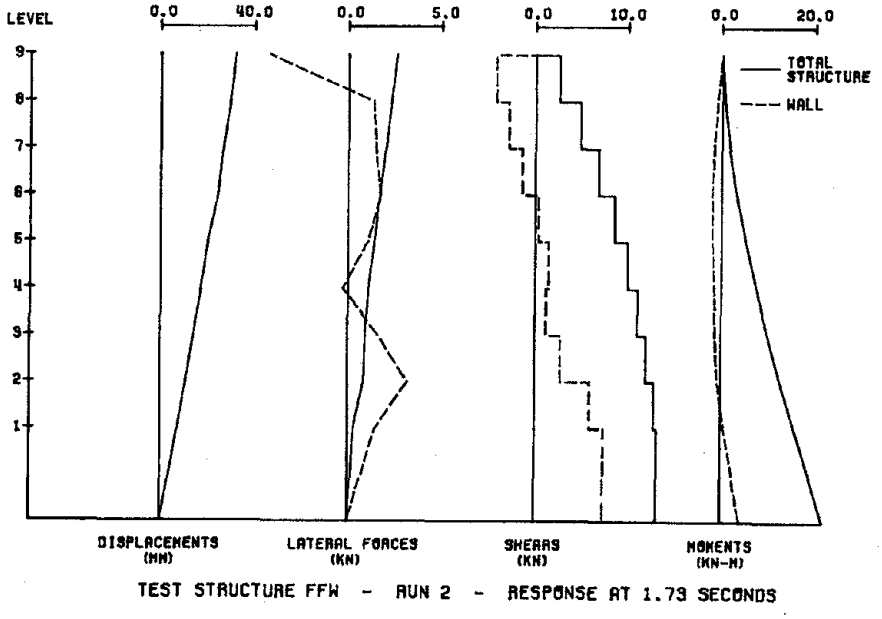


Fig. 4.18 (contd.) Distributions of Response to Second Simulations

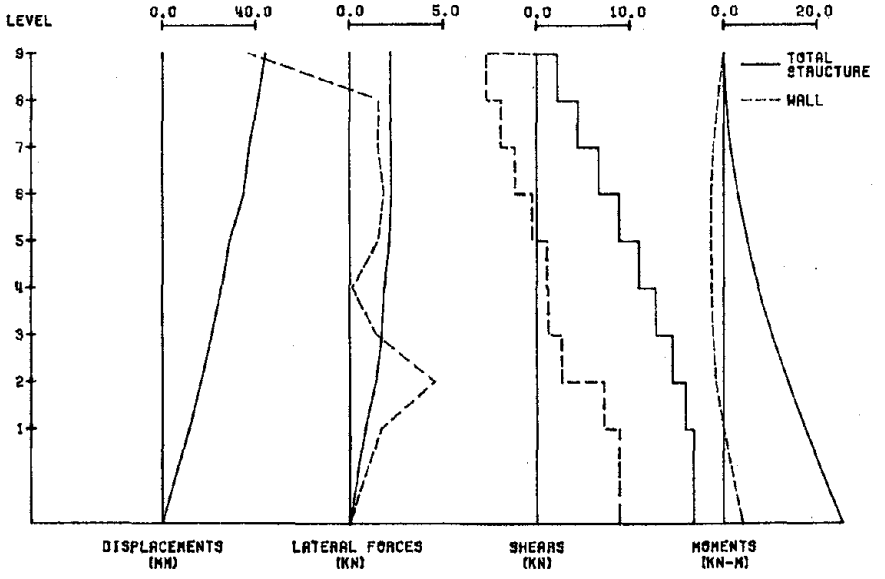


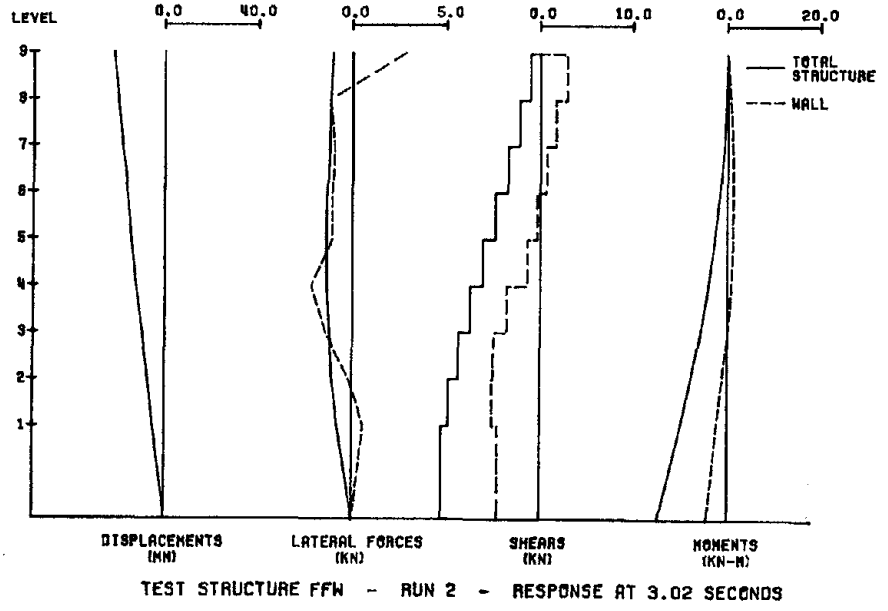


Fig. 4.18 (contd.) Distributions of Response to Second Simulations

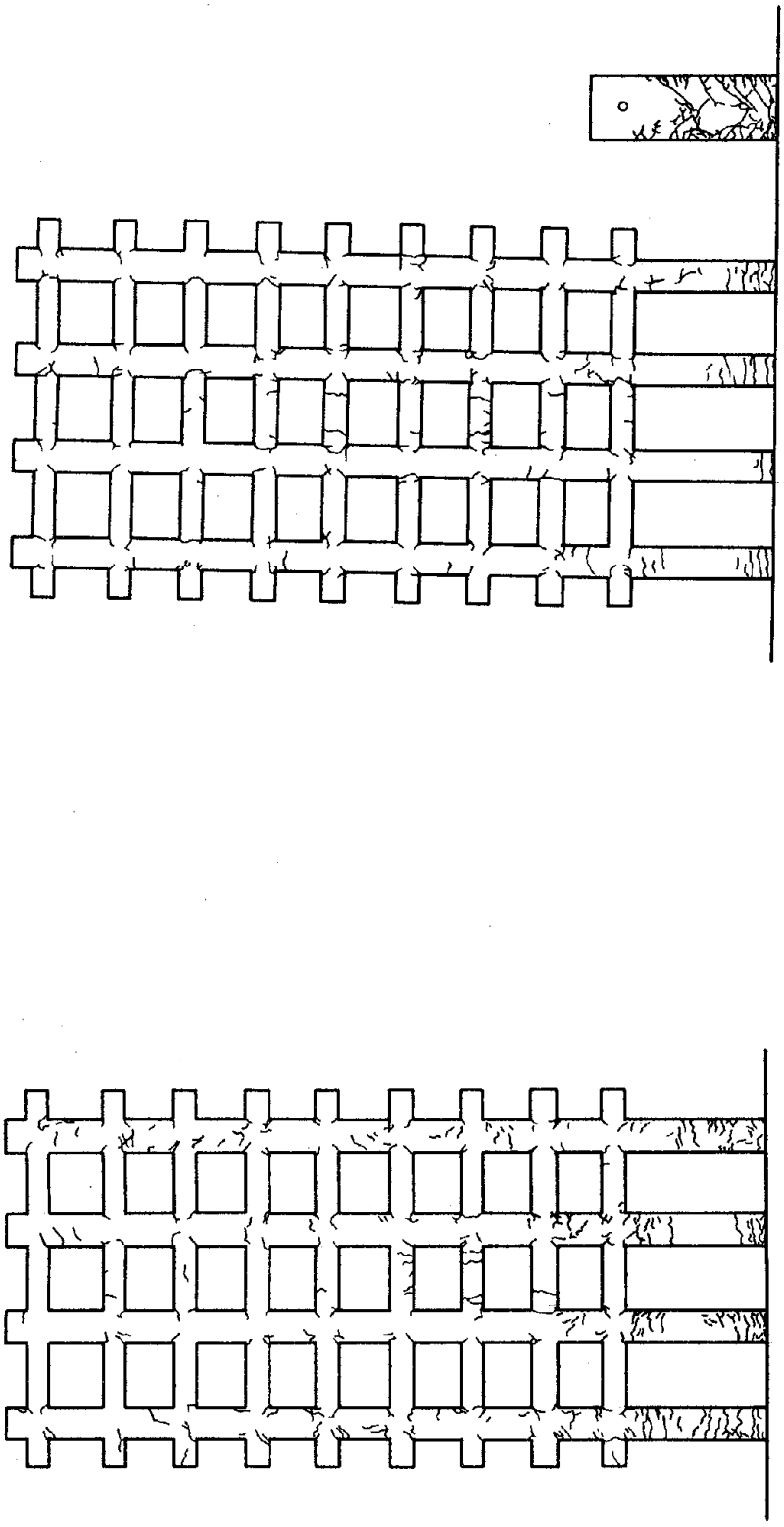

Fig. 4.19 Cracks Observed following Second Simulations

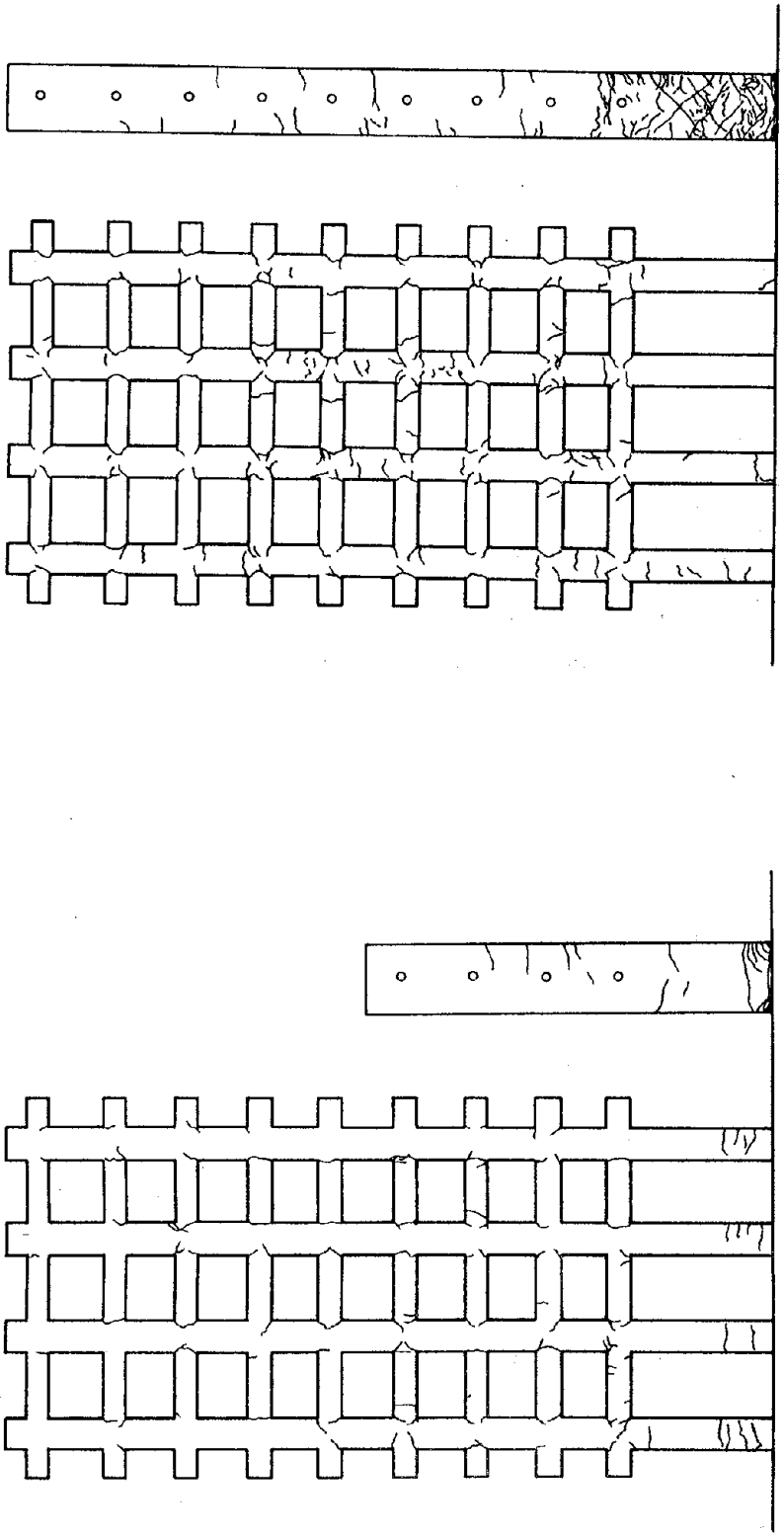

Fig. 4.19 (contd.) Cracks Observed following Second Simulations

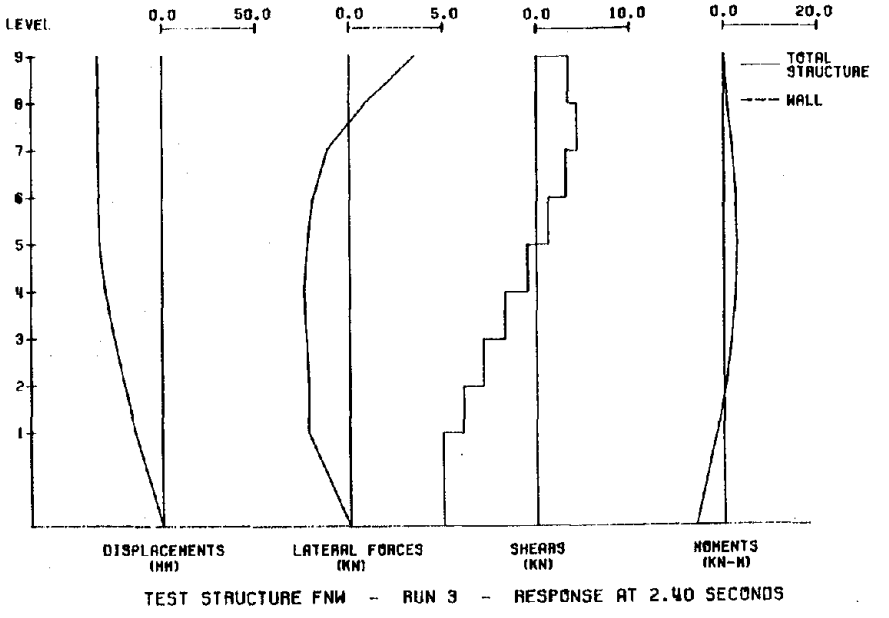


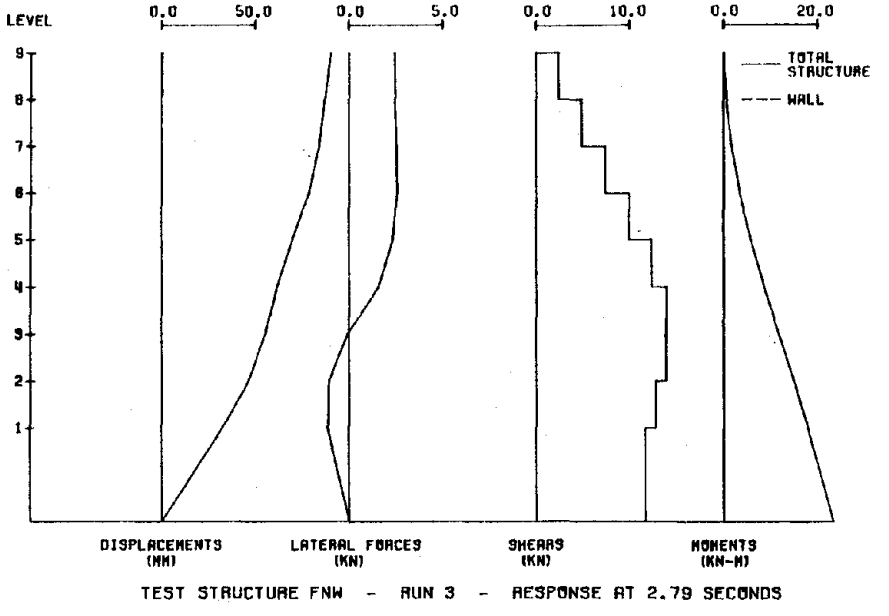


Fig. 4.20 Distributions of Response to Third Simulations

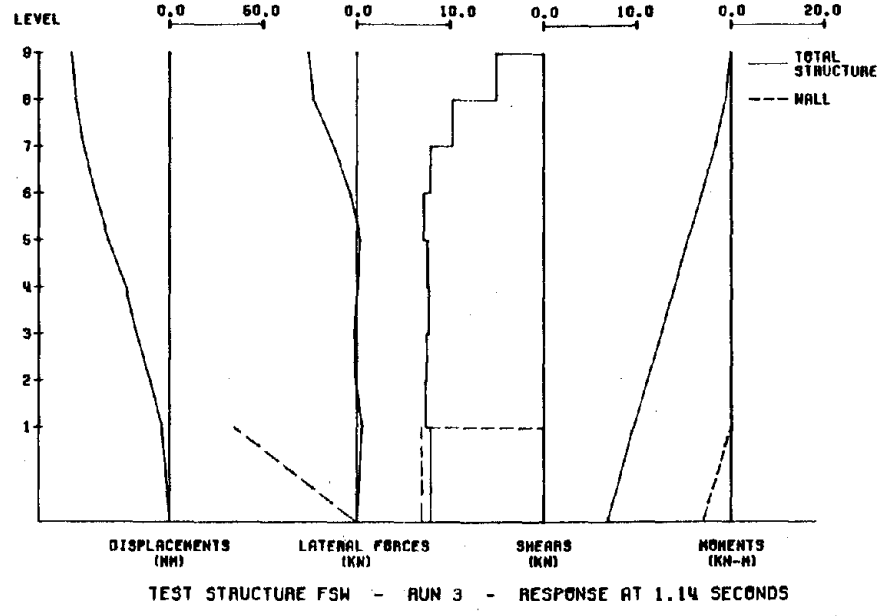


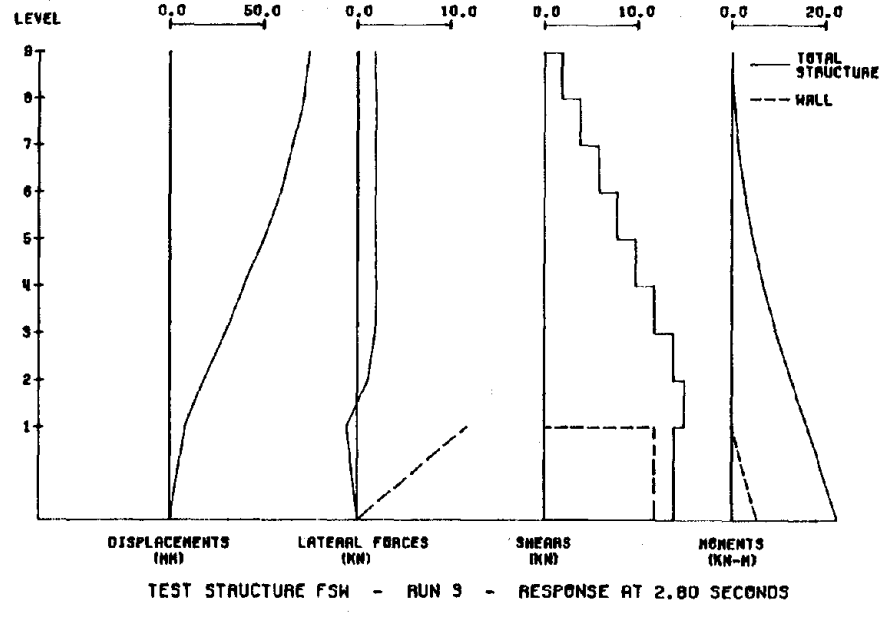


Fig. 4.20 (contd.) Distributions of Response to Third Simulations

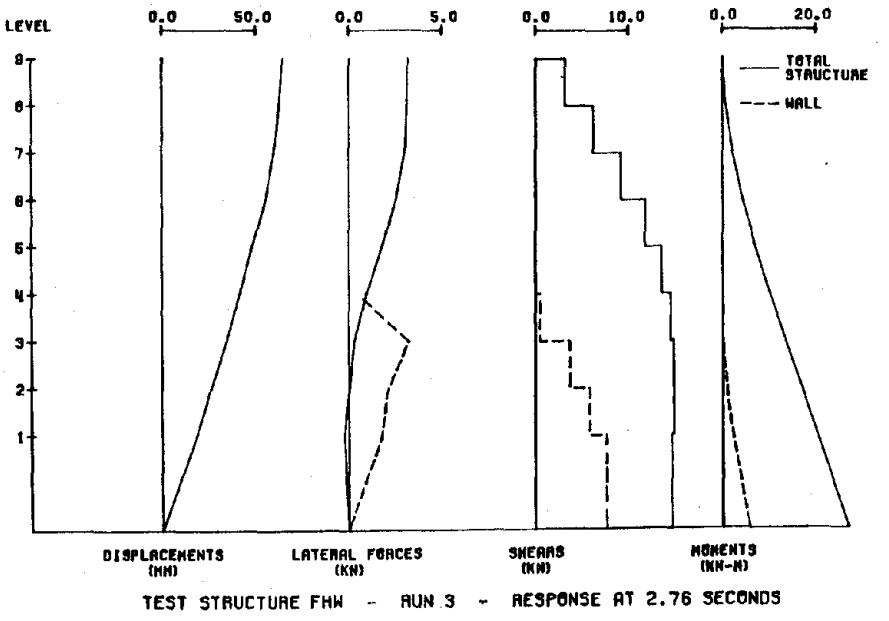


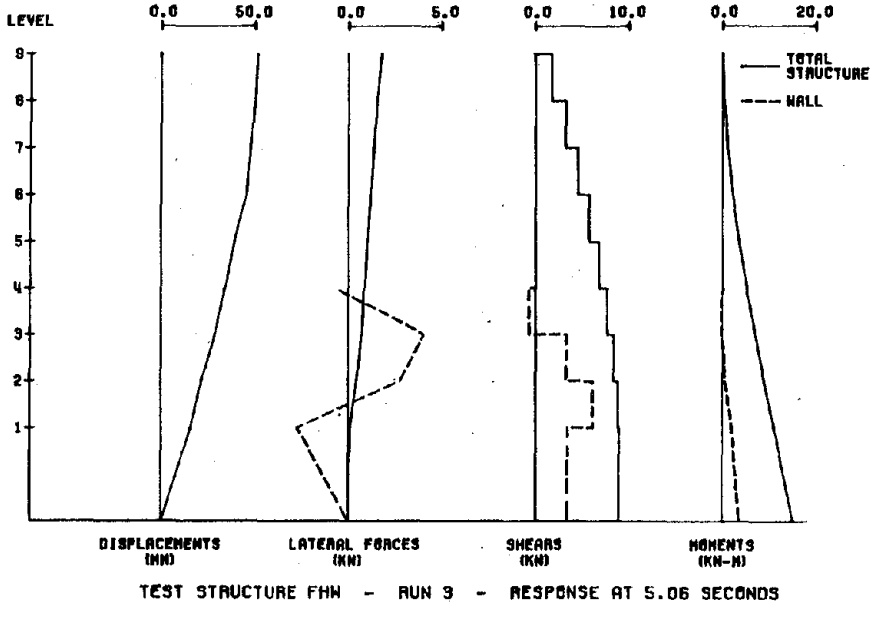


Fig. 4.20 (contd.) Distributions of Response to Third Simulations

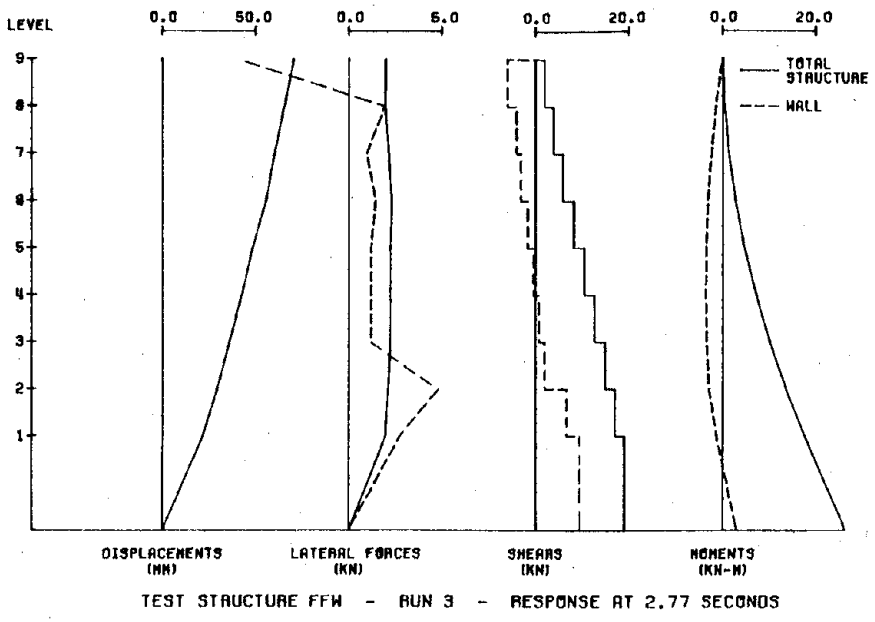


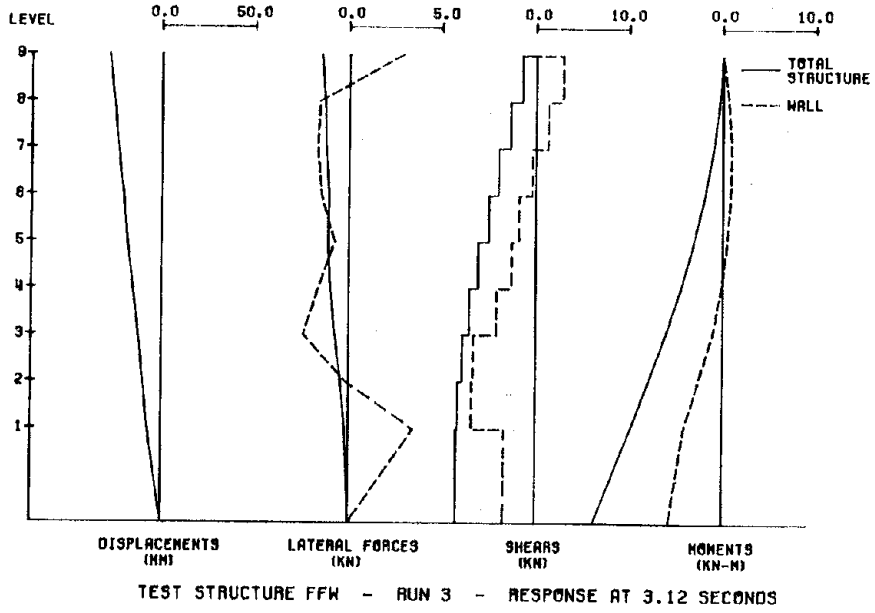


Fig. 4.20 (contd.) Distributions of Response to Third Simulations

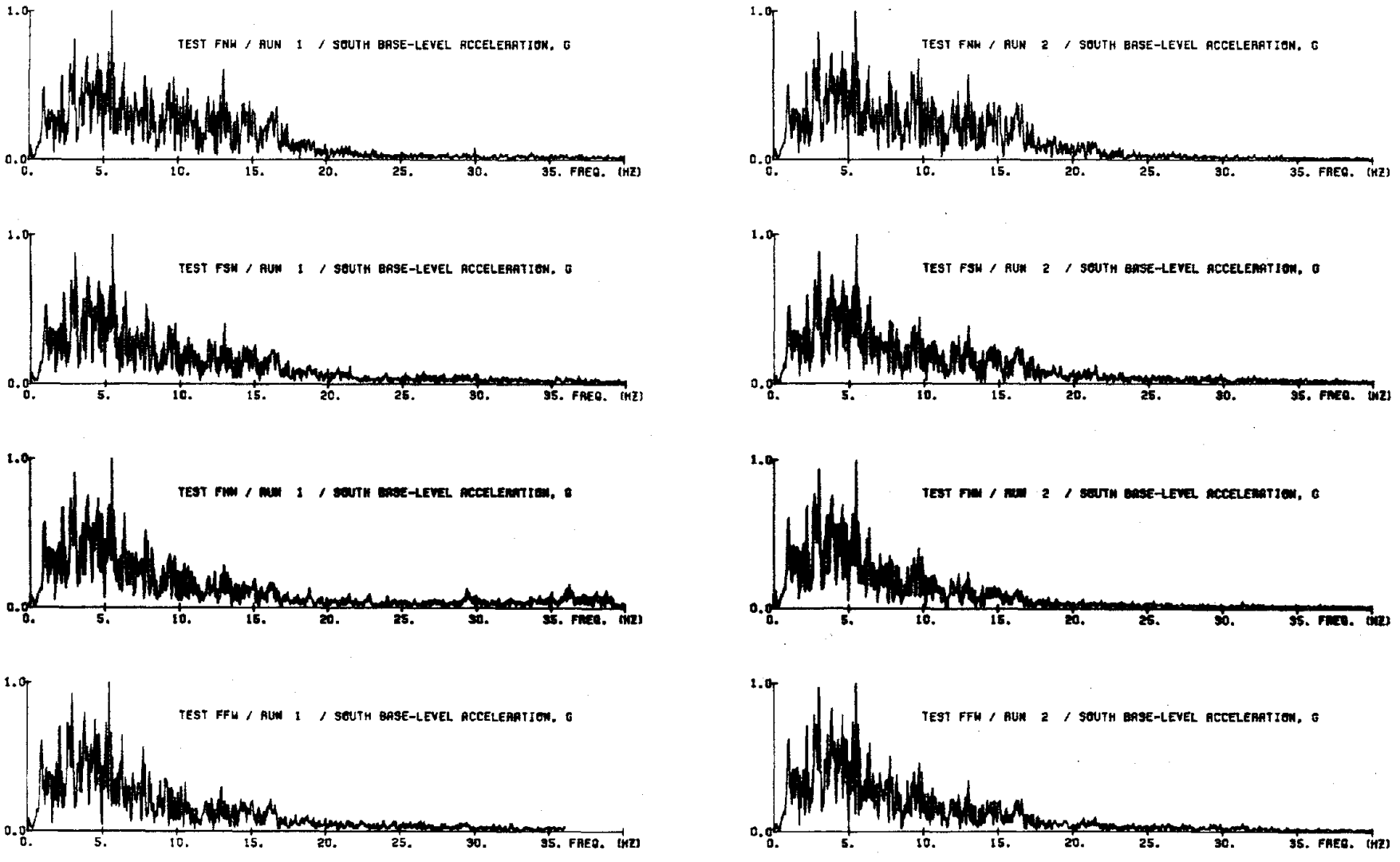


Fig. 5.1 Fourier-Amplitude Spectra of Base Accelerations

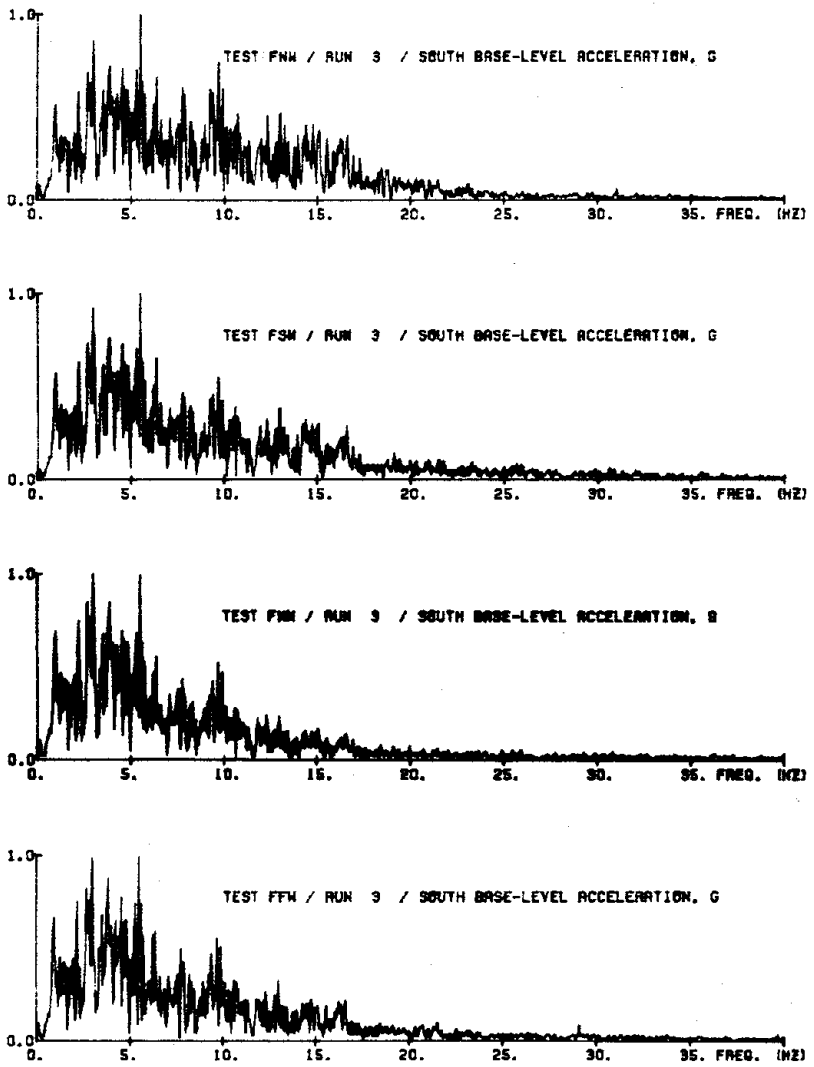


Fig. 5.1 (contd.) Fourier-Amplitude Spectra of Base Accelerations

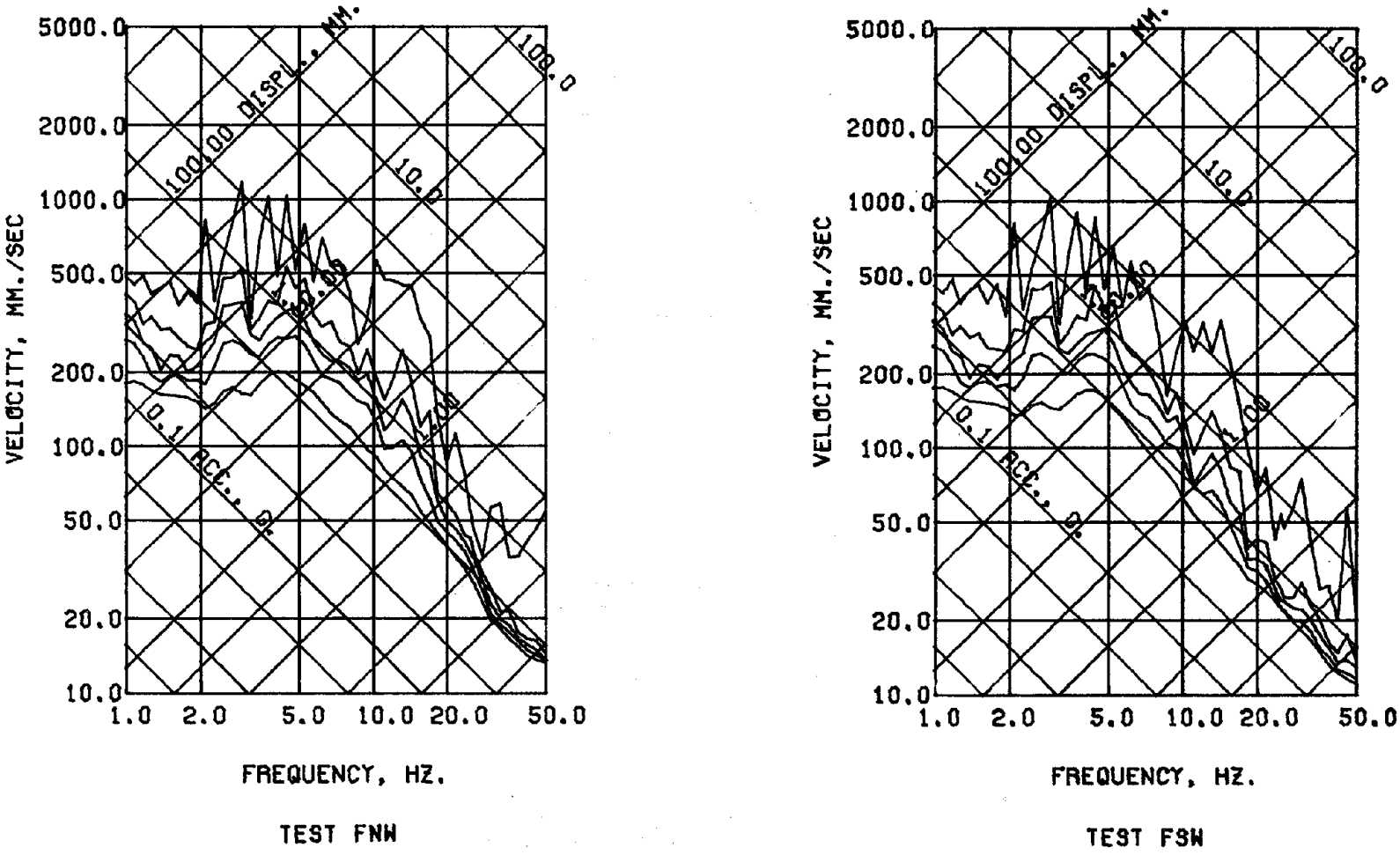


Fig. 5.2 Pseudo Relative Velocity Spectral-Response Curves

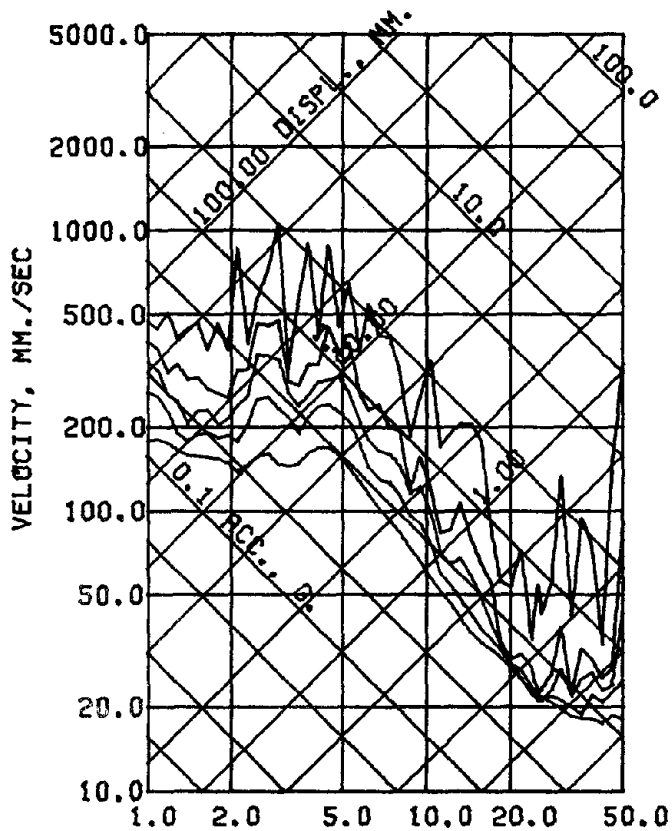


TEST FHW

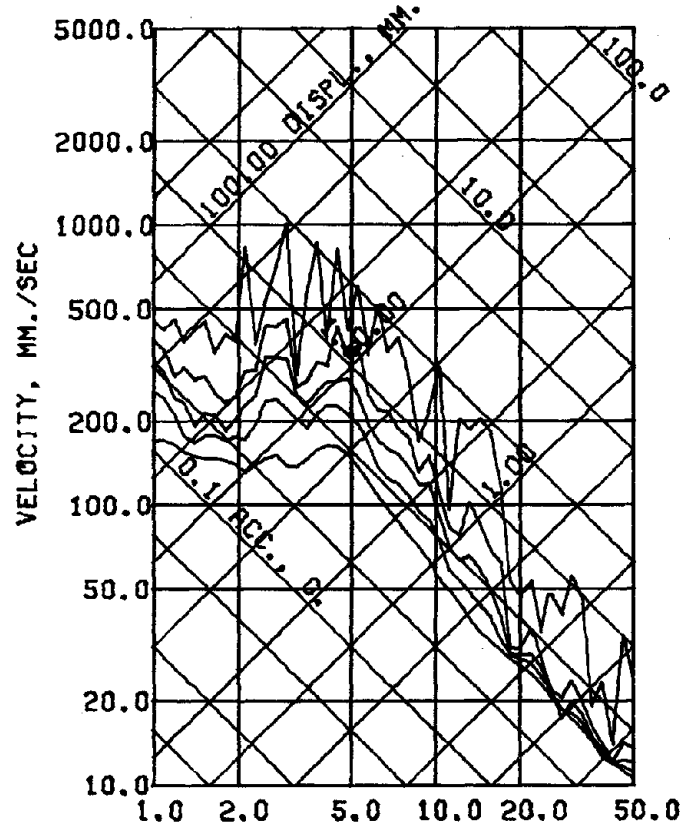


TEST FFW

RUN 1 / SOUTH BASE-LEVEL ACCELERATION, G
DAMPING FACTOR =0.00 0.02 0.05 0.10 0.20

Fig. 5.2 (contd.) Pseudo Relative Velocity Spectral-Response Curves

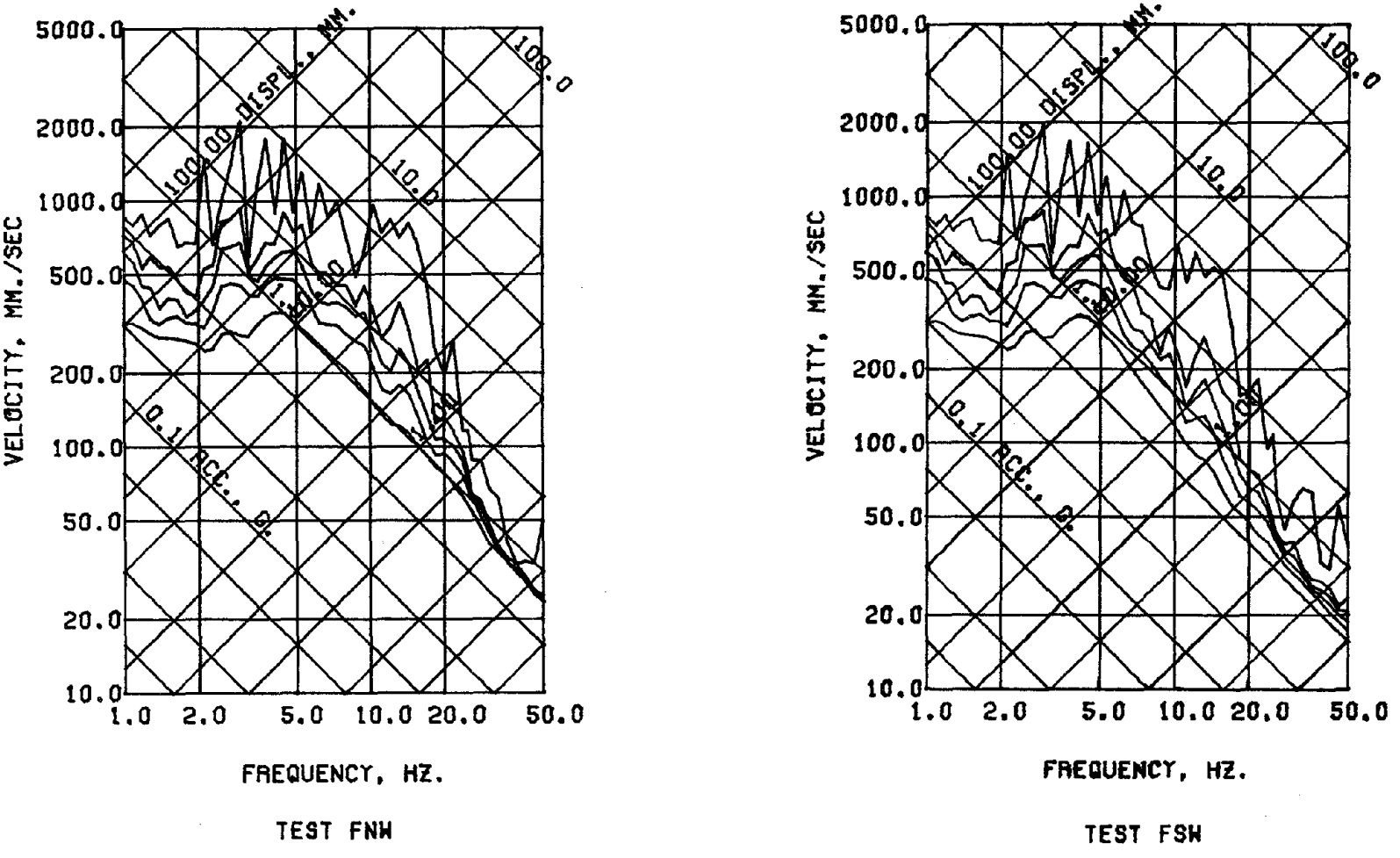


Fig. 5.2 (contd.) Pseudo Relative Velocity Spectral-Response Curves

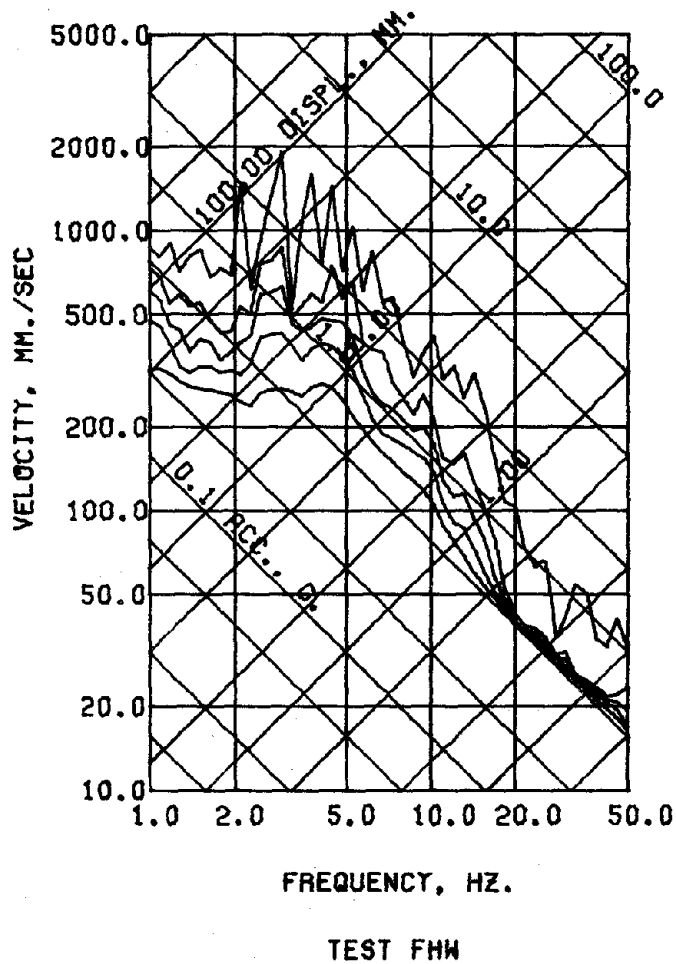


TEST FHW

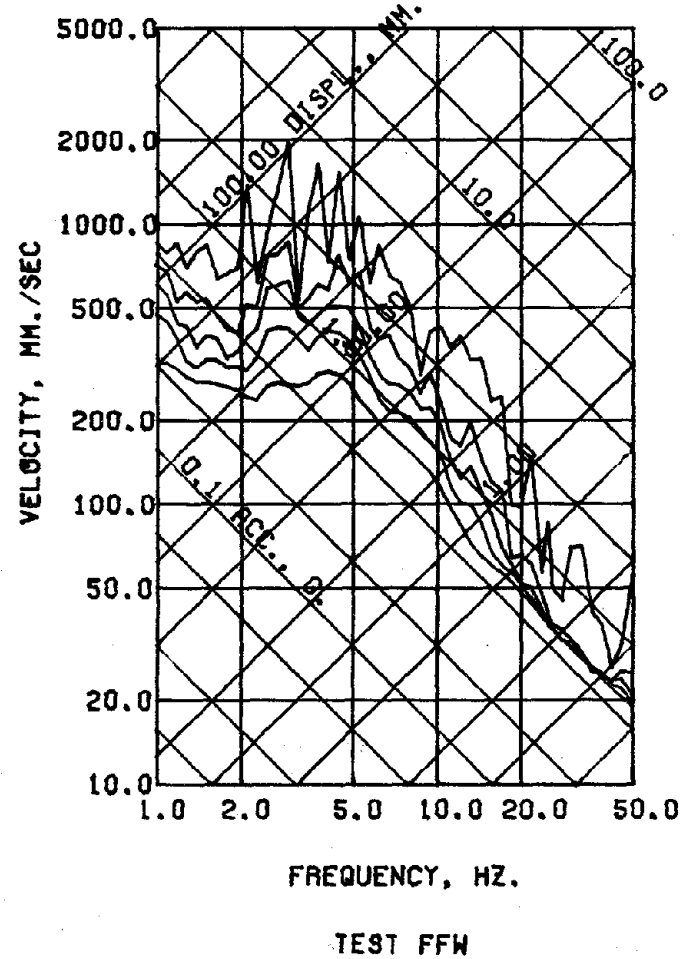


TEST FFW

RUN 2 / SOUTH BASE-LEVEL ACCELERATION, G
DAMPING FACTOR =0.00 0.02 0.05 0.10 0.20

Fig. 5.2 (contd.) Pseudo Relative Velocity Spectral-Response Curves

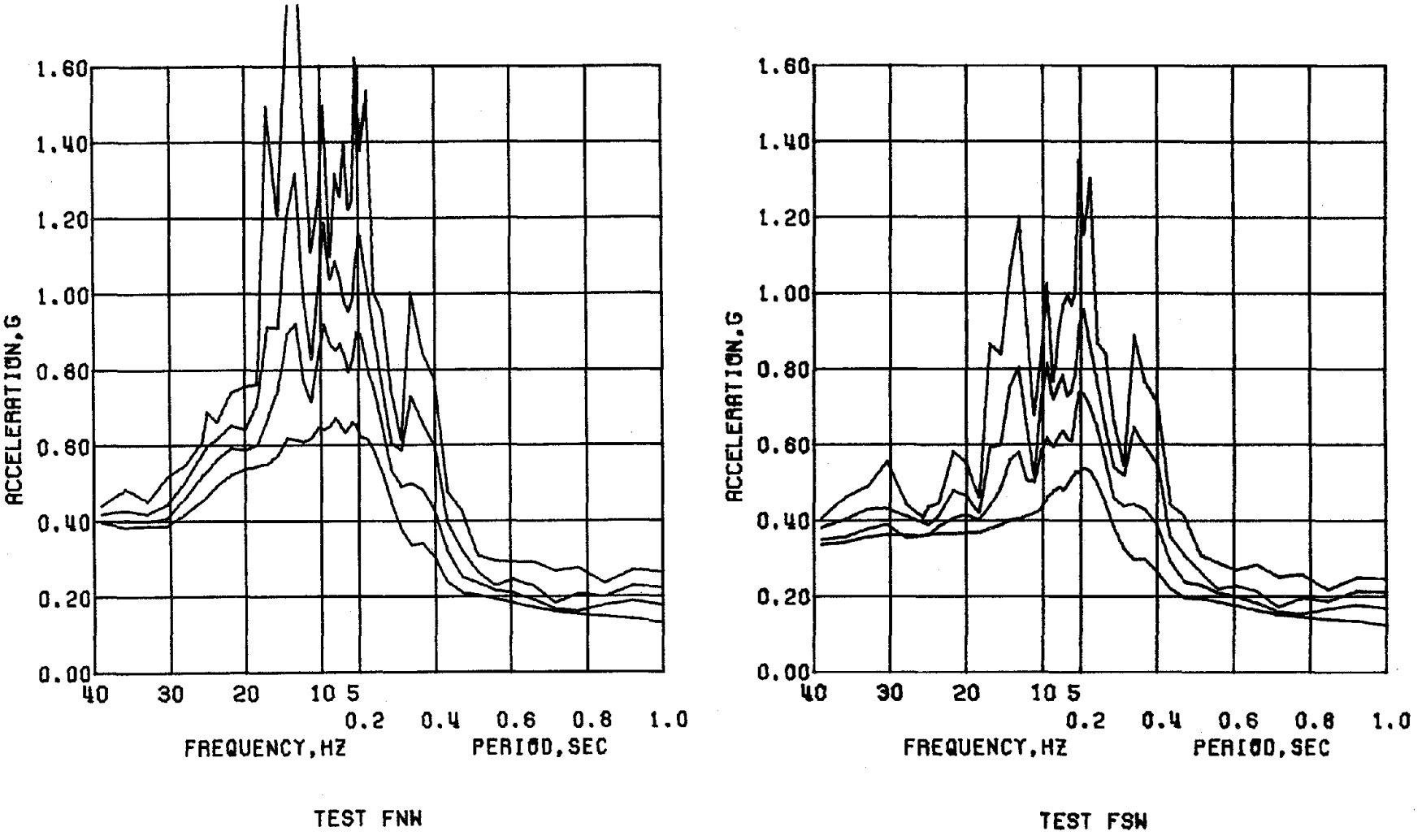


Fig. 5.3 Acceleration and Displacement Spectral-Response Curves

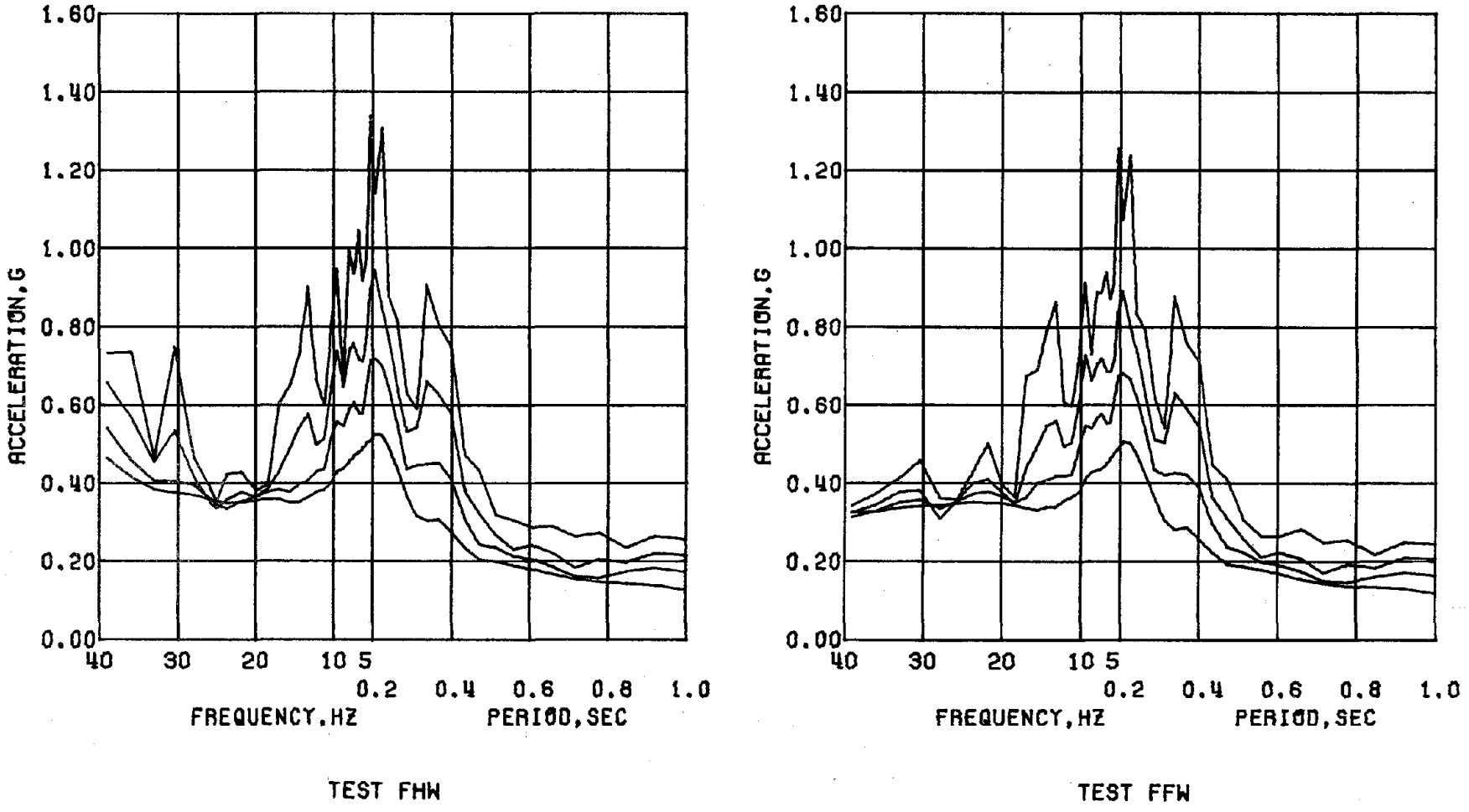


Fig. 5.3 (contd.) Acceleration and Displacement Spectral-Response Curves

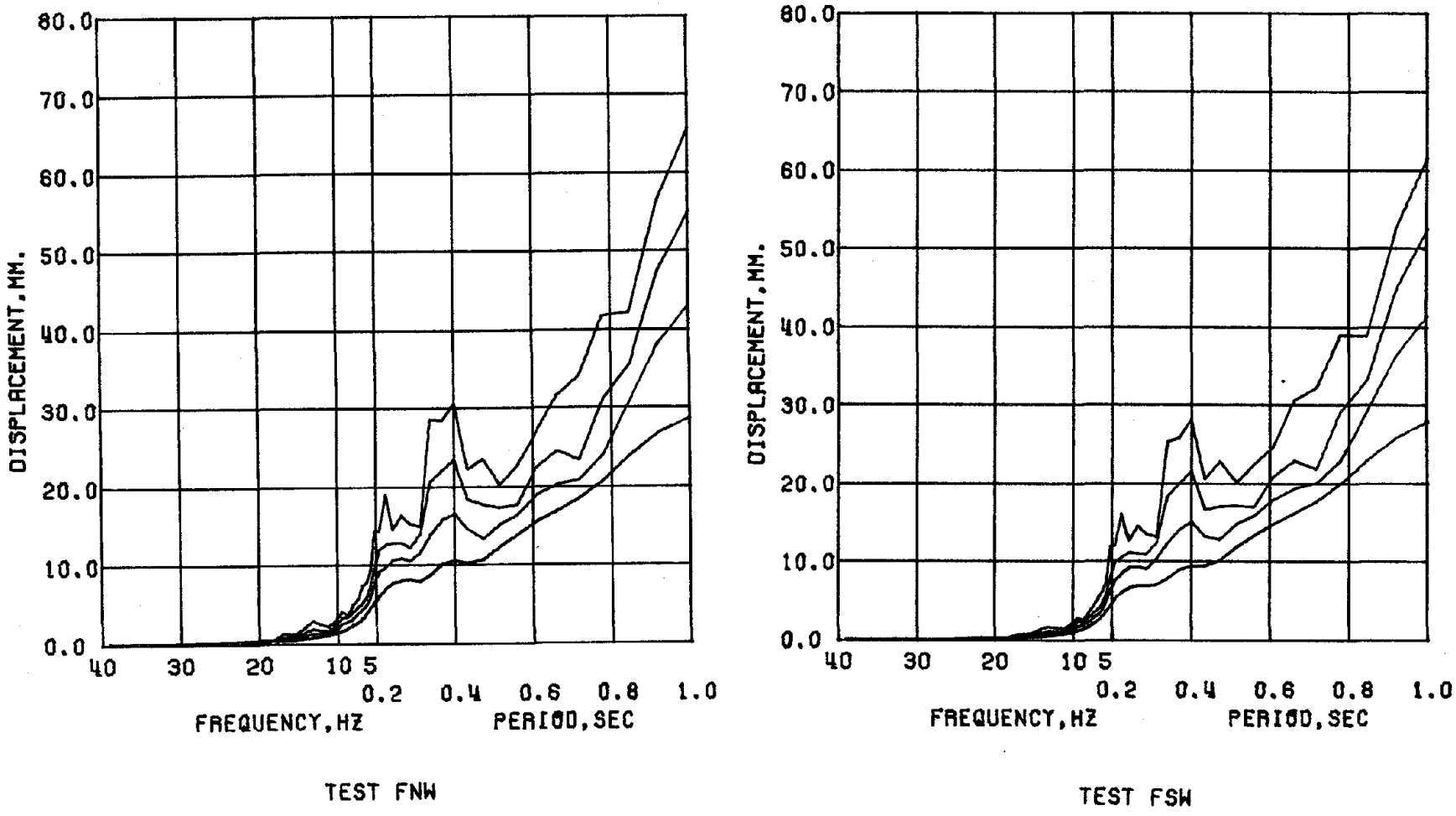


Fig. 5.3 (contd.) Acceleration and Displacement Spectral-Response Curves

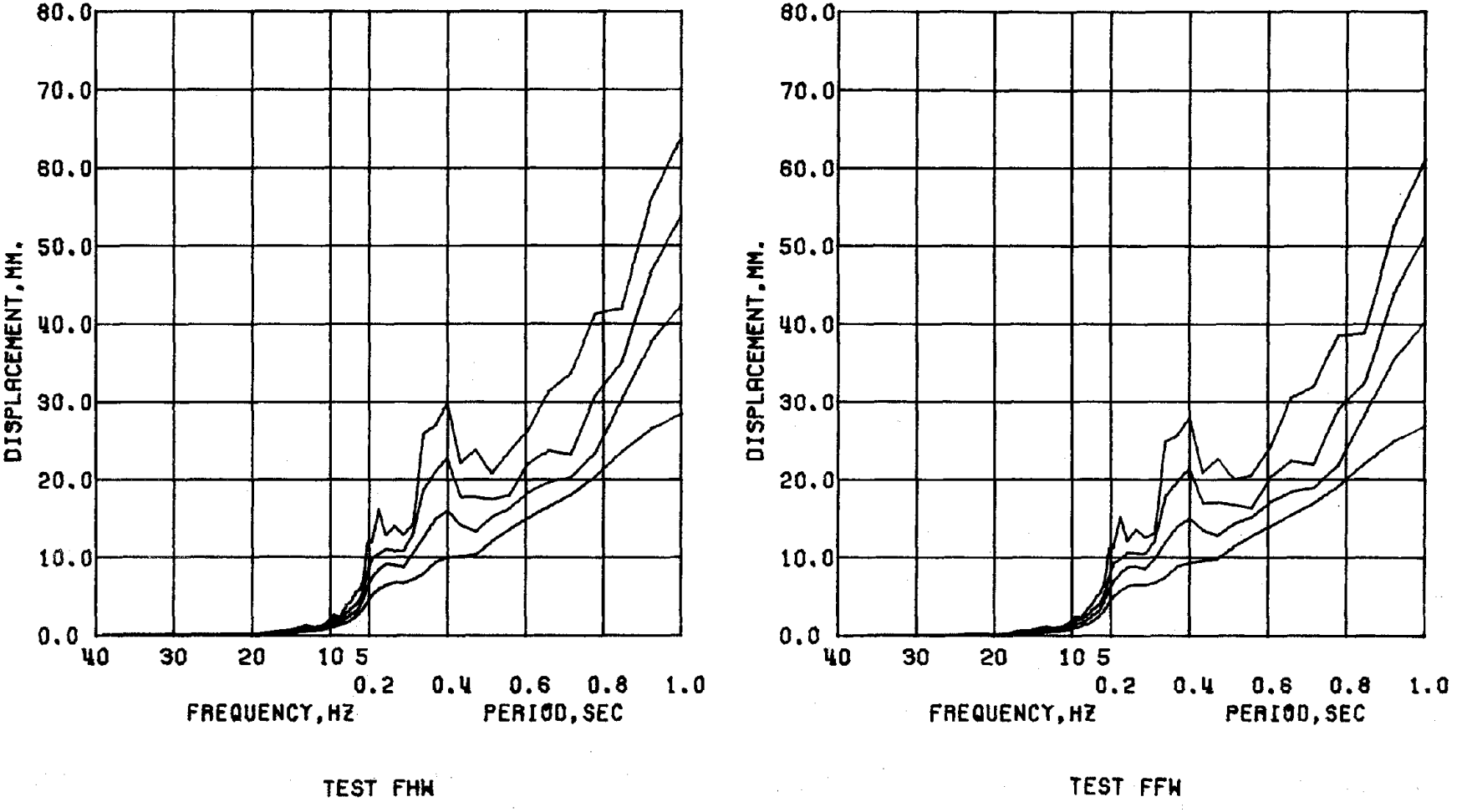


Fig. 5.3 (contd.) Acceleration and Displacement Spectral-Response Curves

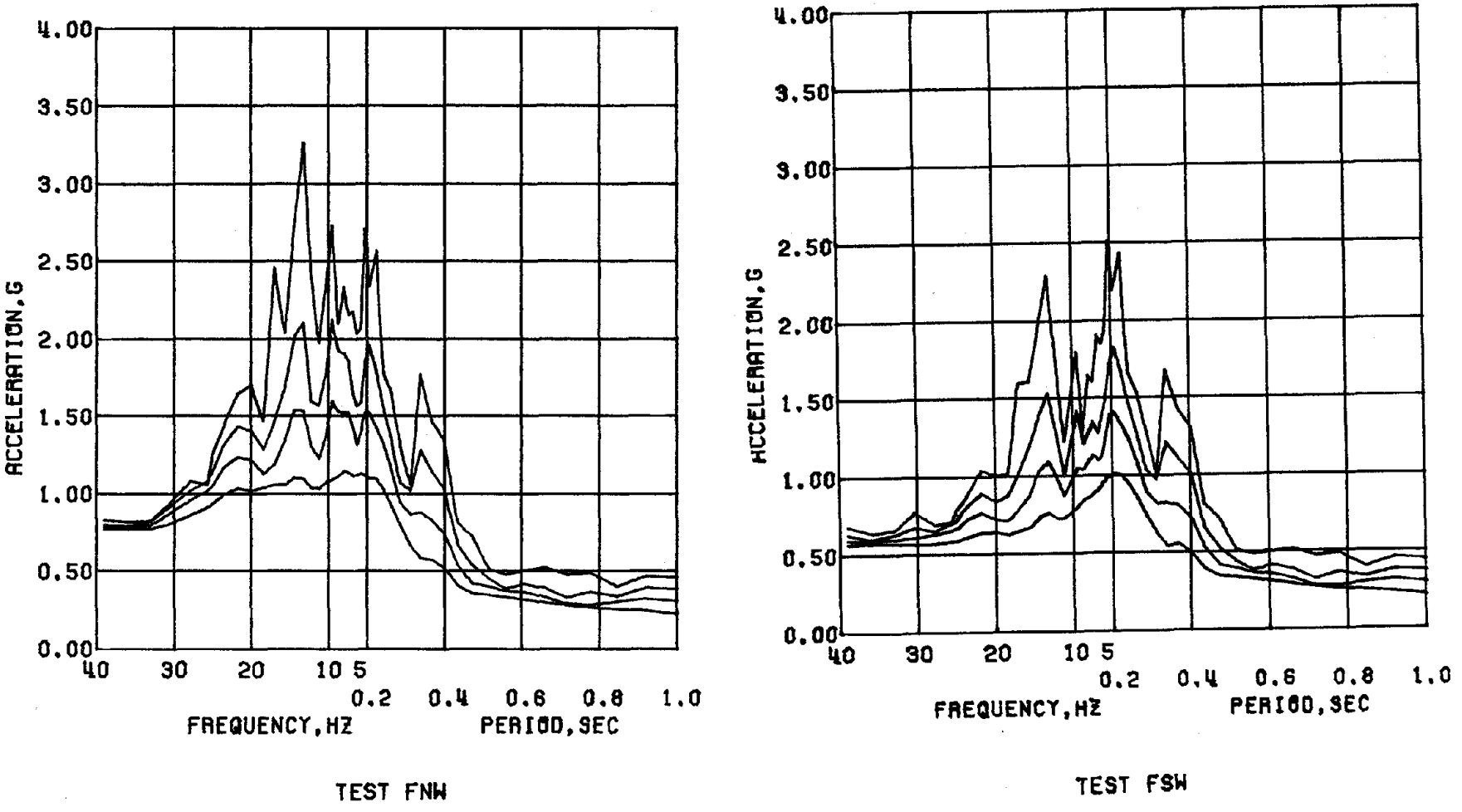


Fig. 5.3 (contd.) Acceleration and Displacement Spectral-Response Curves

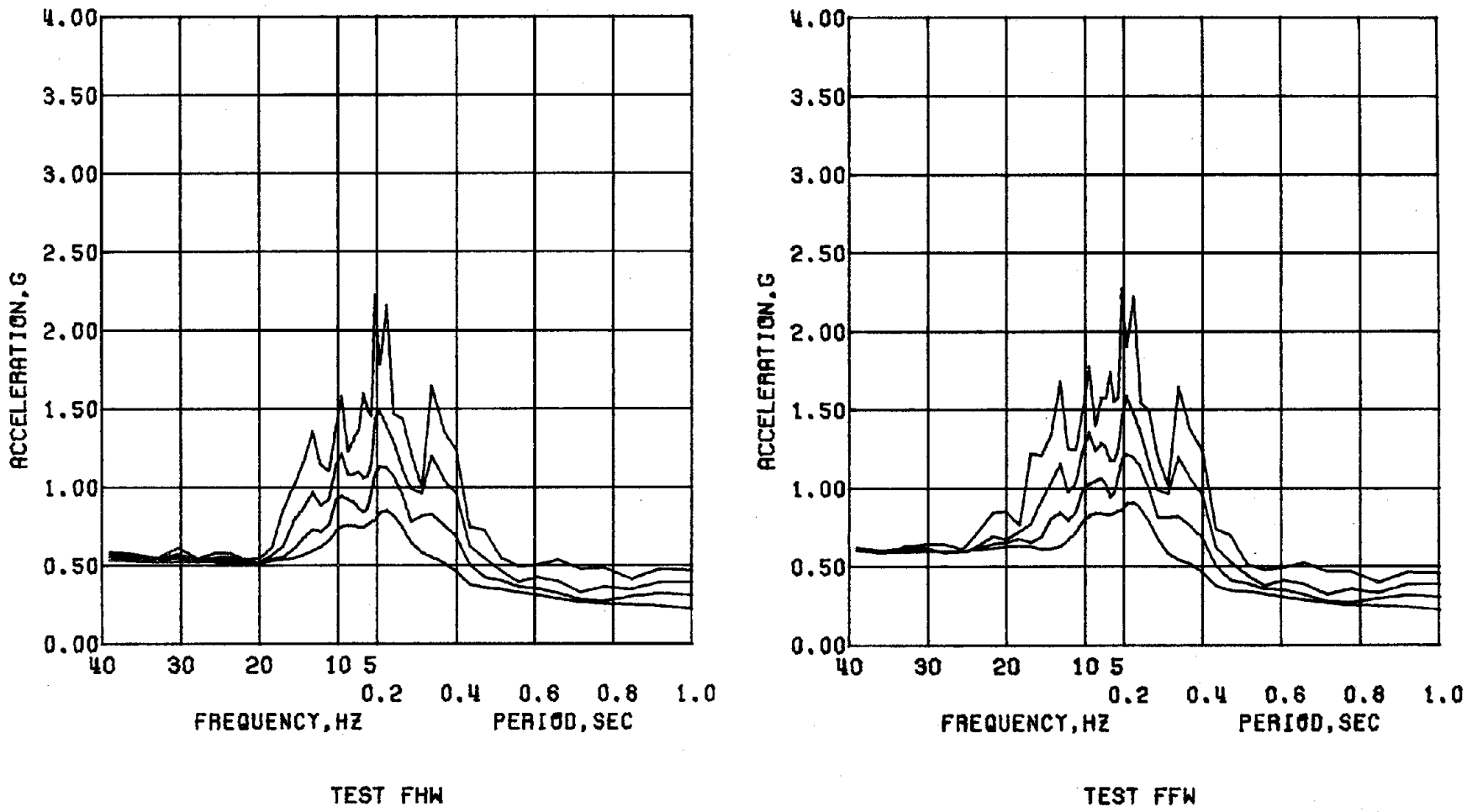


Fig. 5.3 (contd.) Acceleration and Displacement Spectral-Response Curves

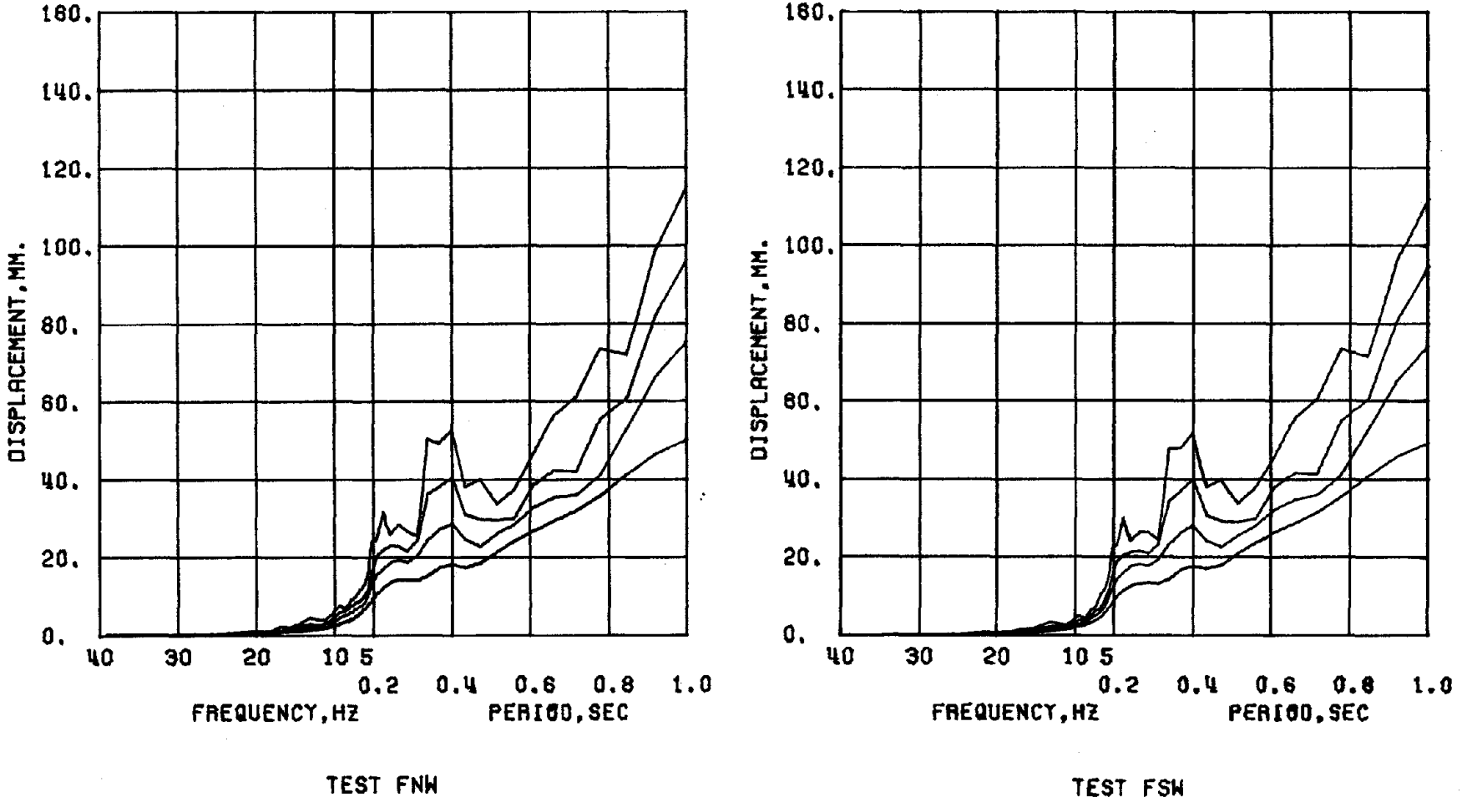


Figure 5.3 (contd.) Acceleration and Displacement Spectral-Response Curves

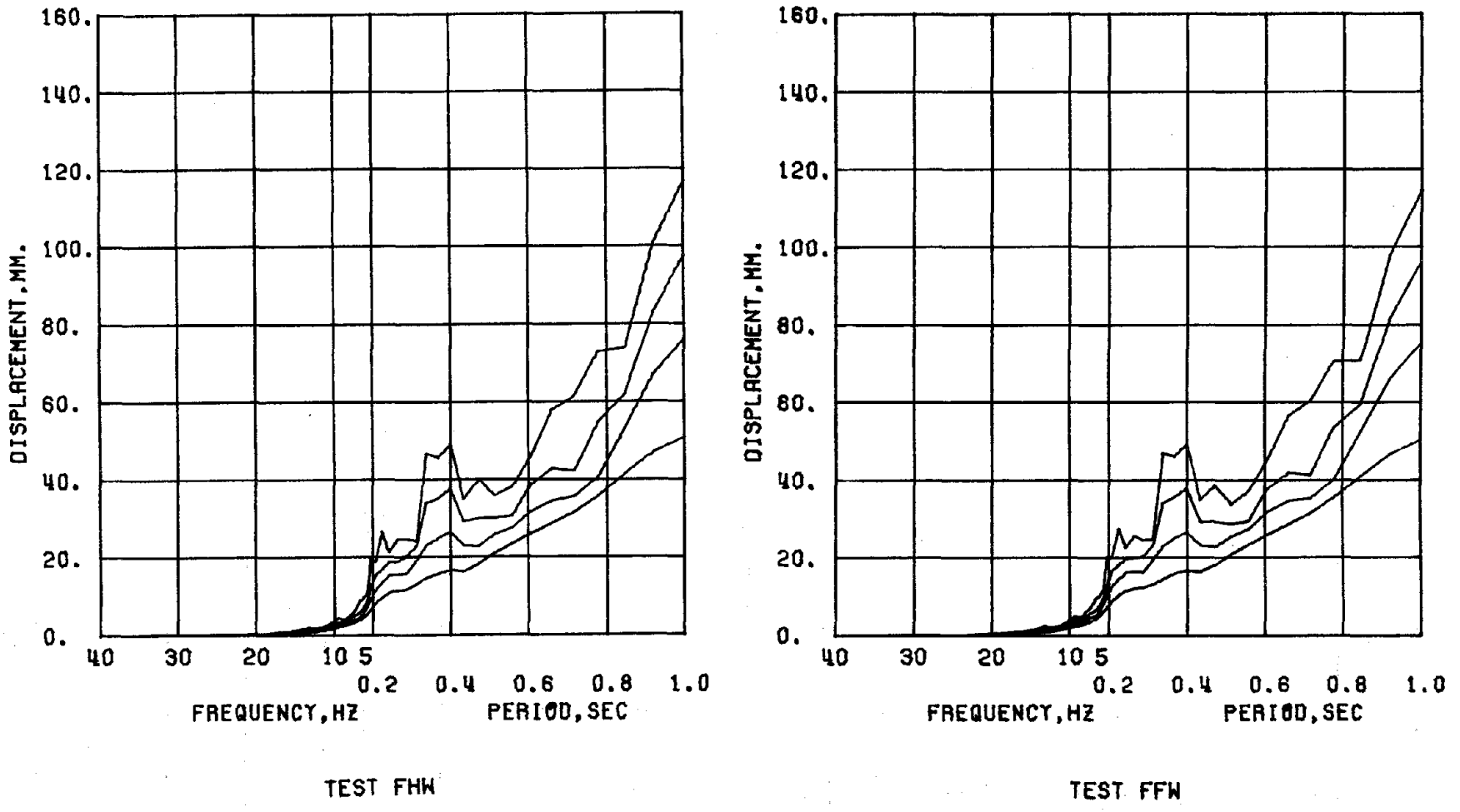


Fig. 5.3 (contd.) Acceleration and Displacement Spectral-Response Curves

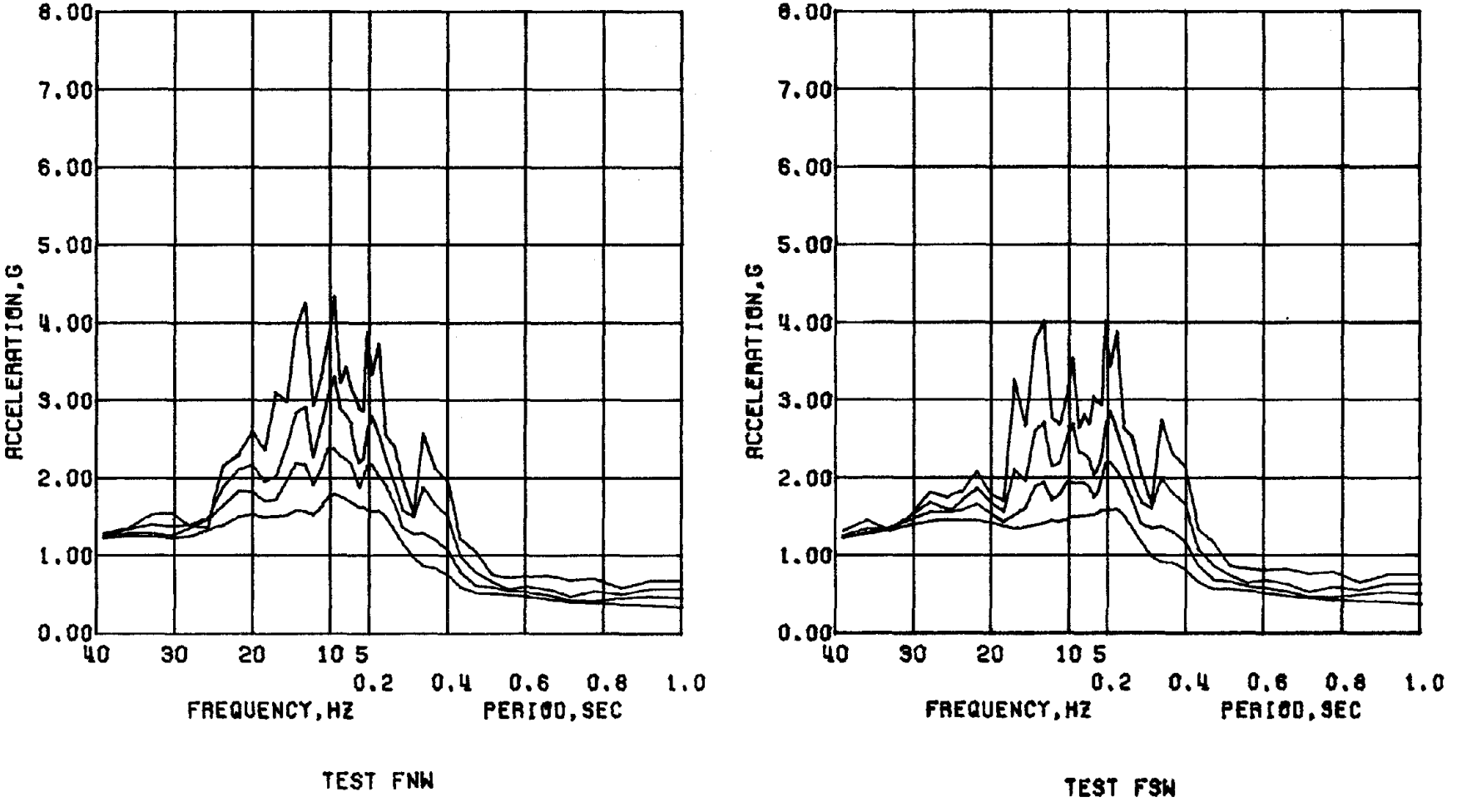


Fig. 5.3 (contd.) Acceleration and Displacement Spectral-Response Curves

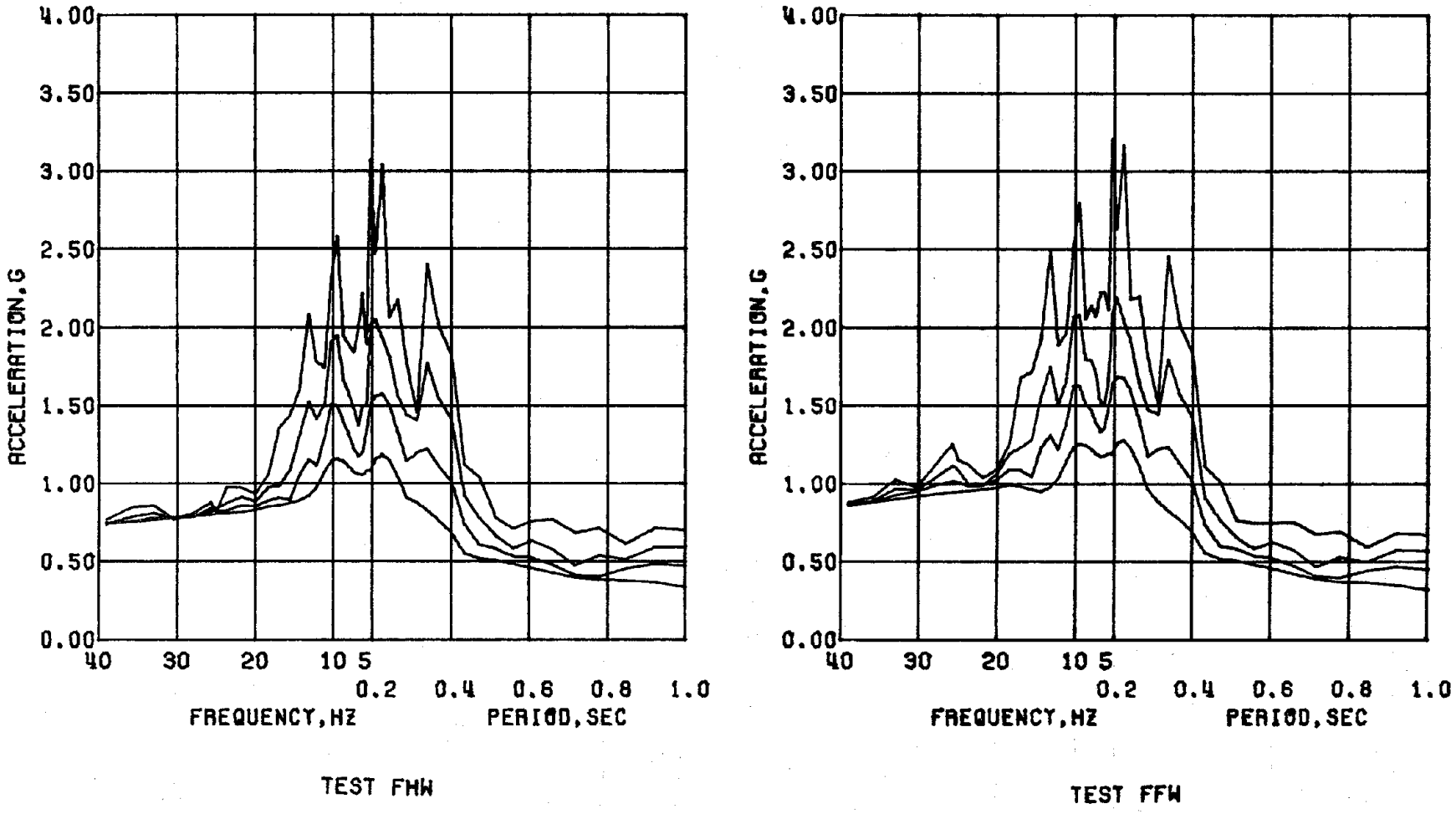


Fig. 5.3 (contd.) Acceleration and Displacement Spectral-Response Curves

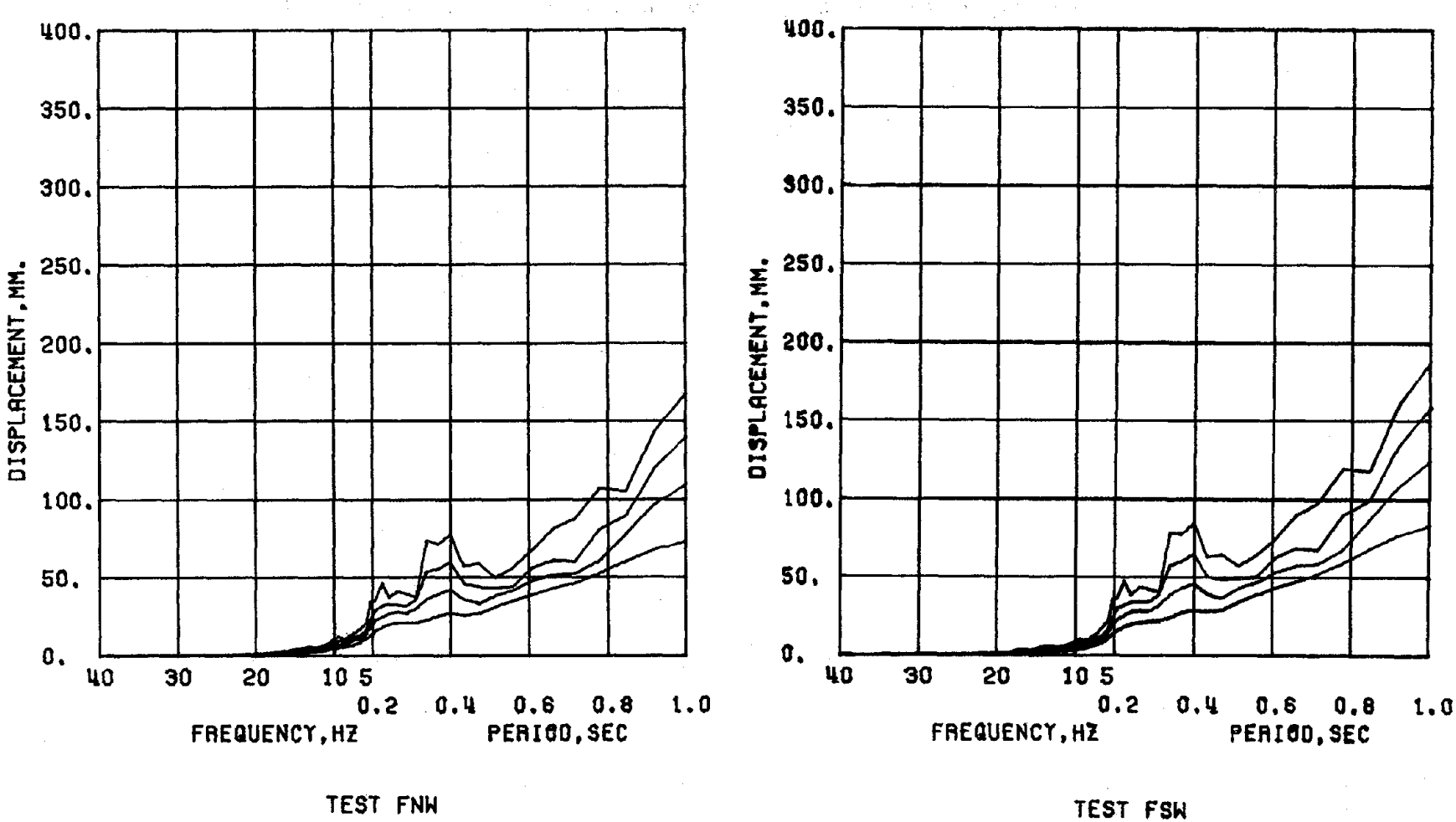


Fig. 5.3 (contd.) Acceleration and Displacement Spectral-Response Curves

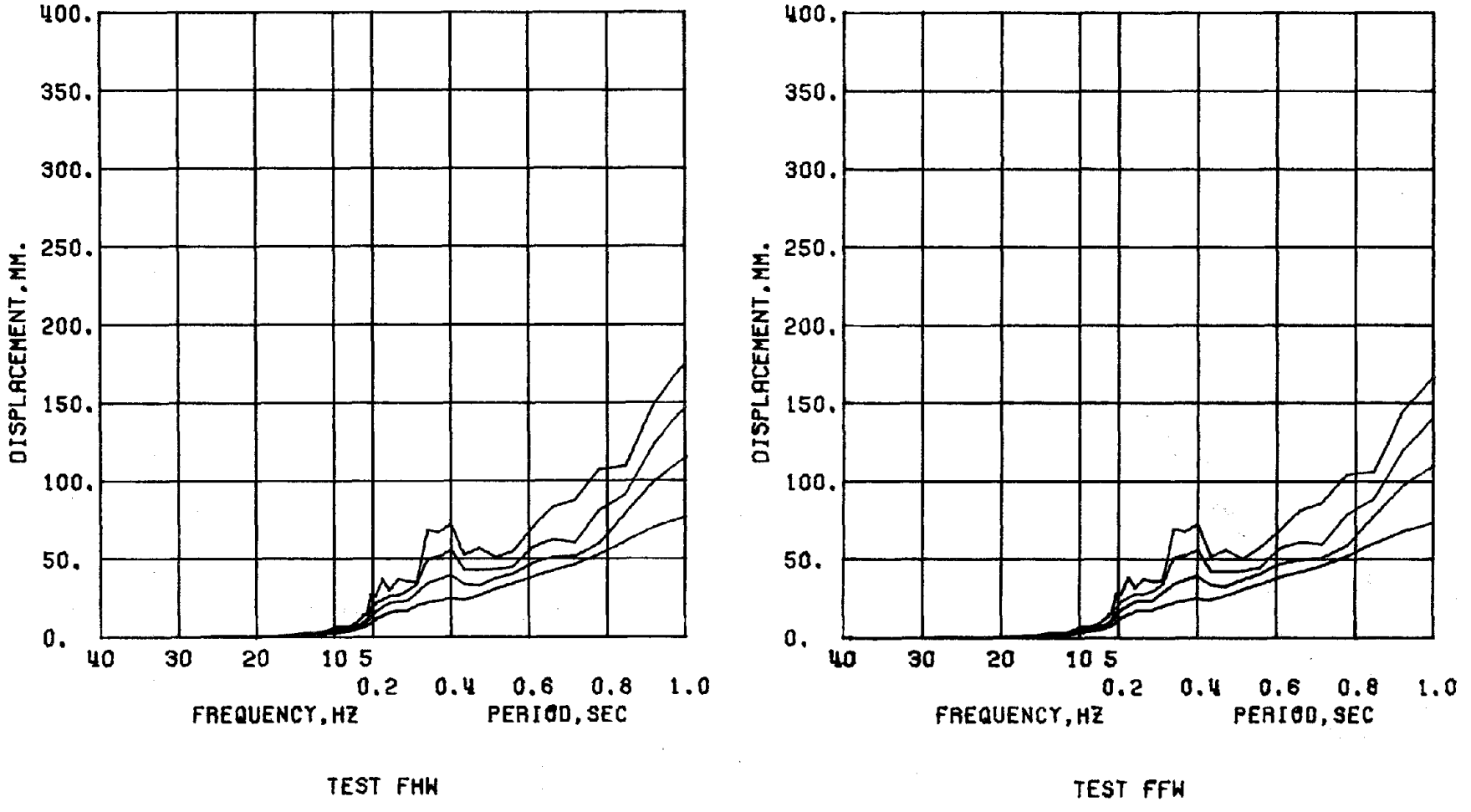


Fig. 5.3 (contd.) Acceleration and Displacement Spectral-Response Curves

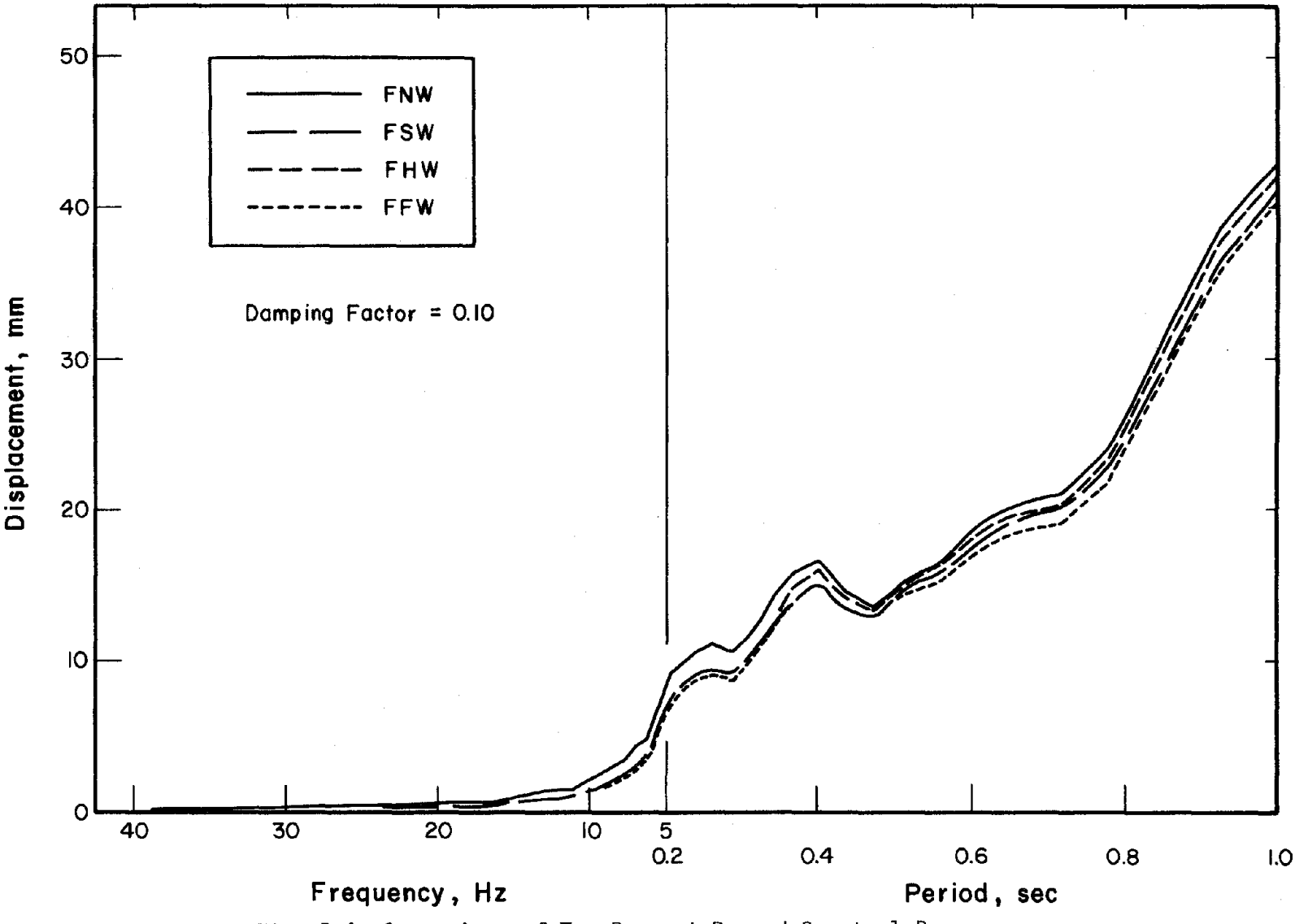


Fig. 5.4 Comparison of Ten-Percent Damped Spectral-Response Curves for Initial Simulations

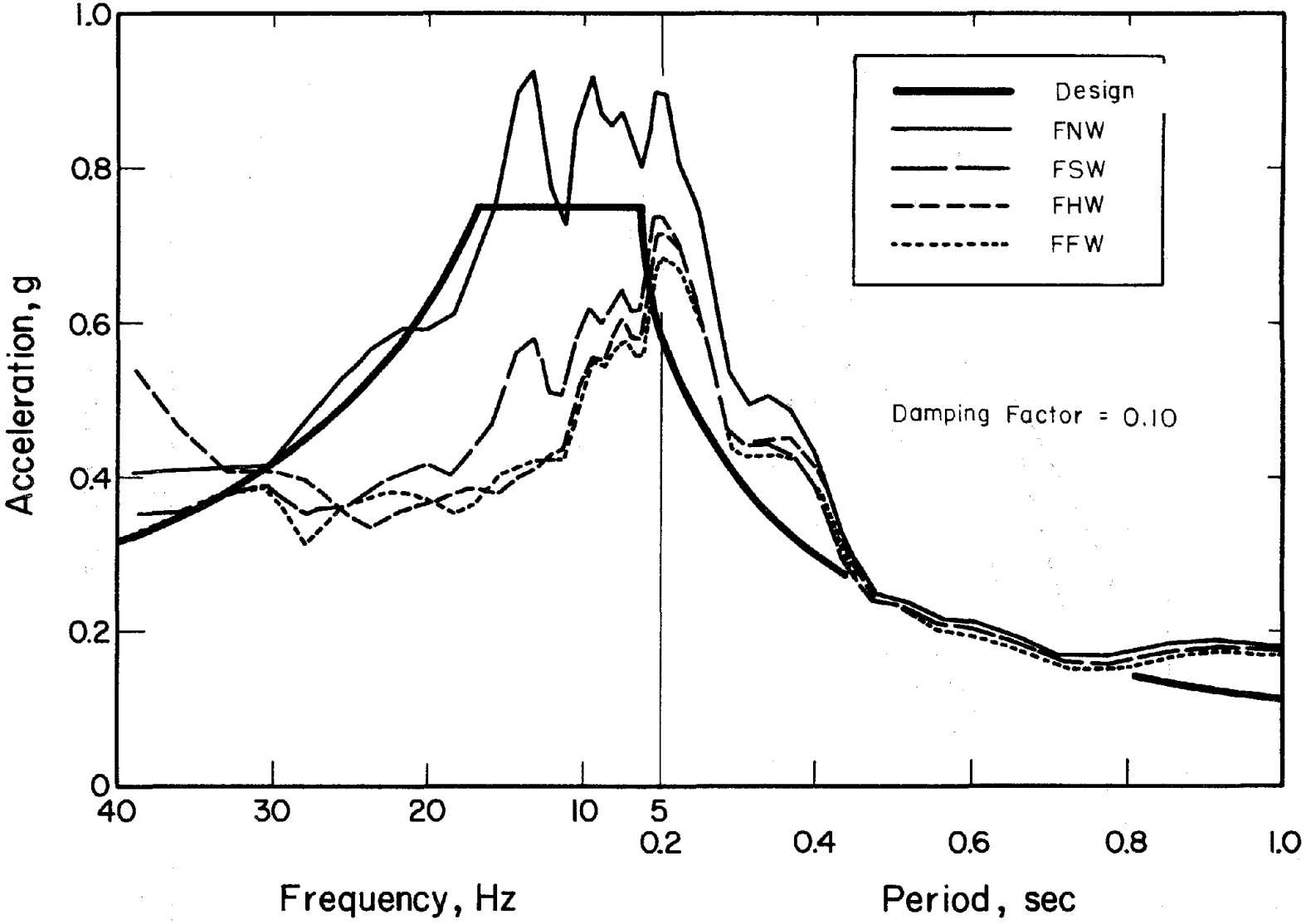


Fig. 5.4 (contd.) Comparison of Ten-Percent Damped Spectral-Response Curves for Initial Simulations

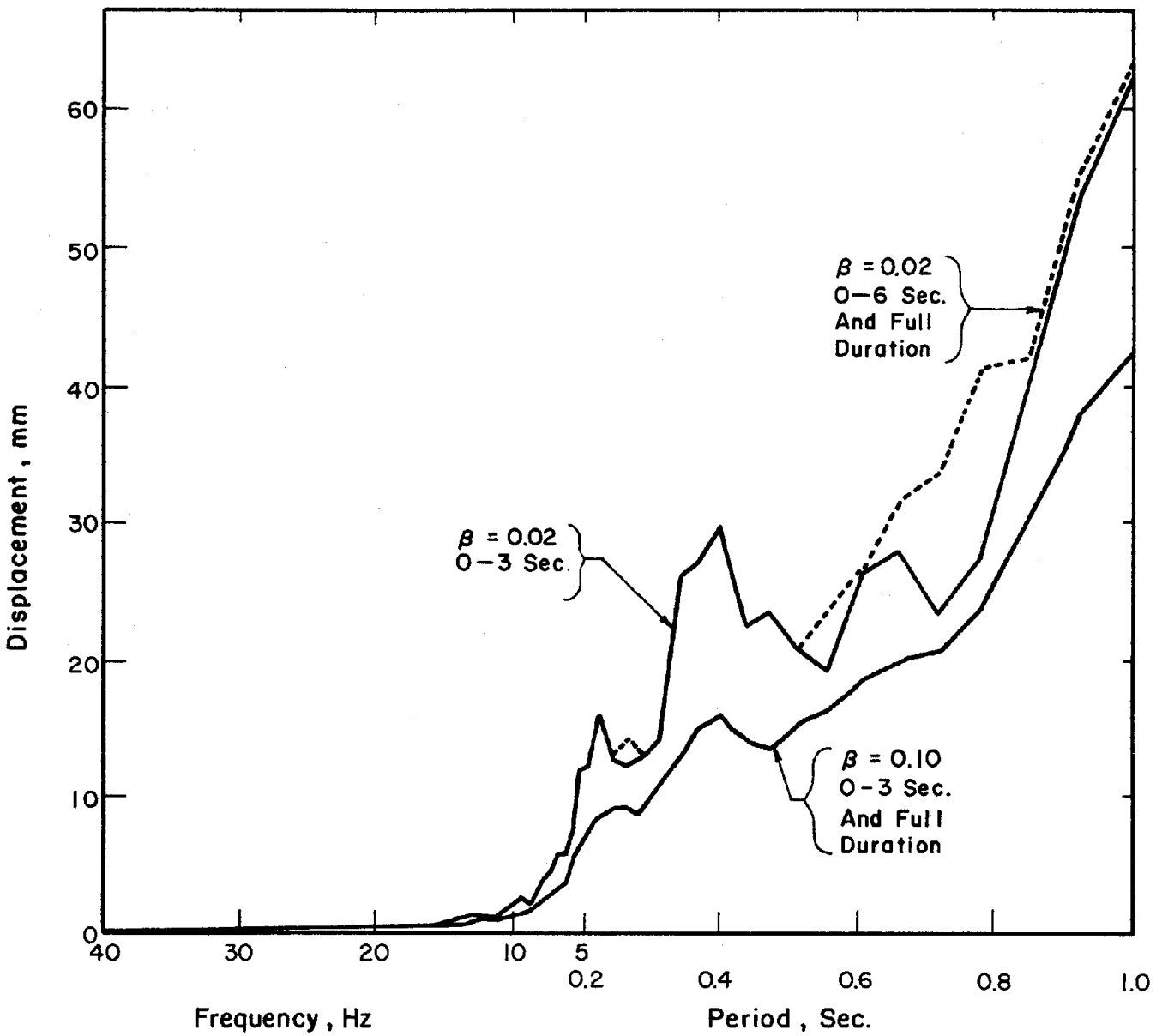


Fig. 5.5 Spectral-Response Curves for Partial Durations

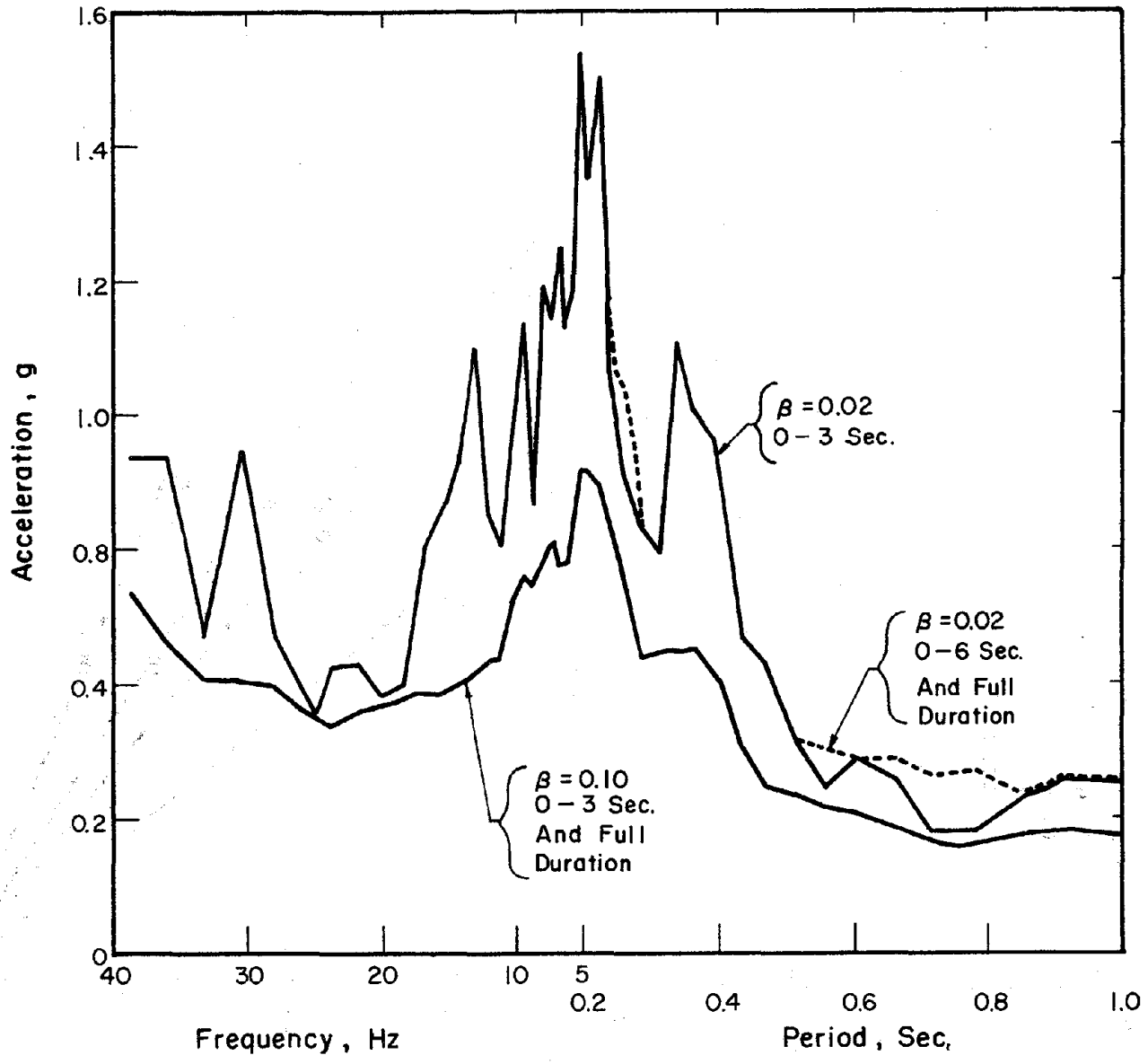


Fig. 5.5 (contd.) Spectral-Response Curves for Partial Durations

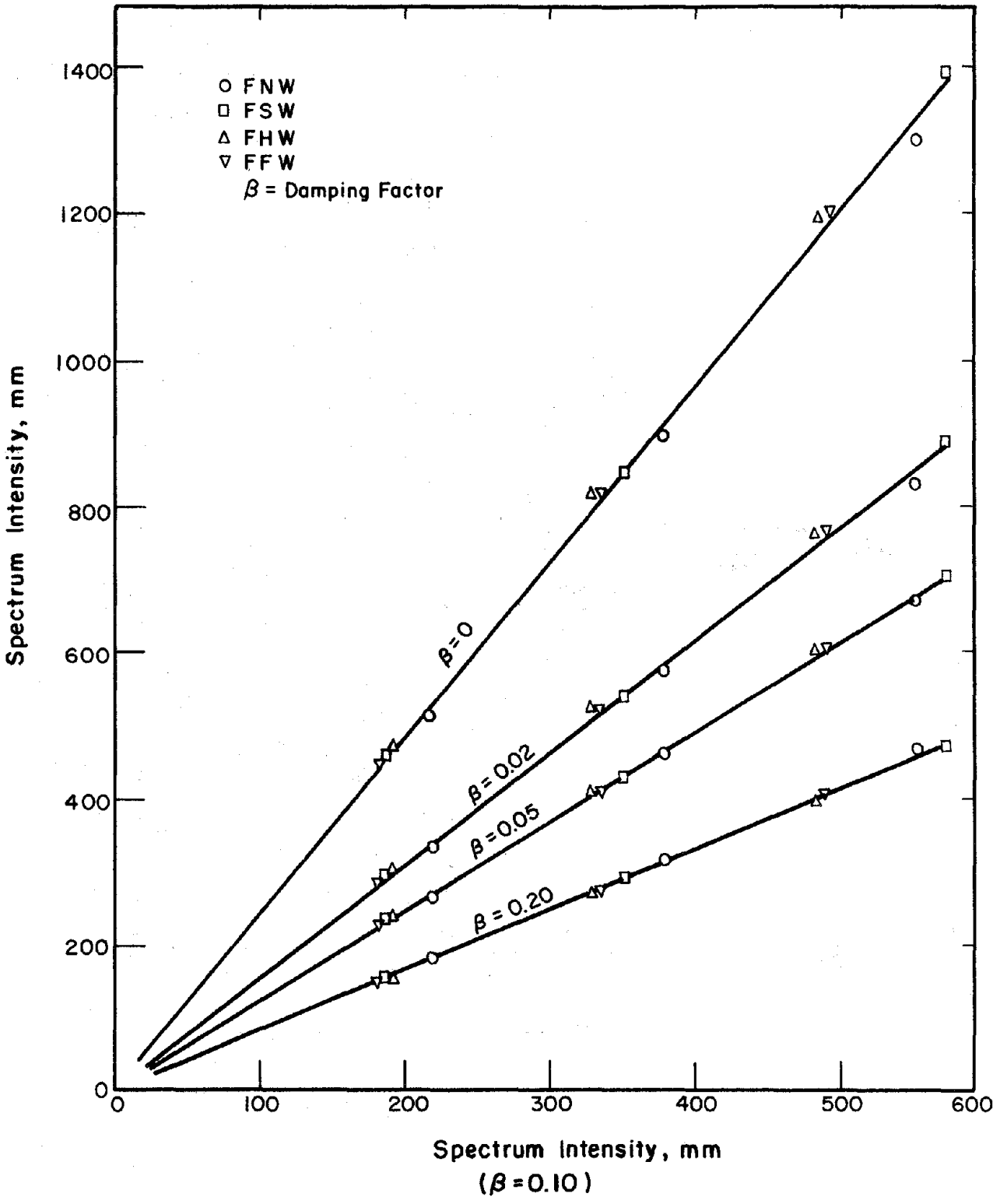


Fig. 5.6 Comparison of Spectrum Intensities for Different Damping Factors

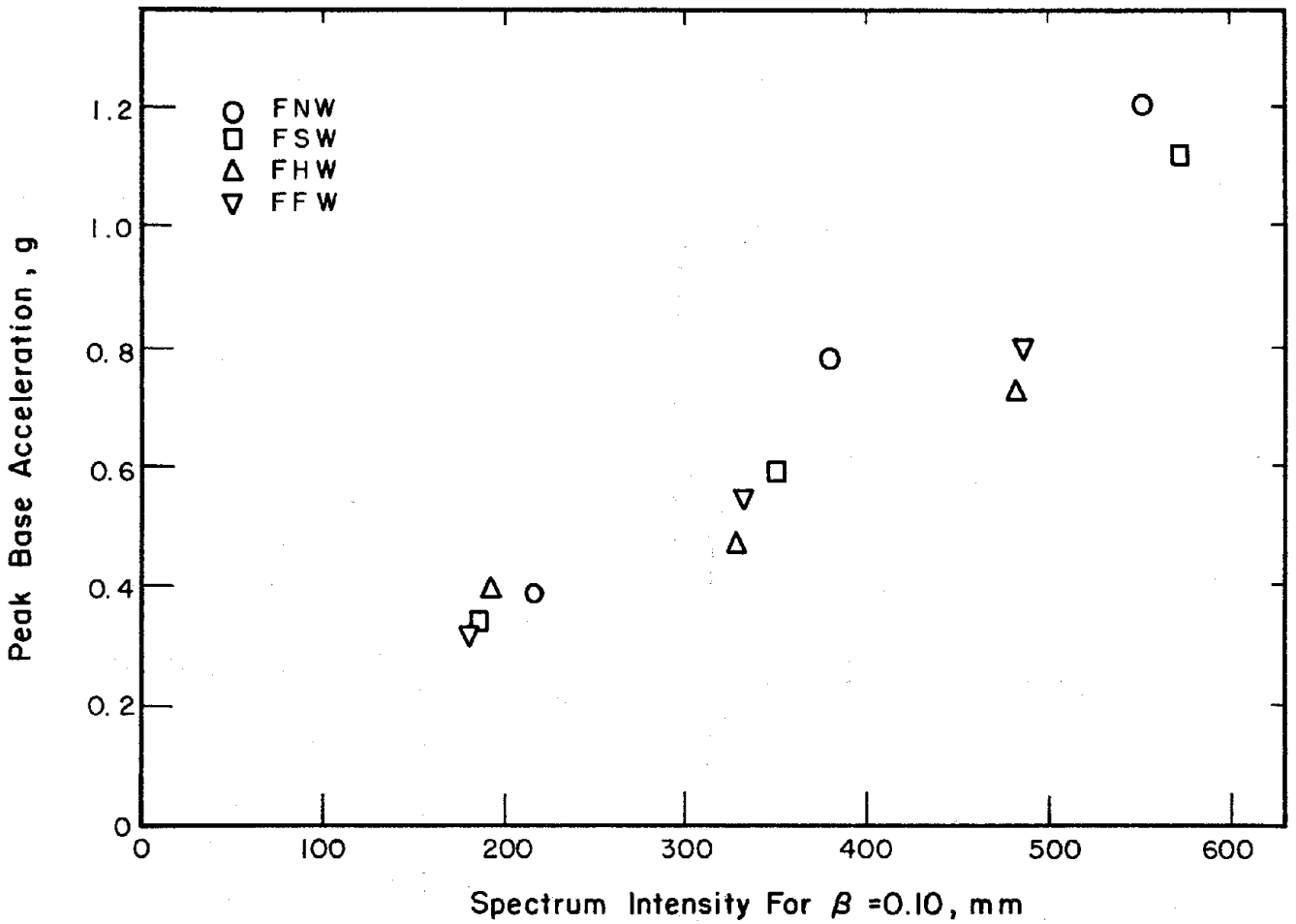


Fig. 5.7 Comparison of Spectrum Intensities and Peak Base Accelerations

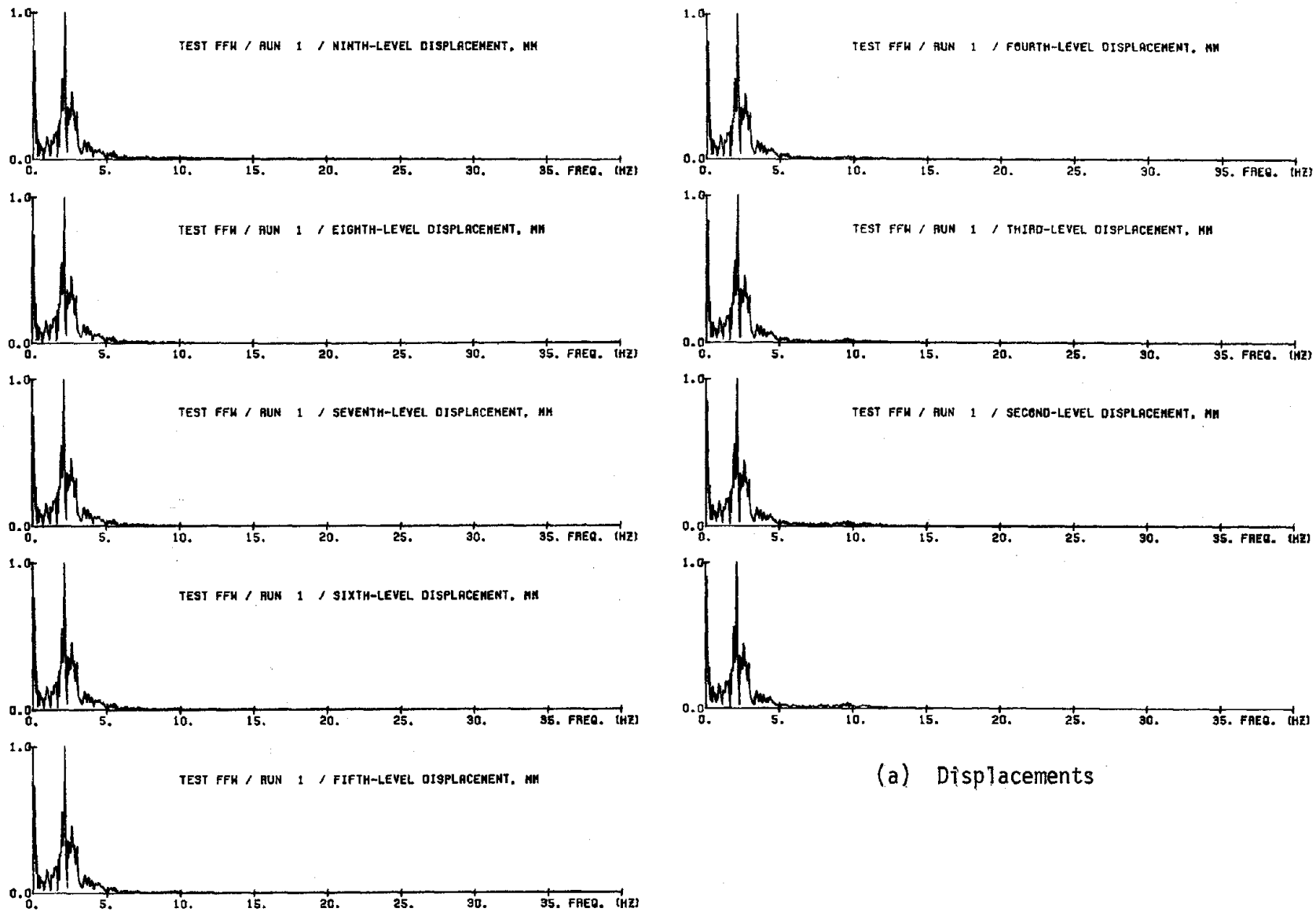


(a) Displacements

Fig. 5.8 Frequency Content of Measured Test-Structure Responses

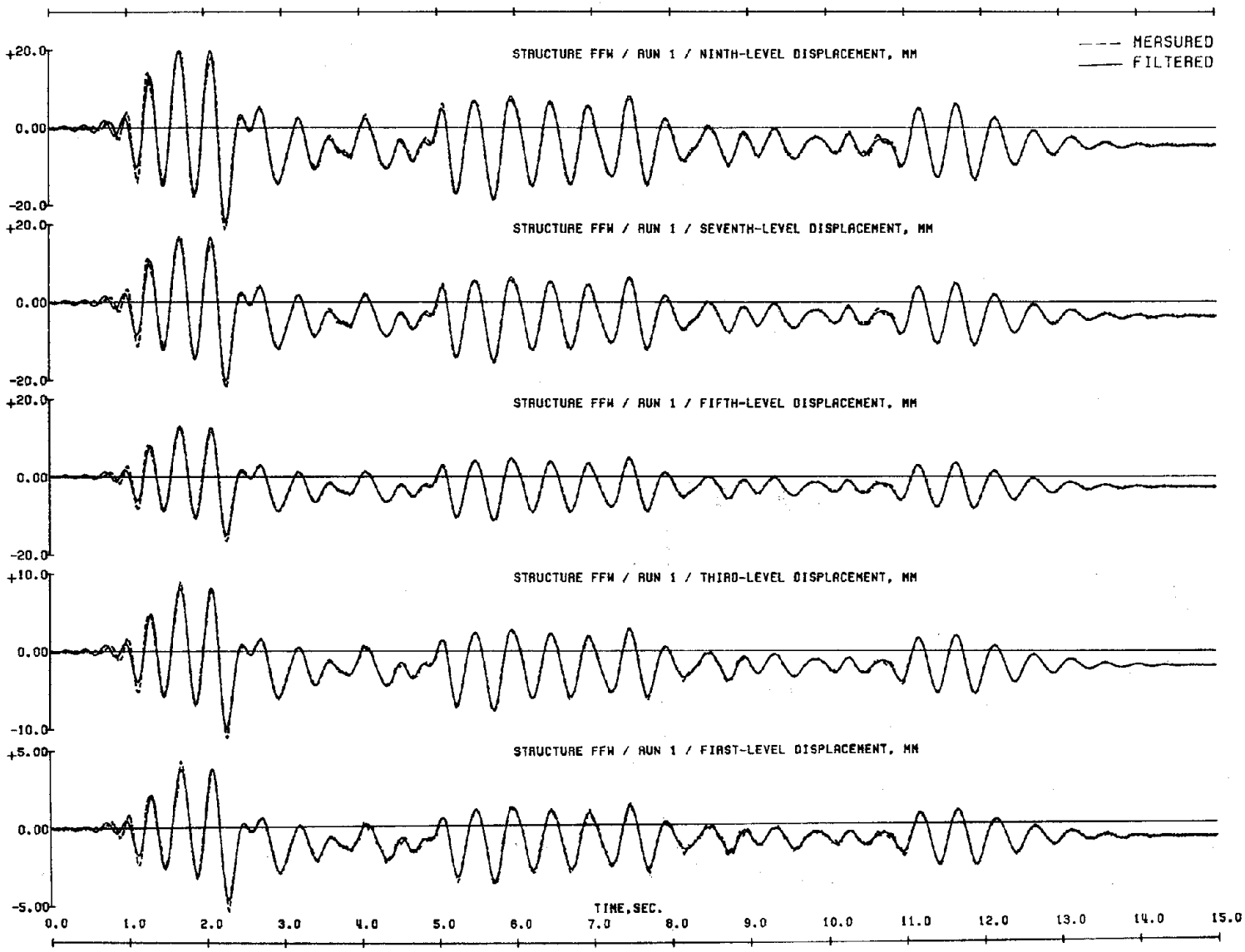


(a) Displacements

Fig. 5.8 (contd.) Frequency Content of Measured Test-Structure Responses

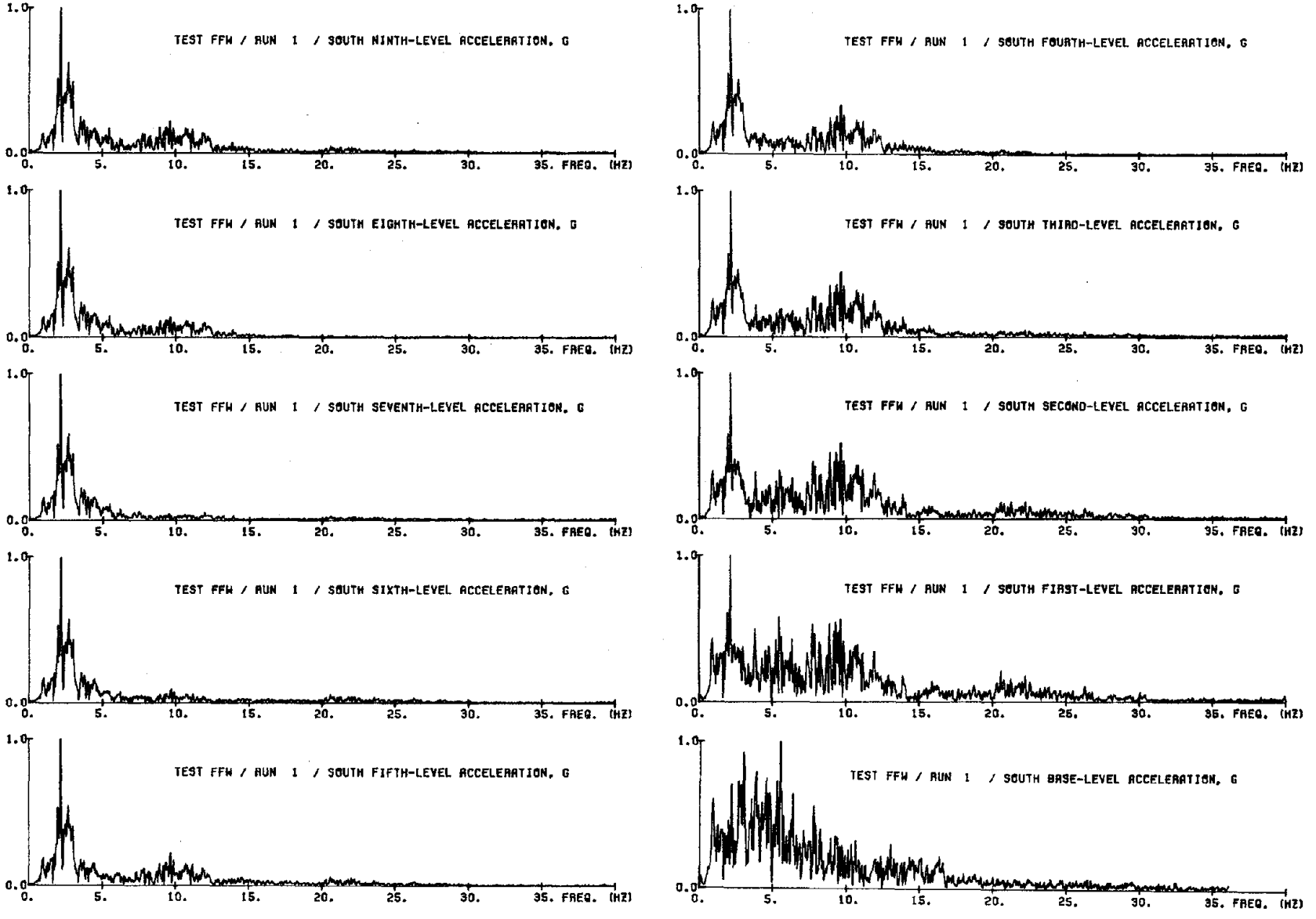


(b) Accelerations

Fig. 5.8 (contd.) Frequency Content of Measured Test-Structure Responses

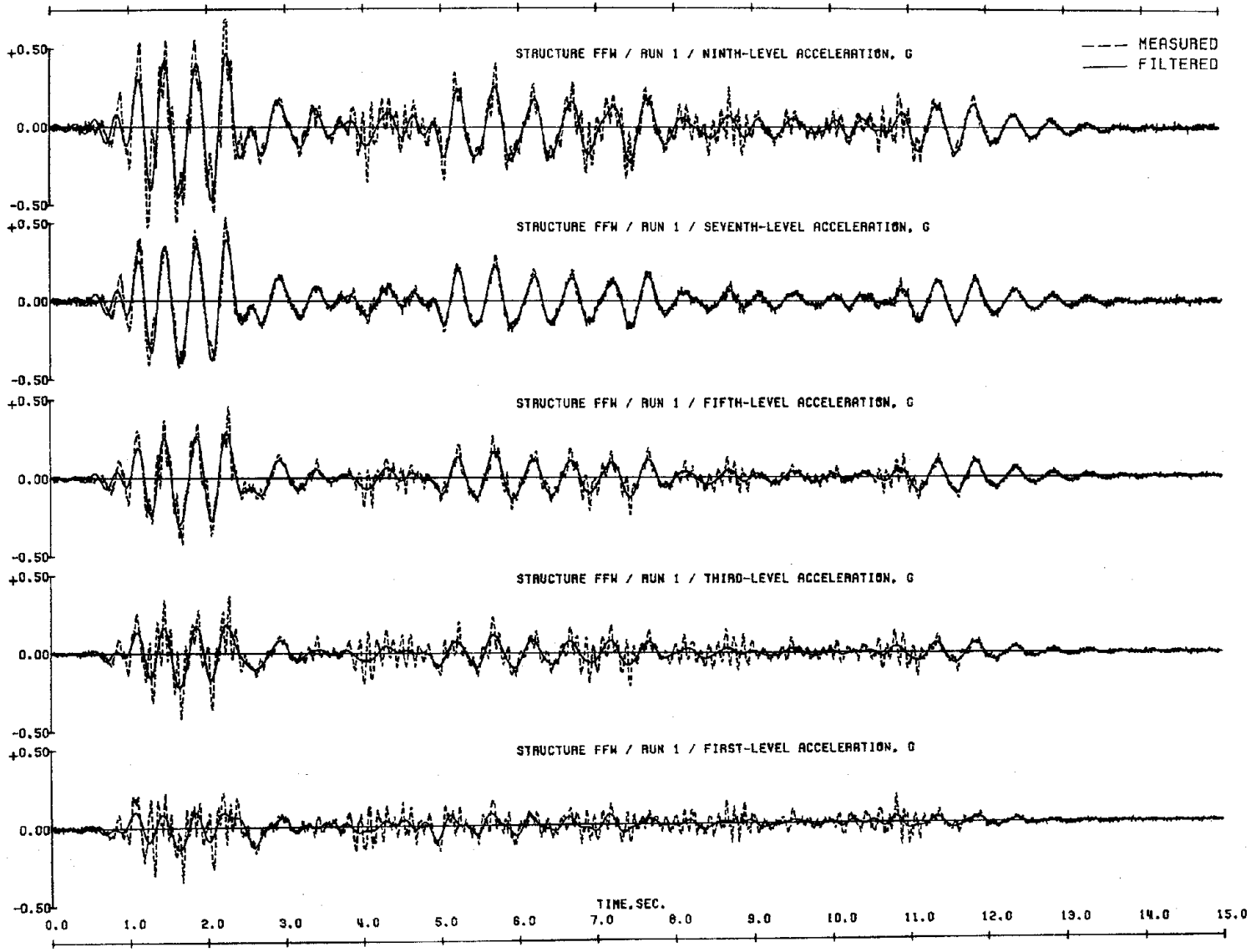


(b) Accelerations

Fig. 5.8 (contd.) Frequency Content of Measured Test-Structure Responses

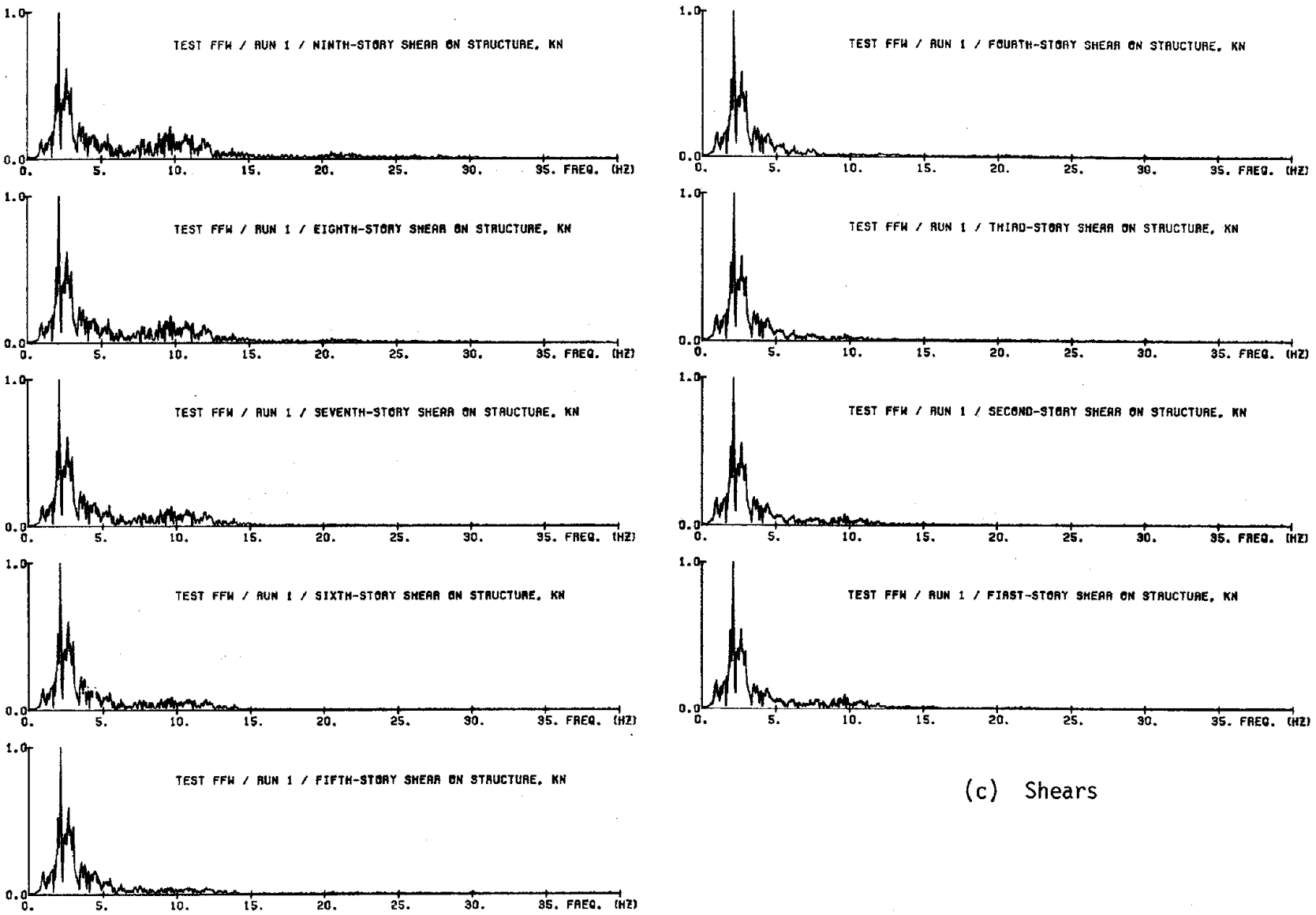


(c) Shears

Fig. 5.8 (contd.) Frequency Content of Measured Test-Structure Responses

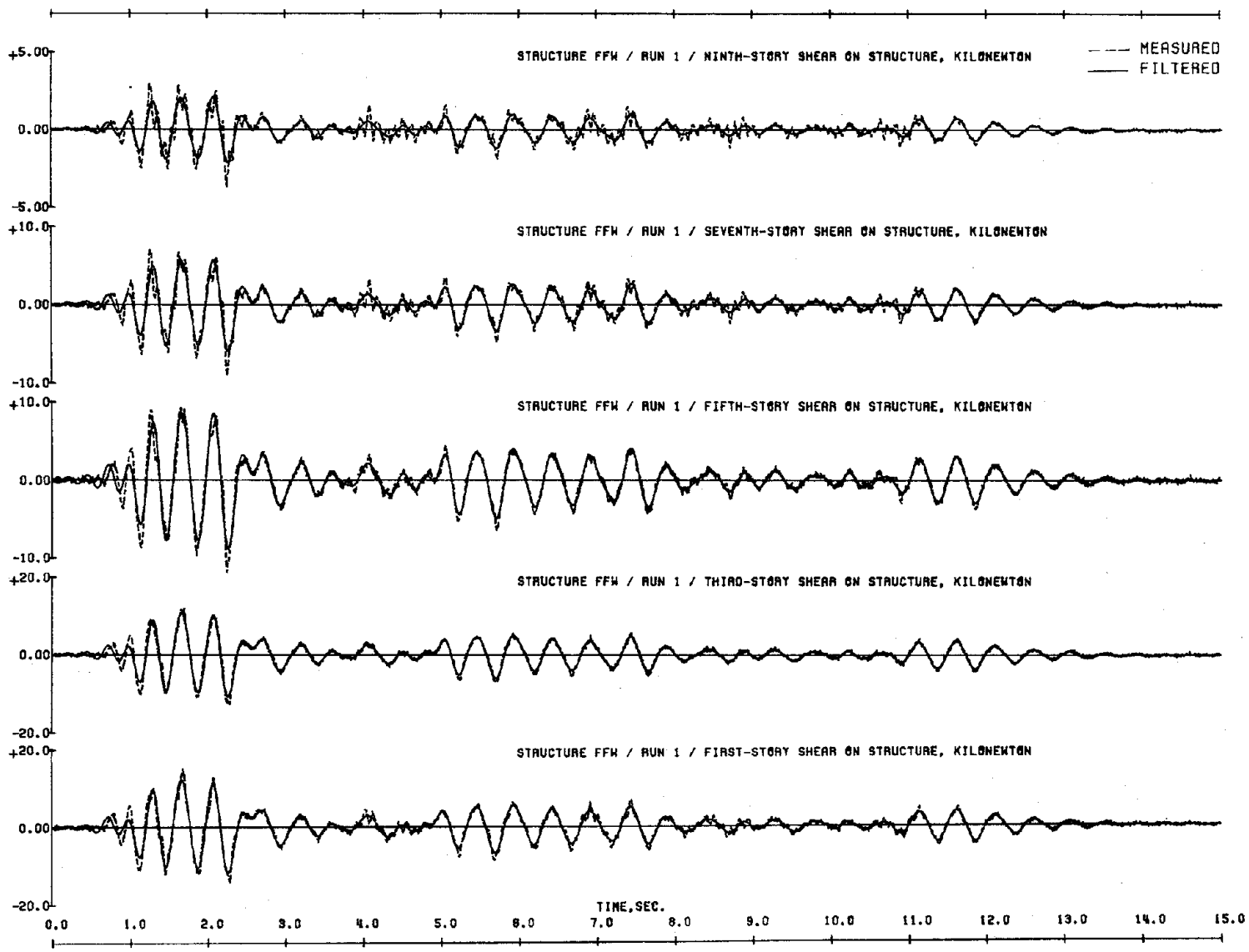


(c) Shears

Fig. 5.8 (contd.) Frequency Content of Measured Test-Structure Responses

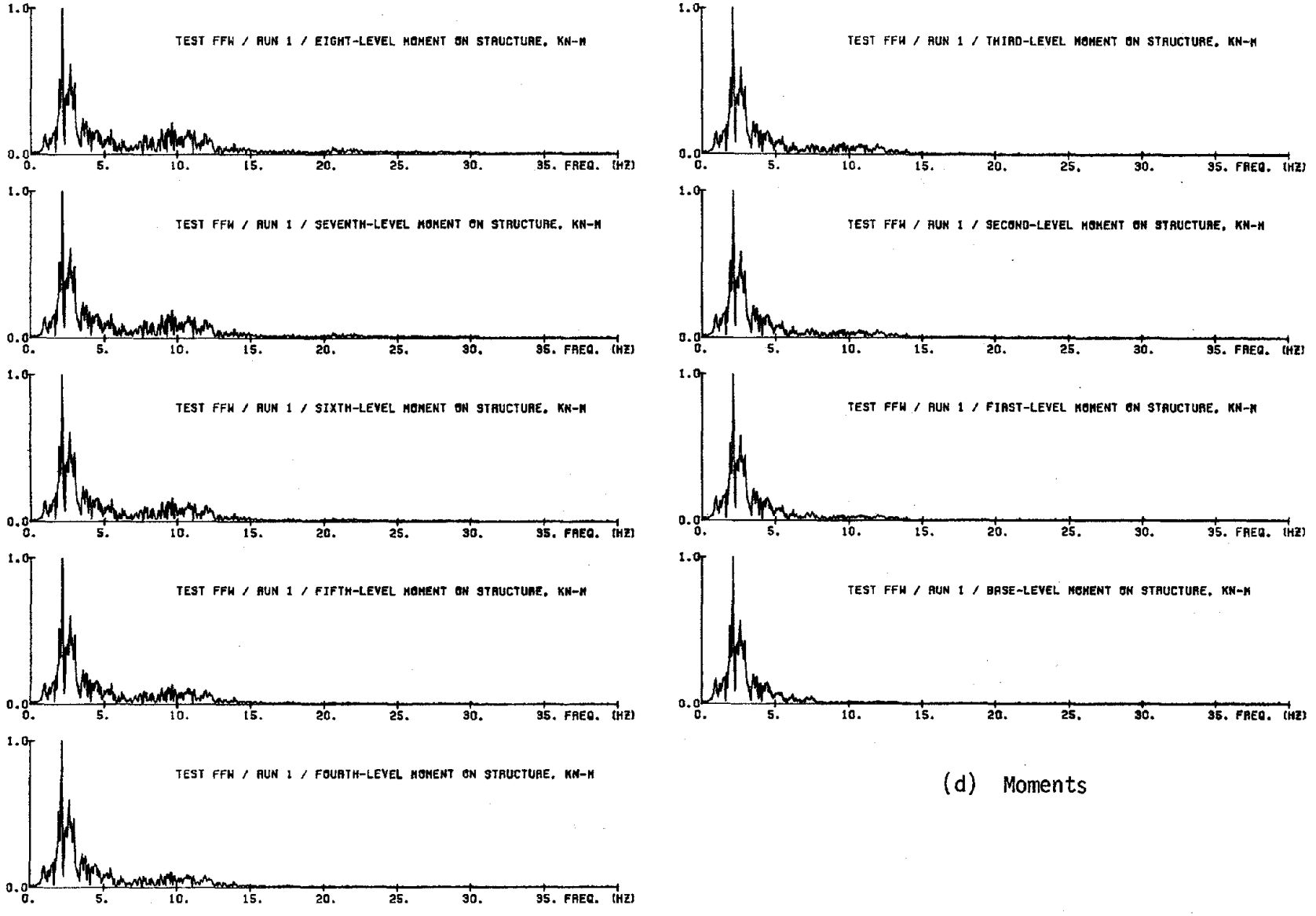


(d) Moments

Fig. 5.8 (contd.) Frequency Content of Measured Test-Structure Responses

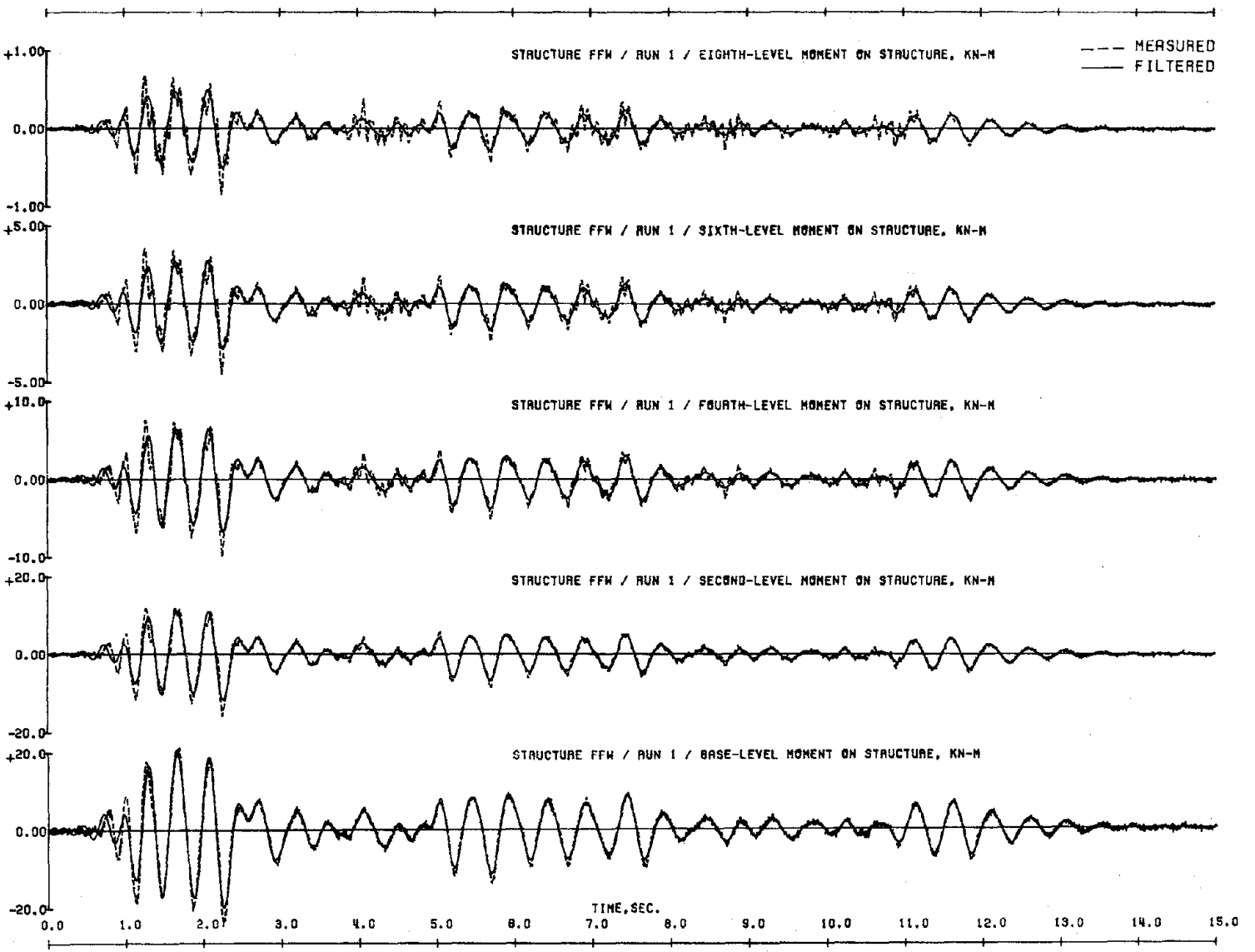


(d) Moments

Fig. 5.8 (contd.) Frequency Content of Measured Test-Structure Responses

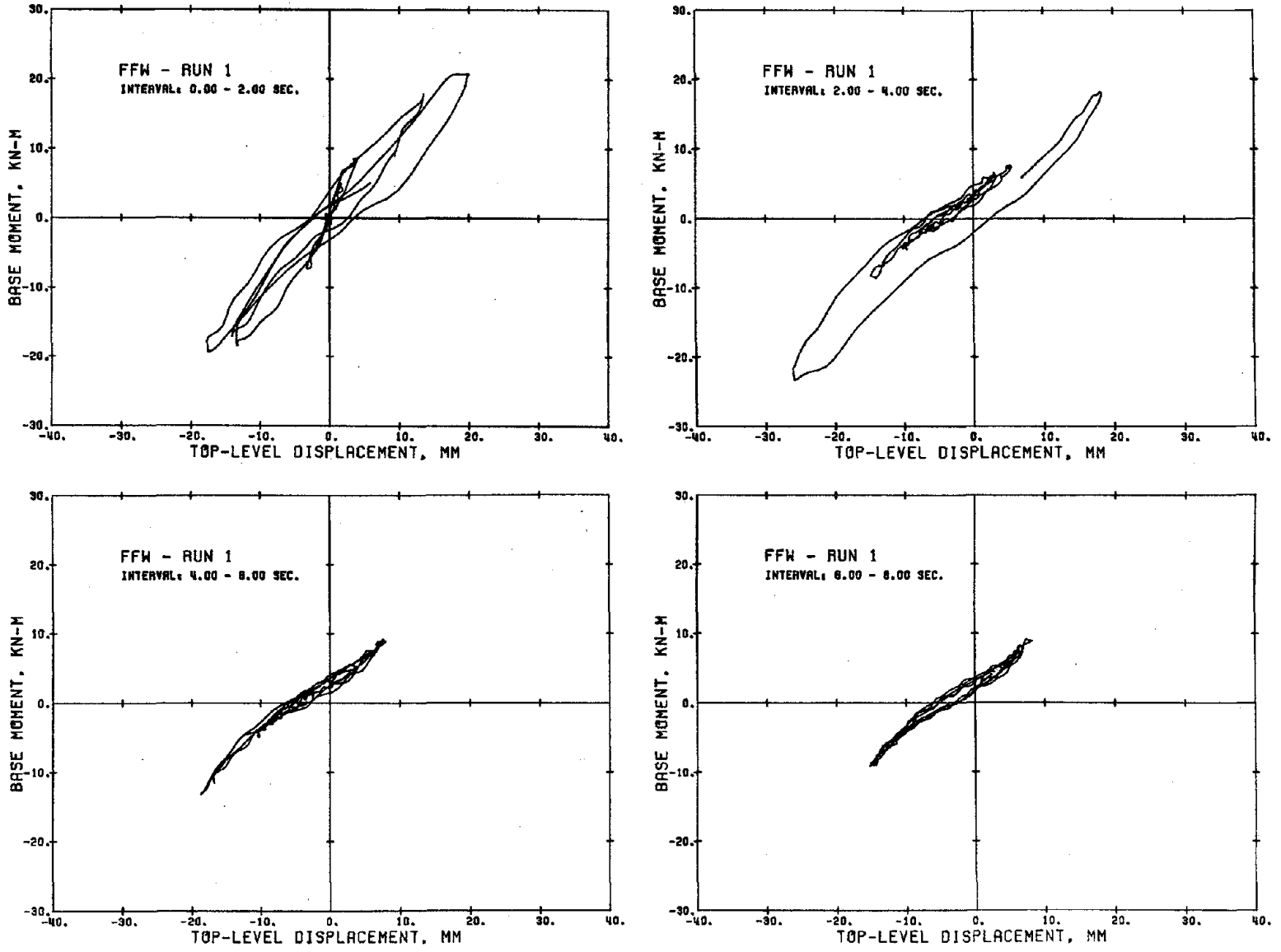


Fig. 5.9 Changes in Base Moment-Top Displacement Relation during an Earthquake Simulation

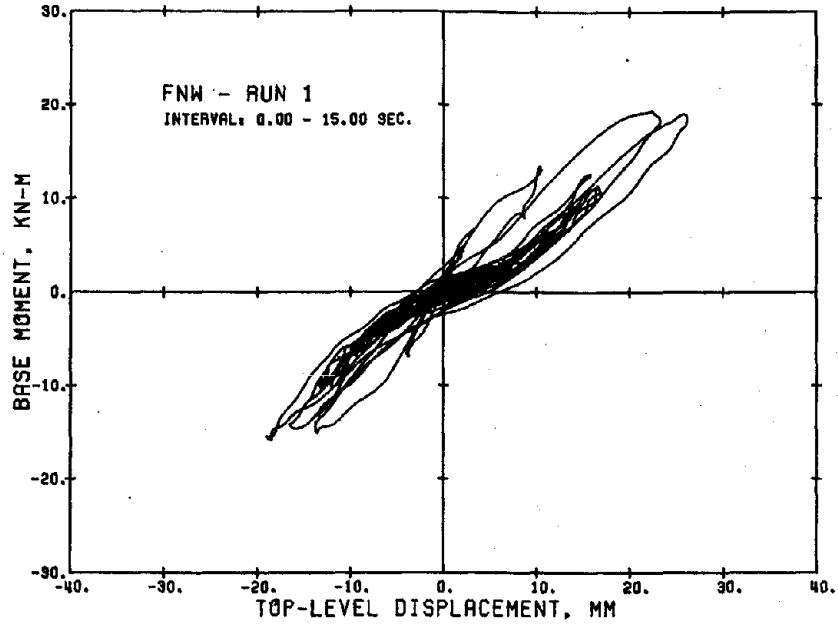


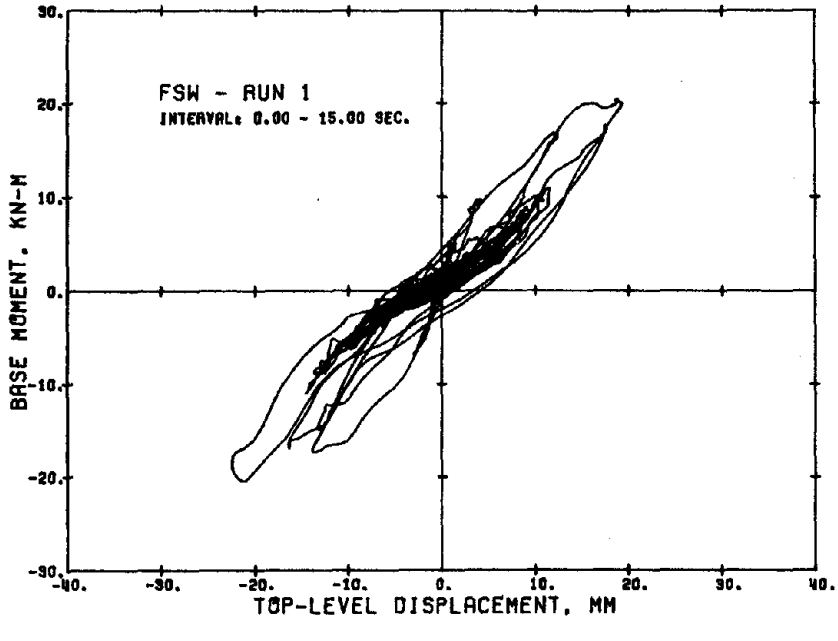


Fig. 5.10 Measured Base Moment-Top Displacement Relations for Initial Simulations

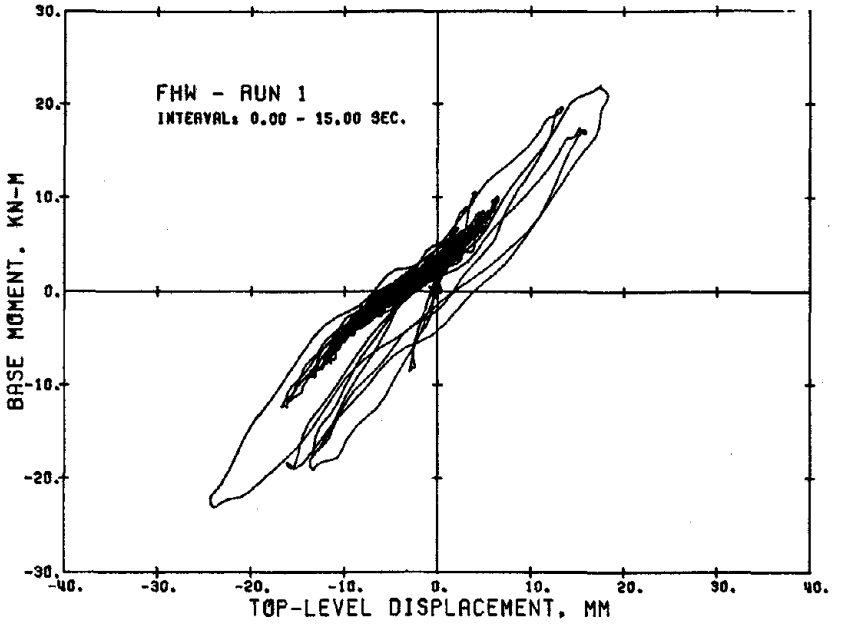


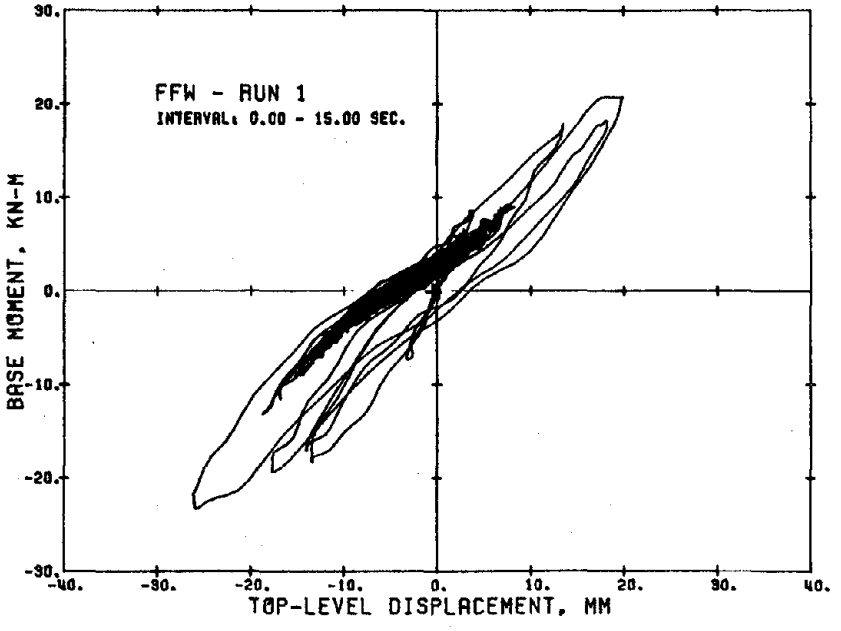


Fig. 5.10 (contd.) Measured Base Moment-Top Displacement Relations for Initial Simulations

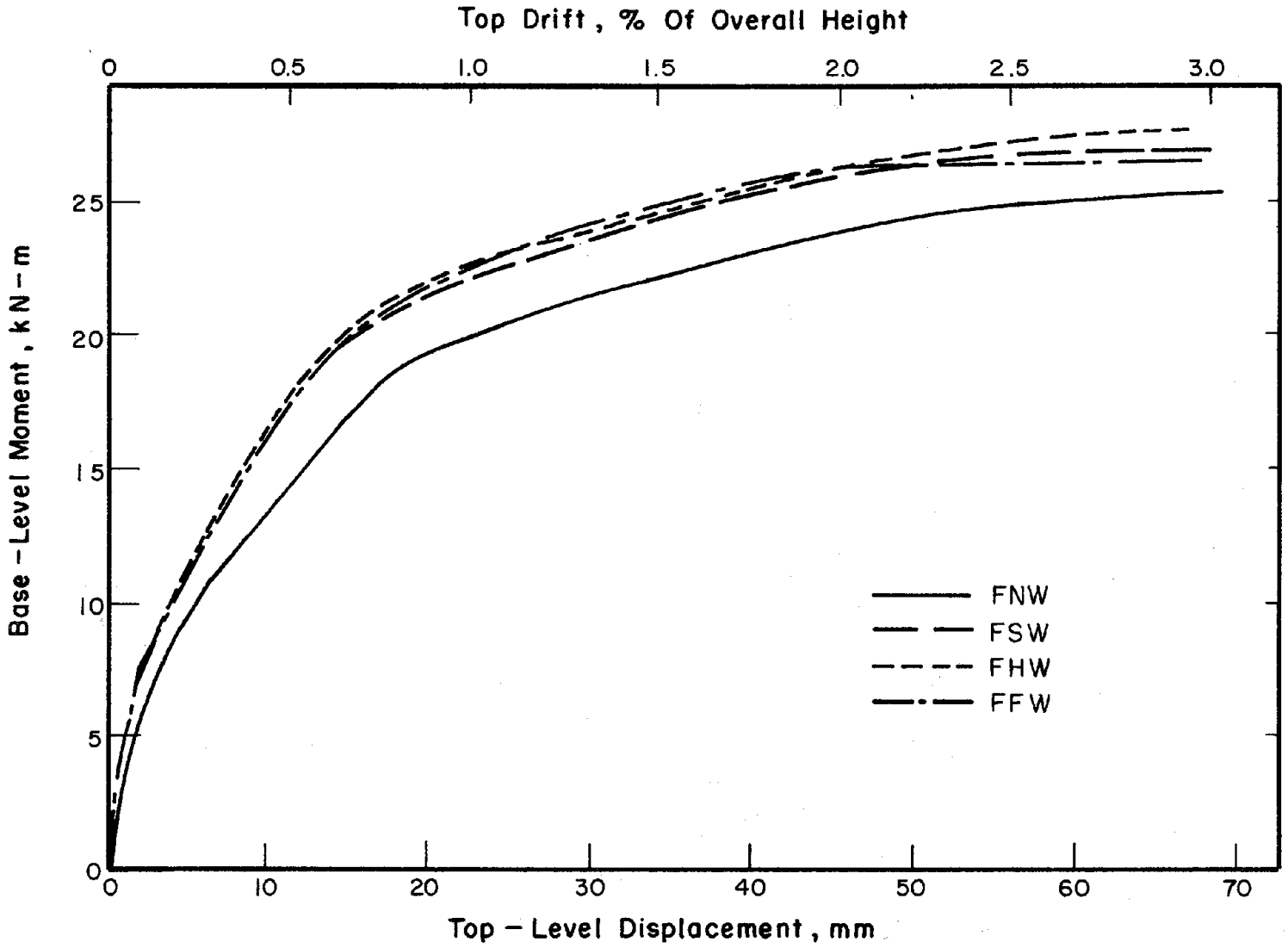


Fig. 5.11 Estimated Primary Curves of Base Moment Versus Top Displacement

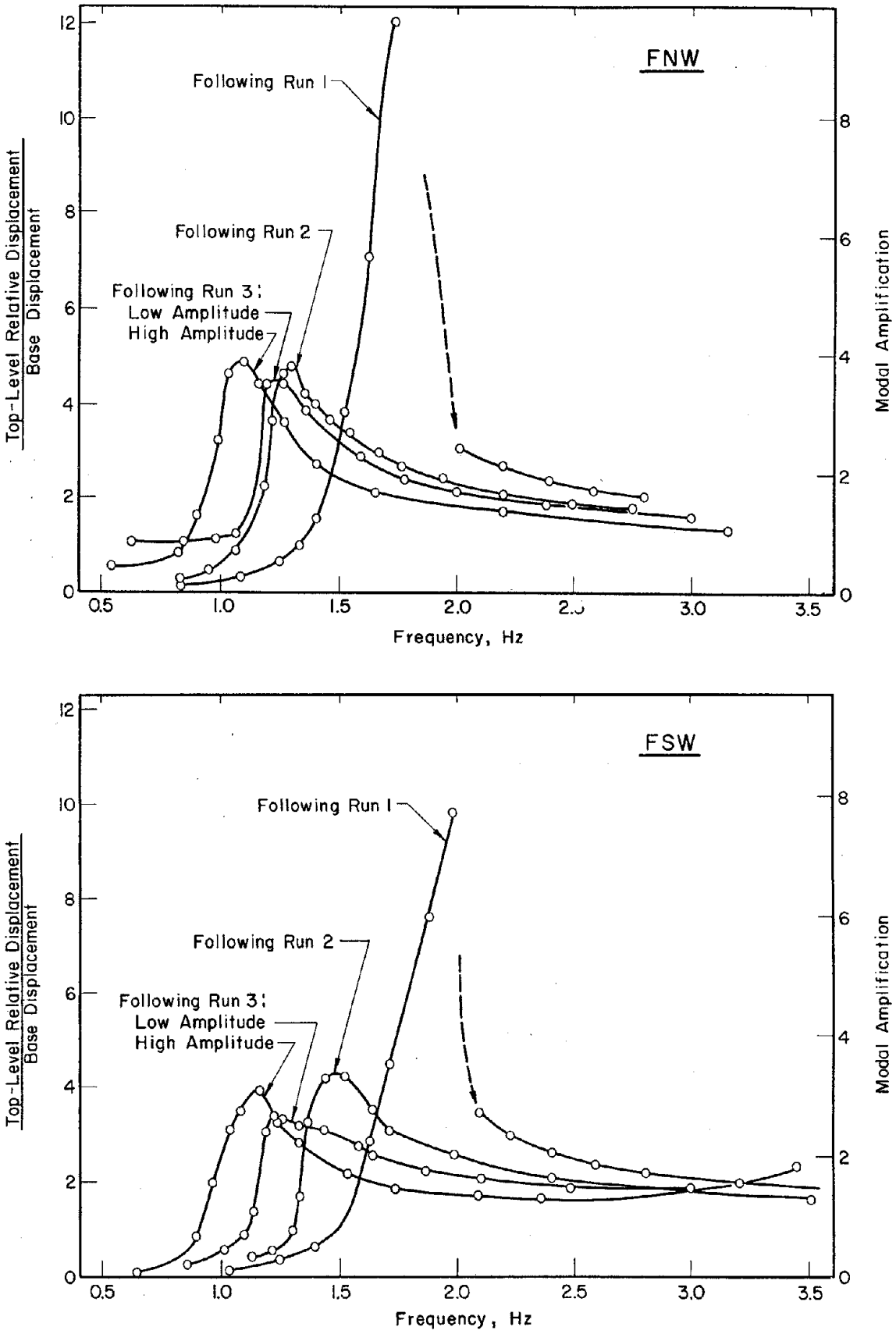


Fig. 5.12 Frequency-Response Curves Measured during Steady-State Tests

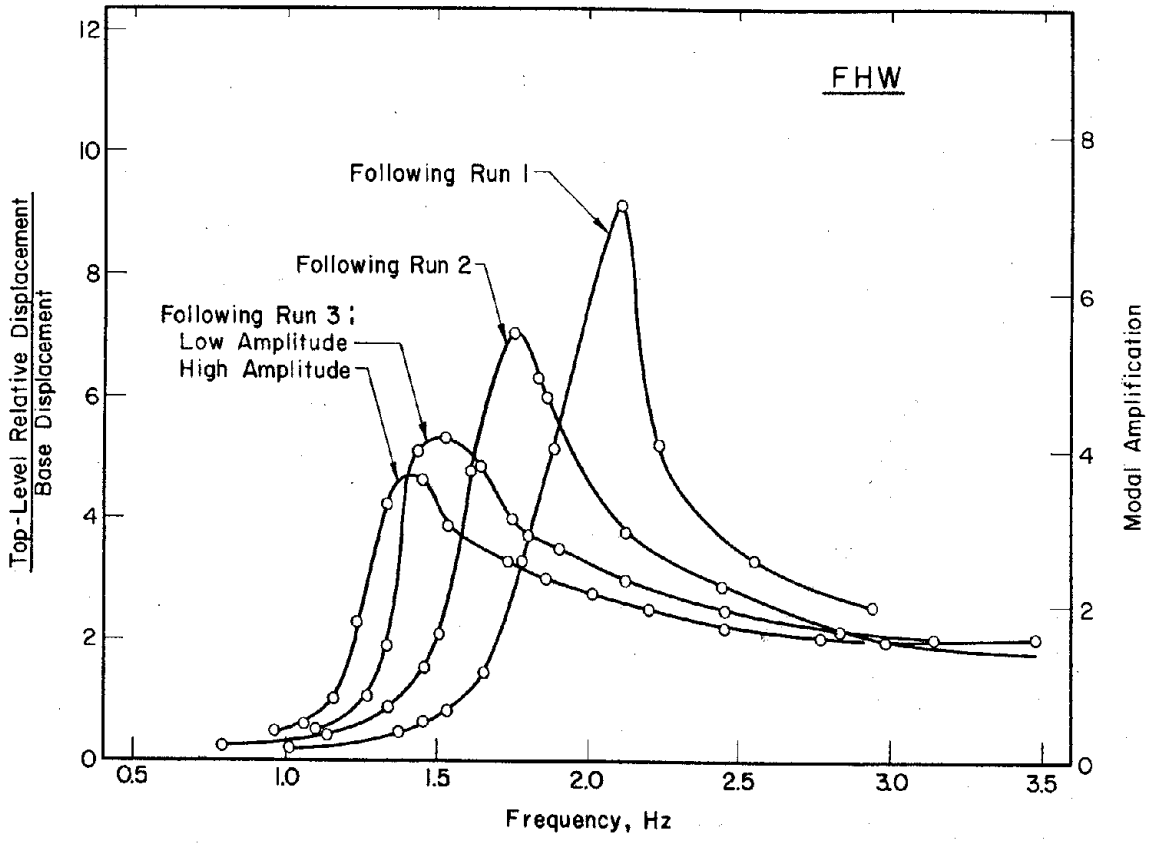


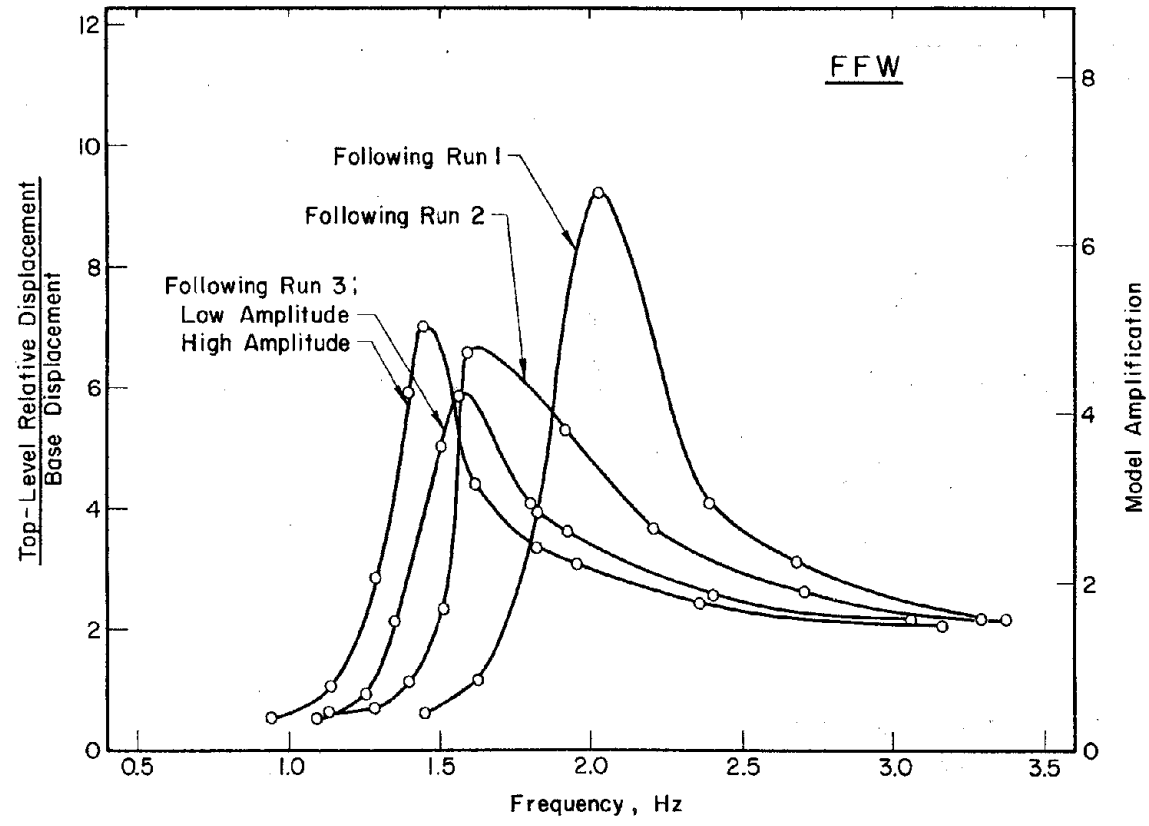


Fig. 5.12 (contd.) Frequency-Response Curves Measured during Steady-State Tests

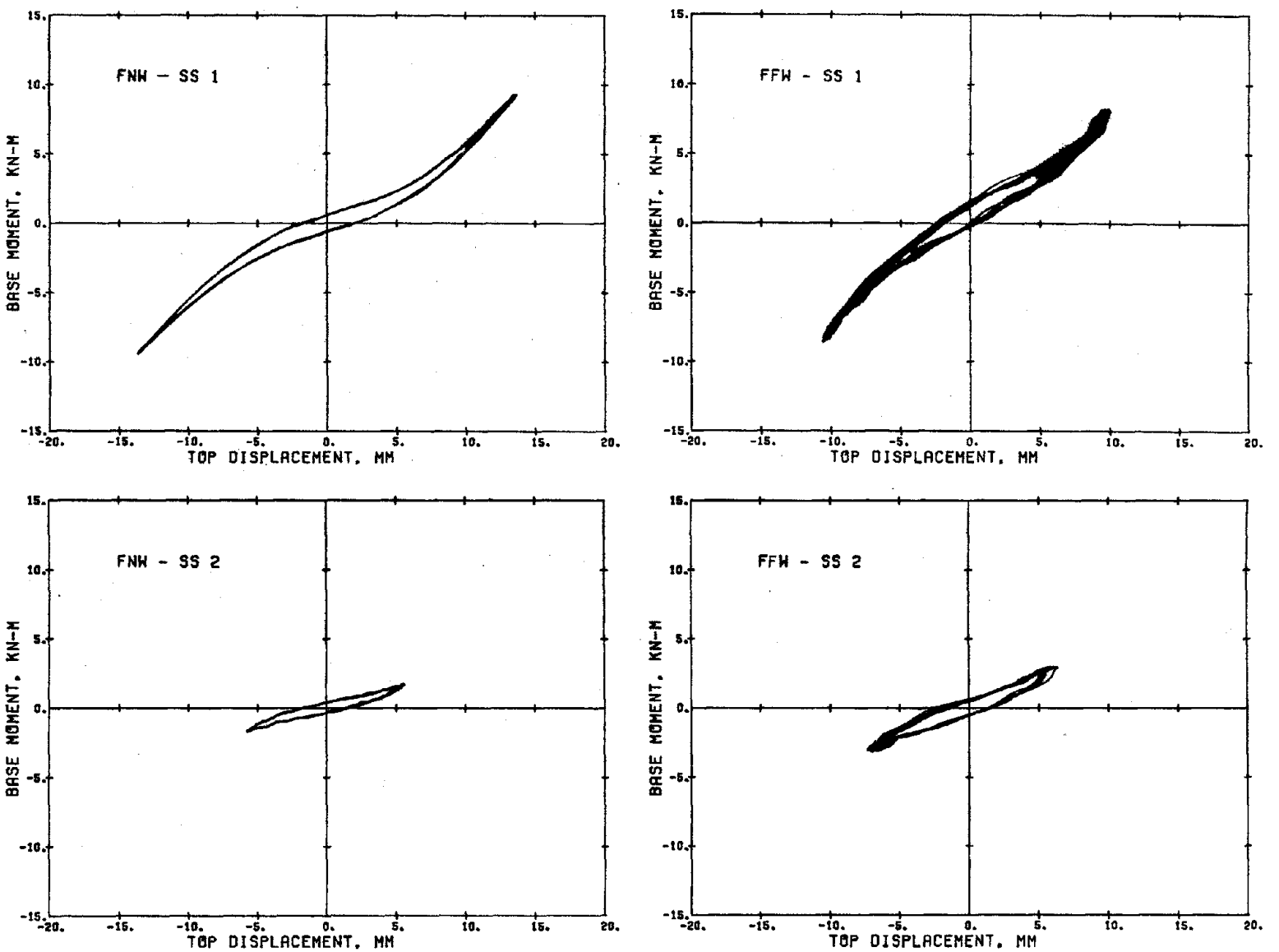


Fig. 5.13 Hysteresis Relations Measured during Steady-State Tests

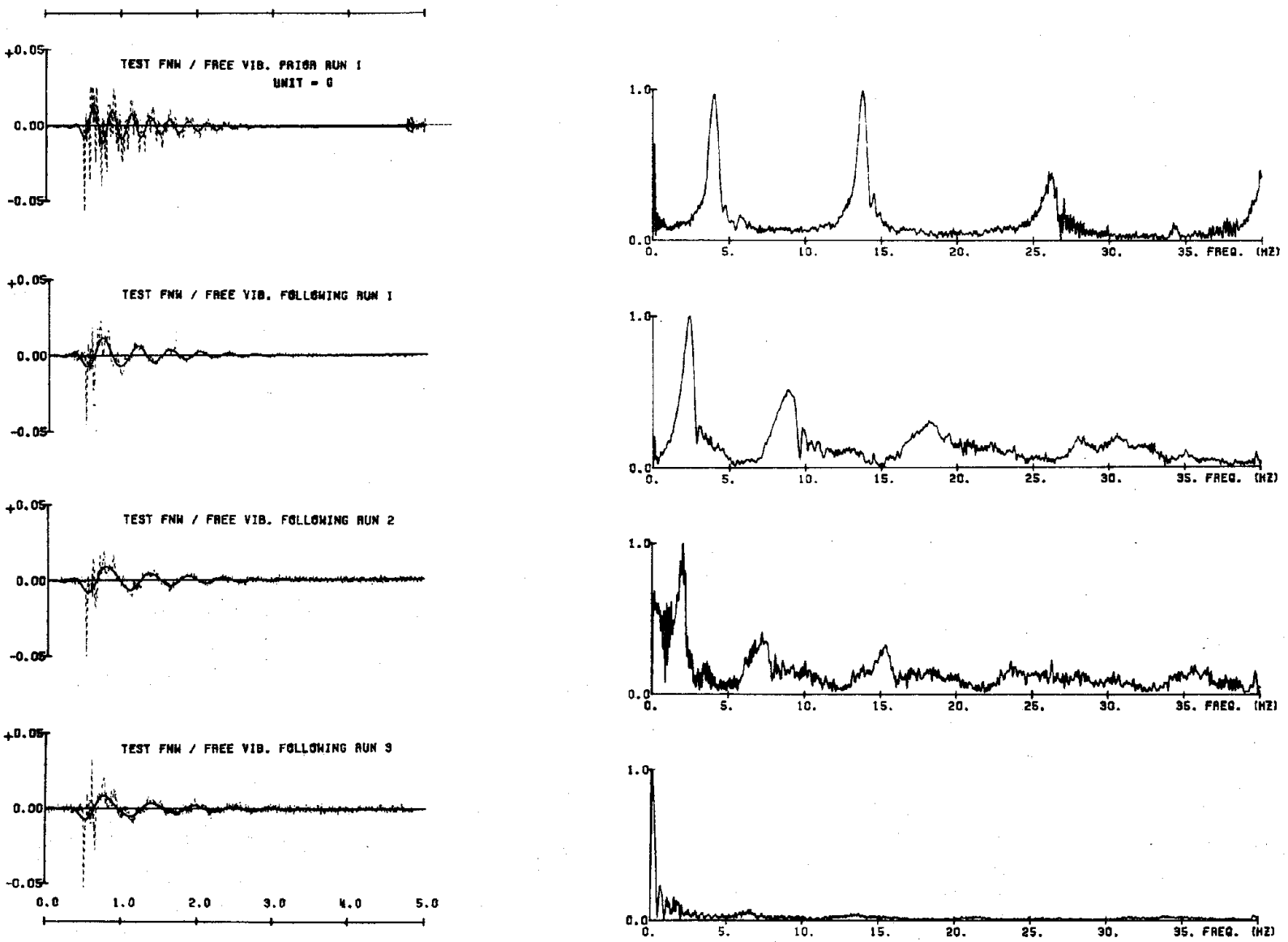


Fig. 5.14 Measured and Filtered Top-Level Free-Vibration Accelerations and Fourier-Amplitude Spectra

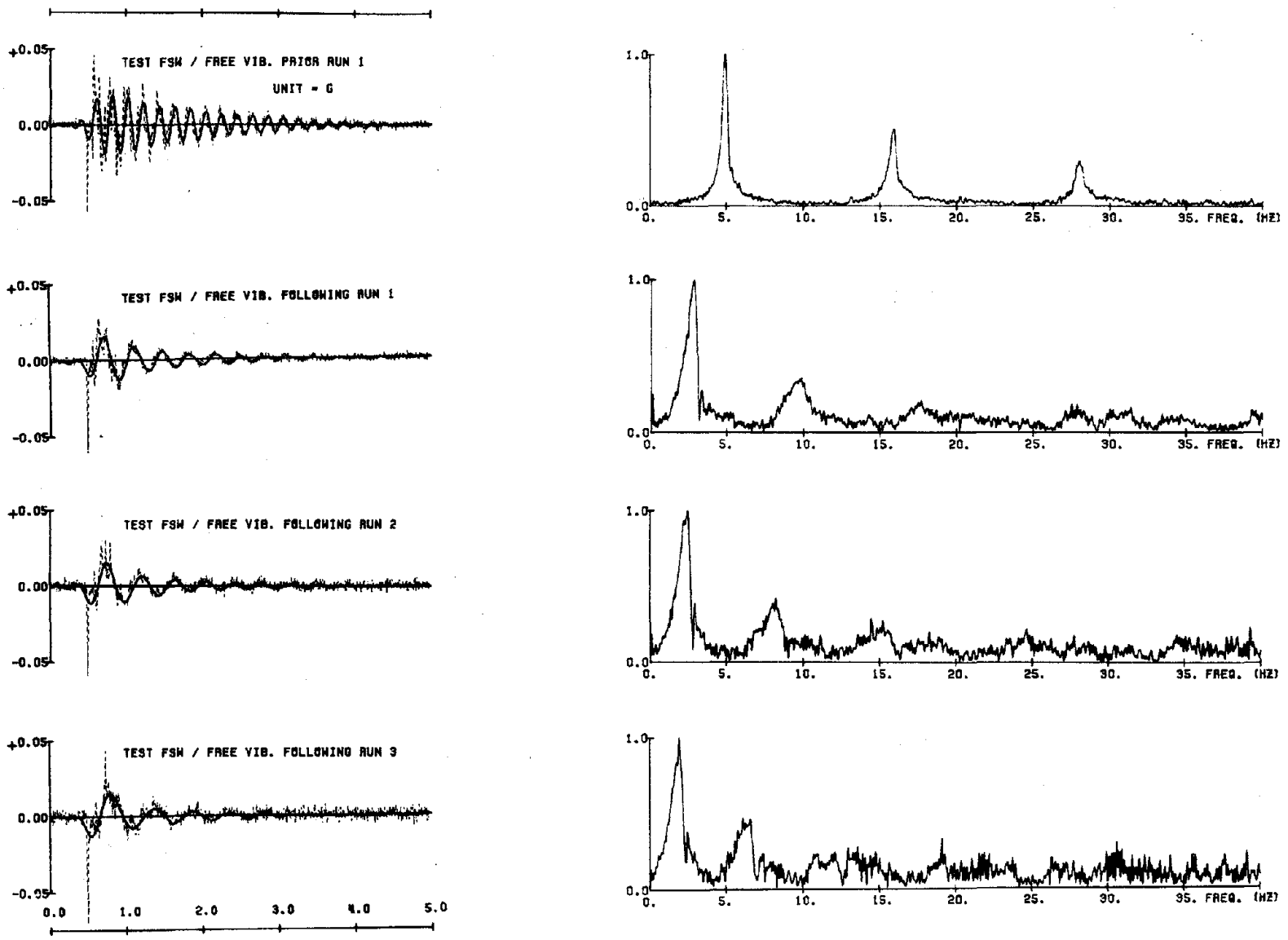


Fig. 5.14 (contd.) Measured and Filtered Top-Level Free-Vibration Accelerations and Fourier-Amplitude Spectra

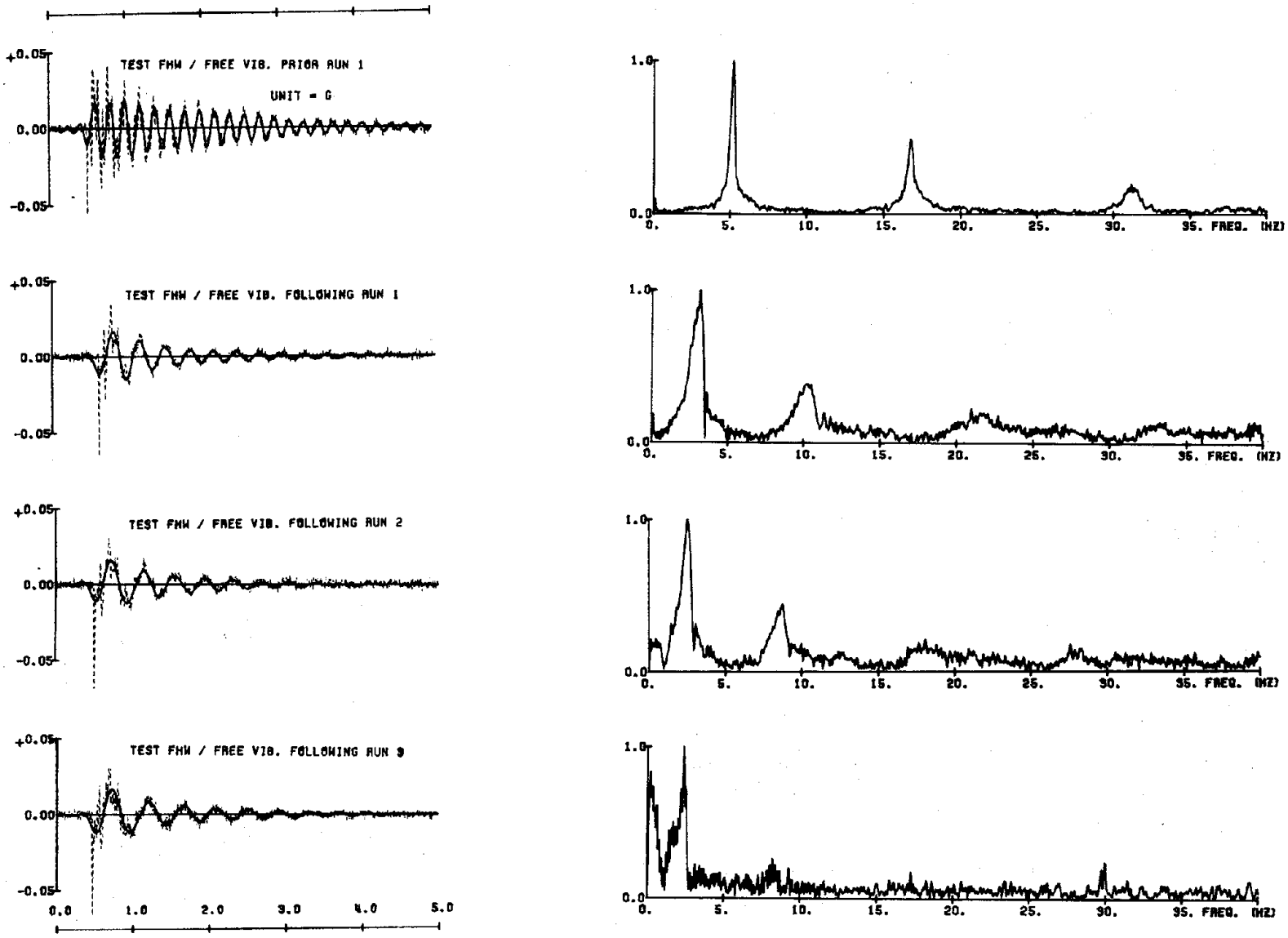


Fig. 5.14 (contd.) Measured and Filtered Top-Level Free-Vibration Accelerations and Fourier-Amplitude Spectra

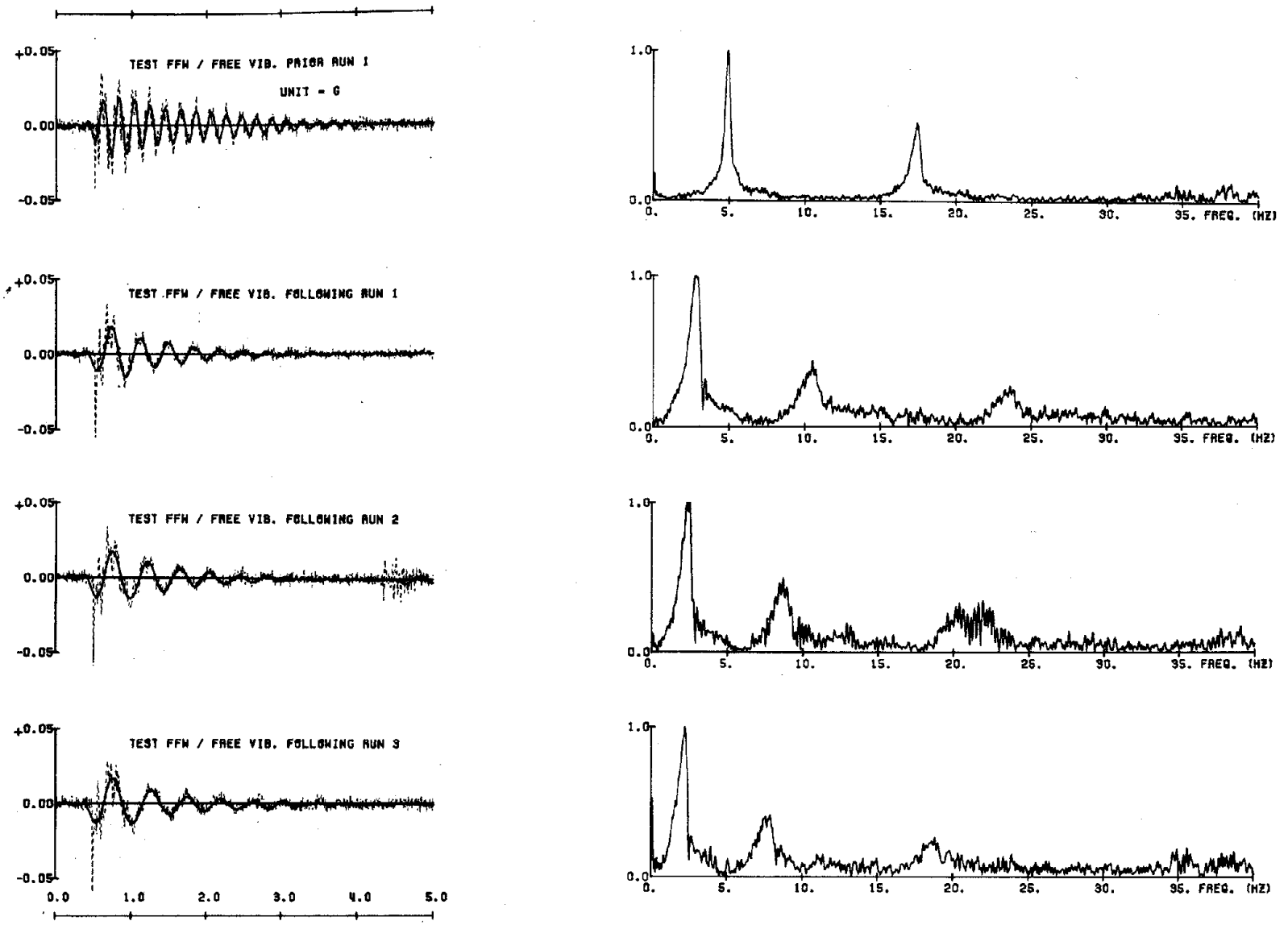


Fig. 5.14 (contd.) Measured and Filtered Top-Level Free-Vibration Accelerations and Fourier-Amplitude Spectra

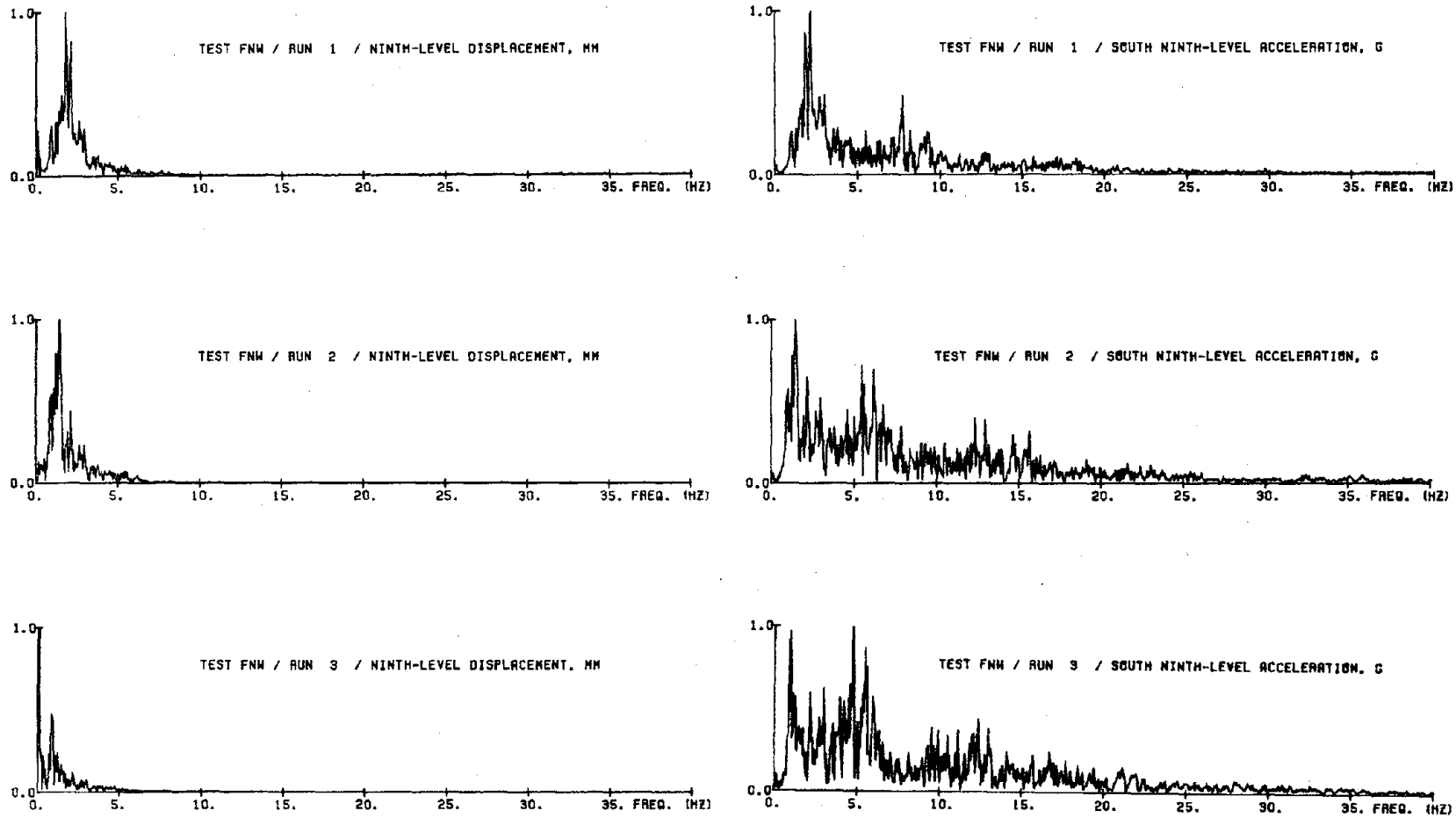


Fig. 5.15 Fourier-Amplitude Spectra of Top-Level Acceleration and Displacement Responses to Earthquake Simulations

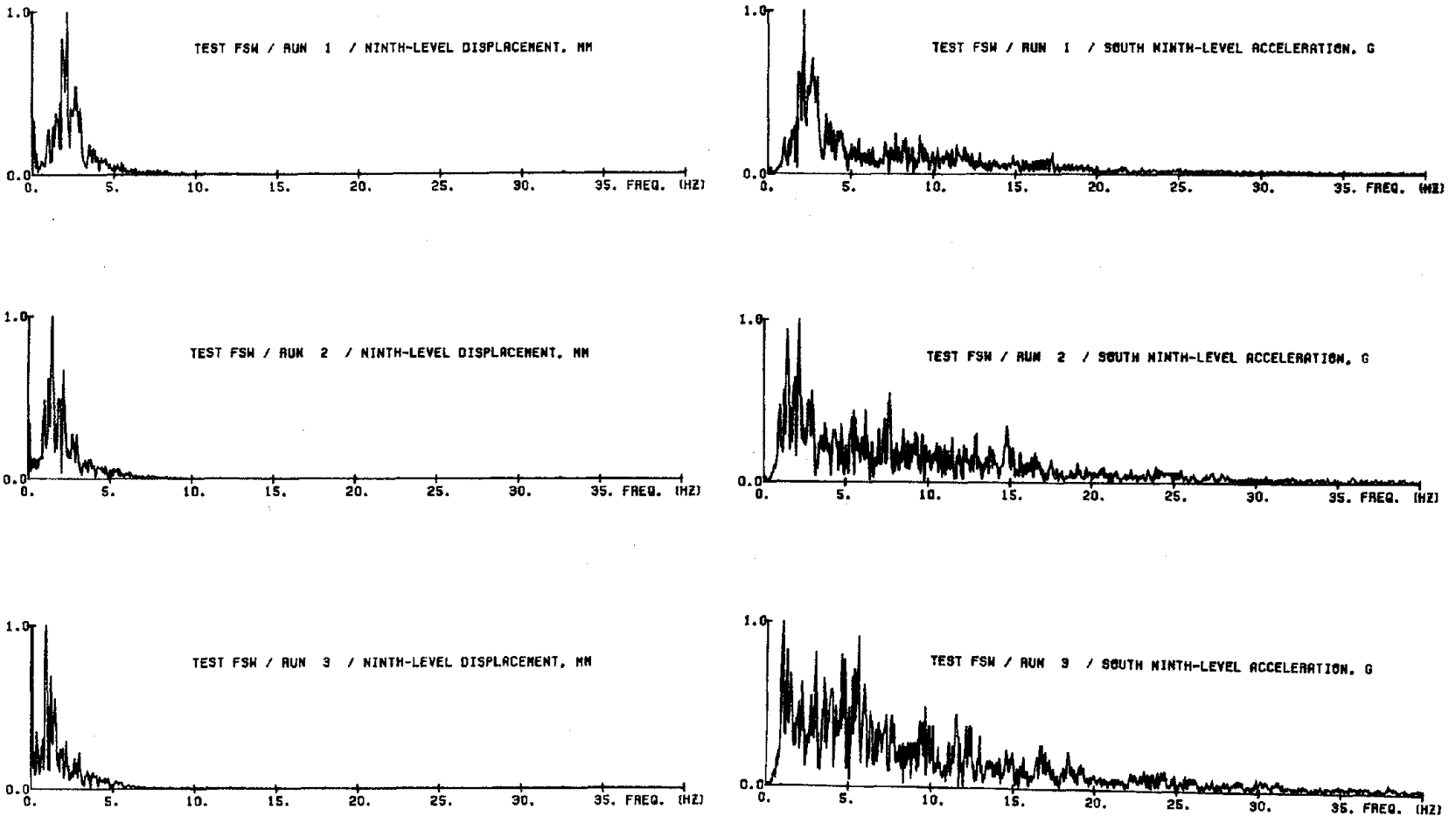


Fig. 5.15 (contd.) Fourier-Amplitude Spectra of Top-Level Acceleration and Displacement Responses to Earthquake Simulations

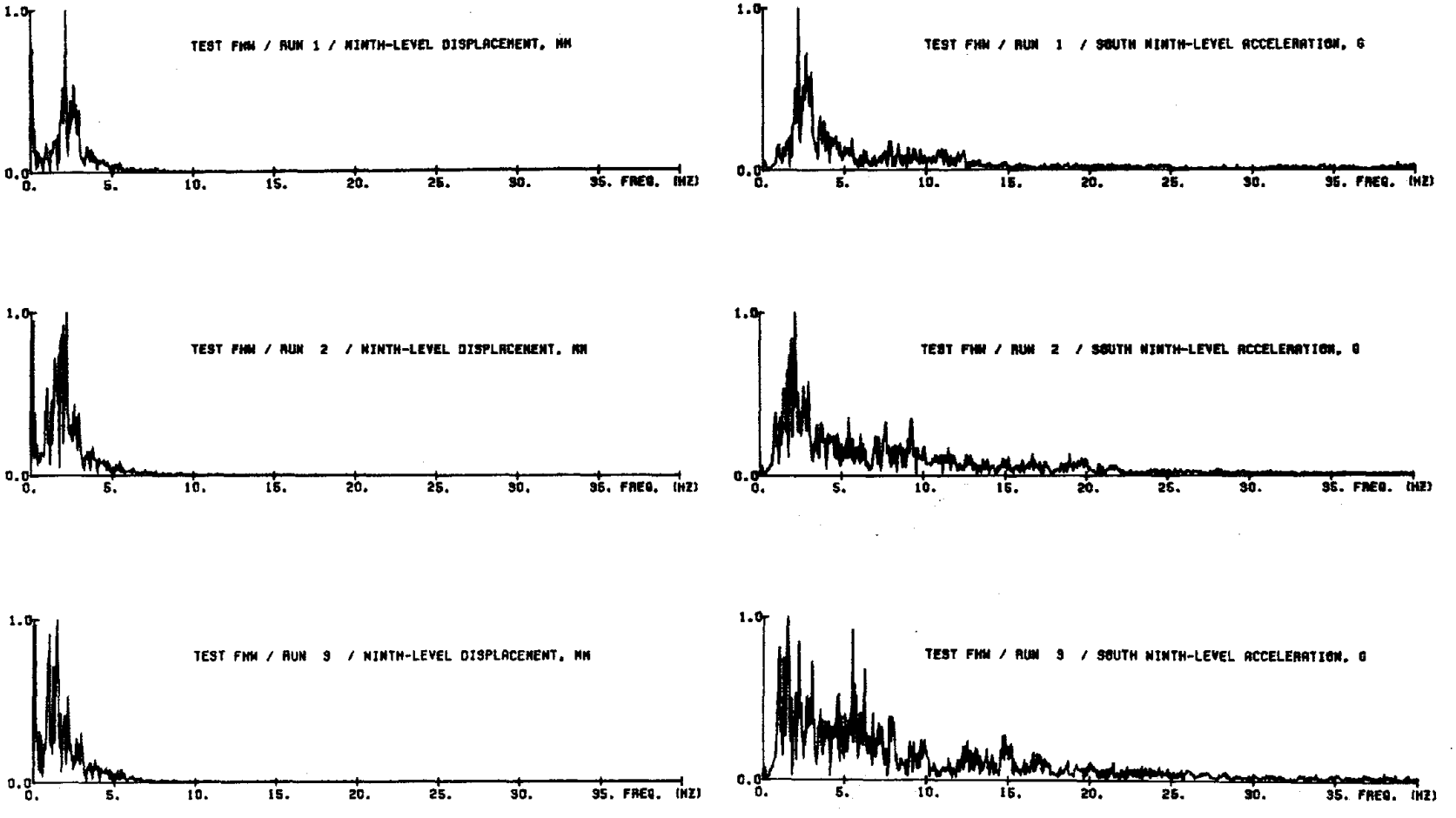


Fig. 5.15 (contd.) Fourier-Amplitude Spectra of Top-Level Acceleration and Displacement Responses to Earthquake Simulations

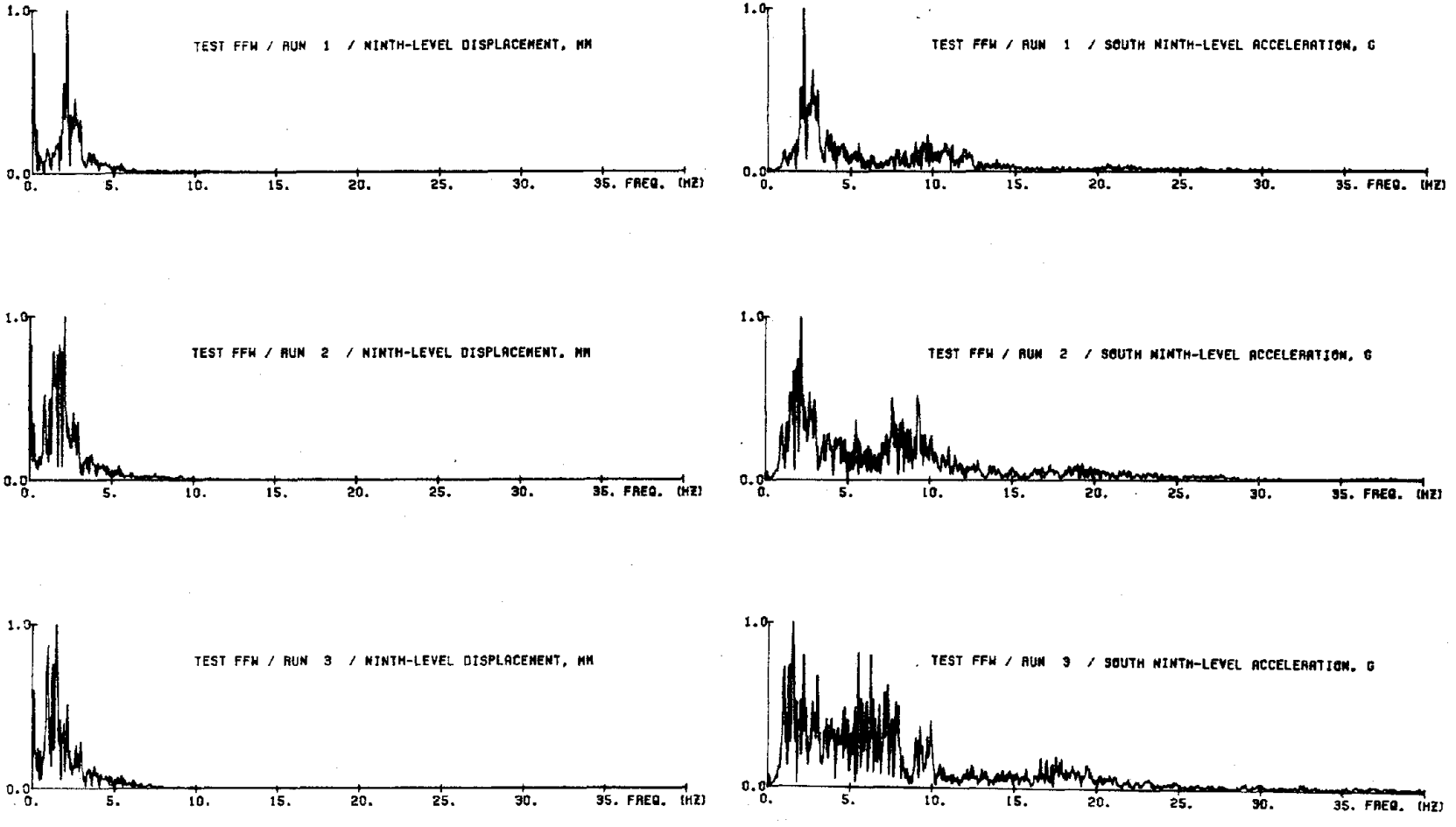


Fig. 5.15 (contd.) Fourier-Amplitude Spectra of Top-Level Acceleration and Displacement Responses to Earthquake Simulations

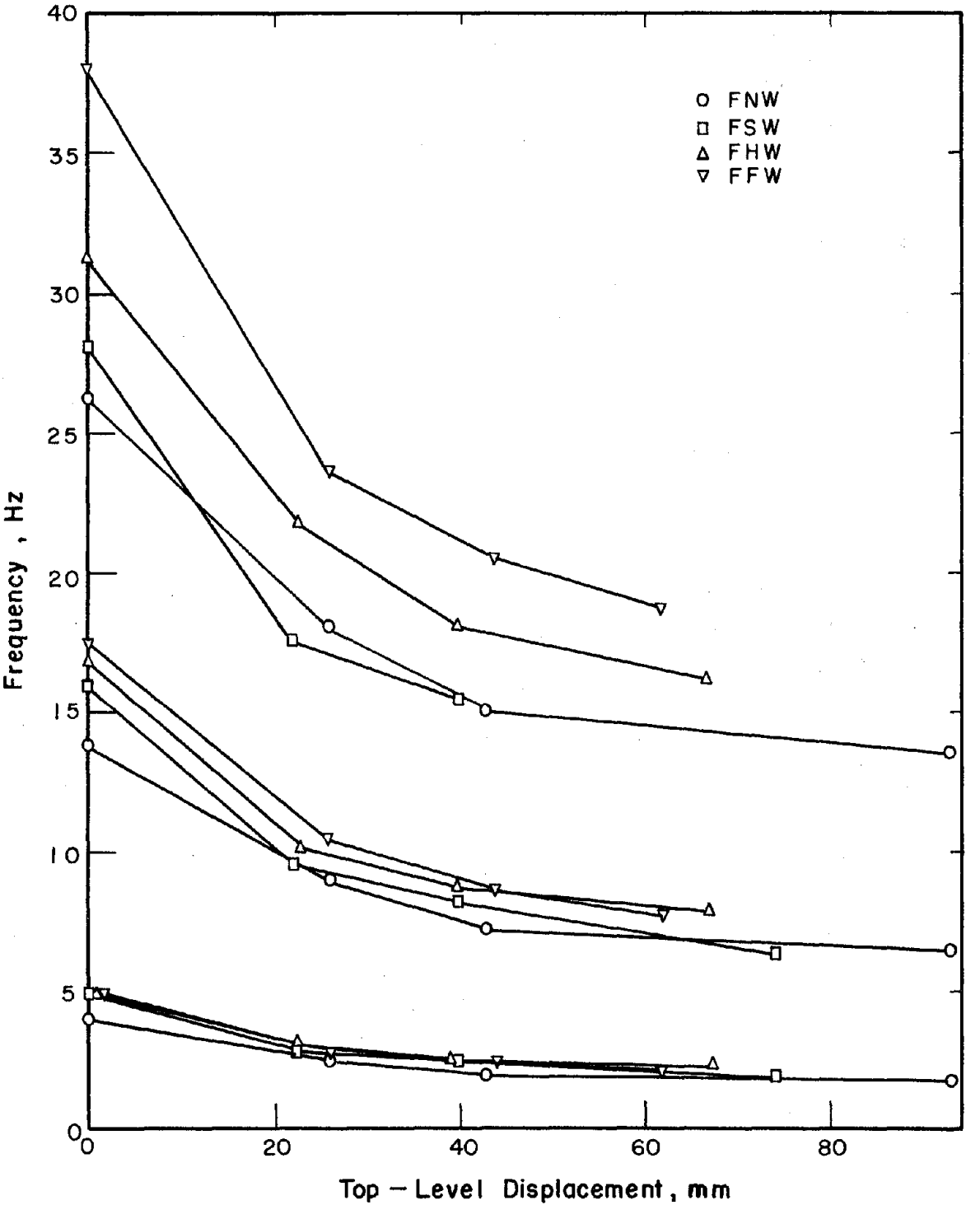


Fig. 5.16 Variation of Dominant Frequencies Measured during Free-Vibration Tests

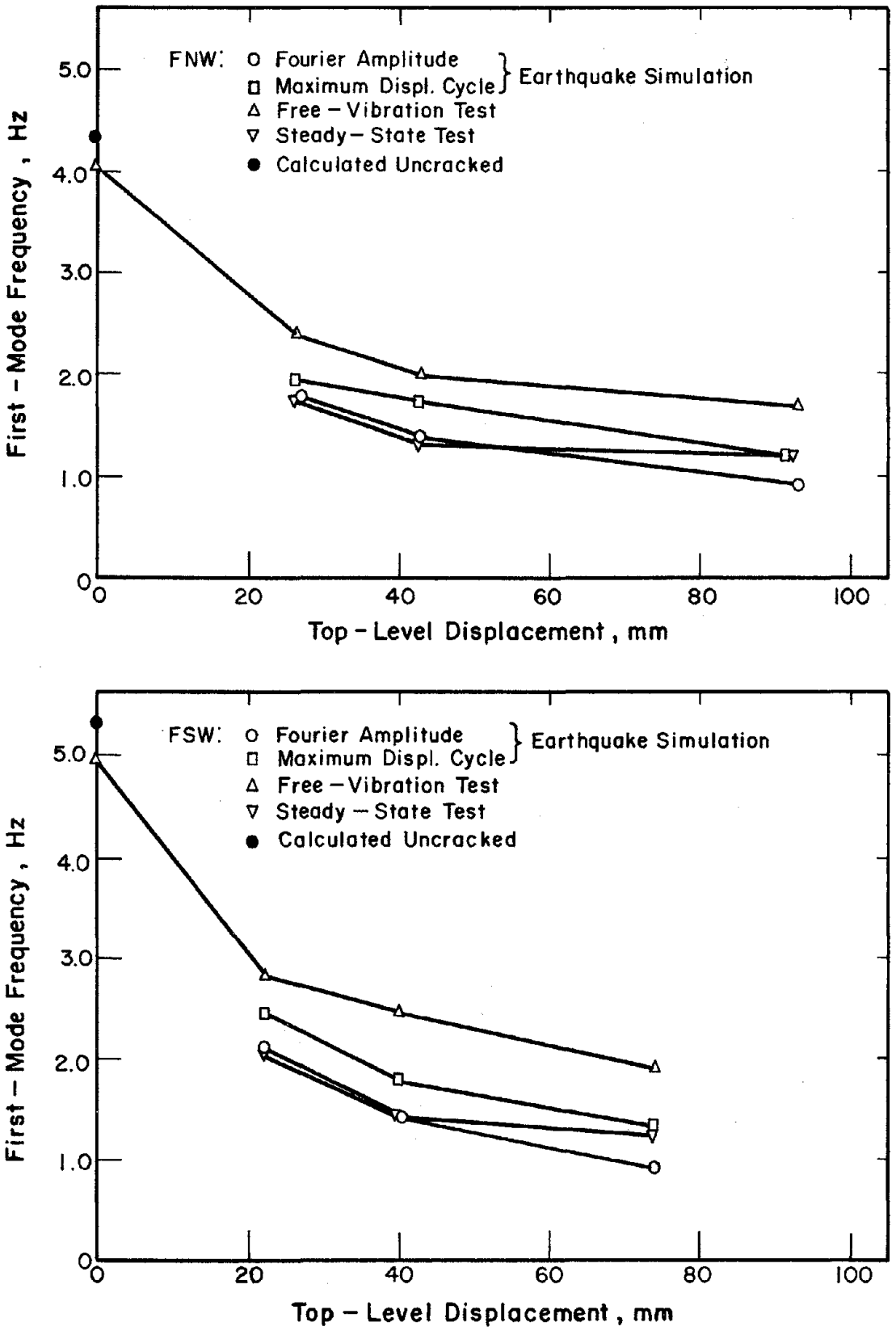


Fig. 5.17 Variation of Apparent Fundamental Frequencies with Maximum Previous Top-Level Displacement

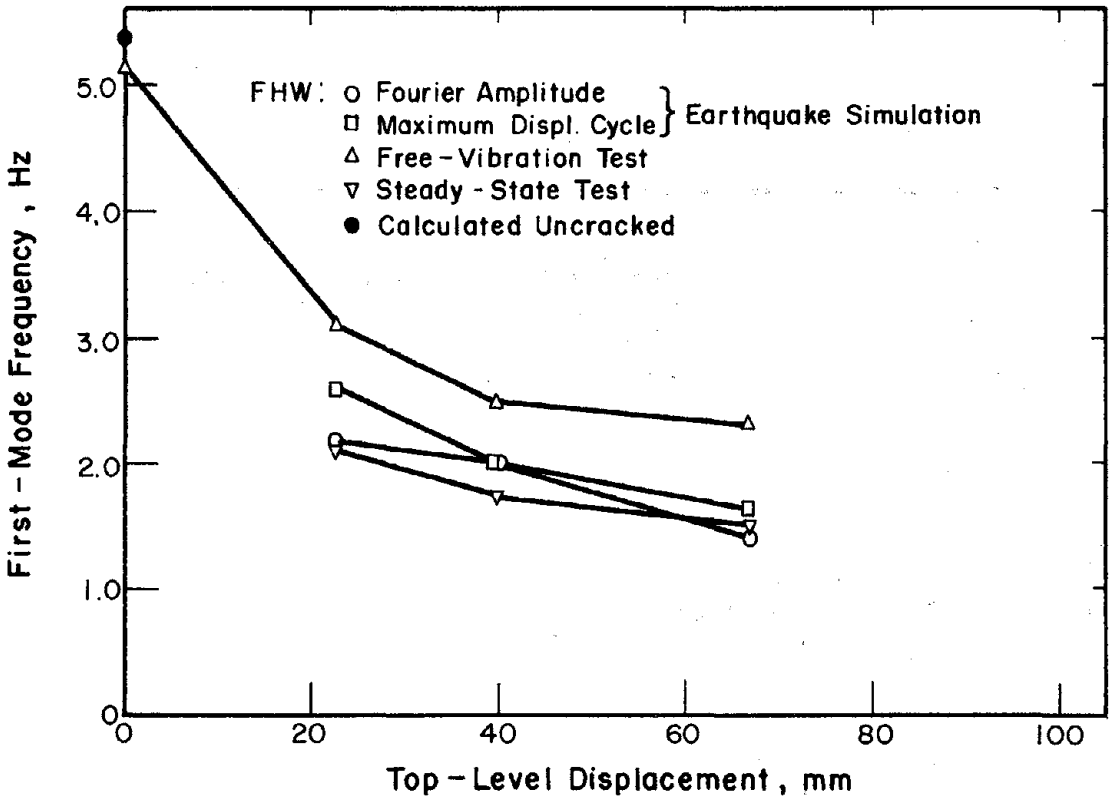


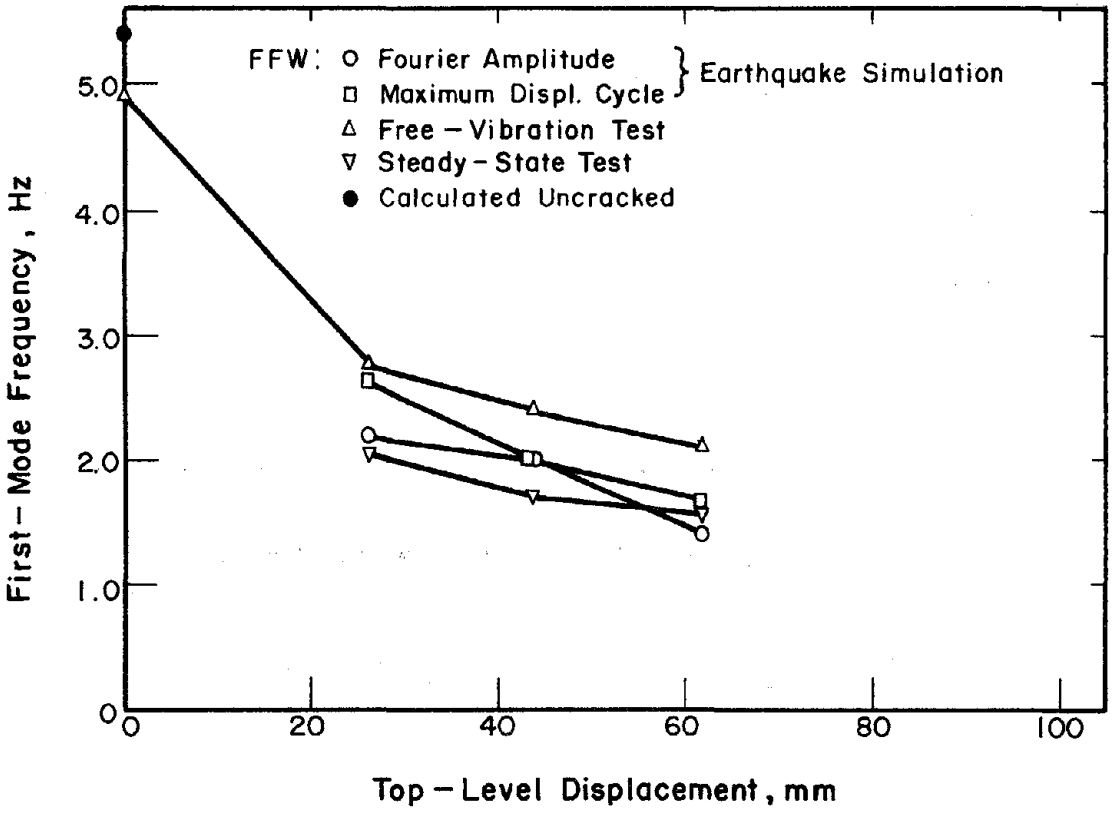


Fig. 5.17 (contd.) Variation of Apparent Fundamental Frequencies with Maximum Previous Top-Level Displacement

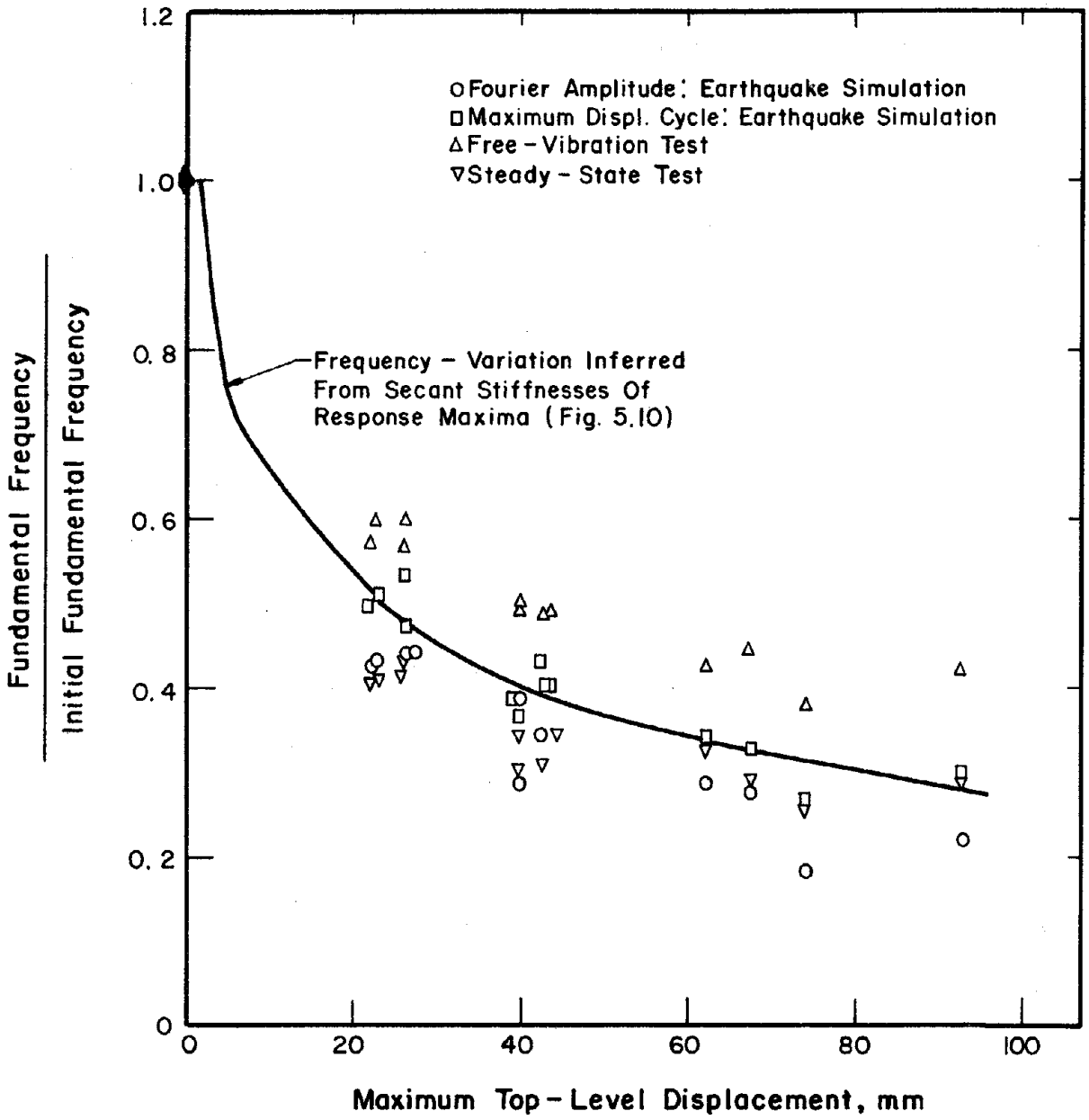


Fig. 5.18 Comparison of Apparent Fundamental Frequency Variation with Variation Inferred from Measured Stiffness

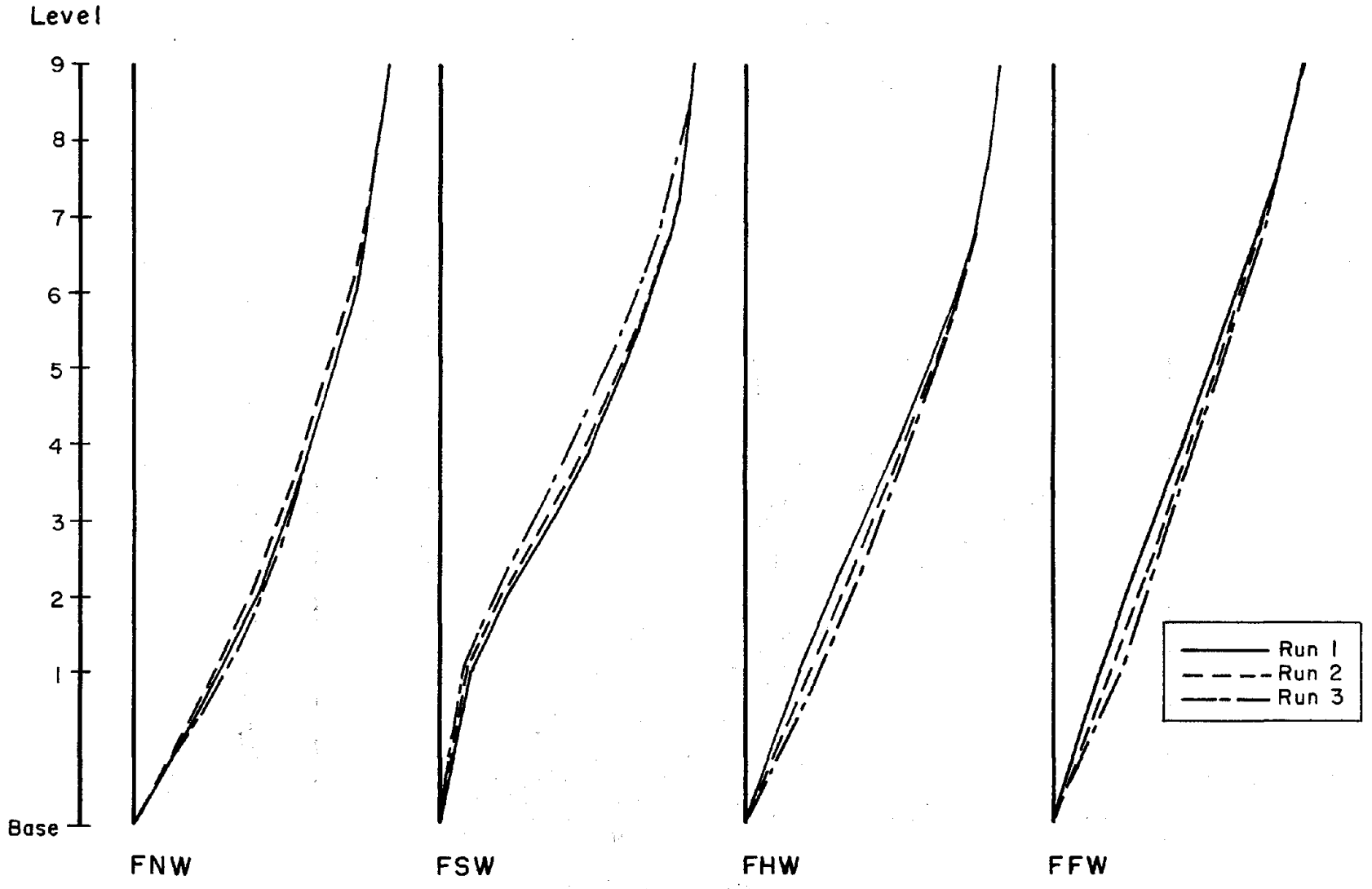


Fig. 5.19 Displaced Shapes Determined from Double-Amplitude Displacements

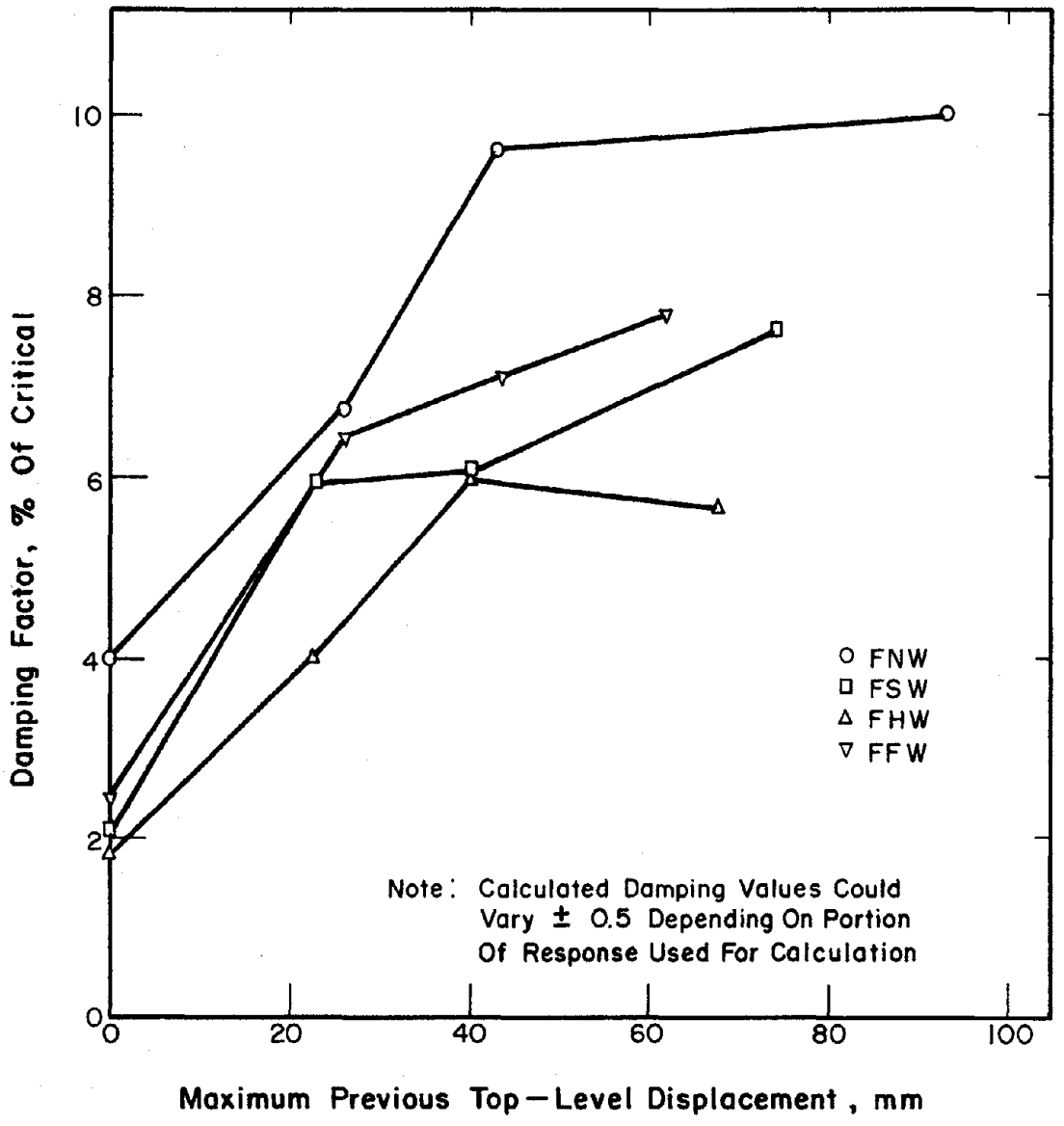


Fig. 5.20 Comparison of Apparent First-Mode Damping Factors Estimated from Free-Vibration Tests

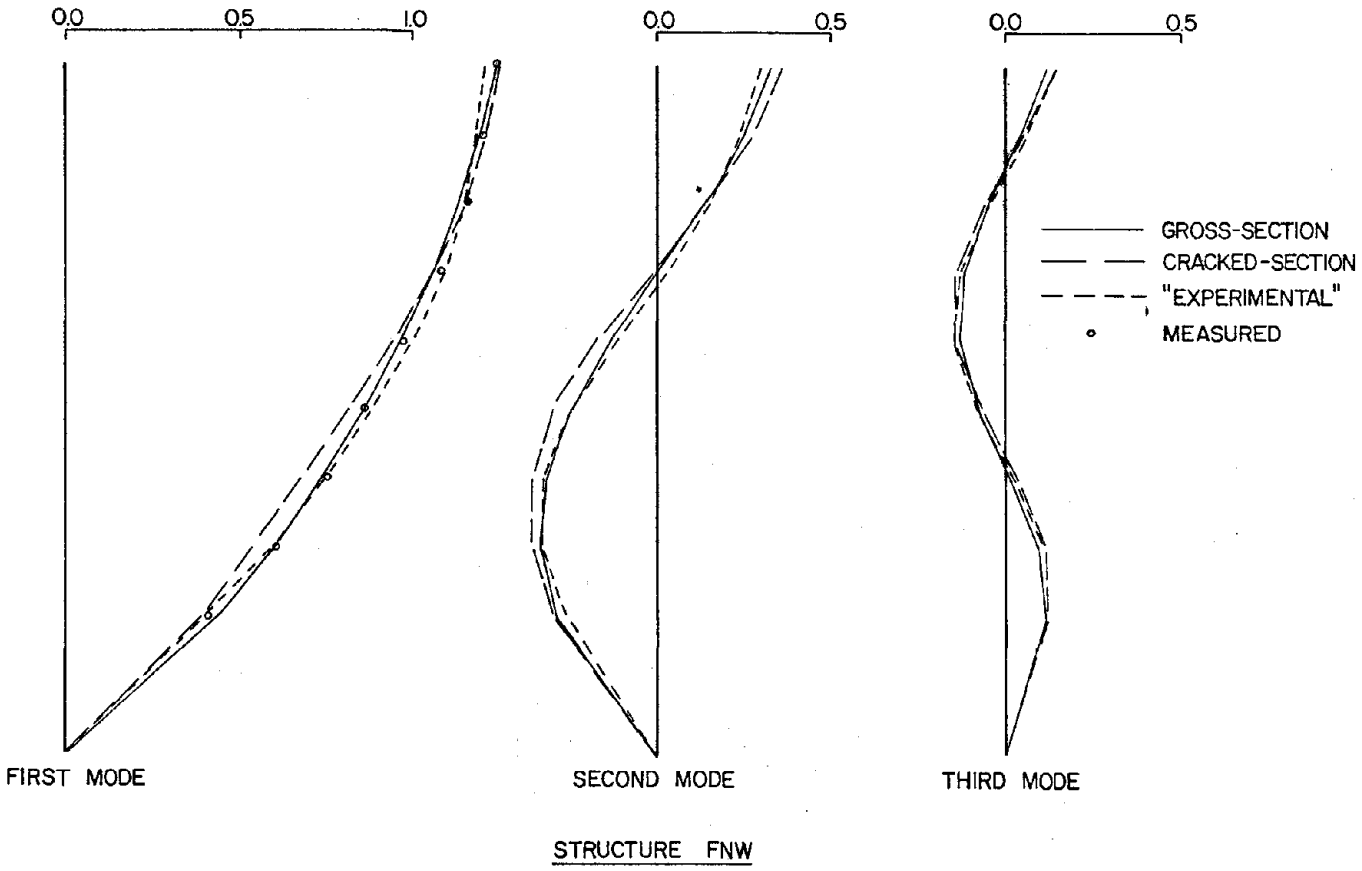


Fig. 6.1 Comparison of Calculated and Measured Mode Shapes

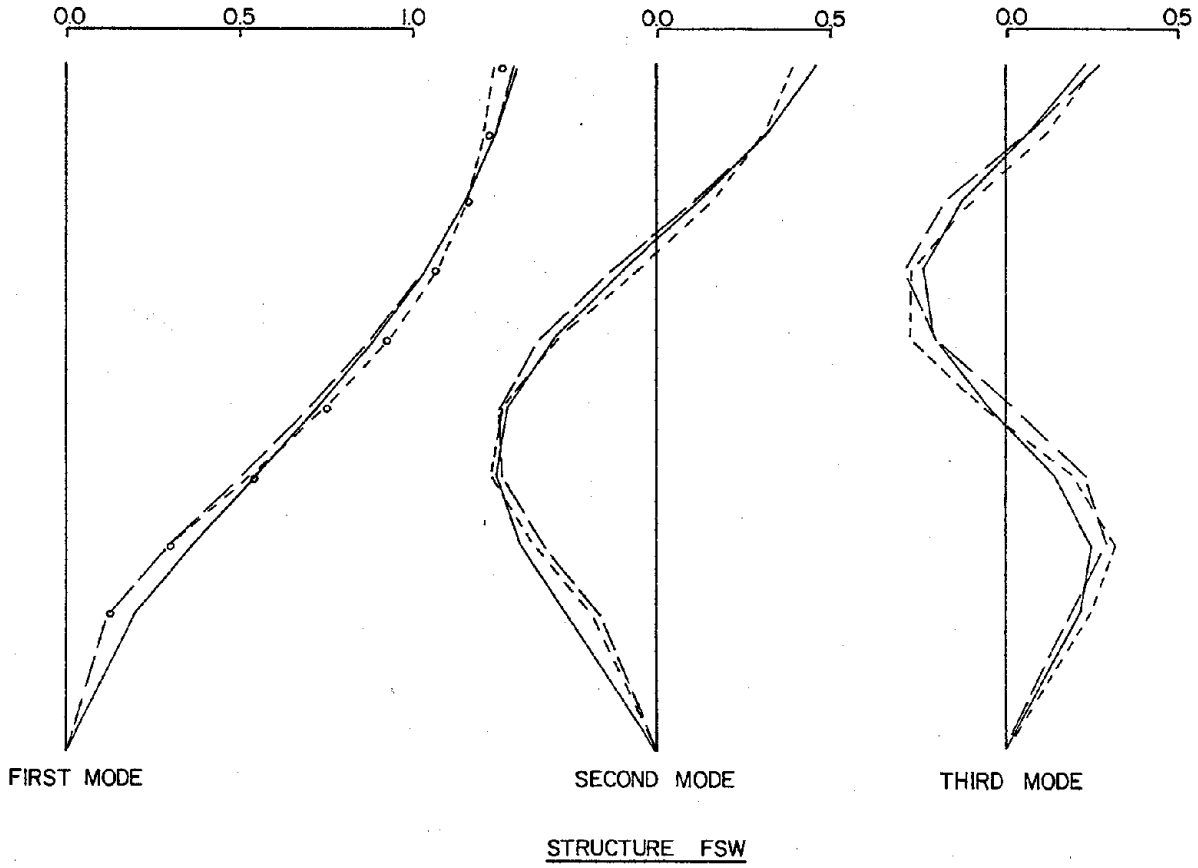


Fig. 6.1 (contd.) Comparison of Calculated and Measured Mode Shapes

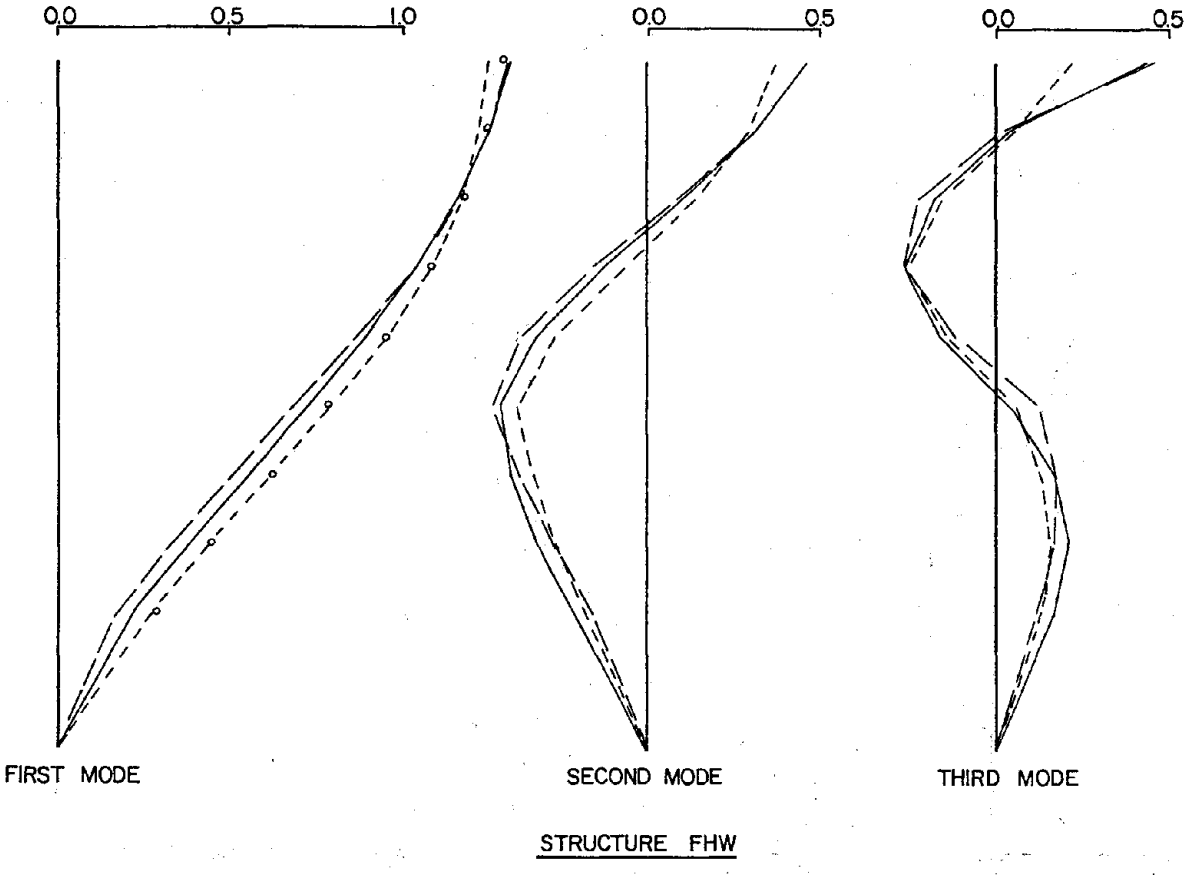


Fig. 6.1 (contd.) Comparison of Calculated and Measured Mode Shapes

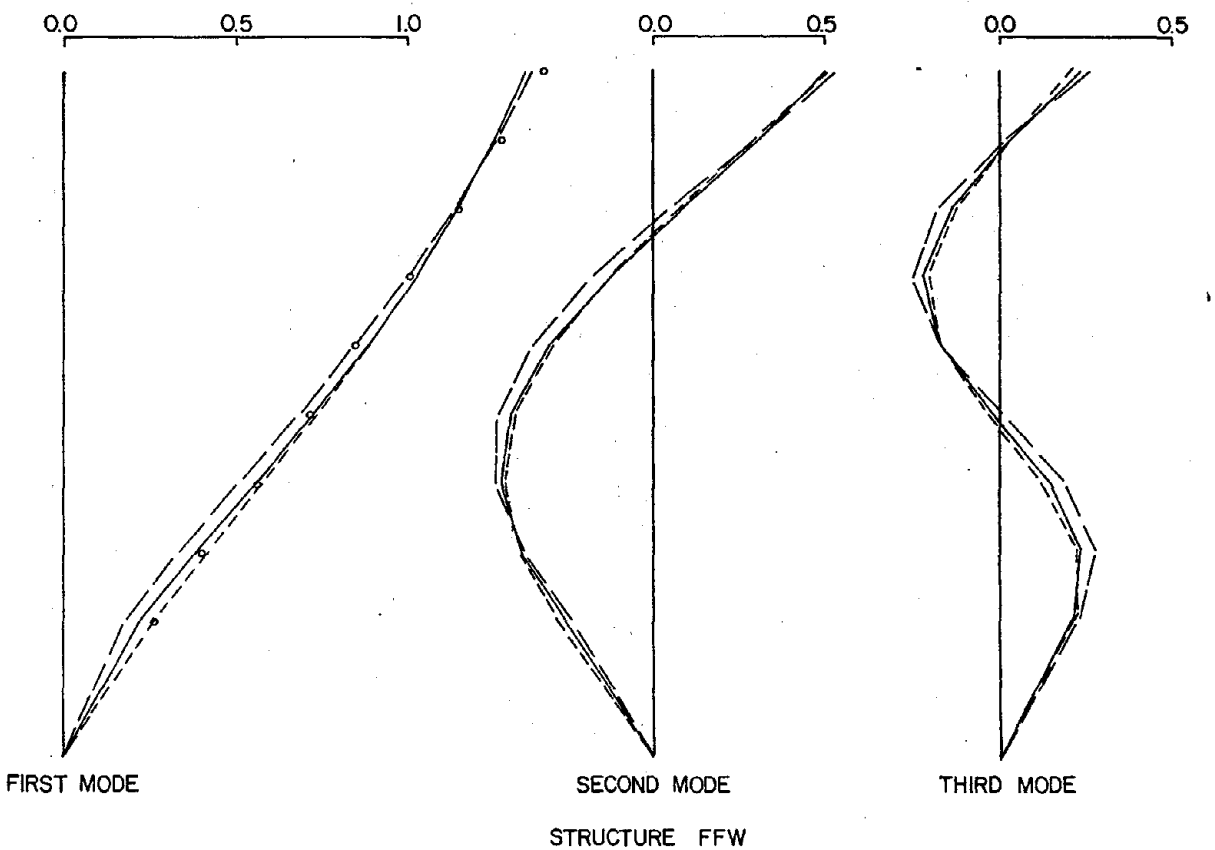


Fig. 6.1 (contd.) Comparison of Calculated and Measured Mode Shapes

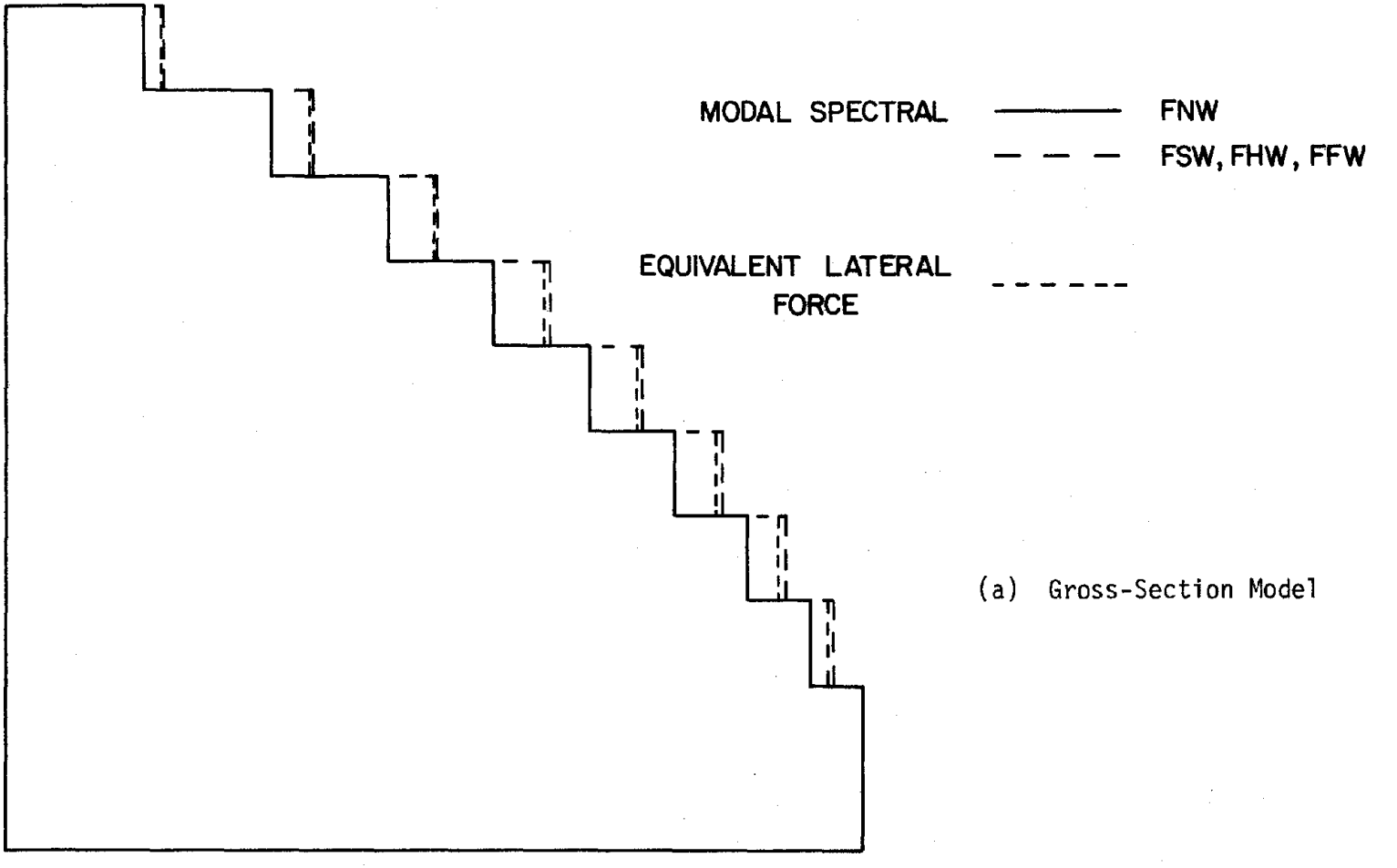


Fig. 6.2 Comparison of Modal-Spectral and Equivalent Static Force Story Shears

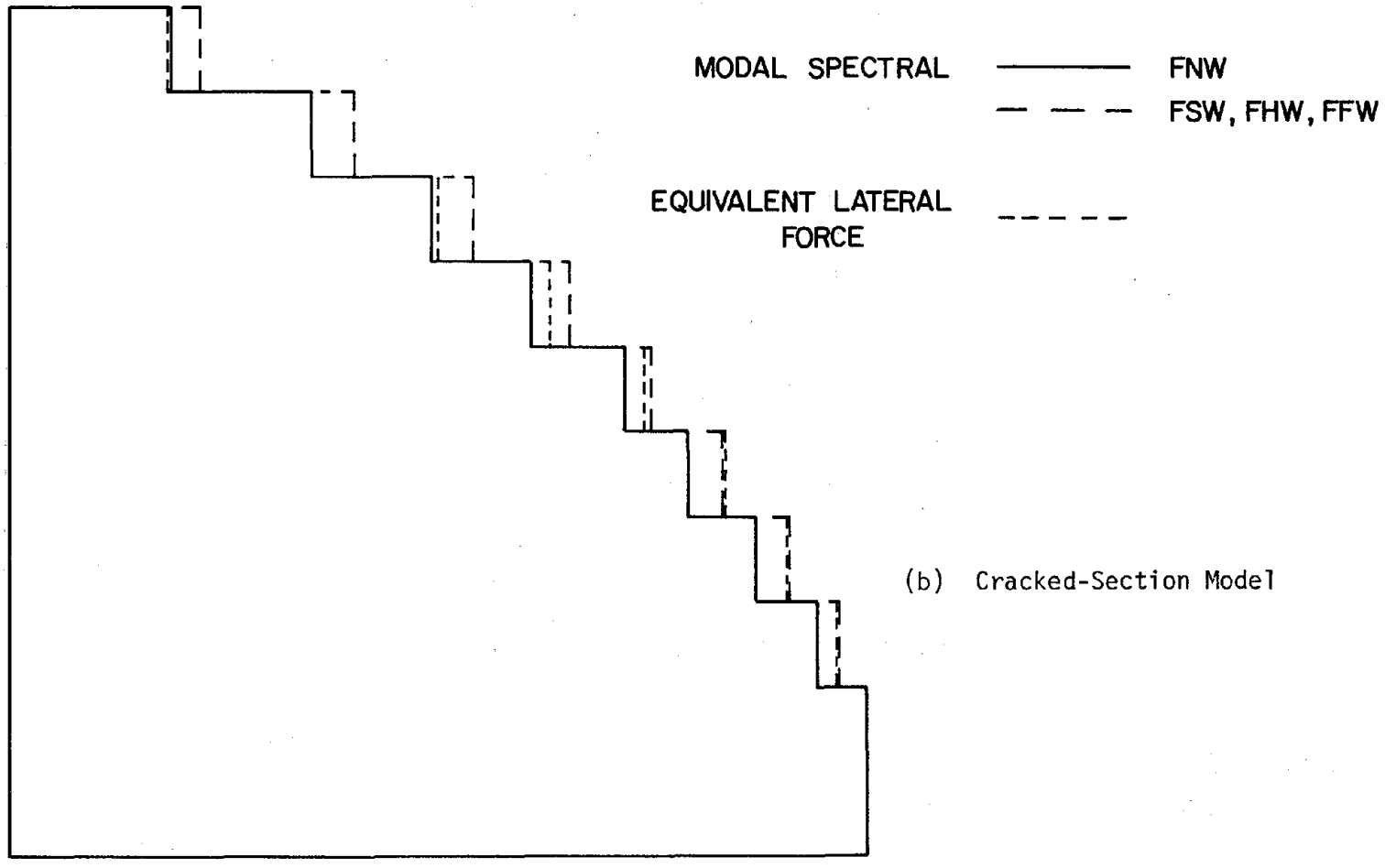


Fig. 6.2 (contd.) Comparison of Modal-Spectral and Equivalent Static Force Story Shears

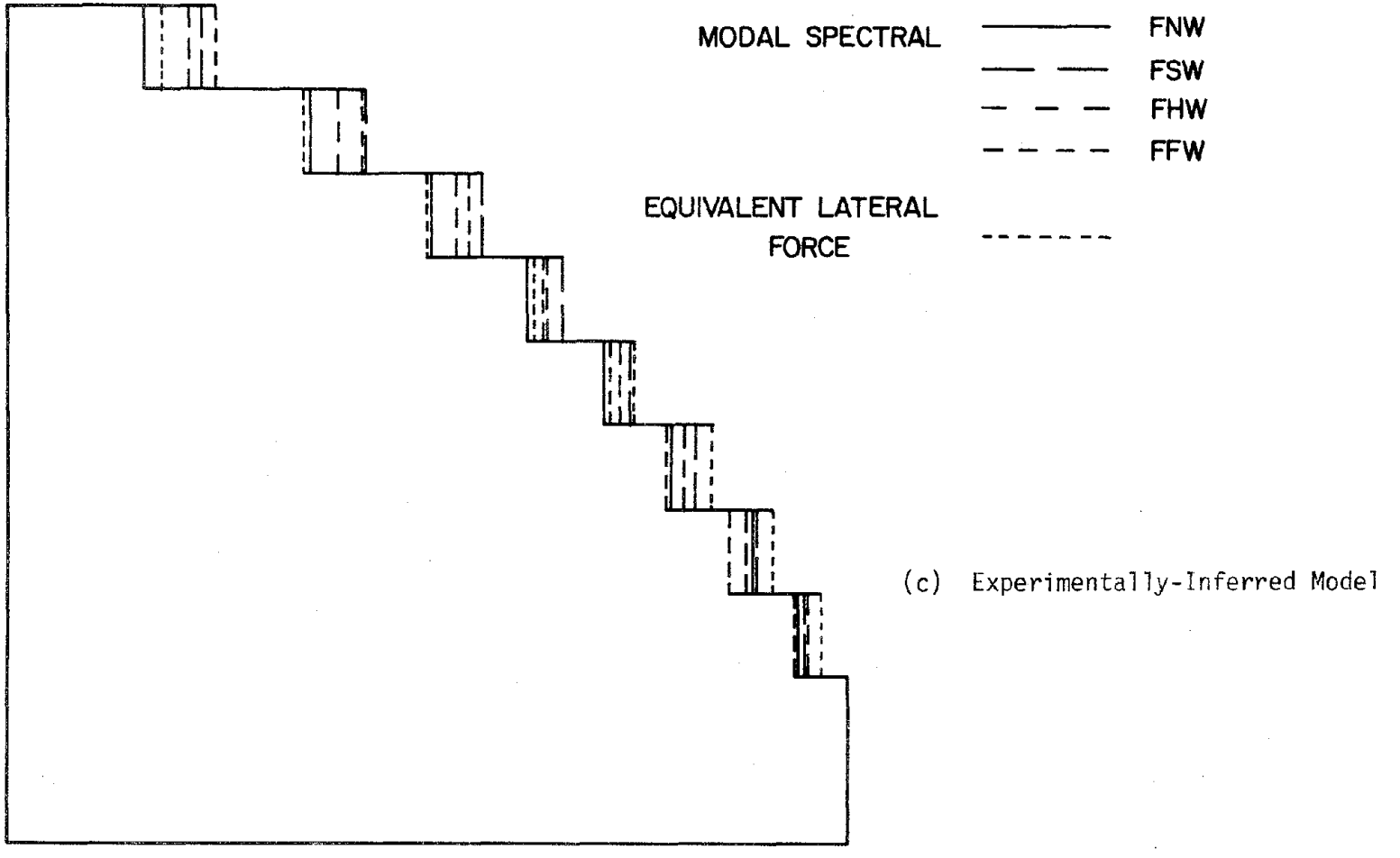


Fig. 6.2 (contd.) Comparison of Modal-Spectral and Equivalent Static Force Story Shears

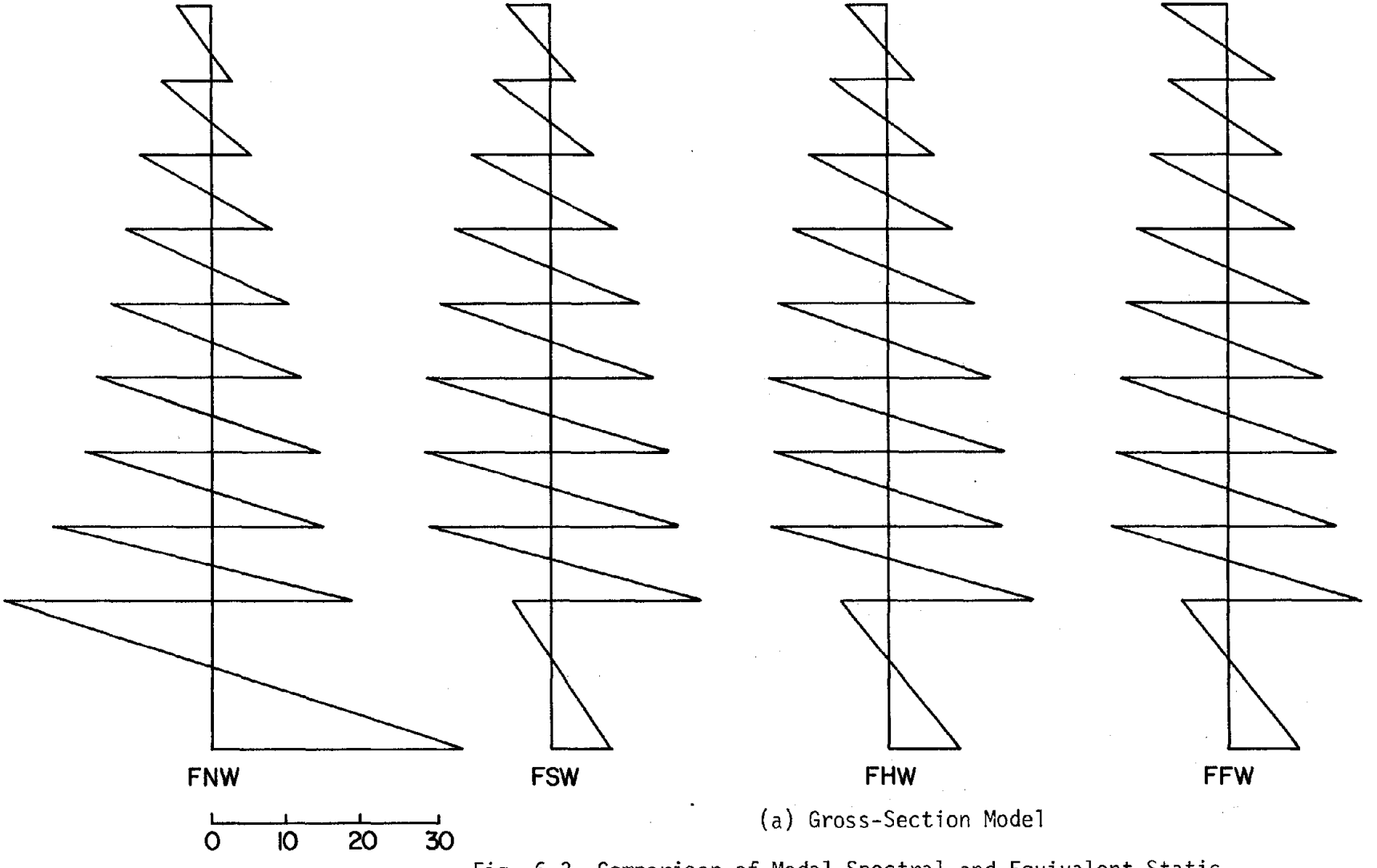


(a) Gross-Section Model

Fig. 6.3 Comparison of Modal-Spectral and Equivalent Static Force Interior Column Moments

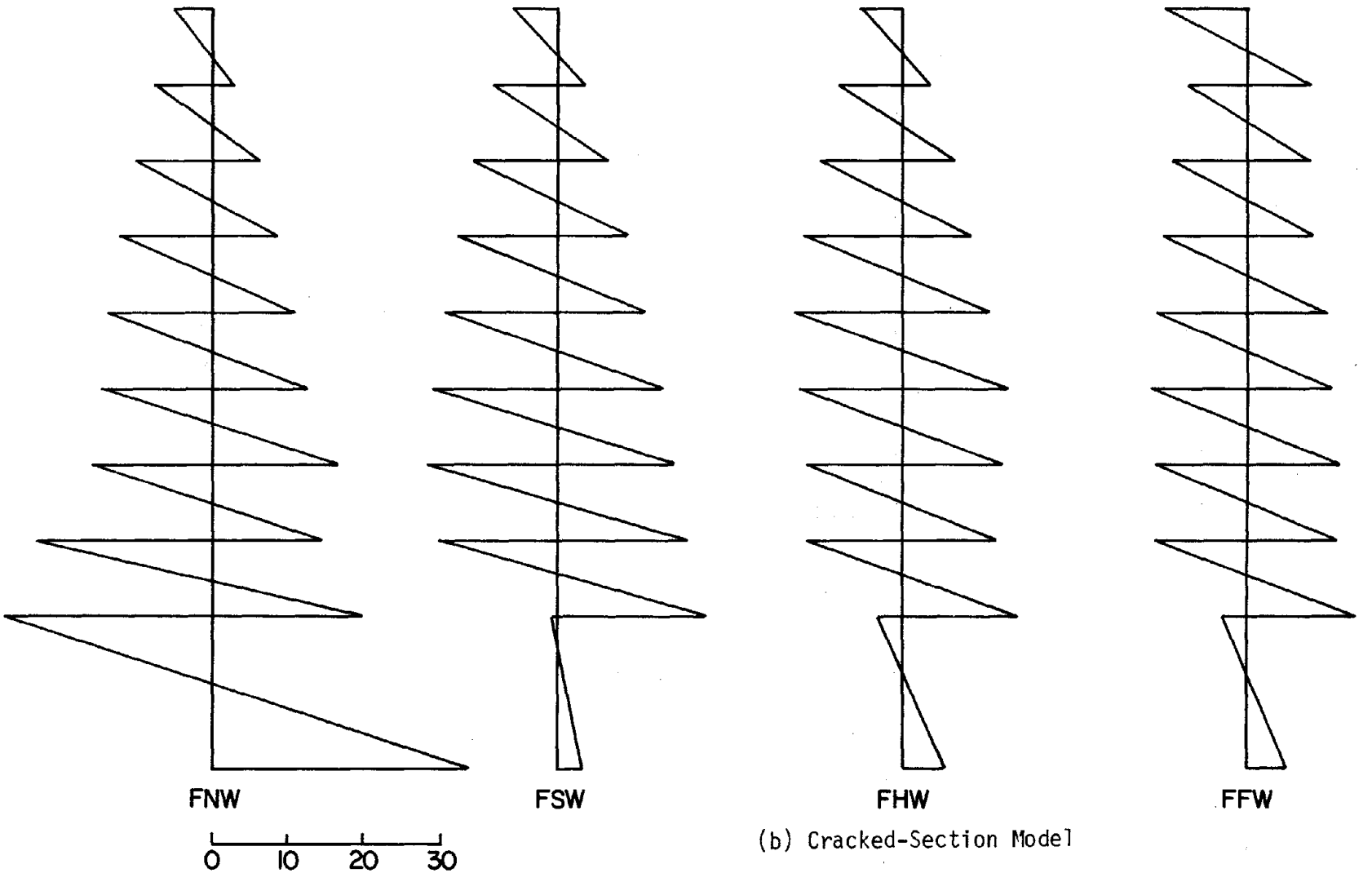


(b) Cracked-Section Model

Fig. 6.3 (contd.) Comparison of Modal-Spectral and Equivalent Static Force Interior Column Moments

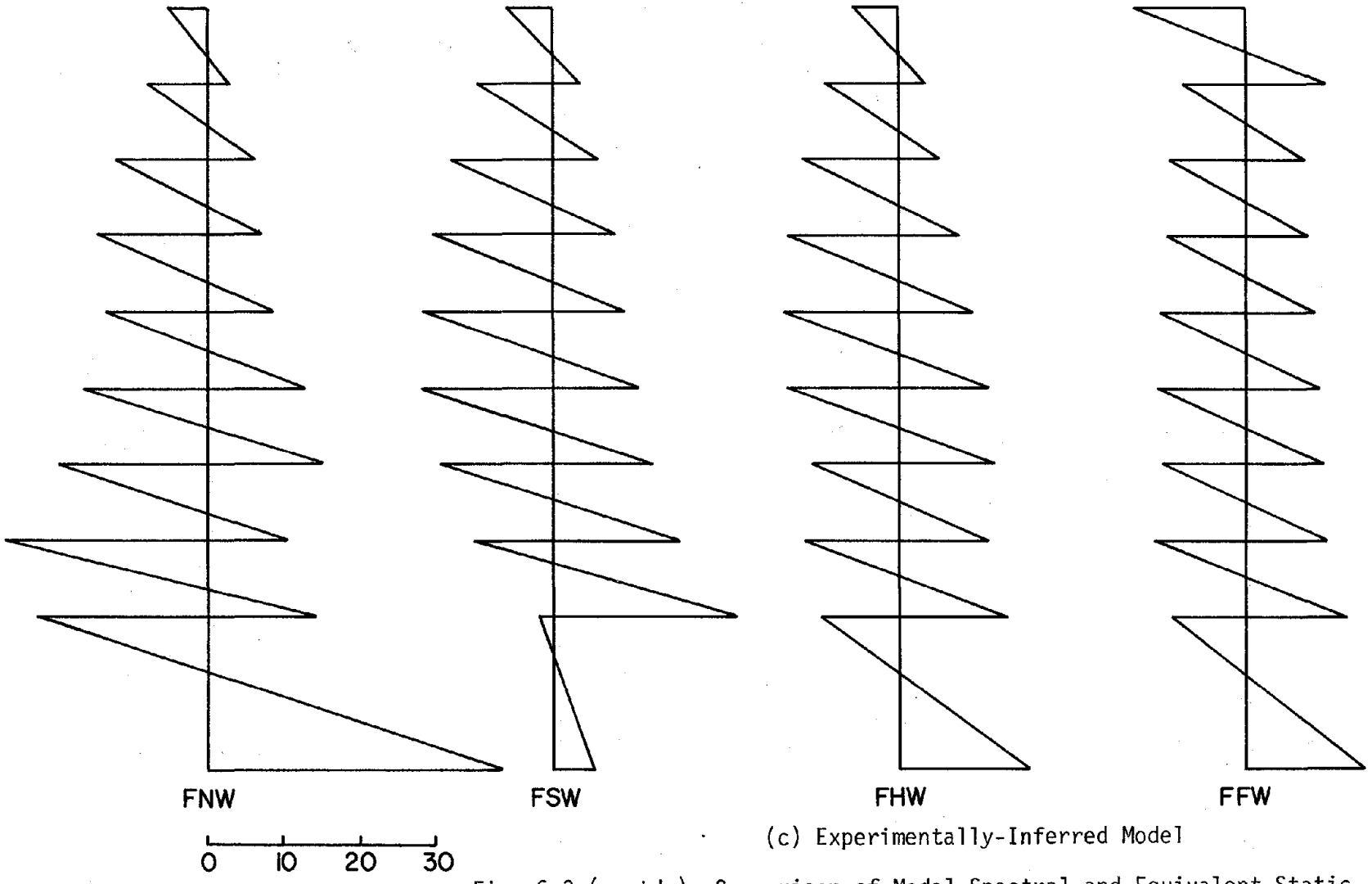


(c) Experimentally-Inferred Model

Fig. 6.3 (contd.) Comparison of Modal-Spectral and Equivalent Static Force Interior Column Moments

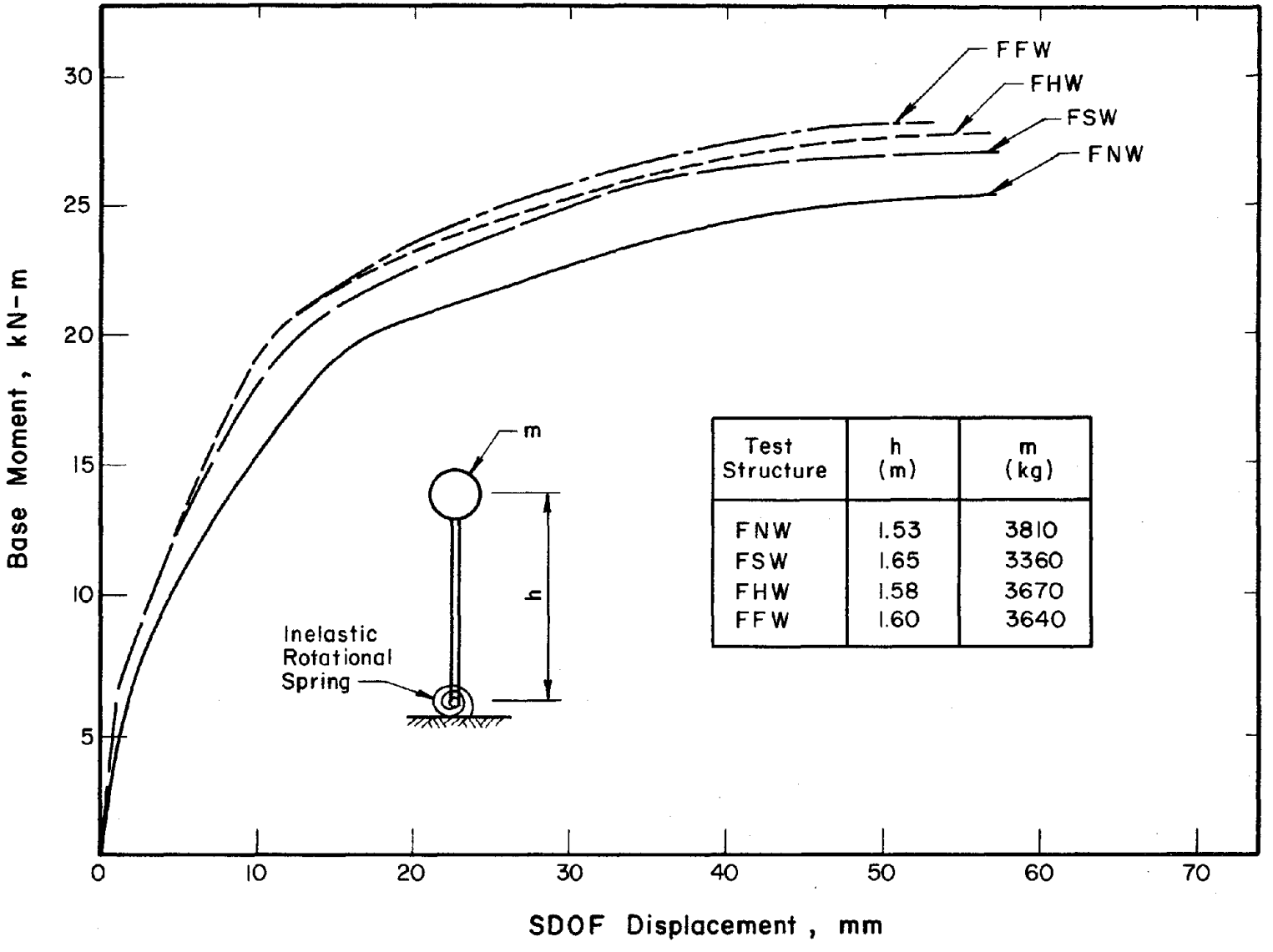


| Test Structure | h (m) | m (kg) |
|---|---|---|
| FNW | 1.53 | 3810 |
| FSW | 1.65 | 3360 |
| FHW | 1.58 | 3670 |
| FFW | 1.60 | 3640 |

Fig. 6.4 Stiffness Variation of Test Structures (a) Moment

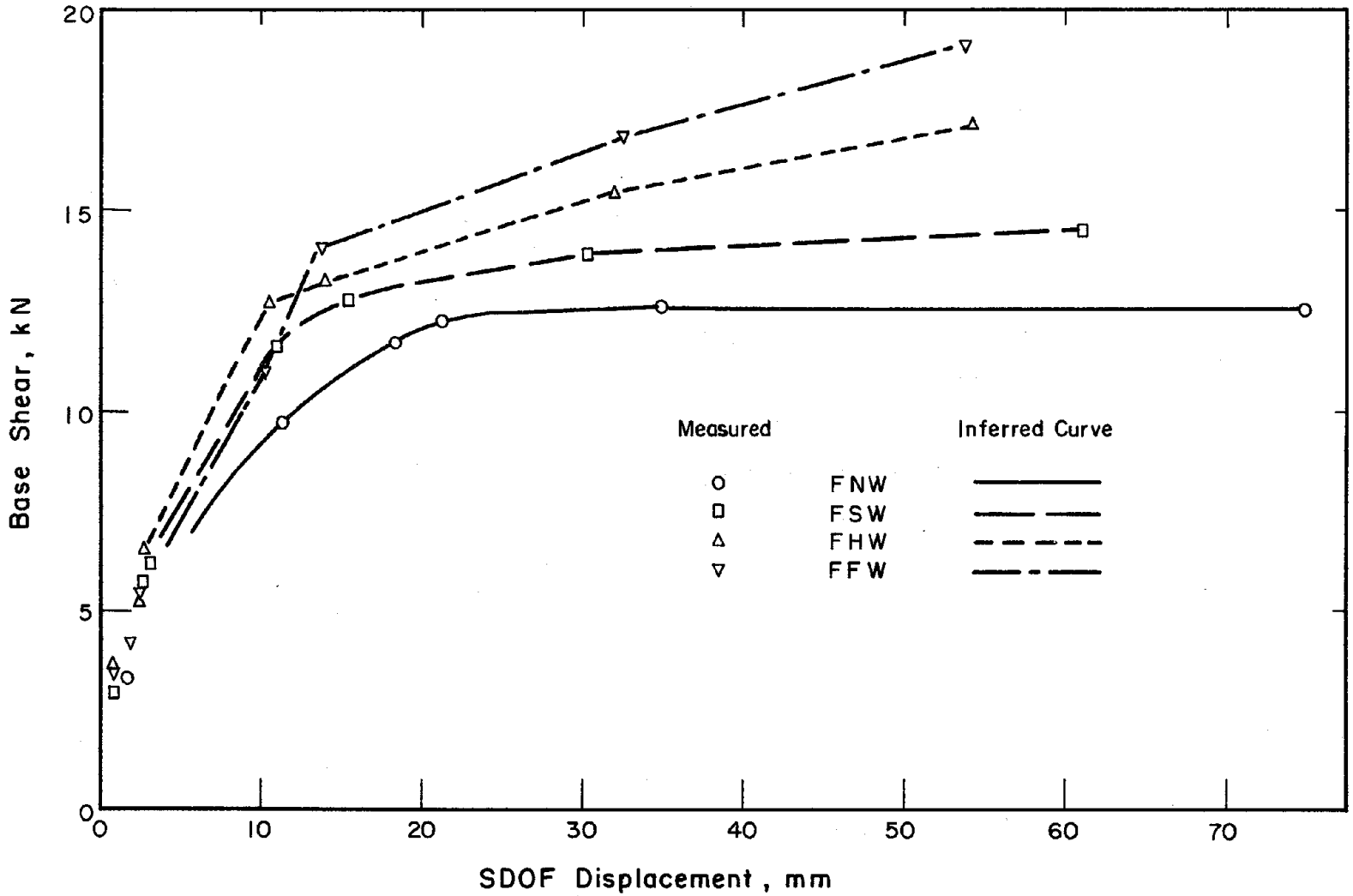


Fig. 6.4 (contd.) Stiffness Variation of Test Structures (b) Shear

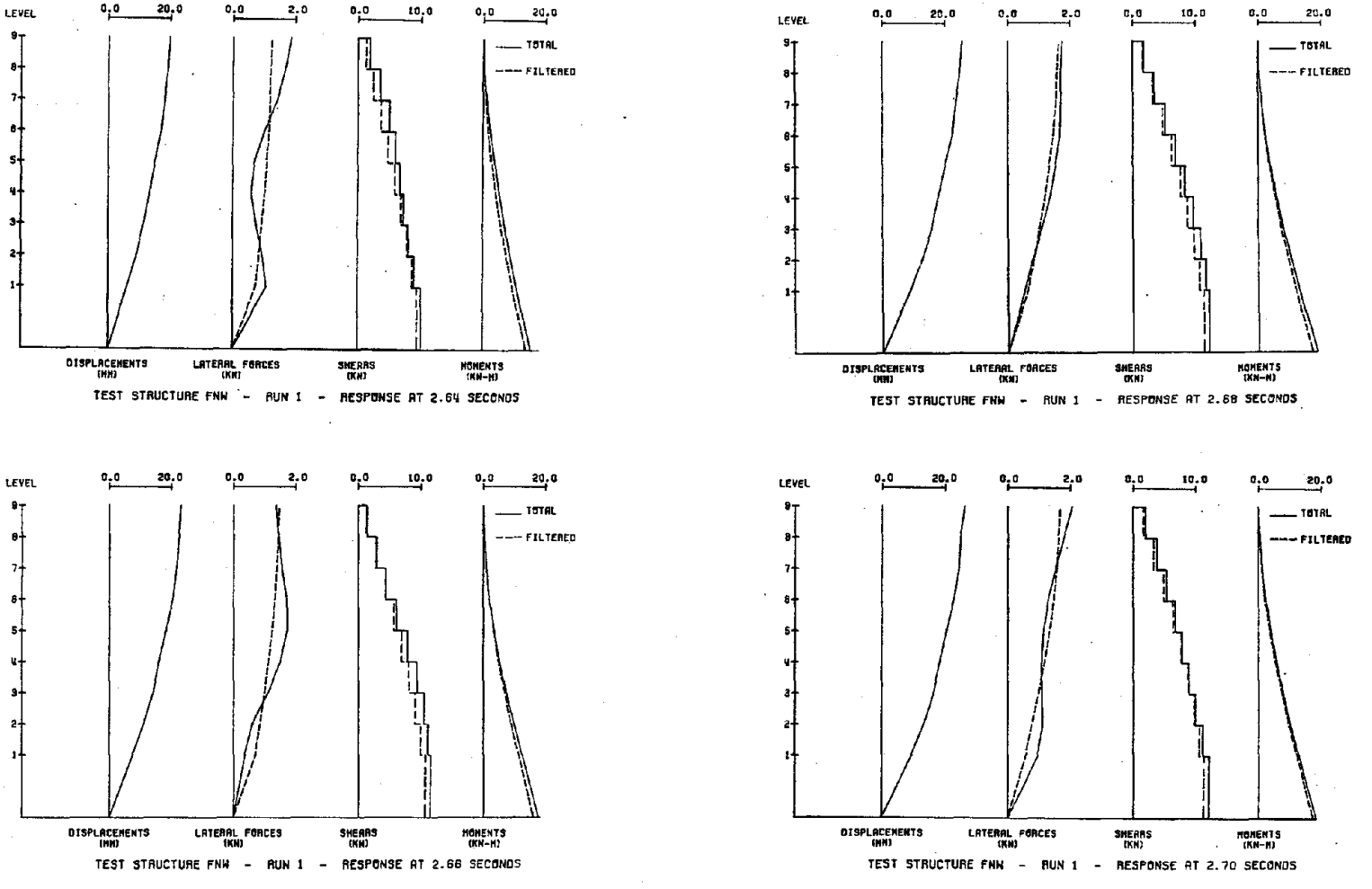


(a) First Test Run

Fig. 6.5 Loading Distribution Observed near Times of Maximum Response

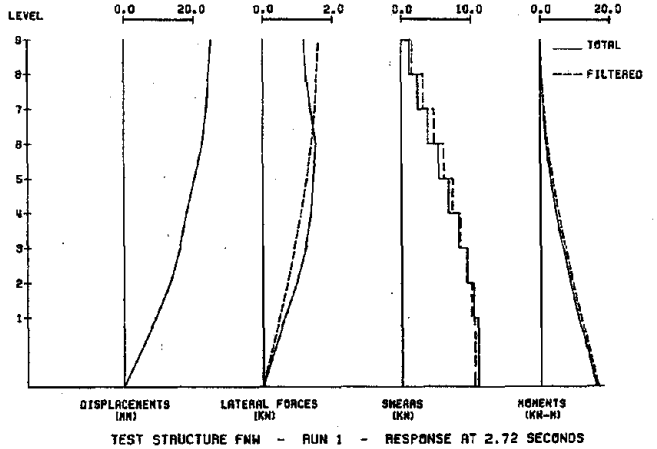


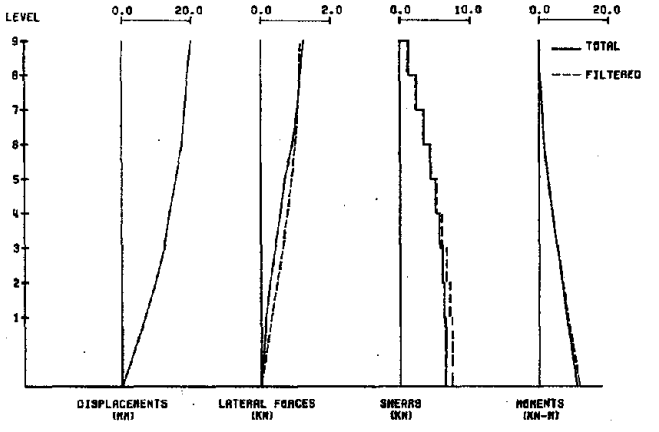


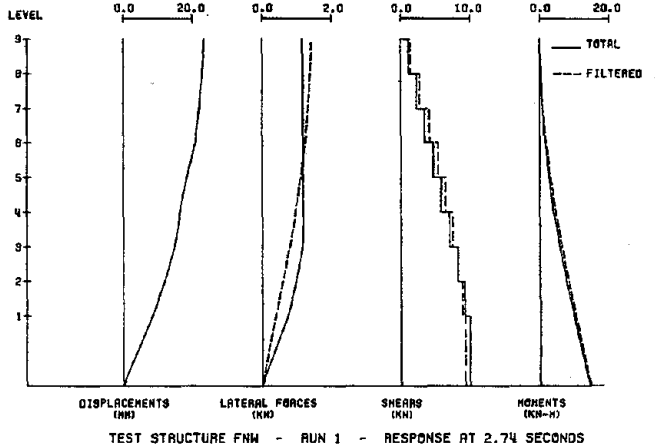


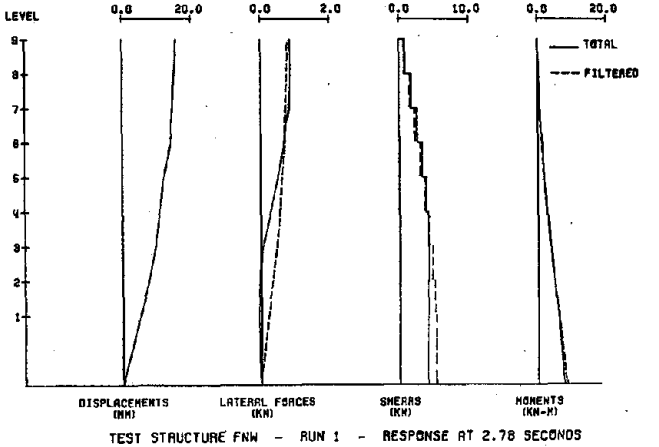


(a) First Test Run

Fig. 6.5 (contd.) Loading Distribution Observed near Times of Maximum Response

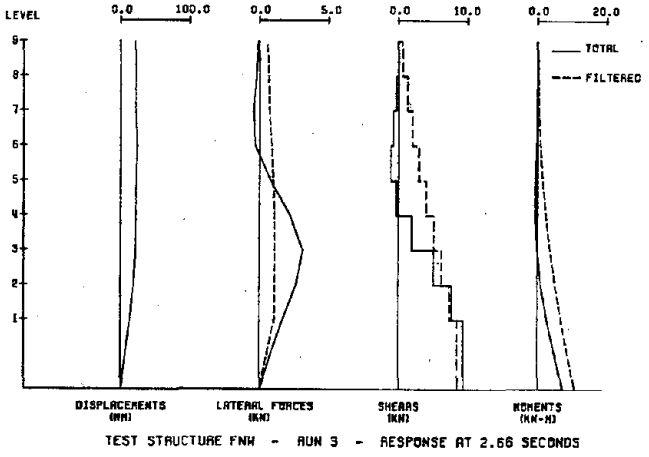


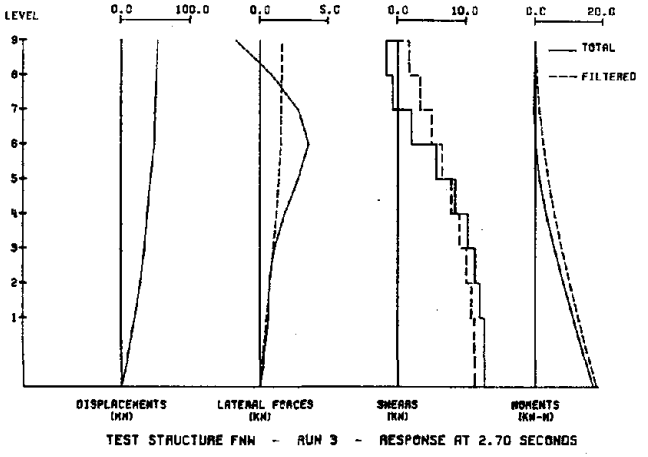


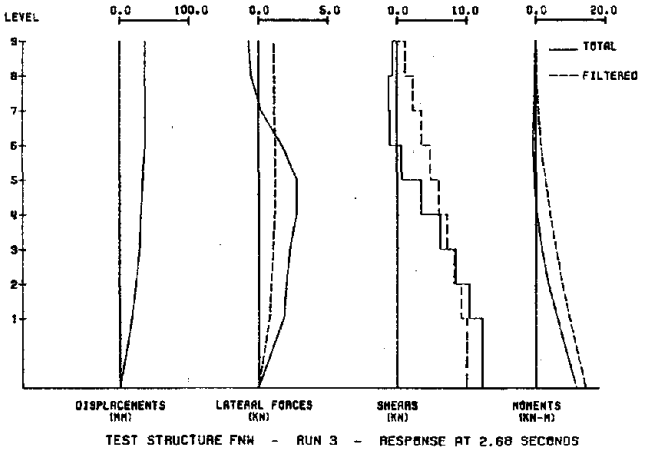


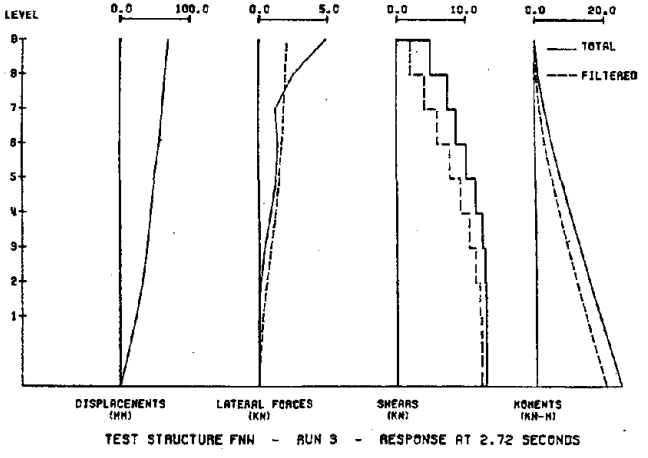


(b) Third Test Run

Fig. 6.5 (contd.) Loading Distribution Observed near Times of Maximum Response

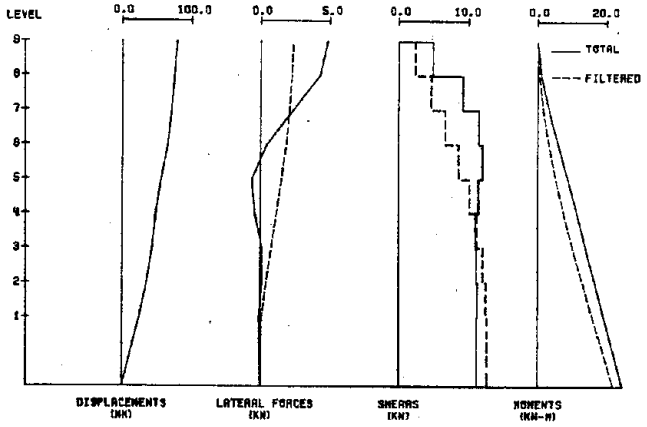


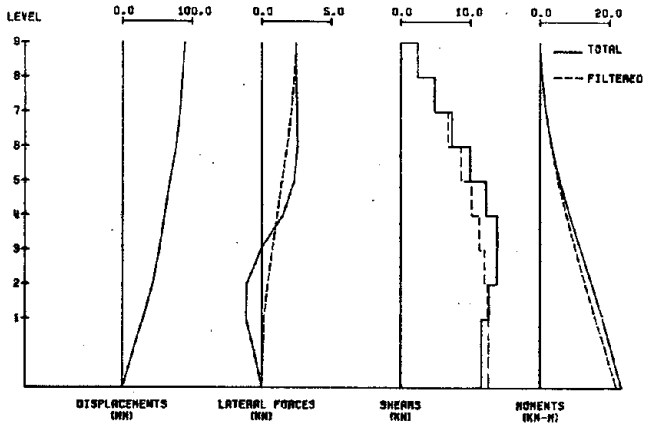


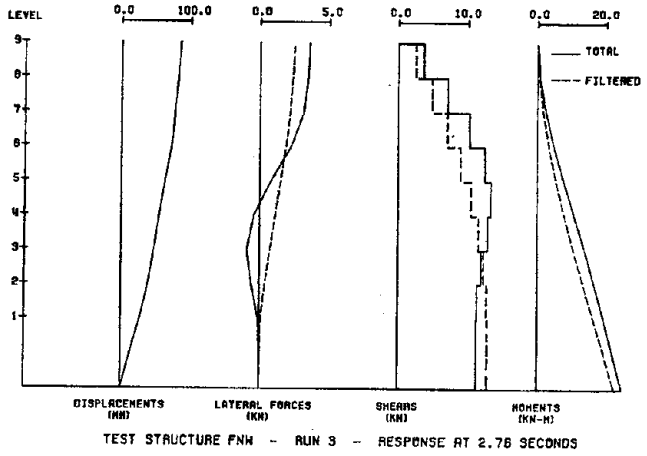


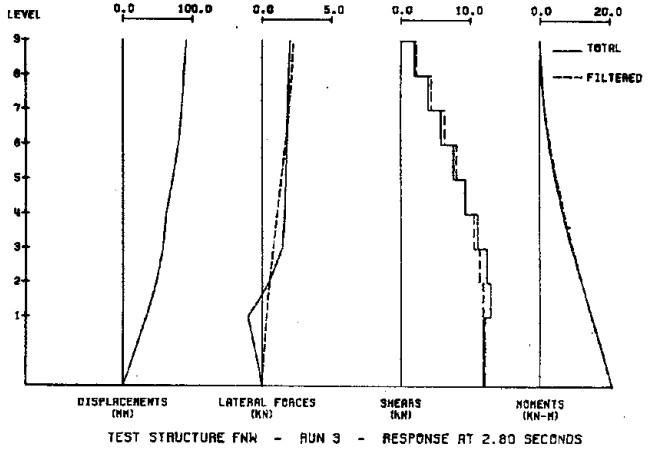


(b) Third Test Run

Fig. 6.5 (contd.) Loading Distribution Observed near Times of Maximum Response

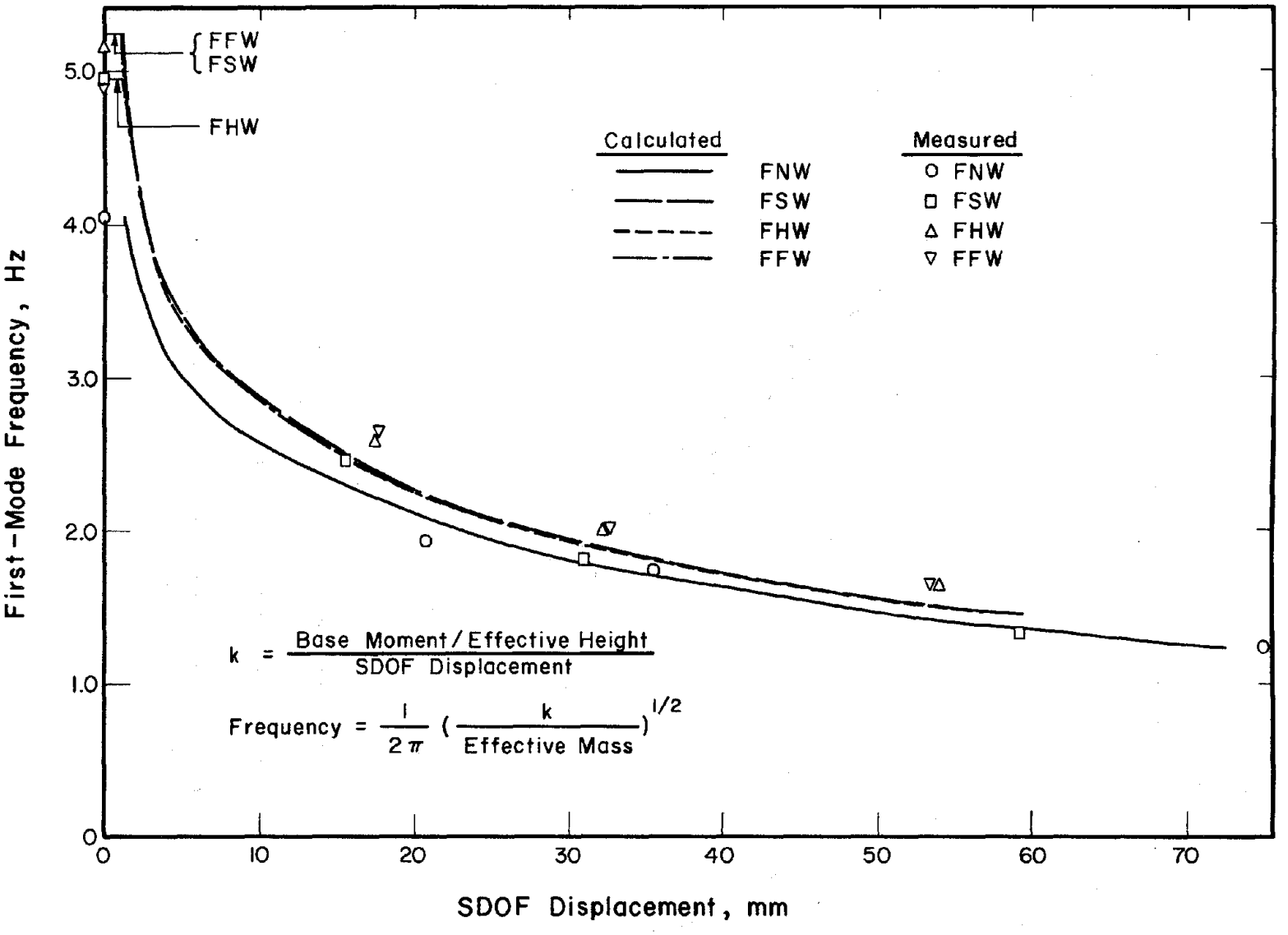


Fig. 6.6 Comparison of Measured and Inferred Relation Between Frequency and Displacement

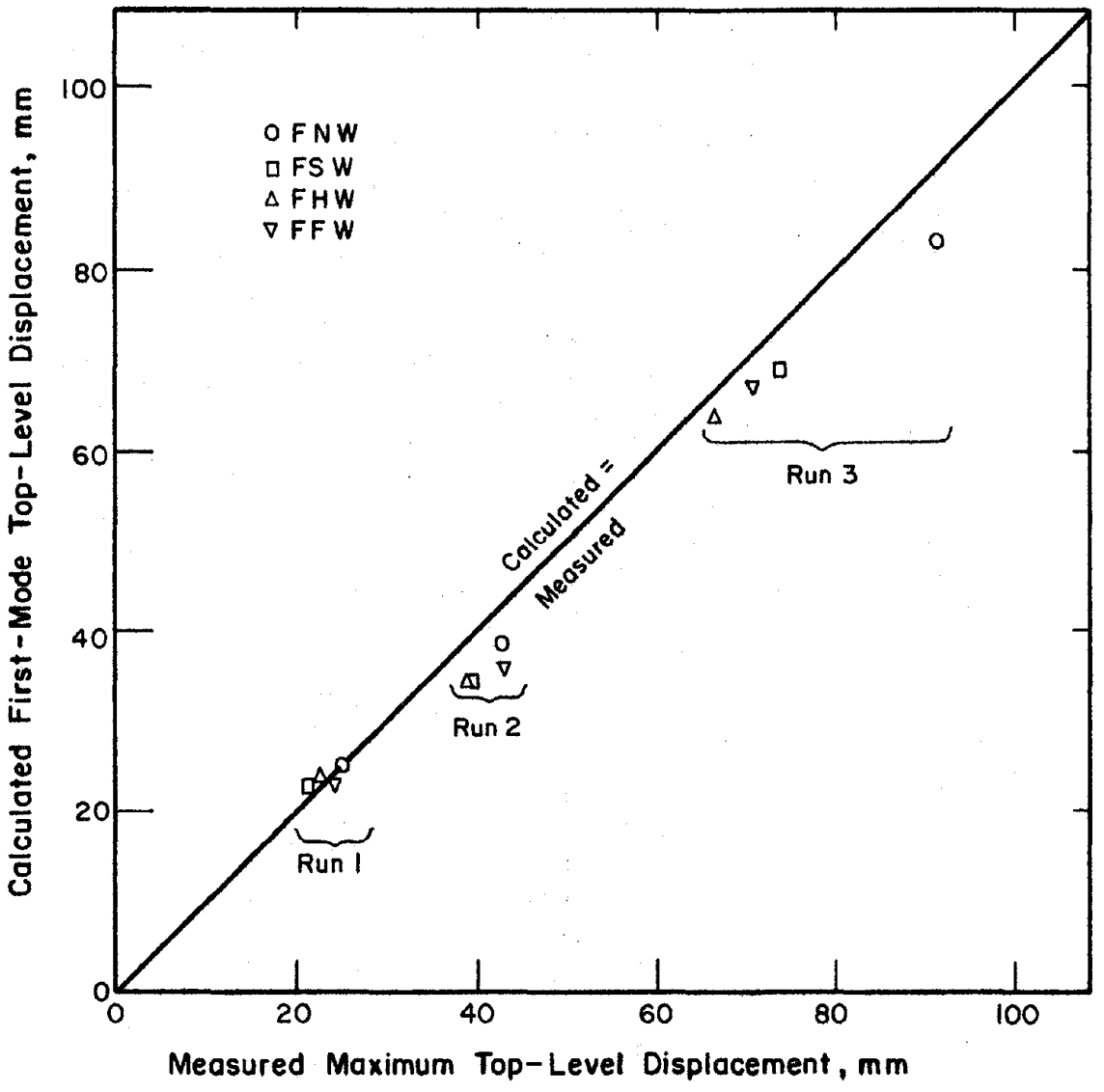


Fig. 6.7 Comparison of Measured and Calculated Response Using Linear Response Spectra and Calculated Damping Factors

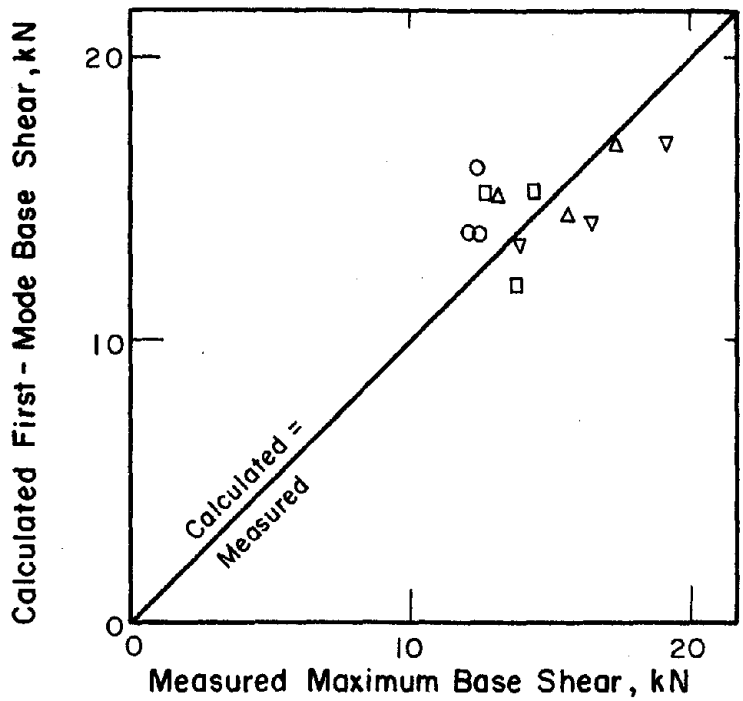


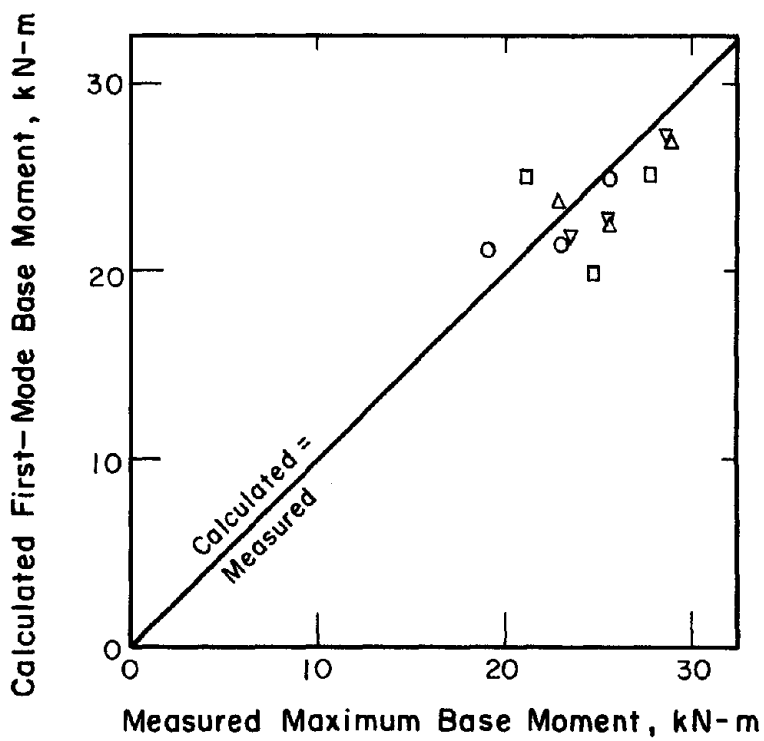


Fig. 6.7 (contd.) Comparison of Measured and Calculated Responses Using Linear Response Spectra and Calculated Damping Factors

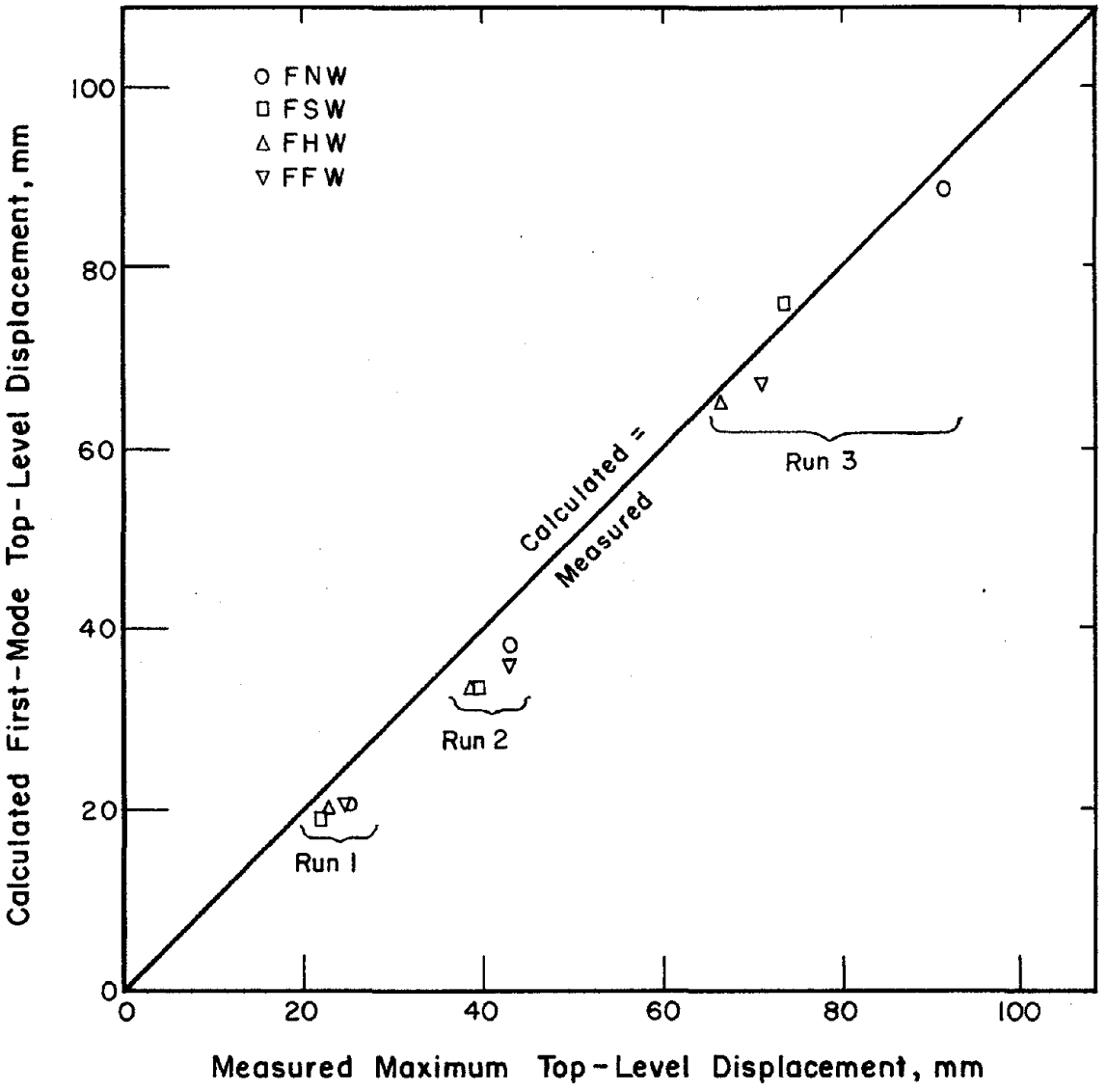


Fig. 6.8 Comparison of Measured and Calculated Responses Using Linear Response Spectra and Ten Percent Damping

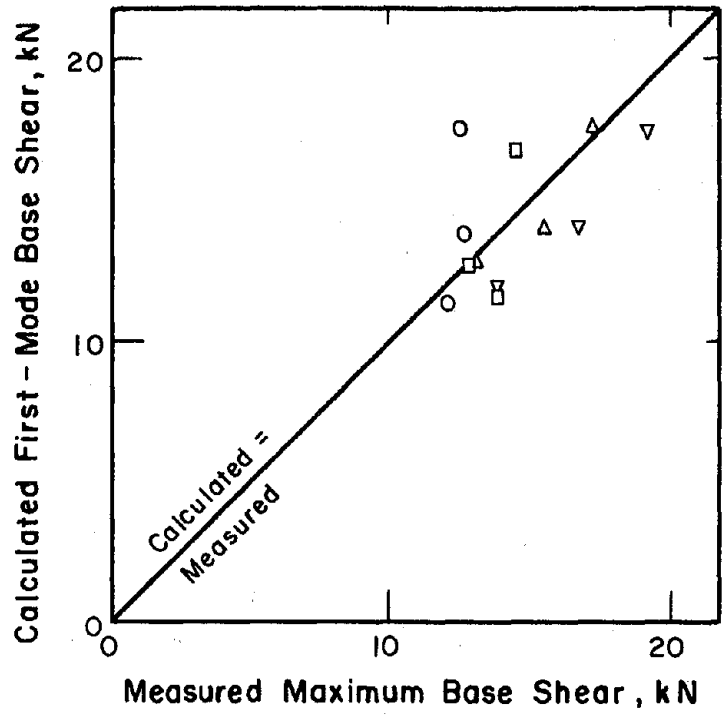


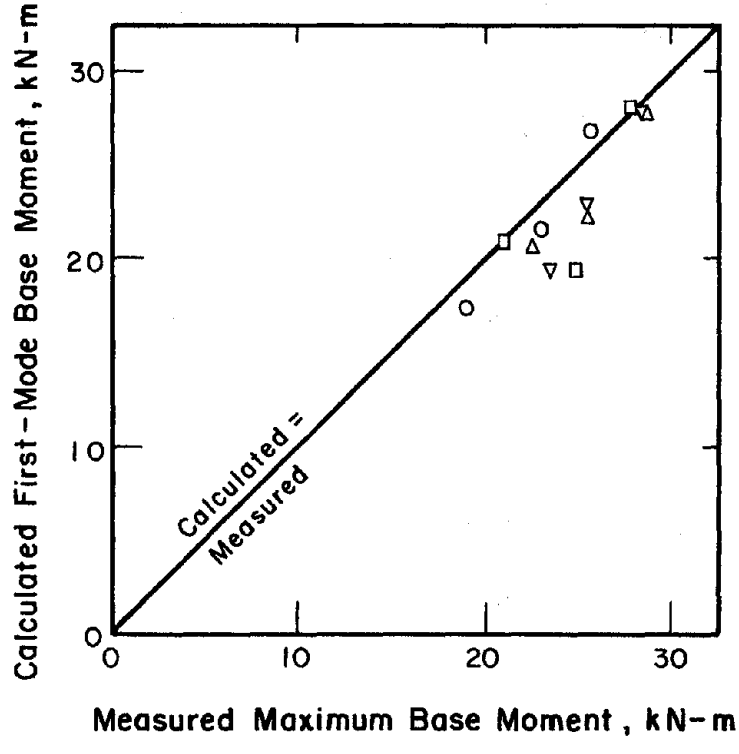


Fig. 6.8 (contd.) Comparison of Measured and Calculated Responses Using Linear Response Spectra and Ten Percent Damping

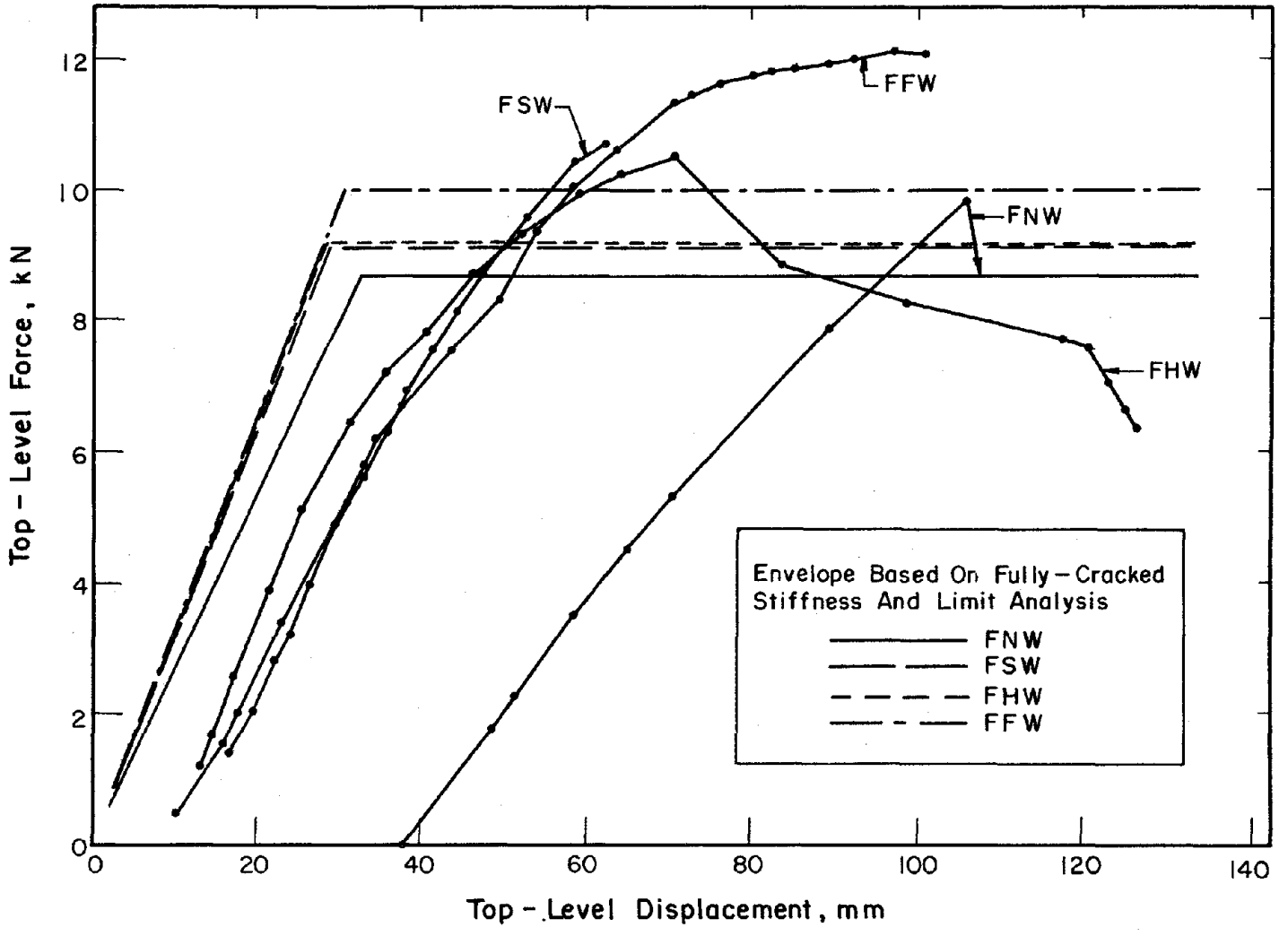


Fig. 7.1 Comparison of Measured and Calculated Strengths for a Top-Level Force

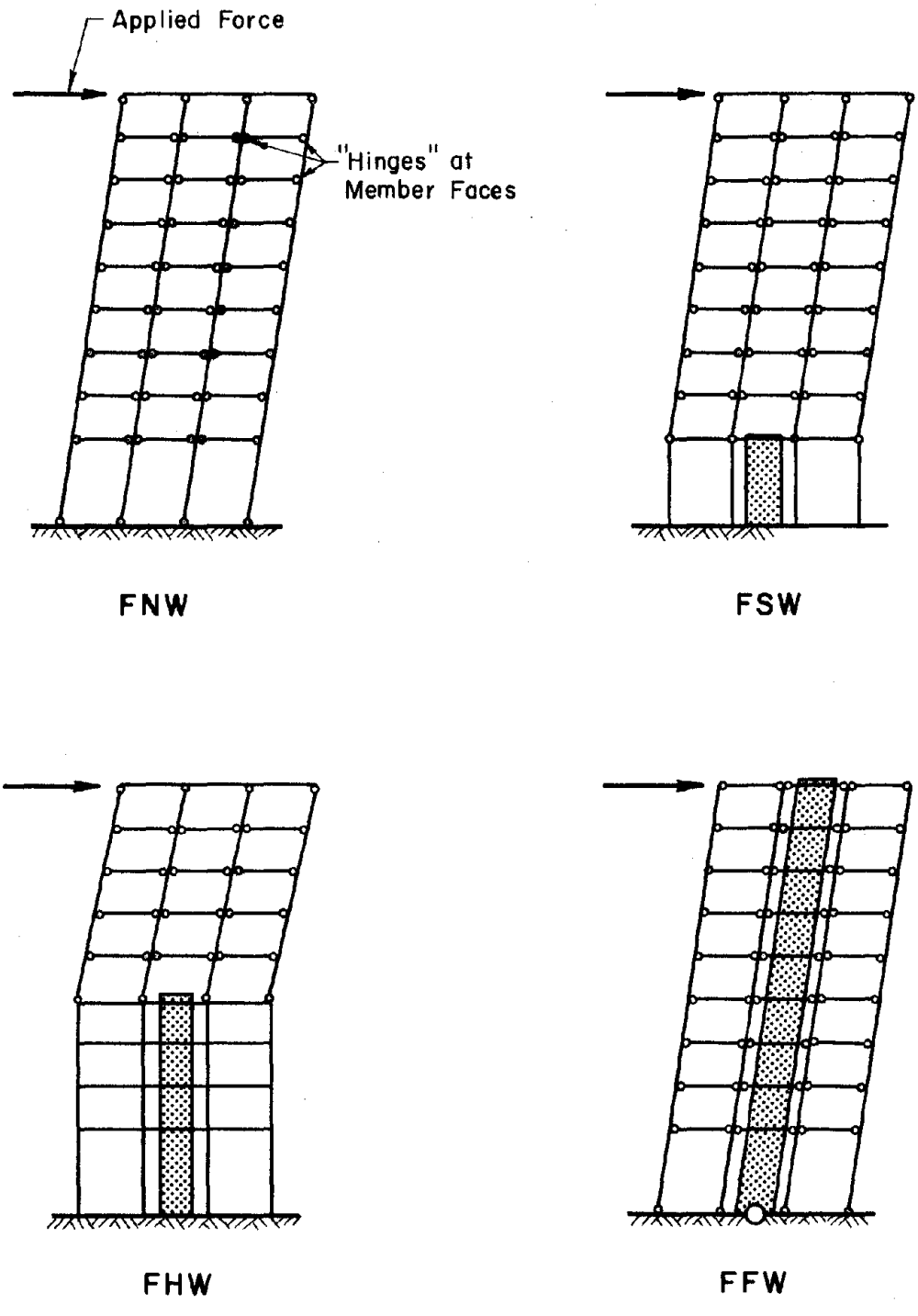


Fig. 7.2 Calculated Collapse Mechanisms for a Top-Level Force

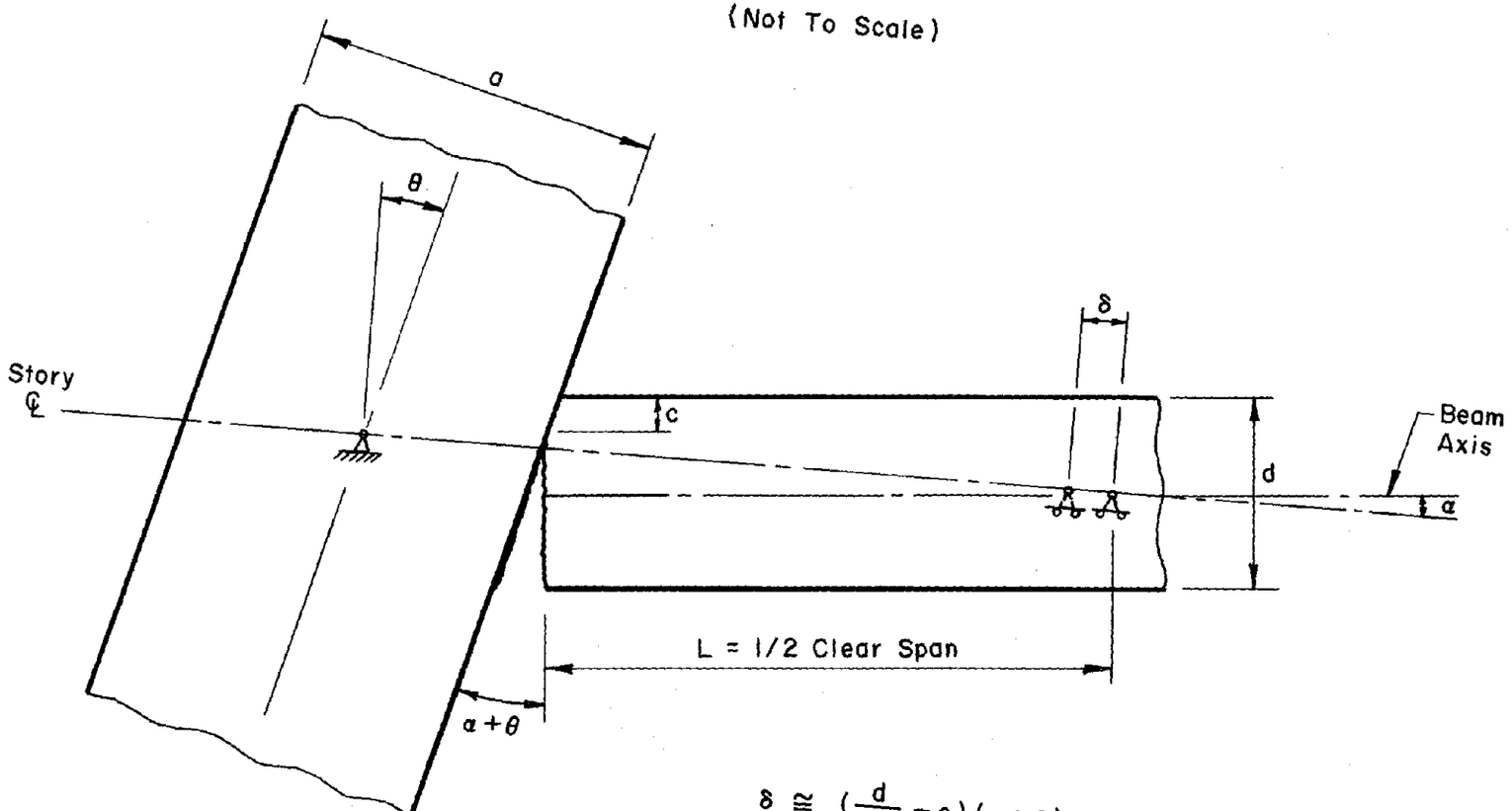


$$\delta \cong \left(\frac{d}{2} - c\right)(\alpha + \theta)$$

$$\cong \left(\frac{d}{2} - c\right)\left(\frac{L + a/2}{L}\right)\theta$$

Fig. 7.3 Model Used to Estimate Frame Joint Separations due to Column Rotation

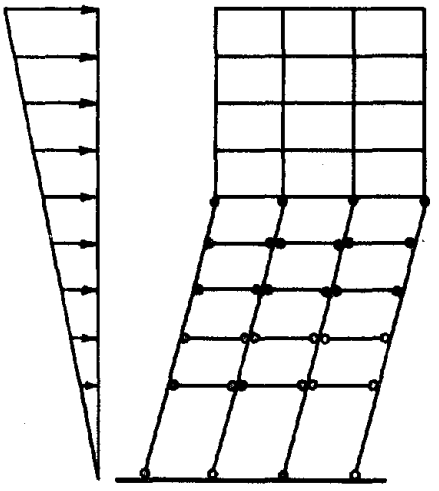

Base Shear = 11 kN
Base Moment = 18 kN-m

FNW

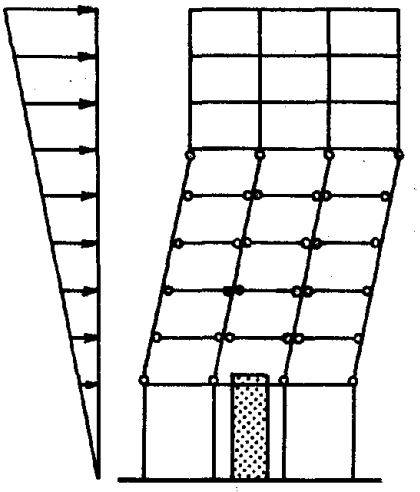

Base Shear = 12 kN
Base Moment = 19 kN-m

FSW

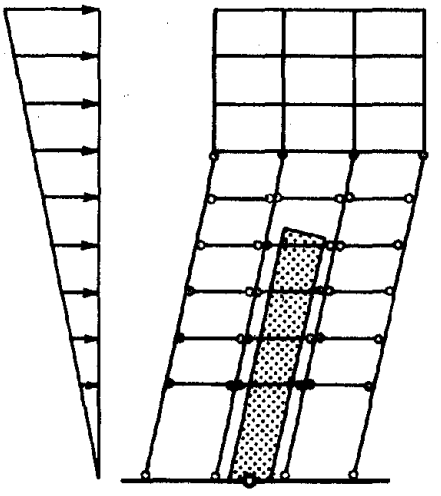

Base Shear = 13 kN
Base Moment = 20 kN-m

FHW

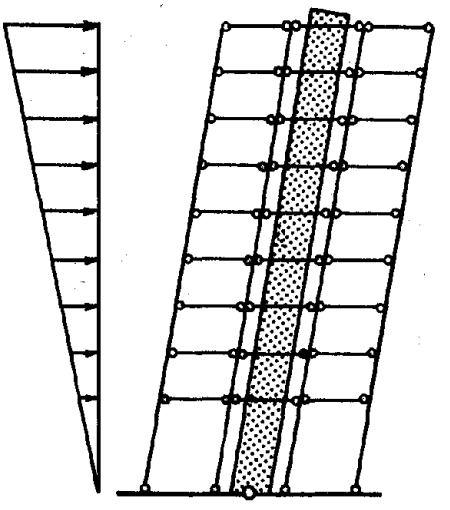

Base Shear = 14 kN
Base Moment = 23 kN-m

FFW

Fig. 7.4 Calculated Collapse Mechanisms for a Linear Loading Distribution

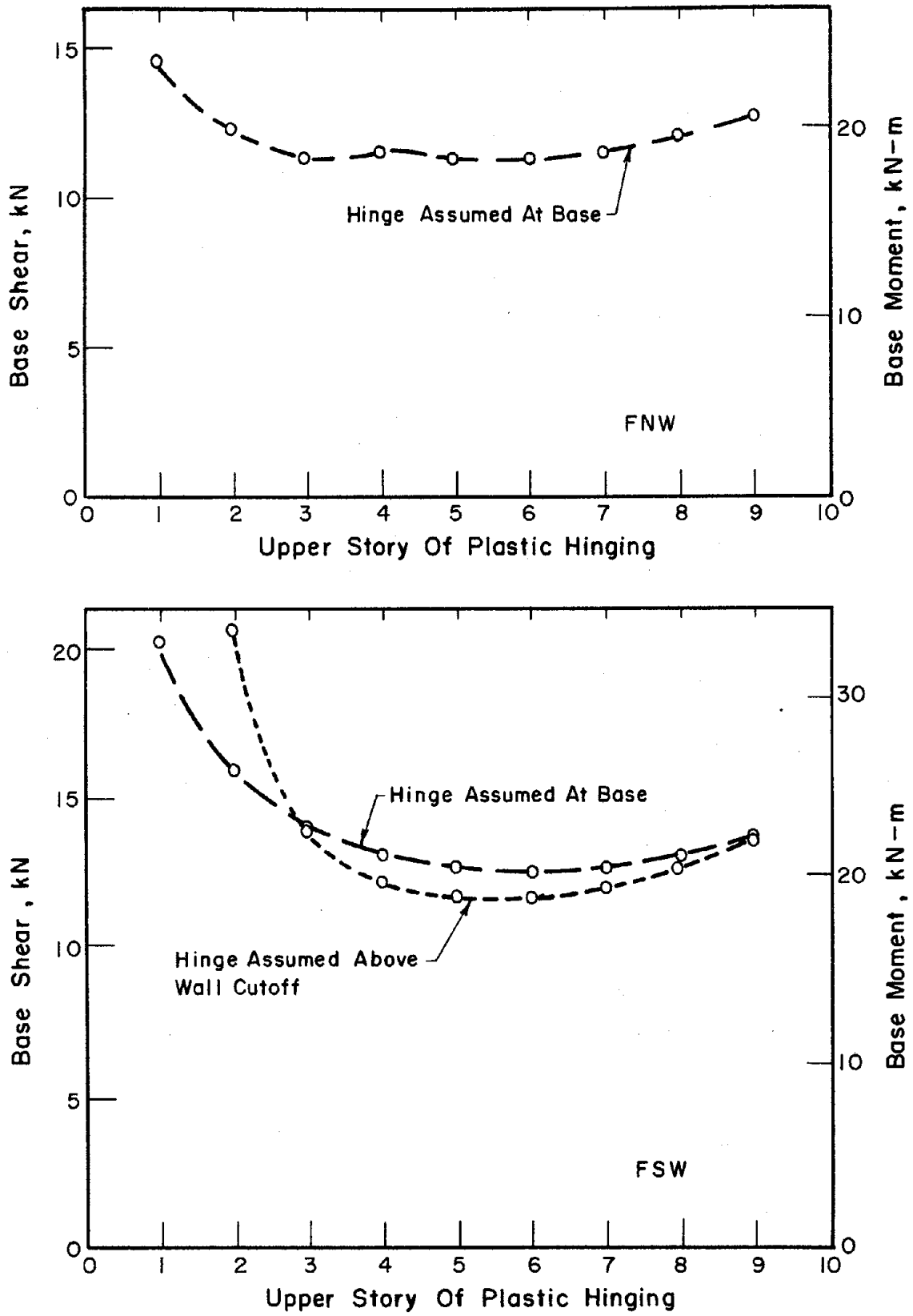


Fig. 7.5 Calculated Collapse Base Forces for a Linear Loading Distribution

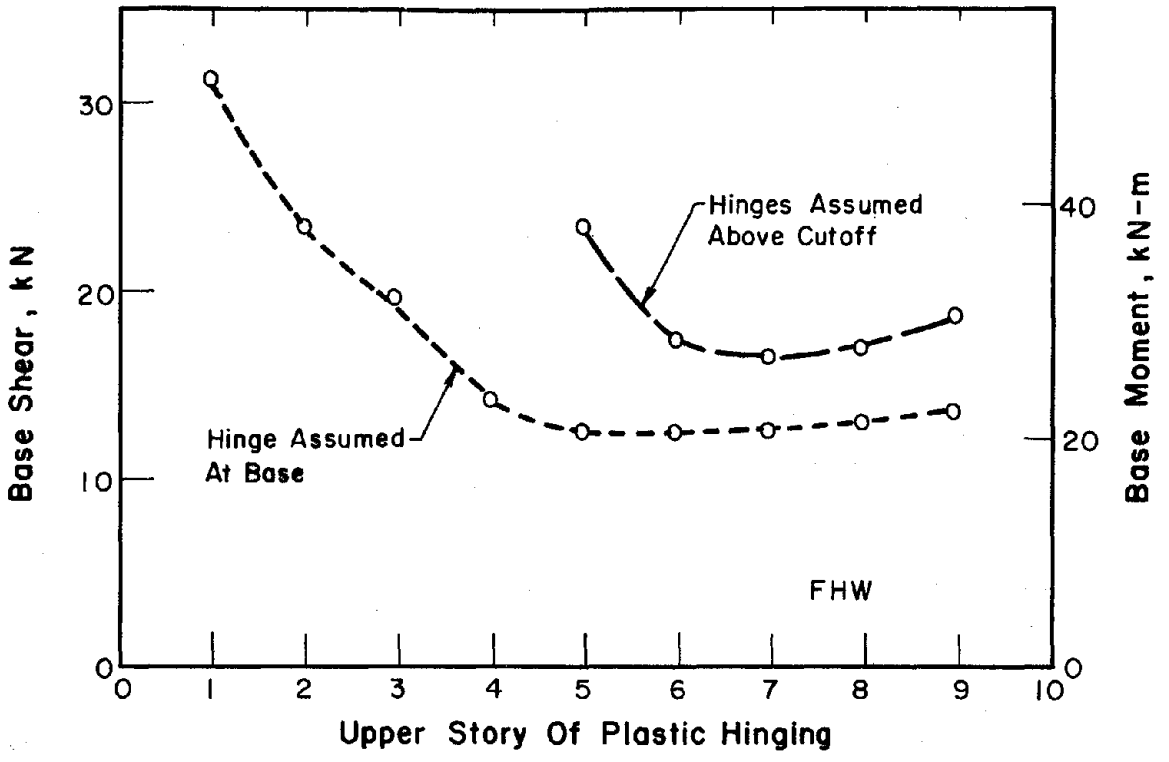


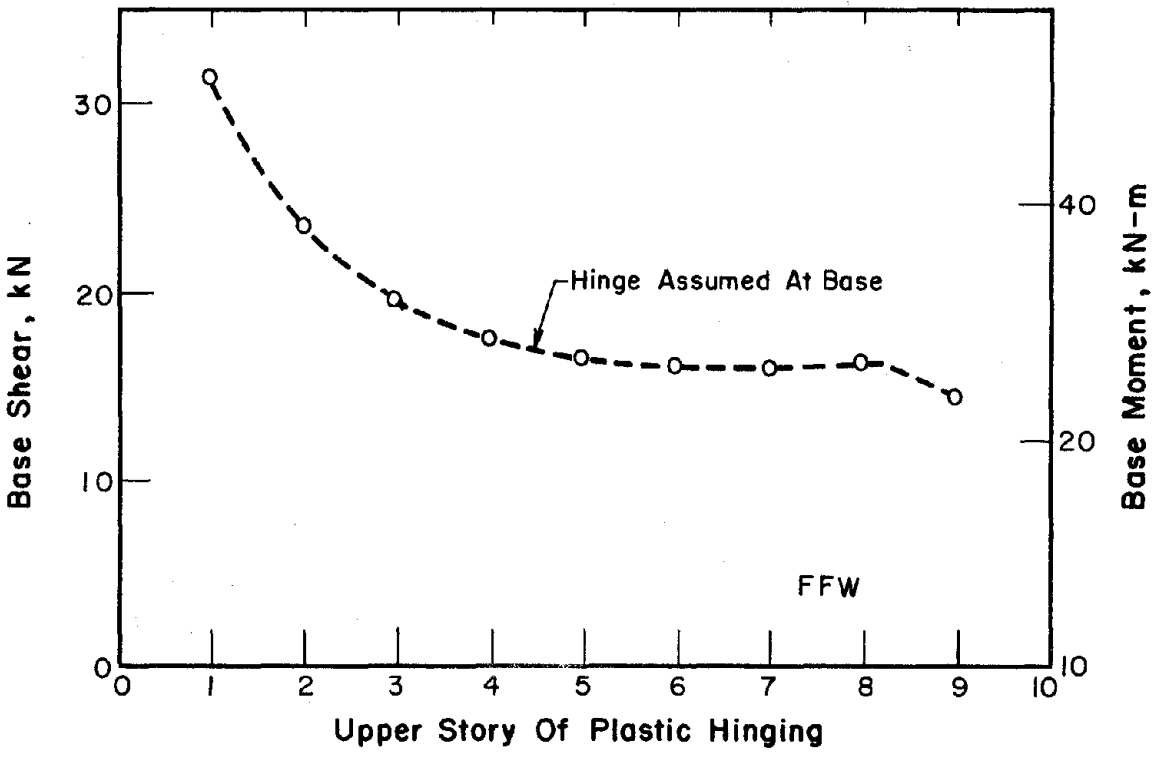


Fig. 7.5 (contd.) Calculated Collapse Base Forces for a Linear Loading Distribution

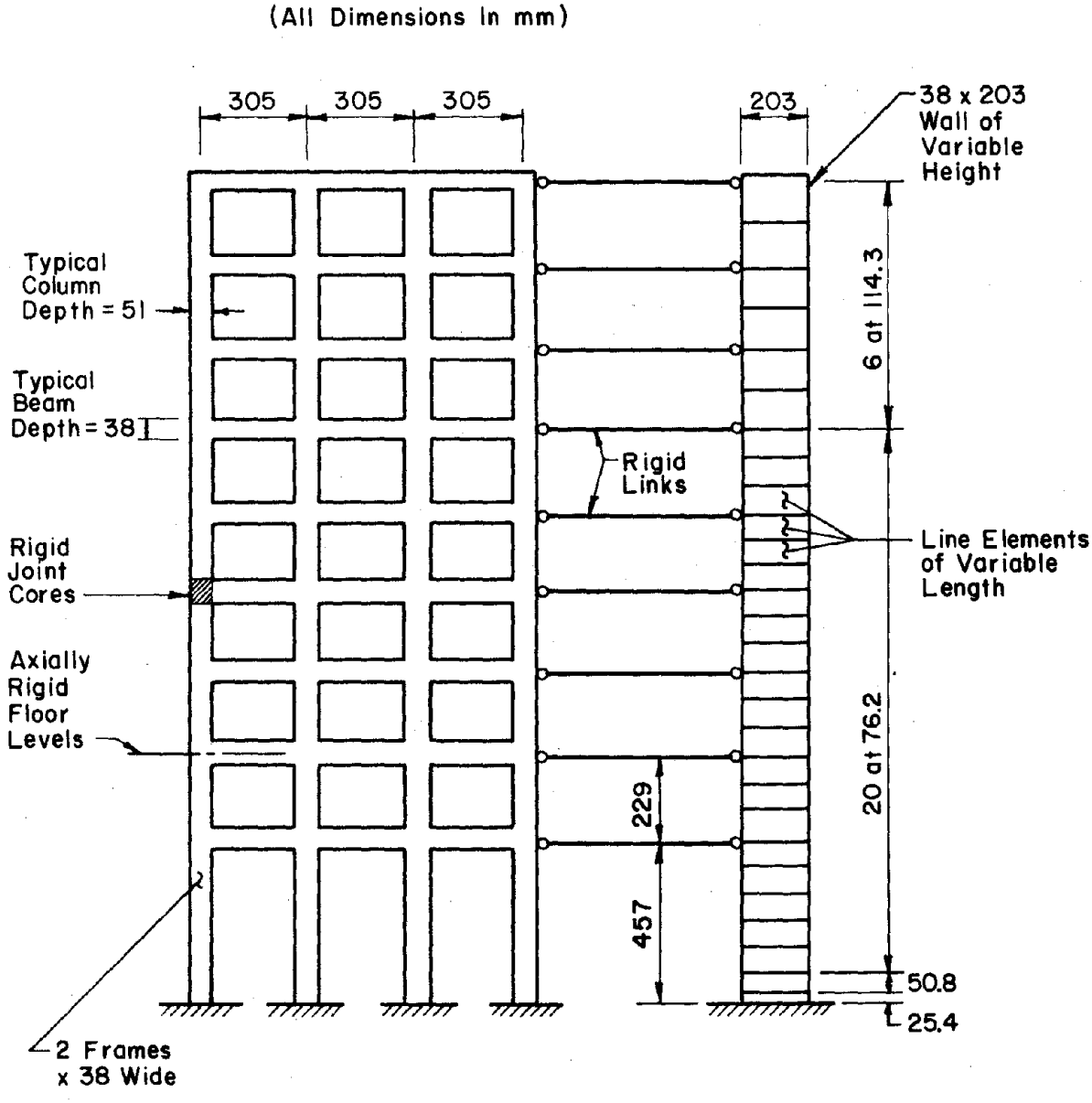


Assumed Column Axial Loads: Stories 1-3 = 1.1 kN
4-6 = 2.8 kN
7-9 = 4.4 kN

Fig. 7.6 Analytical Model Used for Nonlinear Static Analysis

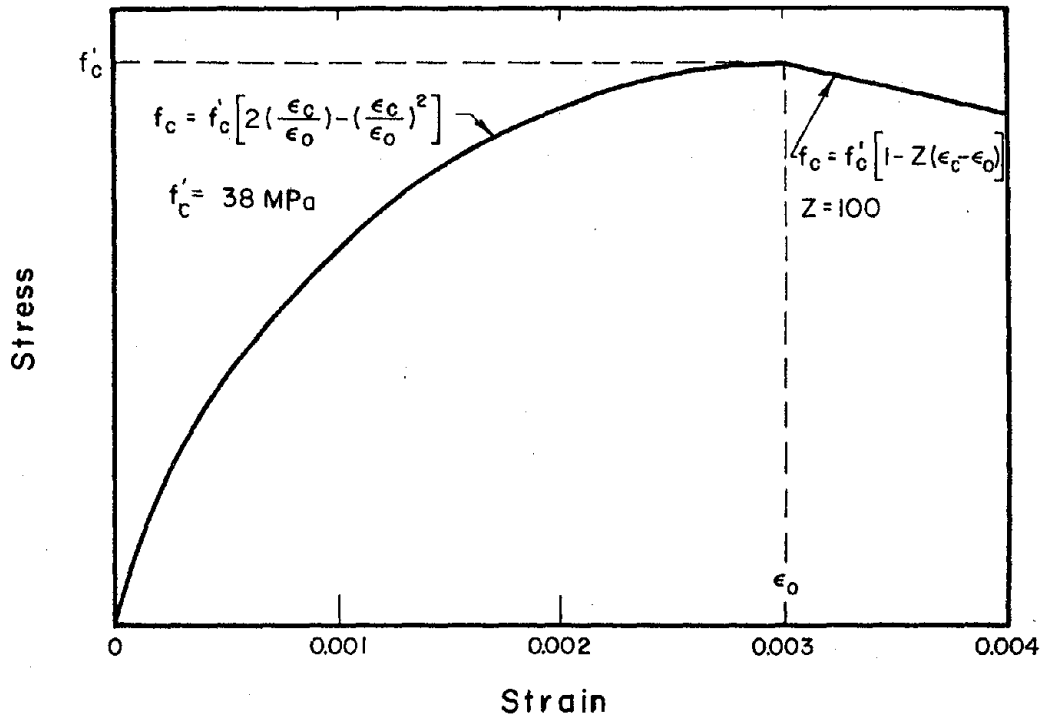


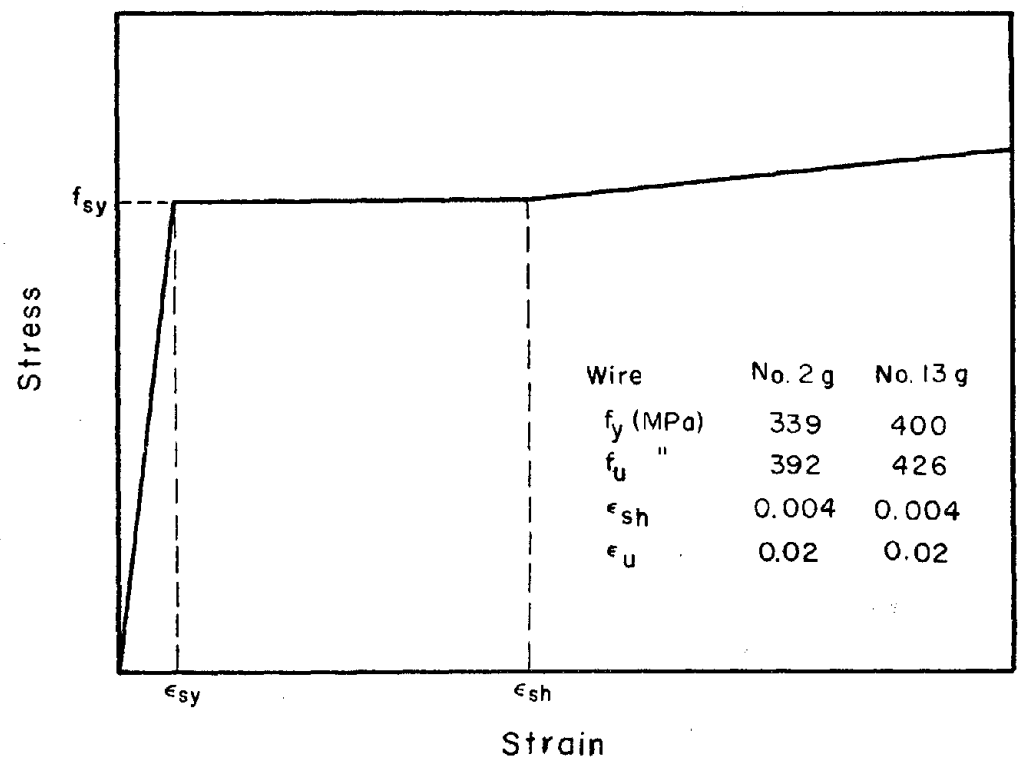


Fig. 7.7 Concrete and Steel Properties Used to Obtain Moment-Curvature Relations

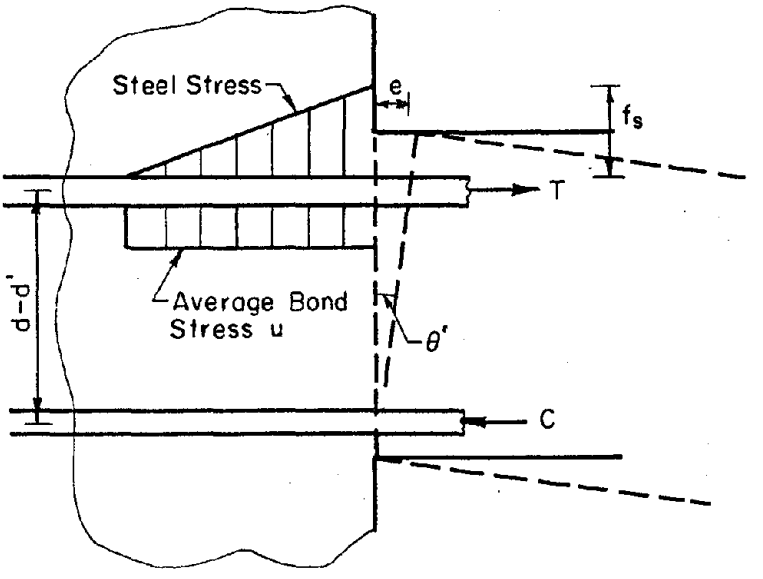


Fig. 7.8 End Rotations due to Reinforcement Pullout

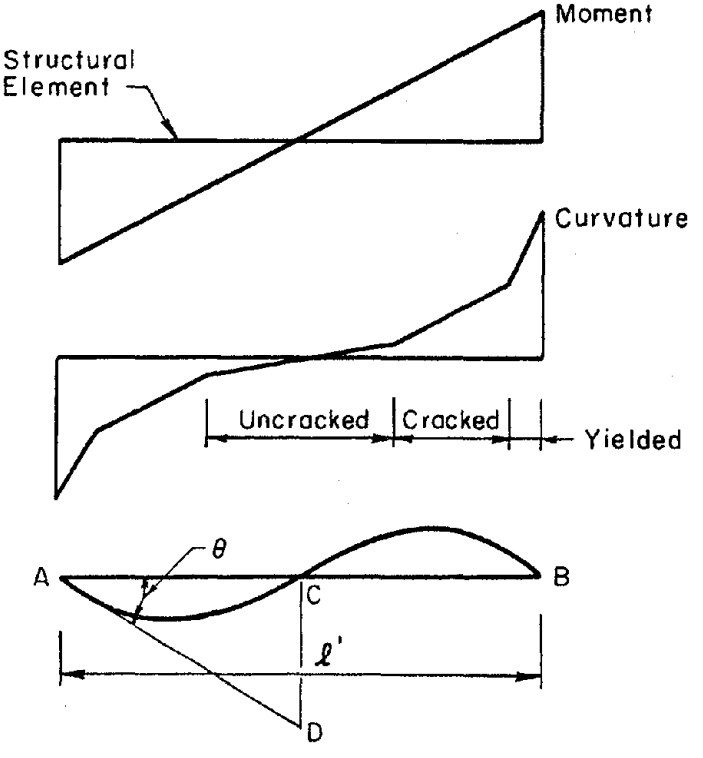


Fig. 7.9 Assumed Curvature Distributions

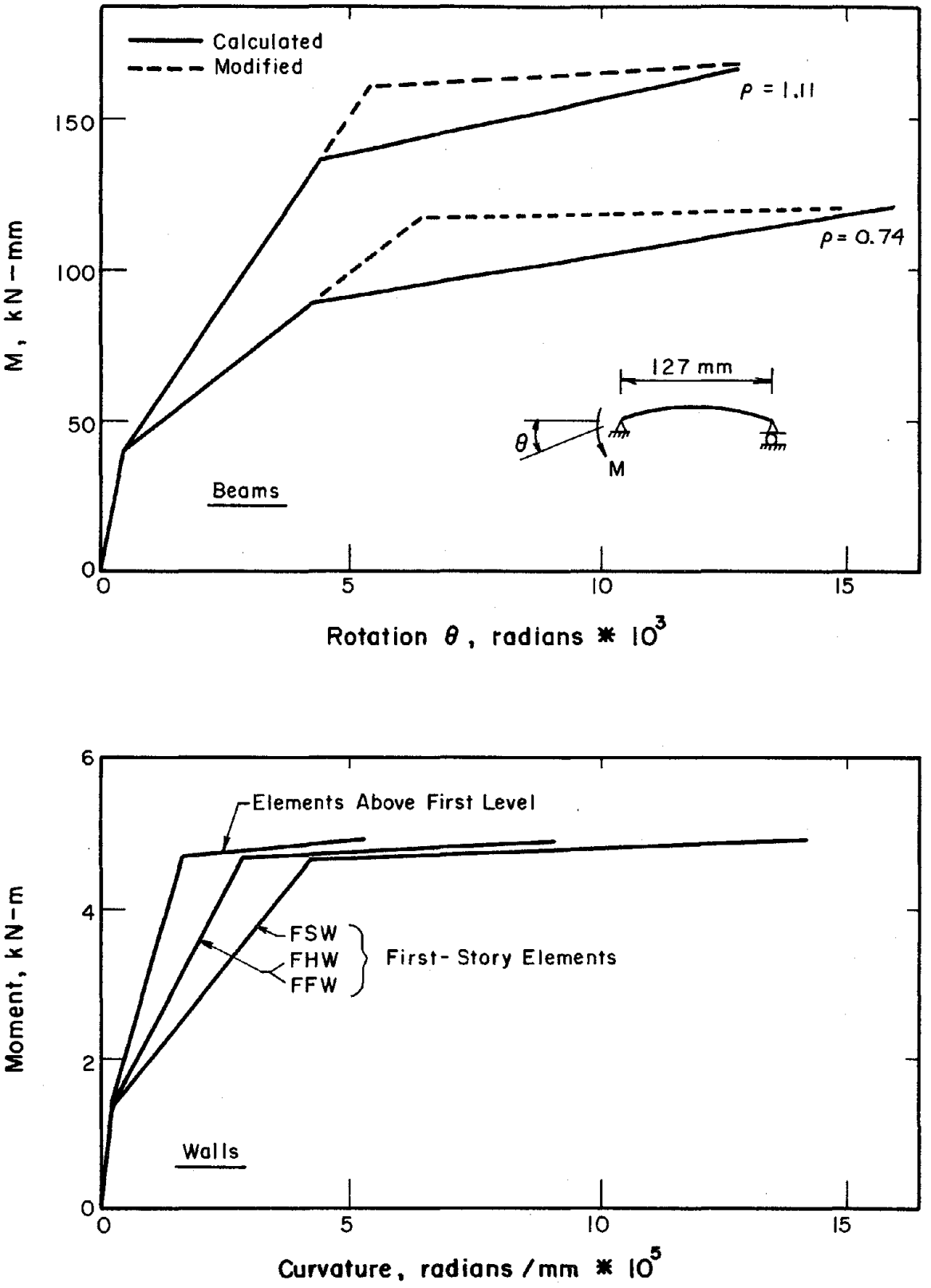


Fig. 7.10 Calculated Moment-Curvature and Moment-Rotation Relations

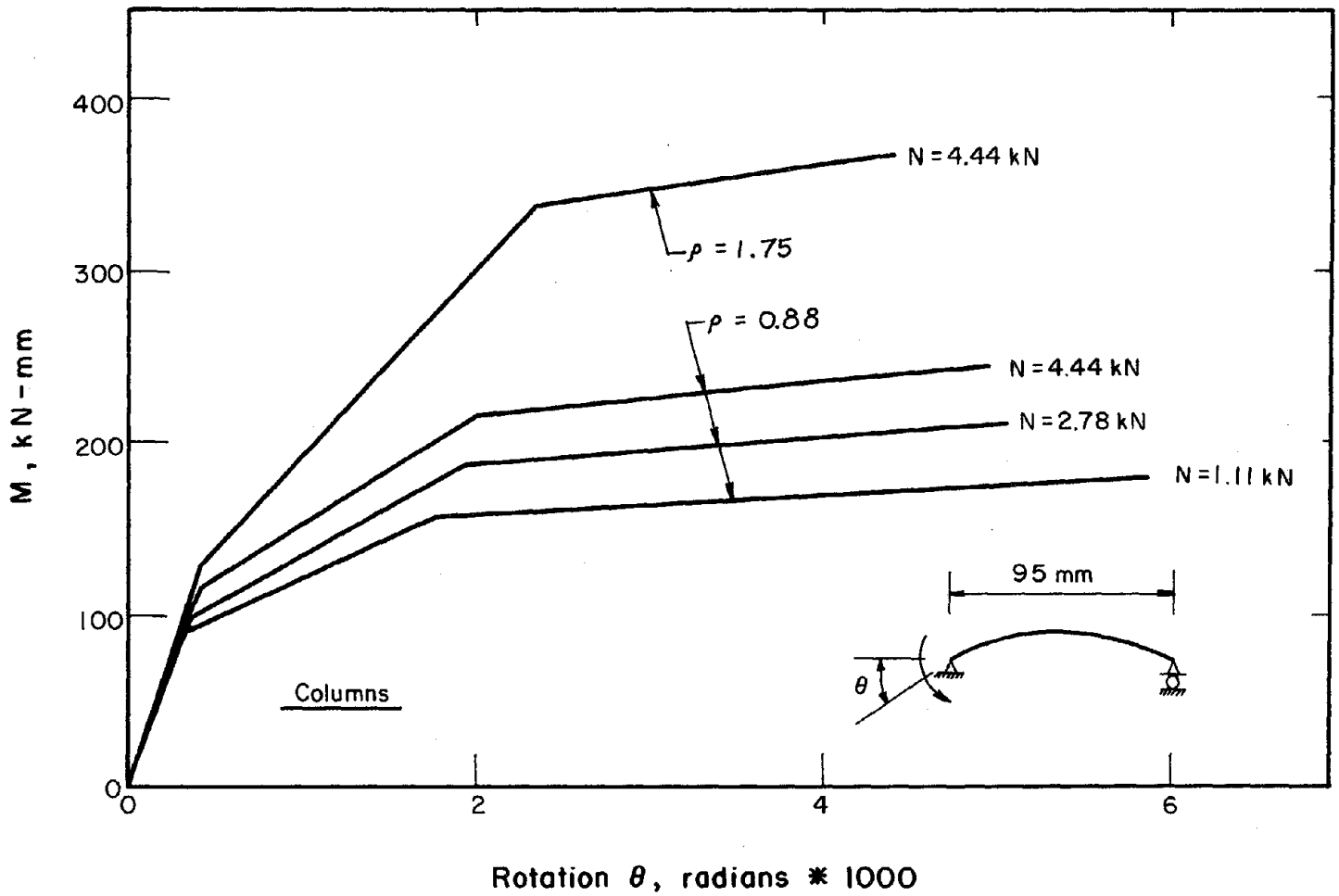


Fig. 7.10 (contd.) Calculated Moment-Curvature and Moment-Rotation Relations

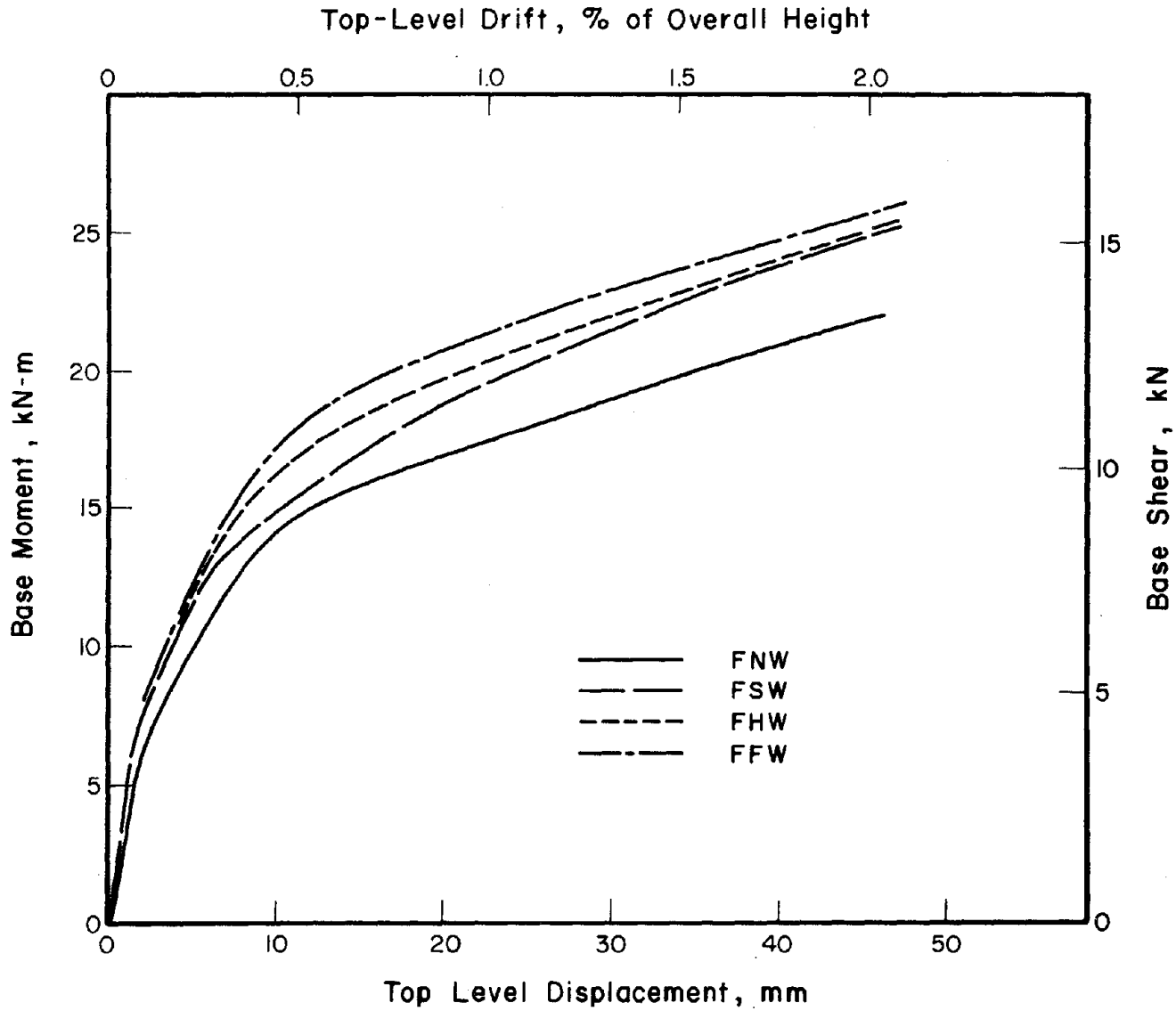


Fig. 7.11 Calculated Moment-Displacement Relations Using Linear Load Distribution and Calculated Beam Properties

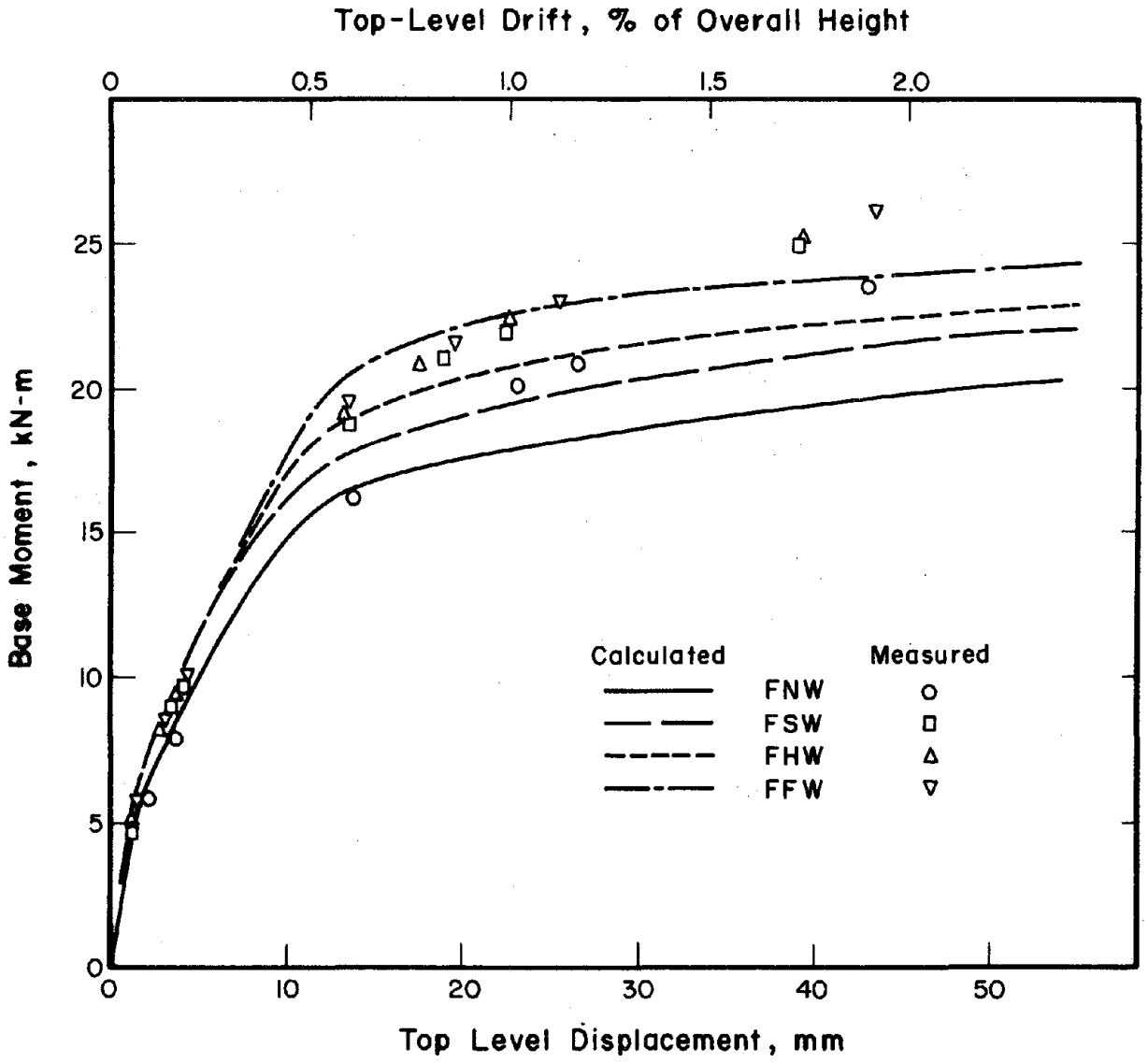


Fig. 7.12 Calculated Moment and Shear Primary Curves Using Linear Load Distribution and Modified Beam Properties

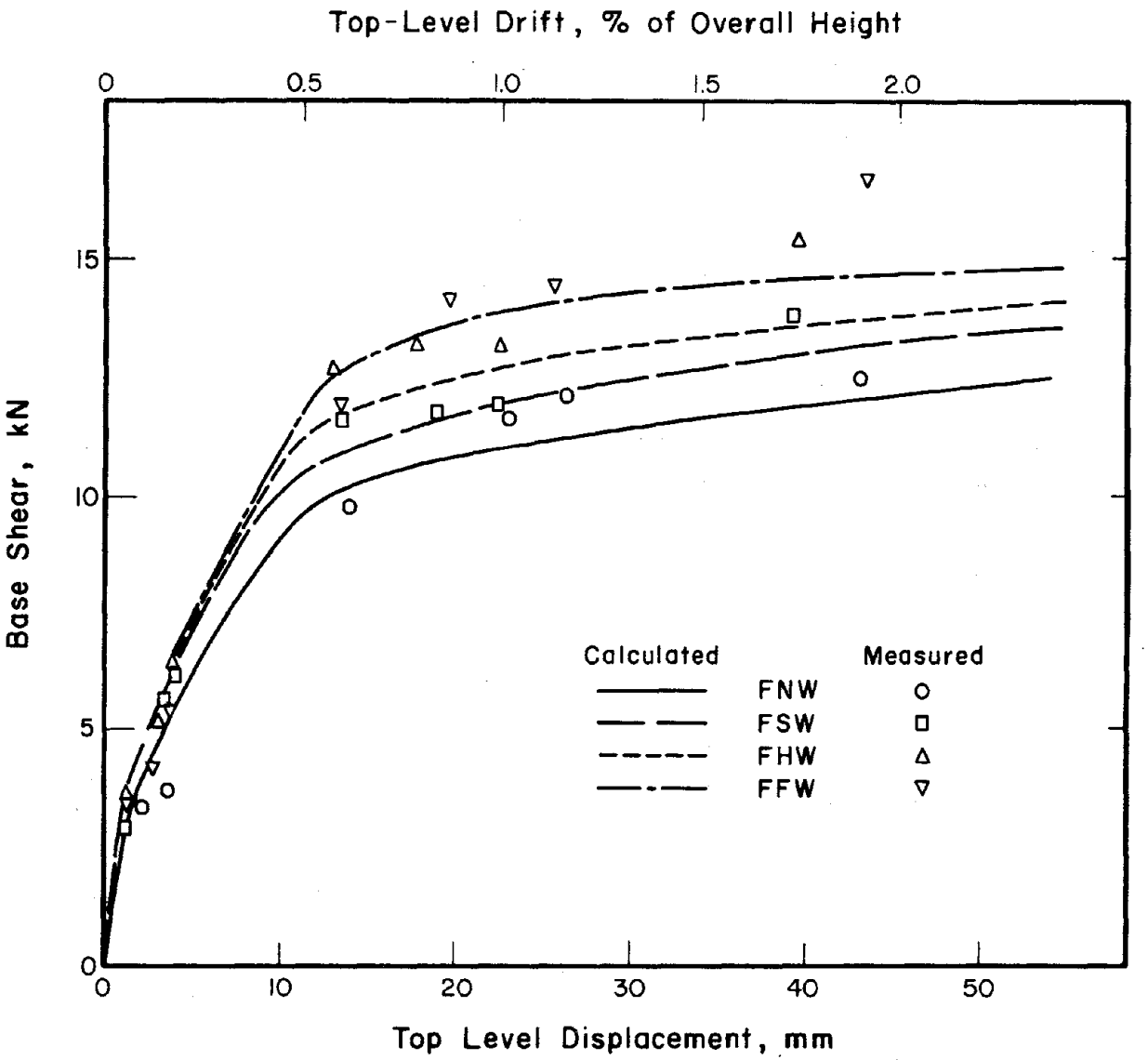


Fig. 7.12 (contd.) Calculated Moment and Shear Primary Curves Using Linear Load Distribution and Modified Beam Properties

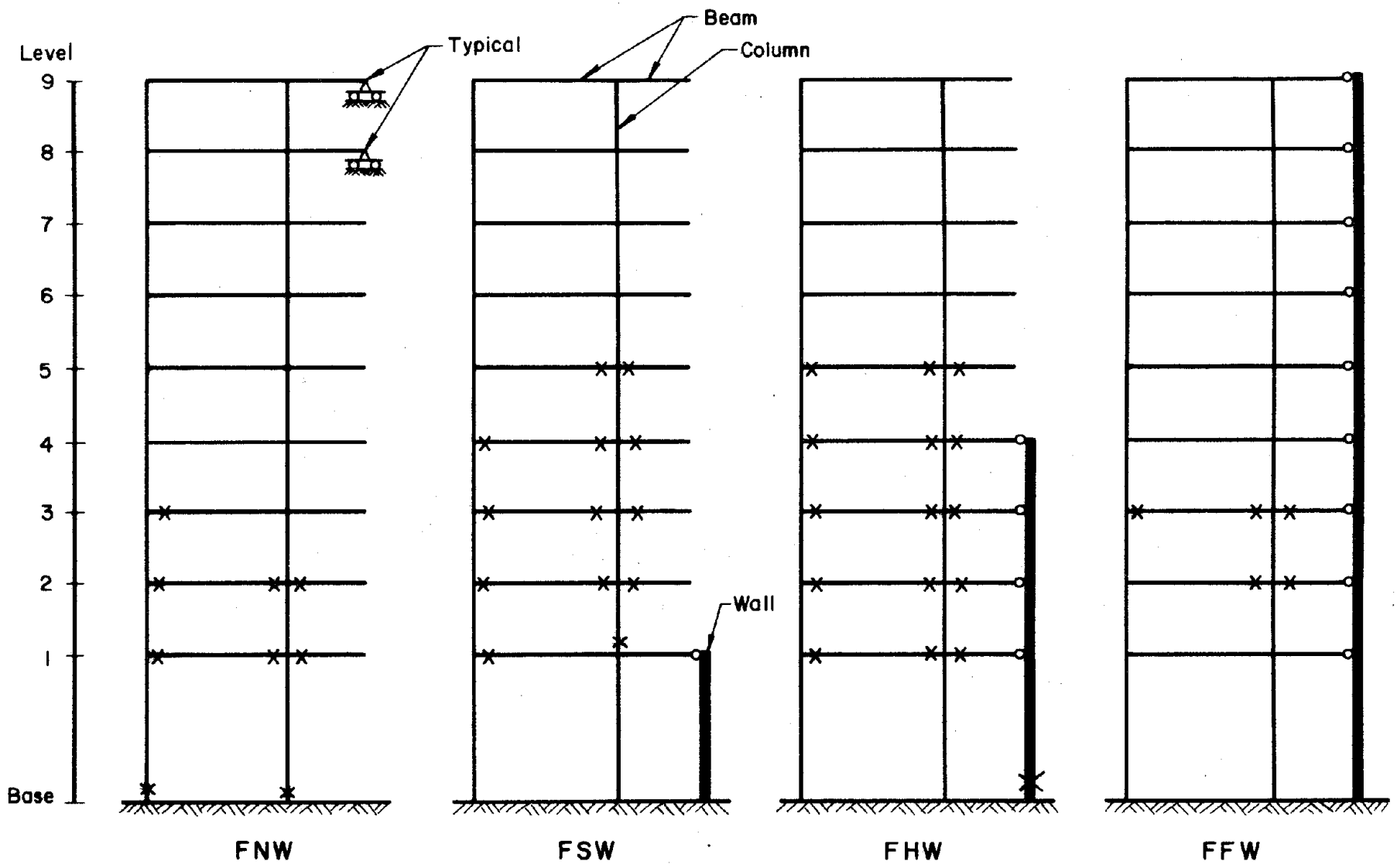


(a) Top Displacement =0.5 % of Height

Fig. 7.13 Calculated Yield Mechanism for Monotonic Loading

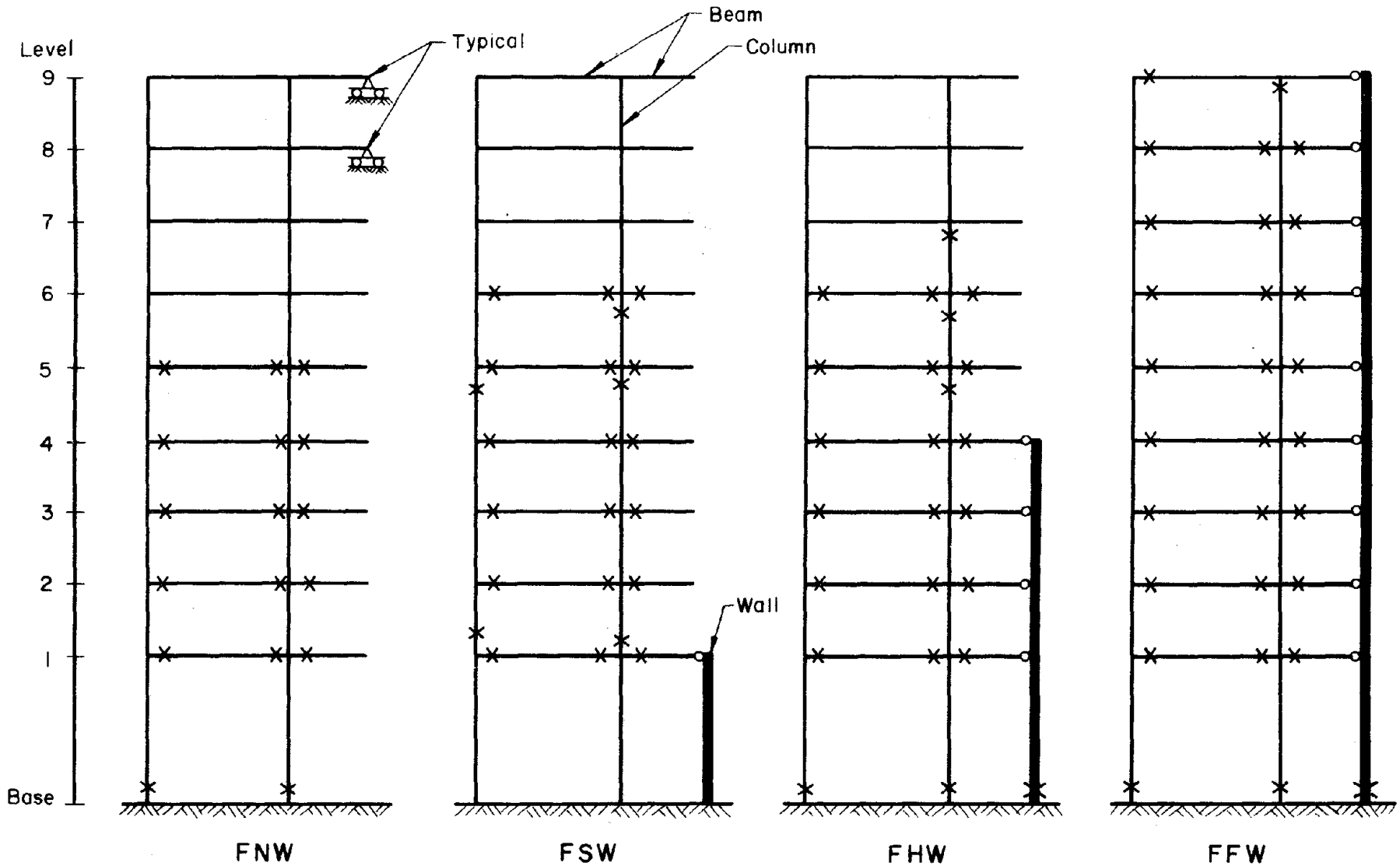


**(b) Top Displacement = 1.0 % of Height**

Fig. 7.13 (contd.) Calculated Yield Mechanism for Monotonic Loading

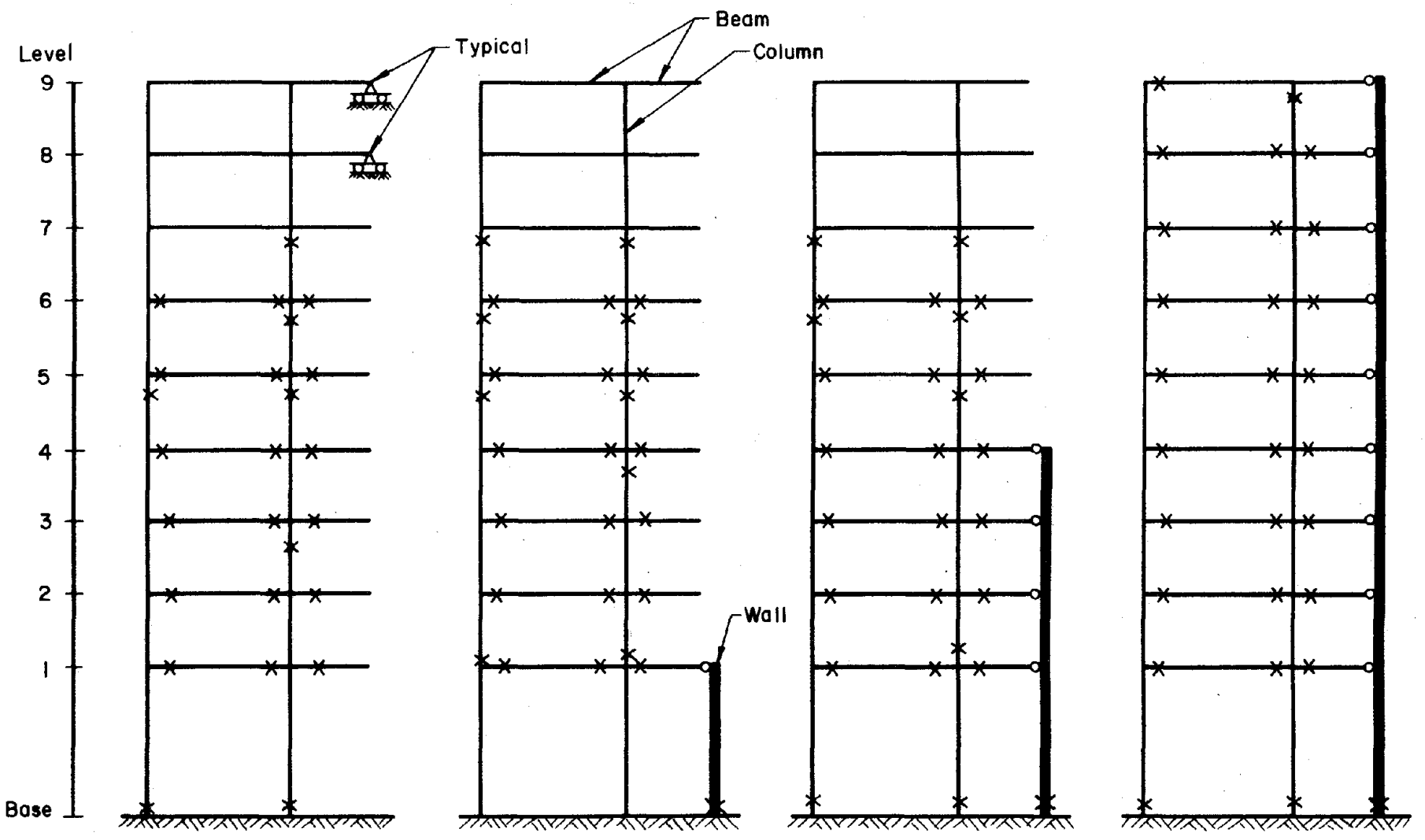


(d) Top Displacement = 1.5% of Height

Fig. 7.13 (contd.) Calculated Yield Mechanism for Monotonic Loading

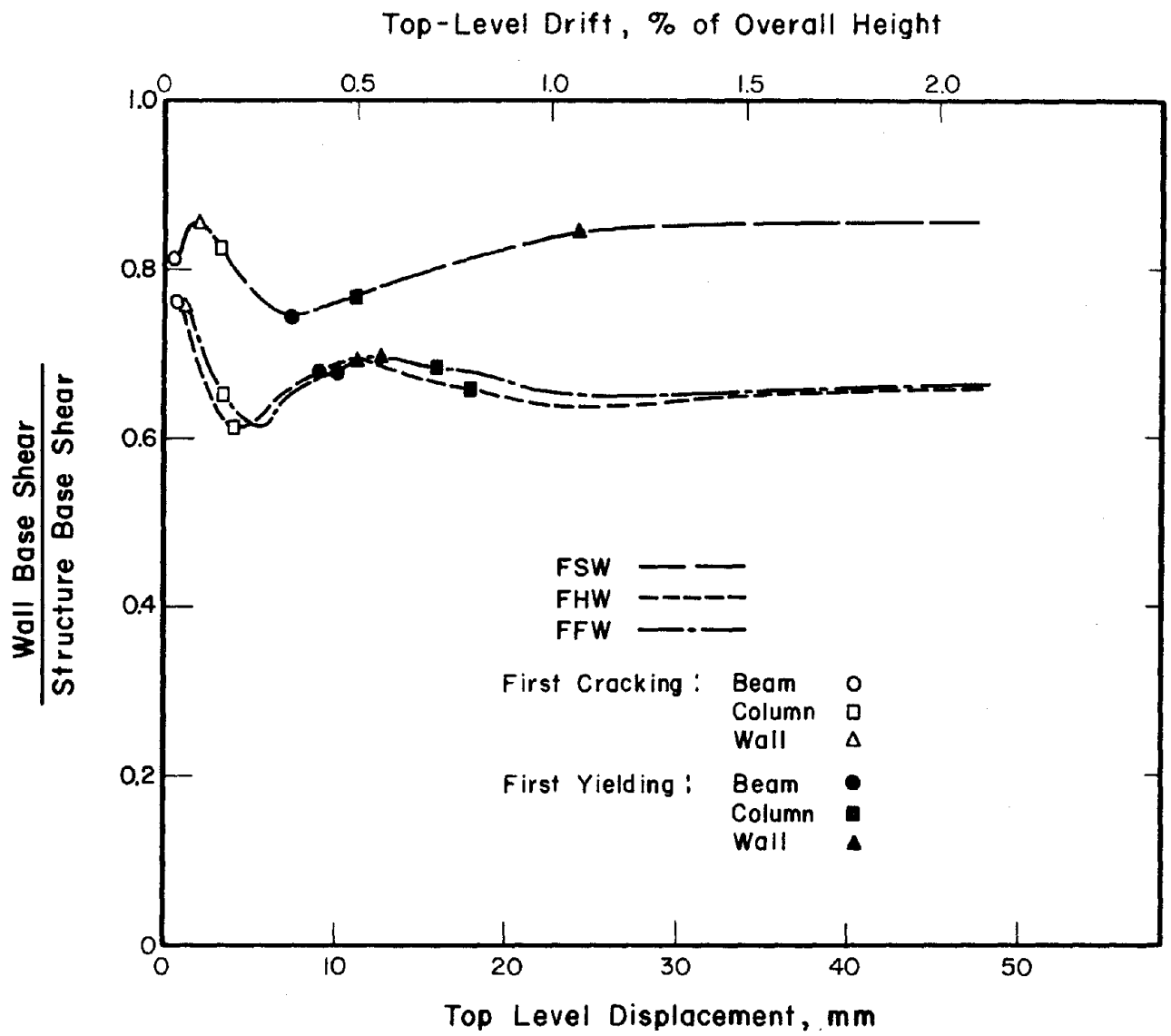


Fig. 7.14 Calculated Wall Base Shear for Monotonic Loading

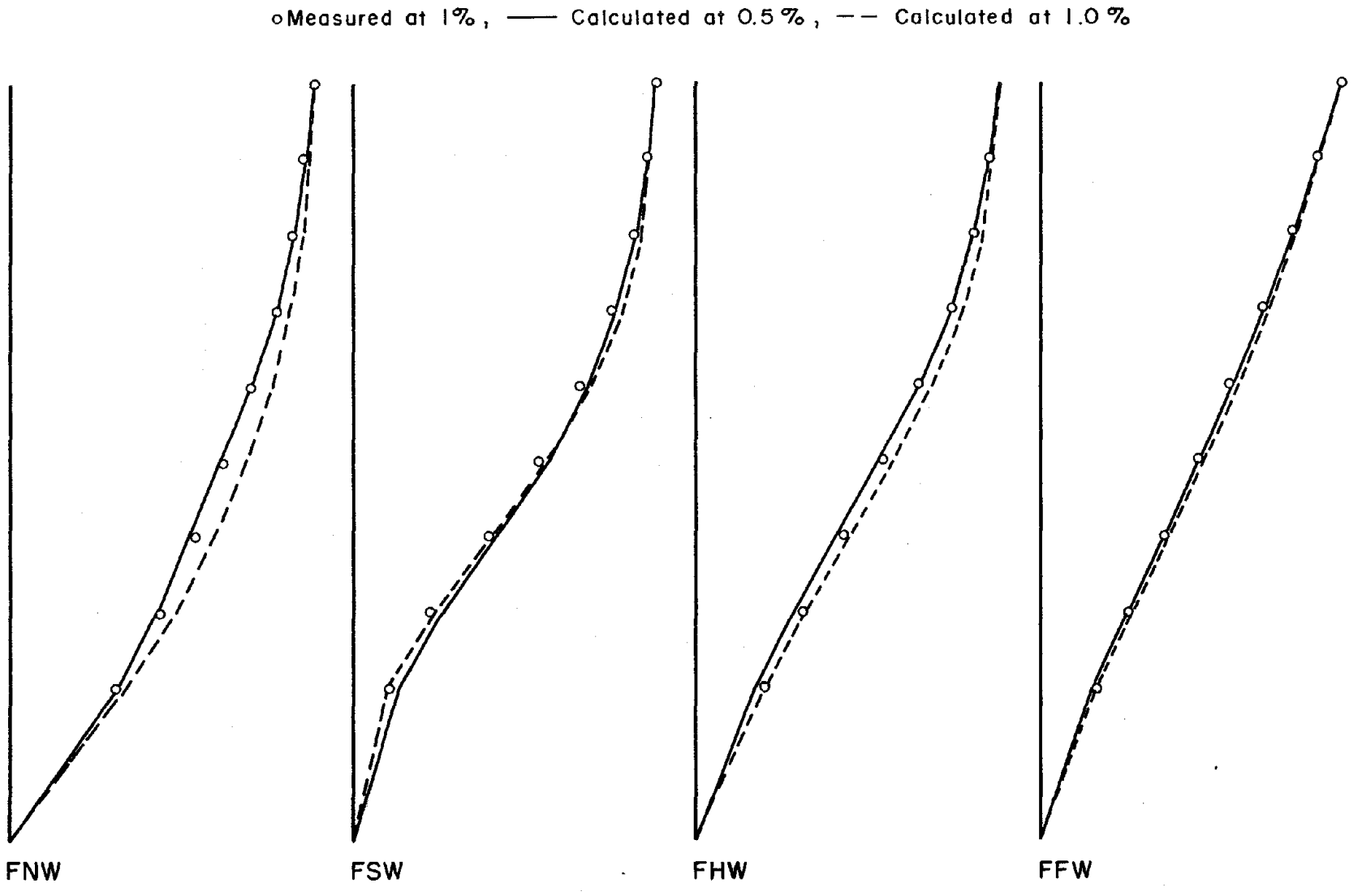


Fig. 7.15 Comparison of Measured Displaced Shapes with Shapes Calculated for Monotonic Loading

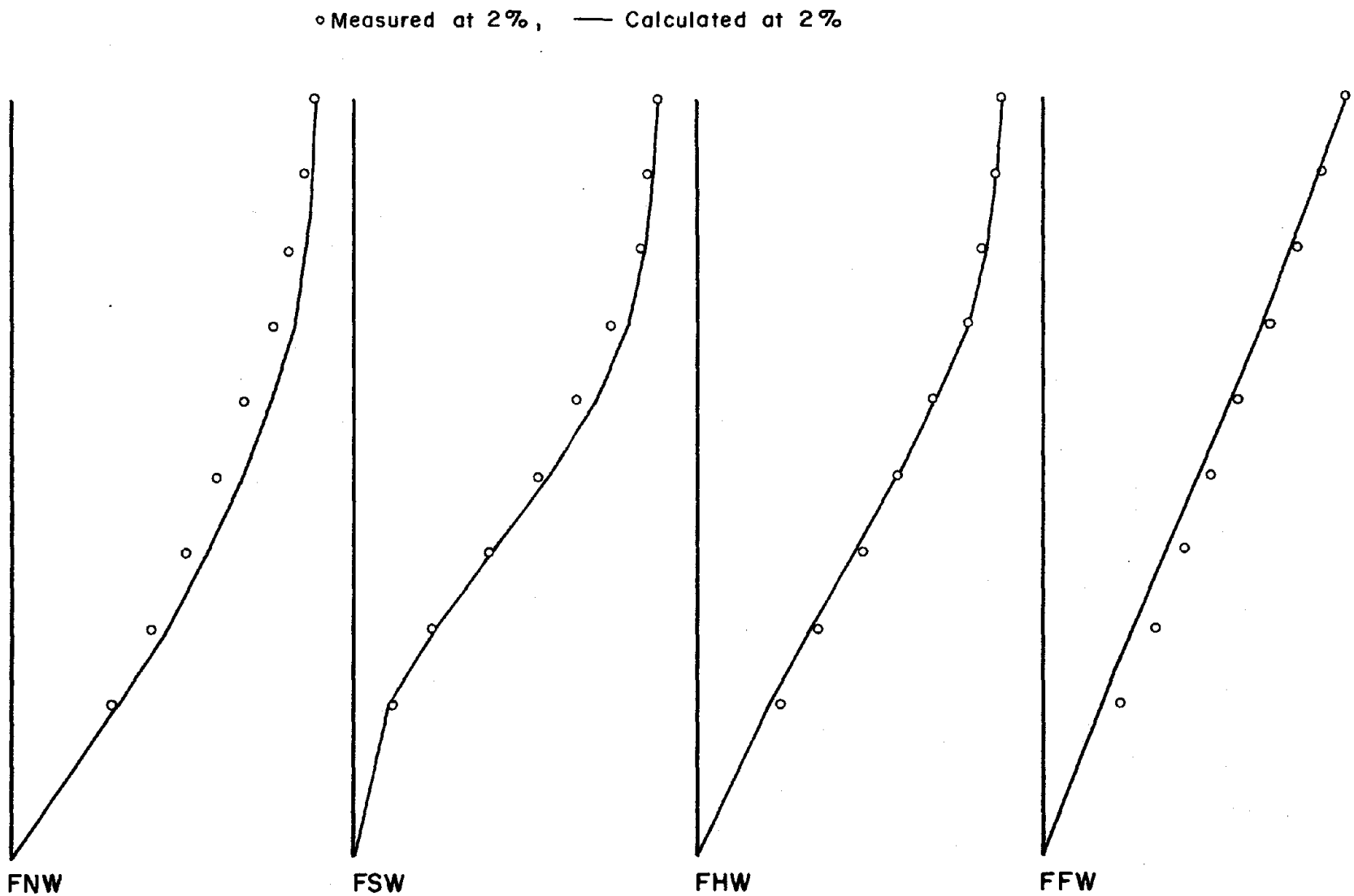


Fig. 7.15 (contd.) Comparison of Measured Displaced Shapes with Shapes Calculated for Monotonic Loading

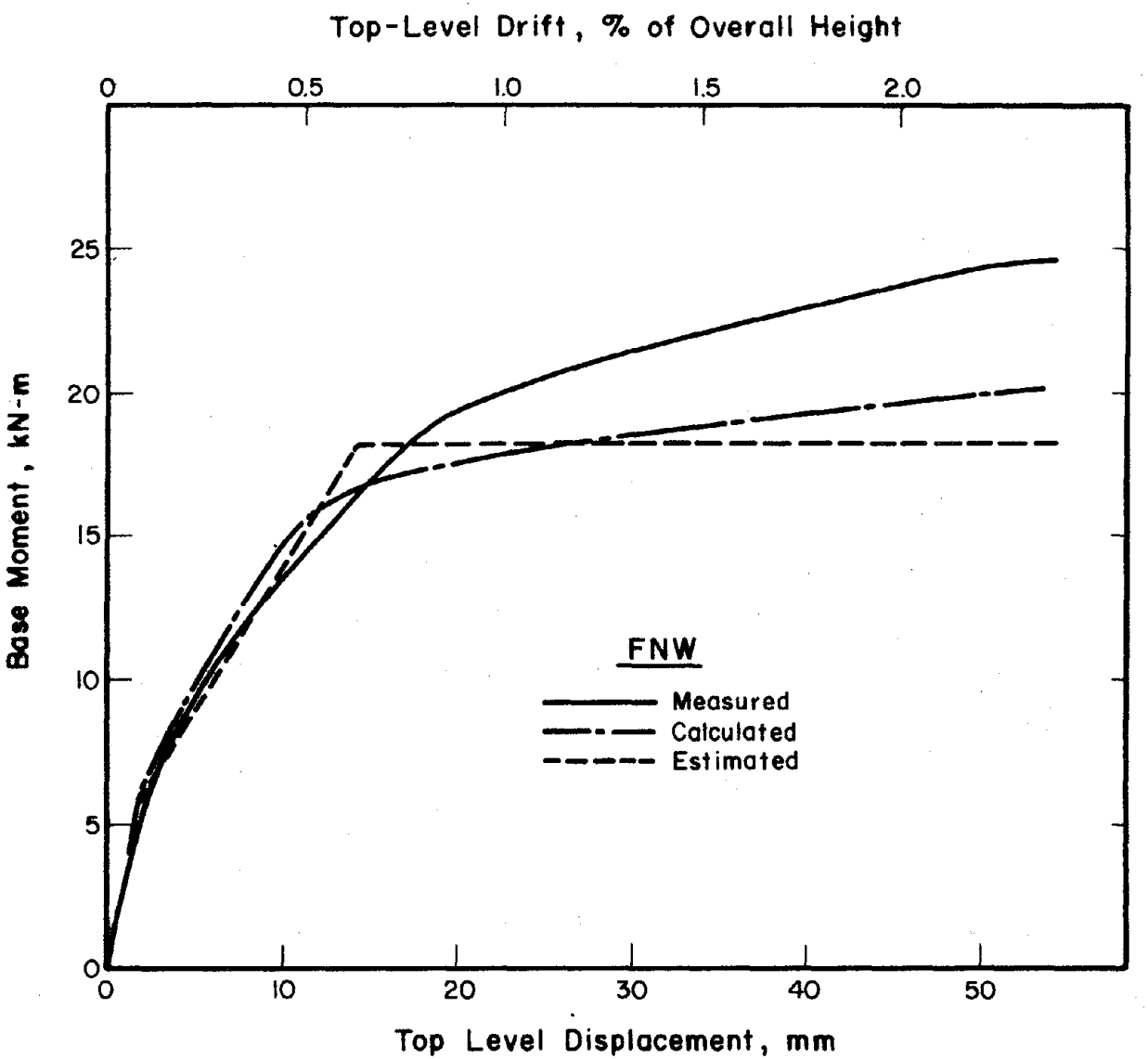


Fig. 7.16 Comparison of Moment-Displacement Primary Curves Used for SDOF Analyses

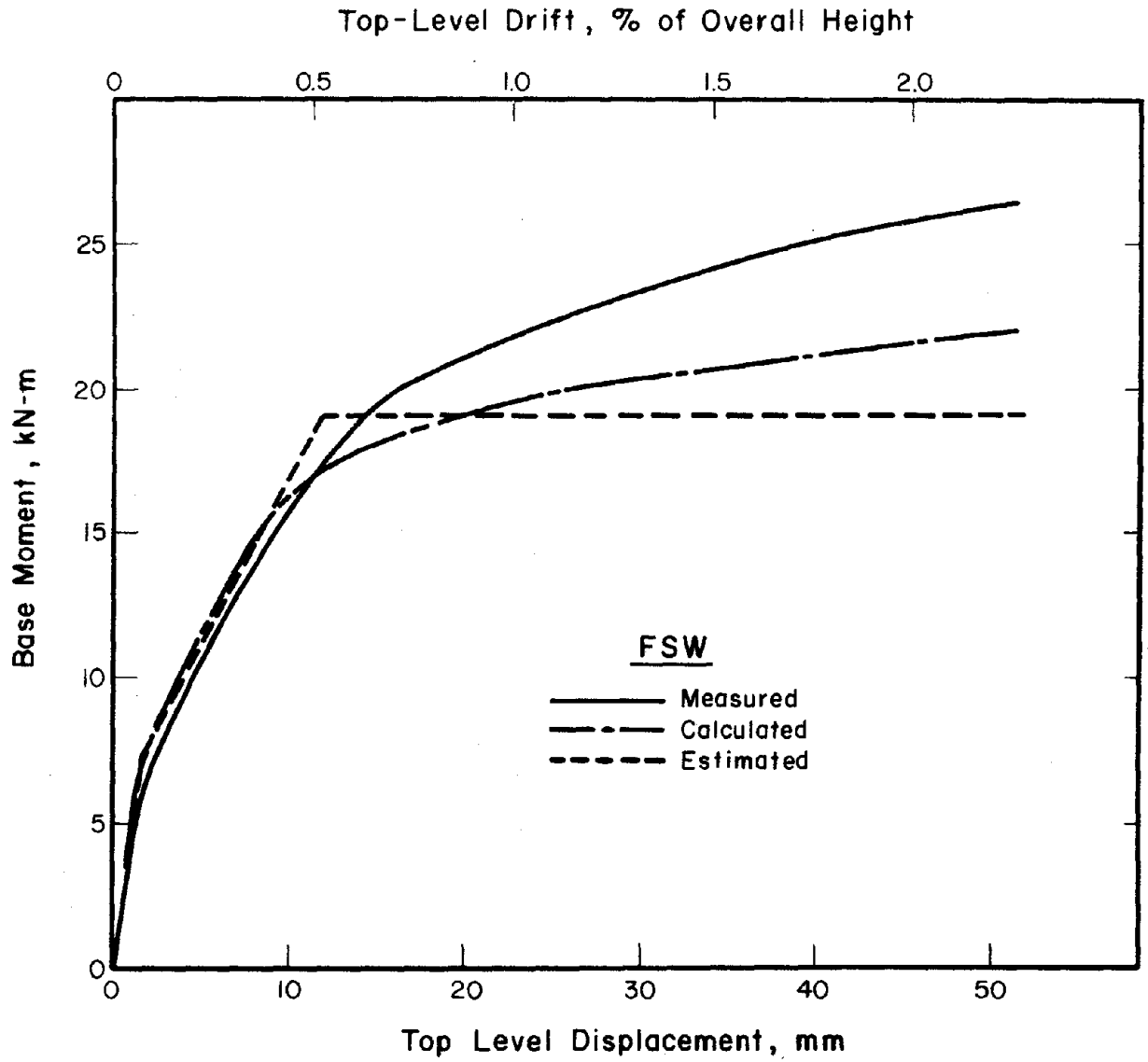


Fig. 7.16 (contd.) Comparison of Moment-Displacement Primary Curves Used for SDOF Analyses

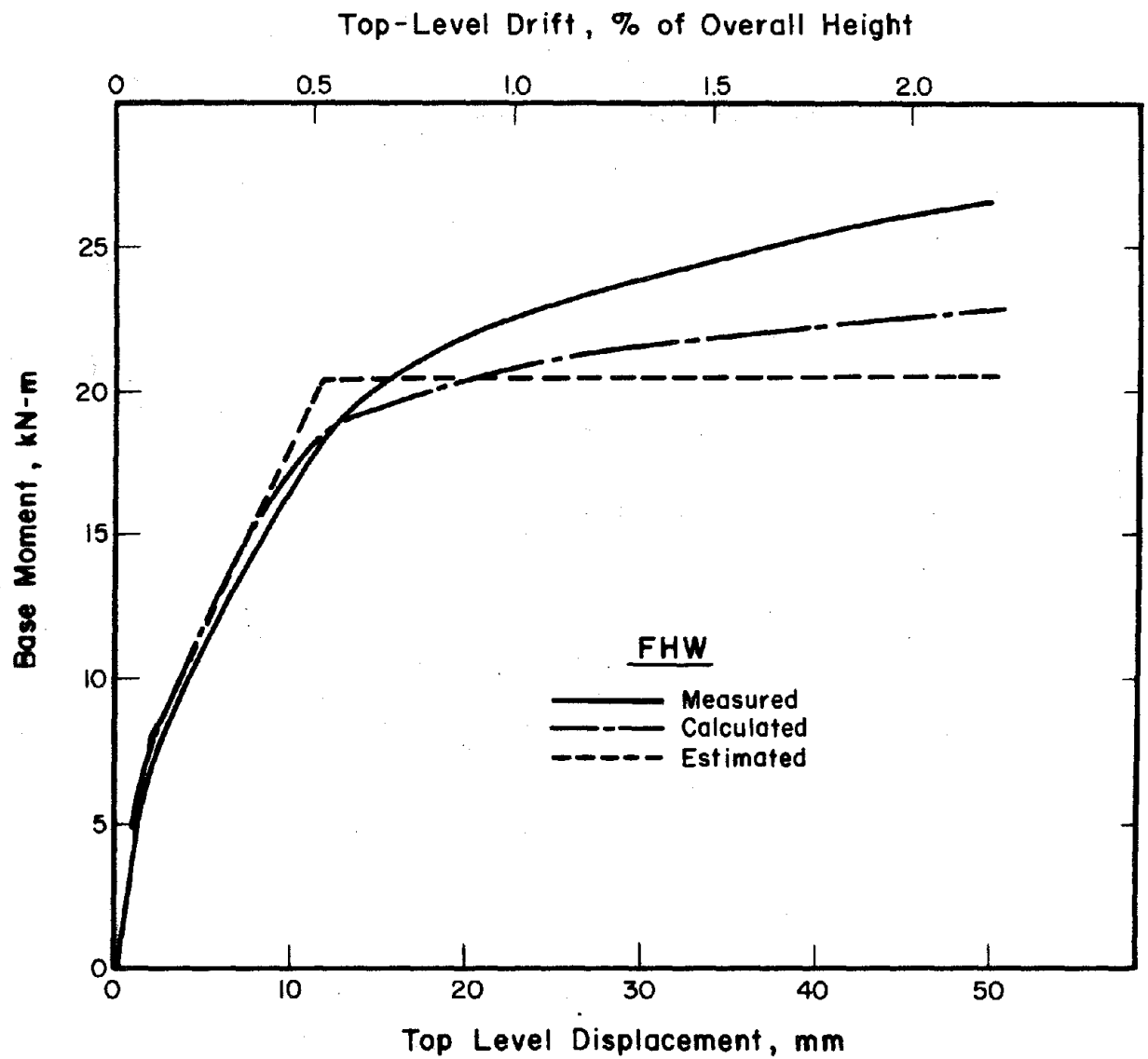


Fig. 7.16 (contd.) Comparison of Moment-Displacement Primary Curves Used for SDOF Analyses

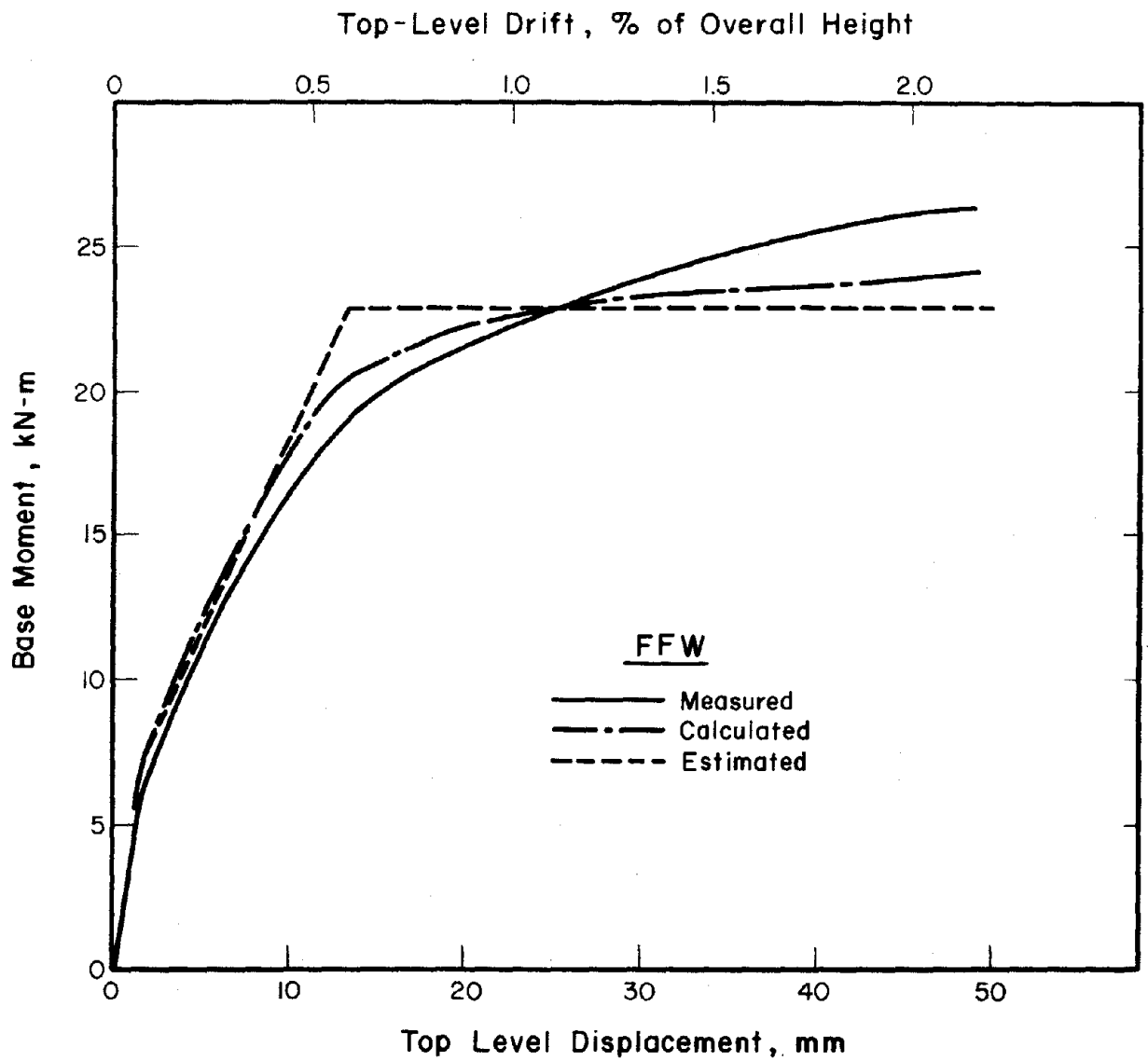


Fig. 7.16 (contd.) Comparison of Moment-Displacement Primary Curves Used for SDOF Analyses

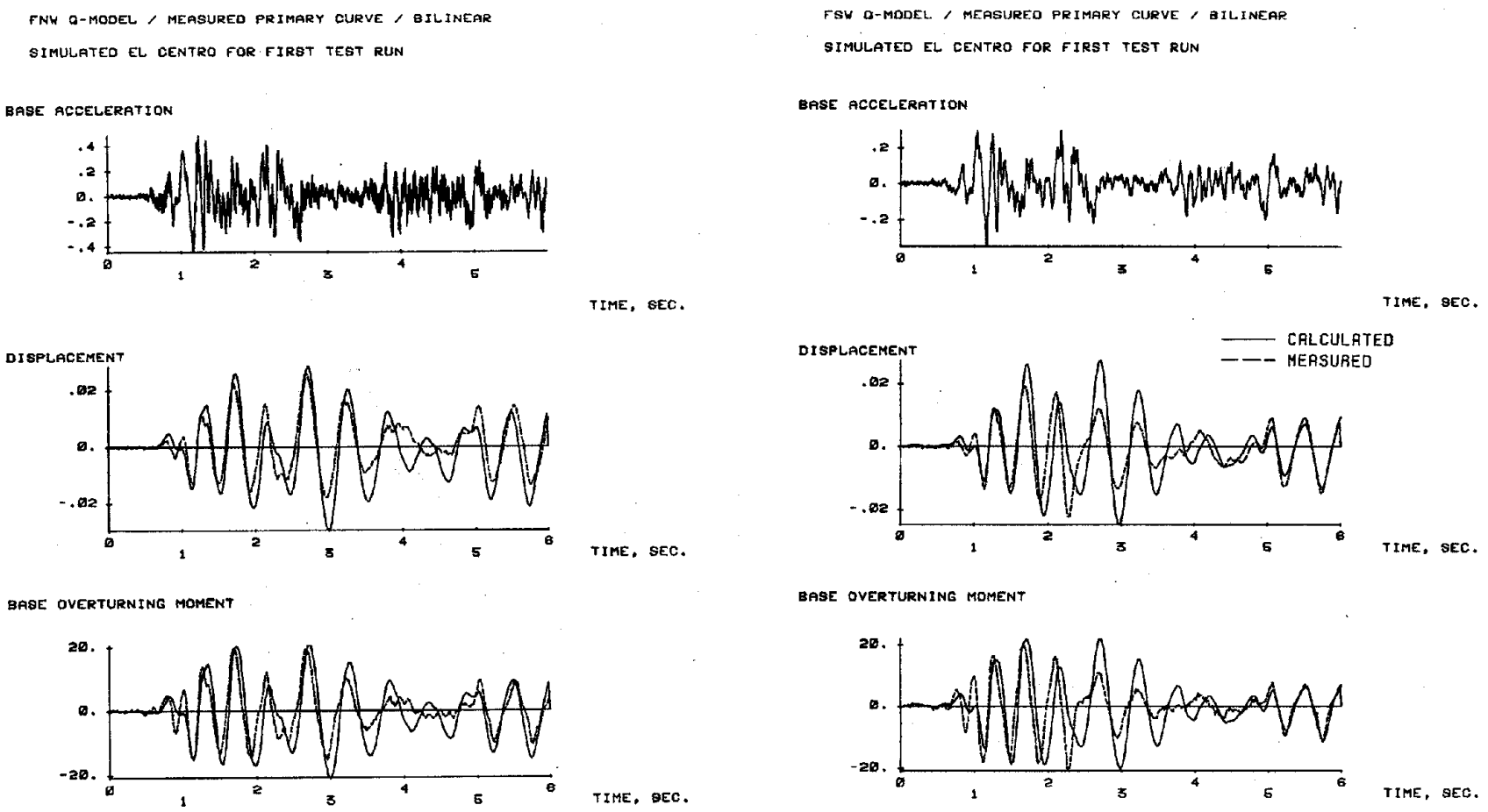


(a) Measured Primary Curve with Bilinear Hysteresis

Fig. 7.17 Top-Displacement and Base-Moment Responses Calculated Using the Q-Model

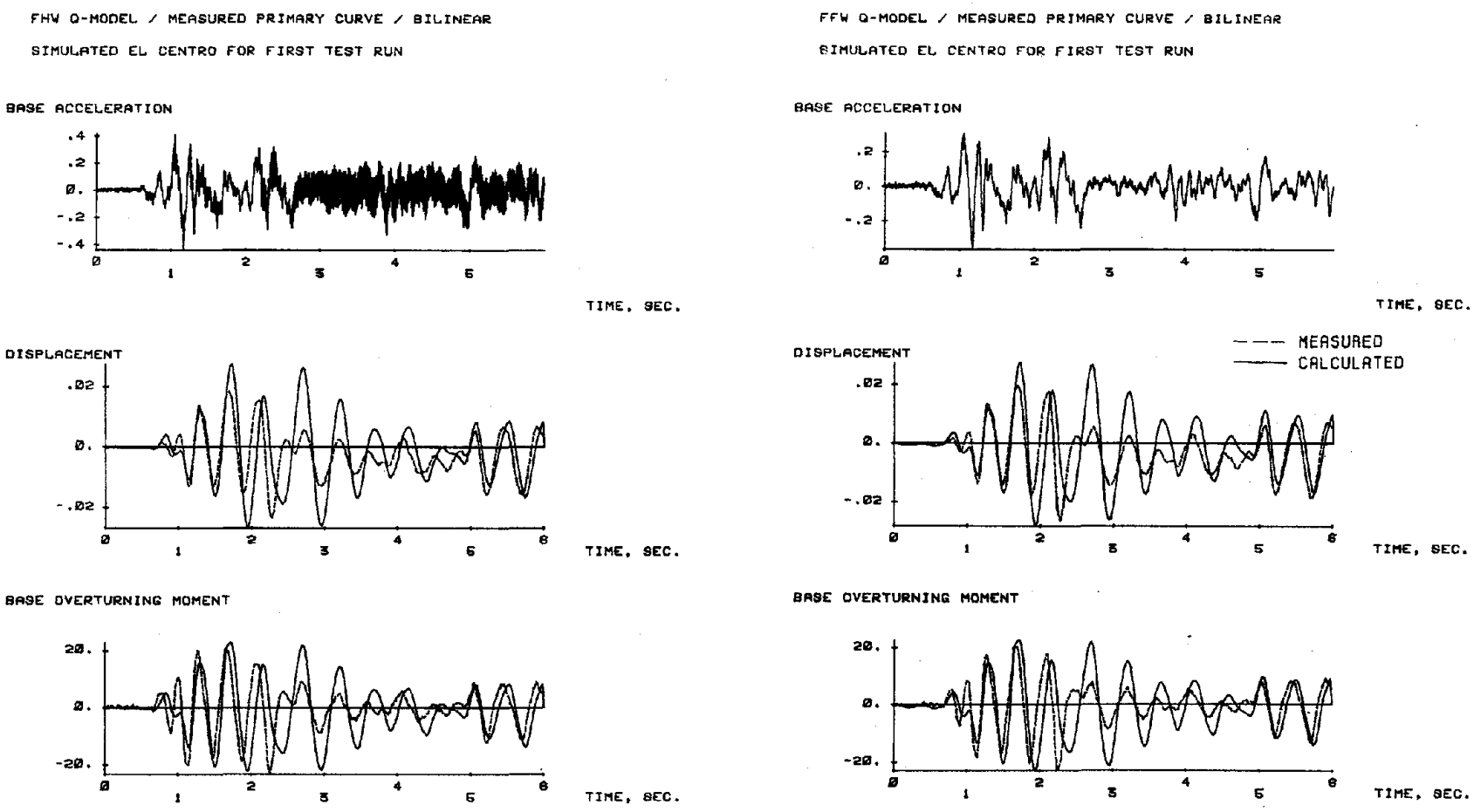


(a) Measured Primary Curve with Bilinear Hysteresis

Fig. 7.17 (contd.) Top-Displacement and Base-Moment Responses Calculated Using the Q-Model

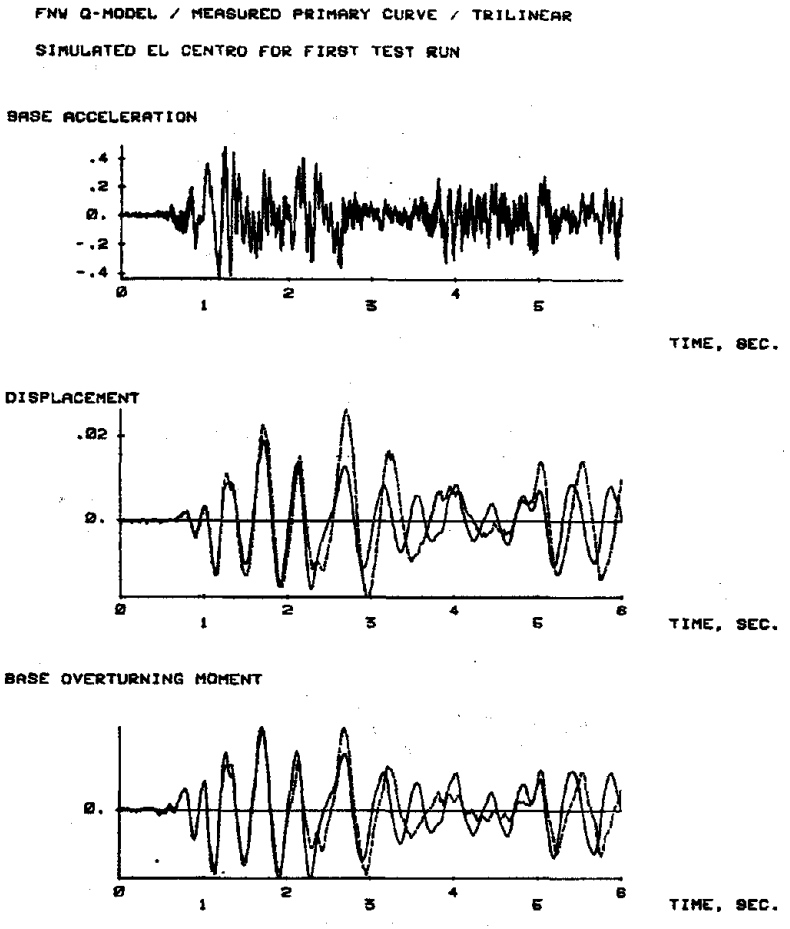


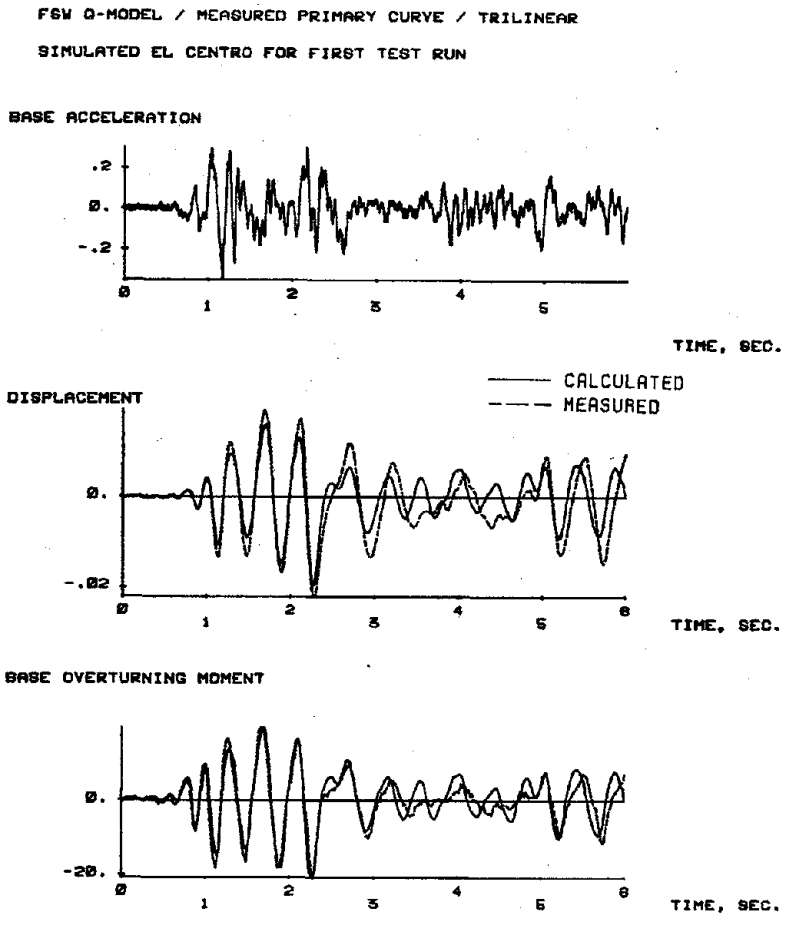


(b) Measured Primary Curve with Trilinear Hysteresis

Fig. 7.17 (contd.) Top-Displacement and Base-Moment Responses Calculated Using the Q-Model

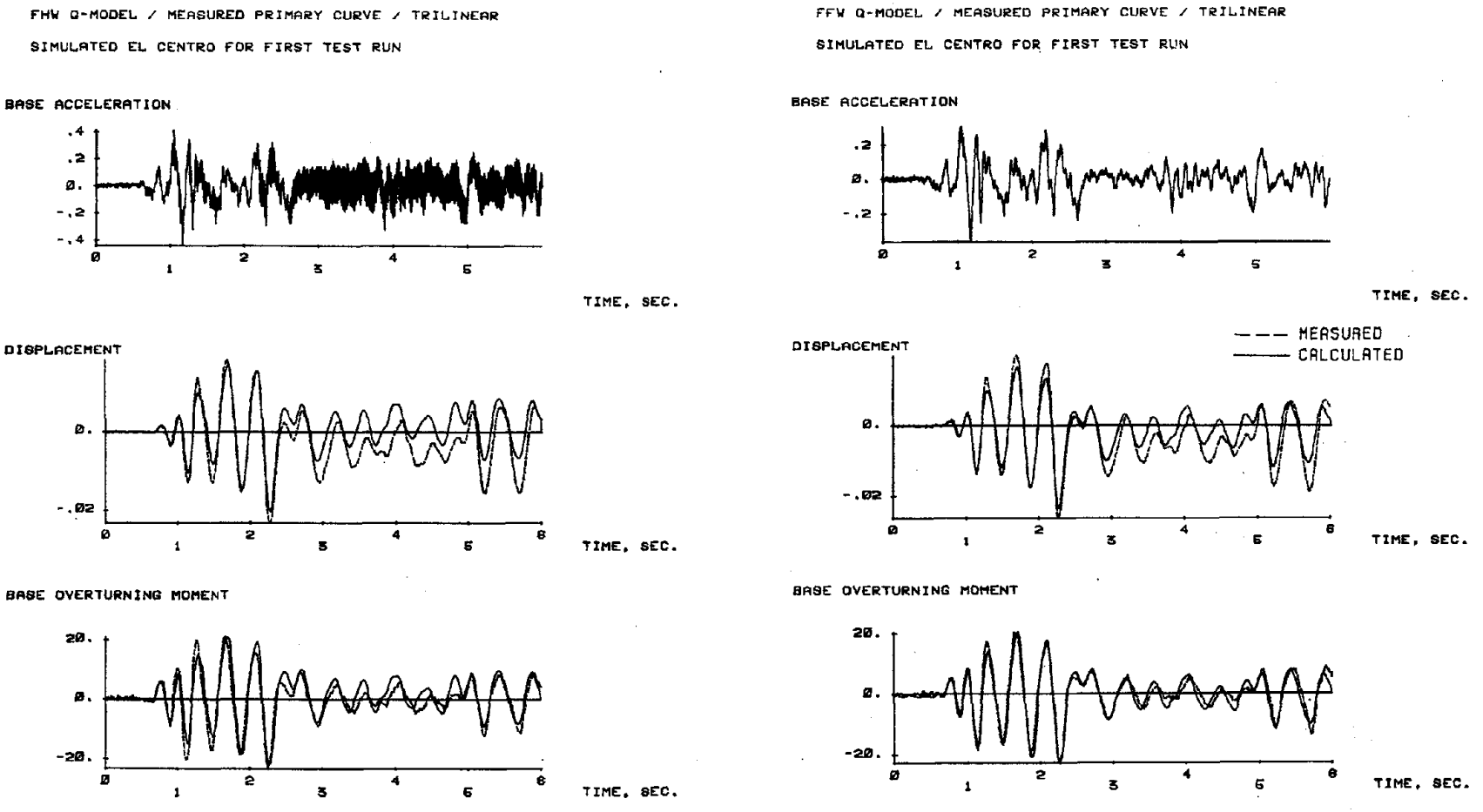


(b) Measured Primary Curve with Trilinear Hysteresis

Fig. 7.17 (contd.) Top-Displacement and Base-Moment Responses Calculated Using the Q-Model

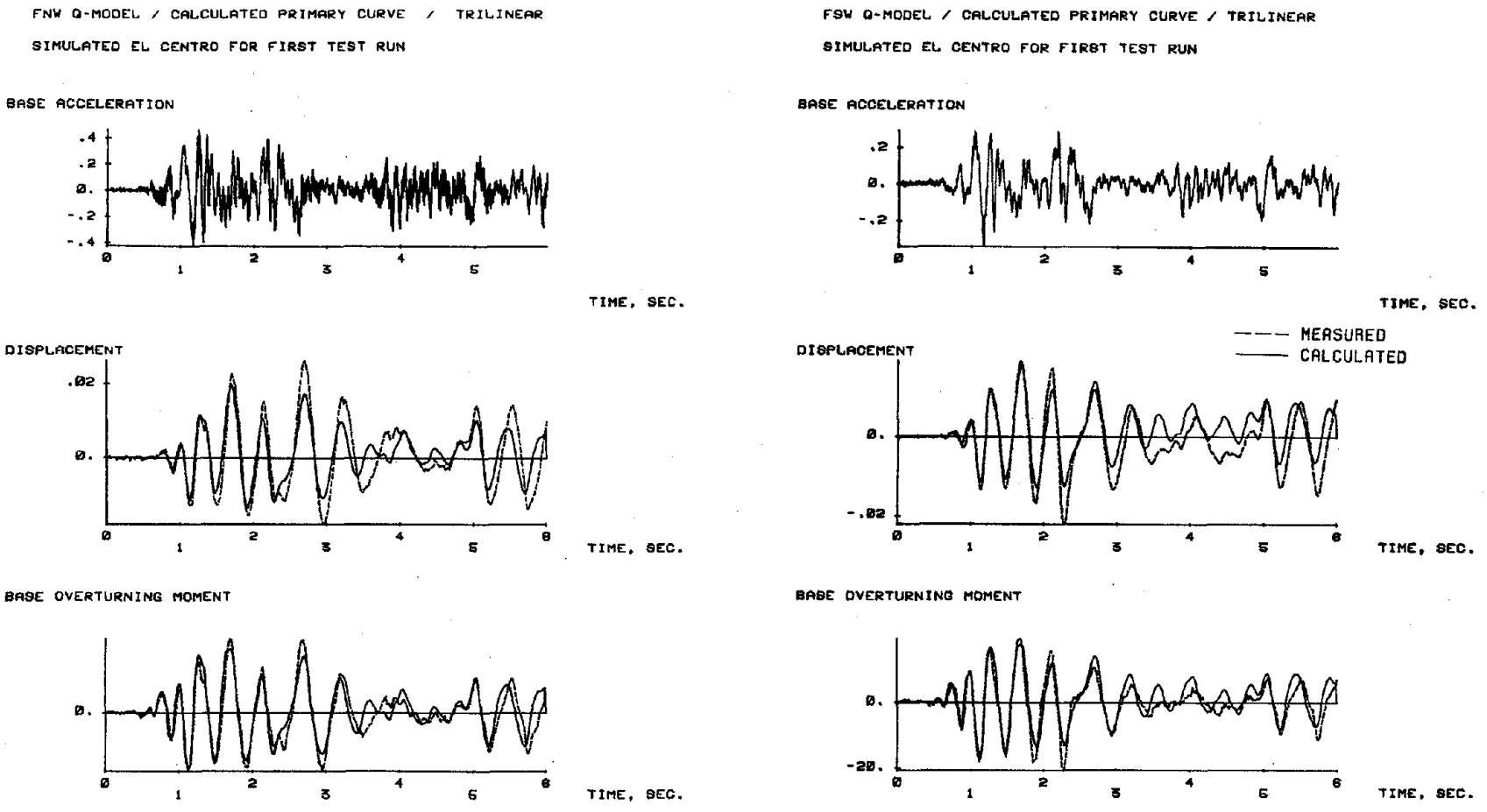


(c) Calculated Primary Curve with Trilinear Hysteresis

Fig. 7.17 (contd.) Top-Displacement and Base-Moment Responses Calculated Using the Q-Model

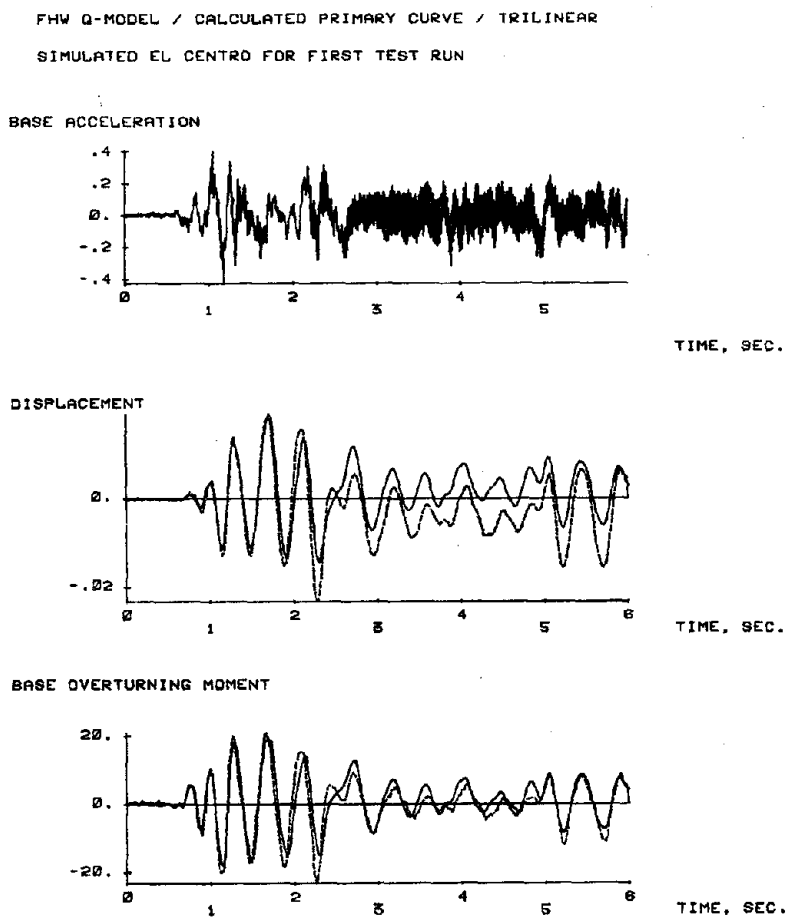


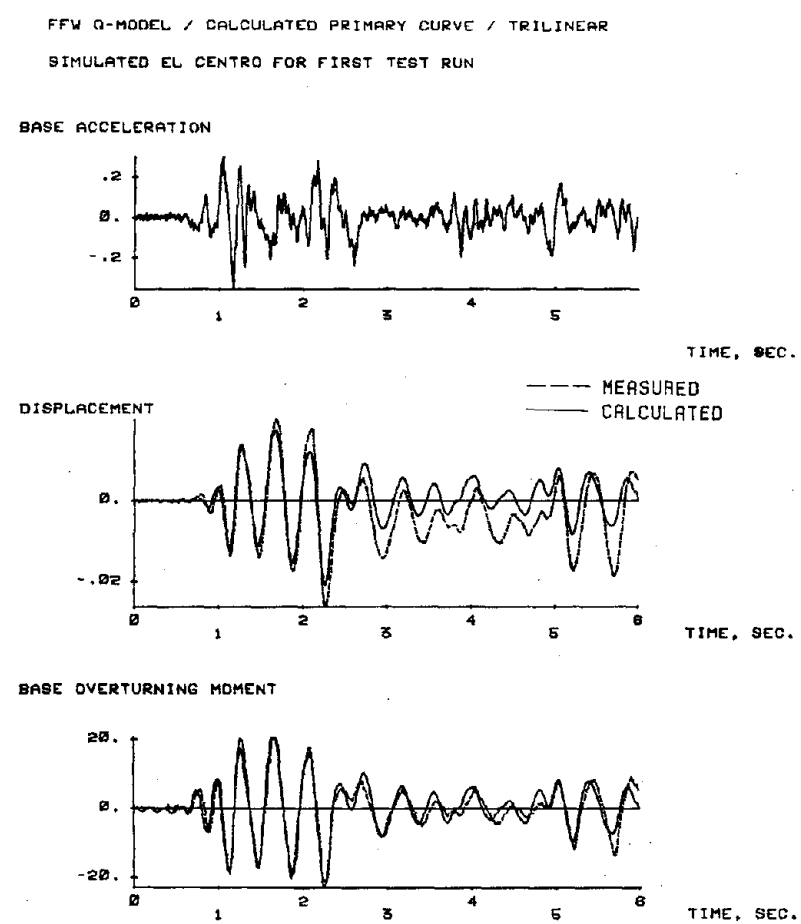


(c) Calculated Primary Curve with Trilinear Hysteresis

Fig. 7.17 (contd.) Top-Displacement and Base-Moment Responses Calculated Using the Q-Model

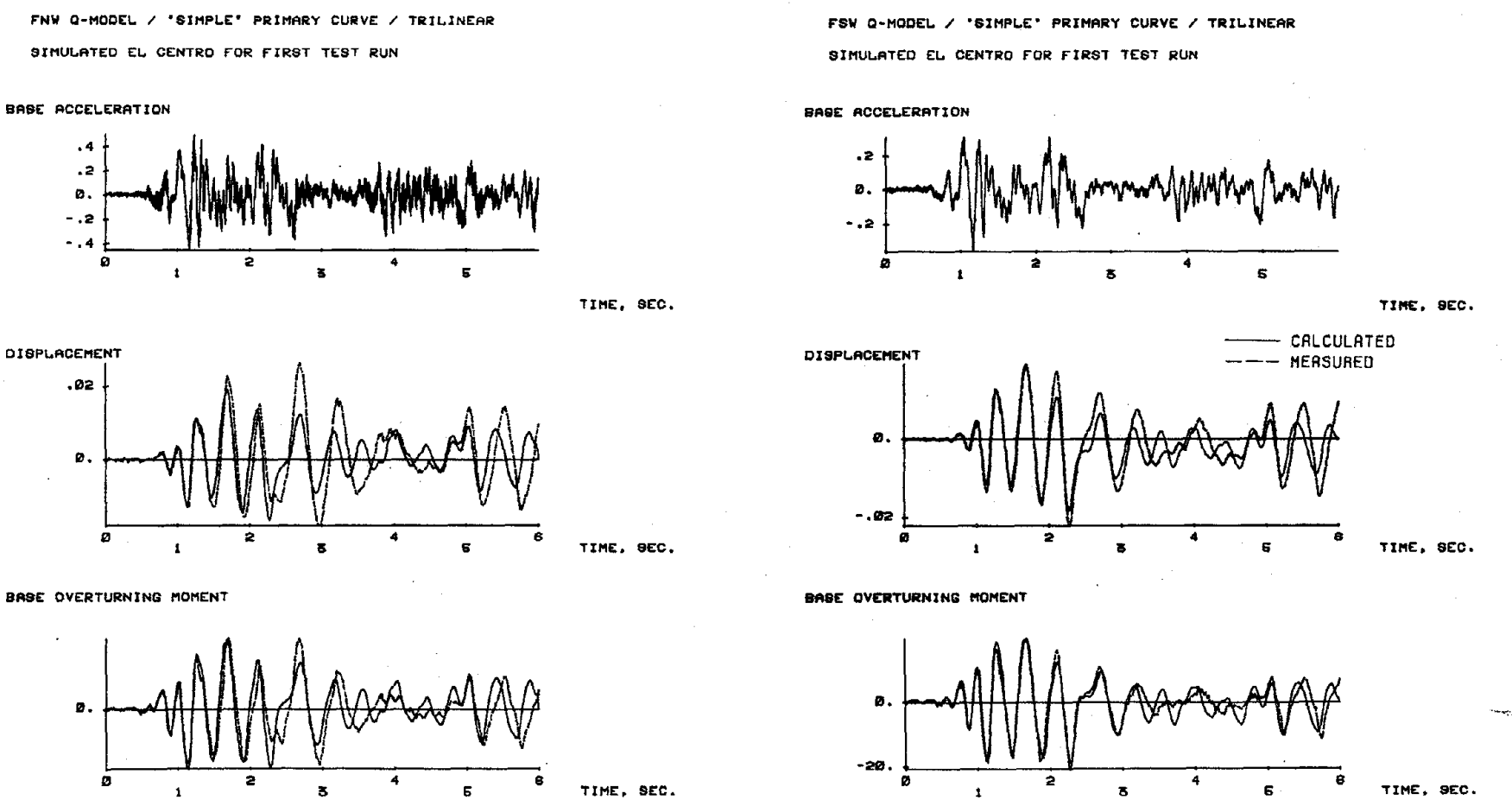


(d) Estimated Primary Curve with Trilinear Hysteresis

Fig. 7.17 (contd.) Top-Displacement and Base-Moment Responses Calculated Using the Q-Model

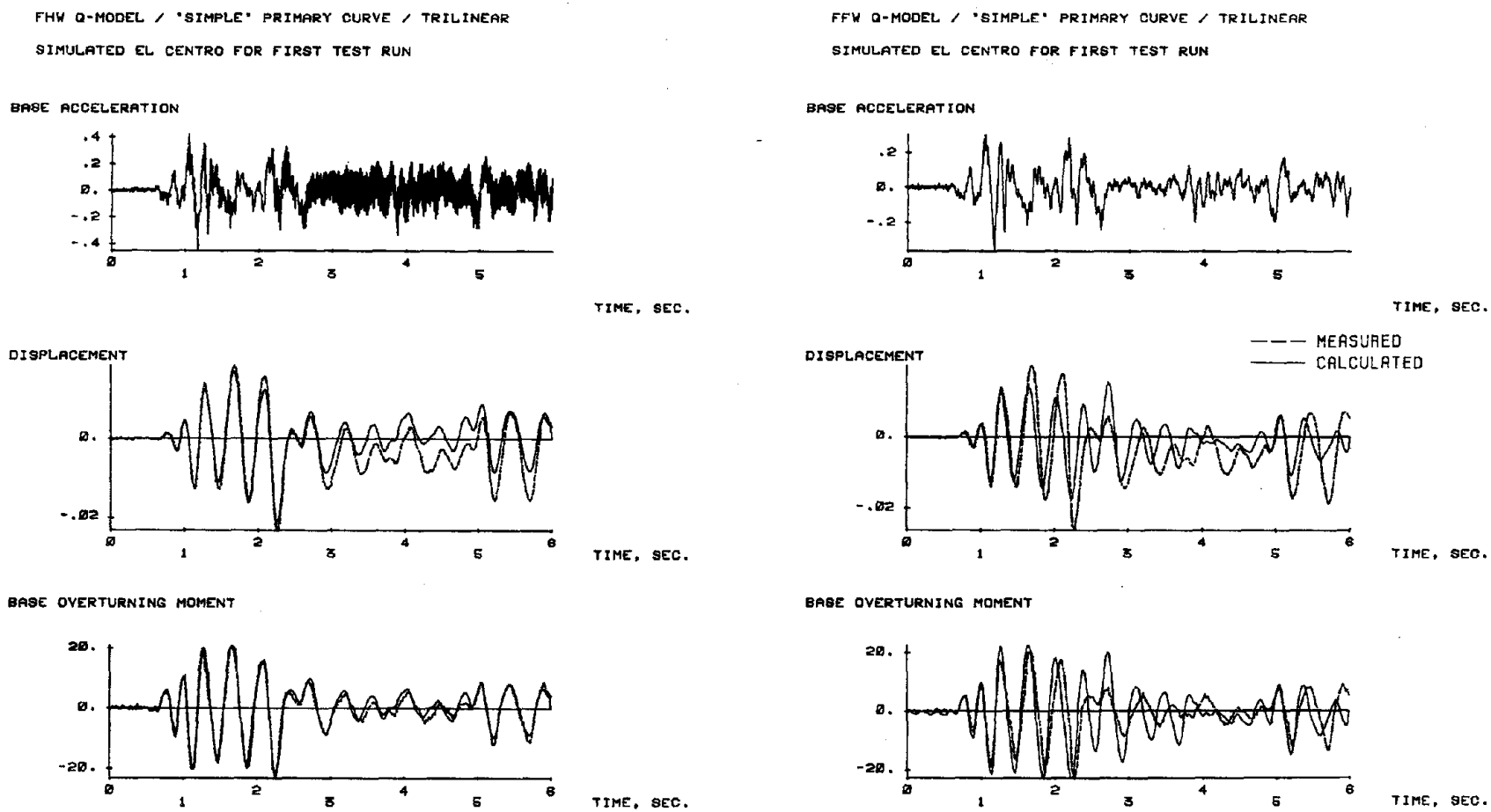


(d) Estimated Primary Curve with Trilinear Hysteresis

Fig. 7.17 (contd.) Top-Displacement and Base-Moment Responses Calculated Using the Q-Model

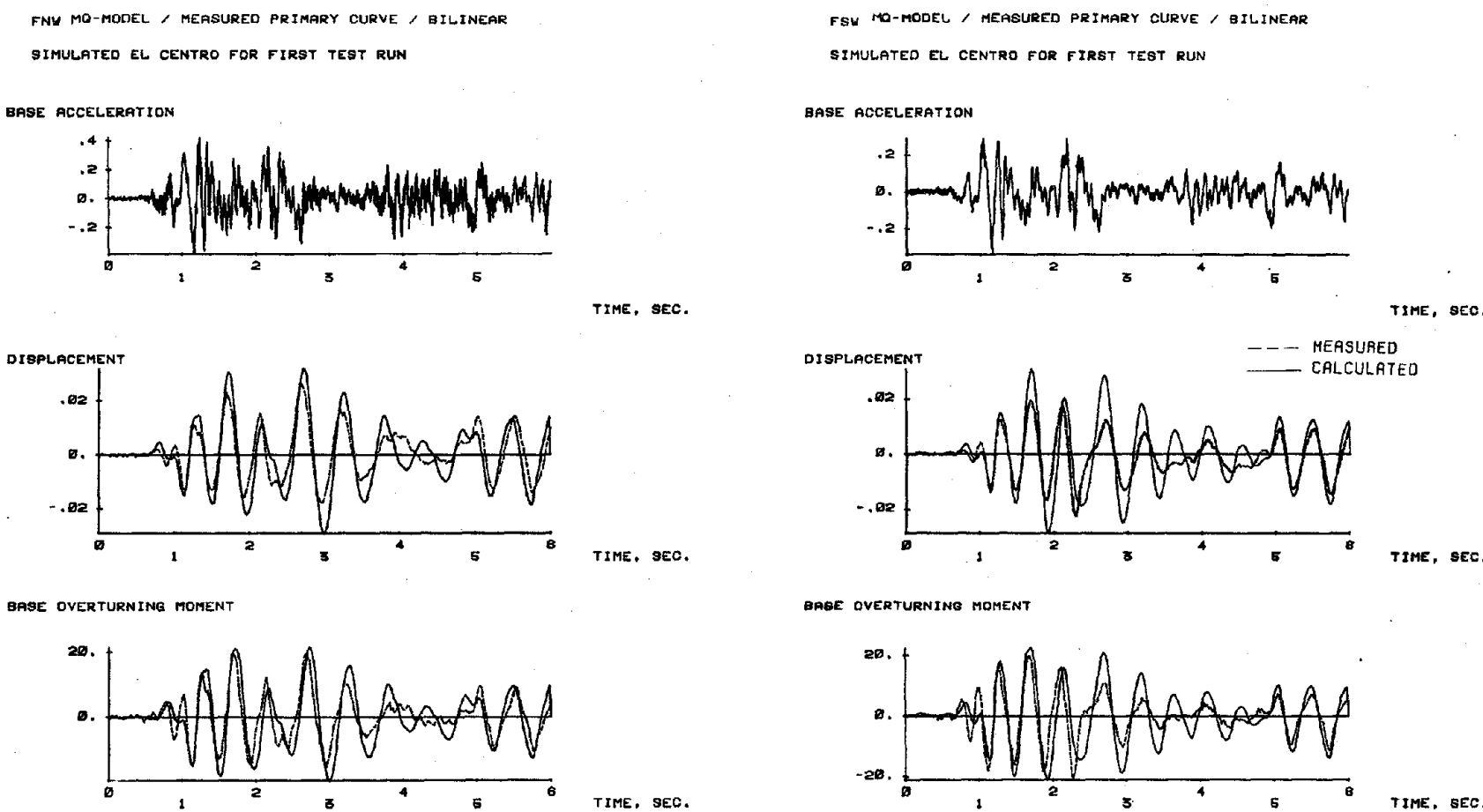


(a) Measured Primary Curve with Bilinear Hysteresis

Fig. 7.18 Top-Displacement and Base-Moment Responses Calculated Using the MQ-Model

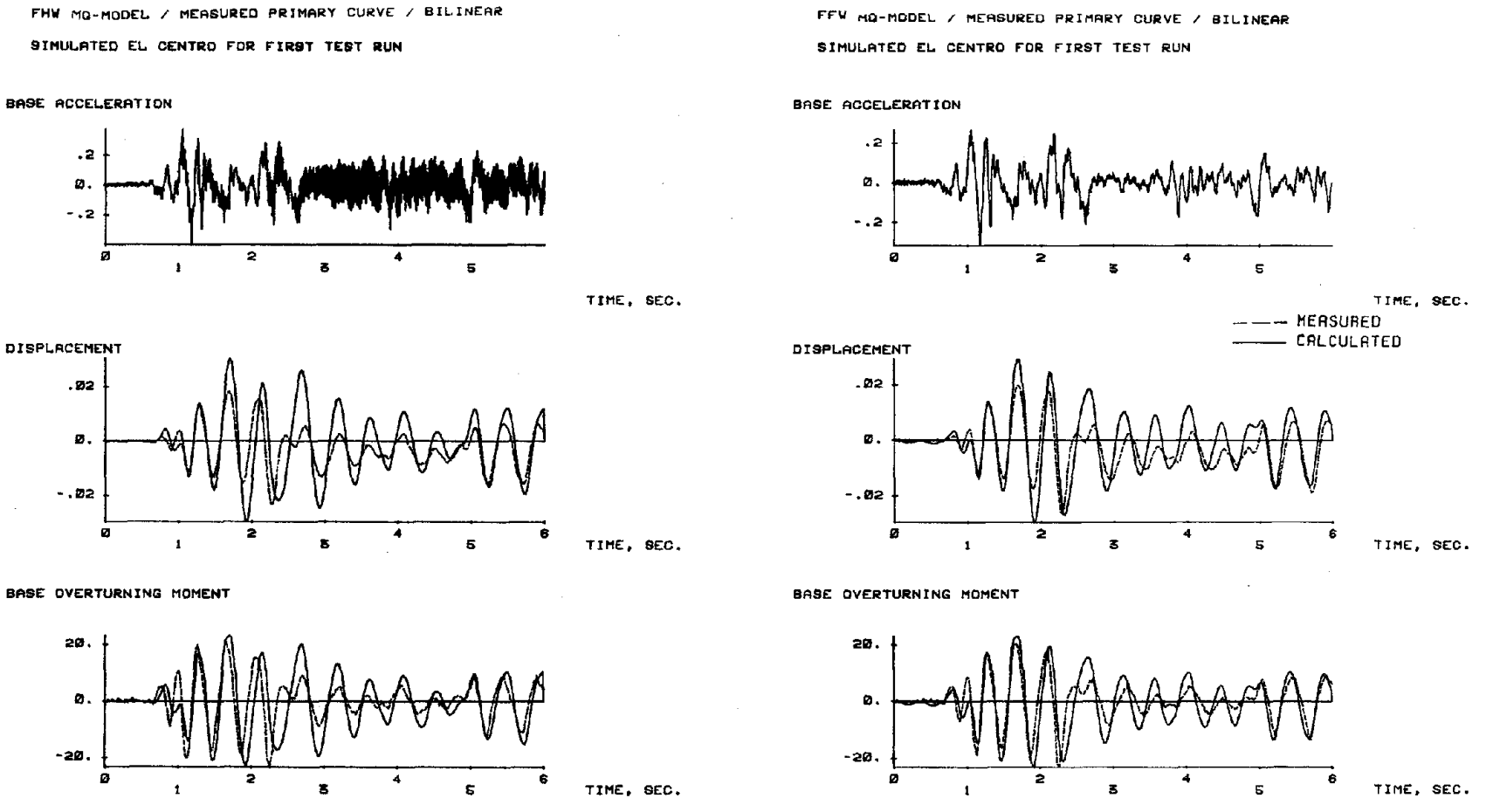


(a) Measured Primary Curve with Bilinear Hysteresis

Fig. 7.18 (contd.) Top-Displacement and Base-Moment Responses Calculated Using the MQ-Model

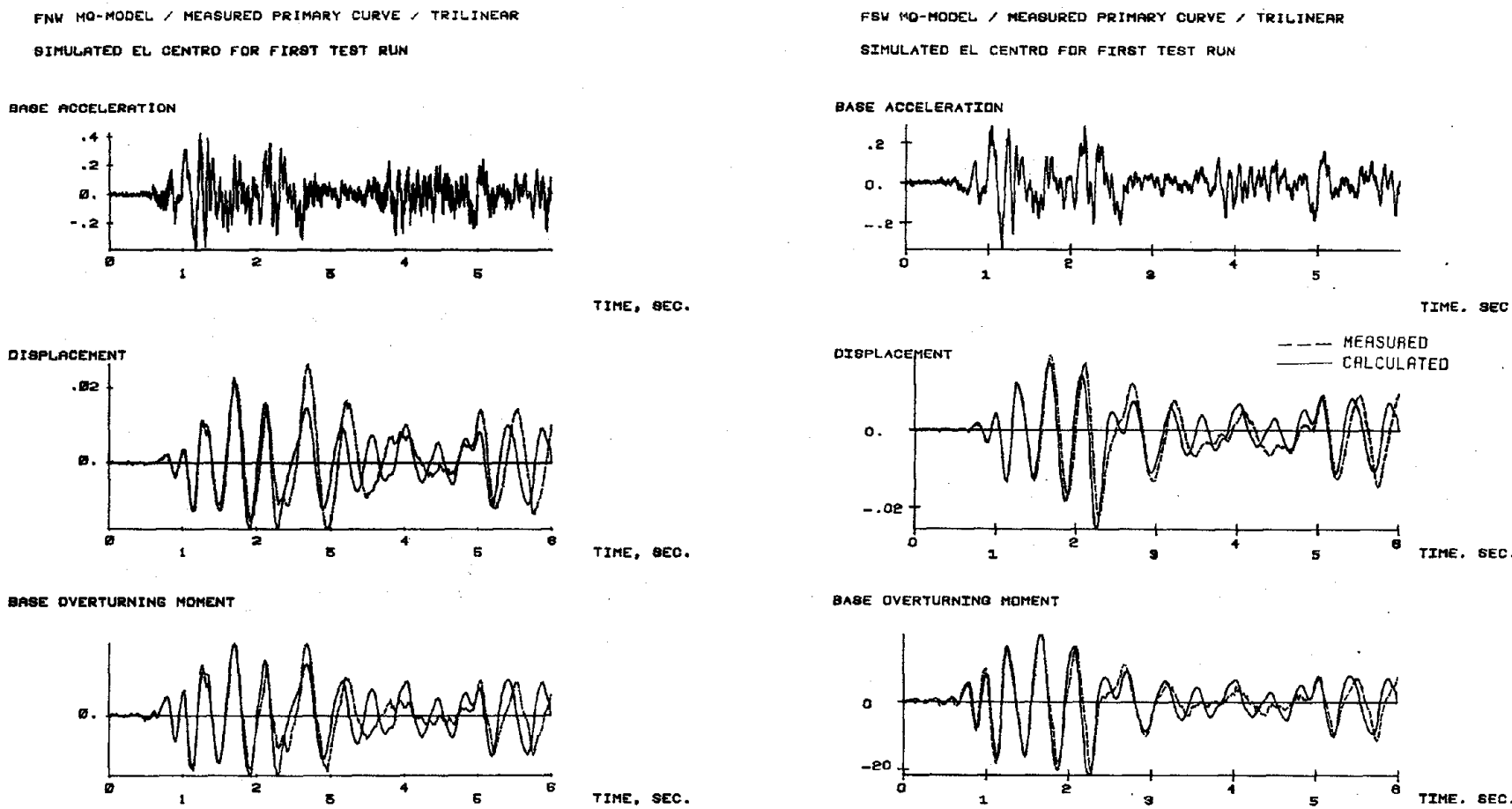


(b) Measured Primary Curve with Trilinear Hysteresis

Fig. 7.18 (contd.) Top-Displacement and Base-Moment Responses Calculated Using the MQ-Model

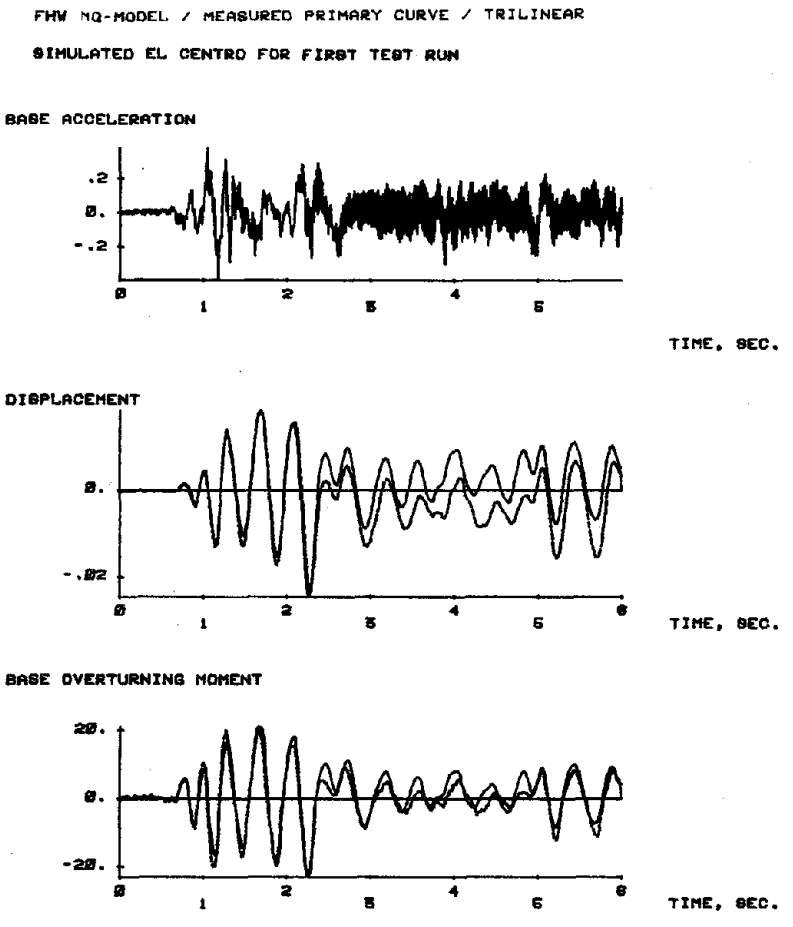


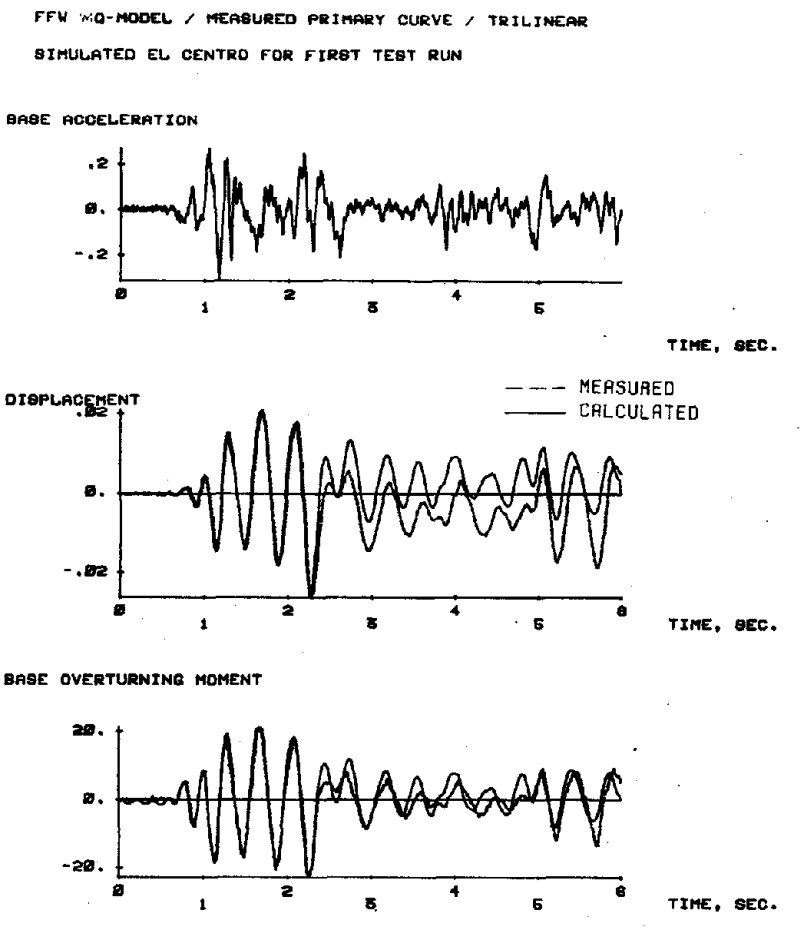


(b) Measured Primary Curve with Trilinear Hysteresis

Fig. 7.18 (contd.) Top-Displacement and Base-Moment Responses Calculated Using the MQ-Model

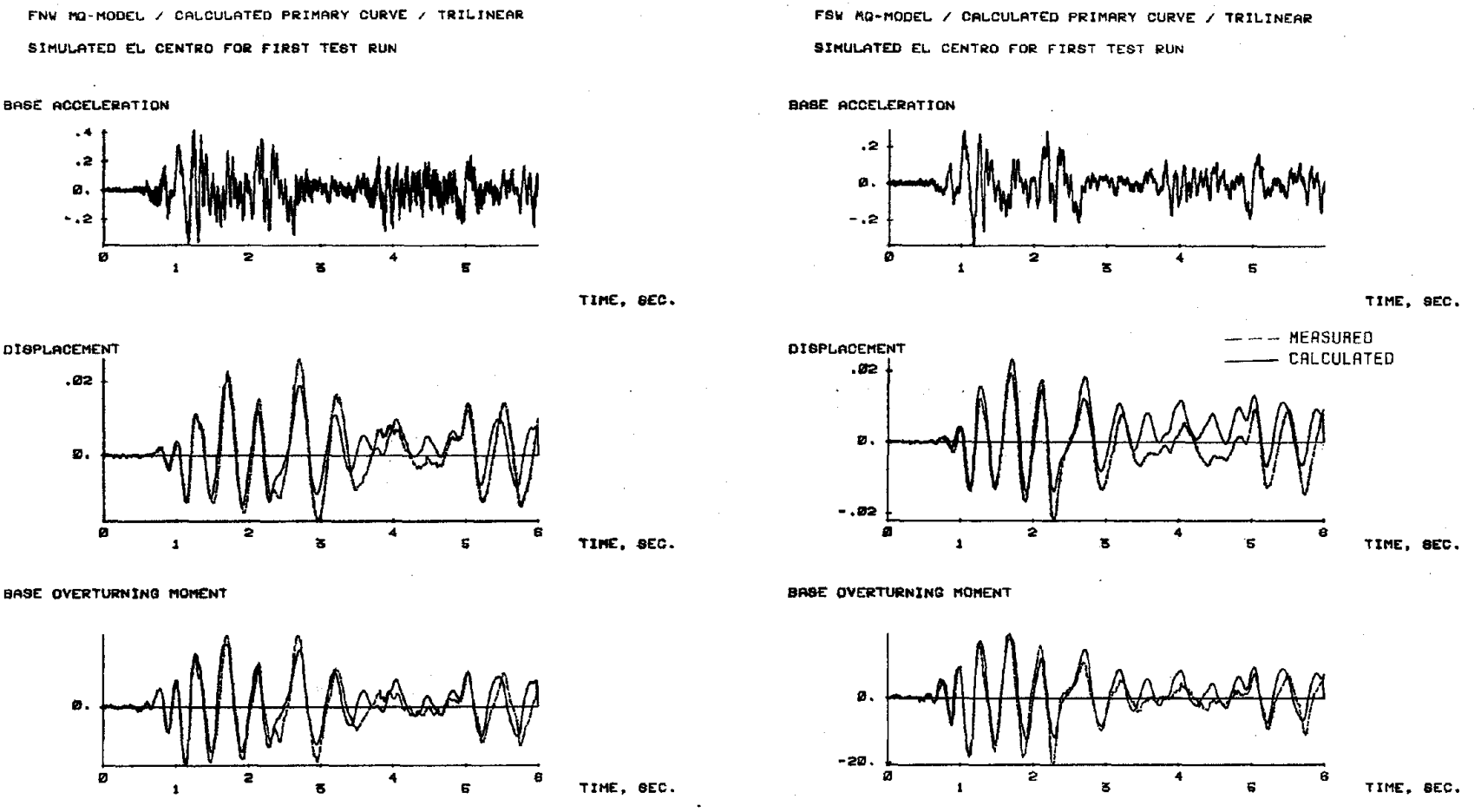


(c) Calculated Primary Curve with Trilinear Hysteresis

Fig. 7.18 (contd.) Top-Displacement and Base-Moment Responses Calculated Using the MQ-Model

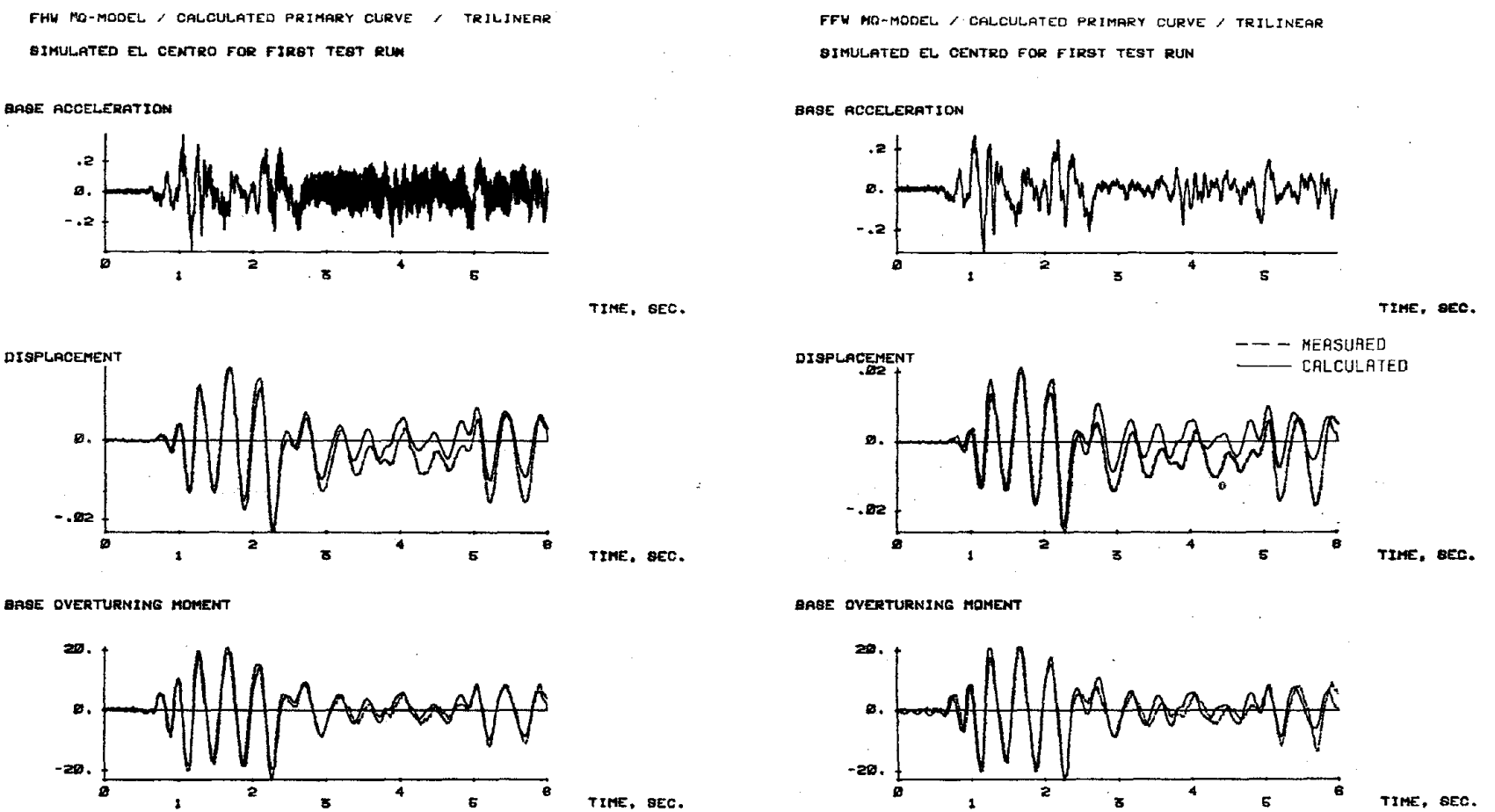


(c) Calculated Primary Curve with Trilinear Hysteresis

Fig. 7.18 (contd.) Top-Displacement and Base-Moment Responses Calculated Using the MQ-Model

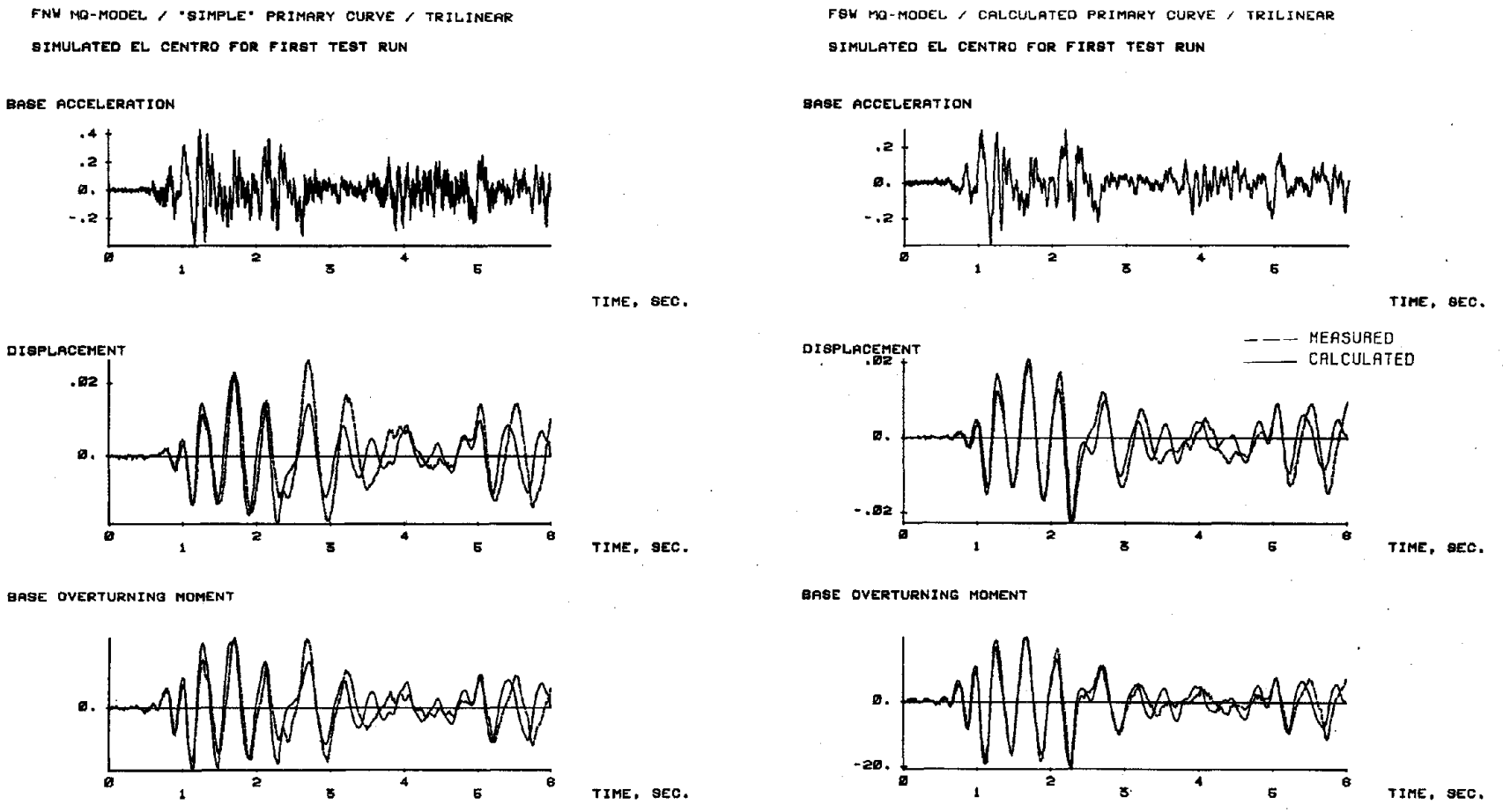


(d) Estimated Primary Curve with Trilinear Hysteresis

Fig. 7.18 (contd.) Top-Displacement and Base-Moment Responses Calculated Using the MQ-Model

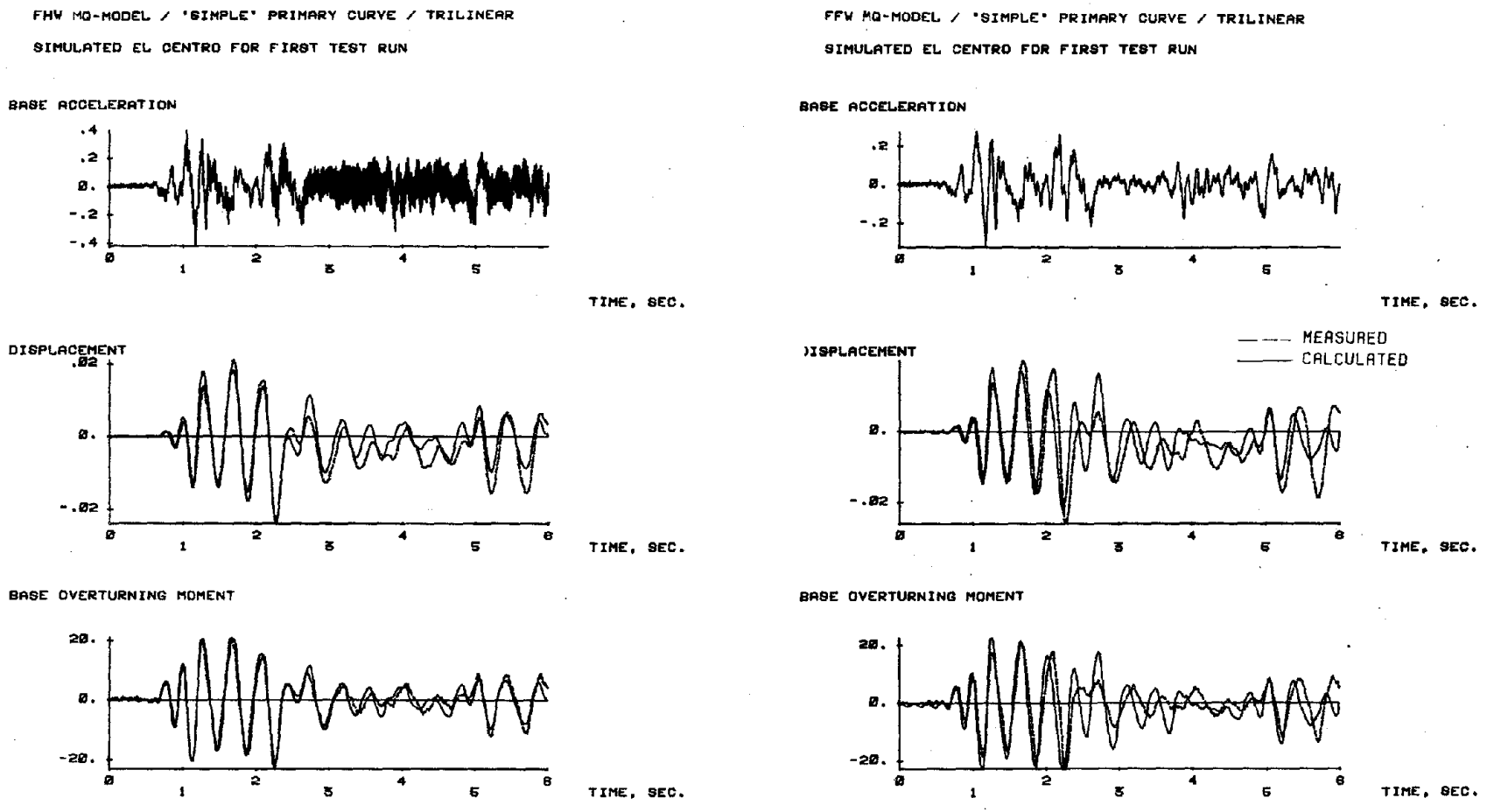


(d) Estimated Primary Curve with Trilinear Hysteresis

Fig. 7.18 (contd.) Top-Displacement and Base-Moment Responses Calculated Using the MQ-Model

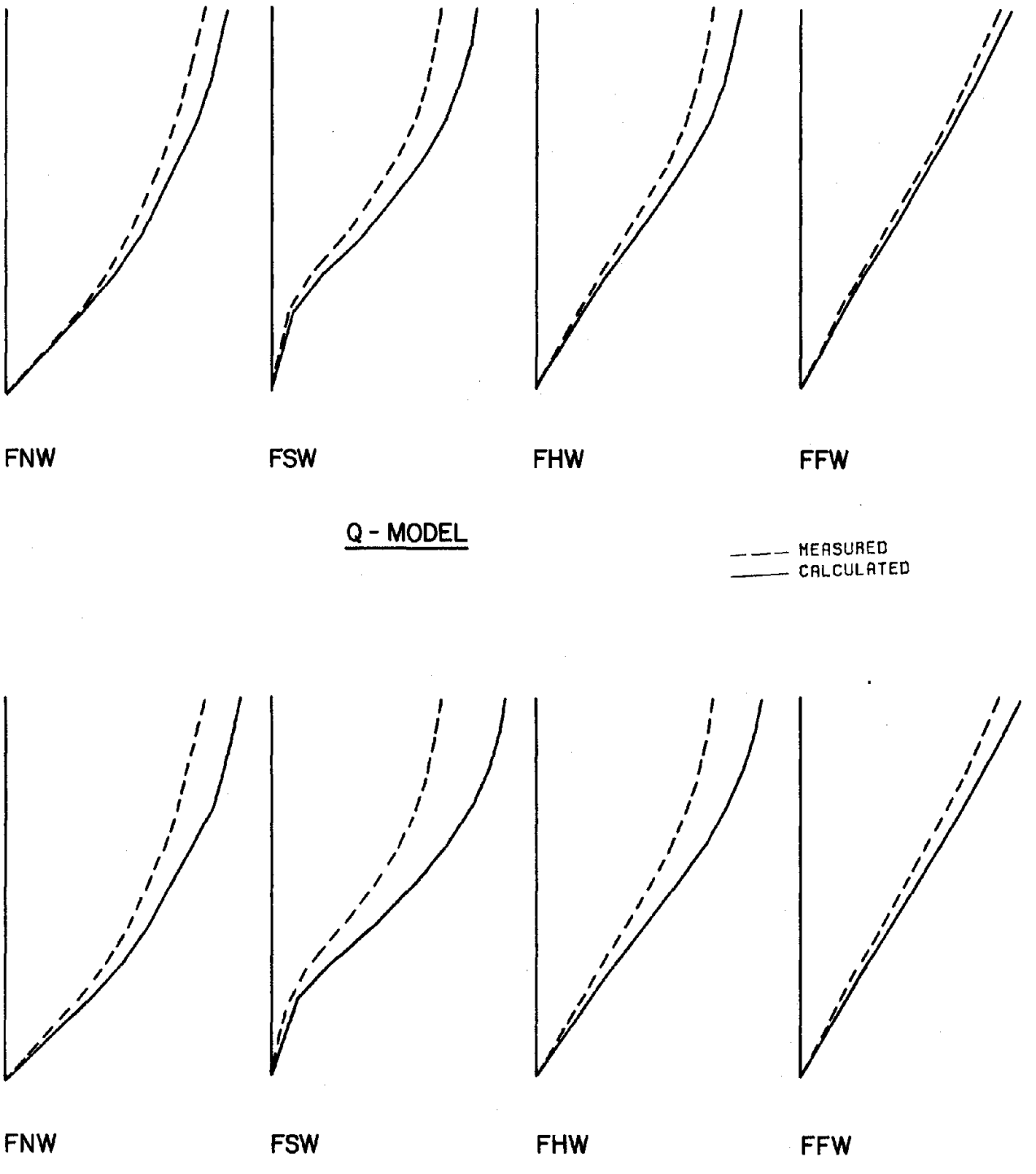


(a) Measured Primary Curve with Bilinear Hysteresis

Fig. 7.19 Comparison of Measured and Calculated Displacement Maxima

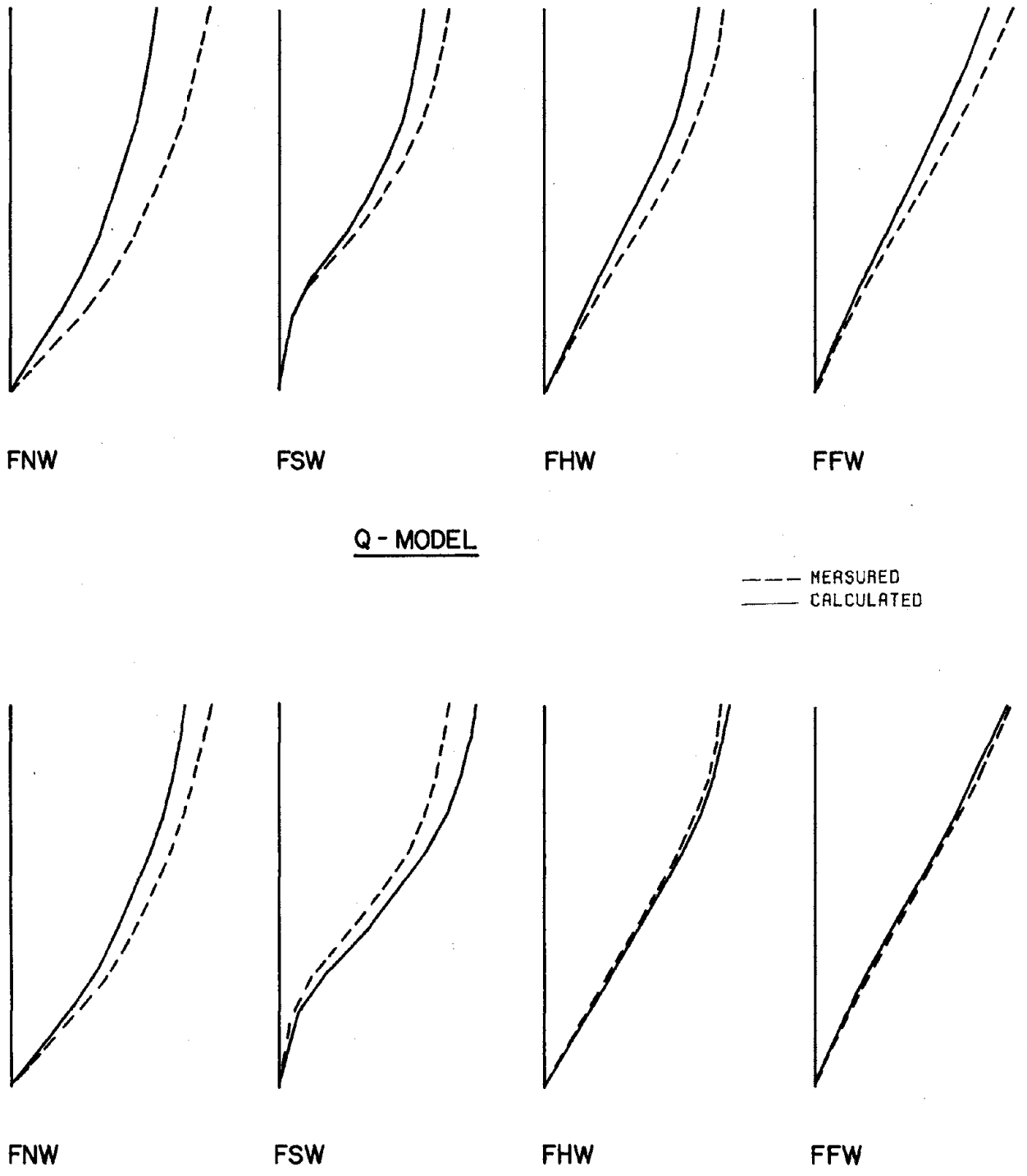


(b) Measured Primary Curve with Trilinear Hysteresis

Fig. 7.19 (contd.) Comparison of Measured and Calculated Displacement Maxima

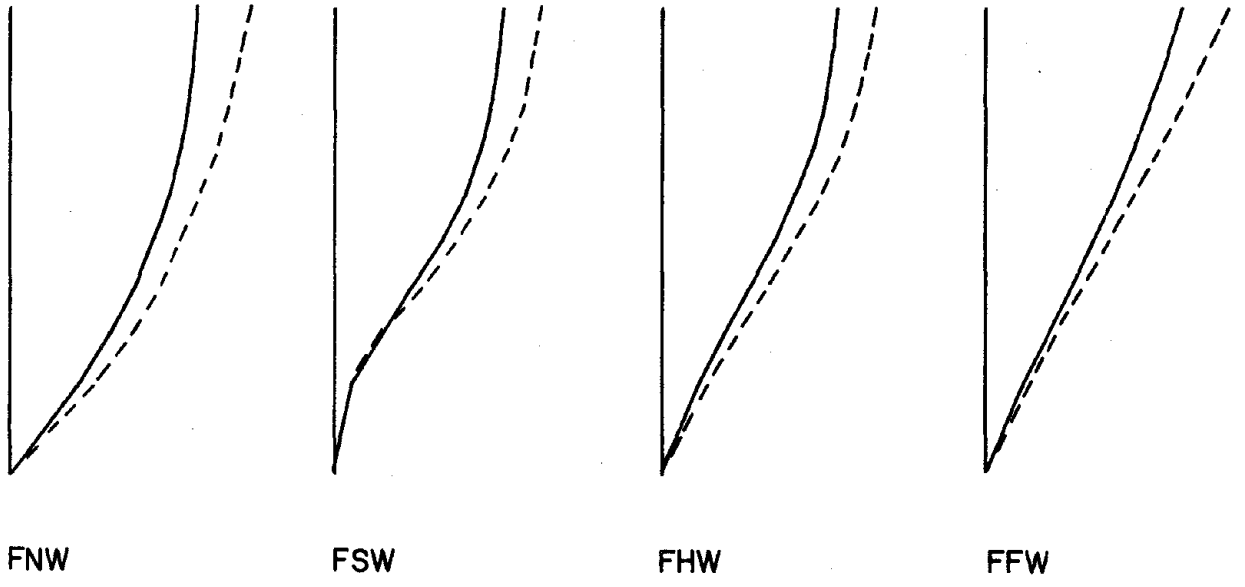


Q - MODEL

MEASURED
CALCULATED

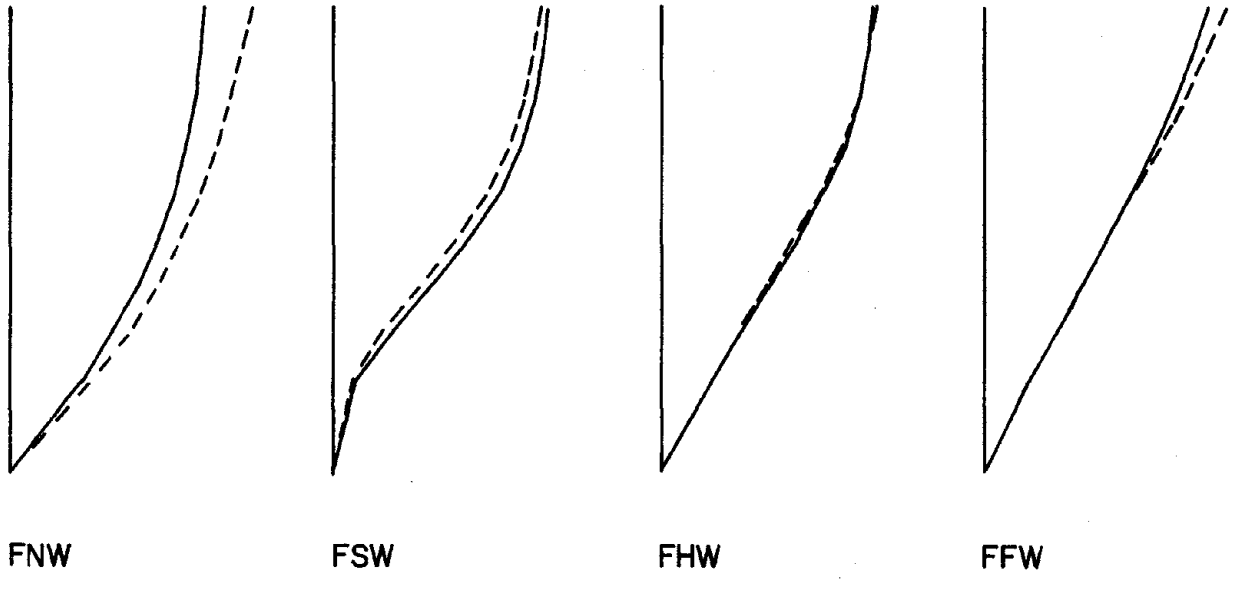


MQ - MODEL

(c) Calculated Primary Curve with Trilinear Hysteresis

Fig. 7.19 (contd.) Comparison of Measured and Calculated Displacement Maxima

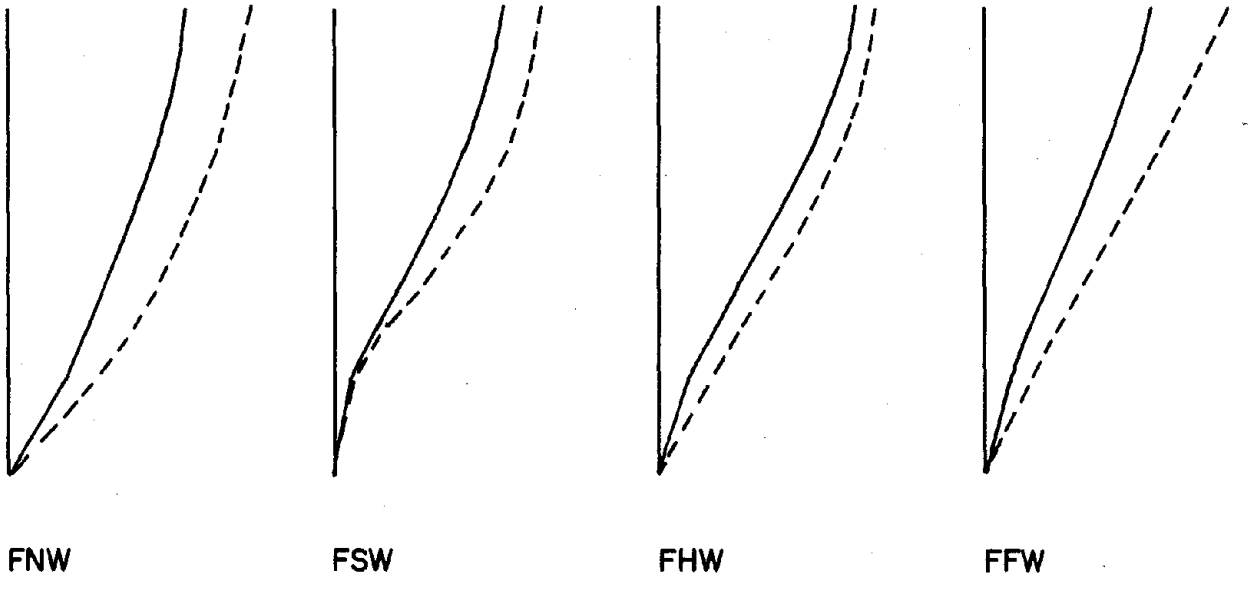


Q - MODEL

--- MEASURED
——— CALCULATED

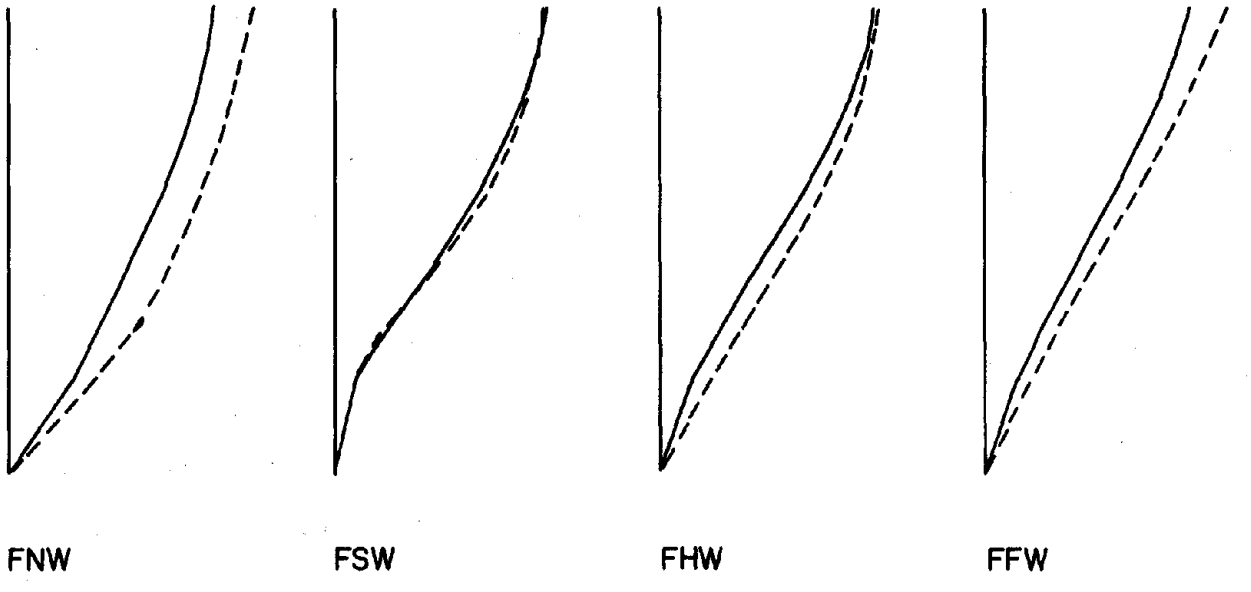


MQ - MODEL

(d) Estimated Primary Curve with Trilinear Hysteresis

Fig. 7.19 (contd.) Comparison of Measured and Calculated Displacement Maxima

# APPENDIX A

# DESCRIPTION OF EXPERIMENTAL WORK

## A.1 Test Structure

### (a) Configuration

Test structures were composed of two frames and one wall which acted in parallel to resist lateral loads (Fig. A.1). Frames had three bays and nine stories at approximately one-twelfth of full scale. Wall heights in each of the four test structures were different (Fig. 2.2). Frames and walls were connected at each of nine story levels so that lateral displacements of all elements at a level would be equal. Rotational restraint of the connections was small. Story weights (which were part of the connecting system) were used to increase lateral inertial forces and vertical load. Base-fixity of frames and walls was insured by prestressing stiff base girders (which had been cast monolithically with the frames and walls) to the testing platform.

### (b) Dimensions

Nominal dimensions of test structures were presented in Chapter 2. Gross concrete cross-sectional dimensions at all beam-column interfaces and at each story level of walls were measured before testing using a mechanical dial gage accurate to 0.01 in. Measured dimensions (Table A.1) were nearly the same as nominal dimensions with small variations. Center-to-center dimensions of story heights and bay widths were identical to the nominal values within the accuracy of the dial gage. Following a test, clear concrete cover for reinforcing steel were checked at twenty random locations per frame and at the base of walls by chipping away concrete cover. Measured depths are presented in Table A.2.

(c) Story Weights

Story weights (Fig. A.1b and A.2d) were made of steel and concrete. Weights were cast with a central opening which allowed penetration of the centrally-located structural walls. A welded box of steel plate and channels formed the inner and outer boundaries of a weight. Embedded No. 4 bars were welded to the plates and channels to insure composite action. Number 11 bars were provided to increase weight. All story weights were cast from a single batch of concrete which included high early-strength cement and pea gravel. Measured weights (including all frame and wall connections) are presented in Table A.3. Measured mass centers were positioned at story-level centerlines in the test setup.

(d) Connections

A nonstructural connection system was required to couple the independent frames and wall into a single unit. Story weights were an integral part of the connecting system. Connections were designed so that (1) displacements of frames and walls would be effectively equal at each level, (2) rotational restraint of connectors on frame and wall elements would be small, (3) frame-wall interaction forces could be measured, and (4) distribution of vertical loads would be determinate.

Frame connections (Fig. A.1c) consisted of a series of channels which distributed vertical and lateral forces to frame-joint centers without eccentricity. Unlike the probably vertical load distribution in a real building, vertical loads were distributed equally to all frame joints at a level. The channels on either side of a frame (Fig. A.1c) were connected to frames with a 7/16-inch diameter bolt passing through tubing which had been cast into joint centers. To reduce rotational re-

sistance, the channels were separated from frames with small-diameter washers and the bolts were tightened "snug" by hand and locked in place with a locknut.

Although it would have been desirable to carry some vertical load in the wall, a connection which transmitted an uncertain amount of vertical load to the wall would have introduced uncertainties in column and wall strengths. For this reason, a steel "link" connection was designed to carry no vertical force (Fig. A.1d). A spherical bearing connection at the mass permitted rotation about three axes. A ball-bearing connection at the wall centerline permitted rotation within the plane of the wall. Using this arrangement, virtually unrestrained rotation of the wall was possible and vertical loads in the wall were avoided. Bolted connections at either end of the connection were tested under reversed loads to insure their adequacy against slip. A necked-down portion of the link was instrumented with strain gages to indicate wall forces (see Section A.3).

A system of bellows (Fig. A.1a) were connected between story weights to increase stiffness in the transverse direction. The bellows were made of hinge-connected steel plates and introduced negligible in-plane resistance. The bellows did not prevent motion transverse to the plane of a structure but did provide some transverse stiffness and stability to the effectively planar structure.

Connections at the base of a test structure (Fig. A.1a) consisted of a series of channels (12 inch) and transverse angles (4 inch) which were used to prestress wall and frame base girders to the test platform. Hydrocal was placed around the channels and angles before tests began.

Absence of cracks in the hydrocal indicated that no base uplift or slippage had occurred during any of the tests.

(e) Frame and Wall Fabrication

Frame reinforcement cages were fabricated by tying plain No. 13 gage bright basic annealed wire (2.32 mm dia.) inside rectangular spirals (Fig. 2.10b). The spirals had been turned from straight lengths of No. 16 gage wire (1.98 mm dia.) on the mandrel of a lathe so that accurate dimensions were obtained. Each spiral was straightened by hand to form the rectangular shapes. For spirals, the quantity $A_v f_y d/s$ (where $A_v$=cross-sectional wire area, $f_y$= yieldstress, d=effective beam or column depth, and s=spacing of transverse wire) was 9.0 kN (minimum) compared with a maximum expected shear of 3.0 kN. Wall reinforcement cages were fabricated by tying knurled No. 2 gage (6.65 mm dia.) wire inside No. 16 gage closed stirrups (Fig. 2.10c). The minimum ratio of the quantity $A_v f_y d/s$ to expected shear was 2.6.

All flexural steel was purchased in straight lengths and was continuous throughout elements so that no splices or welding were required within members or joints. Treatment of all steel included cleaning with a petroleum-based solvent and then wiping clean with acetone. Following tying, cages were sprayed with ten-percent hydrochloric acid solutions and removed to a "fog" room to rust for 72 hours. Following this period, loose rust particles were removed by spraying with a "high-pressure" water stream and scrubbing with a wire brush.

All frames and walls for a single test specimen were cast from a single batch of concrete. The specimens were cast in a horizontal position with the stiff base girders. Frame and wall forms are pictured in Fig. A.2.

Forms were prepared by oiling steel form beds and steel side pieces. Reinforcement cages were held in place by fixing them to tubing which had been bolted to the form beds at joint centers and which would later be used as joint reinforcement for attaching story weights. Steel embedment plates were welded to longitudinal steel within the base girders (Fig. 2.10d and e and A.2b and c).

The concrete mix had dry-weight proportions of 4.0:1.0:1.1 (coarse Wabash River sand:fine lake sand:Type III high early-strength cement) with a water:cement ratio of 0.75. Concrete was consolidated with a stud vibrator and all concrete was in place and finished within two hours of mixing. Forms were struck approximately eight hours afterwards so that frames and wall would be unrestrained on the form beds. The curing period lasted two weeks. During this period, frames and walls were covered with soaked burlap and plastic sheets to prevent moisture loss. Control specimen for determining concrete properties received identical treatment as frames and walls.

Following the curing period, the form beds were lifted to a vertical position so that the attached frame and wall specimens would be upright. The forms were then separated from frames and walls. Frames and walls were allowed to cure approximately two additional weeks before being moved to the earthquake simulator test platform for erection of a test structure. Specimen ages at testing time are presented in Table A.5.

(f) Material Properties

Concrete

The concrete was a small-aggregate concrete with mix proportions identified in Section A.1(e). Control specimens for determining concrete

properties comprised ten 100 by 200mm cylinders for compression tests, six 100 by 200mm cylinders for splitting tests, and twelve 50 by 50 by 200mm prisms for modulus-of-rupture tests. The stress-strain relations were determined from compression tests with strains measured over a 125-mm gage length. It was not possible to measure the descending portion of the stress-strain curve because of equipment limitations. The bounds of measured relations are shown in Fig. A.3. Splitting strengths were determined by loading cylinders along the diameter. Moduli of rupture were determined by loading the prisms at the center of a 150-mm span. Measured concrete properties are summarized in Table A.5.

Reinforcing Steel

Longitudinal steel used in frames was plain No. 13 gage bright-basic annealed wire. Longitudinal steel used in walls was knurled No. 2 gage bright-basic annealed wire. All wires were purchased in straight lengths from Wire Sales Company, Chicago. Ten samples of each wire were tested in tension at strain rates of 0.001/sec. and ten at 0.005/sec. Mean yield stresses (at a strain rate of 0.005/sec.) were 399 and 339 MPa for the No. 13 and No. 2 gage wire, respectively. Stress-strain curves are plotted in Fig. A.4 and a summary of properties is listed in Table A.4.

Wire used for helical, spiral, and stirrup reinforcement was No. 16 gage. Helical and spiral shapes were formed on the mandrel of a lathe and turned to final shapes by hand. Stirrups were bent from straight wire. Because of the extent of overdesign with regard to shear failure, extensive wire testing was not required. A minimum yeild stress of 750 MPa was obtained in tension.

(g) Test Structure Erection

Following frame and wall fabrication, a test structure was erected on the test platform of the University of Illinois Earthquake Simulator (Fig. A.1a and A.5). Construction was begun by positioning a wall on the test platform. Channel sections which were bolted to the test platform on either side of the wall were used as a foundation for stacking story weights. Each weight was lowered about the wall onto collapsible wooden blocks. The blocks had greased teflon pads above them which allowed the weights to be easily and precisely positioned. After positioning, the weight was connected to the wall. During connection, the wall force was monitored continuously with a strain indicator and kept at a low level. The weight was then locked in place with bolts bearing against an erection cage which surrounded the specimen under construction. After all weights were in place, the test frames were positioned and attached on either side of the stacked weights. The collapsible wooden blocks and erection cage were removed one hour before testing began.

## A.2 Test Equipment

(a) Earthquake Simulator

All testing was conducted on the test platform of the University of Illinois Earthquake Simulator. Major components of the simulator system include a hydraulic ram, a power supply, a command center, and a test platform. The overall configuration of the ram and test platform (with a test structure in place) is shown in Fig. A.5. The steel test platform is 3.66 m square in plan with tapped holes which facilitated prestressing of frame and wall base girders. Motion of the test platform (limited to one horizontal direction) is controlled by input from the command center where

an appropriate acceleration record is integrated twice to produce a displacement signal. A servomechanism interprets this signal to reproduce the desired motion.

Detailed descriptions of performance and characteristics of the simulator can be found in References [ 26 ] and [ 33 ].

(b) Free-Vibration Setup

Free vibration of a test structure was imparted by laterally displacing the top level of a test structure with a known force and suddenly releasing the force (Fig. A.6). The procedure and force were the same for all tests.

(c) Static Test Setup

Static test equipment included a loading cable, hydraulic jack, and reaction frame. Story-level centerlines were loaded individually by pulling the center of a story weight with a cable attached to the reaction frame. Loads were attained using a hand-pumped hydraulic jack. A "soft" spring attached in series with the loading jack and cable aided in maintaining constant load levels during data readings. A story level was loaded in three increments with data readings after each load increment. Loads were applied individually to each level working from the top to the bottom. All loads were applied in the same direction for every test.

The strength test was an extension of the static tests conducted following all other testing. In this test, the structure was loaded at the top level in increments until failure was deemed imminent.

## A.3 Instrumentation

Instrumentation was organized so that displacements, accelerations, and wall forces could be measured. Instrument location and orientation

is indicated schematically in Fig. A.7. Photographs appear in Fig. A.8.

Displacements of story-weight centerlines were measured relative to a stiff A-frame fixed to the test platform (Fig. A.5). The A-frame was sufficiently stiff (natural frequency of approximately 50 Hz) that displacements measured relative to the A-frame can be considered measured relative to the base. Additional LVDT's were attached to the top level of north and south test frames as a check on torsional motion.

Accelerometers were used to measure in-plane, transverse, and vertical accelerations. Accelerometers measuring in-plane accelerations at each story level were Endevco piezoresistive type. All others were Endevco Q-flex accelerometers. Base accelerations were measured by accelerometers attached to the top of north and south base girders. Story-level accelerations were measured with accelerometers fixed to north and south frames at story-level centerlines. An additional accelerometer to measure in-plane accelerations was attached to the top of the ninth-level story weight. Transverse accelerations were measured on the top of the ningh level weight. Each transverse accelerometer was offset 500 mm from the center of the test structure. Accelerometers fixed to the top of columns and wall measured vertical accelerations.

Manufacturer's ratings for the two accelerometer types (Q-flex and piezoresistive) are listed below.

| Parameter | Piezoresistive Accelerometers | Q-flex Accelerometers |
|---|---|---|
| Range | ± 25 g | ± 15 g |
| Linearity | 1.0% | 0.03% |
| Frequency Response (5%) | 0-750 Hz | 0-500 Hz |
| Natural Frequency | 2500 Hz | 1000 Hz |
| Damping | 0.7 | 0.6 |

Wall forces were determined from strains measured along a necked-down portion of the link which connected the wall to story weights (Fig. A.1d). The necked-down portion was drilled hollow to form a thin-walled cylinder. Electronic strain gages were arranged in a four-arm bridge so that strains due to flexure of the link would cancel (Fig. A.8d).

## A.4 Recording of Data

### (a) Dynamic Tests

Signals from electronic instruments were amplified and recorded on four separate magnetic analog tape recorders. Each recorder had fourteen channels. One channel per recorder was reserved for the simulator input signal which was later used to synchronize records on different recorders. An additional channel recorded a signal which controlled digitization of records.

It is important to note that exact synchronization of signals from different recorders was not possible because of inherent variation in recorder speeds. Only signals recorded on the same recorder could be directly compared. Layout of instruments on the various recorders is indicated in Fig. A.9.

Calibration was performed by recording the signal produced by known quantities. LVDT's were calibrated by displacing LVDT rods a known distance. Accelerometers were calibrated statically by alternately pointing them toward and away from the floor for negative and positive one-g accelerations. Wall-connection gages were calibrated by applying a known force before erection of a test structure. Electrical calibrations were used to monitor and correct electrical variations throughout a test.

Response signals were recorded for all tests. Full-scale recorder settings were varied for different tests of a structure to accommodate anticipated signal amplitudes. Each electrical calibration was maintained at its original voltage so as to provide a common basis for calibrating a given signal for different tests.

(b) Static Tests

Measurements during static tests included loads, displacements, and wall forces. Loads were inferred from a transducer signal which had been calibrated with a known force. Calibration of LVDT's and wall load-indicators were made during calibrations for dynamic tests. Applied loads were maintained constant while data readings were taken. Electrical signals were received by a 100-channel VIDAR data acquisition system and recorded on paper tape.

(c) Visible Damage

Observation of visible damage was made immediately before any testing began and again immediately following each earthquake simulation. Observations included spalling and crack locations and widths. Crack location was aided through the use of a fluorescent fluid (Partek P1-A Fluorescent, Magnaflux Corporation, Chicago, Illinois) which collected in cracks when washed over specimens and which reflected "black light" to show crack locations. Visible damage was recorded on data sheets.

## A.5 Test Procedure

The test procedure is described in detail in Section 3.2. The test sequence is indicated in Fig. 3.2. Test-structure connections were checked following every earthquake simulation and no loose connections were located. Fixity of test-structure base girders was indicated by the absence of cracks

in hydrocal placed around the foundation connections. Test activities were carefully monitored and compared with a checklist of planned activities. All dynamic tests were completed in a single day. A second day was required for completion of static and strength tests for structures FNW, FHW, and FFW.

## A.6 Data Reduction

Test data that had been recorded on analog magnetic tape was "digitized" and recorded on digital magnetic tape using the Spiras-65 computer of the Department of Civil Engineering. Each recorded signal was digitized at a rate of 200 points per second. Sprias tapes were copied using a Burrough's 6700 system so that tapes could be read using the CDC-Cyber 175 system of the Department of Computer Science. Calibrations that had been recorded before each earthquake simulation, free-vibration, and steady-state test were used to calibrate recorded signals. Shear and moment responses were determined using measured story heights and weights (including all connections and lumped portions of frames and walls). A system of computer programs was used to obtain CALCOMP and Hewlett-Packard 7221A plots and numerical values of data presented in this report.

Data from static tests were recorded on paper tape. These tapes were read into disc files and manipulated using the Cyber system and CALCOMP and H-P 7221A plotters.

## A.7 Description of Wall Tests

### (a) Description of Walls

Four small-scale walls were tested with slowly-varying load reversals. The walls were identical in dimensions and fabrication to the lower four stories of walls used in test structures. The walls were cast as cantilevers with stiff base girders (Fig. A.10). Longitudinal reinforcement had the

same properties as described for walls in nine-story test structures. The concrete, which was nominally the same as that used in test structures, had mean initial and secant moduli of 26.5 and 21.5 MPa and mean compression, splitting, and rupture strengths of 43, 3.5, and 7.4 MPa.

(b) Experimental Setup and Loading Program

The experimental setup is illustrated in Fig. A.10 and B.3. In the setup, the base girder was fixed to a strong floor so that the wall projected as a vertical cantilever. Base fixity was the same as that used in test structures. A single load was applied at one of four story levels through one of the wall "link" connections used in test structures (Fig. A.1d, A.10, and B.3). The loading program is described in Sec. B.1c and Fig. B.2. A load cell indicated applied lateral load and LVDT's measured displacements at each of four story levels and rigid-body translations of a radial bar fixed to the test specimen 50.8 mm above the base of the wall. Dial gauges were used as a check of displacement at loading level and of motion of the base girder relative to the LVDT support. Negligible base-girder motion was observed during testing. Electrical instrument signals were received by a 100-channel VIDAR data acquisition system and recorded on paper tape.

(c) Data Reduction

Paper tape data were read into a disc file on the CYBER 175 computer system. Electrical signals were calibrated using the signals resulting from known force or displacement quantities which were recorded approximately one hour before testing began. Measured displacements of the radial bar attached to the test specimen (Fig. A.10) were used to determine rigid-body rotations and translations at a level 50.8 mm above the base of the wall. Data were plotted (Fig. B.7) using CALCOMP plotting routines.

Table A.1 Measured Cross-Sectional Dimensions

| Structure FNW | | | | | | | | |
|---|---|---|---|---|---|---|---|---|
| Level/ Story | Beam Depth (mm) | | Beam Width (mm) | | Column Depth (mm) | | Column Width (mm) | |
| | Mean | Std. Dev. | Mean | Std. Dev. | Mean | Std. Dev. | Mean | Std. Dev. |
| 9 | 38.4 | 0.85 | 38.1 | 0.30 | 50.9 | 0.51 | 38.8 | 0.42 |
| 8 | 38.1 | 0.48 | 39.0 | 0.36 | 51.0 | 0.47 | 38.9 | 0.52 |
| 7 | 38.1 | 0.35 | 39.2 | 0.49 | 51.0 | 0.45 | 39.0 | 0.45 |
| 6 | 37.7 | 0.60 | 39.2 | 0.43 | 50.9 | 0.54 | 39.1 | 0.41 |
| 5 | 38.1 | 0.33 | 39.0 | 0.41 | 50.8 | 0.44 | 38.9 | 0.33 |
| 4 | 38.4 | 0.44 | 39.0 | 0.41 | 50.8 | 0.79 | 38.7 | 0.45 |
| 3 | 38.8 | 0.56 | 39.1 | 0.39 | 50.9 | 0.41 | 39.1 | 0.46 |
| 2 | 37.9 | 0.36 | 39.1 | 0.35 | 51.3 | 0.50 | 38.8 | 0.41 |
| 1 | 38.1 | 0.31 | 39.0 | 0.29 | 51.0 | 0.42 | 38.5 | 0.33 |
| All Levels | 38.1 | 0.53 | 39.1 | 0.39 | 51.0 | 0.52 | 38.9 | 0.46 |

Table A.1 (contd.) Measured Cross-Sectional Dimensions

| Structure FSW | | | | | | | | |
|---|---|---|---|---|---|---|---|---|
| Level/ Story | Beam Depth (mm) | | Beam Width (mm) | | Column Depth (mm) | | Column Width (mm) | |
| | Mean | Std. Dev. | Mean | Std. Dev. | Mean | Std. Dev. | Mean | Std. Dev. |
| 9 | 38.4 | 0.55 | 38.2 | 0.29 | 51.2 | 0.41 | 38.5 | 0.36 |
| 8 | 38.3 | 0.38 | 38.8 | 0.43 | 51.2 | 0.32 | 38.6 | 0.32 |
| 7 | 38.2 | 0.50 | 38.8 | 0.29 | 51.0 | 0.35 | 38.4 | 0.30 |
| 6 | 38.0 | 0.36 | 38.7 | 0.37 | 51.1 | 0.36 | 38.6 | 0.57 |
| 5 | 38.1 | 0.40 | 39.0 | 0.48 | 51.2 | 0.33 | 38.5 | 0.31 |
| 4 | 38.2 | 0.38 | 38.5 | 0.41 | 51.2 | 0.35 | 38.7 | 0.40 |
| 3 | 38.2 | 0.25 | 38.8 | 0.41 | 51.1 | 0.38 | 38.8 | 0.49 |
| 2 | 38.3 | 0.35 | 38.0 | 0.51 | 51.1 | 0.33 | 38.7 | 0.45 |
| 1 | 38.1 | 0.49 | 38.8 | 0.43 | 51.2 | 0.37 | 38.6 | 0.47 |
| All Levels | 38.2 | 0.41 | 38.7 | 0.44 | 51.2 | 0.35 | 38.6 | 0.42 |

Table A.1 (contd.) Measured Cross-Sectional Dimensions

| Structure FHW | | | | | | | | |
|---|---|---|---|---|---|---|---|---|
| Level/ Story | Beam Depth (mm) | | Beam Width (mm) | | Column Depth (mm) | | Column Width (mm) | |
| | Mean | Std. Dev. | Mean | Std. Dev. | Mean | Std. Dev. | Mean | Std. Dev. |
| 9 | 38.3 | 0.42 | 38.4 | 0.33 | 51.1 | 0.26 | 38.6 | 0.38 |
| 8 | 38.4 | 0.27 | 38.7 | 0.39 | 51.2 | 0.24 | 38.6 | 0.51 |
| 7 | 38.3 | 0128 | 38.7 | 0.39 | 51.0 | 0.26 | 38.5 | 0.32 |
| 6 | 38.1 | 0.33 | 38.6 | 0.35 | 50.9 | 0.32 | 38.5 | 0.40 |
| 5 | 38.2 | 0.49 | 38.7 | 0.32 | 51.1 | 0.35 | 38.6 | 0.48 |
| 4 | 38.3 | 0.29 | 38.6 | 0.39 | 51.1 | 0.26 | 38.6 | 0.36 |
| 3 | 38.0 | 0.34 | 38.7 | 0.40 | 51.3 | 0.42 | 38.6 | 0.43 |
| 2 | 38.2 | 0.43 | 38.8 | 0.49 | 51.1 | 0.36 | 38.6 | 0.32 |
| 1 | 38.1 | 0.19 | 38.6 | 0.35 | 51.1 | 0.47 | 38.5 | 0.35 |
| All Levels | 38.2 | 0.36 | 38.6 | 0.38 | 51.1 | 0.34 | 38.6 | 0.39 |

Table A.1 (contd.) Measured Cross-Sectional Dimensions

| Structure FFW | | | | | | | | |
|---|---|---|---|---|---|---|---|---|
| Level/ Story | Beam Depth (mm) | | Beam Width (mm) | | Column Depth (mm) | | Column Width (mm) | |
| | Mean | Std. Dev. | Mean | Std. Dev. | Mean | Std. Dev. | Mean | Std. Dev. |
| 9 | 38.6 | 0.36 | 38.6 | 0.44 | 51.1 | 0.34 | 38.7 | 0.23 |
| 8 | 38.5 | 0.24 | 38.7 | 0.37 | 51.1 | 0.35 | 38.7 | 0.45 |
| 7 | 38.2 | 0.47 | 39.0 | 0.30 | 51.1 | 0.29 | 38.8 | 0.38 |
| 6 | 38.2 | 0.43 | 38.9 | 0.30 | 51.1 | 0.29 | 30.9 | 0.47 |
| 5 | 38.2 | 0.57 | 39.9 | 0.26 | 51.3 | 0.35 | 38.7 | 0.29 |
| 4 | 38.5 | 0.38 | 39.0 | 0.42 | 51.1 | 0.24 | 38.7 | 0.27 |
| 3 | 38.0 | 0.30 | 38.9 | 0.35 | 51.3 | 0.28 | 38.8 | 0.34 |
| 2 | 38.4 | 0.30 | 38.9 | 0.48 | 51.1 | 0.26 | 38.9 | 0.24 |
| 1 | 38.3 | 0.16 | 39.0 | 0.25 | 51.3 | 0.36 | 38.9 | 0.33 |
| All Levels | 38.3 | 0.41 | 38.9 | 0.37 | 51.2 | 0.31 | 38.8 | 0.35 |

Table A.1 (contd.) Measured Cross-Sectional Dimensions

| Level/ Story | Wall Dimensions, mm | | | | | |
|---|---|---|---|---|---|---|
| | FSW | | FHW | | FFW | |
| | Depth | Width | Depth | Width | Depth | Width |
| 9 | -- | -- | -- | -- | 205 | 38.4 |
| 8 | -- | -- | -- | -- | 205 | 38.5 |
| 7 | -- | -- | -- | -- | 206 | 38.5 |
| 6 | -- | -- | -- | -- | 205 | 39.0 |
| 5 | -- | -- | -- | -- | 204 | 38.5 |
| 4 | -- | -- | 204 | 39.5 | 204 | 38.2 |
| 3 | -- | -- | 203 | 39.0 | 204 | 38.5 |
| 2 | -- | -- | 203 | 39.4 | 203 | 38.6 |
| 1 | 203 | 38.6 | 203 | 39.1 | 203 | 38.1 |
| Base | 202 | 38.2 | 203 | 38.2 | 203 | 38.9 |

Table A.2 Concrete Cover for Longitudinal Steel*

| Test Structure | Beams** | | Columns** | | Wall Base | |
|---|---|---|---|---|---|---|
| | Mean | Std. Dev. | Mean | Std. Dev. | East | West |
| FNW | 6.5 | 1.1 | 5.9 | 0.8 | -- | -- |
| FSW | 6.1 | 0.9 | 5.8 | 1.2 | 5.6 | 6.4 |
| FHW | 5.6 | 0.9 | 6.0 | 1.1 | 7.1 | 7.1 |
| FFW | 6.0 | 0.5 | 5.7 | 0.8 | 6.4 | 6.4 |

* All dimensions in mm

** Beam and column values based on 20 samples each

Table A.3 Measured Story Weights*

| Level | Weight, kN |
|---|---|
| 9 | 4.55 |
| 8 | 4.54 |
| 7 | 4.57 |
| 6 | 4.55 |
| 5 | 4.56 |
| 4 | 4.56 |
| 3 | 4.53 |
| 2 | 4.56 |
| 1 | 4.51 |

* Includes lumped portions of frames and walls and all connections. Subtract 0.04 kN if no wall.

Table A.4 Steel Properties

| Wire Gage | Diameter (mm) | Strain Rate (1/sec) | Yield Stress** MPa | Strength** MPa |
|---|---|---|---|---|
| No. 2 | 6.65 | 0.001 | 330 ± 3 | 388 ± 2 |
| | | 0.005 | 339 ± 6 | 392 ± 5 |
| No. 13 | 2.32 | 0.001 | 384 ± 11 | 417 ± 9 |
| | | 0.005 | 399 ± 12 | 426 ± 15 |

** Mean ± standard deviation based on ten samples each.

Table A.5 Concrete Properties

| Test Structure | Age at Testing (days) | Initial Modulus (MPa) | Secant Modulus (MPa) | Compression* Strength (MPa) | Splitting Strength (MPa) | Modulus of* Rupture (MPa) |
|---|---|---|---|---|---|---|
| FNW | 49 | 23,000 | 20,000 | 40(1.4) | 3.5 | 8.7(0.6) |
| FSW | 44 | 20,000 | 18,000 | 35(1.3) | 3.0 | 7.8(0.3) |
| FHW | 43 | 21,000 | 19,000 | 36(1.3) | 3.6 | 8.5(0.5) |
| FFW | 52 | 22,000 | 19,000 | 37(2.3) | 3.1 | -- |
| overall | -- | 22,000 | 19,000 | 37 | 3.3 | 8.3 |

* Mean (Standard Deviation)

Table A.6 Chronology of Experiment*

| Event | Structure | | | |
|---|---|---|---|---|
| | FNW | FSW | FHW | FFW |
| Casting | 9/14/78 | 3/7/79 | 2/16/79 | 12/18/79 |
| Remove Specimen from Forms | 9/28/78 | 3/20/79 | 3/2/79 | 1/2/79 |
| Begin Testing | 11/1/78 | 4/18/79 | 3/28/79 | 2/7/79 |
| End Testing | 11/2/78 | 4/19/79 | 3/29/79 | 2/8/79 |
| Test Coupons | 11/3/78 | 4/20/79 | 3/30/79 | 2/9/79 |

*Dates are month/day/year.

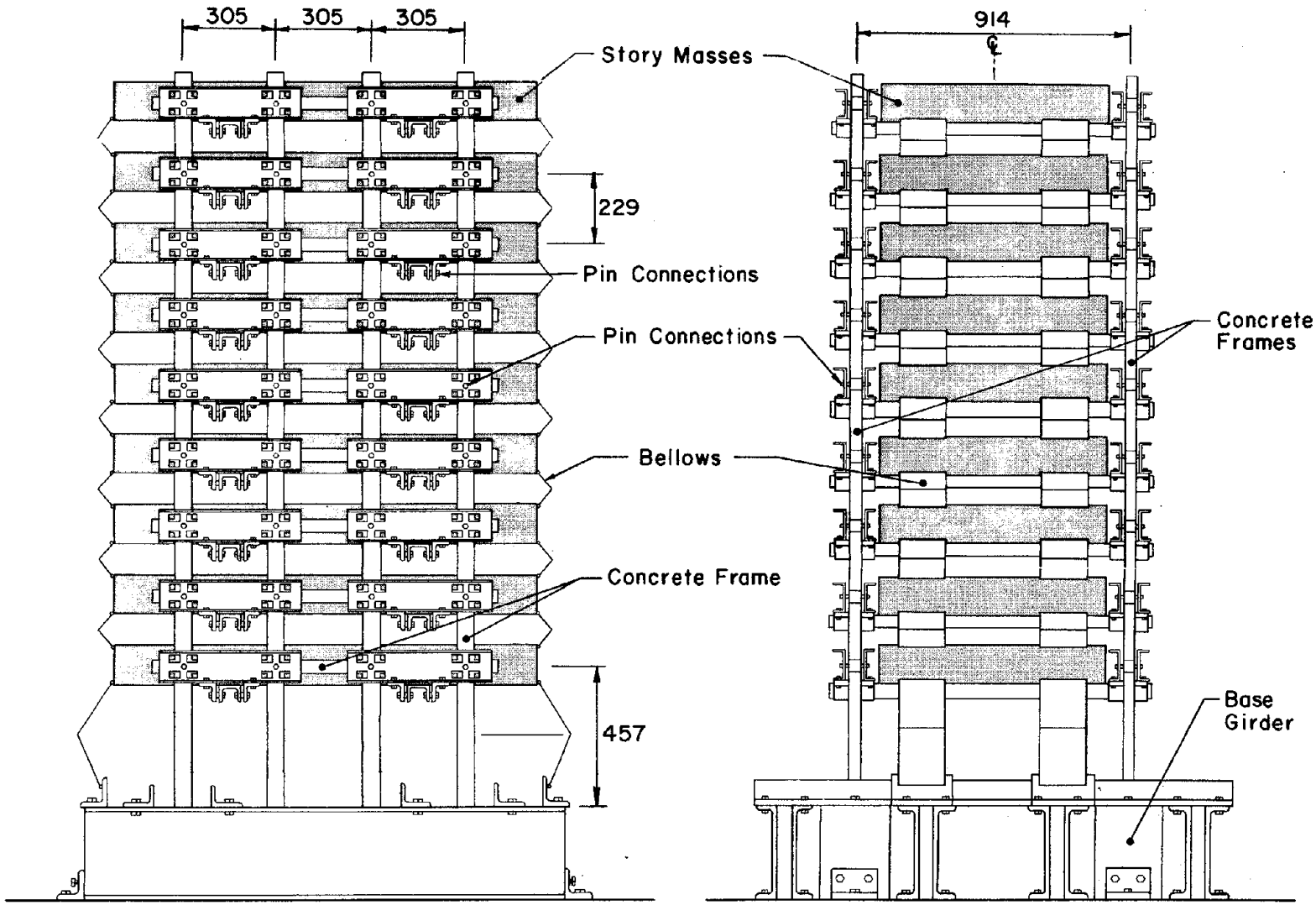


Fig. A.1 Test Structure and Connections

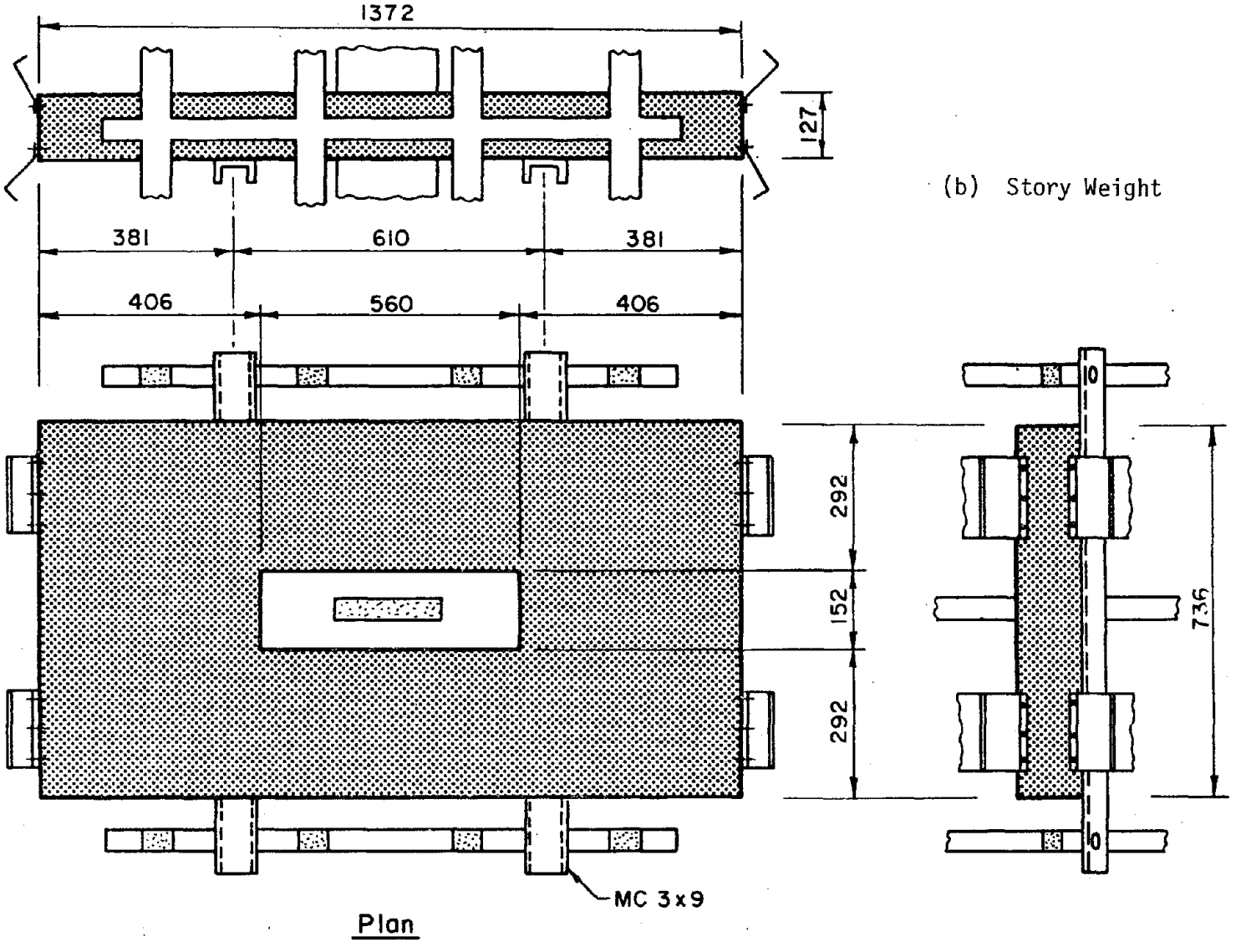


Fig. A.1 (contd.) Test Structure and Connections

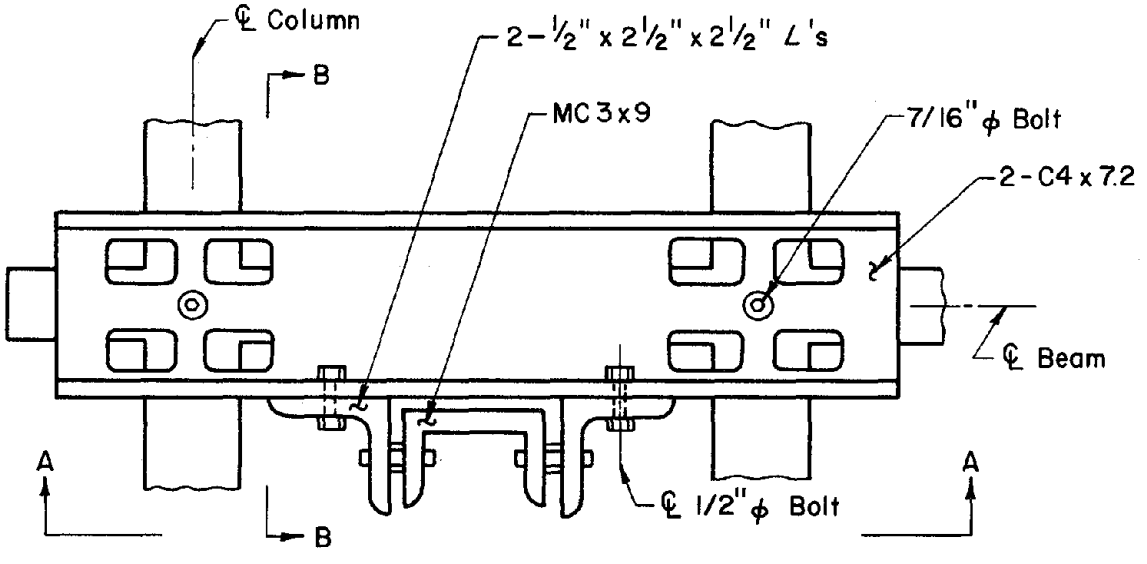


Elevation

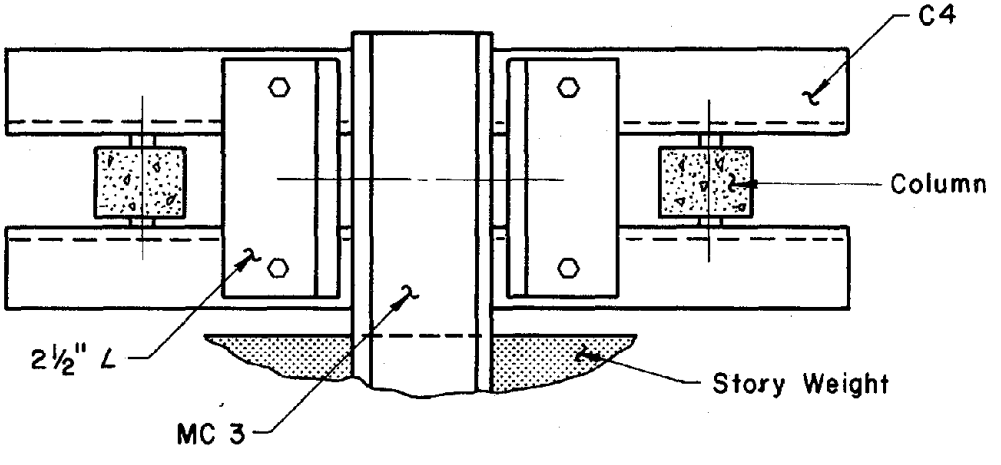


Section A-A

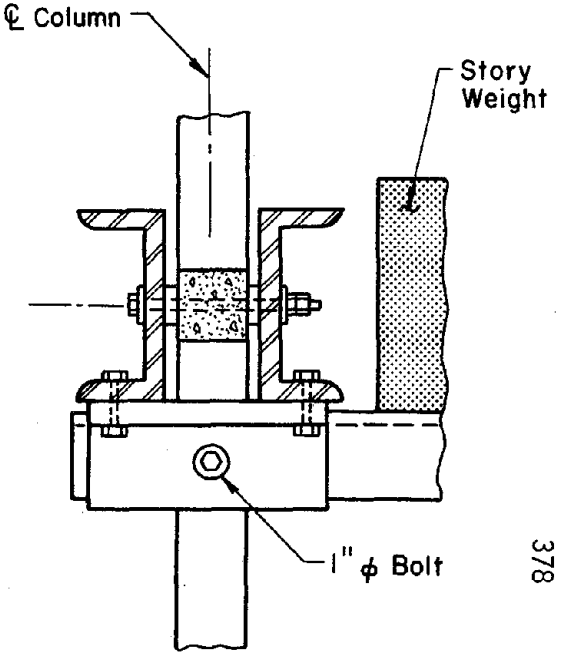


Section B-B

(c) Frame Connection

Fig. A.1 (contd.) Test Structure and Connections

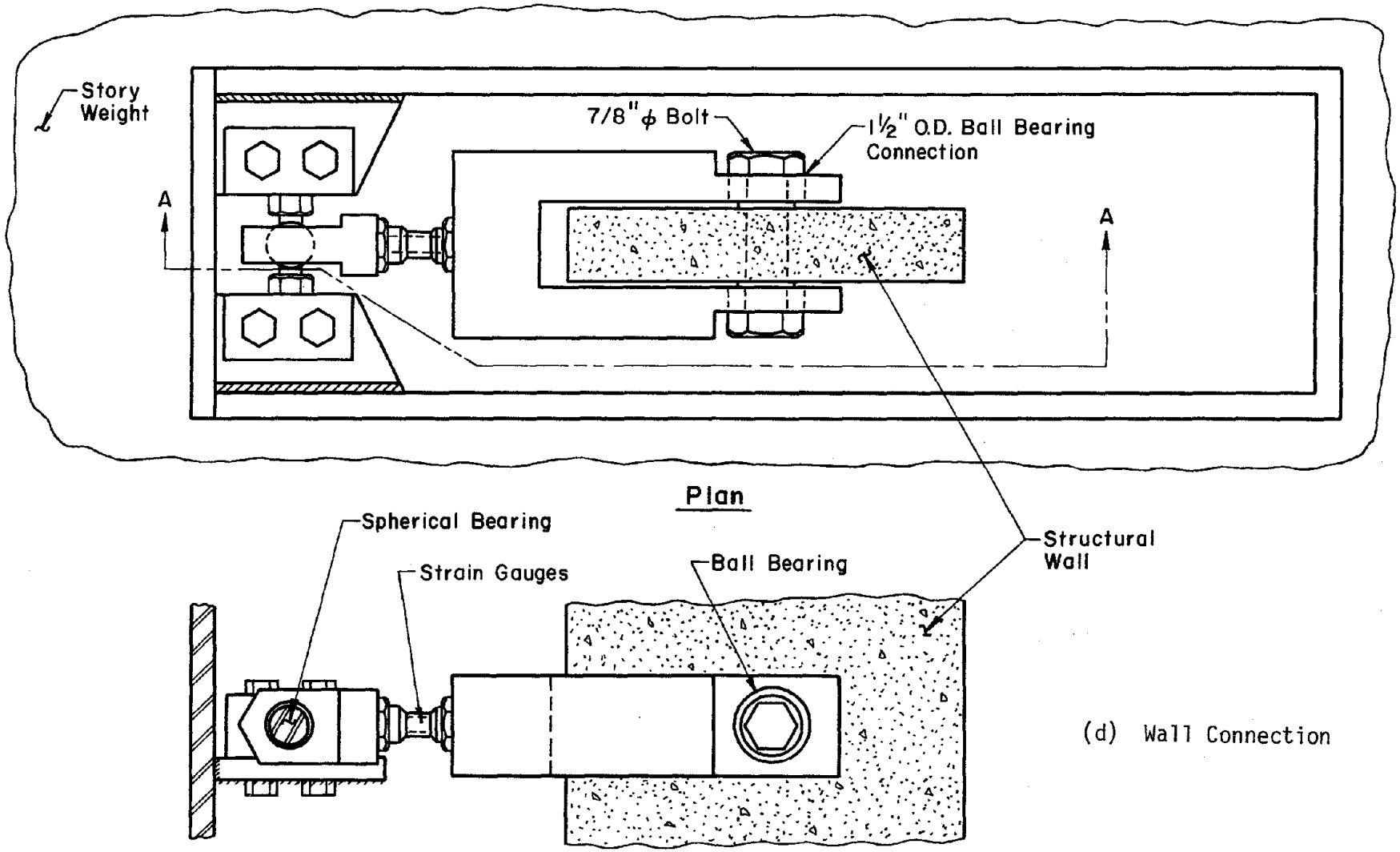


(d) Wall Connection

Fig. A.1 (contd.) Test Structure and Connections

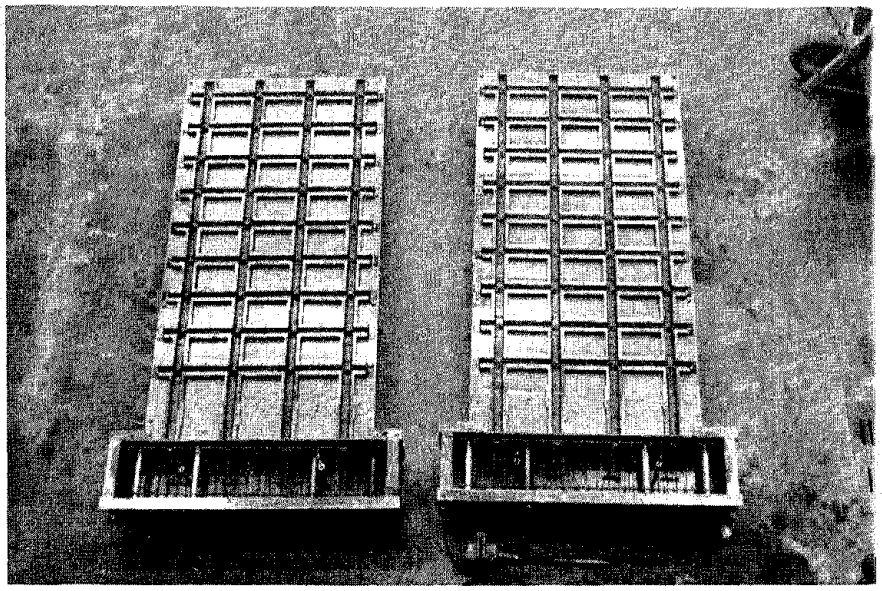

(a) Frame Reinforcement

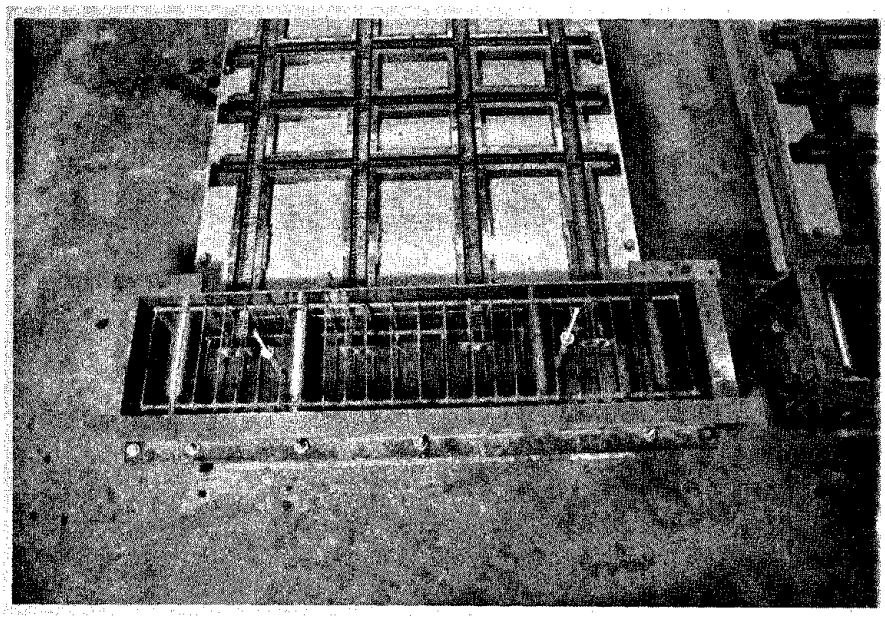

(b) Frame Anchorage

Fig. A.2 Forms and Reinforcement for Story Weights, Frames, and Walls

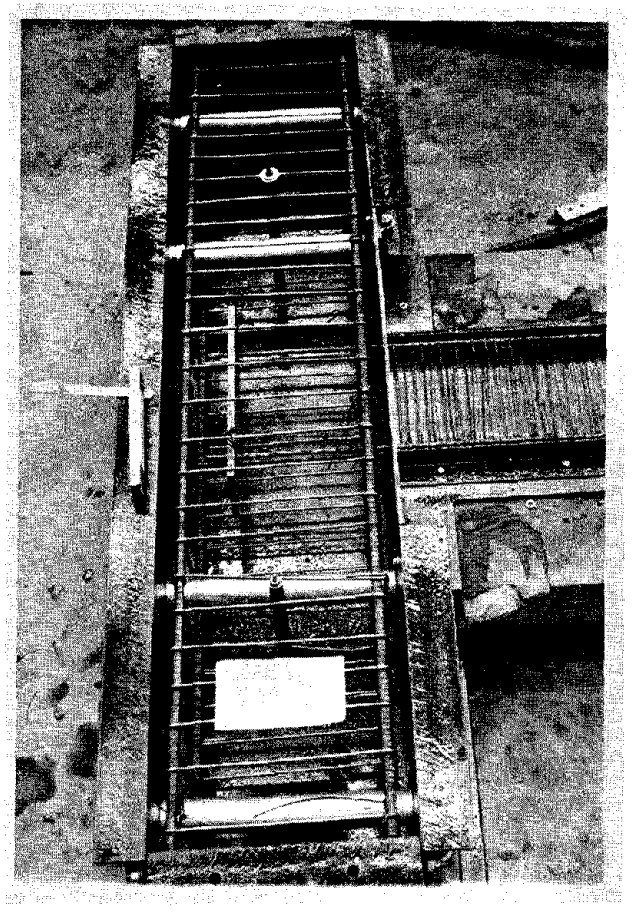

(c) Wall Anchorage

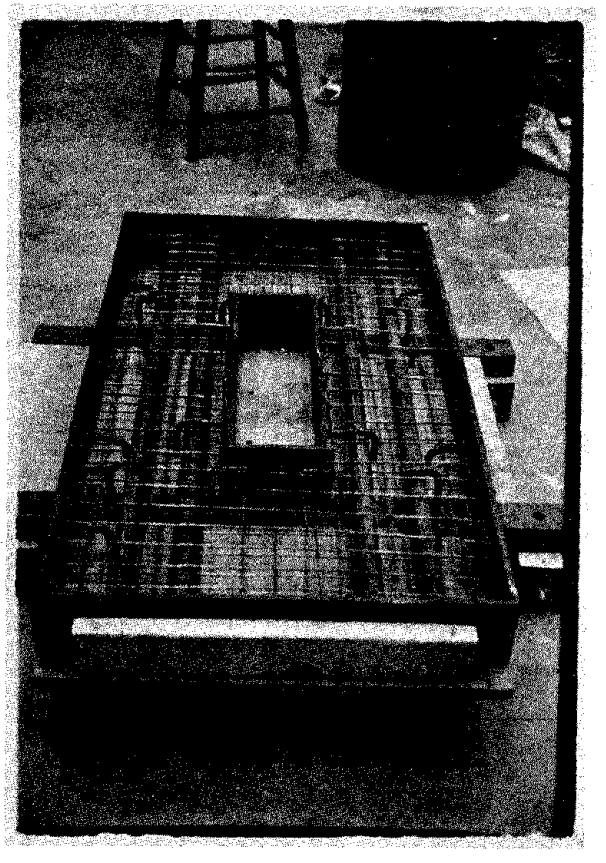

(d) Story Weight

Fig. A.2 (contd.) Forms and Reinforcement for Story Weights, Frames, and Walls

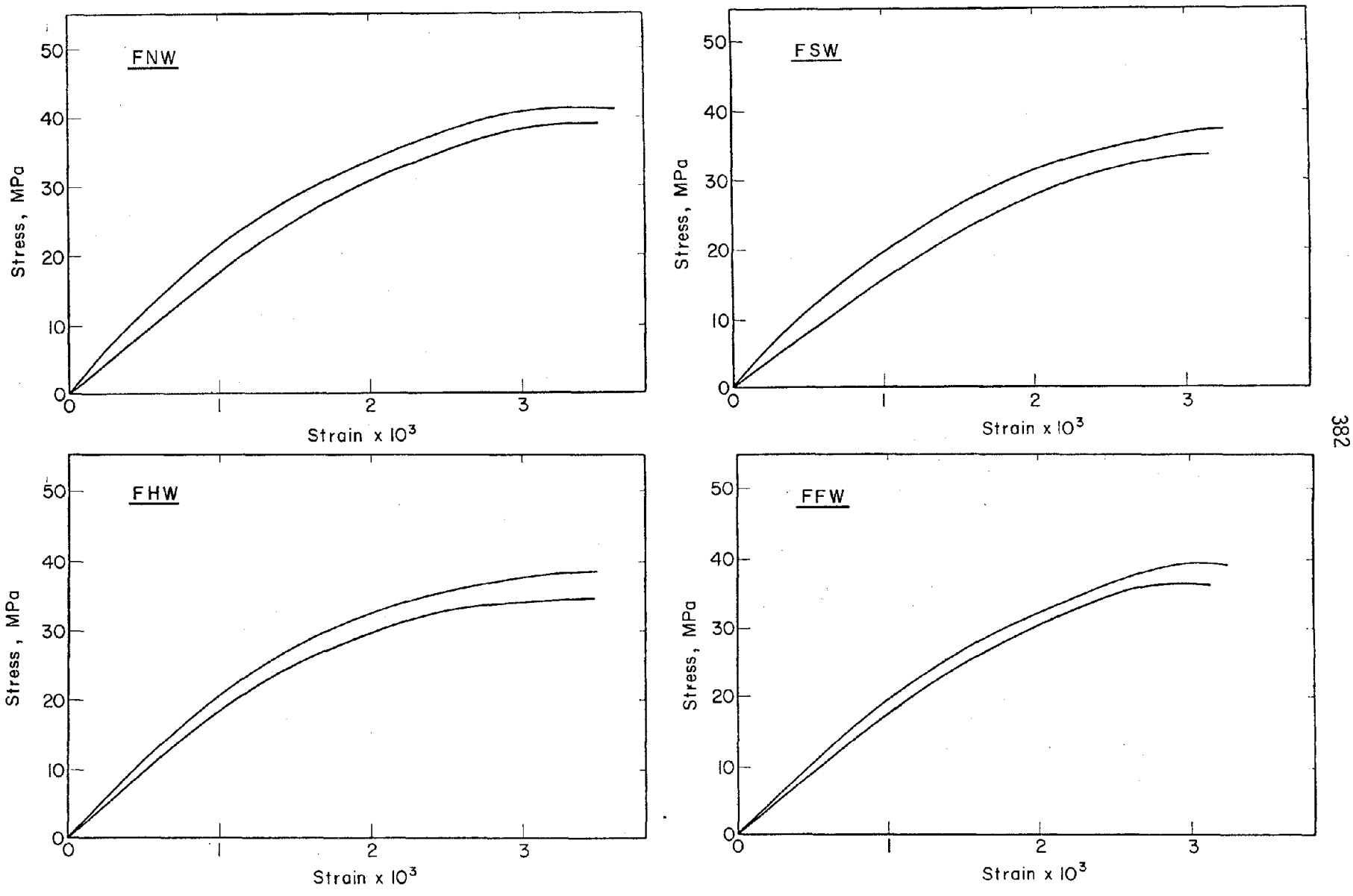


Fig. A.3 Bounds of Concrete Stress-Strain Relations

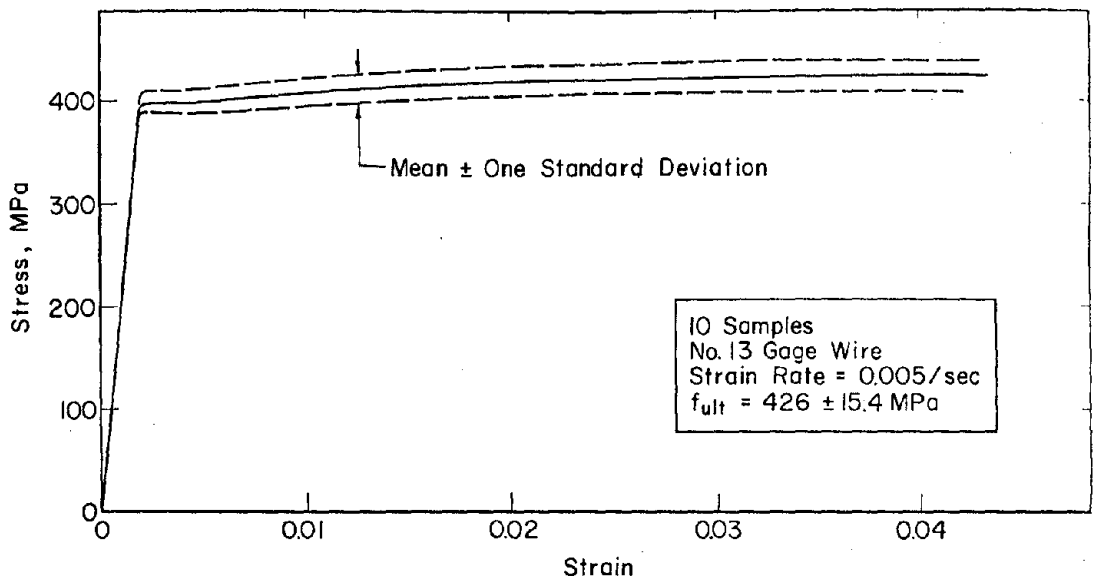


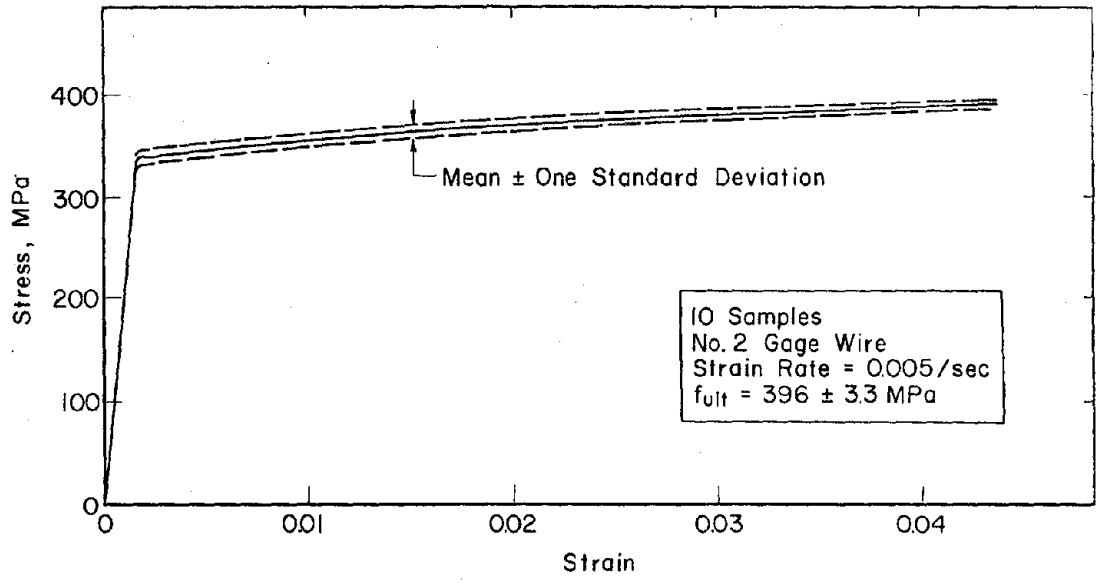


Fig. A.4 Stress-Strain Curves for Longitudinal Wires

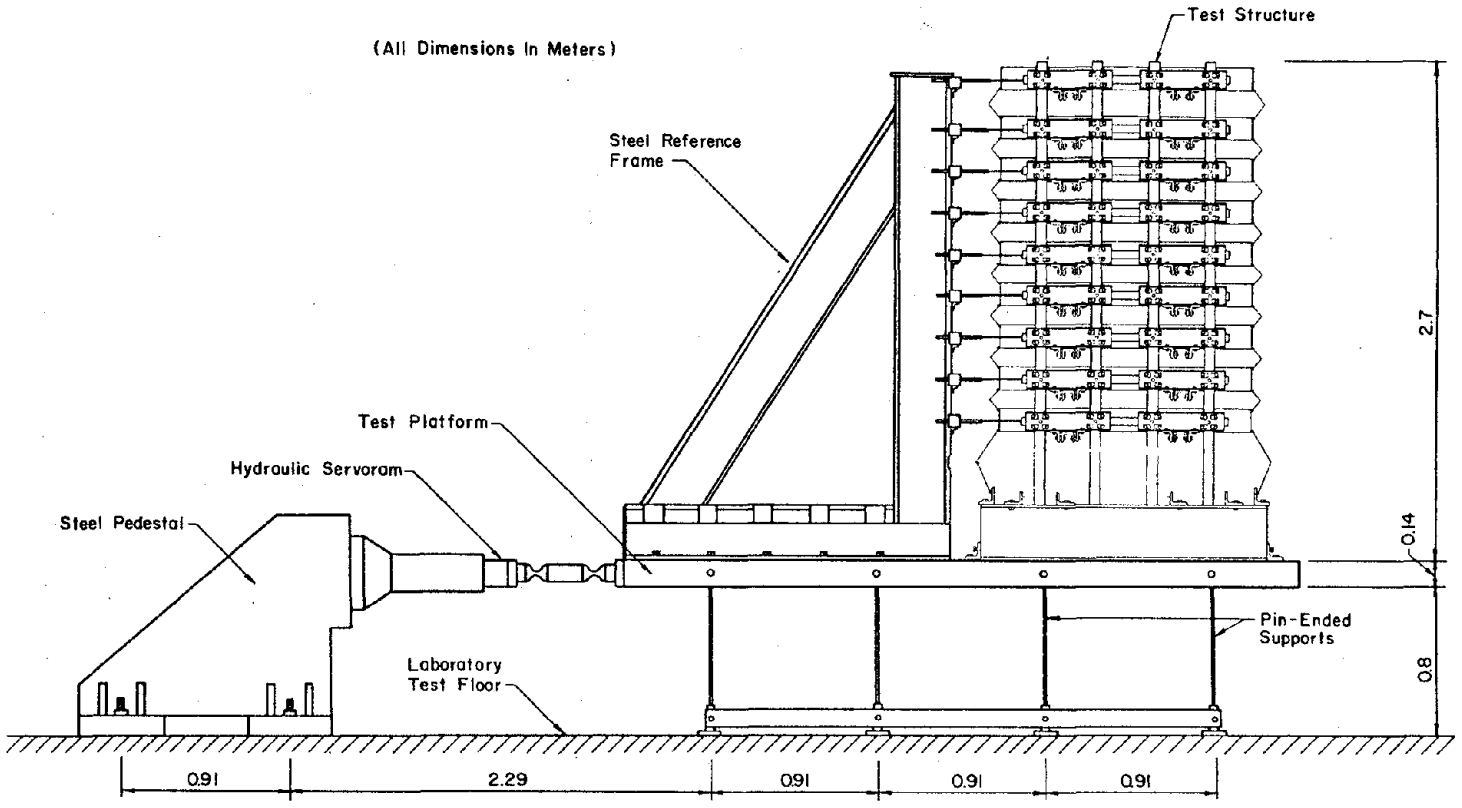


Fig. A.5 Earthquake Simulator and Test Structure

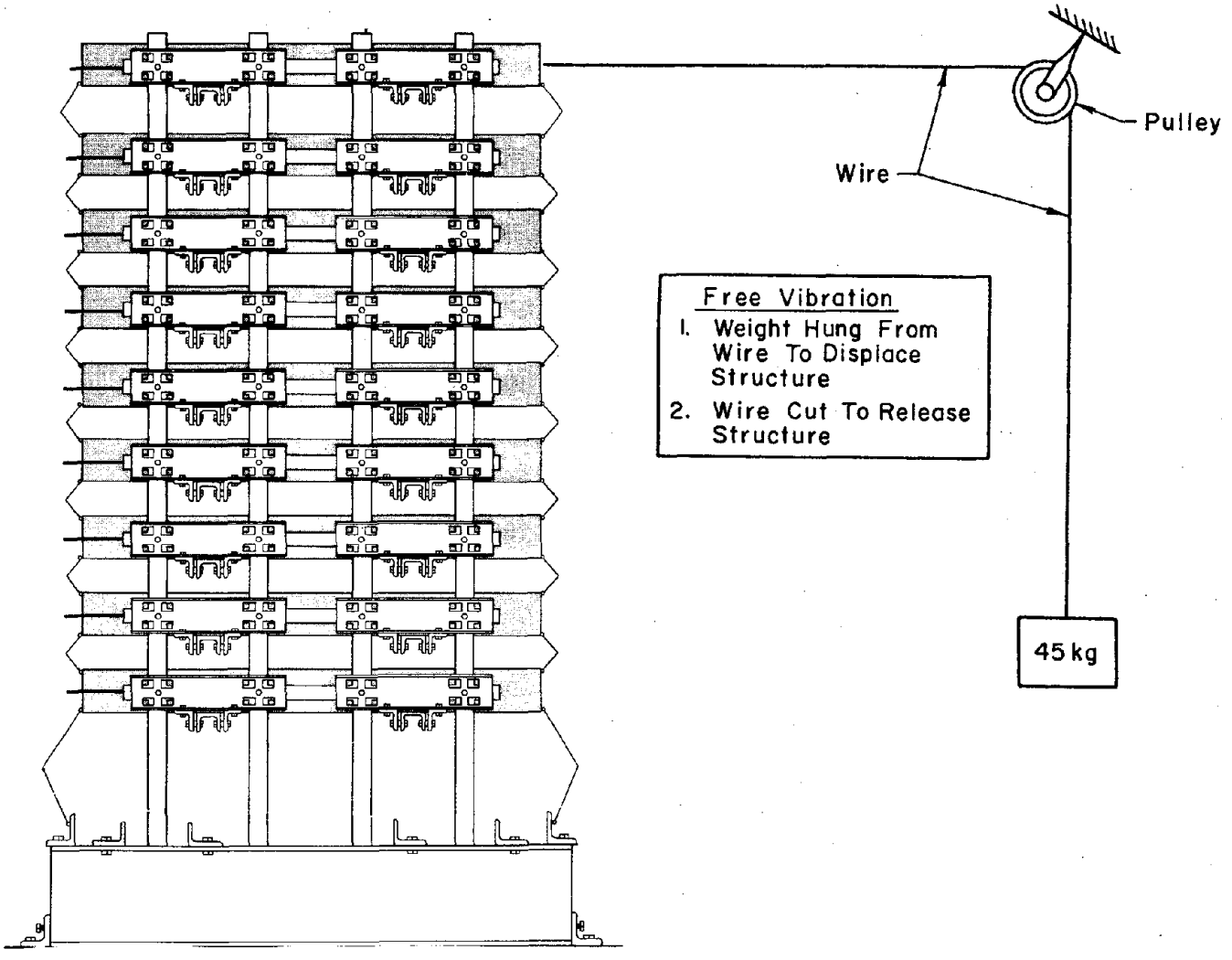


Fig. A.6 Free-Vibration Test Setup

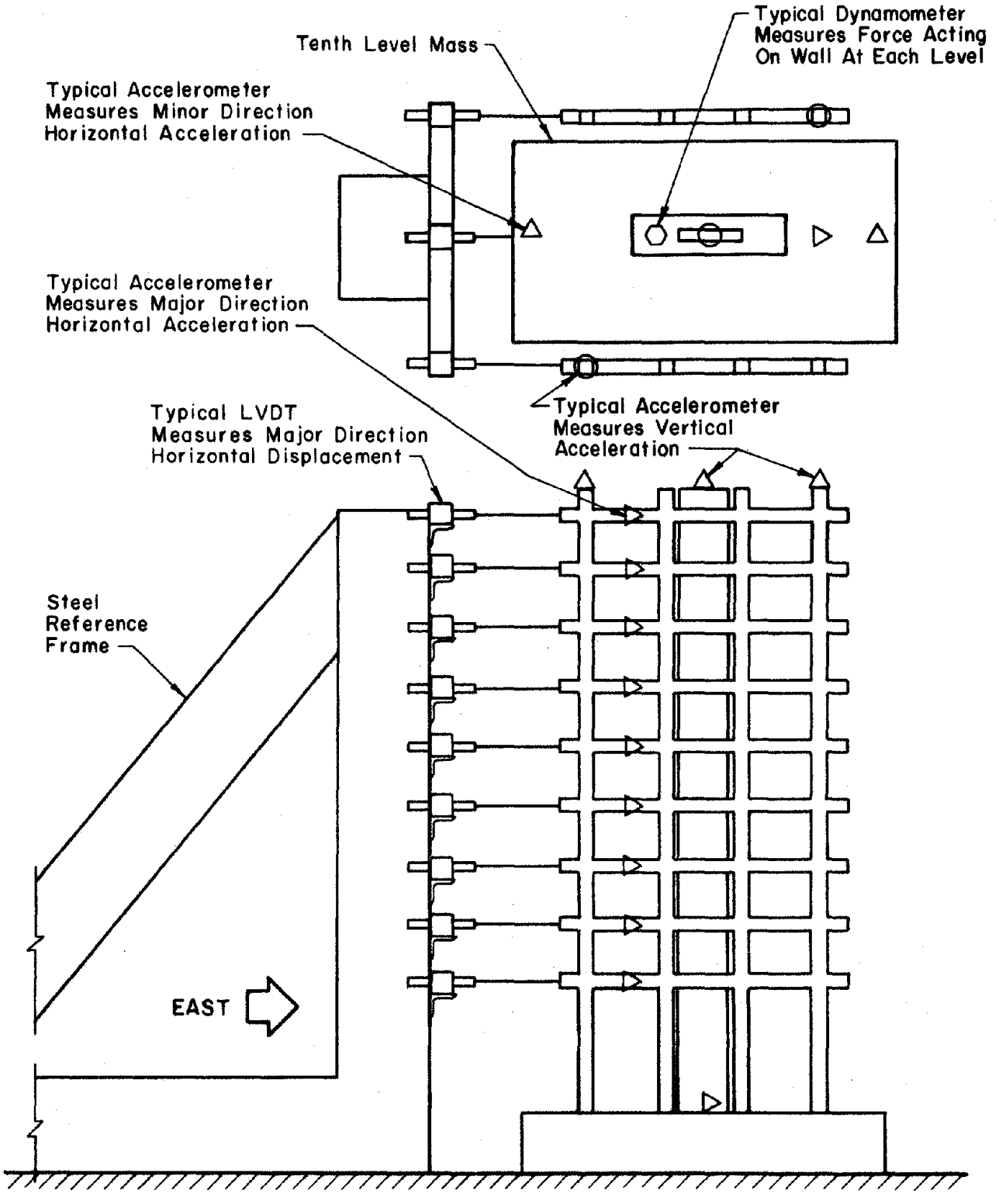


Fig. A.7 Instrumentation Location and Orientation

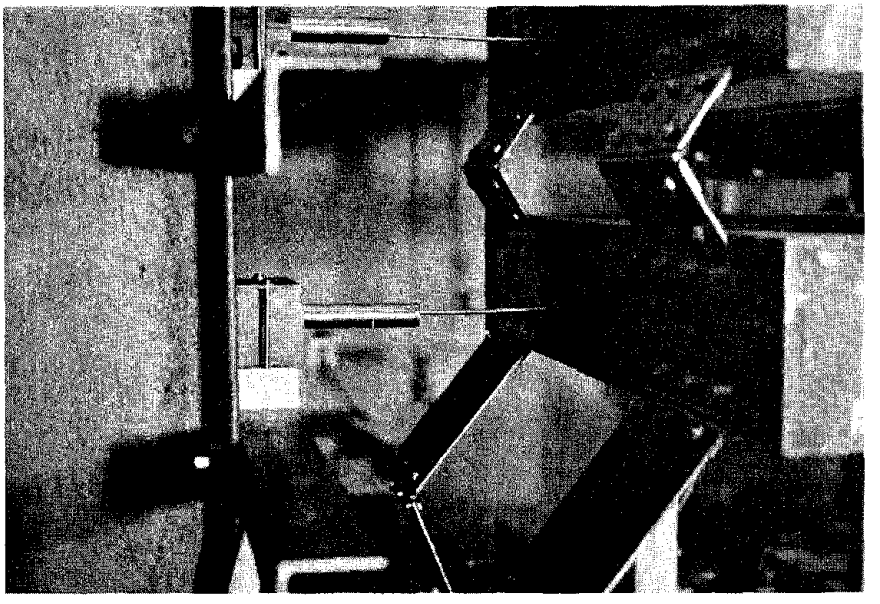

(a) LVDT's

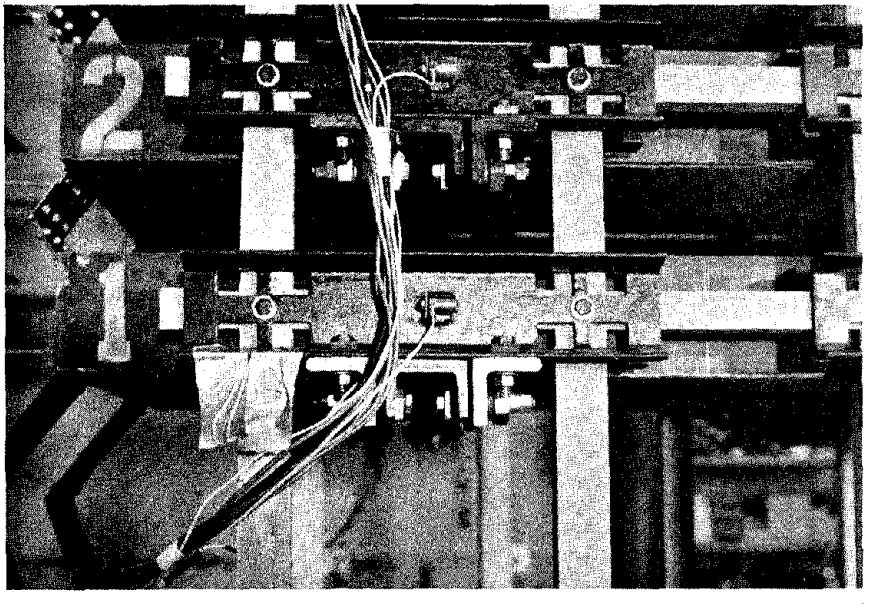

(b) Story-Level Accelerometers

Fig. A.8 Photographs of Instrumentation

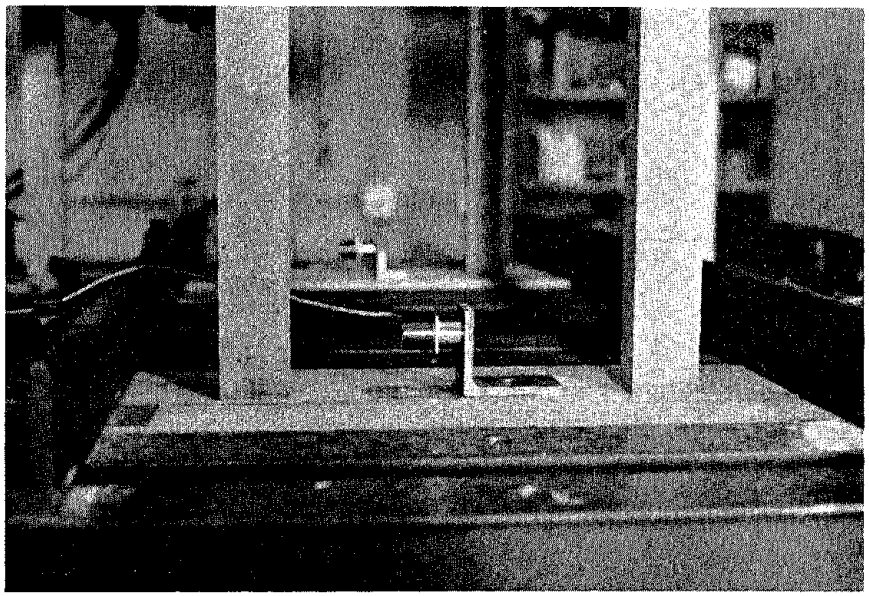

(c) Base-Level Accelerometer

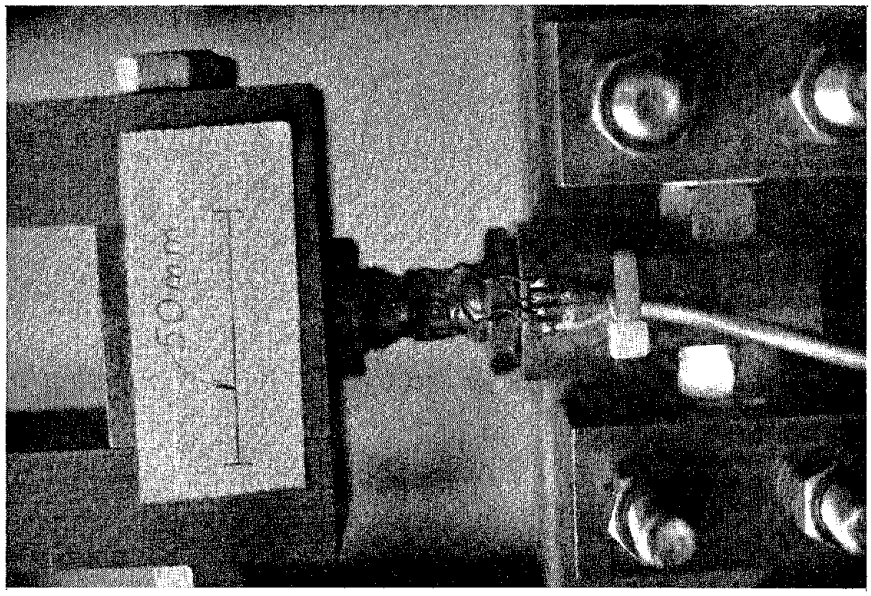

(d) Strain-Gages on Wall Connection

Fig. A.8 (contd.) Photographs of Instrumentation

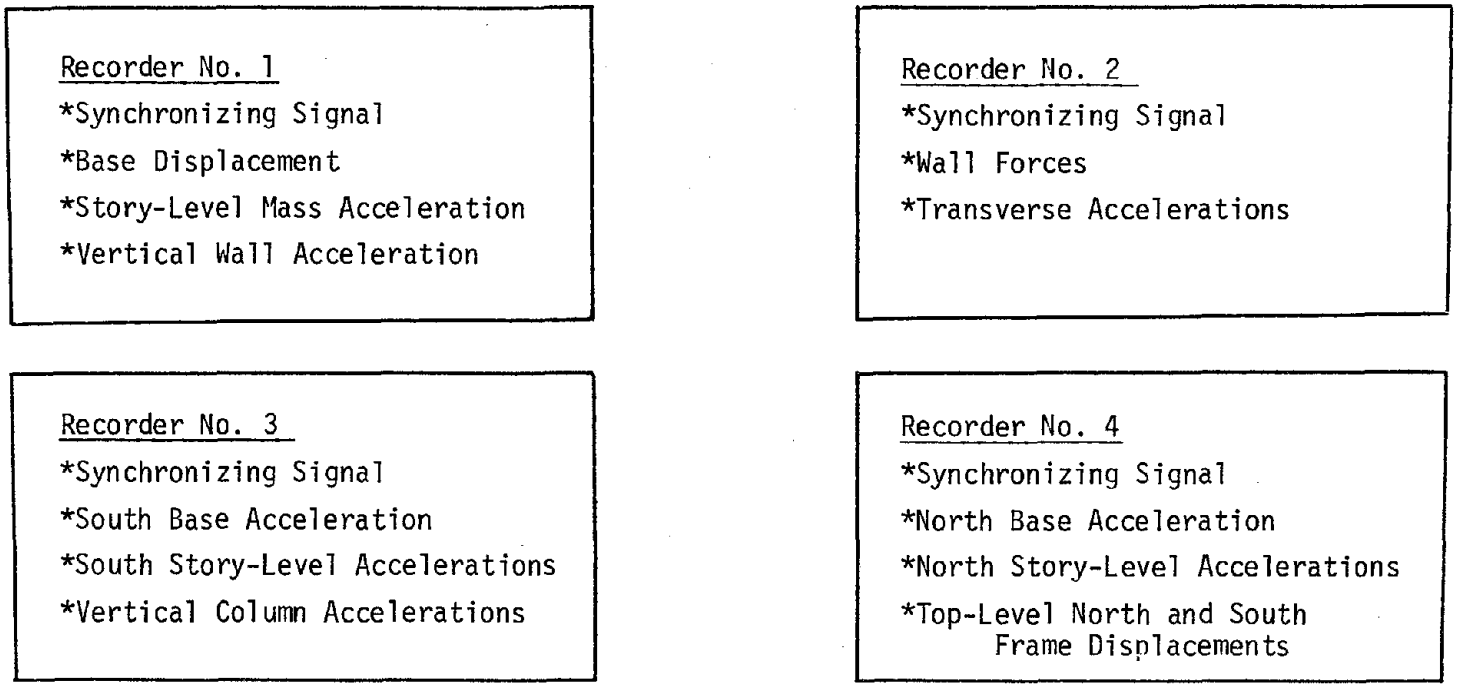


Fig. A.9 Organization of Instruments and Tape Recorders

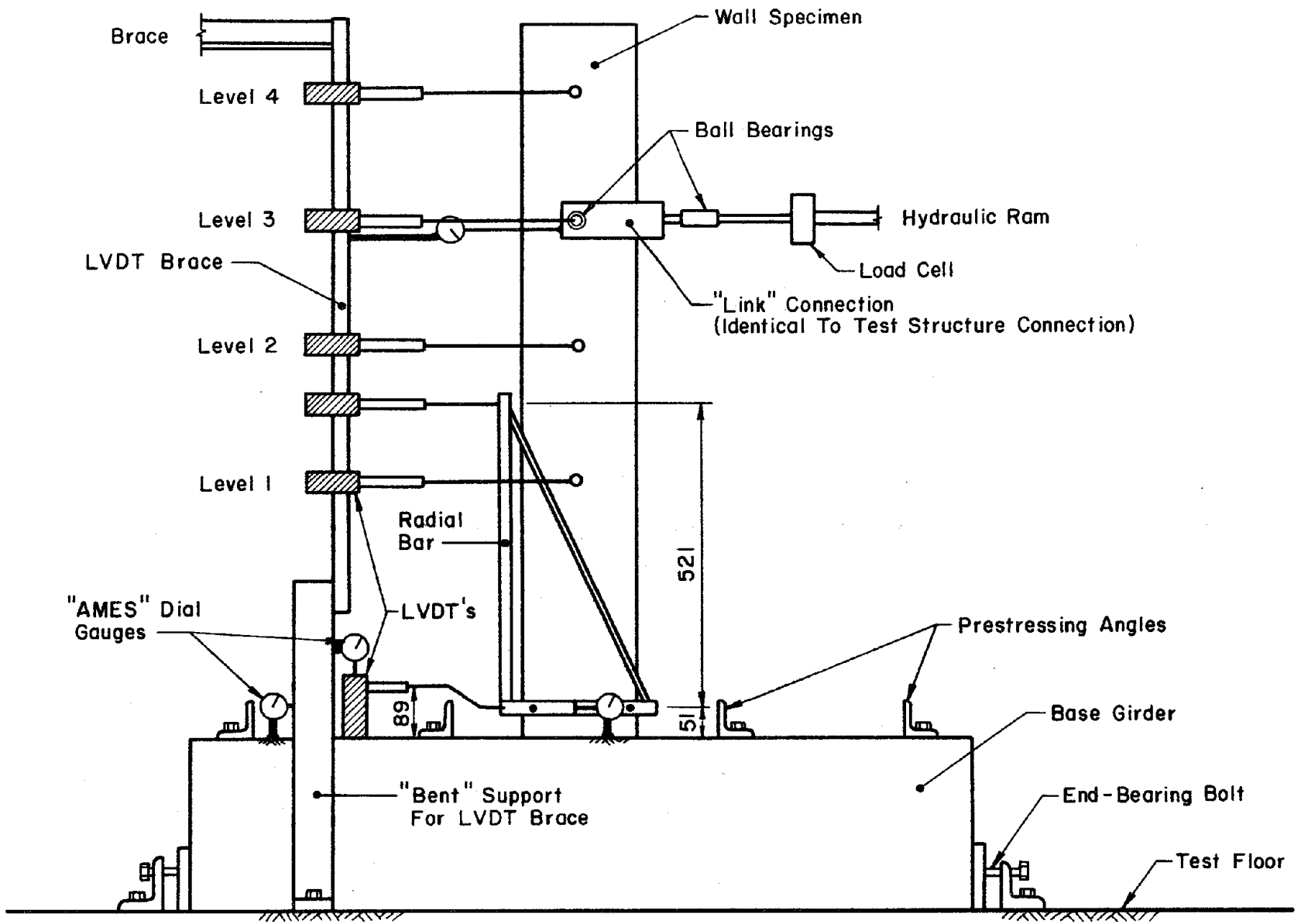


Fig. A.10 Test Setup for Wall Tests

# APPENDIX B

# BEHAVIOR OF MEMBERS SUBJECTED TO SLOW LOAD REVERSALS

Small-scale members and member assemblies were tested to determine the static stiffness and strength characteristics of members composing the test structures. Specimen configurations and loading programs were chosen to be representative of those in the nine-story test structures. Test descriptions and observed behavior are presented in this appendix. Additional details can be found in References [ 12 ] and [ 23 ] and in Sec. A.7 of this report.

## B.1 Description of Test Specimens and Loading Programs

Test specimens included beam-column assemblies, first-story columns, and walls. The relations of the test specimens to the nine-story test structures are indicated in Fig. B.1.

### (a) Beam-Column Assemblies

Configurations of beam-column assemblies were chosen to represent interior and exterior joints (Fig. B.1). Points of contraflexure were fixed at the centers of beam spans and column heights. The assemblies were subjected to a programmed displacement history by loading laterally the top of the column (Fig. B.1). Two loading patterns were used (Fig. B.2a). Pattern "A" was representative of average story distortions measured during design simulations of nine-story test structures. Pattern "B" displacements exceeded distortions measured for design simulations of test structures and are used in this report primarily to study characteristics of the primary curve. The test setup is pictured in Fig. B.4a. Measurements during testing included applied load, displacement at load level, and rotation of beam-column joint (Fig. B.3a).

Specimens subjected to Pattern "A" loading were reinforced with two or three longitudinal wires per face in beams and two per face in columns. Only interior joints, reinforced with two wires per face in beams and columns, were loaded with Pattern "B". The mean yield stress of longitudinal wires was 358 MPa (compared with 399 MPa for nine-story test structures). Fabrication and reinforcement details were the same as those described for test structures (Chapter 2 and Appendix A) with the exception that reinforcement cages were not rusted before casting. Further details are given in Reference [ 23].

(b) First-Story Columns

Column configurations were selected to provide insight into behavior of interior and exterior first-story columns (Fig. B.1). Columns were cast monolithically with stiff base girders and extended as vertical cantilevers to a load point 254 mm above the base. Two loading patterns were used (Fig. B.2b). In pattern "A", a vertical dead load stress equal to that in test structures ($0.07\ f'_c$) was imposed and the loading point subjected to a cyclic displacement pattern. In pattern "B", the same displacement pattern was used but vertical load was cycled in proportion with applied shear (Fig. B.2b). Pattern "A" was intended to be representative of the loading history of interior columns during design simulations of test structures while pattern "B" was intended to provide insight into the effects of overturning on exterior columns. The bounds of axial loads in pattern "B" were similar to those expected in test structures considering dead load and yield moments at all beam-column joints. The test setup (Fig. B.4c) included a loading frame which was loaded at various heights to produce the overturning effect. Measurements during testing included applied horizontal and vertical load, displacement at load level, and rotation at a level 25.4 mm above the

column-base girder interface (Fig. B.3b).

Specimens were reinforced with either two or four longitudinal wires per face. Fabrication and reinforcement properties were the same as those described for test structures in Chapter Two and Appendix A. Additional details are given in Reference [ 12 ].

(c) Walls

Wall specimens were cast as vertical cantilevers with stiff base girders (Fig. A.10). So that a range of moment-to-shear ratios could be studied, four specimens were tested, each by loading laterally at one of four story levels (Fig. B.3c). A single displacement pattern was used (Fig. B.2c). In that pattern, the amplitude of the first quarter cycle was selected as three times the yield displacement calculated based on fully cracked section properties. A photograph of the test setup appears in Fig. B.4b. Measurements during testing included applied load, displacement at each story level, and rotation and translation at a level 50.8 mm above the wall-base girder interface (Fig. B.3c).

Fabrication and reinforcement details were identical to the lower four stories of walls used in test structures (Chapter Two and Appendix A). Details of the tests are presented in Sec. A.7.

## B.2 Observed Behavior

(a) Beam-Column Assemblies

Specimens subjected to loading pattern "A", which was representative of average story distortions during design simulations, indicated that significant inelastic behavior could be expected of frame joints during design simulations (Fig. B.5). Effective stiffnesses generally decreased whenever

new displacement maxima were reached. Pinching of moment-rotation curves (low incremental stiffness at low moment levels followed by higher stiffness) was apparent for interior and exterior joints. Because of (1) more-pronounced pinching for interior joints, (2) the similarity between displacement and rotation curves, and (3) concentration of cracks in beams rather than columns, it may be concluded that the majority of inelastic action occurred in beams.

Specimens subjected to loading Pattern "B" reached apparent strengths during the first quarter cycle (Fig. B.5). Under both loading patterns, strengths were maintained to equivalent interstory drifts exceeding five percent after which strength decreased gradually. No joint cracks or excessive column damage was observed at this level of distortion. However, joint deterioration in terms of apparent bond slip was significant.

(b) First-Story Columns

Moment at the base of columns was calculated (including the P-delta moment) and is plotted versus displacement or rotation in Fig. B.6. Although it is difficult to relate column behavior directly to test structure behavior because of uncertainty in location of the point of contraflexure, the measurements indicate yield of flexural steel at displacement of approximately one percent lateral drift. As was true for beam-column joints, stiffnesses generally decreased whenever new distortion maxima were reached. Pinching of the curves was much less pronounced than for the beam-column joints, indicating that the anchorage of longitudinal steel at the base of columns was adequate. Similarity in shapes of moment-displacement and -rotation curves and a concentration of cracking near the base indicate that the majority of inelastic action occurred near the base of the columns.

Several effects of the loading pattern were apparent. Specimens subjected to constant axial load (pattern "A") responded symetrically about the origin. Specimens subjected to varying axial load (pattern "B") exhibited higher stiffness and strength in the quadrant of increasing axial load than under decreasing axial load. Strengths of specimens under constant axial load were maintained to displacement limits of six percent. Under varying axial load, apparent strengths decreased rapidly when cycled into the quadrant of increasing axial load (particularly the "more-heavily" reinforced columns) but did not decrease with increasing distortion under decreasing axial load. Failure of all specimens was precipitated by reinforcement fracture at extreme displacements. Nominal concrete spalling was symmetric for specimens under constant axial load but more severe on the high-compression side for specimens subjected to varying axial load.

(c) Walls

Hysteretic relations obtained from wall tests (Fig. B.3c) are presented in Fig. B.7. The data include displacement at load level and first level, and translation and rotation at a level 50 mm ahove the base for wall specimens TW2, TW3, and TW4. For TW1 (which was loaded at the first level) translation resulting from distortions at 50 mm were not recorded, so only first-level displacement and base rotation are presented (Fig. B.7).

During the first quarter cycle, specimens loaded at higher story levels (e.g. TW4) were displaced well beyond apparent yield while specimens loaded at lower levels (e.g. TW1) were displaced only moderately beyond apparent yield, even though all specimens were displaced to three times the yield displacement calculated based on fully-cracked section properties.

The discrepancy was apparently caused by reinforcement pullout from base girders which caused the "shorter" walls to be effectively more flexible before yield. Hysteresis for wall specimens was similar to that observed for columns (under constant axial force). Apparent yield was observed to occur at first-level displacements of approximately 0.5 percent of first-level height and was not affected significantly by the moment-to-shear ratio (loading height). Thus, walls in test structures FSW, FHW, and FFW would be expected to yield during design simulations.

Failure of walls occurred at first level displacements exceeding 20 mm and was accompanied by nominal concrete crushing, reinforcement fracture, and, for specimens TW3 and TW4, buckling of compression steel. Primary shear failure was not observed. However, failure was preceded by shear sliding across the main flexural crack near the wall-base girder interface. This is indicated by relative translation between wall and base girder near the base (Fig. B.7). Shear resistance along the crack deteriorated rapidly when first level displacements exceeded approximately five mm. Thus, sliding of the wall should be expected for structures FHW and FFW during second and third simulations and for FSW during the third simulation.

## B.3 Comparison of Measured and Calculated Stiffnesses and Strengths

Measured stiffnesses are compared with calculated quantities to verify experimental results and to provide a basis for estimating stiffnesses and strengths in test structures.

(a) Beam-Column Assemblies

Column stiffnesses in the assemblies were interpreted from displacement and joint rotation measurements by Abrams [ 1 ]. As inferred from these measurements and demonstrated in Fig. B.8, column behavior could be represented satisfactorily by linear elements with stiffness based on fully-cracked section properties.

Beam stiffnesses below apparent yield could not be satisfactorily represented with cracked-section properties because of bond slip. For specimens subjected to loading pattern "A", yield of reinforcement was not readily apparent at any distortion limit, because of gradual stiffness loss (largely attributable to bond slip) as distortion amplitudes increased gradually (Fig. B.5 and B.9). For specimens subjected to loading pattern "B", yield of reinforcement was apparent during the first quarter cycle (Fig. B.5)

Strengths of beam-column assemblies were limited by beam strengths. Measured strengths of specimens subjected to loading pattern "A" are indicated in Fig. B.10. Strengths calculated using measured dimensions and considering both layers of reinforcement to be fully stressed are taken from Kreger [ 23 ]. Measured strengths consistently exceeded calculated strengths by five to ten percent (Fig. B.10).

(b) First-Story Columns

Primary moment-displacement relations were constructed from measured responses and are compared in Fig. B.11. The curves include two specimens for each type of loading program and reinforcement ratio. Stiffnesses based on three different assumptions are compared with measured curves. Gross- and cracked-section stiffnesses were based on cross-sectional and material

properties ignoring axial load. A third stiffness, $EI_5$, was based on a linear curvature variation with curvature at the base equal to the yield curvative calculated using fully-cracked section properties and an axial load of 5 kN. Stiffness $EI_5$ compares well with measured stiffnesses for specimens with two wires per face but not so well for specimens reinforced with four wires per face.

Flexural strengths were calculated considering two layers of steel for specimens subjected to constant or increasing axial load. A couple formed by longitudinal steel alone was considered for specimens under tensile axial load because concrete near the compression face was probably ineffective due to previous plastic elongation of compression steel. Measured and calculated strengths agreed satisfactorily. Further discussion of stiffness and strength can be found in Reference [ 12 ].

(c) Walls

Stiffnesses of walls before apparent cracking could be represented satisfactorily using uncracked, transformed-section properties (Fig. B.12). Following cracking, overall wall stiffness reduced to less than the fully-cracked stiffness because of concentrated base rotations caused by slip of anchored longitudinal reinforcement from base girders. Stiffnesses were well-represented by fully-cracked section when measured components of base rotation and translation (extrapolated linearly to the base girder face) were subtracted (Fig. B.12). After several cycles at first-level drifts exceeding three percent, the stiffness above the base did not soften to less than 80 percent of the fully-cracked stiffness for any specimen. From this it may be inferred that wall stiffnesses above the base in test structures could be

represented by either gross- or cracked-section properties for all three earthquake simulations.

Measured and calculated strengths are compared in Fig. B.13. Cracking strengths were based on measured moduli of rupture. Ultimate capacities were calculated considering usable concrete strain of 0.003, measured steel properties, and the Whitney rectangular stress block [ 38 ]. Ultimate capacities compared well. Measured cracking strengths were below calculated strengths, possibly because of initial stresses at the wall-base girder interface caused by differential shrinkage.

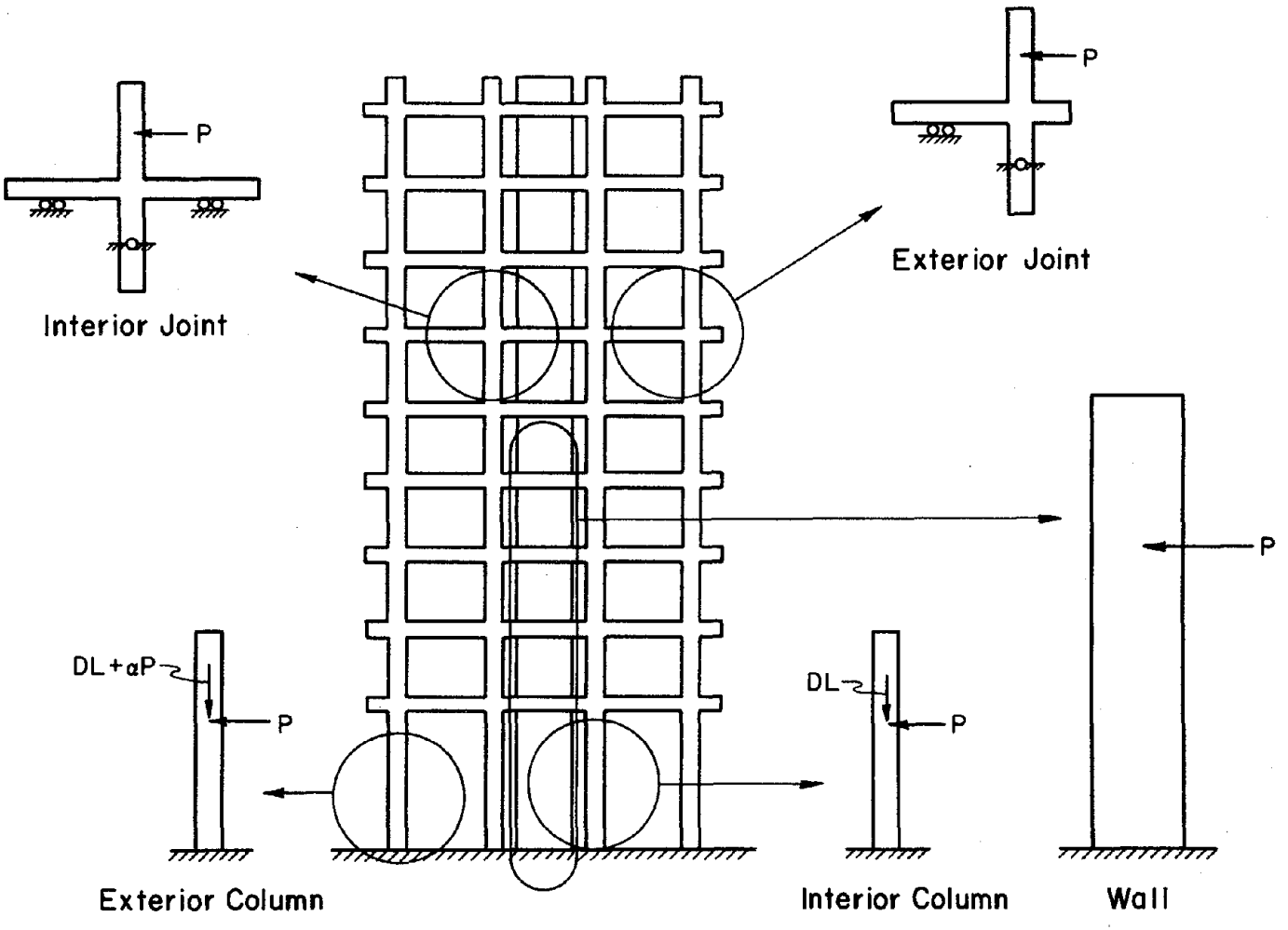


Fig. B.1 Idealizations of Test-Structure Members

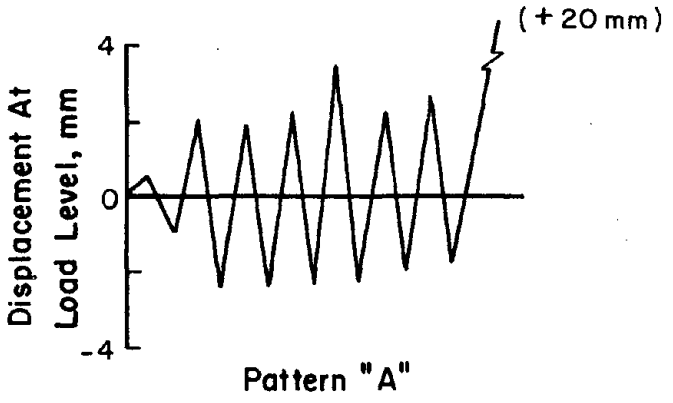


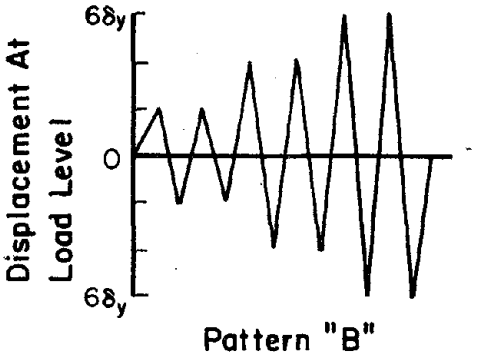


(a) Loading Patterns For Beam - Column Assemblies

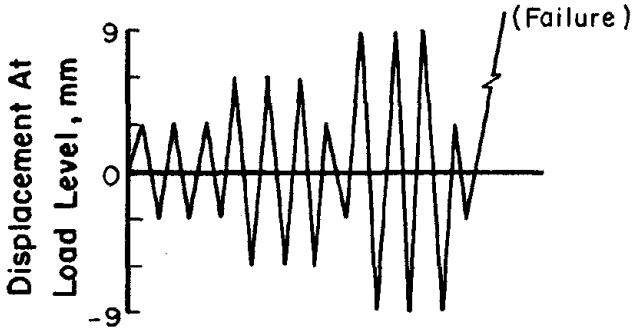


Axial Load = ( DL + α x Shear ) kN

| Pattern | No. Wires | DL | α |
|---|---|---|---|
| A | 2 | 5.4 | 0 |
| A | 4 | 5.4 | 0 |
| B | 2 | 2.4 | 6.0 |
| B | 4 | 3.3 | 4.0 |

Axial Load Patterns "A" & "B"

(b) Loading Patterns For Columns

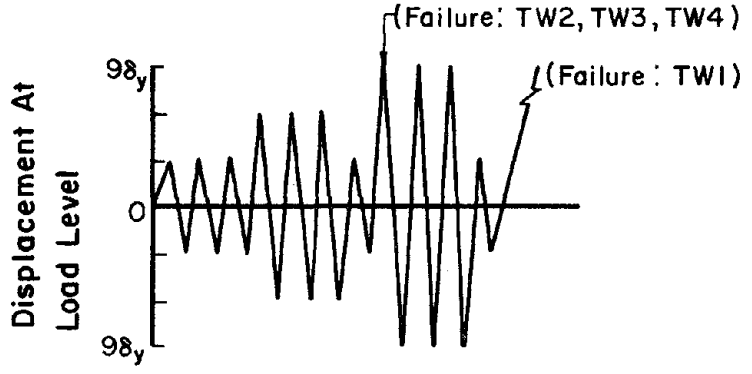


(c) Loading Patterns Walls

Fig. B.2 Loading Patterns for Member Tests

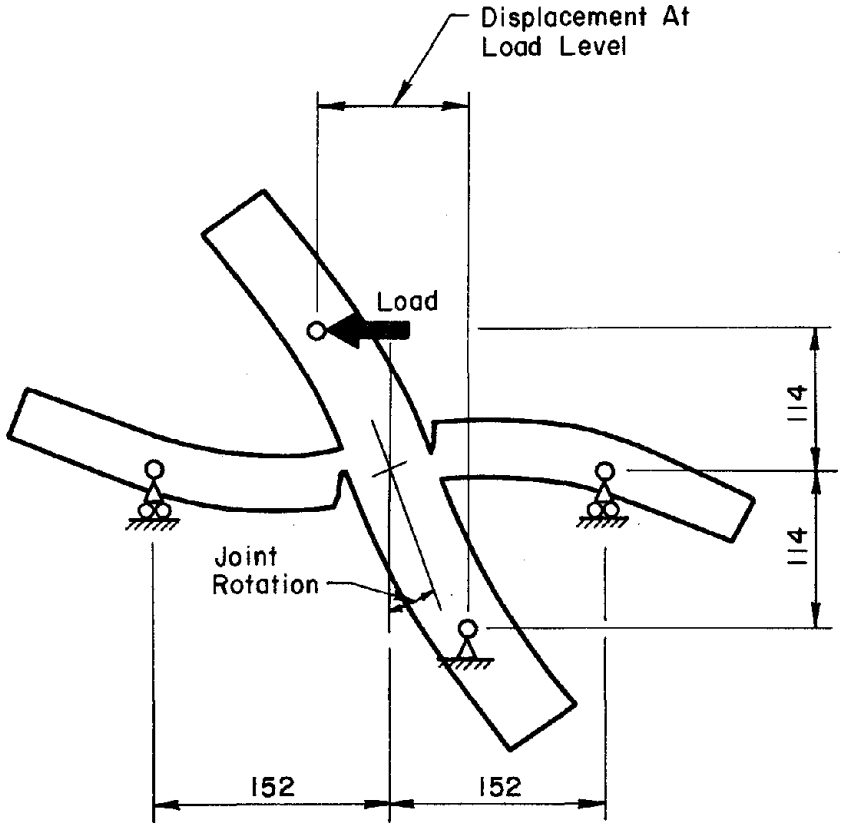


(a) Beam-Column Assemblies

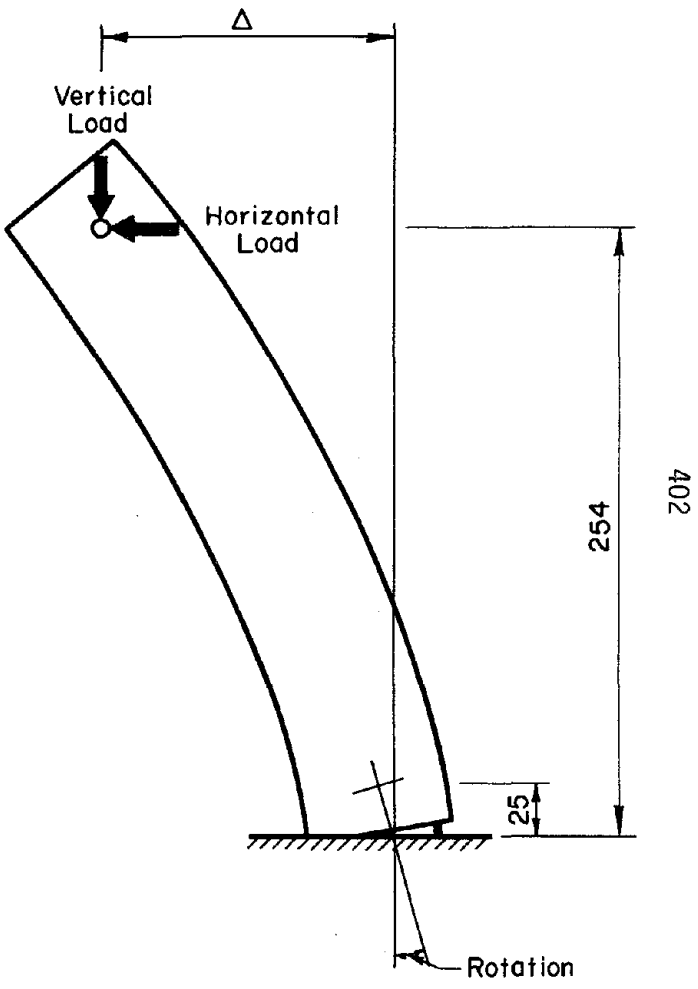


(b) First-Story Columns

Fig. B.3 Description of Measurements for Member Tests

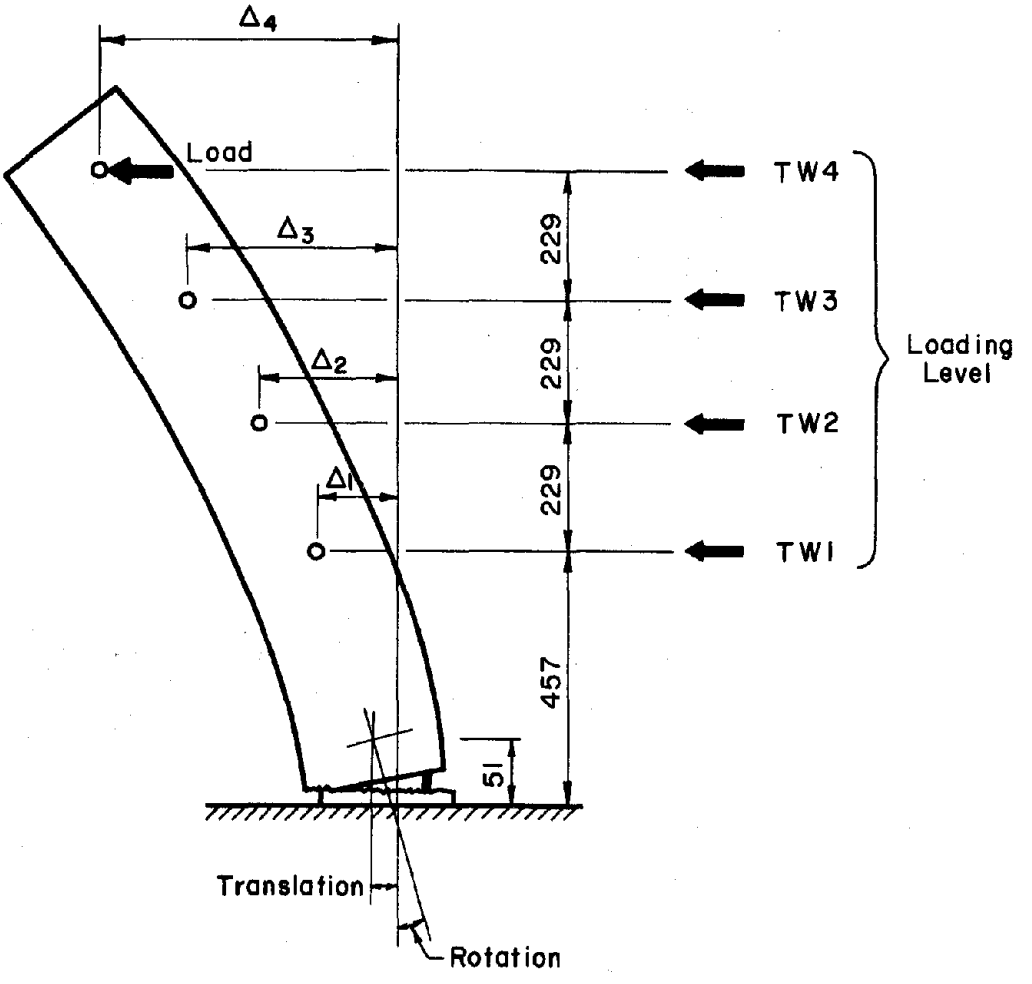


(c) Walls

Fig. B.3 (contd.) Description of Measurements for Member Tests

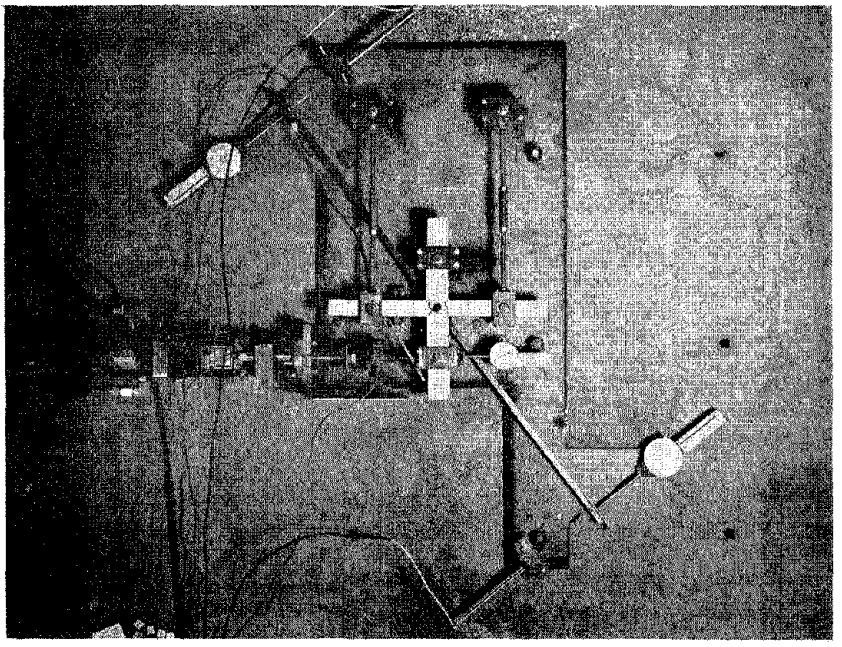

(a) Beam-Column Assembly

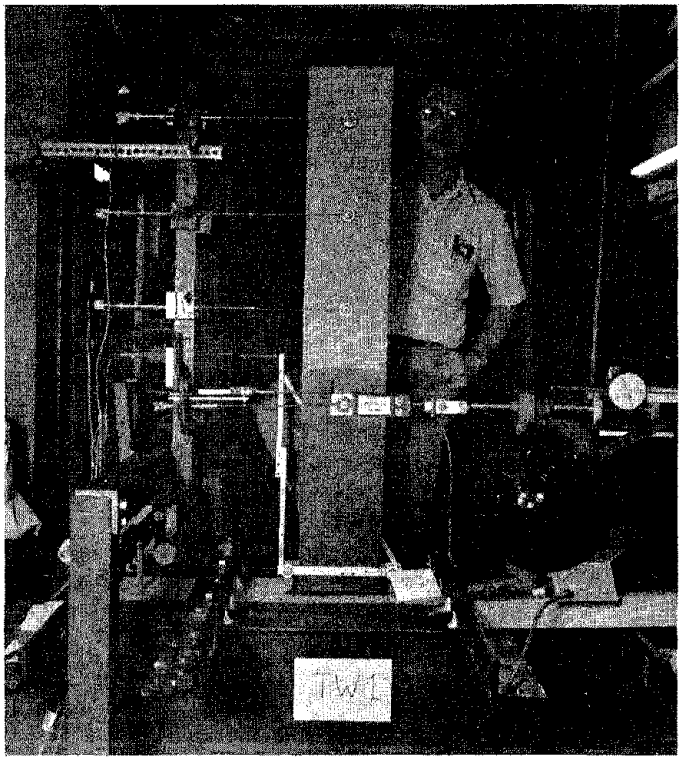

(b) Wall

Fig. B.4 Photographs of Experimental Setup for Member Tests

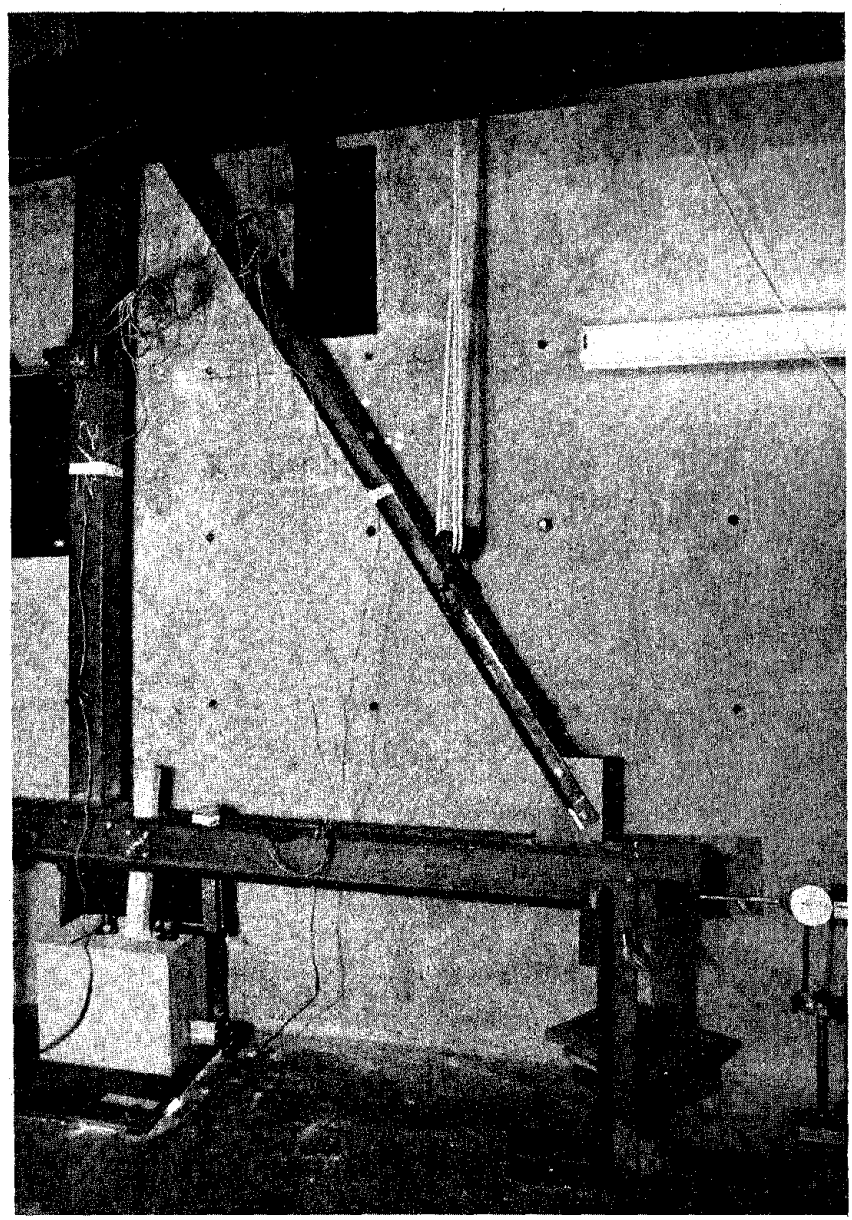

(c) Column

Fig. B.4 (contd.) Photographs of Experimental Setup for Member Tests

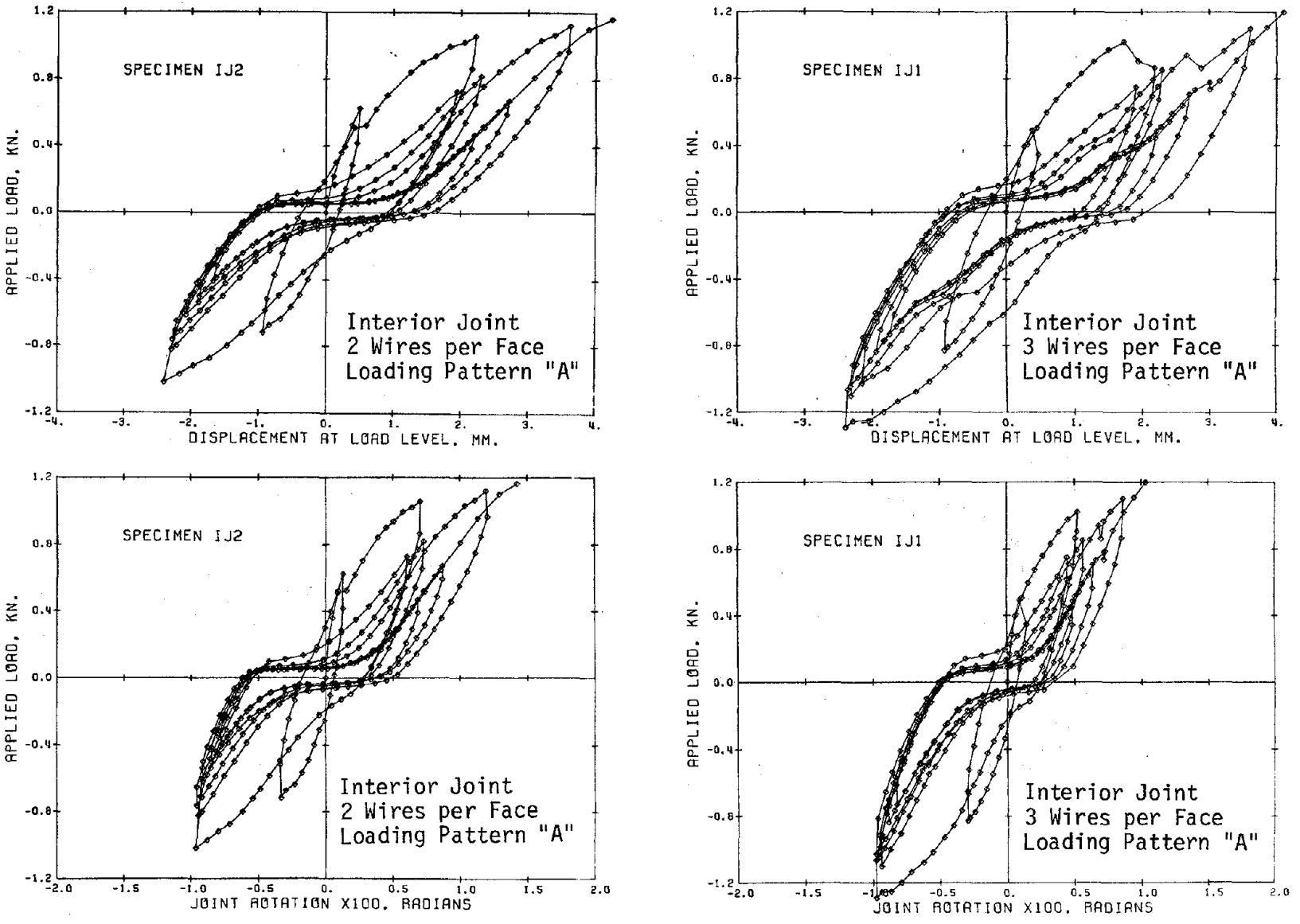


Fig. B.5 Measured Response of Beam-Column Joint Assemblies

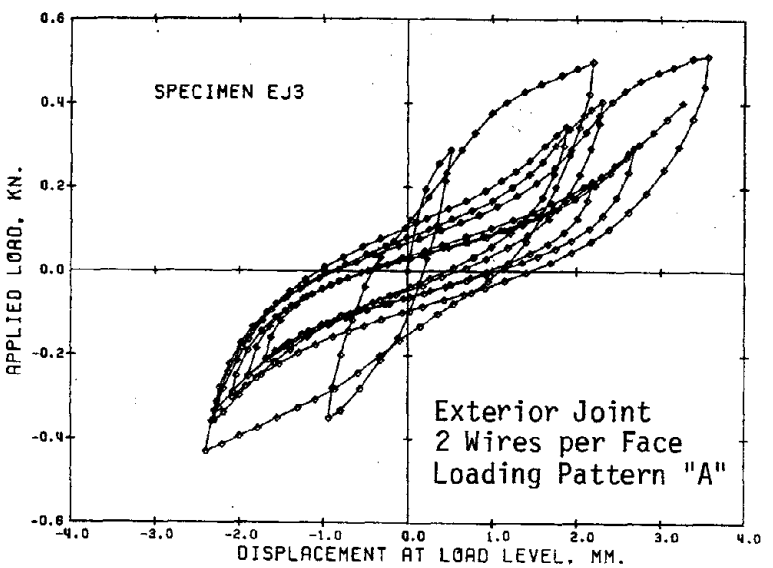


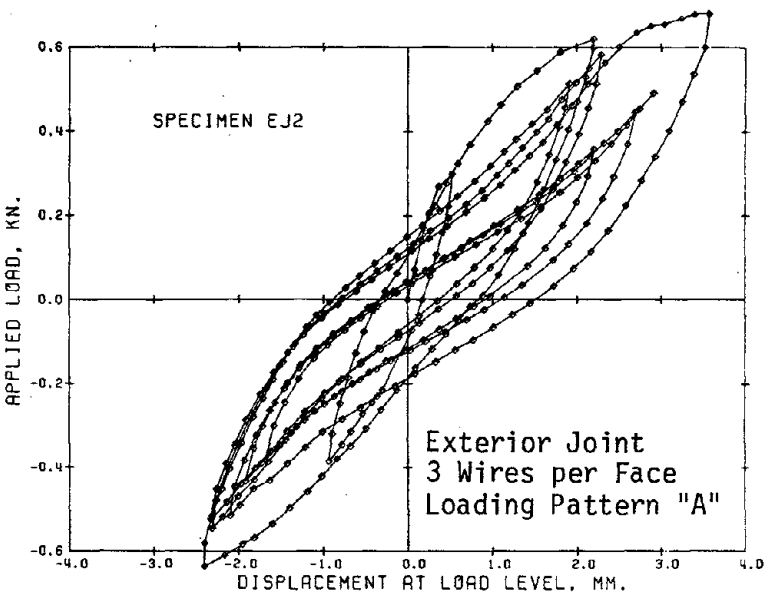


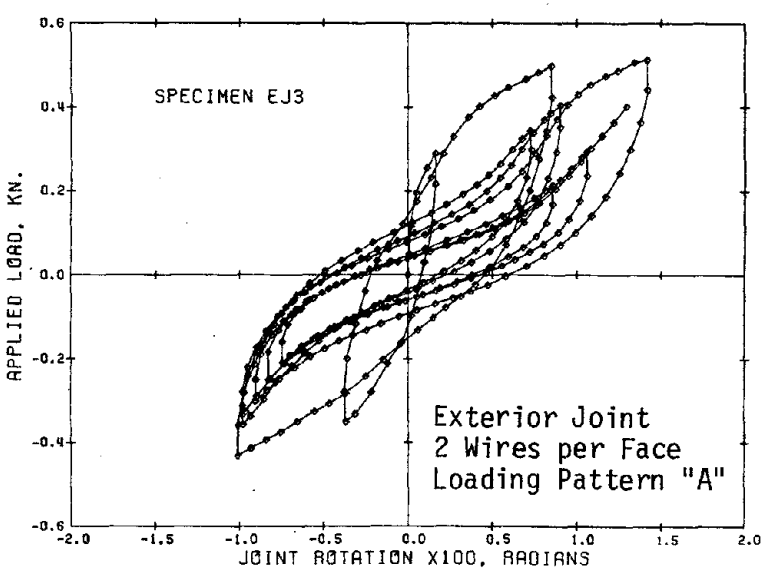


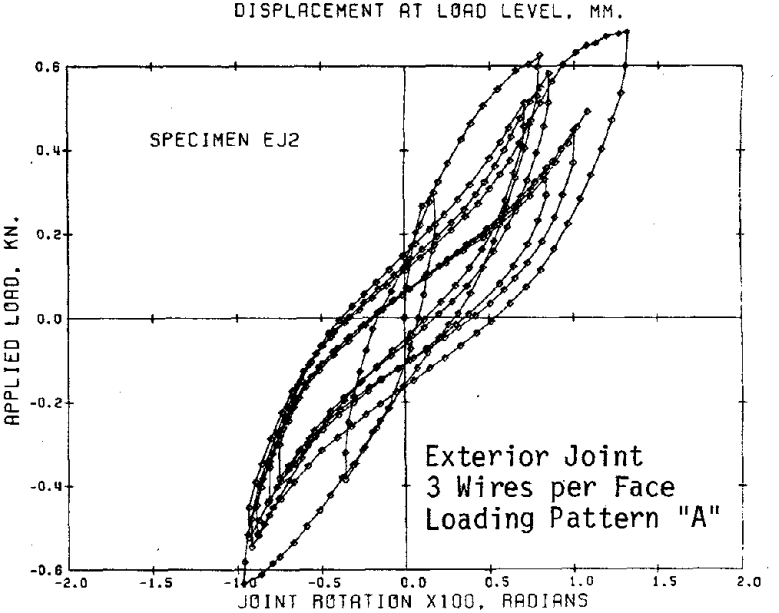


Fig. B.5 (contd.) Measured Response of Beam-Column Joint Assemblies

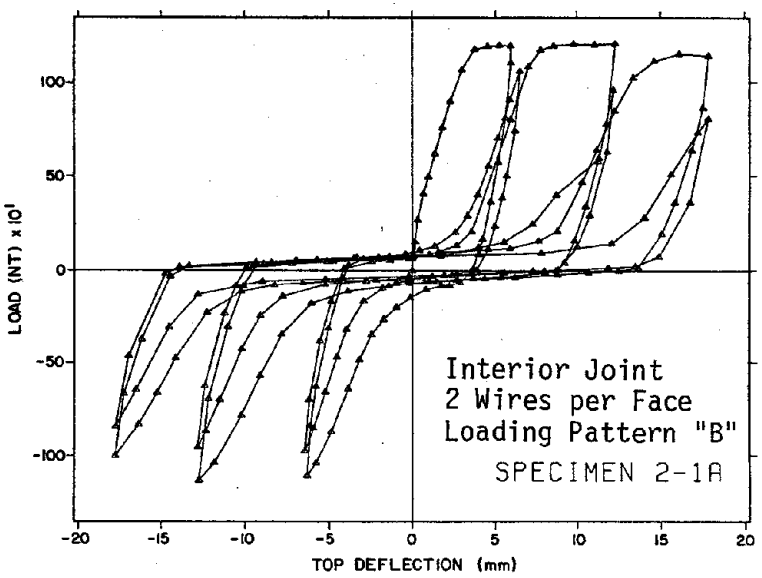


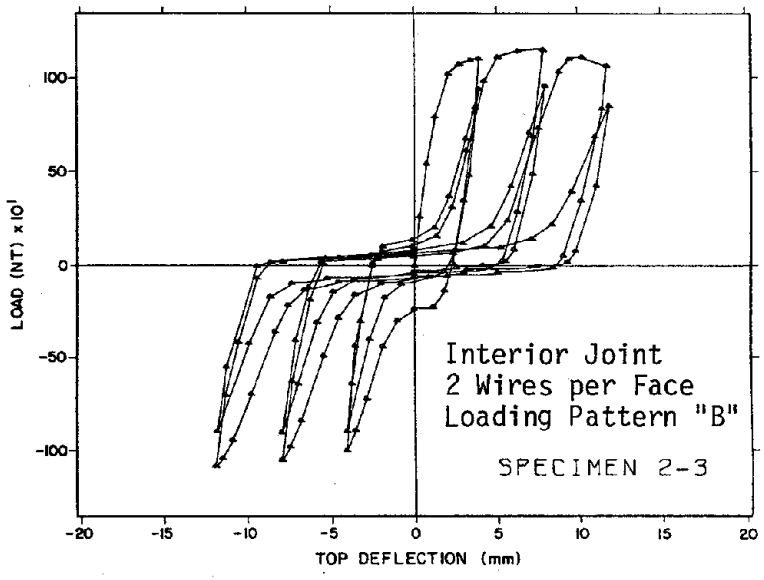


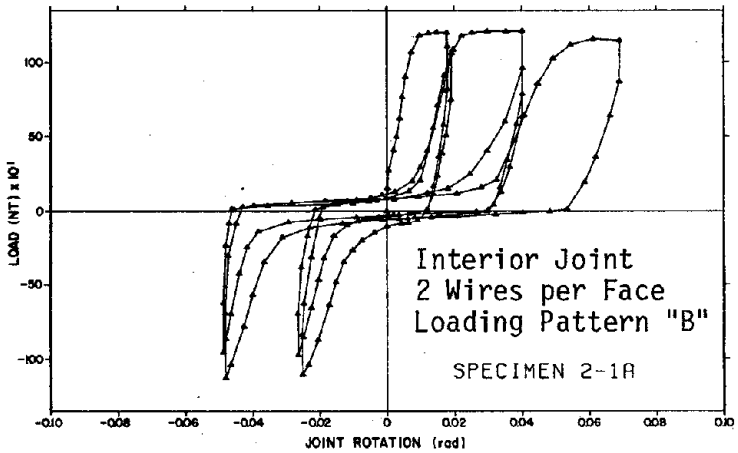


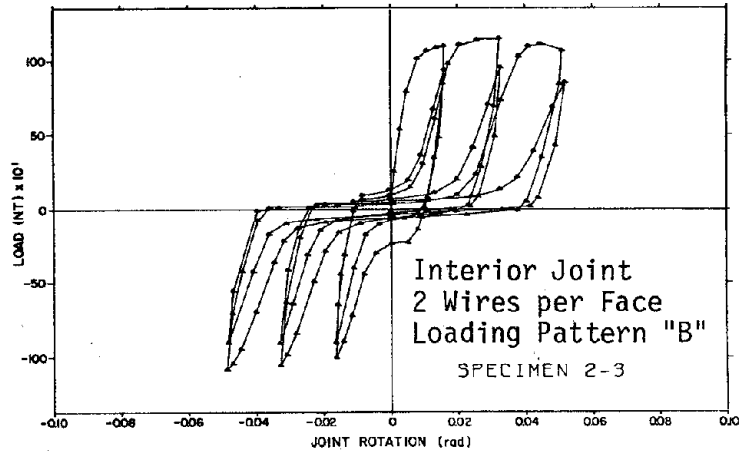


Fig. B.5 (contd.) Measured Response of Beam-Column Joint Assemblies

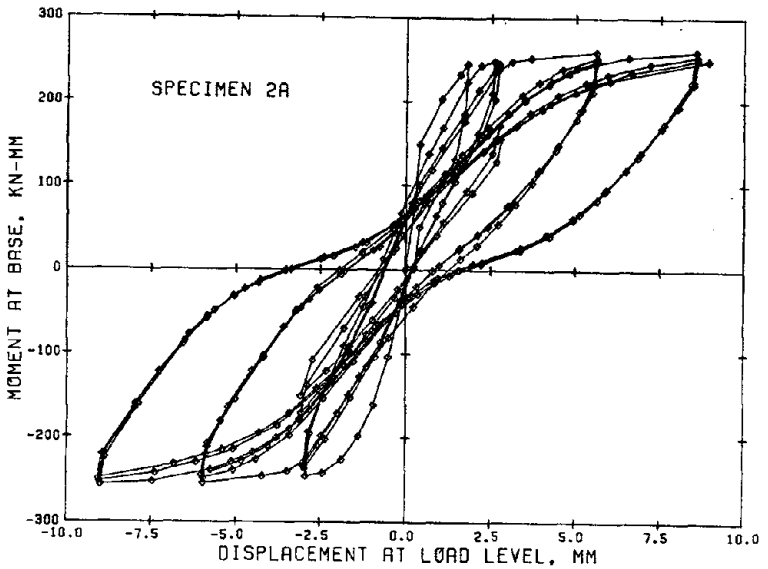


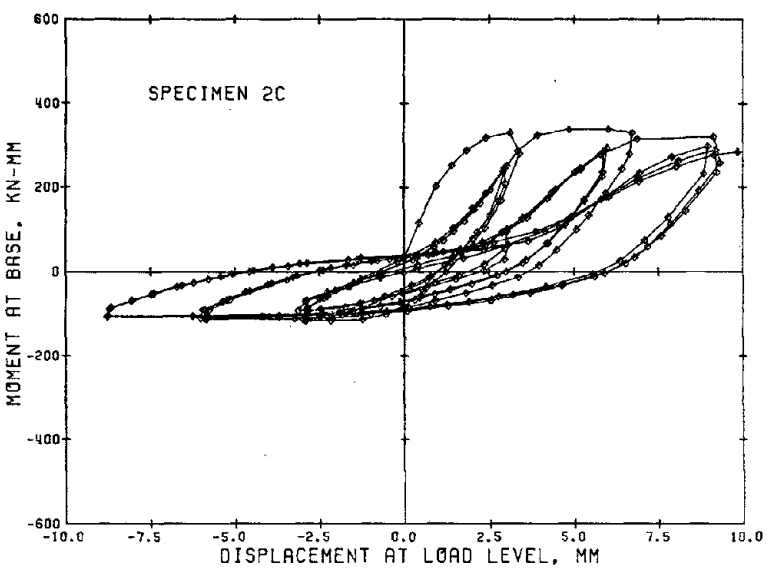


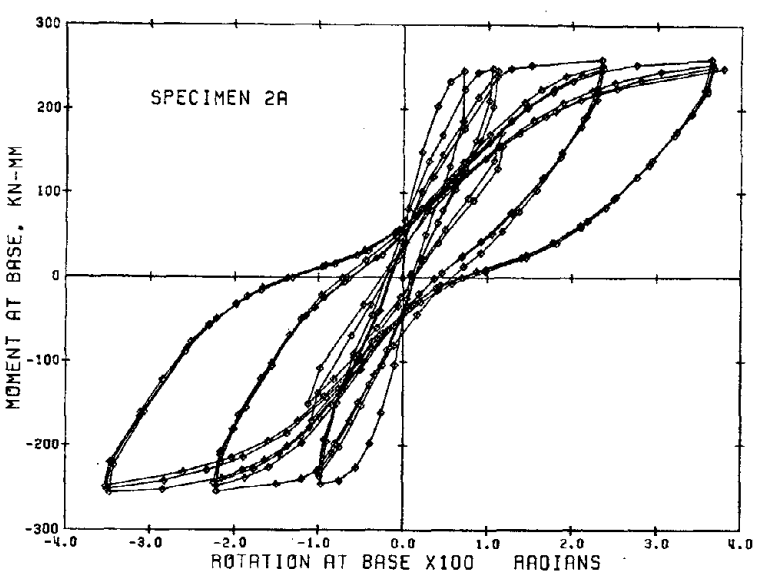


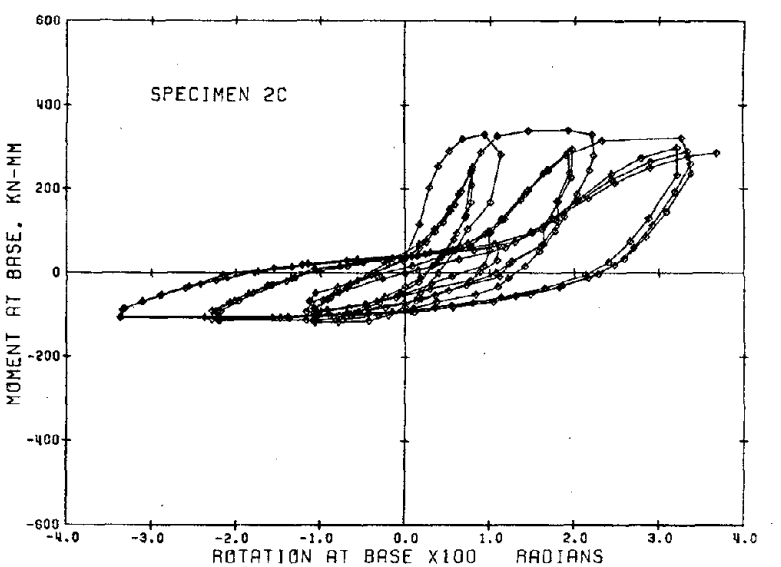


Fig. B.6 Measured Response of First-Story Columns

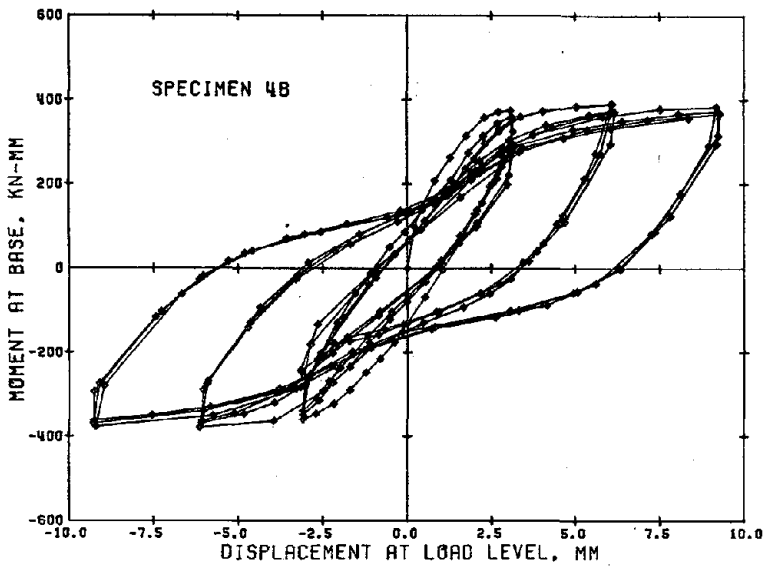


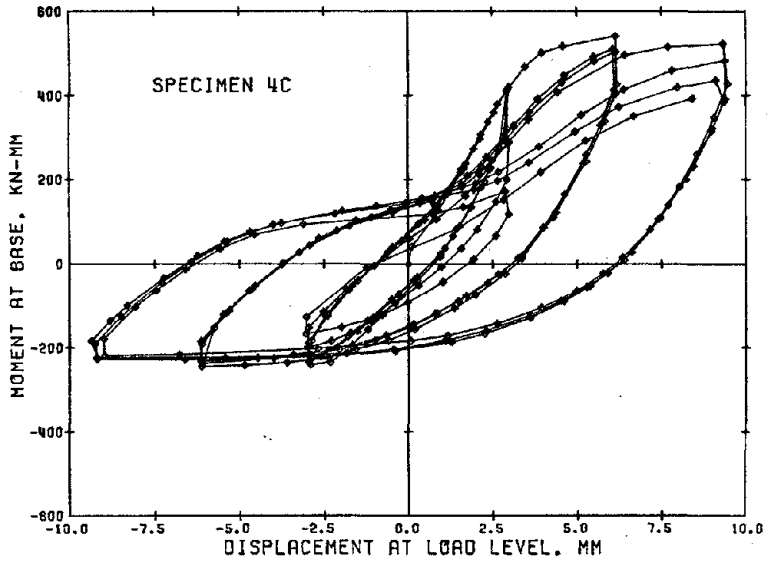


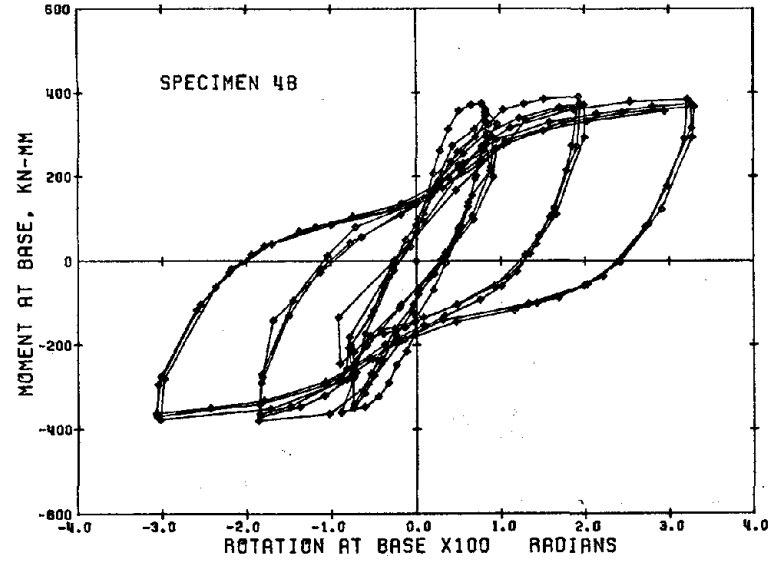


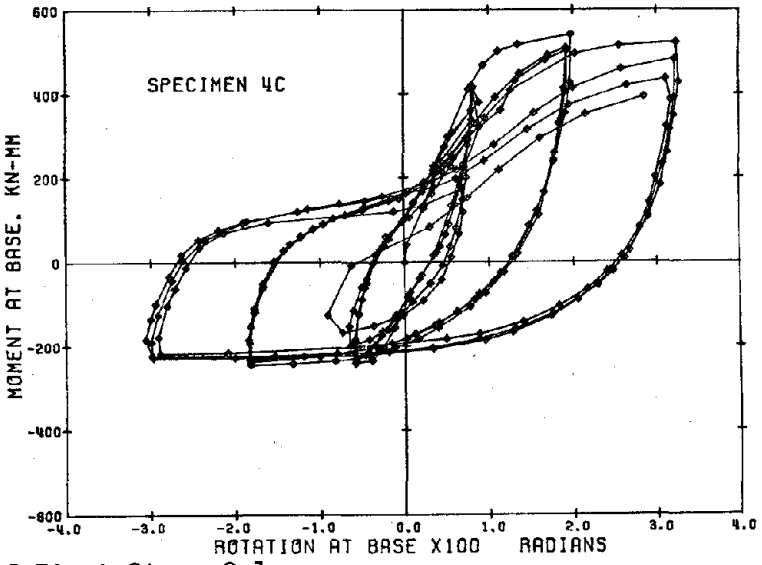


Fig. B.6 (contd.) Measured Response of First-Story Columns

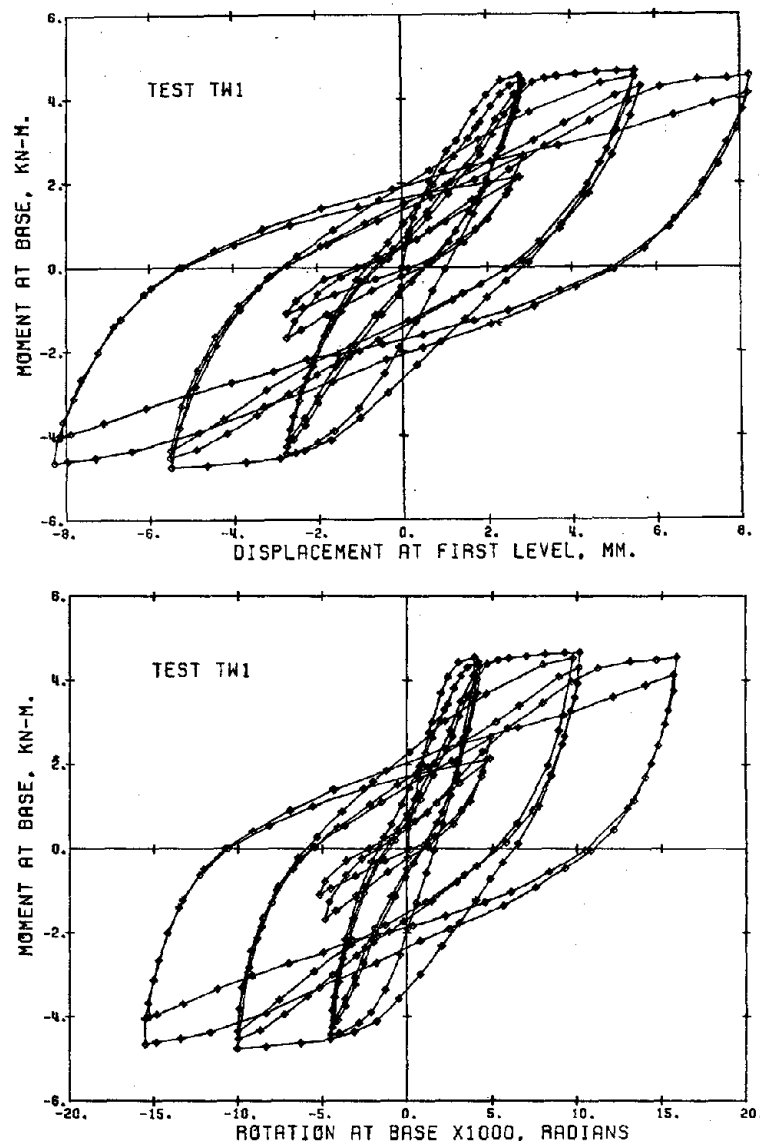


Fig. B.7 Measured Response of Walls

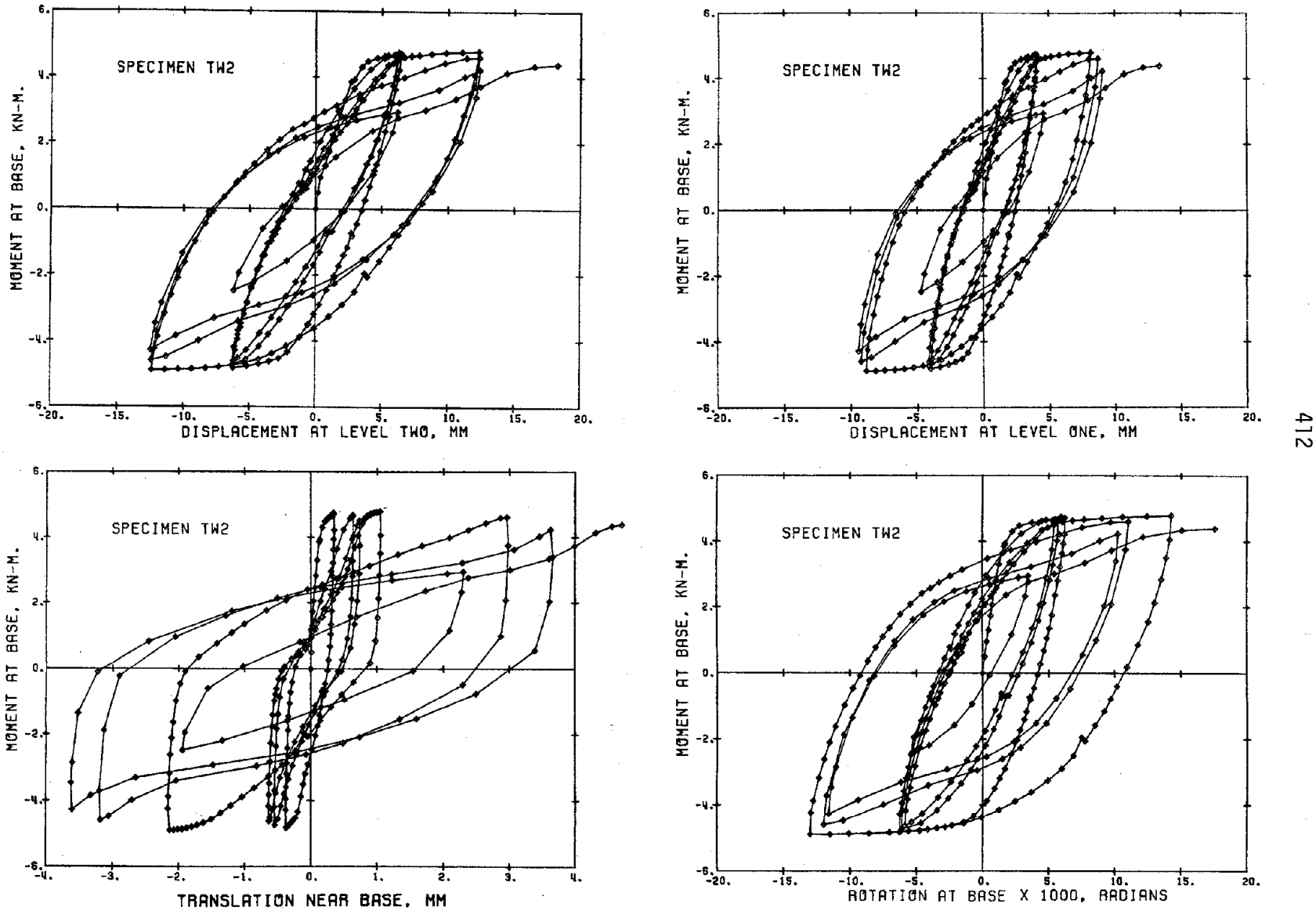


Fig. B.7 (contd.) Measured Response of Walls

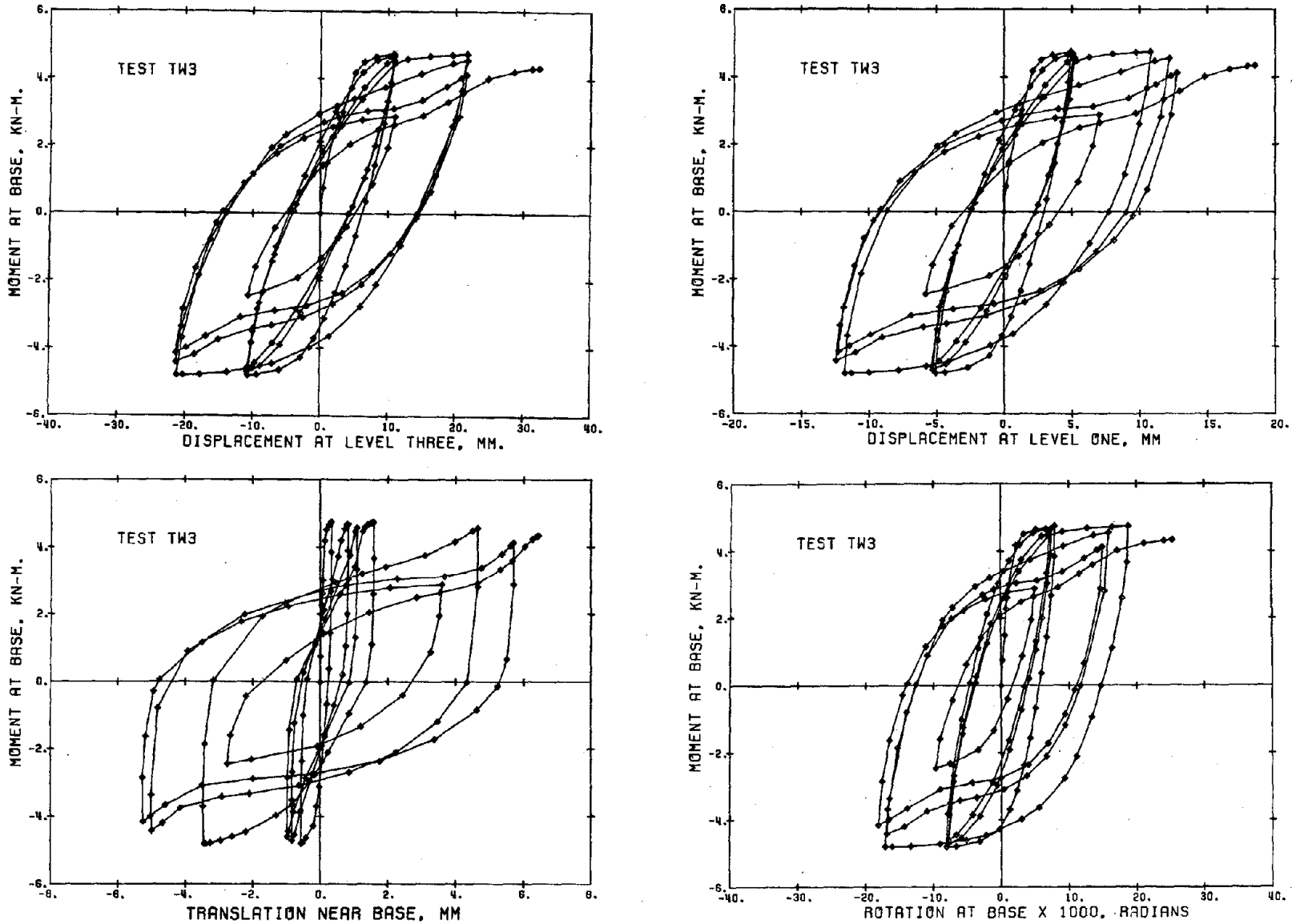


Fig. B.7 (contd.) Measured Response of Walls

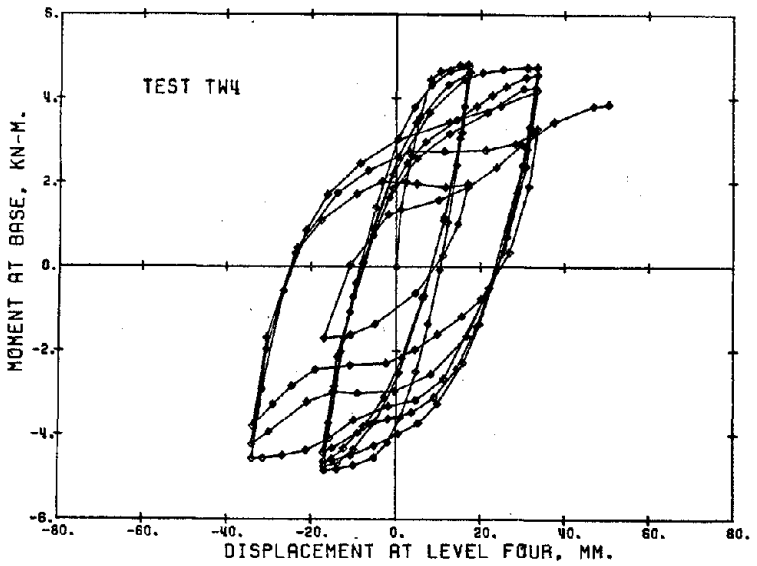


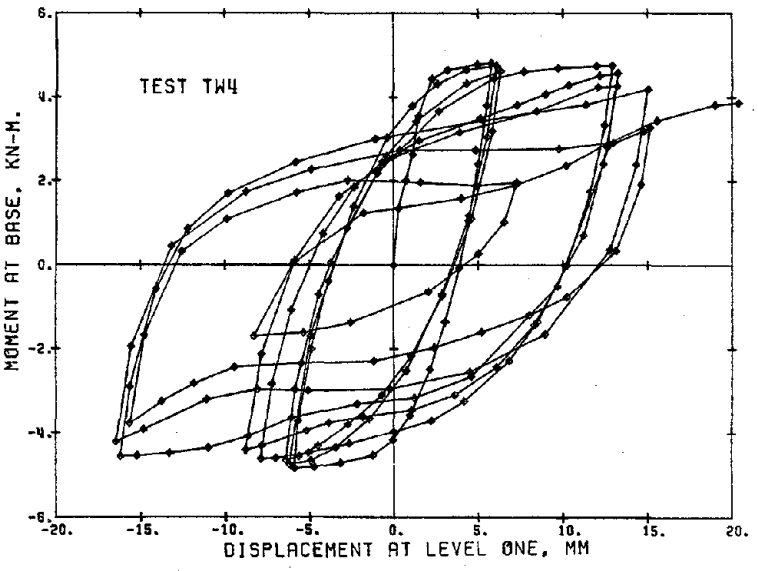


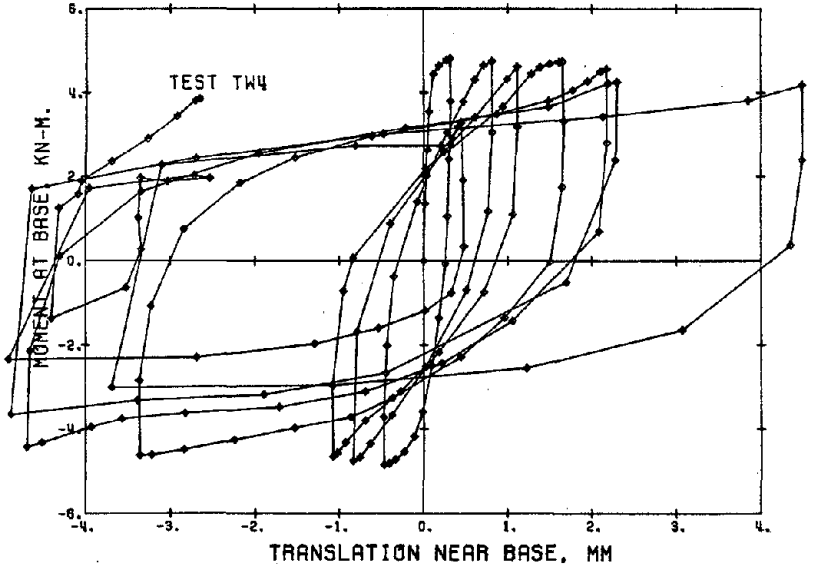


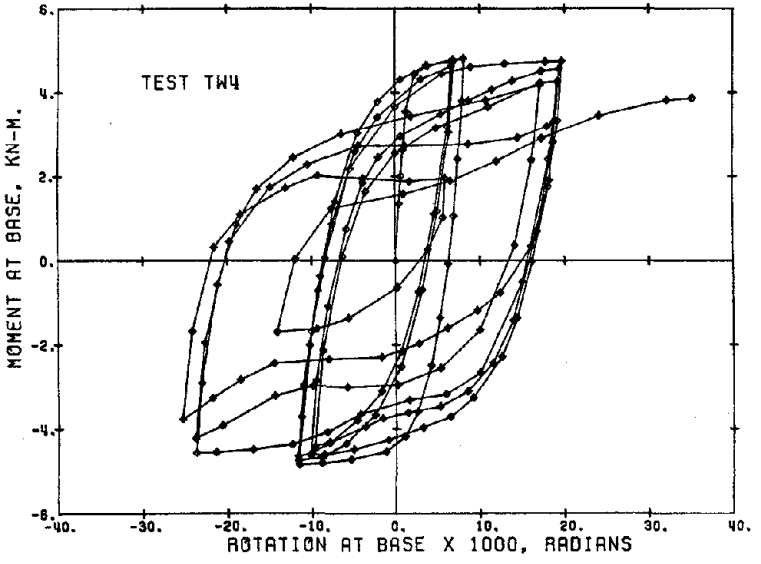


Fig. B.7 (contd.) Measured Response of Walls

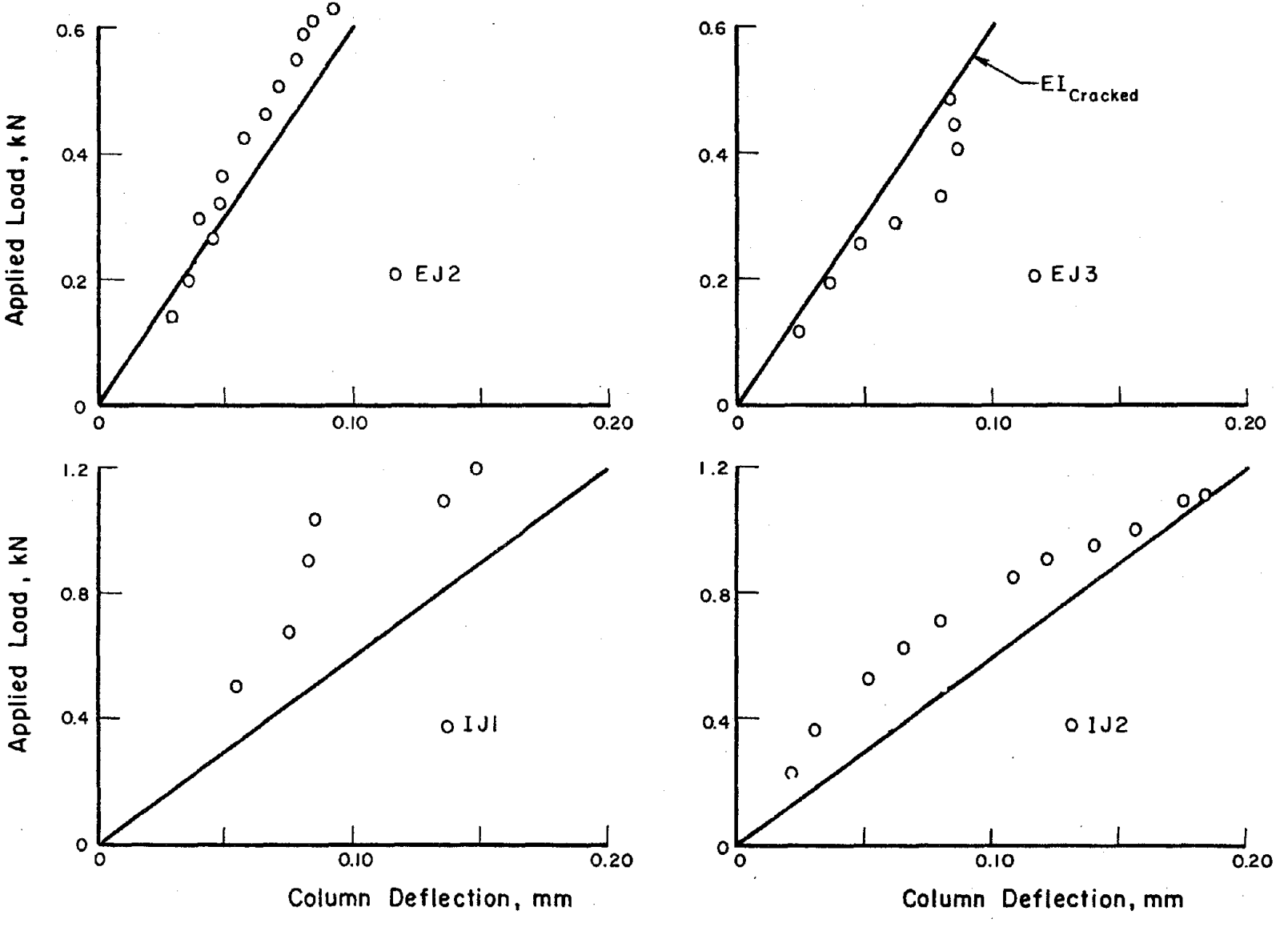


Fig. B.8 Comparison of Measured and Calculated Column Stiffness in Joint Assemblies

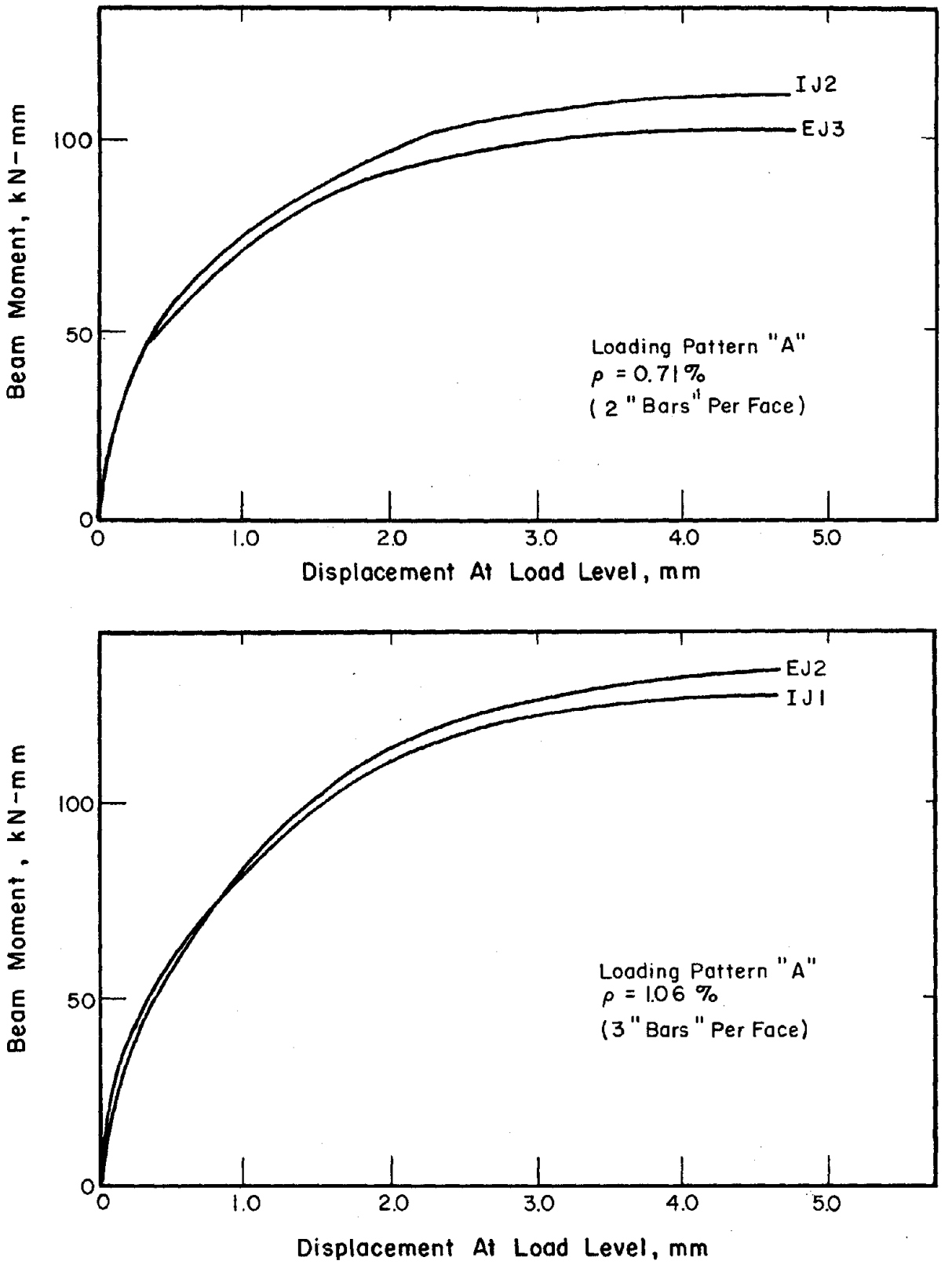


Fig. B.9 Envelopes of Measured Beam-Column Stiffnesses in Joint Assemblies for Pattern "A"

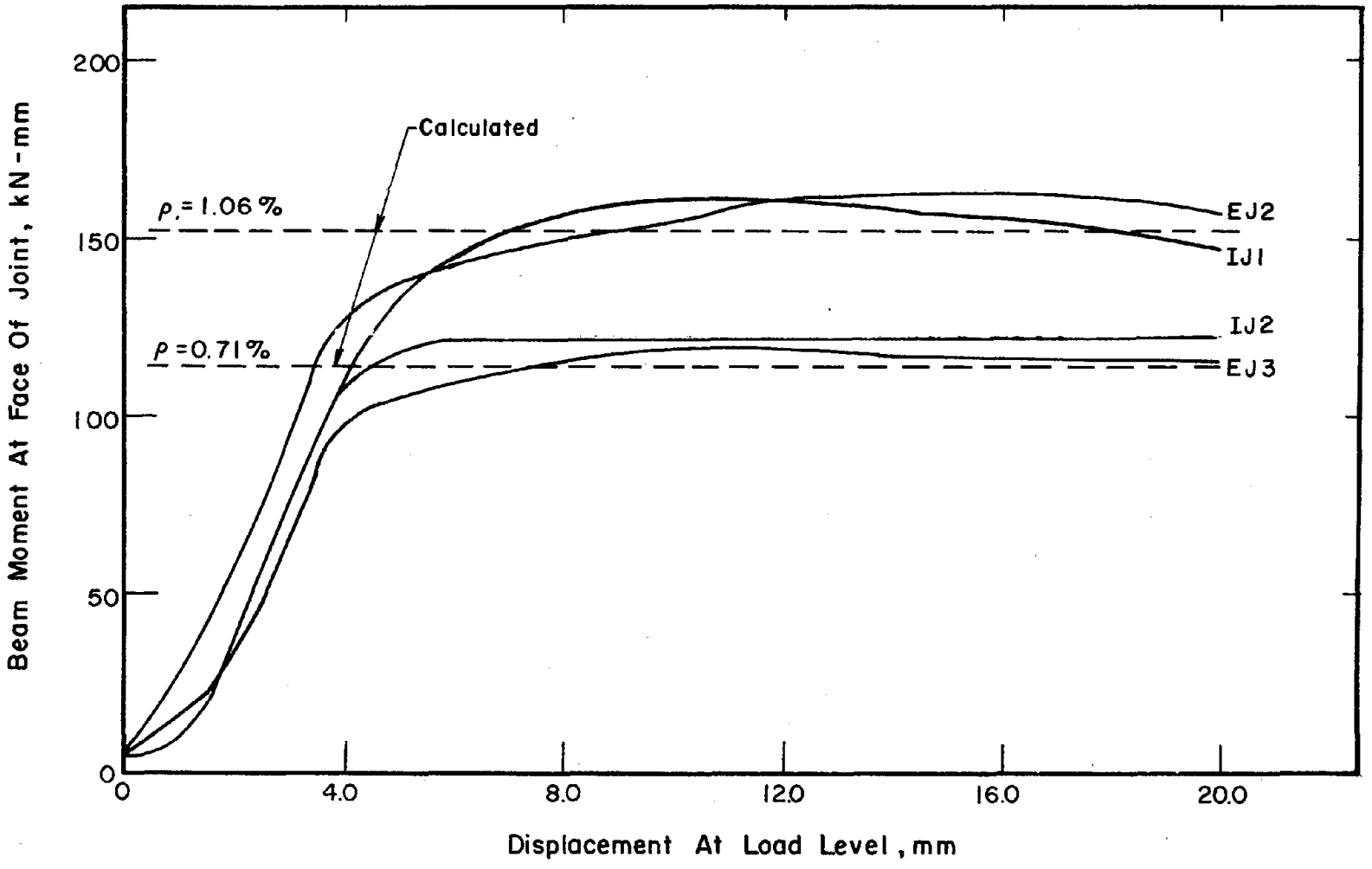


Fig. B.10 Comparison of Measured and Calculated Beam Strengths

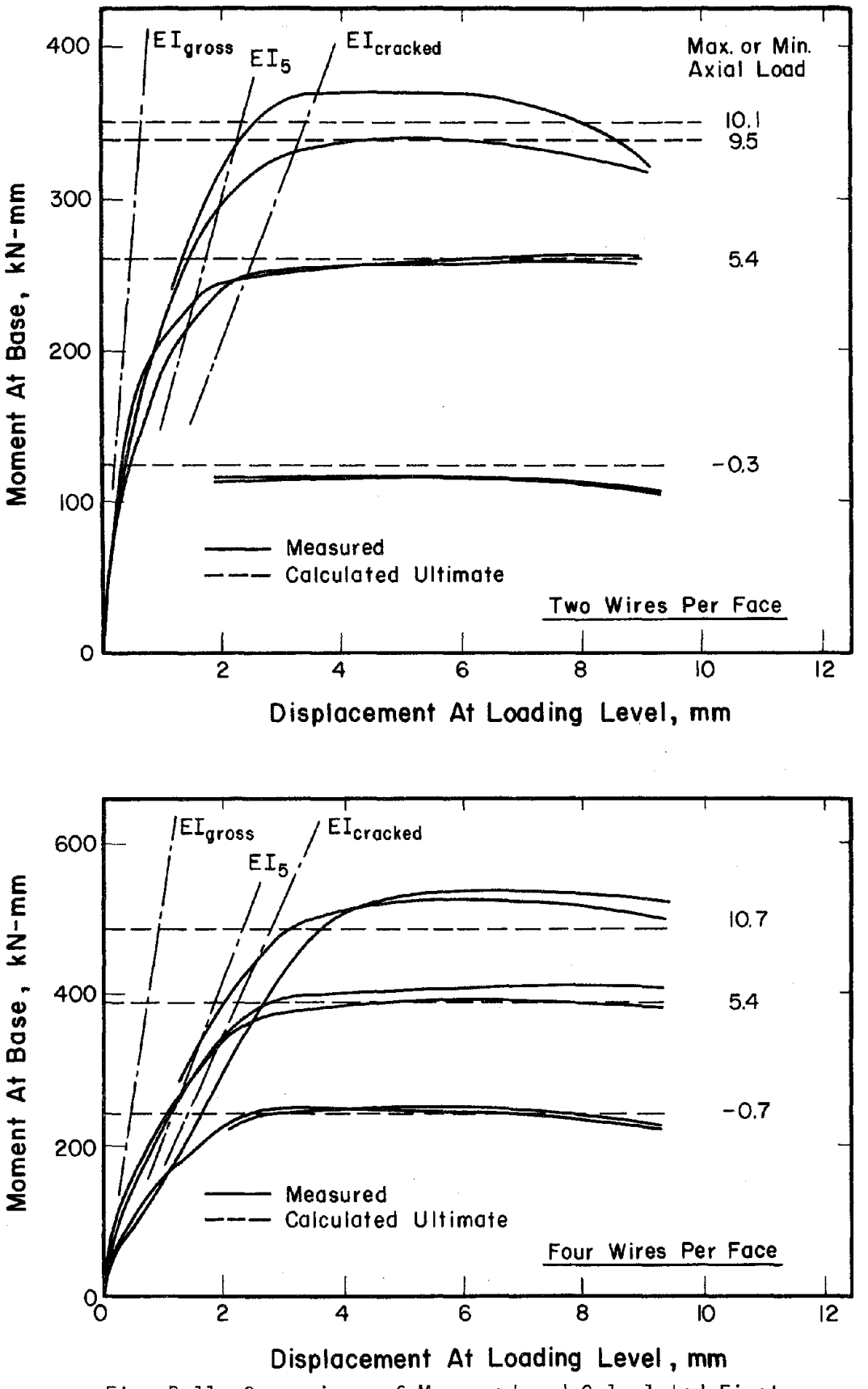


Fig. B.11 Comparison of Measured and Calculated First-Story Column Response

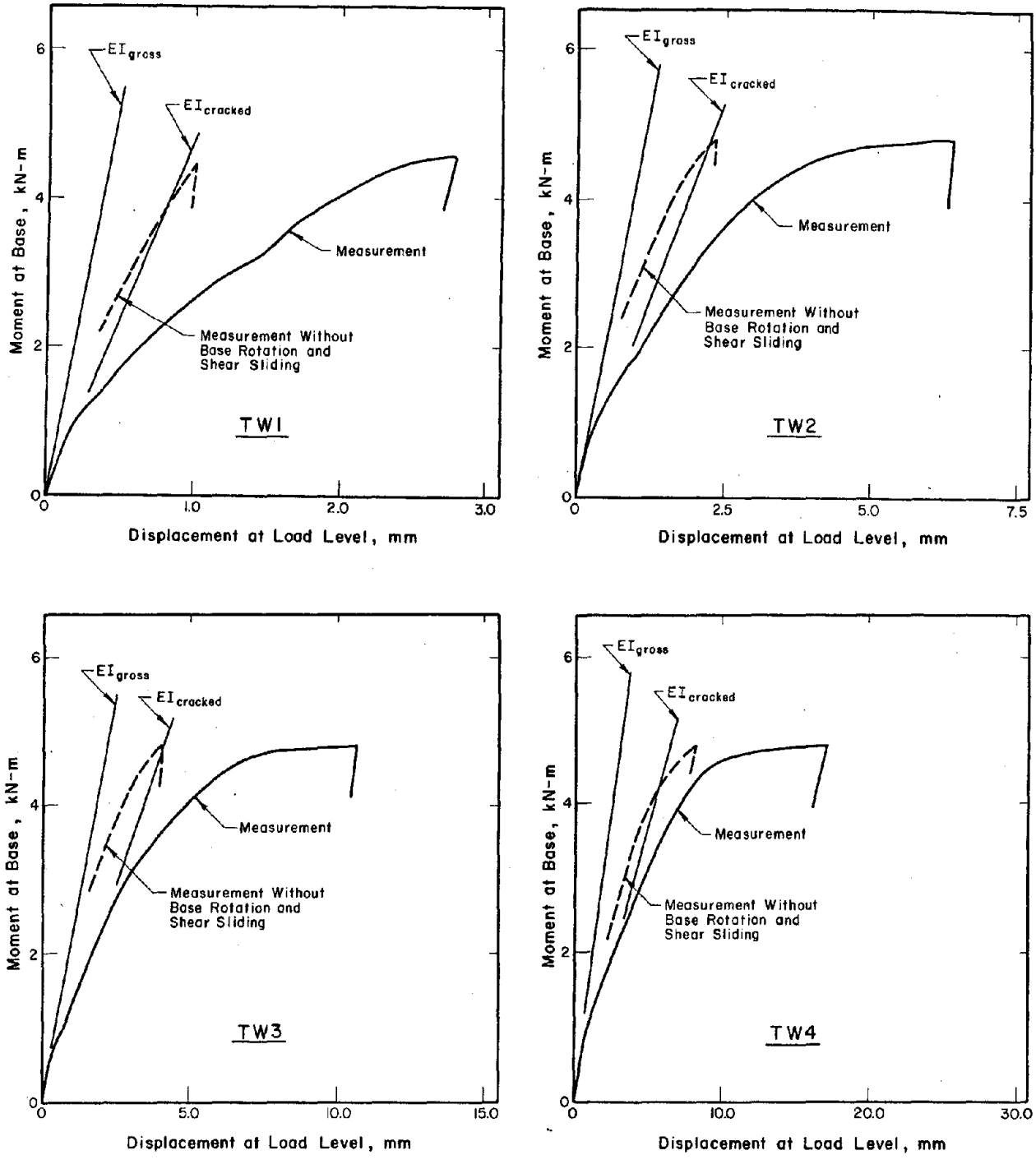


Fig. B.12 Comparison of Measured and Calculated Wall Stiffnesses

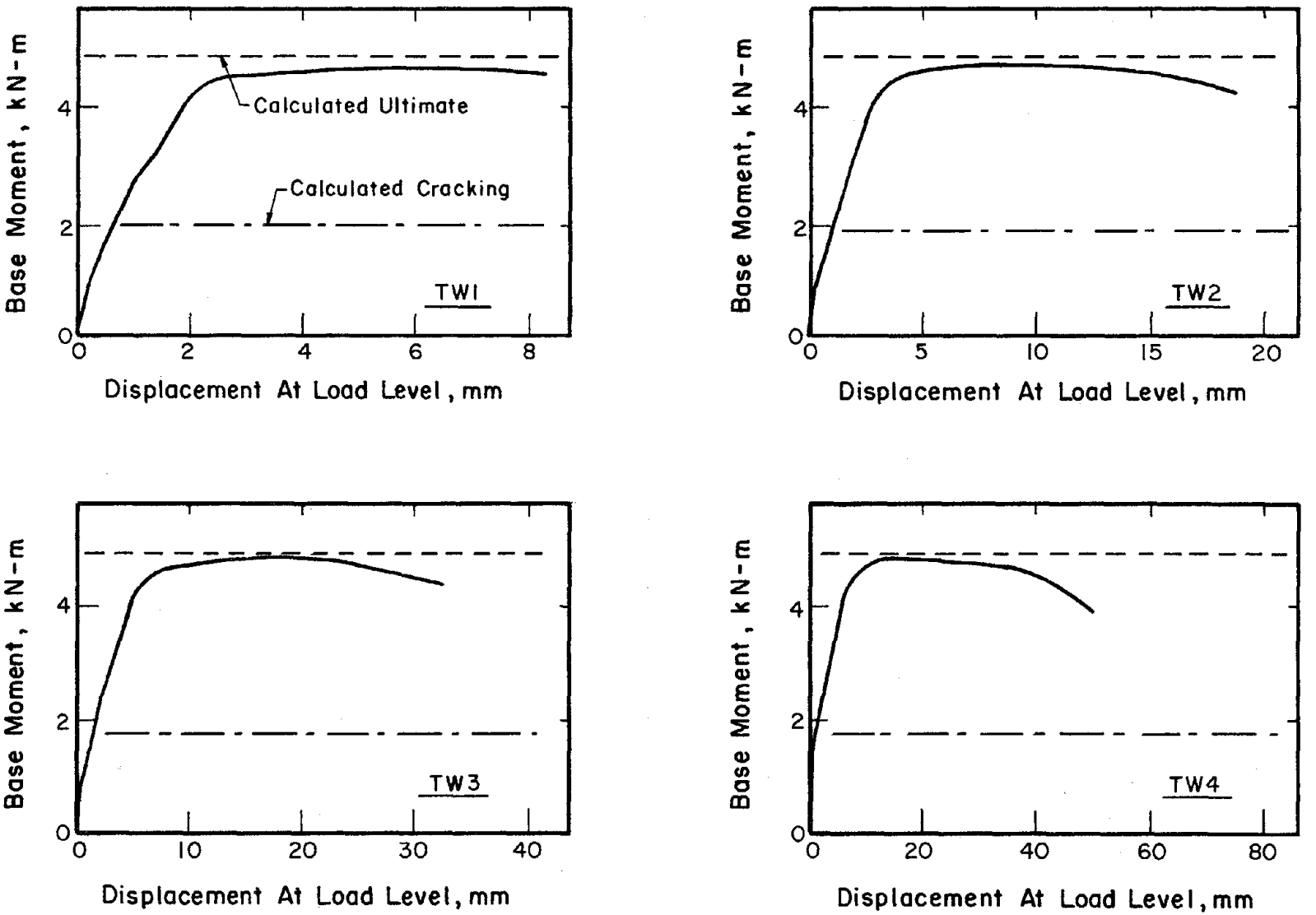


Fig. B. 13 Comparison of Measured and Calculated Wall Strengths

# APPENDIX C

## A FEW NOTES ON THE MQ-MODEL

A simple, approximate method for analyzing structures as nonlinear SDOF systems (the MQ-Model) was introduced in Sec. 7.4. The model was initially developed for an N-degree of freedom shear beam system for equal masses (m) and for stiffnesses $k_i$. For free-vibration in the first mode, the equation of motion can be written

$$m \sum_{i=1}^{N} \phi_i \ \ddot{X} + k_1 \phi_1 \ X = 0 \qquad (C.1)$$

where X is the coordinate having $\phi = 1$. Equation C.1 is not limited to shear beam systems. For example, Eq. C.1 can be used to estimate the fundamental frequency of a cantilever beam by suitable subdivision of the beam into elements.

For the MQ-Model, the right-hand side of Eq. C.1 was substituted by the product of the base acceleration and total mass resulting in Eq. C.2,

$$m \sum_{i=1}^{N} \phi_i \ \ddot{X} + k_1 \phi_1 \ X = -N \ m \ \ddot{X}_g \qquad (C.2)$$

The linear loading with lateral loads proportional to mass and height is used to define the stiffness and shape for convenience. It should be noted that, for displaced shapes which are significantly different from the linear shape, improved frequency and shape estimates can be obtained iteratively by replacing the linear load distribution with a distribution proportional to the shape obtained using the linear distribution.